Modelling and Numerical Simulation of Contact and Lubrication

DISSERTATION
zur Erlangung des Grades eines Doktors der Naturwissenschaften

vorgelegt von
M. Sc. Frank Gimbel

eingereicht bei der Naturwissenschaftlich-Technischen Fakultät
der Universität Siegen

Siegen 2012

1. Gutachter: Prof. Dr. F.-T. Suttmeier
2. Gutachter: Prof. Dr. H.-J. Reinhardt
Datum der mündlichen Prüfung: 28.11.2012

Abstract

This thesis considers the simulation of a steel forming process including the lubricant between tool and workpiece. The model equations, that describe deformation, contact and hydrodynamic flow, are derived from fundamental physical laws.

For the contact-simulation the two models of Signorini- and z-contact are introduced. The 3-dimensional Stokes problem for a thin fluid film is condensed to the 2-dimensional SubStokes model (for velocity and pressure) and further reduced to the Reynolds model, which is an equation for the pressure only. All fluid models are extended to variational inequations to consider cavitation.

Basic mathematical concepts for the numerical treatment with the finite element method and the corresponding analysis are presented.

Error estimation is done separate for the modelling error and discretisation error. An algorithm for model adaptivity is given and model error estimates are derived out of the physical models for z- and Signorini-contact aswell as SubStokes- and Reynolds-fluids.

Error estimates for the discretisation error of elliptic problems – deformation and Reynolds-flow – are presented. The SubStokes problem is stabilized to apply linear finite elements. To estimate the discretisation error of the SubStokes inequation a Lagrangian multiplier is introduced.

An algorithm for a simultanous refinement of model and grid is given.

Finally the presented methods and estimates are validated by the application to various prototype examples. The results allow to compare the different models (z- and Signorini-contact, Reynolds- and SubStokes-fluid).

Zusammenfassung

Diese Arbeit behandelt die Simulation eines Stahlformungsprozesses einschließlich des Schmieröls zwischen Werkzeug und Werkstück. Die Modellgleichungen, die Deformation, Kontakt und Hydrodynamik zugrunde liegen, werden aus physikalischen Gesetzen abgeleitet. Für die Kontakt-Simulation werden die beiden Modelle des Signorini- und z-Kontaktes vorgestellt. Das 3-dimensionale Stokes-Problem für eine dünne Schicht wird zum 2-dimensionalen SubStokes-Modell verdichtet und weiter vereinfacht zum Reynolds-Modell, das nur noch eine Gleichung für den Druck ist. Alle Fluid-Modelle werden zu Variationsungleichungen erweitert, um Kavitation abzubilden.

Mathematische Grundlagen zur numerischen Simulation mittels Finiter Elemente und die zugehörige Analyse werden bereitgestellt.

Modell- und Diskretisierungsfehler werden separat abgeschätzt. Es wird ein Algorithmus zur Modelladaptivität aufgestellt und aus den physikalischen Modellen für z- und Signorini-Kontakt sowie für SubStokes- und Reynolds-Fluide Modellfehlerschätzer hergeleitet. Fehlerschätzer für den Diskretisierungsfehler elliptischer Probleme – Deformation und Reynolds-Strömung – werden präsentiert.

Das SubStokes-Problem wird stabilisiert, um lineare Finite Elemente darauf anzuwenden. Um den Diskretisierungsfehler der SubStokes-Ungleichung abzuschätzen, wird ein Lagrange-Multiplikator eingefügt.

Ein Algorithmus zur simultanen Modell- und Gitter-Verfeinerung wird aufgestellt.

Schließlich werden die vorgestellten Methoden und Schätzer durch die Anwendung auf vielfältige Beispiele validiert. Die Ergebnisse gewähren einen Vergleich der unterschiedlichen Modelle von Kontakt und Fluid.

Contents

Introduction

This thesis is motivated by a project in the field of steel forming. In the industry there is a need for fast or even online simulation of the process of steel forming including the behaviour of the lubricant between tool and workpiece.
This demand can be split into several tasks

- To describe the real world (i. e. the technological process) computationally, firstly we need a **mathematical model** of it. For our application this means
  - a model of the deformated material (the steel sheet)
  - a contact model for the interaction of tool and steel sheet
  - a model of the lubricant between tool and work piece.
- Each of these **continuous models has to be discretised**, to handle it numerically.
- To minimize computational costs (i. e. time and computer capacity) we have to **control the error** of the model *and* of the discretisation.

This already prescribes the structure of the thesis on hand:

I Physics
We derive the models we need from fundamental physical laws.
In section I.1 we provide mechanical **preservation laws of mass and impulse**, introduce tensors of deformation, stress and elasticity and derive **Hook's law for elastic material** (I.11).
Furthermore in section I.1.4 we present two models of **two-body-contact**, that are distinguished by the use of two different projections – a projection in one fixed direction (I.20) on the one hand and the **Signorini-projection** (I.21), that allows tangential surface forces, on the other hand.

Figure 1: Projection in z-direction (left) and Signorini projection (right).

Finally in section I.2 we scatch the theory of hydrodynamics, starting in section I.2.1 with the derivation of the **Stokes model** for three dimensional fluids (I.29). In section I.2.3 this model is simplified for **thin fluid films** to the two dimensional **SubStokes model** (I.57). Therefor we replace the three dimensional velocity and pressure fields v and p by two dimensional ones χ and ψ ((I.44) and (I.45)).
Because in our field of application the unit of interest is the pressure, in a further simplification in section I.2.4 we even omit the calculation of the velocity field and state the **Reynolds model** for thin fluid films (I.77).

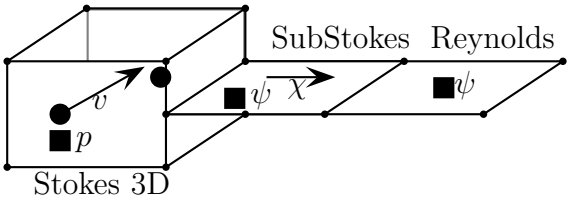

Figure 2: Velocity- and pressure-fields of the different fluid models.

In regions of low pressure, the lubricant might vaporize and thus violate the law of mass conservation – this phenomenon is called **cavitation**.
Therefor we finally derive formulations of all three models, which consider cavitation, what leads to the variational inequations (I.38) (Stokes model for cavitation), (I.66) (SubStokes model for cavitation) and (I.81) (Reynolds model for cavitation).

II Mathematics

Firstly in section II.1 we provide some basic definitions and theorems about **functional analysis**. Especially we define Hölder- and Sobolev-spaces, needed for the weak formulation of the differential equations in section I, which is the basis for the finite element discretisation below.
For the handling of the different saddle point problems, that arise in the field of fluid dynamics, in section II.1.1 we examine saddle point problems from an abstract point of view.
In section II.1.4 we modify the scalar product $\langle \cdot, \cdot \rangle_{H^1}$ under consideration of the width of the fluid film and introduce the **Reynolds scalar product** $\langle \cdot, \cdot \rangle_R$ to cope with this concrete physical situation.
At next section II.3 gives a brief introduction into the **Finite Element Method**. Sections II.3.1 and II.3.2 introduce the appropriate finite elements for the different problems of section I. Because both – the deformation problem and the Reynolds problem – are elliptic, section II.3.1 considers these two problems and gives the discretisation with (bi-) linear elements Q^1. Section II.3.2 considers the Stokes (saddle point-) problem, that is eventually stabilised to gain an elliptic problem too. In section II.3.2.1 the Q_1-element even is applied to this **stabilised Stokes problem**.

III Error Estimates

Firstly the total error between the physical model of the real world and the numerical solution of an (even coarser) mathematical model is split into **modelling and discretisation error** (III.3).
In III.1 we shortly describe the general handling of different models for a physical phenomenon. Therefor we introduce algorithm III.1 for **model adaptivity** and its variants for different refinement strategies – firstly the refinement on a fixed fraction of the coarse cells (analogue to the grid refinement) and secondly a sorted error strategy, that ensures that the model error on each cell in the coarse model's region is lower than on any cell in the accurate model's region. In sections III.1.1 and III.1.2 the model error estimators for the different contact– and fluid–models respective are derived and applied to the variants of algorithm III.1.
At next in section III.2 we present error estimates for the **discretisation error**, i. e. the difference between the mathematical model and the numerical solution.
We consider each class of problem separate. In section III.2.1.1 we develop a-priori-estimates for the discretization error of elliptic variational equations (III.31) and inequations (III.33). These estimates (corollary III.8 and theorem III.10) imply the convergence of the used FE-methods and furthermore they are of optimal order (with respect to the maximal cell-diameter h of the triangulation), i. e. of the same order as the interpolation error in the corresponding finite-dimensional spaces.
In sections III.2.1.2 – III.2.1.5 the estimates of section III.2.1.1 are applied to the problems of deformation, contact and the Reynolds-fluid with and without cavitation.
Section III.2.2.1 gives a brief overview over error estimates for non stabilised saddle point problems. The discrete spaces have to fulfill the inf-sup-condition (II.3) to guarantee stability. The Taylor-Hood-Element, a stable element for the Stokes problem, is introduced. Because in all our applications we only consider stabilised saddle point problems, this section is rather short and there are not given further estimates.
In section III.2.3.1 we describe the **stabilization of a saddle point problem**, replace the inf-sup-condition by the **generalised inf-sup-condition** (III.70) and give error estimates for the stabilisation error (theorem III.20) on the one hand and for the total error of the stabilized problem (corollary III.21) on the other hand.
In section III.2.3.2 we quote an a-posteriori estimate for the stabilised SubStokes problem (theorem III.23).
In section III.2.3.3 we derive an a-posteriori error estimate for the SubStokes problem with cavitation (I.66), introducing an additional Lagrangian parameter.

Finally in section III.3 we briefly discuss, how to refine both, the **model and the numerical approximation in a balanced way**. Additional in section III.3 we present the algorithms, that are used to produce the numerical results of section IV.

IV Applications

In the last part of this work we present some numerical results of the introduced models, error-estimates and solvers. All calculations are obtained with the use of the `deal.II`-library (Bangerth et al. [2007]).

The most basical applications are presented in section IV.1, where we apply our model for **linear elasticity** (I.17) to a box-shaped domain (IV.1) for different cases of external force fields to test the error estimators for these examples.
For all examples, we see that the error estimate of theorem III.12 decreases with the expected order of $O(n_{dofs}^{-1/2})$ that corresponds the reduction of the estimate by the factor $1/\sqrt{2}$. Also the output of the adaptively refined grids shows a refinement in zones of high stresses and rather coarse cells in regions of low stresses.

In the next section IV.2 we consider the **contact problem**. We apply the different contact algorithms to several physical examples.
Section IV.2.1 contains the results of a grid-adaptive algorithm, using the a-posteriori-error of theorem III.15 to the contact problem (I.23) with the simple **projection in only one direction**.
The computations, presented in sections IV.2.1.1 – IV.2.1.6, confirm, that the error estimate in theorem III.15 is of optimal order, because all convergence tables basically show the decrease of the estimate with the order of $O(n_{dofs}^{1/2})$ as we expect for the energy-norm under adaptive refinement.
In the cases of the jump-like obstacles (sections IV.2.1.4 and IV.2.1.5) the grid has to be refined around the jump regions before the error estimate decreases with the expired speed. This can be seen in the corresponding tables IV.9 and IV.10. These critical regions are localised correctly by our estimate too.
Furthermore the plotted grid series (e. g. figure IV.19 and IV.21) illustrate the geometrical correct refinement near the contact zones especially at the rather rough parts of the obstacles. On the other hand the grids stay coarse in regions of a plain obstacle.

At next in section IV.2.2 the results of the grid-adaptive algorithm for the contact problem with the more accurate **Signorini projection** are presented.
The calculations for Signorini contact presented in sections IV.2.2.1 – IV.2.2.6 supply sufficiant results too. The zones of high stress and rough obstacles are detected correctly (compare e. g. figures IV.31 and IV.33).
Furthermore we see the advantage of the Signorini solver regarding rough obstacles and rather high deformations. Especially a comparison of the result of the z-solver and the one of the Signorini solver (figure 3) for the two-obstacle-problem illustrates, that the Signorini solver does not hurt the contact condition, while the z-projection results in an obstacle penetration. This advantage is balanced out against the higher speed of the z-solver in section IV.2.3.

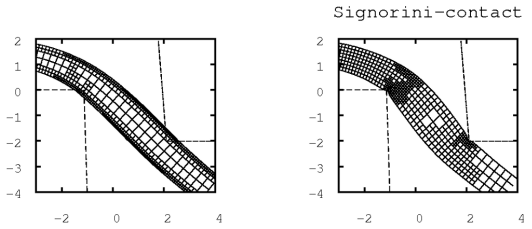

Figure 3: Comparison of z-contact and Signorini-contact

In the third part IV.2.3 the **model adaptive schemes**, based on algorithm III.1, are applied to each of the examples considered in the previous sections IV.2.1 and IV.2.2.
In the application of the different model refinement schemes – namely algorithm III.2 for the fixed fraction strategy and algorithm III.3 for the sorted error strategy – to our model examples (sections IV.2.3.1 – IV.2.3.6) we see that the modelling error estimate (III.16) decreases for both strategies. Furthermore we see the supremacy of the sorted error strategy over the fixed fraction strategy. For example in section IV.2.3.3 the comparison of the number of faces on which we have to use the more expensive Signorini-model to the modelling error results in the following table:

fixed fraction		sorted error	
# S-faces	model-error	# S-faces	model-error
0	6.8e-02	0	6.8e-02
10	4.7e-02	12	4.3e-02
20	3.0e-02	22	2.6e-02
29	9.1e-02	32	3.1e-02

We see, that the modelling error can be reduced without an remarkable increase of the number of accurate faces. In general we can say that after the same number of refinement cycles the error estimate for the sorted error algorithm III.3 is lower than that of the fixed-fraction algorithm III.2 and demands for the more expensive model on a lower number of faces.

Finally in the fourth part IV.2.4 we apply the **model- and grid-adaptive algorithm** III.25 to each of the previous examples, to refine both, the contact model and the grid, in a balanced way.
A comparison of the results of the model- and grid-adaptive solver with the model-refinement-solver (MA-solver), affirms, that the critical points for the contact are detected correctly (compare figure 4).

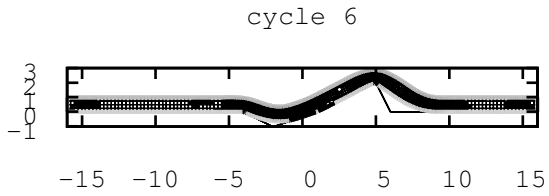

Figure 4: Simultanuous model- and grid-refinement. The zone of Signorini contact is colored black, that of z-contact gray.

If we compare the results of the MGA-solver with the ones of the Signorini-solver (given in section IV.2.2) we see, that the grid is refined in the same regions of high stress or rough obstacle respective as before.
Furthermore we see, that the balanced refinement strategy of algorithm III.25 lets the error contributions of modelling error and discretisation error converge to the same order from initially different orders. For example in table IV.35 the estimates start at $\|e_m\| = O(0.1)$ and $\|e_d\| = O(1.0)$ and reach $\|e_m\|, \|e_d\| = O(0.01)$.

In section IV.3 we present numerical results for the Reynolds– and SubStokes–model with and without cavitation considering some prototype examples on the unit square ((IV.7)–(IV.20), figure IV.55).
Firstly in section IV.3.1 and IV.3.2 we solve the **Reynolds equation** (I.77) and the **SubStokes equations** (I.58) for all examples.

The results, given in sections IV.3.1.1–IV.3.1.14, show a decrease of the error estimate, given in theorem III.16, of the expected order $O(n_{dofs}^{1/2})$. For the more sophisticated gap-shapes, the wave– and hill–gaps (sections IV.3.1.9–IV.3.1.14), one sees that the grid refinement, controlled by the estimate of theorem III.16, takes place around the most wide and most narrow parts of the gap, if the surface's velocity is just in vertical direction (figures IV.72, IV.74, IV.78 and IV.80). For the horizontal velocity (section IV.3.1.11 and IV.3.1.14) we see, that the grid refinment is concentrated on the narrow regions for the wave-shaped gap (see figure IV.76). In the case of more complicated gap geometries refinement also depends on the normal vector of the surface.
All calculations for the non-cavitational SubStokes model in sections IV.3.2.1–IV.3.2.14 show a decrease of the error estimate, given in theorem III.23, of the expected order $O(n_{dofs}^{1/2})$ too. In general the grid-refinement is not as strongly localised as it was for the Reynolds-calculations. In contrast to those refinement here is concentrated around the maxima of the gap width.
The comparison of the SubStokes- and the Reynolds-model in sections IV.3.3 and IV.3.7 reveals, that the Reynolds model supplies rather sufficiant results for mainly vertical velocities of the gap's surface (compare figure 5). If the horizontal component in direction

of the surface's gradient is the dominating part of the velocity the Reynolds-model can only be used as a rough guess for the SubStokes-model.

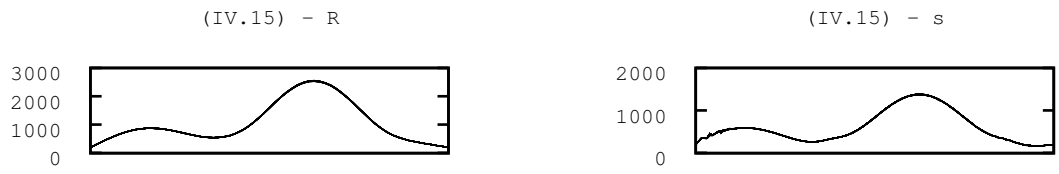

Figure 5: Comparison of Reynolds- and SubStokes pressure ψ for a wave shaped gap and vertical velocity.

Additionaly in section IV.3.4 we present one short example regarding model adaptivity for fluids.

In the last two sections IV.3.5 and IV.3.6 we examine **cavitation models** for those examples, where the pressure in sections IV.3.1 and IV.3.2 took negative values, what indicates the occurance of cavitation. The calculations regarding the Reynolds model for cavitation (sections IV.3.5.1–IV.3.5.6) show a decrease of the error estimate, given in theorem III.17, of the expected order $O(n_{dofs}^{1/2})$. For most of the more sophisticated gap-shapes, the wave– and hill–gaps (sections IV.3.5.3–IV.3.5.5), one sees that the grid refinement takes place around the most narrow parts of the gap (figures IV.123, IV.125, IV.127). A comparison to the results of section IV.3.1 shows, that the regions of cavitation are detected correctly.
All calculations of the SubStokes model for cavitation (sections IV.3.6.1–IV.3.6.6) show the expected decrease of the error estimate, given in theorem III.24. The most visible effect regarding the grid-refinement is, that in regions of cavitation (where ψ is constant) the grid is rather coarse (compare e. g. figure IV.136) in contrast to the refined grids in section IV.3.5. The most refined regions are those where the variation of ψ is rather high. A comparison to the results of section IV.3.2 shows, that the regions of cavitation are detected correctly.

I

Physics

I.1 Mechanics

In this section we introduce the fundamentel laws of continuum mechanics by following and extending Brandt and Dahmen [1996], Fließbach [2003] and especially Stephani and Kluge [1995]. We start with preservation laws of mass and impulse (sections I.1.1, I.1.2), we introduce the tensors of deformation ε_{ij} (I.5), stress σ_{ij} (I.3) and the modules of elasticity C_{ijkl} (I.6). Finally we follow Stephani and Kluge [1995] to derive Hook's law for an isotropic elastic material (I.11). The last part of this section I.1.4 describes two models of two-body-contact, that are distinguished by the use of two different projections – the Signorini-projection (I.21) on the one hand and a projection in one fixed direction (I.20) on the other hand.

I.1.1 Mass bilance

The mass in a given volume V at the time t is given by the **density**

$$\rho : V \times \mathbb{R} \to \mathbb{R}$$

through the integral

$$M(t) = \int_V \rho(x,t)dx.$$

The derivation with respect to the time t of this equation yields

$$\frac{dM}{dt} = \frac{d}{dt}\int_V \rho(x,t)dx = \int_V \partial_t \rho(x,t)dx. \tag{I.1}$$

The second equation is true for time-independend volumes V.
This change of mass dM/dt has to be equal to the mass that enters the volume through its boundary:

$$\frac{dM}{dt} = -\int_{\partial V} \rho v_i n_i d\sigma = -\int_V \text{div } (\rho v)dx. \tag{I.2}$$

For the transformation of the surface integral into a volume integral we used Gauß's theorem II.29.
Equations (I.1) and (I.2) lead to the equation

$$\int_V (\partial_t \rho + \text{div } (\rho v)) dx = 0,$$

which has to be valid for arbitrary volumes V. This forces the integrand to vanish and we achieved the continuity equation

$$\dot{\rho} + \text{div } (\rho v) = \partial_t \rho + \partial_j (\rho v_j) = 0.$$

Here we used Einstein's notation of sums, that also is used in Fließbach [2003] and Stephani and Kluge [1995]:

$$a_i b_i := \sum_{i=1}^{3} a_i b_i$$

as well as the abbreviation

$$\dot{f}(t,x) := \partial_t f(t,x).$$

I.1.2 Impulse bilance

Newton introduced the impulse of a mass point $p = mv$. For a continuous mass distribution one should extend this to an **impulse density** ρv. Furthermore he introduced the field of **accelleration** f, that applies the force

$$F = m \cdot f$$

on a given mass m.
One example is the gravity field on the surface of the earth $f_g = 9.81 ms^{-2}$.
On the surface A with the outer normal n_i of a given volume there act face-forces $(F_A)_i = A \cdot t_i$, that can be written as a **vector of tension**, depending on the outer normal of the surface n in a linear way:

$$t_i(n) = \sigma_{ij} n_j. \tag{I.3}$$

This linear mapping is defined by the **stress tensor** σ_{ij}.
Newtons second law applied to the mass in an arbitrary volume V is

$$\int_V \rho \frac{dv_i}{dt} dx = \int_{\partial V} t_i da + \int_V \rho f_i dx.$$

Introduction of the stress tensor σ_{ij} and application of Gauß's theorem II.29 yields:

$$\int_V \rho \frac{dv_i}{dt} dx = \int_{\partial V} \sigma_{ij} n_j da + \int_V \rho f_i dx$$

$$\Rightarrow \qquad 0 = \int_V \left(\rho \frac{dv_i}{dt} - \partial_j \sigma_{ij} - \rho f_i \right) dx$$

$$\Rightarrow \qquad 0 = \rho \frac{dv_i}{dt} - \partial_j \sigma_{ij} - \rho f_i.$$

I.1.3 Basic Solid Body Mechanics

In this section we examine small deformations of a solid body. Therefore we introduce the tensor of deformation ε_{ik} (I.5) and the moduli of elasticity C_{ijkl} to formulate Hook's law (I.6). We learn, that in the case of an isotropic elastic material C_{ijkl} can be described by the two Lamé moduli μ and λ (I.11). Finally formulate the energy functional of an elastic body (I.15), that has to be minimized in mechanical equilibrium (I.17).

I.1.3.1 Displacement and Deformation

In an relaxed (i. e. force free) solid body the single mass elements (e. g. atoms, molecules or ions in a crystal latice) are at the position x. If any forces are acting on the body the mass elements move to the position $x' = x + s$. The vector s_i is called **displacement**. For every position x there is a given $s(x)$, so the displacement is a function in space. The field of displacement $s(x)$ describes the complete condition of the deformed elastic body. The total differential dx' can be written as

$$dx'_i = dx_i + \partial_l s_i dx_l = (\delta_{il} + \partial_l s_i)\, dx_l. \tag{I.4}$$

The **distortion** tensor $\partial_l s_i$ can be split into its symmetric and antisymmetric part:

$$\partial_l s_i = \frac{1}{2}(\partial_l s_i + \partial_i s_l) + \frac{1}{2}(\partial_l s_i - \partial_i s_l) = \varepsilon_{il} + D_{il}.$$

Now one can write the tensor in (I.4) as a product

$$dx'_i = (\delta_{il} + \partial_l s_i)\, dx_l = (\delta_{il} + \varepsilon_{il} + D_{il})\, dx_l = (\delta_{ij} + D_{ij})(\delta_{jl} + \varepsilon_{jl})\, dx_l.$$

The first factor of this linear mapping $(\delta_{ij} + D_{ij})$ describes a rotation, because it preserves length: Therefore let $a \in \mathbb{R}^3$ an arbitrary vector:

$$\begin{aligned}
|(\delta_{ij} + D_{ij})a_j|^2 &= (\delta_{ik} + D_{ik})a_k(\delta_{ij} + D_{ij})a_j \\
&\approx (\delta_{jk} + D_{jk} + D_{kj})a_k a_j && \text{(neglect of } (\partial_l x_l)^2\text{)} \\
&= a_k a_k + (D_{jk} - D_{jk})a_k a_j && \text{(antisymmetry of } D_{jk}\text{)} \\
&= a_k a_k = |a|^2.
\end{aligned}$$

The symmetric part of the distortion

$$\varepsilon_{il} = \frac{1}{2}(\partial_l s_i + \partial_i s_l) \tag{I.5}$$

is called **deformation**.
So one can interpret the transformation of the differentials (I.4) as concatenation of a rotation and a deformation.

I.1.3.2 Hook's Law

In an elastic body with only small deformations one can assume **Hook's law**, i. e. a linear relation between deformation ε_{kl} and stress tensor σ_{ij}:

$$\sigma_{ij} = C_{ijkl}\varepsilon_{kl}. \tag{I.6}$$

The forth order tensor C_{ijkl} contains the **moduli of elasticity**. In three spacial dimensions at first there are 81 of these values. In the following we will find some restrictions, that will reduce this number.
Because σ_{ij} is symmetric there holds

$$C_{ijkl} = C_{jikl} \tag{I.7}$$

and only $6 \times 9 = 54$ independend values are left.
Usually the relation between deformation and stress tensor can be written in an alternative way by the introduction of a potential field Φ:

$$\sigma_{ij} = \frac{d\Phi}{d\varepsilon_{ij}} = C_{ijkl}\varepsilon_{kl}.$$

If one assumes a sufficiently smooth function Φ the theorem of Schwarz holds and the derivations commute:

$$C_{ijkl} = \frac{d^2\Phi}{d\varepsilon_{kl}d\varepsilon_{ij}} = \frac{d^2\Phi}{d\varepsilon_{ij}d\varepsilon_{kl}} = C_{klij}. \tag{I.8}$$

At first this together with (I.7) implies the symmetry with respect to (k, l):

$$C_{ijkl} = C_{klij} = C_{lkij} = C_{ijlk}$$

so that there are $6 \times 6 = 36$ remaining independend moduli.
At next the same symmetry $C_{ijkl} = C_{klij}$ implies that there are just 21 independend numbers left.

If the considered material fulfills further symmetries one can reduce the number of independend moduli even more:
Here the material is supposed to be isotrope. I. e. C_{ijkl} has to be invariant under arbitrary rotations T_{pq} ($T_{pq}T_{rq} = \delta_{pr}$):

$$C_{ijkl} = T_{ip}T_{jq}T_{kr}T_{ls}C_{pqrs} \tag{I.9}$$

- The symmetry (I.9) with

$$T = \begin{pmatrix} 0 & 1 & 0 \\ 0 & 0 & 1 \\ 1 & 0 & 0 \end{pmatrix}$$

  yields

$$C_{1111} = C_{2222} = C_{3333} \text{ and } C_{1122} = C_{2233} = C_{1133}.$$

With

$$T = \begin{pmatrix} 0 & 0 & 1 \\ 1 & 0 & 0 \\ 0 & 1 & 0 \end{pmatrix}, \begin{pmatrix} 0 & 1 & 0 \\ 1 & 0 & 0 \\ 0 & 0 & -1 \end{pmatrix}, \begin{pmatrix} -1 & 0 & 0 \\ 0 & 0 & 1 \\ 0 & 1 & 0 \end{pmatrix}$$

we proceed

$$\begin{aligned} C_{1122} = C_{3311}, \quad C_{1122} = C_{2211}, \quad C_{2233} = C_{3322} \\ \Rightarrow C_{1122} = C_{1133} = C_{2233} = C_{2211} = C_{3311} = C_{3322}. \end{aligned}$$

- Now we find, that C_{1123} vanishes:
  With

$$T = \begin{pmatrix} 1 & 0 & 0 \\ 0 & 1/\sqrt{2} & 1/\sqrt{2} \\ 0 & -1/\sqrt{2} & 1/\sqrt{2} \end{pmatrix} \tag{I.10}$$

  (I.9) yields

$$C_{1122} = \frac{1}{2}\Big(C_{1122} + C_{1123} + C_{1122} + C_{1123}\Big) \Rightarrow C_{1123} = 0.$$

  For the sake of symmetry there also holds

$$C_{1123} = C_{2213} = C_{3312} = 0 = C_{2311} = C_{3211} = C_{1132} = \dots.$$

- A similar treatment of the entry C_{2223} yields

$$\begin{aligned} C_{2223} =& \frac{1}{4}\Big(-C_{2222} + C_{3333} + C_{2223} - 3C_{2223} - C_{3332} + 3C_{3332} + \\ & + C_{2233} - C_{3322} + C_{2323} - C_{2332} + C_{3223} - C_{3232}\Big) \ (\ T \text{ above}) \\ =& \frac{1}{4}\Big(\underbrace{-C_{2222} + C_{3333}}_{=0} - 2C_{2223} + 2C_{3332}\Big) \\ \Rightarrow \ 3C_{2223} =& C_{3332} \end{aligned}$$

  The analogue calculation for C_{3332} yields

$$3C_{3332} = C_{2223}$$

  and both together

$$C_{2223} = C_{3332} = 0 = C_{1112} = C_{1113} = C_{2221} = C_{3331}$$

  where the last equations are results of similar calculations.

After all just the entries

$$\begin{aligned} C_{1111} = C_{2222} = C_{3333} =: \nu, \\ C_{1122} = C_{1133} = C_{2233} = C_{2211} = C_{3311} = C_{3322} =: \lambda, \\ C_{1212} = C_{1313} = C_{2323} = C_{1221} = \dots =: \mu \end{aligned}$$

remain. Again with the symmetry (I.9) for T (I.10) yields:

$$\begin{aligned} C_{2222} &= \frac{1}{4}\Big(C_{2222} + 4C_{2223} + 4C_{3332} + 2C_{2233} + 4C_{2323} + C_{3333}\Big) \\ \Rightarrow \qquad 4\nu &= 2\nu + 2\lambda + 4\mu \\ \Rightarrow \qquad \nu &= \lambda + 2\mu \end{aligned}$$

and after all **Hook's law for an isotropic elastic material** just depends on the two constants λ and μ:

$$\sigma_{ij} = 2\mu\varepsilon_{ij} + \lambda\delta_{ij}\varepsilon_{ll}. \tag{I.11}$$

The values μ and λ are called **Lamé moduli**.

I.1.3.3 Deformation of an elastic body

We consider an elastic body, that satisfies Hook's law (I.11).
The internal energy, i. e. the energy, stored in the volume Ω of this body due to the deformation described by $x' = x + s$, is

$$\begin{aligned} E_{int} &= \int_\Omega dE = \int_\Omega dF_i ds_i \overset{(I.3)}{=} \int_\Omega \sigma_{ij} n_j da \varepsilon_{il} dx_l \overset{(I.11)}{=} \int_\Omega \left(2\mu\varepsilon_{ij} + \lambda\delta_{ij}\varepsilon_{pp}\right) n_j da \varepsilon_{il} dx_l \\ &= \int_\Omega (2\mu\varepsilon_{ij} + \lambda\delta_{ij}\varepsilon_{pp})\delta_{jl}\varepsilon_{il} dx = \int_\Omega (2\mu\varepsilon_{ij}\varepsilon_{ij} + \lambda\varepsilon_{ii}\varepsilon_{ll}) dx. \end{aligned} \tag{I.12}$$

The potential energy of this deformed body in the external field f is

$$E_f = -\int_\Omega \rho f_i s_i dx. \tag{I.13}$$

Similar to this volume force one can apply an external stress field τ_{ij} on a part of the surface of the body $\Gamma_\tau \subset \partial\Omega$. The energy with respect to τ_{ij} is

$$E_\tau = -\int_{\Gamma_\tau} s_i \tau_{ij} dA_j. \tag{I.14}$$

The total energy of this body is the sum of the three different energies:

$$E(s) = E_{int}(s) + E_f(s) + E_\tau(s) = \int_\Omega \left[2\mu\varepsilon_{ij}\varepsilon_{ij} + \lambda\varepsilon_{ll}\varepsilon_{jj} - \rho f_i s_i\right] dx - \int_{\Gamma_\tau} s_i \tau_{ij} n_j dA. \tag{I.15}$$

Boundary conditions
On another part of the boundary $\Gamma_0 \subset \partial\Omega$ the elastic body may be fixed:

$$s(x) = 0 \text{ on } x \in \Gamma_0. \tag{I.16}$$

In mechanical equilibrium the field of displacement $s(x)$ of the solid body under the given forces f_i and τ_{ij} and the boundary condition (I.16) has to minimize the energy functional (I.15), i. e. in a given function space V we search

$$s \in V_0 := \left\{ v \in V \middle| v|_{\Gamma_0} = 0 \right\}$$

such that

$$\begin{aligned}
\forall r \in V_0: \quad & E'(s)(r) = 0 \\
\Leftrightarrow \forall r \in V_0: \quad & \int_\Omega \left[2\mu \varepsilon_{ij}(s)\varepsilon_{ij}(r) + 2\lambda \varepsilon_{ll}(s)\varepsilon_{jj}(r) - \rho f_i r_i \right] dx - \int_{\Gamma_\tau} r_i \tau_{ij} n_j da = 0 \\
\Leftrightarrow \forall r \in V_0: \quad & 2\mu \left\langle \varepsilon_{ij}(s), \varepsilon_{ij}(r) \right\rangle_\Omega + 2\lambda \left\langle \varepsilon_{ll}(s), \varepsilon_{jj}(r) \right\rangle_\Omega = \left\langle \rho f_i, r_i \right\rangle_\Omega + \left\langle \tau_{ij} n_j, r_i \right\rangle_{\Gamma_\tau}
\end{aligned} \tag{I.17}$$

I.1.4 Contact mechanics

In this section we introduce two models of body-body-contact, that are distinguished by the use of two different projections – the Signorini-projection (I.21) on the one hand and a projection in one fixed direction (I.20) on the other hand. To find the correct displacement of this restricted problem, we have to adjust the minimization problem (I.17) and yield (I.23).

In section I.1.3 we introduced a simple energy functional for an elastic body (I.15). The displacement $s(x)$ of the elastic body under the fields f and τ with respect to the Dirichlet condition (I.16) is the solution of the minimization problem

$$\forall t : t|_{\Gamma_0} = 0: \quad E(s) \leq E(t). \tag{I.18}$$

Examples for this kind of problem are a free membrane or the deformation of an elastic bar. A more complicated problem is given, if the body is not permitted to penetrate some given obstacle, i. e. the displacement $s(x)$ has to fulfill a restriction of the kind

$$P(x + s(x)) = x + s(x). \tag{I.19}$$

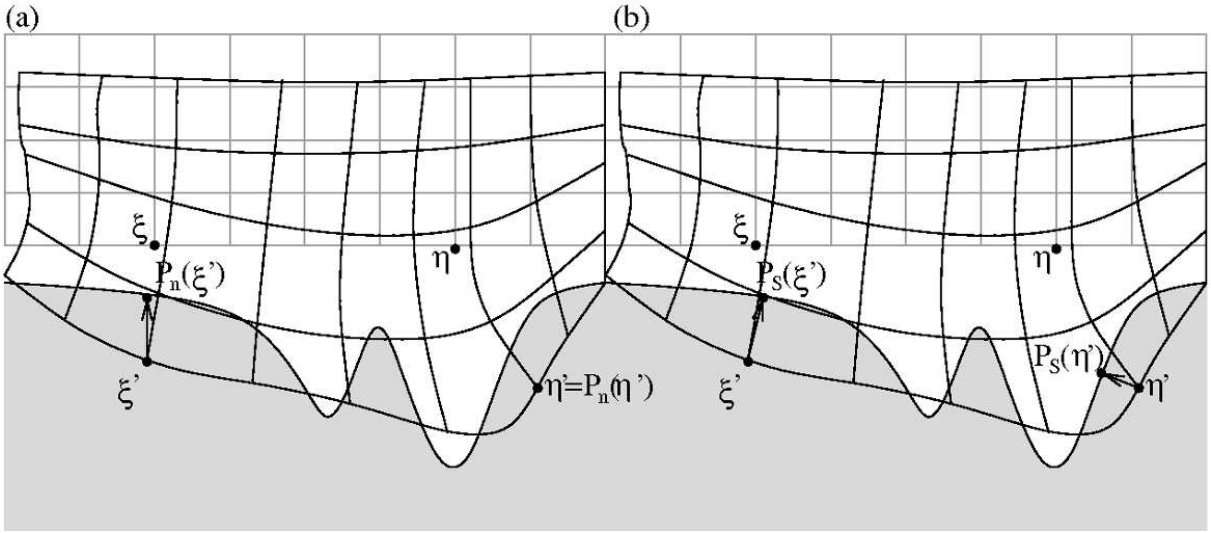

Figure I.1: The simple one-direction projection (a) and the Signorini projection (b). Both figures show the undeformed body (gray), the deformed body (black) and the projection of two displaced points ξ' and η'.

Geometrically P is a projection to a permitted domain. Here two kinds of projection are distinguished (see figure I.1). The more simple projection P_n (figure I.1 (a)) just acts in the direction of one vector n (e. g. $n = e_z$).
The second projection P_s – the Signorini-Projection (figure I.1 (b)) – in every point x of the treated surface acts in the direction of the outer normal $n(x)$ in this point.
The comparison of both shows that the two projections act quite similar, if the obstacle is rather plain (here at point ξ'). But if the obstacle gets more rough (e. g. at point η') the simple projection P_n can permit even obvious wrong solutions, while the Signorini-Projection acts in a reasonable way. For a given obstacle function $b : \mathbb{R}^{d-1} \to \mathbb{R}$, that declares the obstacle relative to a plane vertical to n_b, the formal definition of the two projections is given by

$$P_n(\xi) = \begin{cases} \xi, & \xi \cdot n \leq b(\xi_\perp) \\ \xi - (\xi \cdot n - b(\xi_\perp))n, & \xi \cdot n > b(\xi_\perp) \end{cases} \tag{I.20}$$

$$P_s(\xi) = \begin{cases} \xi, & \xi \cdot n(\xi) \leq b(\xi_\perp) \\ \xi - (\xi \cdot n(\xi) - b(\xi_\perp))n(\xi), & \xi \cdot n(\xi) > b(\xi_\perp) \\ \xi, & \xi \notin \partial\Omega \end{cases} . \tag{I.21}$$

n_b is a fixed chosen vector, that gives the direction of the plane on which the obstacle-defining function b is declared. In the case of P_n there is $n_b = n$, while for P_s n_b can be chosen arbitrary but reasonable.
$\xi_\perp$ means the orthogonal projection of ξ to that plane, i. e. if one has got the base vectors $b_1, \ldots, b_{d-1}$ of this plane, relative to that the function b is declared, ξ can be written as $\alpha_1 b_1 + \ldots + \alpha_{d-1} b_{d-1} + \alpha_d n_b$ and furthermore the projection $\xi_\perp = \alpha_1 b_1 + \ldots + \alpha_{d-1} b_{d-1}$.

On first sight there does not seem to be any difference between both projections despite of the additional case in the Signorini-projection.
The difference is the role of the vector n in both mappings. In the Signorini-projection P_s $n = n(\xi)$ depends on the mapping's argument ξ and stands for the outer normal of the surface. This indeed is the reason, why P_s is not declared for internal points of the body. In the simple projection P_n $n = n_b$ is given as constant direction for all points ξ. One interpretation is, that this fixed n is an approximation of the actual space dependant outer normal $n(\xi)$.
The restriction of P_s to points of the surface of the body will not take any effect to later applications, because the projections only will be applied to points on the surface of Ω.
If we now divide the boundary of our body into three parts

$$\partial\Omega = \Gamma_0 \cup \Gamma_\tau \cup \Gamma_c$$

with $\Gamma_\tau \cap \Gamma_0 = \Gamma_\tau \cap \Gamma_c = \Gamma_0 \cap \Gamma_c = \emptyset$ to declare the conditions

$$\begin{aligned} s &= 0 \text{ on } \Gamma_0 \\ \sigma_{ij} n_j &= \tau_{ij} n_j \text{ on } \Gamma_\tau \\ P(x + s(x)) &= x + s(x) \text{ on } \Gamma_c, \end{aligned}$$

we have to adjust problem (I.18) to:
Find

$$s \in \Pi(V_0) := \left\{ r \in V_0 \middle| P(x + r(x)) = x + r(x),\ x \in \Gamma_c \right\} \tag{I.22}$$

with

$$\forall t \in \Pi(V_0): \quad E(s) \leq E(t).$$

This leads to a variational problem analogue to (I.17):
Find

$$s \in \Pi(V_0)$$

such that

$$\forall r \in \Pi(V_0): \quad E'(s)(r - s) \geq 0. \tag{I.23}$$

I.2 Hydrodynamics

In this section the physical theory of hydrodynamics is scatched and different fluid models are introduced. Therfor we follow the basic introductions in Shivamoggi [1985], Stephani and Kluge [1995] and Fließbach [2003]. In section I.2.1 the Stokes equations (I.29) are derived as minimization of the power-application on a fluid. In section I.2.2 we introduce cavitation into this model, i. e. the possibility of a vaporising fluid. For thin fluid-films these equations are reduced to a model in two dimensions (section I.2.3). The two-dimensional problem can be simplified even more by eliminating the velocity field to achieve the Reynolds equation (section I.2.4).

Between the two interacting bodies (scatched in figure I.1) there is a lubricant, for which we have to calculate the velocity- and pressure-field. Therefor we assume quasistationarity, i. e. that the two contact partners do not move, even though the velocity of them is taken as boundary-condition for the Stokes equation or Reynolds equation respectively.

I.2.1 Stokes equations

In contrast to the classical introductions in physics (e. g. Brandt and Dahmen [1996] we do not derive the Stokes equations from the equilibrium of forces, but as solution of a minimisation problem of the total power (I.25).

We consider an isotrope viscous fluid. If the fluid moves with a (spacial) constant velocity there will not be any loss of energy due to friction, because the different layers of the fluid do not rub against each other. So the tension caused by friction will only depend on the derivative of the velocity $\partial_j v_i$.
This tensor can be split into its symmetric and antisymmetric component:

$$\partial_j v_i = \frac{1}{2}\left(\partial_j v_i + \partial_i v_j\right) + \frac{1}{2}\left(\partial_j v_i - \partial_i v_j\right).$$

The symmetric component

$$V_{ij} = \frac{1}{2}\left(\partial_j v_i + \partial_i v_j\right)$$

is called **strain rate**, while the antisymmetric component can be contracted to the curl density

$$w_l := \frac{1}{2}\varepsilon_{lji}\frac{1}{2}\left(\partial_j v_i - \partial_i v_j\right) = \frac{1}{2}\frac{1}{2}\left(\varepsilon_{lji}\partial_j v_i + \varepsilon_{lij}\partial_i v_j\right) = \frac{1}{2}\varepsilon_{lji}\partial_j v_i = \frac{1}{2}(\mathbf{rot}\ v)_l.$$

(Consider that ε_{lji} denotes the third order Levi-Civita-Tensor.)
Analogue to the independence on the velocity of translation, described above, we assume, that curling of the fluid does not have any effect on the internal friction, consequently friction will only depend on the (symmetric) strain rate.
The most simple relation between the stress tensor σ_{ij} and the strain rate is the multiplication with a scalar 2η:

$$\sigma_{ij} = 2\eta V_{ij}, \qquad \eta \in \mathbb{R}. \tag{I.24}$$

η is called **viscosity** of the fluid.
Finally the force, that is acting on a volume element of the fluid $\delta V = \delta x_1 \delta x_2 \delta x_3$ due to friction is

$$(\delta F_{dis})_i = -\sigma_{ij} \delta A_j,$$

where δA_j are the faces of δV (for example $\delta A_1 = \delta x_2 \delta x_3$, see figure I.2).

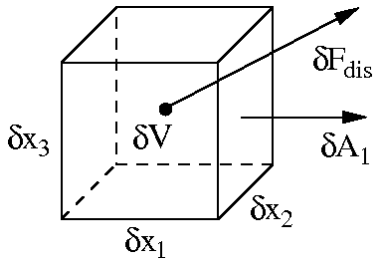

Figure I.2: Volume element $\delta V = \delta x_1 \delta x_2 \delta x_3$ and friction force δF_{dis}

The dissipative energy loss results in a power

$$\delta P_{dis} = -\overline{\delta v_i} (\delta F_{dis})_i$$

with the mean change of velocity in the volume element $\overline{\delta v_i} = \frac{1}{2} \partial_l v_i \delta x_l$. Inserting all the abbreviations into the expression for δP_{dis} results in

$$\begin{aligned} \delta P_{dis} &= \frac{1}{2} \partial_l v_i \delta x_l \sigma_{ij} \delta A_j \\ &= \eta \partial_l v_i V_{ij} \underbrace{\delta A_j \delta x_l}_{\approx \delta_{jl} \cdot \delta x_1 \delta x_2 \delta x_3} \\ &= \eta \partial_j v_i V_{ij} \delta x_1 \delta x_2 \delta x_3. \end{aligned}$$

Integration over the whole fluid volume gives the total dissipative power loss:

$$P_{dis} = \eta \int_\Omega \partial_j v_i V_{ij} dx.$$

The power applied by the volume force f_i is given by

$$P_f = -\int_\Omega \rho f_i v_i dx.$$

The total power bilance is now

$$P(v) = P_f(v) + P_{dis}(v) = -\rho \int_\Omega f_i v_i dx + \eta \int_\Omega \partial_j v_i V_{ij} dx. \tag{I.25}$$

Principles of physics say that this value has to be minimized in a stable system. The minimization has to consider the restriction of a divergence free flow

$$\text{div } v = \partial_l v_l = 0. \tag{I.26}$$

In section I.2.2 we diminish this condition to pay account for the phenomenon of cavitation.
To minimize the power functional under the restriction (I.26), we have to introduce a Lagrange-parameter p into our problem and to solve the two Lagrange conditions:

$$\begin{array}{rll} \forall w \in V: & P'(v)(w) - \langle \partial_l w_l, p\rangle_\Omega & = 0 \\ \forall q \in \Pi: & \langle \partial_l v_l, q\rangle_\Omega & = 0 \end{array}$$

where $\langle f, g\rangle_\Omega = \int\limits_\Omega f \cdot g dx$ denotes the L^2-product.

I.2.1.1 Boundary Conditions I

If we want to proscribe a **Dirichlet boundary condition** on one part of the boundary $\Gamma_v \subset \partial\Omega$ we do this by modification of the space V and the corresponding test space. We now search

$$v \in V_D = \left\{ w \in V \middle| w|_{\Gamma_v} = v_0 \right\} \text{ and } p \in \Pi$$

such that

$$\begin{array}{rll} \forall w \in W: & P'(v)(w) - \langle \partial_l w_l, p\rangle_\Omega & = 0 \\ \forall q \in \Pi: & \langle \partial_l v_l, q\rangle_\Omega & = 0 \end{array},$$

where the velocity-test-space is

$$\tilde{V} = \left\{ w \in V \middle| w|_{\Gamma_v} = 0 \right\}.$$

We write these two equations out:

$$\begin{array}{rll} \forall w \in \tilde{V}: & -\rho \langle f_i, w_i\rangle_\Omega + \underbrace{\eta\Big(\langle \partial_j w_i, V_{ij}\rangle_\Omega + \Big\langle \partial_j v_i, \dfrac{\partial_i w_j + \partial_j w_i}{2}\Big\rangle_\Omega\Big)}_{\eta\langle \partial_j w_i, \partial_i v_j\rangle_\Omega + \eta\langle \partial_i w_j, \partial_i v_j\rangle_\Omega} - \langle \partial_l w_l, p\rangle_\Omega & = 0 \\ \forall q \in \Pi: & \langle \partial_l v_l, q\rangle_\Omega & = 0. \end{array} \tag{I.27}$$

At this point we should mention, that the Dirichlet boundary condition $v|_{\Gamma_v} = v_0$ is restricted by the condition of divergence free flow – at least, if $\Gamma_v = \partial\Omega$. This can be seen by application of the Gauß theorem II.29

$$0 = \int\limits_\Omega \text{div } v dx = \int\limits_{\partial\Omega} v_i n_i da = \int\limits_{\partial\Omega} (v_0)_i n_i d\sigma.$$

Physically this is a consequence of mass conservation. The bilance of mass leaving the volume Ω through the surface $\partial\Omega$, i. e. the last integral, has to be zero if there are no sources or drains in Ω.

I.2.1.2 Classical Formulation

To achieve the Stokes equations in their classical form we apply Green's formula (theorem II.30) on the first equation of (I.27) several times:

$$\begin{aligned}
0 &= -\rho \langle f_i, w_i \rangle_\Omega + \eta \langle \partial_j w_i, \partial_j v_i + \partial_i v_j \rangle_\Omega - \langle \partial_i w_i, p \rangle_\Omega \\
&= -\langle \rho f_i, w_i \rangle_\Omega - \eta \Big\langle w_i, \partial_j \partial_j v_i + \partial_i \underbrace{\partial_j v_j}_{=0} \Big\rangle_\Omega + \eta \int\limits_{\partial\Omega} w_i n_j (\partial_j v_i + \partial_i v_j) da + \\
&\quad + \langle w_i, \partial_i p \rangle_\Omega - \int\limits_{\partial\Omega} w_i n_i p da \\
&= \langle -\rho f_i - \eta \Delta v_i + \partial_i p, w_i \rangle_\Omega + \int\limits_{\Gamma_p} w_i \left(\eta \left(\partial_n v_i + n_j \partial_i v_j \right) - n_i p \right) da
\end{aligned}$$

The reduction of the integration domain of the boundary integral to

$$\Gamma_p = \partial\Omega \setminus \Gamma_v$$

is possible because $w \in \tilde{V}$ vanishes on Γ_v.
First this equation has to be fulfilled by an arbitrary function $w \in \tilde{V}$ that vanishs on Γ_p, i. e. $w|_{\Gamma_p} = 0$. In this case the boundary integral is zero and the first argument of the scalar product must be zero (almost everywhere):

$$-\rho f_i - \eta \Delta v_i + \partial_i p = 0 \qquad \text{on } \Omega.$$

Testing with an arbitrary $w \in \tilde{V}$, enforces the remaining integral to tend zero, which only can be true for:

$$n_i p = \eta \left(\partial_n v_i + n_j \partial_i v_j \right) = \eta n_j \left(\partial_j v_i + \partial_i v_j \right) = n_j 2 \eta V_{ij} \overset{\text{(I.24)}}{=} \sigma_{ij} n_j, \text{ on } \Gamma_p. \tag{I.28}$$

I. e. the pressure on the surface Γ_p has to be an eigenvalue of the stress tensor σ_{ij} with the normal on the surface of Ω as corresponding eigenvector.
This relation rectifies the interpretation of the Lagrange parameter as pressure of the fluid.
Finally we can conclude the result of this section in the **Stokes equations**

$$\begin{aligned}
\eta \Delta v - \nabla p &= -\rho f && \text{on } \Omega \\
\operatorname{div} v &= 0 && \text{on } \Omega \\
v &= v_0 && \text{on } \Gamma_v \subset \partial\Omega \\
pn &= \sigma n && \text{on } \Gamma_p = \partial\Omega \setminus \Gamma_v.
\end{aligned} \tag{I.29}$$

Because only derivatives of the pressure occure in this classical form of the Stokes equations, there must be an additional condition to guarantee a unique pressure. This might be a Dirichlet condition $p = p_0$ on Γ_p, which is discussed below. Sufficiant for this purpuse would also be another condition, e. g. a given value for the average pressure $\int\limits_\Omega p = P = \text{const.}$.

I.2.1.3 Variational Formulation

To gain a **variational formulation** of the Stokes equations we modify the first equation of (I.27) one more time:

$$\begin{aligned}
&\frac{\rho}{\eta}\left\langle f_i, w_i\right\rangle_\Omega + \frac{1}{\eta}\left\langle \partial_l w_l, p\right\rangle_\Omega \\
&= \left\langle \partial_i v_j, \partial_i w_j\right\rangle_\Omega + \left\langle \partial_i v_j, \partial_j w_i\right\rangle_\Omega \\
&= \left\langle \partial_i v_j, \partial_i w_j\right\rangle_\Omega - \langle \underbrace{\partial_j \partial_i v_j}_{\partial_i(\text{div } v)=0}, w_i\rangle_\Omega + \int\limits_{\Gamma_p} n_j \partial_i v_j w_i da \qquad \text{(Green's formula)} \\
&= \left\langle \partial_i v_j, \partial_i w_j\right\rangle_\Omega + \int\limits_{\Gamma_p} n_j \partial_i v_j w_i da \\
&= \left\langle \partial_i v_j, \partial_i w_j\right\rangle_\Omega + \int\limits_{\Gamma_p} \left(2 n_j V_{ij} - n_j \partial_j v_i\right) w_i da \qquad \text{(with (I.28))} \\
&= \left\langle \partial_i v_j, \partial_i w_j\right\rangle_\Omega + \int\limits_{\Gamma_p} \left(2 n_j V_{ij} - \partial_n v_i\right) w_i da \qquad \text{(I.30)}
\end{aligned}$$

I.2.1.4 Boundary Conditions II

As usual there are different kinds of possible boundary conditions for this minimization problem.

- Dirichlet boundary conditions $v|_{\Gamma_v} = v_0$ are already introduced in (I.27) by the restriction of the test space $\tilde{V}$.
- On Γ_p we give a Neumann boundary condition for the velocity field $\partial_n v|_{\Gamma_p} = V_0$ and Dirichlet data for the pressure $p|_{\Gamma_p} = p_0$. Insertion into the boundary integral of (I.30) and application of equation (I.28) yield

$$\int\limits_{\Gamma_p} \left(2 n_j V_{ij} - \partial_n v_i\right) w_i da = \int\limits_{\Gamma_p} \left(\frac{p_0}{\eta} n_i - (V_0)_i\right) w_i da.$$

  The restriction of the pressure leads to modifications of the function space Π analogue to that of the velocity:

$$\begin{aligned}
\Pi_D &= \left\{ q \in \Pi \middle| q|_{\Gamma_p} = p_0 \right\} \\
\tilde{\Pi} &= \left\{ q \in \Pi \middle| q|_{\Gamma_p} = 0 \right\}.
\end{aligned}$$

We can conclude with the **variational formulation of the Stokes equations**:
Search $v \in V_D$ and $p \in \Pi_D$ such that

$$\begin{aligned}
\forall w \in \tilde{V}: \quad \eta \left\langle \partial_i v_j, \partial_i w_j\right\rangle_\Omega - \left\langle \partial_l w_l, p\right\rangle_\Omega &= \rho \left\langle f_i, w_i\right\rangle_\Omega + \int\limits_{\Gamma_p} \left(-p_0 n_i + \eta (V_0)_i\right) w_i da \\
\forall q \in \tilde{\Pi}: \qquad \left\langle \partial_l v_l, q\right\rangle_\Omega &= 0.
\end{aligned} \qquad \text{(I.31)}$$

At this point we have to remark one constraint for the different boundary conditions for the velocity-field: If the field of outer normals n_j on the boundary part Γ_p is not continuous along one line $c(t) = p_0 + td$, $0 \leq t \leq l$ (with direction $d \in \mathbb{R}^3$), i. e. the boundary is not continuously differentiable, e. g. the edge of a box-domain (figure I.3), there are two outer normals n and $\tilde{n}$ available.
If c connects two points $p_0 = c(0), p_l = c(l) \in \Gamma_v$ there must hold

$$\begin{aligned} d \cdot (v_0(c(l)) - v_0(c(0))) =& d \cdot (v(c(l)) - v(c(0))) \\ =& d \cdot \int_0^l v'(c(t))c'(t)dt = \int_0^l d_i d_j \partial_j v_i(c(t))dt \end{aligned}$$

With

$$m = \frac{1}{\|\tilde{n} - (\tilde{n} \cdot n)n\|}(\tilde{n} - (\tilde{n} \cdot n)n) =: \alpha n + \beta \tilde{n}$$

we build up the orthonormal system $\{n, m, d\}$ to write div $v = 0$ as

$$\text{div } v = d_i d_j \partial_j v_i + n_i n_j \partial_j v_i + m_i m_j \partial_j v_i = 0$$

and to replace d in the equation above:

$$\begin{aligned} d \cdot (v_0(c(l)) - v_0(c(0))) &= \int_0^l \Big(-n_i n_j \partial_j v_i(c(t)) - m_i m_j \partial_j v_i(c(t)) \Big) dt \\ &= -\int_0^l \Big(n_i \partial_n v_i(c(t)) + m_i \alpha \partial_n v_i(c(t)) + m_i \beta \partial_{\tilde{n}} v_i(c(t)) \Big) dt \\ &= -\int_0^l \Big((n + \alpha m)_i (V_0(c(t)))_i + \beta m_i (\tilde{V}_0(c(t)))_i \Big) dt \\ &= -\int_0^l \Big(((1 + \alpha^2) n_i + \alpha \beta \tilde{n}_i)(V_0(c(t)))_i + \\ &\qquad + (\alpha \beta n + \beta^2 \tilde{n})_i (\tilde{V}_0(c(t)))_i \Big) dt. \end{aligned} \tag{I.32}$$

If we choose the two kinds of boundary-conditions for the velocity

$$v = v_0 \text{ on } \Gamma_v \text{ and } \partial_n v = V_0 \text{ on } \Gamma_p$$

and our domain's boundary contains nondifferentiable edges we have to take care of the restriction (I.32).
For a box-like domain (as in figure I.3) and

$$c(t) = te_3, \quad n = -e_2, \quad \tilde{n} = -e_1$$

(I.32) takes the form

$$(v_0)_3(c(l)) - (v_0)_3(c(0)) = \int_0^l \Big((V_0(c(t)))_2 + (\tilde{V}_0(c(t)))_1 \Big) dt. \tag{I.33}$$

I.2.2 Stokes Model with Cavitation

In this section we take account for cavitation, i. e. that the fluid might vaporise in some parts of the domain Ω. This leads to Stokes equations with an inequality constraint for the pressure (I.37) and the corresponding variational formulation (I.38).

We return to the minimization of the power application $P(v)$ (I.25).
If the phenomenon of cavitation has to be taken into account for the considered fluid we have to replace the restriction of a divergence free flow (I.26).
Cavitation of a certain liquid means that the substance is able to change its thermodynamical phase from fluid to gaseous. This results in a higher demand for space and so there might be a source of fluid, such that condition (I.26) has to be changed to an inequality condition:

$$\text{div } v = \partial_l v_l \geq 0. \tag{I.34}$$

Of course the changed restriction leads to a changed treatment of the minimization of $P(v)$. Now we search for

$$v \in V \quad \text{and} \quad p \in \Pi_{\geq 0} = \{q \in \Pi | q \geq 0\}$$

that satisfy the variational problem

$$\begin{array}{lll} \forall w \in V: & P'(v)(w) - \langle \partial_l w_l, p \rangle_\Omega & = 0 \\ \forall q \in \Pi_{\geq 0}: & \langle q - p, \partial_l v_l \rangle_\Omega & \geq 0. \end{array}$$

We proceed with the calculations analogue to that of the equation case:

$$\begin{aligned} 0 &= -\rho \langle f_i, w_i \rangle_\Omega + \eta \langle \partial_j v_i + \partial_i v_j, \partial_j w_i \rangle_\Omega - \langle \partial_i w_i, p \rangle_\Omega \\ &= \langle -\rho f_i - \eta \partial_i \partial_j v_j - \eta \partial_j \partial_j v_i + \partial_i p, w_i \rangle_\Omega + \int\limits_{\partial\Omega} \left[\eta n_j (\partial_i v_j + \partial_j v_i) - n_i p \right] w_i da. \end{aligned} \tag{I.35}$$

As above firstly we apply the Dirichlet boundary conditions for v_i to this equation by the modification of the space V such that there remains the search for $v \in V_D$:

$$\forall w \in \tilde{V}: \quad 0 = \langle -\rho f_i - \eta \partial_i \text{div } v - \eta \Delta v_i + \partial_i p, w_i \rangle_\Omega + \int\limits_{\Gamma_p} \left[2\eta n_j V_{ij} - n_i p \right] w_i da$$

with the same spaces V_D and $\tilde{V}$ as in (I.31).
Here again we first test with functions that vanish on Γ_p, $w|_{\Gamma_p} = 0$, to force the first argument of the scalar product to tend zero (almost everywhere)

$$\rho f + \eta \nabla (\nabla \cdot v) + \eta \Delta v - \nabla p = 0,$$

which reinserted into the last variational equation, yields

$$2\eta V_{ij} n_j = n_i p \quad \text{on } \Gamma_p. \tag{I.36}$$

Altogether we achieve the classical notation of the cavitation problem:
Find $v \in V$ and $p \in \Pi_{\geq 0}$ with

$$\begin{aligned} \eta\Delta v + \eta\nabla(\nabla \cdot v) - \nabla p &= -\rho f \quad \text{on } \Omega \\ v &= v_0 \quad \text{on } \Gamma_v \\ \sigma n &= pn \quad \text{on } \Gamma_p \\ \text{div } v &\geq 0 \quad \text{on } \Omega \\ p \cdot \text{div } v &= 0 \quad \text{on } \Omega. \end{aligned} \tag{I.37}$$

For the variational formulation we treat the minimization problem (I.35) in another manner:

$$\begin{aligned} 0 =& -\langle \rho f_i, w_i \rangle_\Omega + \eta \langle \partial_j v_i + \partial_i v_j, \partial_j w_i \rangle_\Omega - \langle \partial_i w_i, p \rangle_\Omega \\ =& -\langle \rho f_i, w_i \rangle_\Omega + \eta \langle \partial_j v_i, \partial_j w_i \rangle_\Omega + \\ &+ \eta \langle \partial_j v_j, \partial_i w_i \rangle_\Omega + \eta \int\limits_{\Gamma_p} [n_j \partial_i v_j w_i - n_i \partial_j v_j w_i]\, da - \langle \partial_i w_i, p \rangle_\Omega , \end{aligned}$$

with the same restriction of the testfunctions as above that leads to the replacement of $\partial\Omega$ by Γ_p in the boundary integral, that is modified again:

$$\begin{aligned} \int\limits_{\Gamma_p} \eta\, [n_j \partial_i v_j - n_i \partial_j v_j]\, w_i da &= \int\limits_{\Gamma_p} [2\eta n_j V_{ij} - \eta n_j \partial_j v_i - \eta n_i \partial_j v_j]\, w_i da \\ &= \int\limits_{\Gamma_p} [pn_i - \eta \partial_n v_i - \eta n_i \text{div } v]\, w_i da. \qquad (\text{ with (I.36)}) \end{aligned}$$

Analogue to the non-cavitational case we can prescribe Dirichlet-data for p and Neumann-data for v on Γ_p. So we achieve the **variational formulation of the Stokes problem with cavitation**:
Find $v \in V_D$ and $p \in (\Pi_D)_{\geq 0} = \left\{ q \in \Pi_{\geq 0} \middle| q|_{\Gamma_p} = p_0 \right\}$ such that

$$\begin{aligned} \forall w \in \tilde{V}: \quad & \eta \langle \partial_j v_i, \partial_j w_i \rangle_\Omega - \langle p, \partial_l w_l \rangle_\Omega + \\ & + \eta \langle \text{div } v, \text{div } w \rangle_\Omega - \int\limits_{\Gamma_p} \eta \text{div } v n_i w_i da &&= \langle \rho f_i, w_i \rangle_\Omega - \int\limits_{\Gamma_p} [p_0 n_i - \eta (V_0)_i]\, w_i da \\ \forall q \in \tilde{\Pi}_{\geq 0}: \quad & \langle q - p, \partial_l v_l \rangle_\Omega &&\geq 0. \end{aligned} \tag{I.38}$$

I.2.2.1 Dimensions

At this point one should discuss the physical dimensions, i. e. the units in which the physical values, e. g. length, mass or time, are measured. It is reasonable to use the SI-System, that uses the following units:

Value	**Sign**	**SI-unit**
Length	s	1 meter = $1m$
Time	t	1 second = $1s$
Velocity	v	1 meter per second = $1\frac{m}{s}$
Force	F	1 Newton = $1N$
Mass	m	1 kilogramm = $1kg$
Pressure	p	1 Pascal = 1Pa = $1\frac{N}{m^2} = 1\frac{kg}{ms^2}$
Density	ρ	1 kilogramm per cubic meter=$1\frac{kg}{m^3}$
Viscosity	η	1Pa s

Table I.1: Different SI-units.

Actually in the following, these units are not used. To simplify the mathematical notation, for a given viscosity $\eta = x_\eta$Pa s with $x_\eta \in \mathbb{R}$ the new unit for the pressure is introduced by

$$1\text{Pa}^* = 1\text{Pa} \cdot x_\eta.$$

This transformation is of the same form as the transfer from meters to feet or miles.
For the unit of mass and the density $\rho = x_\rho \frac{kg}{m^3}$ one can proceed in an analogue way to introduce

$$1kg^* = 1kg \cdot x_\rho.$$

By using these new units the values of η and ρ become one

$$\eta = x_\eta \text{Pa s} = x_\eta \frac{1\text{Pa}^*}{x_\eta} s = 1\text{Pa}^* s$$
$$\rho = x_\rho \frac{kg}{m^3} = x_\rho \frac{\frac{kg^*}{x_\rho}}{m^3} = 1\frac{kg^*}{m^3}$$

and can be neglected in further discussions and especially in numerical simulations.

I.2.3 Subdimensional Stokes Equation

In this section we reduce the dimension of the Stokes Problem (I.29) for thin domains Ω_3 to gain a two-dimensional Stokes problem (I.57) for two-dimensional velocity- and pressure-fields χ and ψ ((I.44) and (I.45)). We also derive the variational formulation (I.58) of this problem. In section I.2.3.3 we also condense the Stokes model with cavitation to its two-dimensional form (I.65) and the corresponding variational formulation (I.66).

The first step to simplify the Stokes equations in three dimensions for a very thin domain

$$\Omega_3 = \left\{ (x_1, x_2, x_3) \in \mathbb{R}^3 \middle| z_0(x_1, x_2) \leq x_3 \leq z_1(x_1, x_2), \quad (x_1, x_2) \in \Omega_2 \right\}$$

is the neglection of the dimension with the least expansion – here the x_3-direction with

$$g(x_1, x_2) := z_1(x_1, x_2) - z_0(x_1, x_2) \ll \operatorname{diam}(\Omega_2),$$

to achieve a two-dimensional problem.

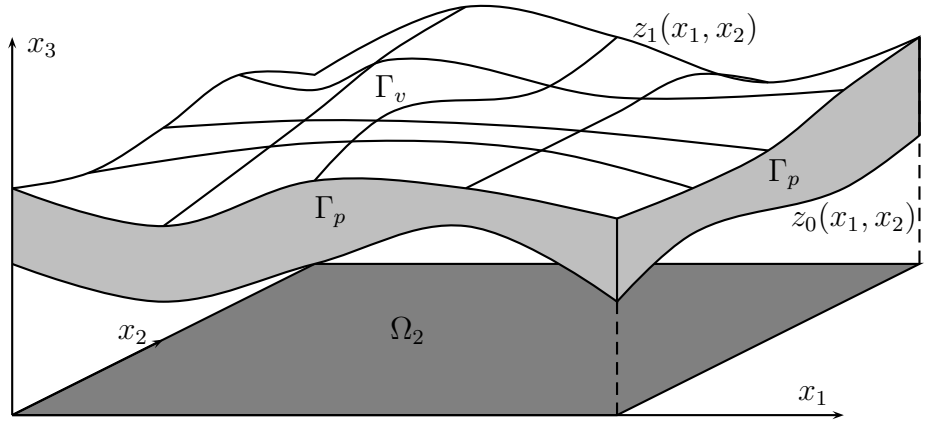

Figure I.3: Reducable domain Ω_3 with gap width $z_1 - z_0$ and corresponding two-dimensional domain Ω_2 that is a rectangle in the $x_1 - x_2$–space.

Starting point are the three-dimensional unitfree Stokes equations (I.29)

$$\begin{aligned} \partial_l \partial_l v_i - \partial_i p &= -f_i && \text{on } \Omega_3 \\ \partial_l v_l &= 0 && \text{on } \Omega_3 \\ v_i &= (v_0)_i && \text{on } \Gamma_v \\ p n_i &= \sigma_{ij} n_j && \text{on } \Gamma_p \\ p &= p_0 && \text{on } \Gamma_p \\ n_j \partial_j v_i &= (V_0)_i && \text{on } \Gamma_p \end{aligned} \tag{I.39}$$

In the following we assume, that Γ_v consists of the opposed parts of the domain Ω_3, that will vanish by the aspired reduction of one dimension. In figure I.3 these are the upper

and the lower face of the domain Ω_3:

$$\Gamma_v = \left\{ (x_1, x_2, z_j(x_1, x_2)) \in \mathbb{R}^3 \middle| (x_1, x_2) \in \Omega_2;\ j = 0, 1 \right\}.$$

On the remaining part of the boundary

$$\Gamma_p = \left\{ (x_1, x_2, x_3) \in \mathbb{R}^3 \middle| z_0(x_1, x_2) \leq x_3 \leq z_1(x_1, x_2); \quad (x_1, x_2) \in \partial\Omega_2 \right\}$$

p and $\partial_n v$ are given.
From this three-dimensional problem we will derive a two-dimensional one by integration with respect to x_3.
To preserve the compact notation through this procedure, from now on a general convention is, that Greek indices $(\mu, \nu, \ldots)$ can have the values 1 or 2, while Roman indices $(i, j, \ldots)$ are out of $\{1, 2, 3\}$. For the Einstein sum convention this implies

$$a_\nu b_\nu := \sum_{\nu=1}^{2} a_\nu b_\nu \quad \text{and} \quad a_i b_i := \sum_{i=1}^{3} a_i b_i.$$

At first we integrate the two Stokes equations with respect to x_3.

- We start with the impulse balance (first equation in (I.39)):

$$-\kappa_i := -\int_{z_0}^{z_1} f_i dx_3 = \int_{z_0}^{z_1} \partial_l \partial_l v_i dx_3 - \int_{z_0}^{z_1} \partial_i p dx_3 \tag{I.40}$$

At first we consider the cases $i = 1, 2$, $i = 3$ is considered in (I.54):

$$\begin{aligned}
-\kappa_\mu =& \partial_\nu \int_{z_0}^{z_1} \partial_\nu v_\mu dx_3 - \partial_\nu v_\mu(z_1)\partial_\nu z_1 + \partial_\nu v_\mu(z_0)\partial_\nu z_0 + \\
&+ g\partial_3^2 v_\mu(\overline{z}) + g^2 O(\left\|\partial_3^3 v_\mu\right\|_\infty) - \partial_\mu \underbrace{\int_{z_0}^{z_1} p dx_3}_{=:\psi} + p(z_1)\partial_\mu z_1 - p(z_0)\partial_\mu z_0 \\
=& \partial_\nu \partial_\nu \underbrace{\int_{z_0}^{z_1} v_\mu dx_3}_{=:\chi_\mu} \underbrace{-\partial_\nu \Big(v_\mu(z_1)\partial_\nu z_1 - v_\mu(z_0)\partial_\nu z_0 \Big) - \partial_\nu v_\mu(z_1)\partial_\nu z_1 + \partial_\nu v_\mu(z_0)\partial_\nu z_0}_{(\gamma_3)_\mu} + \\
&+ g\partial_3^2 v_\mu(\overline{z}) + g^2 O(\left\|\partial_3^3 v_\mu\right\|_\infty) - \partial_\mu \psi + p(z_1)\partial_\mu z_1 - p(z_0)\partial_\mu z_0 \\
=& \Delta\chi_\mu + (\gamma_3)_\mu + \underbrace{g\partial_3^2 v_\mu(\overline{z})}_{= \frac{12}{g^2}\left(g\overline{v}_\mu - \chi_\mu + g^4 O(\left\|\partial_3^3 v_\mu\right\|_\infty)\right),\ \text{(A.6)}} + g^2 O(\left\|\partial_3^3 v_\mu\right\|_\infty) - \partial_\mu \psi + \\
&+ \underbrace{\frac{1}{2}(p(z_1) + p(z_0))}_{= \overline{p} = \frac{\psi}{g} + g^2 O(\left\|\partial_3^2 p\right\|_\infty),\ \text{(A.4)}} \cdot \partial_\mu(z_1 - z_0) + \frac{1}{2}\underbrace{(p(z_1) - p(z_0))}_{=:\delta p}\partial_\mu(z_1 + z_0) \\
=& \Delta\chi_\mu - \frac{12}{g^2}\chi_\mu - \partial_\mu\psi + (\gamma_3)_\mu + \underbrace{\frac{12}{g}\overline{v}_\mu + g^2 O(\left\|\partial_3^3 v_\mu\right\|_\infty)}_{=:(\gamma_v)_\mu} + \qquad \text{(I.41)} \\
&+ \frac{\partial_\mu g}{g}\left(\psi + g^3 O(\left\|\partial_3^2 p\right\|_\infty)\right) + \partial_\mu \overline{z}\delta p \\
=& \Delta\chi_\mu - \frac{12}{g^2}\chi_\mu - g\partial_\mu\left(\frac{\psi}{g}\right) + (\gamma_3 + \gamma_v + \gamma_p)_\mu \qquad \text{(I.42)}
\end{aligned}$$

(with $(\gamma_p)_\mu = \partial_\mu g \cdot g^2 O(\|\partial_3^2 p\|_\infty) + \partial_\mu \overline{z}\delta p$, see (I.48))

- and proceed with the mass balance (second equation in (I.39)) in an analogue way:

$$\begin{aligned}
0 =& \int_{z_0}^{z_1} \partial_l v_l dx_3 \\
=& \partial_\mu \chi_\mu - v_\mu(z_1)\partial_\mu z_1 + v_\mu(z_0)\partial_\mu z_0 + \underbrace{v_3(z_1) - v_3(z_0)}_{=:\delta v_3} \\
=& \partial_\mu \chi_\mu - \delta v_\mu \partial_\mu \overline{z} - \overline{v}_\mu \partial_\mu g + \delta v_3 \\
\overset{(A.4)}{=}& \partial_\mu \chi_\mu + \frac{\partial_\mu g}{g}\Big(\underbrace{\int_{z_0}^{z_1} v_\mu dx_3}_{\chi_\mu} - g\overline{v}_\mu + \underbrace{\frac{g^3}{12}\partial_3^2 v_\mu(\zeta_v)}_{=:-\varepsilon_v \cdot g/\partial_\mu g}\Big) + \\
& - \delta v_\mu \partial_\mu \overline{z} - \overline{v}_\mu \partial_\mu g + \delta v_3 \\
=& \frac{1}{g}\partial_\mu(g\chi_\mu) \underbrace{-2\partial_\mu g \overline{v}_\mu - \partial_\mu \overline{z}\delta v_\mu + \delta v_3}_{-\sigma_3} - \varepsilon_v \\
=& \frac{1}{g}\partial_\mu\left(g\chi_\mu\right) - \varepsilon_v - \sigma_3
\end{aligned} \tag{I.43}$$

The introduction of

$$\chi_\mu(x_1, x_2) := \int_{z_0(x_1,x_2)}^{z_1(x_1,x_2)} v_\mu(x_1, x_2, x_3) dx_3 \tag{I.44}$$

$$\text{and} \quad \psi(x_1, x_2) := \int_{z_0(x_1,x_2)}^{z_1(x_1,x_2)} p(x_1, x_2, x_3) dx_3 \tag{I.45}$$

by the reduction of one dimension corresponds to the change of a flux through an (two-dimensional) interface (in three dimensions) to a flux through an (one-dimensional) edge (in two dimensons).
So after all we obtain a pair of two-dimensional Stokes equations ((I.42) and (I.43))

$$\begin{aligned}
\Delta\chi - \frac{12}{g^2}\chi - g\nabla(\psi/g) &= -\kappa - \gamma_3 - \gamma_p - \gamma_v \\
\frac{1}{g}\nabla \cdot (g\chi) &= \sigma_3 + \varepsilon_v
\end{aligned} \tag{I.46}$$

with the force-correction γ_3 which only depends on the geometrical properties of Ω_3 and the (given) boundary-conditions, the correction-terms γ_v, γ_p and ε_v and the source-term σ_3 in the law of mass-conservation. Furthermore we employed the abbreviations

- average velocity $\overline{v}_i = \frac{1}{2}(v_i(z_1) + v_i(z_0))$
- velocity-difference $\delta v_i = v_i(z_1) - v_i(z_0)$
- average pressure $\overline{p} = \frac{1}{2}(p(z_1) + p(z_0))$
- pressure-difference $\delta p = p(z_1) - p(z_0)$
- the gap-center $\overline{z} = \frac{1}{2}(z_1 + z_0)$
- gap width $g = z_1 - z_0$.

The latter also can be used for simplification of $\gamma_3,\ \gamma_v,\ \varepsilon_v$ and σ_3:

$$\begin{aligned}
(\gamma_3)_\mu =& -\partial_\nu\Big(v_\mu(z_1)\partial_\nu z_1 - v_\mu(z_0)\partial_\nu z_0\Big) - \partial_\nu v_\mu(z_1)\partial_\nu z_1 + \partial_\nu v_\mu(z_0)\partial_\nu z_0\\
=& -\Delta\Big(v_\mu(z_1)z_1 - v_\mu(z_0)z_0\Big) + \Delta v_\mu(z_1)z_1 - \Delta v_\mu(z_0)z_0\\
=& -\Delta\Big(\overline{v}_\mu g + \delta v_\mu \overline{z}\Big) + \Delta\overline{v}_\mu g + \Delta(\delta v_\mu)\overline{z}\\
=& -2\partial_\nu\overline{v}_\mu\partial_\nu g - 2\partial_\nu(\delta v_\mu)\partial_\nu\overline{z} - \overline{v}_\mu\Delta g - \delta v_\mu\Delta\overline{z} \qquad \text{(I.47)}\\
(\gamma_p)_\mu =& \partial_\mu\overline{z}\delta p + \partial_\mu g g^2 O(\left\|\partial_3^2 p\right\|_\infty)\\
=& \partial_\mu\overline{z} g O(\|\partial_3 p\|_\infty) + g^2\partial_\mu g O(\left\|\partial_3^2 p\right\|_\infty) \qquad \text{(I.48)}\\
(\gamma_v)_\mu =& \frac{12}{g}\overline{v}_\mu + g^2 O(\left\|\partial_3^3 v_\mu\right\|_\infty) \qquad \text{(I.49)}\\
\sigma_3 =& -\delta v_3 + \delta v_\mu\partial_\mu\overline{z} + 2\overline{v}_\mu\partial_\mu g \qquad \text{(I.50)}\\
\varepsilon_v =& -\partial_\mu g\frac{g^2}{12}\partial_3^2 v_\mu(\zeta_v) = g^2\partial_\mu g O(\left\|\partial_3^2 v_\mu\right\|_\infty). \qquad \text{(I.51)}
\end{aligned}$$

One must be aware that the two-dimensional flow is **not divergence free** any more, due to the velocity boundary condition on the former parts of the boundary Γ_v that comes with the second Stokes equation in (I.46) via the source-term σ_3 (I.50). Further below we discuss a way to replace the Dirichlet-condition for the velocity.

By the neglecting the error-terms in (I.46) and introduction of

$$\gamma = \gamma_3 + \frac{12}{g}\overline{v}_\mu, \qquad \text{(I.52)}$$

we state the **Subdimensional Stokes Problem**

$$\begin{aligned}
\Delta\chi - \frac{12}{g^2}\chi - g\nabla(\psi/g) &= -\kappa - \gamma \qquad \text{(I.53)}\\
\frac{1}{g}\nabla\cdot(g\chi) &= \sigma_3
\end{aligned}$$

Integration of the first of the three-dimensional Stokes equations (I.39) for $i = 3$ yields

$$\begin{aligned}
-\kappa_3 := -\int_{z_0}^{z_1} f_3 dx_3 &= \int_{z_0}^{z_1} \Delta v_3 dx_3 - \int_{z_0}^{z_1} \partial_3 p dx_3 \\
&= \underbrace{\partial_3 v_3(z_1) - \partial_3 v_3(z_0)}_{=:\delta(\partial_3 v_3)} + \partial_\mu \int_{z_0}^{z_1} \partial_\mu v_3 dx_3 + \\
&\quad - \partial_\mu v_3(z_1)\partial_\mu z_1 + \partial_\mu v_3(z_0)\partial_\mu z_0 - \delta p \\
&= \delta(\partial_3 v_3) + \partial_\mu \partial_\mu \underbrace{\int_{z_0}^{z_1} v_3 dx_3}_{=:\chi_3} - \partial_\mu \left(\delta v_3 \partial_\mu \overline{z} + \overline{v}_3 \partial_\mu g\right) + \\
&\quad - \partial_\mu \overline{v}_3 \partial_\mu g - \partial_\mu(\delta v_3)\partial_\mu \overline{z} - \delta p \\
\Rightarrow \qquad \Delta\chi_3 - \delta p &= -\kappa_3 - \delta(\partial_3 v_3) + \underbrace{2\partial_\mu(\delta v_3)\partial_\mu \overline{z} + 2\partial_\mu \overline{v}_3 \partial_\mu g + \delta v_3 \Delta \overline{z} + \overline{v}_3 \Delta g}_{=:-(\gamma_3)_3} \\
&= -\kappa_3 - g\partial_3^2 v_3(\overline{z}) + g^2 O(\left\|\partial_3^3 v_3\right\|_\infty) - (\gamma_3)_3 \\
&\overset{(A.6)}{=} -\kappa_3 - (\gamma_3)_3 - \frac{12}{g^2}\left(g\overline{v}_3 - \chi_3\right) + g^2 O(\left\|\partial_3^3 v_3\right\|_\infty) \\
\Rightarrow \quad \Delta\chi_3 - \frac{12}{g^2}\chi_3 - \delta p &= -\kappa_3 \underbrace{-(\gamma_3)_3 - \frac{12}{g}\overline{v}_3}_{=:(\gamma)_3} + g^2 O(\left\|\partial_3^3 v_3\right\|_\infty)
\end{aligned} \tag{I.54}$$

with $(\gamma_3)_3$ and $(\gamma)_3$ analogue to (I.47) and (I.52).

I.2.3.1 Boundary Conditions for the Subdimensional Stokes Equations

At last we derive boundary conditions for the two-dimensional problem (I.53) based on the ones of (I.39).
This is easy done for Dirichlet-conditions for the pressure ψ and the Neumann-conditions for the velocity χ_i $(i = 1, 2, 3)$. On the whole boundary of the subdimensional domain $\partial\Omega_2$ there hold

$$\begin{aligned}
\psi &= \int_{z_0}^{z_1} p dx_3 = \int_{z_0}^{z_1} p_0 dx_3 =: \psi_0 \\
\text{and } \partial_n \chi_i &= \partial_n \int_{z_0}^{z_1} v_i dx_3 = \int_{z_0}^{z_1} \partial_n v_i dx_3 = \int_{z_0}^{z_1} (V_0)_i dx_3 =: (X_0)_i.
\end{aligned} \tag{I.55}$$

To determine a unique velocity χ we will need a Dirichlet-boundary condition for χ on a part of $\partial\Omega_2$ too. Since we already have Neumann-conditions for χ on the entire boundary $\partial\Omega_2$, we will prescribe the velocity χ only in single points $P \in \partial\Omega_2$ of this boundary component by the use of (A.4):

$$\chi(P) = g\overline{v}(P) - \frac{g^3}{12}\partial_3^2 v(\zeta_v) =: g\overline{v}(P) + g^3\rho(P). \tag{I.56}$$

So after all we assemble (I.53), (I.55) and (I.56) to the two-dimensional Stokes problem: Find $\chi \in X$ and $\psi \in \Psi$ such that

$$\begin{aligned} \Delta\chi - \tfrac{12}{g^2}\chi - g\nabla(\psi/g) &= -\kappa - \gamma && \text{on } \Omega_2 \\ \tfrac{1}{g}\nabla\cdot(g\chi) &= \sigma_3 && \text{on } \Omega_2 \\ \psi &= \psi_0 && \text{on } \partial\Omega_2 \\ \partial_n\chi &= X_0 && \text{on } \partial\Omega_2 \\ \chi(P) &= (g\overline{v})(P) + g^3\rho(P) && \text{at a point } P \in \partial\Omega_2 \end{aligned} \tag{I.57}$$

where κ, γ and σ_3 are defined in (I.40), (I.52) and (I.50).
We remark, that (I.54)

$$\Delta\chi_3 - \frac{12}{g^2}\chi_3 - \delta p = -\kappa_3 - (\gamma_v - \gamma_3)_3$$

has the same form as the first equation of (I.57), despite this χ_3 is not part of the subdimensional Stokes problem.

I.2.3.2 Variational Formulation of the 2D-Stokes problem

To gain a variational formulation of the 2D-Stokes-problem (I.57) we proceed analogue to section I.2.1.3 and allocate (affine) subspaces of X and Ψ that allow the treatment of the different boundary-conditions:

$$\begin{aligned} X_D &:= \left\{\xi \in X \middle| \xi(P) = (g\overline{v})(P)\right\} & \Psi_D &:= \left\{\phi \in \Psi \middle| \phi = \psi_0\right\} \\ \tilde{X} &:= \left\{\xi \in X \middle| \xi(P) = 0\right\} & \tilde{\Psi} &:= \left\{\phi \in \Psi \middle| \phi|_{\partial\Omega_2} = 0\right\} \end{aligned}$$

(While prescripting the boundary conditions in X_D, we neglected the term $g^3\rho(P)$.)
As usual we multiply the classical equations (I.57) with adequate testfunctions $\xi \in \tilde{X}$ and $\phi \in \tilde{\Psi}$ and employ Green's formula:

- $$\begin{aligned} &\int_{\Omega_2} (\kappa_\mu + \gamma_\mu)\xi_\mu da \\ &= \int_{\Omega_2} \left[-\Delta\chi_\mu\xi_\mu + \frac{12}{g^2}\chi_\mu\xi_\mu + g\partial_\mu\frac{\psi}{g}\xi_\mu\right] da \\ &= \int_{\Omega_2} \left(\partial_\nu\chi_\mu\partial_\nu\xi_\mu + \frac{12}{g^2}\chi_\mu\xi_\mu\right) da - \int_{\partial\Omega_2} n_\nu\partial_\nu\chi_\mu\xi_\mu ds - \int_{\Omega_2}\frac{\psi}{g}\partial_\mu(g\xi_\mu)da + \int_{\partial\Omega_2} n_\mu\xi_\mu\psi ds \\ &= \int_{\Omega_2} \left(\partial_\nu\chi_\mu\partial_\nu\xi_\mu + \frac{12}{g^2}\chi_\mu\xi_\mu\right) da - \int_{\Omega_2}\frac{\psi}{g}\partial_\mu(g\xi_\mu)da + \int_{\partial\Omega_2} \left(\psi n_\mu - n_\nu\partial_\nu\chi_\mu\right)\xi_\mu ds \\ &= \int_{\Omega_2} \left(\partial_\nu\chi_\mu\partial_\nu\xi_\mu + \frac{12}{g^2}\chi_\mu\xi_\mu\right) da - \int_{\Omega_2}\frac{\psi}{g}\partial_\mu(g\xi_\mu)da + \int_{\partial\Omega_2} \left(\psi_0 n_\mu - (X_0)_\mu\right)\xi_\mu ds \end{aligned}$$
- $$\int_{\Omega_2} (\sigma_3)\phi da = \int_{\Omega_2}\frac{\phi}{g}\partial_\nu\left(g\chi_\nu\right) da$$

Alltogether the variational form of the two-dimensional Stokes equations is:
Find $\chi \in X_D$ and $\psi \in \Psi_D$ such that

$$\begin{aligned} \forall \xi \in \tilde{X}: \quad & \langle \partial_\mu \chi_\nu, \partial_\mu \xi_\nu \rangle_{\Omega_2} + 12 \langle \chi/g, \xi/g \rangle_{\Omega_2} - \left\langle \tfrac{\psi}{g}, \partial_\nu (\xi_\nu g) \right\rangle_{\Omega_2} = \\ & \langle \kappa_\mu + \gamma_\mu, \xi_\mu \rangle_{\Omega_2} - \langle \psi_0 n_\mu - (X_0)_\mu, \xi_\mu \rangle_{\partial\Omega_2} \\ \forall \phi \in \tilde{\Psi}: \quad & \left\langle \tfrac{\phi}{g}, \partial_\nu \left(g \chi_\nu \right) \right\rangle_{\Omega_2} = \langle \sigma_3, \phi \rangle_{\Omega_2} . \end{aligned} \tag{I.58}$$

I.2.3.3 2D-Model with Cavitation

The Stokes model with cavitation is given in (I.37):
Find $v \in V$ and $p \in \Pi_{\geq 0}$ with

$$\begin{aligned} \Delta v + \nabla(\nabla \cdot v) - \nabla p &= -f \quad \text{on } \Omega \\ v &= v_0 \quad \text{on } \Gamma_v \\ \sigma n &= pn \quad \text{on } \Gamma_p \\ \text{div } v &\geq 0 \quad \text{on } \Omega \\ p \cdot \text{div } v &= 0 \quad \text{on } \Omega. \end{aligned} \tag{I.59}$$

Firstly it differs from the original Stokes Problem (I.29) in the additional term $\partial_i \partial_j v_j$, which now is condensed separately to one involving χ_μ:

$$\begin{aligned} \int_{z_0}^{z_1} \partial_\mu \partial_j v_j dx_3 = & \ \partial_\mu \int_{z_0}^{z_1} \partial_j v_j dx_3 - \partial_j v_j(z_1) \partial_\mu z_1 + \partial_j v_j(z_0) \partial_\mu z_0 \\ = & \ \partial_\mu \partial_\nu \int_{z_0}^{z_1} v_\nu dx_3 - \partial_\mu \Big(v_\nu(z_1) \partial_\nu z_1 - v_\nu(z_0) \partial_\nu z_0 \Big) + \partial_\mu \delta v_3 + \\ & - \Big(\overline{\partial_j v_j} \partial_\mu g + \delta(\partial_j v_j) \partial_\mu \overline{z} \Big) \\ = & \ \partial_\mu \partial_\nu \chi_\nu - \partial_\mu \Big(\overline{v}_\nu \partial_\nu g + \delta v_\nu \partial_\nu \overline{z} \Big) + \partial_\mu \delta v_3 + \\ & - \Big(\partial_\nu \overline{v}_\nu \partial_\mu g + \partial_\nu \delta v_\nu \partial_\mu \overline{z} + \overline{\partial_3 v_3} \partial_\mu g + \delta(\partial_3 v_3) \partial_\mu \overline{z} \Big) \\ = & \ \partial_\mu \partial_\nu \chi_\nu \underbrace{- \partial_\mu \partial_\nu \Big(\overline{v}_\nu g + \delta v_\nu \overline{z} \Big) + \Big(\partial_\mu \partial_\nu \overline{v}_\nu g + \partial_\mu \partial_\nu \delta v_\nu \overline{z} \Big)}_{=: \gamma_3 - \gamma_{3c} - g \partial_\mu (\delta v_3 / g), \text{ with } \gamma_3 \text{ of (I.47)}} + \partial_\mu \delta v_3 + \\ & - \overline{\partial_3 v_3} \partial_\mu g - \delta(\partial_3 v_3) \partial_\mu \overline{z} \\ = & \ \partial_\mu \partial_\nu \chi_\nu + \gamma_3 - \gamma_{3c} - g \partial_\mu \tfrac{\delta v_3}{g} + \partial_\mu \delta v_3 - \tfrac{\partial_\mu g}{g} \delta v_3 + \tfrac{g^2 \partial_\mu g}{12} \partial_3^3 v_3(\zeta_1) + \\ & \qquad \text{(with (A.4))} \\ & - \partial_\mu \overline{z} \left(\tfrac{g}{2} (\partial_3^2 v_3(z_1) + \partial_3^2 v_3(z_0)) + \tfrac{g^2}{4} (\partial_3^3 v_3(r) - \partial_3^3 v_3(s)) \right) \quad \text{(with (A.5))} \\ = & \ \partial_\mu \partial_\nu \chi_\nu + \gamma_3 - \gamma_{3c} - g \partial_\mu \overline{z} \partial_3^2 v_3(\zeta_{01}) + \tfrac{g^2 \partial_\mu (g + 3\overline{z})}{12} \partial_3^3 v_3(\zeta_{1s}) - \tfrac{g^2 \partial_\mu \overline{z}}{4} \partial_3^3 v_3(r). \end{aligned}$$

If we add this term to the first equation of the original two-dimensional Stokes model (I.57) we have the first equation of the two-dimensional cavitation model:

$$\partial_\nu \partial_\nu \chi_\mu - \frac{12}{g^2} \chi_\mu + \partial_\mu \partial_\nu \chi_\nu - g \partial_\mu \frac{\psi}{g} = -\kappa_\mu - \gamma_{vc} - \gamma_{3c} - \gamma_p \tag{I.60}$$

with the new corrective terms

$$(\gamma_{3c})_\mu = (\gamma_3)_\mu + \partial_\mu\partial_\nu\Big(\overline{v}_\nu g + \delta v_\nu \overline{z}\Big) - \Big(\partial_\mu\partial_\nu \overline{v}_\nu g + \partial_\mu\partial_\nu \delta v_\nu \overline{z}\Big) - g\partial_\mu \frac{\delta v_3}{g} \tag{I.61}$$

$$\gamma_{vc} = \gamma_v + g\partial_\mu \overline{z}\partial_3^2 v_3(\zeta_{01}) - \frac{g^2\partial_\mu(g+3\overline{z})}{12}\partial_3^3 v_3(\zeta_{1s}) + \frac{g^2\partial_\mu \overline{z}}{4}\partial_3^3 v_3(r). \tag{I.62}$$

At next, we have to transform the last condition in (I.59):

$$p = 0 \quad \text{or} \quad \text{div } v = 0. \tag{I.63}$$

Integration over $z_0 \le x_3 \le z_1$ with the help of (I.45) and (I.43) yields

$$\psi = 0 \quad \text{or} \quad \frac{1}{g}\partial_\mu(g\chi_\mu) = \varepsilon_v + \sigma_3. \tag{I.64}$$

Finally we combine the results to the two-dimensional Stokes model with cavitation:
Find $\chi \in X_D$ and $\psi \in (\Psi_D)_{\ge 0} := \{\phi \in \Psi_D | \phi \ge 0\}$ such that

$$\begin{aligned}
\Delta\chi - \tfrac{12}{g^2}\chi + \nabla\nabla\cdot\chi - g\nabla(\psi/g) &= -\kappa - \gamma_c && \text{on } \Omega_2\\
\tfrac{1}{g}\nabla\cdot(g\chi) &\ge \sigma_3 && \text{on } \Omega_2\\
\psi\cdot\Big(\tfrac{1}{g}\nabla\cdot(g\chi) - \sigma_3\Big) &= 0 && \text{on } \Omega_2\\
\psi &= \psi_0 && \text{on } \partial\Omega_2\\
\partial_n\chi &= X_0 && \text{on } \partial\Omega_2\\
\chi(P) &= (g\overline{v})(P) + g^3\rho(P) && \text{at a point } P \in \partial\Omega_2.
\end{aligned} \tag{I.65}$$

with

$$\gamma_c = \gamma_{3c} + \frac{12}{g}\overline{v}$$

defined in (I.61) and κ and σ_3 are already defined in (I.40) and (I.50).
Multiplication with appropriate test functions

$$\xi \in \tilde{X} \quad \text{and} \quad \phi \in \tilde{\Psi}_{\ge 0}$$

and the application of Green's formula (theorem II.30)

$$\begin{aligned}
\langle(\kappa+\gamma_c)_\mu, \xi_\mu\rangle_{\Omega_2} &= -\langle\Delta\chi_\mu, \xi_\mu\rangle_{\Omega_2} + 12\left\langle\frac{\chi_\mu}{g}, \frac{\xi_\mu}{g}\right\rangle_{\Omega_2} - \langle\partial_\mu\partial_\nu\chi_\nu, \xi_\mu\rangle_{\Omega_2} + \langle g\partial_\mu(\psi/g), \xi_\mu\rangle_{\Omega_2}\\
&= \langle\partial_\nu\chi_\mu, \partial_\nu\xi_\mu\rangle_{\Omega_2} + 12\left\langle\frac{\chi_\mu}{g}, \frac{\xi_\mu}{g}\right\rangle_{\Omega_2} - \langle n_\nu\partial_\nu\chi_\mu, \xi_\mu\rangle_{\partial\Omega_2} + \langle\partial_\nu\chi_\nu, \partial_\mu\xi_\mu\rangle_{\Omega_2} +\\
&\quad - \langle n_\mu\partial_\nu\chi_\nu, \xi_\mu\rangle_{\partial\Omega_2} - \langle\psi/g, \partial_\mu(g\xi_\mu)\rangle_{\Omega_2} + \langle\psi/g, gn_\mu\xi_\mu\rangle_{\partial\Omega_2}\\
&= \langle\partial_\nu\chi_\mu, \partial_\nu\xi_\mu\rangle_{\Omega_2} + 12\left\langle\frac{\chi_\mu}{g}, \frac{\xi_\mu}{g}\right\rangle_{\Omega_2} + \langle\partial_\nu\chi_\nu, \partial_\mu\xi_\mu\rangle_{\Omega_2} - \langle\psi/g, \partial_\mu(g\xi_\mu)\rangle_{\Omega_2} +\\
&\quad + \langle -(X_0)_\mu - \text{div }\chi n_\mu + \psi_0 n_\mu, \xi_\mu\rangle_{\partial\Omega_2}\\
\langle\sigma_3, \phi\rangle_{\Omega_2} &\le \langle\phi/g, \partial_\nu(g\chi_\nu)\rangle_{\Omega_2}
\end{aligned}$$

leads to the variational formulation of the two-dimensional cavitation problem:
Find $\chi \in X_D$ and $\psi \in (\Psi_D)_{\geq 0}$ such that

$$\begin{array}{lll} \forall \xi \in \tilde{X}: & \langle \partial_\nu \chi_\mu, \partial_\nu \xi_\mu \rangle_{\Omega_2} + 12 \left\langle \frac{\chi_\mu}{g}, \frac{\xi_\mu}{g} \right\rangle_{\Omega_2} + \langle \partial_\nu \chi_\nu, \partial_\mu \xi_\mu \rangle_{\Omega_2} + \\ & - \langle \psi/g, \partial_\mu (g \xi_\mu) \rangle_{\Omega_2} - \langle \partial_\nu \chi_\nu, n_\mu \xi_\mu \rangle_{\partial\Omega_2} \\ & = \langle (\kappa + \gamma_c)_\mu, \xi_\mu \rangle_{\Omega_2} + \langle (X_0 - \psi_0 n)_\mu, \xi_\mu \rangle_{\partial\Omega_2} \\ \forall \phi \in \tilde{\Psi}_{\geq 0}: & \langle (\phi - \psi)/g, \partial_\nu (g \chi_\nu) \rangle_{\Omega_2} \\ & \geq \langle \sigma_3, \phi - \psi \rangle_{\Omega_2} . \end{array} \tag{I.66}$$

I.2.4 Reynolds Model

In this section we will expand the approximation of χ (I.56) to the entire domain Ω_2. This approach will lead us to the Reynolds-equation (I.77) – a differential equation for the pressure ψ only. In section I.2.4.1 we formulate the Reynolds model under consideration of cavitation (I.81). In the last section I.2.4.2 we reformulate the Reynolds model for the original pressure p.

We recall the two-dimensional Stokes equations (I.57) and the approximation for χ (I.56):

$$\Delta\chi_\mu - \frac{12}{g^2}\chi_\mu - g\partial_\mu\frac{\psi}{g} = -\kappa_\mu - \gamma_\mu \qquad \text{on } \Omega_2 \tag{I.67}$$

$$\frac{1}{g}\partial_\nu(g\chi_\nu) = \sigma_3 \qquad \text{on } \Omega_2 \tag{I.68}$$

$$\chi_\mu = g\overline{v}_\mu + g^3\rho_\mu \qquad \text{on } \Omega_2 \tag{I.69}$$

$$\psi = \psi_0 \qquad \text{on } \partial\Omega_2 \tag{I.70}$$

$$n_\nu\partial_\nu\chi_\mu = (X_0)_\mu \qquad \text{on } \partial\Omega_2 \tag{I.71}$$

The correction terms γ, σ and ρ are defined in (I.47), (I.50) and (I.56):

$$\begin{aligned}(\gamma)_\mu =&(\gamma_3)_\mu + \frac{12}{g}\overline{v}_\mu = -2\partial_\nu\overline{v}_\mu\partial_\nu g - 2\partial_\nu(\delta v_\mu)\partial_\nu\overline{z} - \overline{v}_\mu\Delta g - \delta v_\mu\Delta\overline{z} + \frac{12}{g}\overline{v}_\mu\\ =&\Delta\overline{v}_\mu g + \Delta\delta v_\mu\overline{z} - \Delta(\overline{v}_\mu g) - \Delta(\delta v_\mu\overline{z}) + \frac{12}{g}\overline{v}_\mu\end{aligned} \tag{I.72}$$

$$\sigma_3 = -\delta v_3 + \delta v_\mu\partial_\mu\overline{z} + 2\overline{v}_\mu\partial_\mu g \tag{I.73}$$

$$\rho_\mu = -\frac{1}{12}\partial_3^2 v_\mu(\overline{\zeta}) = -\frac{1}{12}\partial_3^2 v_\mu(\overline{z}) + gO(\left\|\partial_3^3 v_\mu\right\|_\infty). \tag{I.74}$$

Firstly we modify (I.67):

$$\frac{\chi_\mu}{g} = \frac{g}{12}\Big[\Delta\chi_\mu - g\partial_\mu\frac{\psi}{g} + \kappa_\mu + (\gamma_3)_\mu + \frac{12}{g}\overline{v}_\mu\Big] \tag{I.75}$$

to insert it into (I.68):

$$\begin{aligned}\sigma_3 =&\frac{\partial_\mu g}{g}\chi_\mu + \partial_\mu\chi_\mu = \frac{\partial_\mu g}{g}\chi_\mu + g\partial_\mu\frac{\chi_\mu}{g} + \frac{\chi_\mu}{g}\partial_\mu g\\ =&g\partial_\mu\frac{\chi_\mu}{g} + 2\frac{\partial_\mu g}{g}\chi_\mu\\ =&2\frac{\partial_\mu g}{g}\chi_\mu + g\partial_\mu\left(\frac{g}{12}\Big[\Delta\chi_\mu + \frac{12}{g}\overline{v}_\mu - g\partial_\mu\frac{\psi}{g} + \kappa_\mu + (\gamma_3)_\mu\Big]\right)\end{aligned}$$

$$\begin{aligned}
\Rightarrow \qquad \frac{g}{12}\partial_\mu\left(g^2\partial_\mu\frac{\psi}{g}\right) =& \frac{g}{12}\partial_\mu\left[g\Delta\chi_\mu + 12\overline{v}_\mu + g\kappa_\mu + g(\gamma_3)_\mu\right] + 2\frac{\partial_\mu g}{g}\chi_\mu - \sigma_3 \\
\overset{\text{(I.69), (I.73)}}{=}& \frac{g}{12}\partial_\mu\Big[g\Delta(g\overline{v}_\mu) + g\Delta(g^3\rho_\mu) + 12\overline{v}_\mu + g\kappa_\mu + g(\gamma_3)_\mu\Big] + \\
&+ 2\partial_\mu g\overline{v}_\mu + 2\partial_\mu g g^2\rho_\mu + \delta v_3 - \delta v_\mu\partial_\mu\overline{z} - 2\overline{v}_\mu\partial_\mu g \\
=& \delta v_3 + \frac{g}{12}\partial_\mu\left(g\kappa_\mu\right) + \underbrace{\frac{g}{12}\partial_\mu\Big(g\Delta(g\overline{v}_\mu) + g(\gamma_3)_\mu\Big)}_{=:R_3} + \\
&+ \underbrace{g\partial_\mu\overline{v}_\mu - \delta v_\mu\partial_\mu\overline{z}}_{=:R_1} + \underbrace{\frac{g}{12}\partial_\mu\left(g\Delta(g^3\rho_\mu)\right) + 2\partial_\mu g g^2\rho_\mu}_{=:R_\rho}.
\end{aligned}$$

Neglection of the error-term

$$R_\rho = \frac{g}{12}\partial_\mu(g\Delta(g^3\rho_\mu)) + 2\partial_\mu g g^2\rho_\mu \tag{I.76}$$

leaves the two-dimensional **Reynolds equation**

$$\frac{g}{12}\partial_\mu\Big(g^2\partial_\mu\frac{\psi}{g}\Big) = \delta v_3 + \frac{g}{12}\partial_\nu\left(g\kappa_\nu\right) + R_1 + R_3 \tag{I.77}$$

with the Dirichlet boundary-condition (I.70)

$$\psi = \psi_0 \qquad \text{on } \partial\Omega_2 \tag{I.78}$$

and the correction terms

$$\begin{aligned}
R_1 =& g\partial_\nu\overline{v}_\nu - \delta v_\nu\partial_\nu\overline{z} \\
R_3 =& \frac{g}{12}\partial_\nu\Big(g\Big(\Delta\overline{v}_\nu g + \Delta\delta v_\nu\overline{z} - \Delta(\delta v_\nu\overline{z})\Big)\Big) = \frac{g}{12}\partial_\nu\Big(g((\gamma_3)_\nu + \Delta(\overline{v}_\nu g))\Big).
\end{aligned}$$

To gain the **variational formulation** of the Reynolds problem (I.77) we multiply a test-function $\phi \in \tilde{\Psi}$ *and* the factor $1/g^2$, to apply Green's formula:

$$\begin{aligned}
-\left\langle \delta v_3 + \frac{g}{12}\cdot\partial_\nu\left(g\kappa_\nu\right) + R_1 + R_3, \phi/g^2\right\rangle_{\Omega_2} =& -\frac{1}{12}\left\langle g\partial_\mu(g^2\partial_\mu(\psi/g)), \phi/g^2\right\rangle_{\Omega_2} \\
=& \frac{1}{12}\left\langle g\partial_\mu(\psi/g), g\partial_\mu(\phi/g)\right\rangle_{\Omega_2}
\end{aligned} \tag{I.79}$$

The solution of (I.79) has to fulfill the Dirichlet boundary condition (I.78):

$$\psi \in \Psi_D.$$

I.2.4.1 Reynolds model for cavitation

To pay account for cavitation we have to transform the two-dimensional cavitation problem (I.65) in the same way as the non-cavitational one in the last section. The single steps are adapted under consideration of the changed constant γ_c and the additional term $\partial_\mu\partial_\nu\chi_\nu$ in the impulse-bilance.

Firstly (I.75) is replaced by

$$\frac{\chi_\mu}{g} = \frac{g}{12}\left(\Delta\chi_\mu + \partial_\mu\partial_\nu\chi_\nu + \frac{12}{g}\overline{v}_\mu - g\partial_\mu\frac{\psi}{g} + \kappa_\mu + (\gamma_{3c})_\mu\right) \tag{I.80}$$

and the following insertion into the inequality of (I.65) $\frac{1}{g}\partial_\nu(g\chi_\nu) \geq \sigma_3$ is extended by additional terms:

$$\begin{aligned}
\sigma_3 \leq& 2\partial_\mu g\frac{\chi_\mu}{g} + g\partial_\mu\Big[\frac{g}{12}\left(\Delta\chi_\mu + \partial_\mu\partial_\nu\chi_\nu + \frac{12}{g}\overline{v}_\mu - g\partial_\mu\frac{\psi}{g} + \kappa_\mu + (\gamma_{3c})_\mu\right)\Big] \\
\overset{(I.69)}{=}& 2\partial_\mu g\left(\overline{v}_\mu + g^2\rho_\mu\right) + \frac{g}{12}\partial_\mu\Big[g\Delta(g\overline{v}_\mu) + g\Delta(g^3\rho_\mu) + g\partial_\mu\partial_\nu(g\overline{v}_\nu) + \\
&+ g\partial_\mu\partial_\nu(g^3\rho_\nu) + 12\overline{v}_\mu - g^2\partial_\mu\frac{\psi}{g} + g\kappa_\mu + g(\gamma_{3c})_\mu\Big]
\end{aligned}$$

$$\begin{aligned}
\overset{(I.73)}{\Rightarrow}\quad \frac{g}{12}\partial_\mu\left(g^2\partial_\mu\frac{\psi}{g}\right) \leq& 2\partial_\mu g\overline{v}_\mu + \underbrace{\frac{g}{12}\partial_\mu\Big[g\Delta(g\overline{v}_\mu) + g\partial_\mu\partial_\nu(g\overline{v}_\nu) + g(\gamma_{3c})_\mu\Big]}_{=:R_{3c}} + \\
&+ \underbrace{g\partial_\mu\overline{v}_\mu - \delta v_\mu\partial_\mu\overline{z}}_{=R_1} + \frac{g}{12}\partial_\mu(g\kappa_\mu) + \delta v_3 - 2\overline{v}_\mu\partial_\mu g \\
&+ \underbrace{2\partial_\mu g g^2\rho_\mu + \frac{g}{12}\partial_\mu\Big[g\Delta(g^3\rho_\mu) + g\partial_\mu\partial_\nu(g^3\rho_\nu)\Big]}_{=:R_{\rho c}}
\end{aligned}$$

to achieve the **Reynolds inequality** for cavitation:

$$\frac{g}{12}\partial_\mu\left(g\partial_\mu\frac{\psi}{g}\right) \leq \delta v_3 + \frac{g}{12}\partial_\nu\left(g\kappa_\nu\right) + R_1 + R_{3c} \tag{I.81}$$

with the modified constants:

$$\begin{aligned}
R_{3c} =& \frac{g}{12}\partial_\mu\Big[g\Delta(g\overline{v}_\mu) + g\partial_\mu\partial_\nu(g\overline{v}_\nu) + g(\gamma_{3c})_\mu\Big] \\
\overset{(I.61)}{=}& \frac{g}{12}\partial_\mu\Big[g\Delta(g\overline{v}_\mu) + g\partial_\mu\partial_\nu(g\overline{v}_\nu) + g(\gamma_3)_\mu + g\partial_\mu\partial_\nu(\overline{v}_\nu g + \delta v_\nu\overline{z}) + \\
&- g(\partial_\mu\partial_\nu\overline{v}_\nu g + \partial_\mu\partial_\nu\delta v_\nu\overline{z}) - g^2\partial_\mu\frac{\delta v_3}{g}\Big] \\
=& R_3 + \frac{g}{12}\partial_\mu\Big[2g\partial_\mu\partial_\nu(g\overline{v}_\nu) + g\partial_\mu\partial_\nu(\delta v_\nu\overline{z}) - g(\partial_\mu\partial_\nu\overline{v}_\nu g + \partial_\mu\partial_\nu\delta v_\nu\overline{z}) - g^2\partial_\mu\frac{\delta v_3}{g}\Big] \\
R_{\rho c} =& R_\rho + \frac{g}{12}\partial_\mu\Big[g\partial_\mu\partial_\nu(g^3\rho_\nu)\Big]
\end{aligned}$$

We remark, that the solution of (I.81) ψ must fulfill

$$\psi \in (\Psi_D)_{\geq 0}.$$

Furthermore ψ must vanish, if there does not hold equality in (I.81).

The **variational formulation of the Reynolds problem with cavitation** is achieved from (I.81) by multiplication with a test-function $\phi \in \tilde{\Psi}_{\geq 0}$ and the factor $1/g^2$ and the use of Green's formula:

$$\begin{aligned} -\left\langle \delta v_3 + \frac{g}{12}\partial_\nu(g\kappa_\nu) + R_{3c} + R_1, \phi/g^2 \right\rangle_{\Omega_2} \leq & -\frac{1}{12}\left\langle g\partial_\mu(g^2\partial_\mu(\psi/g)), \phi/g^2 \right\rangle_{\Omega_2} \\ = & \frac{1}{12}\left\langle g\partial_\mu(\psi/g), g\partial_\mu(\phi/g) \right\rangle_{\Omega_2} \end{aligned}$$

So we achieved the variational problem
Find $\psi \in (\Psi_D)_{\geq 0}$ such that for all $\phi \in \tilde{\Psi}_{\geq 0}$:

$$\frac{1}{12}\left\langle g\partial_\mu\frac{\phi-\psi}{g}, g\partial_\mu\frac{\psi}{g} \right\rangle_{\Omega_2} \geq -\left\langle \frac{\phi-\psi}{g^2}, \delta v_3 + \frac{g}{12}\partial_\mu(g\kappa_\mu) + R_{3c} + R_1 \right\rangle_{\Omega_2}. \tag{I.82}$$

I.2.4.2 Three-dimensional Reynolds Equation

The two-dimensional Reynolds Equation (I.77) is a differential equation for a two-dimensional pressure ψ – i. e. force per length. To transform this pressure to one with the original physical unit – i. e. force per area – we substitute by using (A.4)

$$\psi(x_1, x_2) = g(x_1, x_2)\overline{p}(x_1, x_2) + g^3 O(\left\|\partial_3^2 p\right\|_\infty). \tag{I.83}$$

Insertion of this expression without the $O(\|\partial_3^2 p\|_\infty)$-term into (I.77) yields

$$\begin{aligned} \delta v_3 + \frac{g}{12}\partial_\nu\left(g\kappa_\nu\right) + R_1 + R_3 = & \frac{g}{12}\partial_\mu(g^2\partial_\mu\overline{p}) \\ = & \frac{1}{12}\partial_\mu\left(g^3\partial_\mu\overline{p}\right) - \frac{g^2}{12}\partial_\mu g\partial_\mu\overline{p} \\ \Rightarrow \qquad \frac{1}{12}\partial_\mu\left(g^3\partial_\mu\overline{p}\right) = & \delta v_3 + R. \end{aligned}$$

This equation has the form of the classical Reynolds-equation as it can be found, e. g. in Hansbo and Nielsson [2010], Sahlin [2005], Lin and Bogy [2001] or Spurk [1989].

I.2.5 Coupling of different Fluid Models

In this section we discuss, how to transform the values of pressure (p, ψ) and velocity (v, χ) from one of the three models (2- and 3-dimensional Stokes model and Reynolds-model) to the next coarser or accurater one respectively. The rules for transformation are given in (I.84) and (I.85) (pressure) and (I.87), (I.89) and (I.90) (velocity).

Our initial problem is the Stokes equation (I.29) that models the velocity- and pressure-fields v_i and p on the three-dimensional domain $\Omega_3 \subset \mathbb{R}^3$.
In section I.2.3 we reduced this three-dimensional problem for a narrow domain Ω_3 – as scatched in figure I.3 – to the two-dimensional Stokes equation (I.57), which models the two-dimensional velocity χ_ν and the pressure ψ on a two-dimensional domain $\Omega_2 \subset \mathbb{R}^2$.
In section I.2.4 this problem is reduced even more to the Reynolds equation (I.77), which is a two-dimensional problem as well, but only for the pressure ψ. Of course we want to use the more simple models (i. e. the two-dimensional ones or even one avoiding the velocity-field) whenever this is possible, or if we need fast results.
Therefor it is necessary to couple the different models on the interfaces of different parts of the domain (figure I.4).
Furthermore a transformation on one complete partition of the domain is needed, if the result of the coarser model is used as initial guess for the more accurate one.

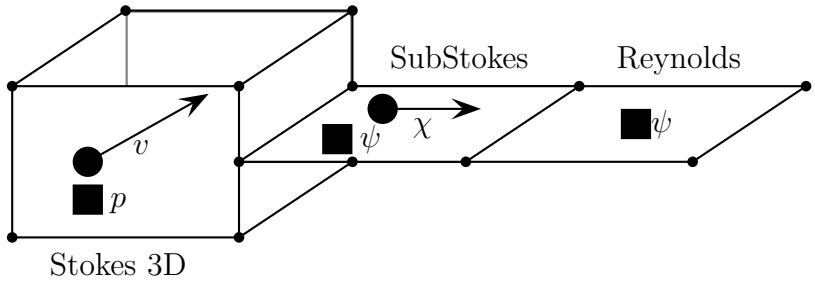

Figure I.4: Velocity- and pressure-fields of the different fluid models.

As one can assume, the way from a more accurate model to a coarser one is easier than the opposite direction:

- The transformation of the pressure ψ of the two-dimensional models – i. e. 2D Stokes and the Reynolds-model is obvious:

$$\psi_{\text{Reynolds}}(x_1, x_2) = \psi_{\text{Stokes}}(x_1, x_2).$$

- The pressure-transformation between the 2D- and 3D-models is given by relation

(I.45):

$$\psi(x_1, x_2) = \int_{z_0(x_1,x_2)}^{z_1(x_1,x_2)} p(x_1, x_2, x_3) dx_3 \tag{I.84}$$

and the opposite direction via the approximation (A.5) (with $p = \partial_z f$):

$$p(x_1, x_2, x_3) = \frac{\psi(x_1, x_2)}{g(x_1, x_2)} + \frac{g}{2}\left(\frac{(x_3 - z_0)^2}{g^2}\partial_3 p(s) - \frac{(z_1 - x_3)^2}{g^2}\partial_3 p(r)\right). \tag{I.85}$$

- The generation of a velocity field χ_ν out of the pressure field ψ of a R-model is given by (I.75), where we replace $\Delta\chi_\mu$ with the help of (I.69) (under neglection of the error term $g^3\rho$):

$$\chi_\mu = g\overline{v}_\mu + \frac{g^2}{12}\left[\Delta\left(g\overline{v}_\mu\right) - g\partial_\mu\frac{\psi}{g} + \kappa_\mu + (\gamma_3)_\mu\right] \tag{I.86}$$

- The transformation for the x_1- and x_2-component of the velocity is given by (I.44):

$$\chi_\mu(x_1, x_2) = \int_{z_0(x_1,x_2)}^{z_1(x_1,x_2)} v_\mu(x_1, x_2, x_3) dx_3. \tag{I.87}$$

For the opposite direction we write the velocity v as linear combination of the boundary-values v_0 in (I.39) and one two-dimensional field $w(x_1, x_2)$, such that the boundary condition $v = v_0$ on Γ_v is fulfilled:

$$\begin{aligned} v_\mu(x_1, x_2, x_3) = &\frac{z_1 - x_3}{g} v_\mu(x_1, x_2, z_0) + \frac{x_3 - z_0}{g} v_\mu(x_1, x_2, z_1) + \\ &+ \frac{(x_3 - z_0)(z_1 - x_3)}{g^2} w_\mu(x_1, x_2) \end{aligned} \tag{I.88}$$

Now $w_\mu(x_1, x_2)$ has to be determined such that the velocity-approximation (I.88) ful-

fills (I.87) for given $\chi_\mu(x_1, x_2)$ and boundary-conditions $v_\mu(x_1, x_2, z_0)$, $v_\mu(x_1, x_2, z_1)$:

$$\begin{aligned}
\chi_\mu(x_1, x_2) =& \int_{z_0}^{z_1} \Big[\frac{z_1 - x_3}{g} v_\mu(x_1, x_2, z_0) + \frac{x_3 - z_0}{g} v_\mu(x_1, x_2, z_1) + \\
&+ \frac{(x_3 - z_0)(z_1 - x_3)}{g^2} w_\mu(x_1, x_2) \Big] dx_3 \\
=& \frac{g}{2} \left(v_\mu(x_1, x_2, z_0) + v_\mu(x_1, x_2, z_1) \right) + \frac{g}{6} w_\mu(x_1, x_2) \\
=& g\overline{v}_\mu + \frac{g}{6} w_\mu(x_1, x_2) \\
\Rightarrow \quad v_\mu(x_1, x_2, x_3) =& \frac{z_1 - x_3}{g} v_\mu(z_0) + \frac{x_3 - z_0}{g} v_\mu(z_1) + \frac{(x_3 - z_0)(z_1 - x_3)}{g^2} \frac{6}{g} (\chi_\mu - g\overline{v}_\mu) \\
=& \frac{z_1 - z_0 + z_0}{g} v_\mu(z_0) + \frac{x_3}{g} (v_\mu(z_1) - v_\mu(z_0)) + \frac{-z_0}{g} v_\mu(z_1) + \\
&+ \frac{6(x_3 - z_0)(z_1 - x_3)}{g^3} (\chi_\mu - g\overline{v}_\mu) \\
=& v_\mu(z_0) + \frac{x_3 - z_0}{g} \delta v_\mu + \frac{6(x_3 - z_0)(z_1 - x_3)}{g^3} (\chi_\mu - g\overline{v}_\mu) \qquad \text{(I.89)}
\end{aligned}$$

- Finally we have to generate the vertical velocity-component $v_3(x_1, x_2, x_3)$ out of the plane data (χ_ν, ψ).
  Therefor we use the solution χ_3 of the Laplace-equation (I.54). The same treatment as that of χ_μ $(\mu = 1; 2)$ leads to an equation analogue to (I.89):

$$v_3(x_1, x_2, x_3) = v_3(z_0) + \frac{x_3 - z_0}{g} \delta v_3 + \frac{6(x_3 - z_0)(z_1 - x_3)}{g^3} (\chi_3 - g\overline{v}_3). \qquad \text{(I.90)}$$

II

Mathematics

II.1 Hilbert Spaces

This section gives some basic definitions and theorems about Functional Analysis, following Dobrowolski [2006] and Brezis [2010]. In the beginning we subsume general properties of Hilbert spaces. In section II.1.1 we examine saddle point problems as they arise in the Stokes models from an abstract point of view. In sections II.1.2 and II.1.3 we summarize basic definitions and theorems about Hölder- and Sobolev spaces that are needed for the weak formulations of our problems. In section II.1.4 we introduce the Reynolds scalar product (II.9) on the Sobolev space $H^1(\Omega)$ to adapt the general Hilbert theory to the concrete fluid-dynamical problems.

Definition II.1 (Scalar product)
A mapping

$$\langle \cdot, \cdot \rangle : \; X \times X \to \mathbb{R}$$

is called **scalar product**, if

- $\langle \cdot, \cdot \rangle$ is linear in the first argument:

$$\forall \lambda \in \mathbb{R},\; x, y, z \in X : \; \langle \lambda x + y, z \rangle = \lambda \langle x, z \rangle + \langle y, z \rangle .$$

- $\langle \cdot, \cdot \rangle$ is symmetric:

$$\forall x, y \in X : \; \langle x, y \rangle = \langle y, x \rangle .$$

- $\langle \cdot, \cdot \rangle$ is positive definite:

$$\forall x \in X \setminus \{0\} : \; \langle x, x \rangle > 0.$$

Lemma II.2 (Cauchy-Schwarz-inequality)
In X with scalar product $\langle \cdot, \cdot \rangle$ there holds

$$| \langle x, y \rangle |^2 \leq \langle x, x \rangle \langle y, y \rangle .$$

Lemma II.3
$\|x\| := \sqrt{\langle x, x \rangle}$ defines a norm on X, i. e.

- $\forall x \in X, \lambda \in \mathbb{R}: \ \|\lambda x\| = |\lambda| \, \|x\|$,
- $\forall x \in X \setminus \{0\}: \ \|x\| > 0$,
- $\forall x, y \in X: \ \|x + y\| \leq \|x\| + \|y\|$.

$\|\cdot\|$ is called induced norm.

Definition II.4 (Hilbert space)
If X is complete (with respect to the induced norm), it is called **Hilbert space**.

Theorem II.5 (Representation Theorem of Riesz)
For any continuous linear form

$$f: \ V \to \mathbb{R}$$

on the Hilbert space V there exists one and only one $v_f \in V$ such that

$$\forall v \in V: \quad f(v) = \langle v_f, v \rangle .$$

Corollary II.6
For any continuous bilinearform

$$b: \ U \times V \to \mathbb{R}$$

on the Hilbert spaces U and V there exists one and only one linear and continuous mapping

$$B: \ U \to V$$

such that for any $(u, v) \in U \times V$ there holds

$$b(u, v) = \langle Bu, v \rangle .$$

Proof. For any $u \in U$ $b(u, \cdot)$ is linear in its second argument. Following theorem II.5, for every $u \in U$ there exits one unique $v_u \in V$, such that for any $v \in V$

$$b(u, v) = \langle v_u, v \rangle .$$

Now we show, that the mapping $B : u \to v_u$ has the requested properties:

- B is linear: for $u, \overline{u} \in U$ and $\lambda \in \mathbb{R}$ it is

  $$\forall v \in V: \ \langle v_u + \lambda v_{\overline{u}}, v \rangle = \langle v_u, v \rangle + \lambda \langle v_{\overline{u}}, v \rangle = b(u, v) + \lambda b(\overline{u}, v) = b(u + \lambda \overline{u}, v)$$

  and hence (and because of the uniqueness of v_u) $v_{u+\lambda\overline{u}} = v_u + \lambda v_{\overline{u}}$.

- The continuity of B is a consequence of that of b:

$$\|Bu\|^2 = \|v_u\|^2 = \langle v_u, v_u \rangle = b(u, v_u) \leq C_b \|u\| \|v_u\| \;\Rightarrow\; \|Bu\| \leq C_b \|u\| .$$

□

Theorem II.7
If $A : V \to V$ is a symmetric, injective operator, its inverse A^{-1} is symmetric too.

Proof. $\forall v, w \in V : \; \langle A^{-1}v, w \rangle = \langle A^{-1}v, A(A^{-1}w) \rangle \overset{A \text{ symm.}}{=} \langle A(A^{-1}v), A^{-1}w \rangle = \langle v, A^{-1}w \rangle .$
□

Theorem II.8
For an operator

$$B : V \to U$$

there exists the **adjoint Operator**

$$B^* : U \to V$$

such that for any $v \in V$ and $u \in U$ there holds

$$\langle Bv, u \rangle = \langle v, B^*u \rangle .$$

Theorem II.9 (Open Range Theorem)
If X and Y are complete spaces and

$$L : X \to Y$$

is continuous and surjective, then L is open, i. e. the image $L(A)$ of any open subset $A \subset X$ is open. Consequently, if L is injective additionally, L is an isomorphism.

Proof. See Dobrowolski [2006]. □

Definition II.10 (Projection)
For a convex, closed subset K of V and $x \in V$ we call $p \in K$ with

$$\|x - p\| = \inf_{y \in K} \|x - y\|$$

projection of x on K and write $p = P_K(x)$.

Theorem II.11
For a convex, closed subset $K \subset V$ and $x \in V$, $P_K(x)$ is well defined.

Proof. Because of $\|x - y\| \geq 0$, there holds

$$m := \inf_{y \in K} \|x - y\| \geq 0$$

and there exists a sequence $(y_l)_{l \in \mathbb{N}} \subset K$ with

$$\|y_l - x\| \to m \; l \to \infty.$$

(y_l) is a Cauchy-sequence:

$$\|y_l - y_{l+\nu}\| \leq \|y_l - x\| + \|x - y_{l+\nu}\| \to 0 \; (l \to \infty),$$

thus, considering the closedness of K, there exists $y \in K$ with $y_l \to y$ $(l \to \infty)$ and

$$\|y - x\| = \lim_{l \to \infty} y_l - x = m.$$

Let now be $y \in K$ and $z \in K$ with $\|y - x\| = \|z - x\| = 0$. Because K is convex, for $a = (y + z)/2 \in K$ we have

$$\|x - a\| = \frac{1}{2} \|x - y + x - z\| \leq \frac{1}{2} \|x - y\| + \frac{1}{2} \|x - z\| = m$$

and thus

$$\begin{aligned}
\frac{1}{4} \|y - z\|^2 = \|y - a\|^2 &= \|y - x\|^2 + \|x - a\|^2 + 2 \langle y - x, x - a \rangle \\
&= m^2 + m^2 - \langle y - x, z - x + y - x \rangle \\
&= m^2 - \langle y - x, z - x \rangle \\
&= m^2 - \langle y - z, z - x \rangle - \langle z - x, z - x \rangle \\
&= \frac{1}{2} \left(- \|y - z + z - x\|^2 + \|y - z\|^2 + \|z - x\|^2 \right) \\
&= - \frac{1}{2} m^2 + \frac{1}{2} \|y - z\|^2 + \frac{1}{2} m^2 = \frac{1}{2} \|y - z\|^2
\end{aligned}$$

leading to $y = z$, the uniqueness of $P_K(x)$. □

Theorem II.12
For a convex, closed subset $K \subset V$ and $x \in V$ there holds

$$p = P_K(x) \quad \Leftrightarrow \quad \forall y \in K: \ \langle y - p, p - x \rangle \geq 0.$$

Proof. Again we set $m := \inf_{y \in K} \|y - x\|$.
For the direction ($\Rightarrow$) let $\|x - p\| = m$ and assume $y \in K$ with:

$$\begin{aligned} & 0 > \langle y - p, p - x \rangle = \langle y - x, p - x \rangle - \|p - x\|^2 \\ \Rightarrow \qquad & m^2 > \langle y - x, p - x \rangle = -\frac{1}{2} \|y - x - p + x\|^2 + \frac{1}{2} \underbrace{\|y - x\|^2}_{\geq m^2} + \frac{1}{2} \|p - x\|^2 \\ & \geq m^2 \quad \lightning \end{aligned}$$

For the opposite direction ($\Leftarrow$) we have $\langle y - p, p - x \rangle \geq 0$ and check the projection condition for an arbitrary $y \in K$:

$$\begin{aligned} \|y - x\|^2 &= \langle y - p + p - x, y - p + p - x \rangle \\ &= \|y - p\|^2 + \|p - x\|^2 + 2 \langle y - p, p - x \rangle \\ &\geq \|y - p\|^2 + \|p - x\|^2 \\ &\geq \|p - x\|^2 \end{aligned}$$

□

II.1.1 Saddle Point Problems

This section gives a short and abstract overview over saddle point problems, as they arise in the weak formulation of the different Stokes models. Basically we follow Braess [1997] and Girault and Raviart [1979]. Section II.1.1.1 also introduces a stabilisation of the general saddle point problem.

Let H and V Hilbert spaces, a and b two continuous bilinearforms

$$\begin{aligned} a : V \times V &\to \mathbb{R} \\ b : V \times H &\to \mathbb{R} \end{aligned}$$

and $f \in V$, $g \in H$ elements in these spaces.
In this section we examine the saddle point problem: Find $u \in V$ and $\lambda \in H$ with

$$\begin{aligned} \forall w \in V: \qquad & a(u, w) - b(w, \lambda) = \langle f, w \rangle \\ \forall \mu \in H: \qquad & b(u, \mu) = \langle g, \mu \rangle . \end{aligned} \tag{II.1}$$

Crucial for solvability and stability of problem (II.1) is

Theorem II.13 (Brezzi)
The linear mapping

$$L:\ (u,\lambda) \to (f,g),$$

defined by (II.1) is an isomorphism (i. e. L is continuous and L^{-1} exists and is continuous), if and only if the following conditions hold:

- a is elliptic on $U = \{v \in V |\ \forall \mu \in H:\ b(v,\mu) = 0\}$:

$$\exists \alpha > 0:\ \forall v \in U:\ a(v,v) \geq \alpha \|v\|^2 \tag{II.2}$$

- b fulfills the inf-sup-condition:

$$\exists \beta > 0:\ \inf_{\mu \in H} \sup_{v \in V} \frac{b(v,\mu)}{\|v\|\,\|\mu\|} \geq \beta \tag{II.3}$$

Proof. See Girault and Raviart [1979]. □

In the following we want to write the bilinear forms with the help of a scalar product, therefor, we employ corollary II.6, that gives the existence of $B:\ H \to V, \quad A:\ V \to V$, such that

$$\forall v,w \in V,\ q \in H:\ b(w,q) = \langle Bq, w\rangle\,; \quad a(v,w) = \langle Av, w\rangle\,. \tag{II.4}$$

Corollary II.14
Under the assumptions of theorem II.13 the **Schur-complement** of (II.1)

$$S = B^* A^{-1} B:\ H \to H$$

exists and is an H-elliptic isomorphism.

Proof. For an arbitrary $\mu \in H$, we set $w := A^{-1}B\mu$, this leads to

$$\begin{aligned}\langle S\mu, \mu\rangle &= \left\langle B^*A^{-1}B\mu, \mu\right\rangle = \left\langle A^{-1}B\mu, B\mu\right\rangle \\ &= \langle w, Aw\rangle \geq \alpha \|w\|^2 \geq \frac{\alpha}{\|A\|^2}\|B\mu\|^2\end{aligned}$$

and with the help of (II.3)

$$\beta\|\mu\| \leq \sup_{v\in V} \frac{b(v,\mu)}{\|v\|} = \sup_{v\in V} \frac{\langle v, B\mu\rangle}{\|v\|} \leq \sup_{v\in V} \frac{\|v\|\,\|B\mu\|}{\|v\|} = \|B\mu\|$$

we achieve the ellipticity of S:

$$\langle S\mu, \mu\rangle \geq \frac{\alpha\beta^2}{\|A\|^2} \|\mu\|^2 .$$

Finally, according the open range theorem II.9 continuity of S is sufficiant to show that S is an isomorphism. This is a consequence of the continuity of A^{-1}, B^* and B: For any $\mu \in H$, there holds

$$\|S\mu\| \leq \|B^*\| \left\|A^{-1}\right\| \|B\| \|\mu\| .$$

□

II.1.1.1 Regularisation of Saddle Point Problems

Following Girault and Raviart [1979] and Becker [1995] we want to solve a regularised adaption of problem (II.1). Therefor we introduce the continuous, symmetric bilinear form

$$c : H \times H \to \mathbb{R}, \quad c(\mu, \nu) = \langle C\mu, \nu\rangle$$

and $\chi \in H$, to state the **regularised problem**:
Find $u^\varepsilon \in V$ and $\lambda^\varepsilon \in H$ such that

$$\begin{array}{rll} \forall v \in V : & a(u^\varepsilon, v) - b(v, \lambda^\varepsilon) = & \langle f, v\rangle \\ \forall \mu \in H : & b(u^\varepsilon, \mu) + \varepsilon c(\lambda^\varepsilon, \mu) = & \langle g, \mu\rangle \end{array} . \tag{II.5}$$

Theorem II.15
If the inf-sup-condition (II.3) for b holds and if c is H-elliptic:

$$\exists \gamma > 0 : \quad \forall \mu \in H : \quad c(\mu, \mu) \geq \gamma \|\mu\|^2$$

and

$$\exists \alpha_c > 0 : \quad \forall v \in V : \quad a(v, v) + \left\langle v, BC^{-1}B^* v\right\rangle \geq \alpha_c \|v\|^2 ,$$

then the regularised and the non-regularised problem are uniquely solvable and for sufficiantly small $\varepsilon > 0$ there holds the estimate

$$\|u - u^\varepsilon\| + \|\lambda - \lambda^\varepsilon\| \leq K\varepsilon \left(\|f\| + \|g\|\right)$$

with a constant K only depending on $\alpha_c, \beta, \|a\|, \|b\|, \|c\|$.

Proof. See Girault and Raviart [1979]. □

The process of stabilisation is discussed in more detail in section III.2.3.

II.1.2 Hölder Spaces

To define the Sobolev Spaces in the following section II.1.3, we need to define Hölder spaces, that contain smooth functions. We do this following Dobrowolski [2006].

In this section $\Omega \subset \mathbb{R}^d$ denotes an open, connected and bounded domain.

Definition II.16
We call $\Omega_0 \subset \Omega$ **strongly included** in Ω and write

$$\Omega_0 \subset\subset \Omega,$$

if $\overline{\Omega_0}$ is compact and $\overline{\Omega_0} \subset \Omega$.

Definition II.17
The **support of a function** $\phi : \Omega \to \mathbb{R}$ is the set

$$\text{supp}(\phi) := \overline{\{x \in \Omega | \phi(x) \neq 0\}}.$$

The following definition declares some function spaces, we will need in the following sections:

Definition II.18

- $C^0(\Omega)$ denotes the **space of continuous functions** on Ω.
- The space of m times **continuously differentiable functions** is written as

  $$C^m(\Omega) = \left\{\phi : \Omega \to \mathbb{R} \middle| \forall |\alpha| \leq m : \partial_\alpha f \in C^0(\Omega)\right\}$$

  and

  $$C^m(\overline{\Omega}) = \left\{\phi : \Omega \to \mathbb{R} \middle| \forall |\alpha| \leq m : \ \partial_\alpha \phi \text{ bounded and uniformly continuous}\right\}.$$

- We call

  $$C_0^m(\Omega) = \{\phi \in C^m(\Omega) | \text{supp}(\phi) \subset\subset \Omega\}$$

  functions with compact support on Ω.
- Analogue for $\Gamma_D \subset \partial\Omega$ we define

  $$C^m_{0,\Gamma_D}(\Omega) := \{\phi \in C^m(\Omega) | \text{dist}(\text{supp}(\phi), \Gamma_D) > 0\}.$$

For $\phi \in C^m(\overline{\Omega})$ we define

$$\|\phi\|_{m,\infty} := \max_{|\alpha|\leq m} \sup_{x\in\Omega} |\partial_\alpha \phi(x)|$$

Definition II.19

- We call $\phi : \Omega \to \mathbb{R}$ **Hölder continuous** (with exponent α), if $0 < \alpha < 1$ and $\exists c : \forall x, y \in \Omega : \ |\phi(x) - \phi(y)| \leq c|x - y|^\alpha$.
  (For $\alpha = 1$ we have Lipschitz continuity.)
- For $0 < \alpha \leq 1$: we define

  $$C^{m,\alpha}(\overline{\Omega}) := \{\phi \in C^m(\overline{\Omega}) | \forall |\beta| \leq m : \partial_\beta \phi \text{ is Hölder continuous with exponent } \alpha\}$$

  and the norm on $C^{m,\alpha}(\overline{\Omega})$:

  $$\|\phi\|_{C^{m,\alpha}} := \|\phi\|_{m,\infty} + \max_{|\gamma|=m} [\partial_\gamma \phi]_{C^\alpha}$$

  with $[\phi]_{C^\alpha} := \sup_{x\neq y} \frac{|\phi(x)-\phi(y)|}{|x-y|^\alpha}$ and for $\alpha = 0$:

  $$C^{m,0}(\overline{\Omega}) := C^m(\overline{\Omega}).$$

Theorem II.20
$\left(C^{m,\alpha}(\overline{\Omega}), \|\cdot\|_{C^{m,\alpha}}\right)$ is a Banach space.

Theorem II.21
For $m \in \mathbb{N}_0$ and $0 \leq \alpha < \beta \leq 1$ there exists a compact embedding

$$C^{m,\beta} \to C^{m,\alpha}.$$

II.1.3 Sobolev Spaces

Here we give a short overview over Sobolev Spaces. Again we follow Dobrowolski [2006]. We omit an introduction into basics about Lebesgue integration theory and weak derivatives and refer to literature like Dobrowolski [2006].

Initially we introduce the weak derivative:

Definition II.22 (Weak derivative)
A function $u \in L^p(\Omega)$ has the **weak derivative** $\partial^\alpha u \in L^p(\Omega)$, if

$$\forall \phi \in C_0^\infty(\Omega): \quad \int_\Omega \partial^\alpha u \phi dx = (-1)^{|\alpha|} \int_\Omega u \partial^\alpha \phi dx.$$

($\alpha = (\alpha_1, \ldots, \alpha_d) \in \mathbb{N}_0^d$ is a multiindex with $\partial^\alpha = \partial_1^{\alpha_1} \ldots \partial_d^{\alpha_d}$ and $|\alpha| = \alpha_1 + \ldots + \alpha_d$.)

$\partial^\alpha u$ is well defined and unique. Furthermore for differentiable functions it coinsides with the classical derivative, thus we use the same notation for both.
With this generalisation of the derivative, we can state a result of the classical analysis under weaker assumptions:

Theorem II.23
A Lipschitz continuous function $u \in C^{0,1}(\overline{\Omega})$ is weakly differentiable and there holds

$$\|\partial_i u\|_\infty \leq \sup_{x \neq y} \frac{|u(x) - u(y)|}{|x - y|}.$$

From now on, we assume Ω to be an open, connected **Lipschitz domain**, i. e. its boundary fulfills certain regularity-requirements:

Definition II.24 (Lipschitz Domain)
$\Omega \subset \mathbb{R}^n$ is called **Lipschitz domain**, if for any boundary point $x_0 \in \partial\Omega$ one can rotate and translate the coordinate system (see the scatch in figure II.1) such that there exits a neighbourhood $U \subset \mathbb{R}^n$ of x_0 and a neighbourhood $W \subset \mathbb{R}^{n-1}$ of the origin $0 \in \mathbb{R}^{n-1}$ and a mapping $h \in C^{0,1}(\overline{W})$ (i. e. h is Lipschitz continuous)

$$h : W \to \mathbb{R}$$

and a constant $r > 0$ with

$$U \cap \Omega = W \times (h(W) + (0; r)); \quad U \cap \Omega^C = W \times (h(W) + (-r; 0)); \quad U \cap \partial\Omega = W \times h(W).$$

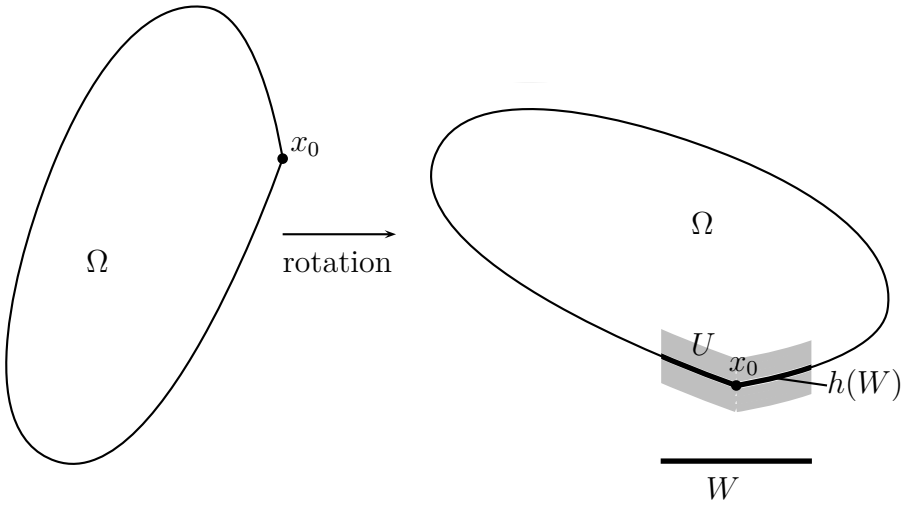

Figure II.1: Parametrisation of a Lipschitz-domain.

After we introduced Lipschitz-domains, we can use them for

Definition II.25 (Sobolev-space)
The space

$$H^{m,p}(\Omega) = \{\phi \in L^p(\Omega) | \forall |\alpha| \leq m \exists \partial^\alpha \phi \in L^p(\Omega)\}$$

with the norm

$$\|\phi\|_{m,p;\Omega} = \left(\sum_{|\alpha| \leq m} \|\partial^\alpha u\|_p^p \right)^{1/p}$$

is called Sobolev-space.
Additionally we define

$$H_0^{m,p} := \left\{ u \in H^{m,p}(\Omega) | \exists u_k \in C_0^\infty(\Omega),\ u_k \underset{H^{m,p}}{\to} u \right\}$$

and for $\Gamma_D \subset \partial\Omega$

$$H_{0,\Gamma_D}^{m,p}(\Omega) := \left\{ u \in H^{m,p}(\Omega) | \exists u_k \in C_{0,\Gamma_D}^\infty(\Omega),\ u_k \underset{H^{m,p}}{\to} u \right\}.$$

In the following, we omit writing out p for the case $p = 2$

On a part $\Gamma \subset \partial\Omega$ of the boundary of a Lipschitz domain Ω we define the **boundary integral**:

Definition II.26 (Boundary integral)
Let $\Gamma \subset \partial\Omega$ with a partition of the kind

$$\Gamma = \overline{\bigcup_{j\in J} r_j(\{(\xi, h_j(\xi))|\xi \in W_j\})}$$

with

$$W_j \subset \mathbb{R}^{d-1},\ h_j \in C^{0,1}(\overline{W}),\ j \in J$$

and mappings

$$r_j : \mathbb{R}^d \to \mathbb{R}^d,\ j \in J$$

which just rotate and translate the coordinate system (compare definition II.24) and

$$r_j(\{(\xi, h_j(\xi))|\xi \in W_j\}) \cap r_k(\{(\xi, h_k(\xi)|\xi \in W_k\}) = \emptyset \text{ for } j \neq k.$$

For a function

$$\phi : \Gamma \to \mathbb{R}$$

we define the **boundary integral**

$$\int_\Gamma \phi da = \sum_{j\in J} \int_{W_j} \phi\Big(r_j(\xi, h_j(\xi))\Big)\sqrt{1 + (\partial_l h_j(\xi))^2}d\xi.$$

If this integral exists, we call ϕ integrable on Γ.

For the sake of clarity this definition is not as accurate as in Dobrowolski [2006].
After this definition we can state

Theorem II.27 (Trace Theorem)
For a Lipschitz domain $\Omega \subset \mathbb{R}^n$, $1 \leq p < \infty$ and

$$q \begin{cases} = (n-1)\frac{p}{n-p} & ,\ p < n \\ < \infty & ,\ p = n \end{cases}$$

there exists a unique continuous linear operator

$$S :\ H^{1,p}(\Omega) \to L^q(\partial\Omega) \text{ with } Su = u\Big|_{\partial\Omega} \text{ for } u \in C^\infty(\overline{\Omega}).$$

Finaly we collect further theorems regarding Hilbert spaces.

Theorem II.28 (Poincaré inequality)
For $\phi \in H^1_{0,\Gamma_D}(\Omega)$ there holds

$$C_P \left|\phi\right|_1 \geq \left\|\phi\right\|_0 \tag{II.6}$$

with a constant C_P that only depends on the geometry of Ω.

Theorem II.29 (Gauss)
For the function $u_i \in H^1(\Omega)$ there holds

$$\int_\Omega \partial_i u_i dx = \int_{\partial\Omega} n_i u_i da,$$

where n_i denotes the outer normal of the boundary $\partial\Omega$ and da implies the integration on $\partial\Omega$.

Theorem II.30 (Green)
For the two functions $u, v \in H^2(\Omega)$ there holds

$$\int_\Omega \partial_i u \partial_i v dx = -\int_\Omega \partial_i \partial_i u v dx + \int_{\partial\Omega} n_i \partial_i u v da, \tag{II.7}$$

where n_i denotes the outer normal on the boundary of Ω.

Proof.

$$\begin{aligned}
\int_\Omega \left[\partial_i u \partial_i v + \partial_i \partial_i u v\right] dx =& \int_\Omega \left[\frac{1}{2}\Big(\partial_i \partial_i (uv) - \partial_i \partial_i u v - u \partial_i \partial_i v\Big) + \partial_i \partial_i u v\right] dx \\
=& \frac{1}{2}\int_\Omega \left[\partial_i \partial_i (uv) + \partial_i \partial_i u v - u \partial_i \partial_i v\right] dx \\
=& \frac{1}{2}\int_\Omega \partial_i \left[\partial_i (uv) + \partial_i u v - u \partial_i v\right] dx \\
=& \frac{1}{2}\int_{\partial\Omega} n_i \left[\partial_i (uv) + \partial_i u v - u \partial_i v\right] da \qquad \text{(with theorem II.29)} \\
=& \int_{\partial\Omega} n_i \partial_i u v da
\end{aligned}$$

□

Corollary II.31

For two functions $u, v \in H^1_{0,\Gamma}(\Omega)^d$ (with $\Gamma \subset \partial\Omega$) there holds

$$\langle \partial_i u_j, \partial_j v_i \rangle_{L^2(\Omega)} = \langle \partial_j u_j, \partial_i v_i \rangle_{L^2(\Omega)} + \langle \partial_i u_j, n_j v_i \rangle_{L^2(\partial\Omega\setminus\Gamma)} - \langle \partial_j u_j, n_i v_i \rangle_{L^2(\partial\Omega\setminus\Gamma)}. \tag{II.8}$$

Proof.
$C^\infty_{0,\Gamma}(\Omega)$ is dense in $H^1_{0,\Gamma}(\Omega)$, so we can choose a sequence $u^k \in C^\infty_0(\Omega)^d$ $(k \in \mathbb{N})$ with

$$\left\|u^k - u\right\|_{H^1(\Omega)} \underset{k\to\infty}{\longrightarrow} 0.$$

Then we have:

$$\begin{aligned}
&\left|\langle \partial_i u_j, \partial_j v_i\rangle_\Omega - \langle \partial_j u_j, \partial_i v_i\rangle_\Omega - \langle \partial_i u_j, n_j v_i\rangle_{\partial\Omega} + \langle \partial_j u_j, n_i v_i\rangle_{\partial\Omega}\right| \\
=&\Big|\left\langle \partial_i(u_j - u_j^k), \partial_j v_i\right\rangle_\Omega + \left\langle \partial_i u_j^k, \partial_j v_i\right\rangle_\Omega + \\
&\quad - \langle \partial_j u_j, \partial_i v_i\rangle_\Omega - \langle \partial_i u_j, n_j v_i\rangle_{\partial\Omega} + \langle \partial_j u_j, n_i v_i\rangle_{\partial\Omega}\Big| \\
\overset{\text{Green}}{=}&\Big|\left\langle \partial_i(u_j - u_j^k), \partial_j v_i\right\rangle_\Omega - \left\langle \partial_j\partial_i u_j^k, v_i\right\rangle_\Omega + \\
&\qquad + \left\langle \partial_i u_j^k, n_j v_i\right\rangle_{\partial\Omega} - \langle \partial_j u_j, \partial_i v_i\rangle_\Omega - \langle \partial_i u_j, n_j v_i\rangle_{\partial\Omega} + \langle \partial_j u_j, n_i v_i\rangle_{\partial\Omega}\Big| \\
\overset{\text{Green}}{=}&\Big|\left\langle \partial_i(u_j - u_j^k), \partial_j v_i\right\rangle_\Omega + \left\langle \partial_j u_j^k, \partial_i v_i\right\rangle_\Omega + \\
&\quad + \left\langle \partial_i(u_j^k - u_j), n_j v_i\right\rangle_{\partial\Omega} - \left\langle \partial_j u_j^k, n_i v_i\right\rangle_{\partial\Omega} - \langle \partial_j u_j, \partial_i v_i\rangle_\Omega + \langle \partial_j u_j, n_i v_i\rangle_{\partial\Omega}\Big| \\
=&\Big|\left\langle \partial_i(u_j - u_j^k), \partial_j v_i\right\rangle_\Omega + \left\langle \partial_j(u_j^k - u_j), \partial_i v_i\right\rangle_\Omega + \\
&\qquad + \left\langle \partial_i(u_j^k - u_j), n_j v_i\right\rangle_{\partial\Omega} - \left\langle \partial_j(u_j^k - u_j), n_i v_i\right\rangle_{\partial\Omega}\Big| \\
\le&\left|u - u^k\right|_{H^1(\Omega)} |v|_{H^1(\Omega)} + \left\|\partial_j(u_j^k - u_j)\right\|_{L^2(\Omega)} \|\partial_i v_i\|_{L^2(\Omega)} + \\
&+ \left|u^k - u\right|_{H^1(\partial\Omega)} |n\cdot v|_{L^2(\partial\Omega)} + \left\|\partial_j(u_j^k - u_j)\right\|_{L^2(\partial\Omega)} \|n\cdot v\|_{L^2(\partial\Omega)} \underset{k\to\infty}{\longrightarrow} 0
\end{aligned}$$

The norms on the boundary $\partial\Omega$ are estimated with the help of the trace theorem II.27. Because of $u, u^k, v \in H^1_{0,\Gamma}(\Omega)^d$ we can replace $\partial\Omega$ by $\partial\Omega \setminus \Gamma$ and gain (II.8). □

II.1.4 Hilbert meets Reynolds

In this section we specialise the general properties of a Hilbert-space to the scalar product (II.9), given by the bilinearform of the Reynolds-equation (I.79).

We recall the bilinear-form of the Reynolds-equation (I.79) on the function space

$$\Psi = H^1_{0,\Gamma_D}(\Omega) :$$

$$\langle \cdot, \cdot \rangle_R : \Psi \times \Psi \to \mathbb{R}, \quad \langle \phi, \psi \rangle_R = \langle g\partial_\mu(\phi/g), g\partial_\mu(\psi/g) \rangle_{L^2} = \int_\Omega g\partial_\mu \frac{\phi}{g} \cdot g\partial_\mu \frac{\psi}{g} dx. \tag{II.9}$$

To guarantee, that this expression is well-defined, we assume the function $g : \Omega \to \mathbb{R}^{>0}$ to be smooth enough, this is the case for

$$g \in H^1(\Omega).$$

With the help of $\langle \cdot, \cdot \rangle_R$ we define the **Reynolds norm**

$$\|\phi\|_R := \sqrt{\langle \phi, \phi \rangle_R} = \sqrt{\int_\Omega \left(g\partial_\nu \frac{\phi}{g} \right)^2 dx}. \tag{II.10}$$

Initially we proove the equivalence between this norm and the H^1-Norm:

Lemma II.32
If the derivative of the function $g : \Omega \to \mathbb{R}^{>0}$ can be estimated by

$$\left| \frac{\partial_\nu g}{g} \right| \leq \gamma \leq \frac{\alpha}{C_P}$$

with $0 < \alpha < 1$ and C_P the constant occuring in the Poincaré-inequality (II.6), then for $\phi \in H^1_{0,\Gamma_D}(\Omega)$ there holds the estimate

$$\frac{1-\alpha}{C_P(1+C_P)} \|\phi\|_{H^1(\Omega)} \leq \|\phi\|_R \leq \max\{\sqrt{1+2\alpha}; \gamma\} \|\phi\|_{H^1(\Omega)}.$$

Proof.

$$\begin{aligned}
\|\phi\|_R^2 &= \int_\Omega \left(g\partial_\nu \tfrac{\phi}{g}\right)^2 dx \\
&= \int_\Omega \left(\partial_\nu\phi - \tfrac{\partial_\nu g}{g}\phi\right)^2 dx \\
&= |\phi|^2_{H^1(\Omega)} + \left\|\tfrac{\partial_\nu g}{g}\phi\right\|^2_{L^2(\Omega)} - 2\left\langle \partial_\nu\phi, \tfrac{\partial_\nu g}{g}\phi\right\rangle_{L^2(\Omega)} \\
&\geq \left(|\phi|_{H^1(\Omega)} - \left\|\tfrac{\partial_\nu g}{g}\phi\right\|_{L^2(\Omega)}\right)^2 \qquad \text{(Cauchy-Schwarz)} \\
&\geq \left(|\phi|_{H^1(\Omega)} - \left\|\tfrac{\partial_\nu g}{g}\phi\right\|_{L^2(\Omega)}\right)^2 + \quad (\|(\partial_\nu g)/g\phi\|_{L^2} \leq \gamma\|\phi\|_{L^2} \leq \alpha/C_P\|\phi\|_{L^2}) \\
&\quad - \underbrace{\left(\gamma\|\phi\|_{L^2(\Omega)} - \left\|\frac{\partial_\nu g}{g}\phi\right\|_{L^2(\Omega)}\right)}_{\geq 0} \underbrace{\left(2|\phi|_{H^1(\Omega)} - \gamma\|\phi\|_{L^2(\Omega)} - \left\|\frac{\partial_\nu g}{g}\phi\right\|_{L^2(\Omega)}\right)}_{\geq 2|\phi|_{H^1} - 2\gamma\|\phi\|_{L^2} \geq 2\left(|\phi|_{H^1} - \alpha/C_P\|\phi\|_{L^2}\right) \geq 0} \\
&= |\phi|^2_{H^1(\Omega)} + \gamma^2\|\phi\|^2_{L^2(\Omega)} - 2\gamma\|\phi\|_{L^2(\Omega)}|\phi|_{H^1(\Omega)} \\
&= \left(|\phi|_{H^1(\Omega)} - \gamma\|\phi\|_{L^2(\Omega)}\right)^2 \\
&\geq \left(|\phi|_{H^1(\Omega)} - \tfrac{\alpha}{C_P}\|\phi\|_{L^2(\Omega)}\right)^2 \geq \tfrac{(1-\alpha)^2}{C_P^2}|\phi|^2_{H^1(\Omega)} \geq \left(\tfrac{1-\alpha}{C_P(1+C_P)}\|\phi\|_{H^1(\Omega)}\right)^2 \\
\|\phi\|_R^2 &= |\phi|^2_{H^1(\Omega)} + \left\|\tfrac{\partial_\nu g}{g}\phi\right\|^2_{L^2(\Omega)} - 2\left\langle \partial_\nu\phi, \tfrac{\partial_\nu g}{g}\phi\right\rangle_{L^2(\Omega)} \\
&\leq |\phi|^2_{H^1(\Omega)} + \gamma^2\|\phi\|^2_{L^2(\Omega)} + 2\gamma|\phi|_{H^1(\Omega)}\|\phi\|_{L^2(\Omega)} \\
&\overset{\text{(II.6)}}{\leq} |\phi|^2_{H^1(\Omega)} + \gamma^2\|\phi\|^2_{L^2(\Omega)} + 2\gamma C_P|\phi|^2_{H^1(\Omega)} \\
&\leq \max\{1+2\gamma C_P;\gamma^2\}\|\phi\|^2_{H^1(\Omega)} \leq \max\{1+2\alpha;\ \gamma^2\}\|\phi\|^2_{H^1(\Omega)}
\end{aligned}$$

□

Lemma II.33
$(\Psi, \langle\cdot,\cdot\rangle_R)$ is a Hilbert-space.

Proof.

- $\langle\cdot,\cdot\rangle_R$ is obviously linear in each argument and symmetric.
- $\langle\cdot,\cdot\rangle_R$ is positive semi-definite: $\langle\phi,\phi\rangle_R = \|g\partial_\nu(\phi/g)\|^2_{L^2(\Omega)} \geq 0$. To see the (strict) definitness, let $\phi\in\Psi$ with $\langle\phi,\phi\rangle_R = 0$. There follows

$$0 = \langle\phi,\phi\rangle_R = \left\|g\partial_\nu\frac{\phi}{g}\right\|^2_{L^2(\Omega)} \Rightarrow 0 = g\partial_\nu\frac{\phi}{g} \overset{g>0}{\Longrightarrow} 0 = \partial_\nu\frac{\phi}{g}$$
$$\Rightarrow \frac{\phi}{g} = \text{const.} \overset{\phi|_{\Gamma_D}=0}{\Longrightarrow} \phi = 0.$$

- Because of the equivalence of $\|\cdot\|_R$ and $\|\cdot\|_{H^1}$ (lemma II.32) the completness of $(\Psi, \|\cdot\|_R)$ is a consequence of the complteness of $(H^1_{0,\Gamma_D}(\Omega), \|\cdot\|_{H^1})$.

□

II.2 Concrete Hilbert Spaces

In part I we analysed the applicational problems (elasticity, contact and fluid dynamics) from the physicists point of view. In particular we did not care about the function spaces that should contain solutions and test-functions of the different problem statements. In the following we will make up for this. The problem of elastic deformation (section II.2.1) is a well known example application, that is analysed e. g. in Braess [1997]. We show, that the Sobolev space $H^1(\Omega)$ or an appropriate subspace (II.12) contains a stable solution of the deformation problem (II.11). In the case of a contact problem (section II.2.2) we have to constrain these subspaces (II.16) and reduce the problem to a projection onto this space. In section II.2.3 we introduce spaces (II.21)– (II.22), containing the solution of the Stokes equation (II.17), that fulfill the inf-sup-condition (theorem II.13). Crucial is the declaration of a Dirichlet boundary condition for the pressure. In section I.2.2 the pressure-space is restricted, to solve the cavitational Stokes problem (II.25). The stability and existence of a solution in these restricted spaces is reduced to the projection problem (II.31), similar to section II.2.2. These results are transfered to the two-dimensional Stokes- and cavitation-problem in sections II.2.5 and II.2.6. Finally sections II.2.7 and II.2.8 consider the Reynolds problem with and without cavitation. Basically we use the similarity of this problem to the problem of deformation (sections II.2.1 and II.2.2) and techniques of section I.2.2 to declare appropriate spaces for this problem.

II.2.1 Deformation of a solid body

The problem of the deformed solid body is given by (I.17): Find $s \in V_0 \subset V$ such that

$$\forall r \in V_0 : \quad 2\mu \langle \varepsilon_{ij}(s), \varepsilon_{ij}(r) \rangle_\Omega + 2\lambda \langle \varepsilon_{ll}(s), \varepsilon_{jj}(r) \rangle_\Omega = \langle \rho f_i, r_i \rangle_\Omega + \langle \tau_{ij} n_j, r_i \rangle_{\Gamma_\tau} \qquad \text{(II.11)}$$

Here the operator $\varepsilon_{ij}(r) = \frac{1}{2}(\partial_i r_j + \partial_j r_i)$ contains weak derivatives and the scalar products $\langle \cdot, \cdot \rangle$ denote the L^2-product on the indicated domains. As preparation, we formulate

Lemma II.34 (Korn's inequation)
If $\Gamma_0 \subset \partial\Omega$ has a positive $d-1$–dimensional meassure, then the bilinear form $\langle \varepsilon(\cdot), \varepsilon(\cdot) \rangle_{L^2(\Omega)}$ is $H^1_{0,\Gamma_0}(\Omega)$-elliptic:

$$\exists c > 0 : \ \forall r \in H^1_{0,\Gamma_0}(\Omega) : \quad \langle \varepsilon(r), \varepsilon(r) \rangle_{L^2(\Omega)} \geq c \, \|r\|^2_{H^1(\Omega)} .$$

Proof. The proof for $d = 3$ is given in Braess [1997]. □

Theorem II.35
If we choose

$$V = H^1(\Omega) \text{ and } V_0 = H^1_{0,\Gamma_0}(\Omega). \qquad \text{(II.12)}$$

problem (II.11) is well posed.

Proof. At first we define the symmetric bilinearform

$$a : V_0 \times V_0 \to \mathbb{R},\ a(s,r) = 2\mu \left\langle \varepsilon_{ij}(s), \varepsilon_{ij}(r) \right\rangle_\Omega + 2\lambda \left\langle \varepsilon_{ll}(s), \varepsilon_{jj}(r) \right\rangle_\Omega \tag{II.13}$$

and the linear form

$$b : V_0 \to \mathbb{R},\ b(r) = \langle \rho f_i, r_i \rangle_\Omega + \langle \tau_{ij} n_j, r_i \rangle_{\Gamma_\tau} \tag{II.14}$$

and farther, following the representation theorem of Riesz II.5 and corollary II.6, a linear, continuous mapping $A : V_0 \to V_0$ and an element $g \in V_0$ with

$$\forall r, s \in V_0 : \quad a(r,s) = \langle Ar, s \rangle_{H^1(\Omega)}, \quad b(r) = \langle g, r \rangle_{H^1(\Omega)}.$$

With the help of these we can abbreviate (II.11): Find $s \in V_0$ such that

$$\begin{aligned} & \forall r \in V_0 : \ \langle As, r \rangle_{H^1(\Omega)} = \langle g, r \rangle_{H^1(\Omega)} \\ \Leftrightarrow \qquad & As = g \end{aligned}$$

To guarantee a unique solution of this problem we have to show, that A is bijective or equivalently

$$a(r,r) = 0 \Rightarrow r = 0 :$$

This is a conclusion of the V_0-ellipticity of $a(\cdot,\cdot)$, that follows from Lemma II.34 under consideration of $\langle \varepsilon_{ll}, \varepsilon_{jj} \rangle \geq 0$.
Because of the Open range theorem II.9 the continuity of A is sufficiant for A to be an isomorphism and so problem (II.11) is well posed. □

II.2.2 Contact

We consider the contact problem for the elastic solid body (I.23)

$$\forall r \in \Pi(V_0) : \quad a(s, r-s) - b(r-s) \geq 0 \tag{II.15}$$

with the linear mappings (II.13) and (II.14) and the restricted subset of V_0 (I.22):

$$\begin{aligned} \Pi(V_0) &= \left\{ r \in V_0 \middle| P(x + r(x)) = x + r(x),\ x \in \Gamma_C \right\} \\ &= \left\{ r \in V_0 \middle| r(x) \cdot n \leq b \text{ on } x \in \Gamma_C \right\}. \end{aligned} \tag{II.16}$$

$V_0 = H^1_{0,\Gamma_0}(\Omega)$ denotes the same Sobolev space as in section II.2.1.
The vectorfield n and the function b are introduced in section I.1.4 to describe the obstacle. In the case of the simple projection n and b only depend on x, while in the case of the Signorini-projection n and b depend on r too.

Theorem II.36
There exists a unique solution of problem (II.15).

Proof. At first we show, that $\Pi(V_0)$ is convex:
Let $r, t \in \Pi(V_0)$ and $\lambda \in [0;1]$. Because of

$$r \cdot n, t \cdot n \leq b$$

there follows

$$(\lambda r + (1-\lambda)t) \cdot n \leq \lambda b + (1-\lambda)b = b$$

and so $\lambda r + (1-\lambda)t \in \Pi(V_0)$.
In the proof of theorem II.35 we proove the positive definiteness of $a(\cdot,\cdot)$, so we can define a scalar product on $H^1(\Omega)$:

$$\langle u, v \rangle_a := a(u,v) = \langle Au, v \rangle_{H^1(\Omega)}.$$

With this definition problem (II.15) can be transformed

$$\begin{aligned} \forall r \in \Pi(V_0): \quad 0 \leq & a(s, r-s) - b(r-s) = \langle s, r-s \rangle_a - \langle g, r-s \rangle_{H^1(\Omega)} \\ & = \langle s, r-s \rangle_a - \left\langle A^{-1}g, r-s \right\rangle_a = \left\langle s - A^{-1}g, r-s \right\rangle_a \end{aligned}$$

A comparison to theorem II.12 reveals, that s is the projection of $A^{-1}g$ on $\Pi(V_0)$ and thus its existence and uniqueness. □

II.2.3 Stokes Model

The Stokes problem (I.31) can be written as:
Find $v \in V_D$ and $p \in \Pi_D$ such that

$$\begin{array}{lrcl} \forall w \in \tilde{V}: & a(v,w) - b(w,p) = & \langle k, w \rangle \\ \forall q \in \tilde{\Pi}: & b(v,q) = & \langle l, q \rangle \end{array} \tag{II.17}$$

with

$$a(u,w) = \langle \partial_i u_j, \partial_i w_j \rangle_{L^2(\Omega)} \tag{II.18}$$

$$b(v,q) = \langle \partial_l v_l, q \rangle_{L^2(\Omega)} \tag{II.19}$$

$$\langle k, w \rangle = \langle f_i, w_i \rangle_{L^2(\Omega)} + \langle -p_0 n_i + (V_0)_i, w_i \rangle_{L^2(\Gamma_p)}. \tag{II.20}$$

For the original Stokes-problem we have $l = 0$, but for sake of generality, we allow an arbitrary right hand side.
For this problem we have to choose spaces $V_D, \tilde{V} \subset V$ and $\Pi_D, \tilde{\Pi} \subset \Pi$ that fulfill the conditions of theorem II.13 to guarantee a solvable (and stable) problem, and the boundary conditions

$$\begin{aligned} v \in V_D \Rightarrow & v|_{\Gamma_v} = v_0, & \qquad v \in \tilde{V} \Rightarrow & v|_{\Gamma_v} = 0 \\ q \in \Pi_D \Rightarrow & q|_{\Gamma_p} = p_0, & \qquad q \in \tilde{\Pi} \Rightarrow & q|_{\Gamma_p} = 0. \end{aligned}$$

Crucial is the Dirichlet boundary condition for the pressure. In more simple applications (compare Girault and Raviart [1979]) one chooses $\Gamma_v = \partial\Omega$ and determines the pressure by the condition

$$\int_\Omega p dx = 0,$$

which allows the choice

$$\tilde{V} = (H_0^1(\Omega))^d \text{ and } \tilde{\Pi} = \left\{ q \in L^2(\Omega) | \int q dx = 0 \right\}.$$

If we want to apply Dirichlet conditions to the space Π, obviously we have to require continuous functions:

Theorem II.37
If we define the (affine) spaces

$$\tilde{\Pi} = L^2(\Omega) \cap C^0_{0,\Gamma_p}(\Omega), \qquad \Pi_D = \{p_0\} + \tilde{\Pi} \tag{II.21}$$

$$\tilde{V} = (H^1_{0,\Gamma_v}(\Omega))^d \cap \text{div}^{-1}(\tilde{\Pi}), \qquad V_D = \{v_0\} + \tilde{V} \tag{II.22}$$

and assume, that the boundary value functions

$$v_0 : \Gamma_v \to \mathbb{R}^d, \quad p_0 : \Gamma_p \to \mathbb{R}$$

can be extended to functions

$$v_0 \in V_D, \quad p_0 \in \Pi_D$$

(we omit a different notation for functions on $\overline{\Omega}$ and $\partial\Omega$), V_D and Π_D contain a unique solution $(v, p) \in (V_D, \Pi_D)$ of problem (II.17) and the mapping $(k, l) \to (v, p)$ is an isomorphism.

Proof. The statement is proven in four steps: Firstly we show, that it is sufficiant to consider the homogenous case of (II.17). Then we show the ellipticity of $a(\cdot,\cdot)$ (II.18) and the inf-sup-condition for $b(\cdot,\cdot)$ (II.19) respectively. After we did this preparational steps, we apply theorem II.13, that deliveres the statement of this theorem.

- For the reduction to homogenous boundary conditions we use the mappings $A : (H^1(\Omega))^d \to (H^1(\Omega))^d$ and $B : L^2(\Omega) \to (H^1(\Omega))^d$ with

  $$\langle Au, w\rangle = a(u, w), \qquad \langle u, Bq\rangle = b(u, q), \qquad u, w \in H^1(\Omega),\ q \in L^2(\Omega)$$

  to modify the right hand side of the system:

  $$\overline{k} = k - Av_0 + Bp_0, \qquad \overline{l} = l - B'v_0.$$

A solution $(\overline{v}, \overline{p}) \in \tilde{V} \times \tilde{\Pi}$ deliveres the solution

$$v = v_0 + \overline{v},\ p = p_0 + \overline{p}$$

of the original system (II.17): For any $(w, q) \in \tilde{V} \times \tilde{\Pi}$ there hold

$$\begin{aligned} a(v,w) - b(w,p) =& a(v_0,w) - b(w,p_0) + a(\overline{v},w) - b(w,\overline{p}) \\ =& a(v_0,w) - b(w,p_0) + \left\langle \overline{k}, w \right\rangle = \left\langle \overline{k} + Av_0 - Bp_0, w \right\rangle = \langle k, w \rangle \\ b(v,q) =& b(\overline{v},q) + b(v_0,q) = \left\langle \overline{l}, q \right\rangle + \langle B'v_0, q \rangle = \langle l, q \rangle . \end{aligned}$$

- The ellipticity of $a(u,w) = \langle \partial_i u_j, \partial_i v_j \rangle_{L^2(\Omega)}$ on $\tilde{V} \subset H^1_{0,\Gamma_D}(\Omega)$ is a conclusion of the Poincaré-inequality II.6

$$a(u,u) = \|\partial_i u_j\|^2_{L^2(\Omega)} \overset{\text{(II.6)}}{\geq} \frac{1}{1+C_P} \|u\|^2_{H^1(\Omega)} .$$

- We have to show that there exists a constant $\beta > 0$ such that for any $q \in \tilde{\Pi}$ there holds

$$\sup_{w \in \tilde{V} \setminus \{0\}} \frac{\langle \text{div } w, q \rangle_{L^2(\Omega)}}{\|w\|_{H^1(\Omega)}} \geq \beta \|q\|_{L^2(\Omega)} . \tag{II.23}$$

For an arbitrary but constant $q \in \tilde{\Pi}$ there exists a function $\phi \in H^2(\Omega)$ with

$$q = \Delta\phi.$$

Then for

$$\overline{w}_i := \partial_i \phi,$$

we have $\partial_i \overline{w}_i = q$, but not $\overline{w} \in H^1_{0,\Gamma_v}(\Omega)$.
To fix this, we find an $u \in H^1(\Omega)$ with $u|_{\Gamma_v} = \overline{w}|_{\Gamma_v}$ and div $u = 0$ (following Temam [1985]) to set

$$w_q := \overline{w} - u,$$

and gain

$$w_q|_{\Gamma_v} = 0,\ \text{div } w_q = q \qquad \Rightarrow \qquad w_q \in \tilde{V}.$$

In the following, we proove, that div $: \tilde{V} \to \tilde{\Pi}$ is an isomorphism (i. e. div $^{-1}$ exists and is bounded: $\left\| \text{div }^{-1}(q) \right\| / \|q\| \leq 1/\beta$), thus we gain estimate (II.23):

$$\sup_w \frac{\langle \text{div } w, q \rangle_{L^2(\Omega)}}{\|w\|_{H^1(\Omega)}} \geq \frac{\langle \text{div } w_q, q \rangle_{L^2(\Omega)}}{\|w_q\|_{H^1(\Omega)}} = \frac{\|q\|_{L^2(\Omega)}}{\left\| \text{div }^{-1}(q) \right\|_{H^1(\Omega)}} \|q\|_{L^2(\Omega)} \geq \beta \|q\|_{L^2(\Omega)} .$$

The fact, that div is an isomorphism is a consequence of the open range theorem II.9. The conditions for this theorem are surjectivity, injectivity and continuity of div . The surjectivity is already proven above. The continutiy is obvious:

$$\|\text{div } w\|^2_{L^2(\Omega)} = \|\partial_i w_i\|^2_{L^2(\Omega)} \leq |w|^2_{H^1(\Omega)} .$$

For the injectivity, let

$$\text{div } w = 0$$

and recall that then there exists an $\phi \in C^2(\Omega)$ with $\partial_i \phi = w_i$ and $\Delta\phi = 0$. Due to the Dirichlet condition for v we have

$$\partial_i \phi|_{\Gamma_v} = 0 \quad \Rightarrow \quad \phi|_{\Gamma_v} = \text{const.}.$$

This Poisson problem has a unique solution (this can be proven analogue to theorem II.35) and thus must be constant on the whole domain Ω. Consequently $w = 0$ is the only function with div $w = 0$ and div is injective.

□

II.2.4 Stokes model with cavitation

In section I.2.2 we introduced cavitation into our fluid model. There we derived the variational formulation of the cavitational Stokes model (I.38), which can be abbreviated by the mappings

$$a_c : V \times V \to \mathbb{R}, \qquad a_c(u,v) = \langle \partial_i u_j, \partial_i v_j \rangle + \langle \partial_i u_i, \partial_j v_j \rangle \tag{II.24}$$

analogue to $a(\cdot,\cdot)$ of (II.18), $b(\cdot,\cdot)$ (II.19) and the functions l and k (II.20), that we already used in the non-cavitational case (II.17):
Find $v \in V_D$ and $p \in (\Pi_D)_{\geq 0} = \left\{ q \in \Pi_{\geq 0} \middle| q|_{\Gamma_p} = p_0 \right\}$ such that

$$\begin{array}{lrl} \forall w \in \tilde{V}: & a_c(v,w) - b(w,p) = & \langle k, w \rangle \\ \forall q \in \tilde{\Pi}_{\geq 0}: & b(v, q-p) \geq & \langle l, q-p \rangle . \end{array} \tag{II.25}$$

At this point we assumed, that the non-symmetric boundary integral

$$\int_{\Gamma_p} \text{div } v n_i w_i da,$$

occuring in I.38 vanishes, which is for instance the case for $p_0 > 0$.
Here the spaces $\tilde{V}$, V_D, $\tilde{\Pi}$ and Π_D are the same as in the non-cavitational case (II.21) and (II.22).
Now we proceed similar to section II.2.2 where we reduced the contact-problem of the solid body to a projection on a convex subset of a Hilbert space.
According to corollary II.6 we can write the two bilinear forms with the help of linear continuous mappings

$$a_c(u,w) = \langle A_c u, w \rangle_{H^1(\Omega)}, \qquad A_c : (H^1(\Omega))^d \to (H^1(\Omega))^d \tag{II.26}$$

$$b(w,q) = \langle w, Bq \rangle_{H^1(\Omega)}, \qquad B : L^2(\Omega) \to (H^1(\Omega))^d. \tag{II.27}$$

Before we prove the well-posedness of the inhomogenous problem (II.25), we show it for the homogenuous case:

Lemma II.38
Under the same assumptions as in theorem II.37 and for

$$v_0 = 0 \text{ and } p_0 = 0,$$

i. e. $V_D = \tilde{V}$ and $\Pi_D = \tilde{\Pi}$ problem (II.25) has a unique solution and the mapping

$$(v, p) \to (k, l)$$

is an isomorphism.

Proof. For the (to $\tilde{V}$ and $\tilde{\Pi}$) restricted mappings (II.26) and (II.27) there hold

$$A_c : \tilde{V} \to \tilde{V}, \quad B : \tilde{\Pi} \to \tilde{V},$$

in particular for any $q, p \in \tilde{\Pi}$

$$B(q - p) \in \tilde{V}$$

is an element of the subset $\tilde{V}$. From the proof of theorem II.37 we know, that $a(\cdot, \cdot)$ is elliptic on $\tilde{V}$ and furthermore

$$\forall u \in \tilde{V} : \quad a_c(u, u) - a(u, u) = \langle \text{div } u, \text{div } u \rangle \geq 0,$$

hence a_c is elliptic and

$$A_c^{-1} B(q - p) \in \tilde{V}$$

exists. Thus we can conclude from the inequality in (II.25) for an arbitrary $q \in \tilde{\Pi}_{\geq 0}$:

$$\begin{aligned}
& b(v, q - p) \geq \langle l, q - p \rangle \\
\Leftrightarrow \quad & \langle B^* v - l, q - p \rangle \geq 0 \\
\Leftrightarrow \quad & \Big\langle B^* A_c^{-1} B p + B^* A_c^{-1} k - l, q - p \Big\rangle \geq 0, \quad \text{with } w = A_c^{-1} B(q - p) \text{ in (II.25)} \\
\Leftrightarrow \quad & \Big\langle S(p + S^{-1}(B^* A_c^{-1} k - l)), q - p \Big\rangle \geq 0, \quad S = B^* A_c^{-1} B \qquad \text{(II.28)}
\end{aligned}$$

Due to corollary II.14, we can introduce the scalar product on Π

$$\langle q, r \rangle_S := \langle Sq, r \rangle_{L^2(\Omega)}, \qquad \text{(II.29)}$$

theorems II.12 and II.11 give us the existence and uniqueness of the pressure p as projection on $\tilde{\Pi}_{\geq 0}$.
Insertion of this p into the equation of (II.25) yields a solution for the velocity

$$v = A_c^{-1} \Big(Bp + k \Big),$$

that is unique because A_c is an isomorphism. □

Now we generalize lemma II.38 to inhomogenuous boundary conditions:

Theorem II.39
Under the assumptions of theorem II.37 problem (II.25) has a unique solution and the mapping

$$(v, p) \to (k, l)$$

is an isomorphism.

Proof. Here again we want to characterize the solution $p \in \Pi_{D,\geq 0}$ of the Schur-complement inequation (II.28)

$$\forall q \in \tilde{\Pi}_{\geq 0}: \quad \Big\langle S(p + S^{-1}(B^* A_c^{-1} k - l)), q - p \Big\rangle \geq 0 \tag{II.30}$$

as projection on $\Pi_{D,\geq 0}$. This is not obvious, because the test function q and the solution p are not elements of the same subspace of Π. In the following we will show the equivalence of (II.30) and

$$\forall r \in \Pi_{D,\geq 0}: \quad \Big\langle S(p + S^{-1}(B^* A_c^{-1} k - l)), r - p \Big\rangle \geq 0. \tag{II.31}$$

- [(II.30) $\Rightarrow$ (II.31)]: For an arbitrary test function

  $$r \in \Pi_{D,\geq 0}$$

  we choose $q \in \tilde{\Pi}_{\geq 0}$ and an open set U_ε such that $\Gamma_p \subset U_\varepsilon$ and

  $$q = r \text{ on } \Omega \setminus U_\varepsilon \text{ and } |q| \leq |r| \text{ on } V_\varepsilon := \Omega \cap U_\varepsilon.$$

  With these and the abbreviations

  $$\begin{aligned} \overline{k} &:= -S^{-1}(B^* A_c^{-1} k - l) \\ \langle p, q \rangle_{S,U} &:= \langle Sp, q \rangle_{L^2(U)} \end{aligned}$$

  we have

  $$\begin{aligned} \Big\langle r - p, p - \overline{k} \Big\rangle_{S,\Omega} &= \Big\langle q - p, p - \overline{k} \Big\rangle_{S,\Omega} + \Big\langle r - q, p - \overline{k} \Big\rangle_{S,\Omega} \\ &\overset{\text{(II.30)}}{\geq} 0 + \Big\langle r - q, p - \overline{k} \Big\rangle_{S,V_\varepsilon} = \int_{V_\varepsilon} (r - q)(p - \overline{k}) dx. \end{aligned}$$

  By definition r, q and p are continuous on $\overline{V_\varepsilon}$ as well as $\overline{k}$ (because S is an isomorphism), such that the integrand is bounded

  $$|r - q| \cdot |p - \overline{k}| \leq R \text{ on } V_\varepsilon,$$

this yields

$$\left\langle r-p, p-\overline{k}\right\rangle_{S,\Omega} \geq -\,R\ \mathrm{vol}(V_\varepsilon).$$

Finally for every $\varepsilon > 0$ we can find an U_ε, such that $\mathrm{vol}(V_\varepsilon) < \varepsilon/R$ and hence there holds

$$\forall \varepsilon > 0: \ \left\langle r-p, p-\overline{k}\right\rangle_{S,\Omega} \geq -\varepsilon \ \Rightarrow \ \left\langle r-p, p-\overline{k}\right\rangle_{S,\Omega} \geq 0 \Rightarrow \text{(II.31)}.$$

- The opposite direction [(II.31) $\Rightarrow$ (II.30)] is proven completely analogue.

Altogether $p \in \Pi_{D,\geq 0}$ is a solution of (II.30) if and only if it is a solution of (II.31)

$$\forall r \in \Pi_{D,\geq 0}: \ \left\langle r-p, p-\overline{k}\right\rangle_{S,\Omega} \geq 0.$$

This characterisation is equivalent to that of the projection on the set $\Pi_{D,\geq 0}$, hence theorem II.11 guarantees existence and uniqueness of p. The solution for the velocity $v \in V_D$ is constructed as in lemma II.38. □

II.2.5 Subdimensional Stokes Model

The two-dimensional approximation of the Stokes-model (I.58) can be written as: Find $\chi \in X_D$ and $\psi \in \Psi_D$, such that

$$\begin{aligned} \forall \xi \in \tilde{X}: \qquad & a_2(\chi,\xi) - b(g\xi, \psi/g) = \langle \kappa+\gamma, \xi\rangle_{\Omega_2} - \langle \psi_0 n - X_0, \xi\rangle_{\partial\Omega_2} \\ \forall \varphi \in \tilde{\Psi}: \qquad & b(g\chi, \phi/g) = \langle \sigma_3, \phi\rangle_{\Omega_2} \end{aligned} \tag{II.32}$$

with

$$a_2(\chi,\xi) := a(\chi,\xi) + 12\,\langle \chi/g, \xi/g\rangle_{L^2(\Omega)} \tag{II.33}$$

and the bilinear forms a and b, defined in (II.18) and (II.19).
To see the well-posedness of this problem, we adapt the proof of the three-dimensional case (theorem II.37) to the subdimensional one. Firstly we define the two-dimensional analoga to the spaces (II.21) and (II.22):

$$\tilde{\Psi} = L^2(\Omega_2) \cap C_0^0(\Omega_2), \qquad \Psi_D = \{\psi_0\} + \tilde{\Psi} \tag{II.34}$$

$$\tilde{X} = (H^1_{0,P}(\Omega_2))^2 \cap \left(\frac{1}{g}\mathrm{div}^{-1}\left(\frac{1}{g}\tilde{\Psi}\right)\right), \qquad X_D = \{v_0(P)\} + \tilde{X} \tag{II.35}$$

We should mention, that the definition of $\tilde{X}$ and X_D is reasonable, because any function in $H^1_{0,P}(\Omega_2)$ is continuous near $P \in \partial\Omega_2$, and hence the declaration of v in the single point P is valid.

Theorem II.40
If the boundary function ψ_0 can be extended to a function $\psi_0 \in \Psi_D$, the two-dimensional Stokes problem (II.32) is well posed for the spaces (II.34) and (II.35).

Proof. We do the same steps as in the proof of theorem II.37:

- The reduction to homogenous boundary conditions is the same as in the three dimensional case.
- The ellipticity of a_2 is even more obvious then in the higher dimensional case:

$$\begin{aligned} a_2(\xi,\xi) =& \langle \partial_i \xi_j, \partial_i \xi_j \rangle_{L^2(\Omega_2)} + 12 \langle \xi/g, \xi/g \rangle_{L^2(\Omega_2)} \\ \geq& \min\left\{1; 12/g_{\max}\right\} \cdot \langle \xi, \xi \rangle_{H^1(\Omega_2)} = C \|\xi\|^2_{H^1(\Omega_2)} \end{aligned}$$

- To proove the inf-sup-condition, we assume an arbitrary $\phi \in \tilde{\Psi}$:

$$\begin{aligned} \sup_{\xi \in \tilde{X}} \frac{b(g\xi, \phi/g)}{\|\xi\|} \geq& \sup \frac{b(g\xi, \phi/g)}{\|g\xi\|} \cdot g_{\min}, && g_{\min} = \inf_{\Omega_2} g > 0 \\ \geq& \beta g_{\min} \left\| \frac{\phi}{g} \right\|, && \text{inf-sup-cond. (II.23)} \\ \geq& \beta \frac{g_{\min}}{g_{\max}} \|\phi\|, && g_{\max} = \sup_{\Omega_2} g \end{aligned}$$

□

II.2.6 Subdimensional Stokes Model with Cavitation

The two-dimensional Stokes cavitation model is given by (I.66): Find $\chi \in X_D$ and $\psi \in (\Psi_D)_{\geq 0}$ such that

$$\begin{aligned} \forall \xi \in \tilde{X}: \quad a_2(\chi,\xi) + \langle \partial_\nu \chi_\nu, \partial_\mu \xi_\mu \rangle_{\Omega_2} - & \langle \psi/g, \partial_\mu(g\xi_\mu) \rangle_{\Omega_2} - \langle \partial_\nu \chi_\nu, n_\mu \xi_\mu \rangle_{\partial\Omega_2} \\ = & \langle (\kappa + \gamma_c)_\mu, \xi_\mu \rangle_{\Omega_2} + \langle (X_0 - \psi_0 n)_\mu, \xi_\mu \rangle_{\partial\Omega_2} \\ \forall \phi \in \tilde{\Psi}_{\geq 0}: \quad \langle (\phi - \psi)/g, \partial_\nu(g\chi_\nu) \rangle_{\Omega_2} \geq & \langle \sigma_3 + \varepsilon_v, \phi - \psi \rangle_{\Omega_2}. \end{aligned} \tag{II.36}$$

Theorem II.41
If ψ_0 can be extended to a function $\psi_0 \in \Psi_D$, problem (II.36) has a unique solution $(\chi, \psi) \in X_D \times \Psi_D$ and the mapping to the right hand side is an isomorphism.

Proof. The proof for the three-dimensional case (theorem II.39) is also valid for the two-dimensional case, because the ellipticity of a_2 and the inf-sup-condition for $b(g\xi, \psi/g)$ holds here too (proof of theorem II.40). □

II.2.7 Reynolds

The Reynolds-problem (I.79) can be reformulated by the use of the Reynolds scalar product: Find $\psi \in \Psi_{R,D}$, such that for all $\phi \in \tilde{\Psi}_R$:

$$\langle \psi, \phi \rangle_R = -12 \left\langle \frac{\delta v_3}{g^2} + \frac{1}{12g} \partial_\nu (g \kappa_\nu) + \frac{R_1 + R_3}{g^2}, \phi \right\rangle_{L^2(\Omega_2)} =: \langle l_R, \phi \rangle_{L^2(\Omega_2)} . \tag{II.37}$$

Because $\langle \cdot, \cdot \rangle_R$ contains derivatives, we use a higher order space for the Reynolds pressure:

$$\Psi_R := H^1(\Omega_2),\ \tilde{\Psi}_R := H_0^1(\Omega_2) \text{ and } \Psi_{R,D} := \{\psi_0\} + \tilde{\Psi}_R. \tag{II.38}$$

Hence the right hand side of equation (II.37) $L_R(\phi)$ is linear in ϕ and $H_0^1(\Omega_2)$ is complete regarding $\|\cdot\|_R$ (lemma II.32), the representation theorem of Riesz II.5 guarantees a unique solution $\tilde{\psi} = \psi - \psi_0 \in \tilde{\Psi}_R$ of

$$\tilde{\psi} \in \tilde{\Psi}_R :\ \forall \phi \in \tilde{\Psi}_R :\ \left\langle \tilde{\psi}, \phi \right\rangle_R = L(\phi) - \langle \psi_0, \phi \rangle_R ,$$

which is just a slightly modified version of (II.37).
Altogether this implies

Theorem II.42
The Reynolds problem (II.37) has a unique solution $\psi \in \Psi_{R,D}$ (II.38) and the mapping

$$l_R \to \psi$$

is an isomorphism.

II.2.8 Reynolds Model with Cavitation

The Reynolds model for a cavitational fluid is given in (I.82): Find $\psi \in \Psi_{R,D,\geq 0}$ with

$$\forall \phi \in \tilde{\Psi}_{R,\geq 0} :\ \langle \phi - \psi, \psi \rangle_R \geq \langle l_{R,c}, \phi - \psi \rangle_{L^2(\Omega_2)} \tag{II.39}$$

with $l_{R,c}$, the analogon to the linear mapping in (II.37), where we just replace R_3 by R_{3c}. Ψ_R, $\tilde{\Psi}_R$ and $\Psi_{R,D}$ denote the same spaces as in (II.38) and

$$\tilde{\Psi}_{R,\geq 0} = \{\phi \in \tilde{\Psi}_R | \phi \geq 0\}, \quad \Psi_{R,D,\geq 0} = \{\phi \in \Psi_{R,D} | \phi \geq 0\} \tag{II.40}$$

respectively.
For this problem there holds

Theorem II.43
There exists a unique solution $\psi \in \Psi_{R,D,\geq 0}$ of (II.39) and the mapping

$$l_{R,c} \to \psi$$

is an isomorphism.

Proof. According section II.2.7 we can write

$$L_{R,c}(\cdot) = \langle l, \cdot \rangle_R$$

with $l \in \Psi_R$.
Analogue to the equivalence of (II.30) to (II.31) we can show the equivalence of (II.39) to

$$\psi \in \Psi_{R,D,\geq 0} : \quad \forall \phi \in \psi_{R,D,\geq 0} : \ \langle \phi - \psi, \psi - l \rangle_R \geq 0, \tag{II.41}$$

but this equation has a unique solution ψ, the projection of l on the convex subset $\Psi_{R,D,\geq 0}$. □

II.3 Finite Element Method

This section firstly gives a brief introduction into the Finite Element Method. Basically we follow Johnson [1987] and Braess [1997]. Sections II.3.1 and II.3.2 introduce the appropriate finite elements for the different model problems of the last section. Because of the classification of the (in–)equations section II.3.1 considers the problems of deformation and Reynolds-lubrication, while section II.3.2 considers the Stokes problem. In section II.3.2.1 the Q_1-element of section II.3.1 even is applied to the stabilised Stokes problem.

The abstract setting of the problems, we have to solve is:
Find $u \in V$, such that

$$\forall v \in V : \ a(u, v) = L(v), \tag{II.42}$$

where

$$L : \ V \to \mathbb{R}, \quad a : V \times V \to \mathbb{R}$$

are (bi-)linear forms on the Hilbert space V.
In our context of **physical models** V is a function space on the domain $\Omega \in \mathbb{R}^d$. One example is $V = H_0^1(\Omega)$ (see section II.1.3).
To treat problem (II.42) numerically, we have to approximate it with a **finite-dimensional problem**. We do this by a restriction of V to a finite-dimensional subspace V_h:
Find $u_h \in V_h \subset V$, such that

$$\forall v \in V_h : \ a(u_h, v) = L(v). \tag{II.43}$$

Once, we have done this, we can introduce a finite base of V_h:

$$V_h = \text{span } \{v_1, \ldots, v_n\}$$

to represent u and v by $\xi, \eta \in \mathbb{R}^n$:

$$u = \xi_i v_i, \quad v = \eta_j v_j$$

and insert this into (II.43):
Find $x \in \mathbb{R}^n$, such that

$$\begin{aligned}
& \forall \eta \in \mathbb{R}^n : && a(\xi_i v_i, \eta_j v_j) &&= L(\eta_j v_j) \\
\Leftrightarrow \quad & \forall \eta \in \mathbb{R}^n : && \xi_i \underbrace{a(v_i, v_j)}_{\alpha_{ji}} \eta_j &&= \eta_j \underbrace{L(v_j)}_{\beta_j} \\
\Leftrightarrow \quad & \forall j = 1, \ldots, n : && \alpha_{ji} \xi_i &&= \beta_j
\end{aligned}$$

So after all we reduced our approximated (finite-dimensional) problem to the linear system of equations

$$\xi \in \mathbb{R}^n : \ \alpha\xi = \beta$$

with

$$\alpha_{ij} = a(v_i, v_j) \text{ and } \beta_j = L(v_j) \qquad (i, j = 1, \ldots, n).$$

This has to be solved with the methods of numerical linear algebra.
Following the finite element method, for the discretisation of our problem firstly we need a triangulation of our domain Ω into certain subdomains. In our case we will always use quadrilaterals (for $\Omega \in \mathbb{R}^2$) and hexaeders (for $\Omega \subset \mathbb{R}^3$) respective. One example triangulation is shown in figure II.2.
One practical reason for the restriction to these geometrical objects is that in this case we can rely on the well developed c++-library deal.II (Bangerth et al. [2007], `www.dealii.org`, Bangerth and Kanschat [2005]), which is the tool of choice for all computations presented in this work.

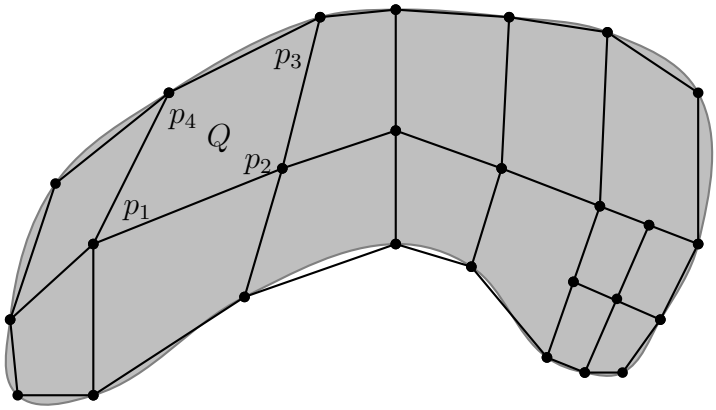

Figure II.2: Partition of the domain $\Omega \subset \mathbb{R}^2$ (gray) into quadrilaterals.

In figure II.2 one sees, that the domain may not be exactly covered by the quadrilaterals. But in the following, we always assume, a polygonal domain, then there holds

$$\overline{\Omega} = \bigcup_{Q \in \mathbb{T}} \overline{Q}$$

with open, pairwise disjoint quadrilaterals (or hexagons respective) $Q \in \mathbb{T}$ and a finite set $\mathbb{T}$.
Once, we have partitioned the domain into such subdomains, we just consider the restriction of the function space V to a single subdomain Q:

$$V(Q) = \{\phi : Q \to \mathbb{R}\}.$$

This function space has to be approximated by a finite-dimensional subspace $V_h(Q)$. Therefore we introduce a set of degrees of freedom Σ, which's elements are certain properties of functions in $V_h(Q)$, for example the function values in the edges of Q.
$V_h(Q)$ and Σ have to correspond in the way, that a certain function $\phi \in V_h(Q)$ is fully determined by the configuration of the degrees of freedom Σ.
One example are bilinear elements on a quadrilateral Q:

$$Q_1(Q) = \{\varphi : Q \to \mathbb{R} |\ \varphi(x) = a_Q + b_Q x_1 + c_Q x_2 + d_Q x_1 x_2\}$$

with

$$\Sigma = \{\varphi(p_1), \varphi(p_2), \varphi(p_3), \varphi(p_4)\},$$

the function values on the vertices p_j of Q (figure II.2).
Following Johnson [1987] the triple $(Q, V_h(Q), \Sigma)$ is called a **Finite Element**.
These ideas can be extended to vector-valued functions $\left(V \subset (L_2(\Omega))^d\right)$ by the use of the cartesian product of the discretised spaces, e. g. we might use $(Q_1)^d$.
Formally, we introduce two kinds of standard elements $V_h(Q)$ on squares (or intervals in one dimension or hexaeders in three dimensions respective) $Q \subset \mathbb{R}^d$:

- Polynomial Elements:

$$P_k(Q) := \left\{ \phi \in C^0(Q) \Big|\ \phi(x) = \sum_{n \in \mathbb{N}_0^d,\, |n| \le k} a_n x_1^{n_1} \dots x_d^{n_d} \text{ with } a_n \in \mathbb{R} \right\} \tag{II.44}$$

- Multilinear Elements:

$$Q_k(Q) := \left\{ \phi \in C^0(Q) \Big|\ \phi(x) = \phi_1(x_1) \dots \phi_d(x_d) \text{ with } \phi_1, \dots, \phi_d \in P_k(\mathbb{R}) \right\} \tag{II.45}$$

$$Q_k(\Omega) := \left\{ \phi \in C^0(\overline{\Omega}) \Big|\ \forall Q \in \mathbb{T} :\ \phi|_Q \in Q_k(Q) \right\} \tag{II.46}$$

  where $P_k(\mathbb{R})$ denotes the space of polynoms of degree k.

The degrees of freedom for $Q_k(Q)$ usually are attached to the function values at the vertices of Q (for Q_1 see above) or at uniformely distributed points, e. g. the four vertices, the centers of all four edges of Q and the center of Q for $Q_2(Q)$.
In the case of P_k (used on quadrilaterals) there is no such canonical connection. Actually these functions have not even to be continuous.

In the following we introduce the finite elements, used for our different applications:

II.3.1 Deformation of an Elastic Body and Pressure of a Reynolds Fluid

In both applications, described in section II.2.1 (deformation) and in section II.2.7 (Reynolds fluid) the solutions are functions

$$s \in (H^1(\Omega))^d,\ \psi \in H^1(\Omega_2) \text{ respective.}$$

For the approximation of $H^1(\Omega)$, we will use linear elements (II.46):

$$s_h \in V_h := (Q_1(\Omega))^d \tag{II.47}$$

$$\psi_h \in \Psi_h := Q_1(\Omega_2). \tag{II.48}$$

In sections II.2.1 and II.2.7 we have seen, that both the elastic deformation model (II.11) and the Reynolds model (II.37) can be written as

$$\text{Find } v \in V: \quad \forall w \in V: \; a(v,w) = L(w), \tag{II.49}$$

with a V-elliptic, continuous bilinear form $a: V \times V \to \mathbb{R}$ and a linear mapping $L: V \to \mathbb{R}$. The V-ellipticity of a was sufficient for the existence of a unique solution of (II.49).
To guarantee a unique solution of the discretisation of (II.49)

$$\text{Find } v_h \in V_h: \quad \forall w \in V_h: \; a(v_h,w) = L(w), \tag{II.50}$$

we remark, that $a(\cdot,\cdot)$ is also V_h-elliptic (because of $V_h \subset V$) and that V_h is complete.

II.3.2 The Stokes Model

For the Stokes Problem (II.17)

$$\text{Find } (v,p) \in V_D \times \Pi_D: \quad \begin{array}{ll} \forall w \in \tilde{V}: & a(v,w) - b(w,p) = \langle k, w\rangle \\ \forall q \in \tilde{\Pi}: & b(v,q) = \langle l, q\rangle . \end{array} \tag{II.51}$$

in section II.2.3 we have learned, that (II.51) is well posed, if and only if

$$\begin{aligned} &a(\cdot,\cdot) \text{ is elliptic on } U = \{v \in \tilde{V} | b(v,\cdot) = 0\} \text{ and} \\ &\text{for } b(\cdot,\cdot) \text{ there exists } \beta > 0: \; \forall \mu \in \tilde{\Pi}: \; \sup_{v \in \tilde{V}} \frac{b(v,\mu)}{\|v\|} \geq \beta \|\mu\| . \end{aligned} \tag{II.52}$$

To guarantee well-posedness for the discrete problem

$$\text{Find } (v_h,p_h) \in V_{D,h} \times \Pi_{D,h}: \quad \begin{array}{ll} \forall w \in \tilde{V}_h: & a(v_h,w) - b(w,p_h) = \langle k, w\rangle \\ \forall q \in \tilde{\Pi}_h: & b(v_h,q) = \langle l, q\rangle . \end{array} \tag{II.53}$$

with the choice

$$V_h^{\text{Stokes}} := (Q_2(\Omega))^d, \qquad V_{D,h} = V_h^{\text{Stokes}} \cap V_D, \qquad \tilde{V}_h = \tilde{V} \cap V_h^{\text{Stokes}} \tag{II.54}$$

$$\Pi_h := Q_1(\Omega), \qquad \Pi_{D,h} = \Pi_h \cap \Pi_D, \qquad \tilde{\Pi}_h = \Pi_h \cap \tilde{\Pi} \tag{II.55}$$

one has to prove the conditions according (II.52):

- $a(\cdot,\cdot)$ is elliptic on
$$U_h := U \cap V_h$$
because U_h is a subspace of U and in section II.2.3 we have seen, that $a(\cdot,\cdot)$ is U-elliptic.

- For the inf-sup-condition on $\tilde{V}_h \times \tilde{\Pi}_h$:
$$\exists \beta_h > 0: \; \forall \mu \in \tilde{\Pi}_h: \; \sup_{v \in \tilde{V}_h} \frac{b(v,\mu)}{\|v\|_{H^1(\Omega)}} \geq \beta_h \|\mu\|_{L^2(\Omega)} \tag{II.56}$$
This proof can be found in Girault and Raviart [1986].

II.3.2.1 Stabilized Stokes Equations

In the previous paragraph, we had to choose a rather rich velocity space $V_h = Q_2(\Omega)$, to fulfill the discrete inf-sup-condition (II.56). To avoid this, we can go an other way, using the results of section II.1.1.1, to regularise the Stokes Equations (II.51) to a system of the kind (II.5):

$$\text{Find } (v^\varepsilon, p^\varepsilon) \in V_D \times \Pi_D, \text{ such that } \begin{array}{rrl} \forall w \in \tilde{V}: & a(v^\varepsilon, w) - b(w, p^\varepsilon) = & \langle k, w\rangle \\ \forall q \in \tilde{\Pi}: & b(v^\varepsilon, q) + \varepsilon c(p^\varepsilon, q) = & \langle l, q\rangle \end{array} . \quad \text{(II.57)}$$

Lemma II.44
If the bilinearforms a and c are elliptic and $\varepsilon > 0$, the bilinear form

$$a_c: \ \Big((u,r);\ (w,q)\Big) \to a(u,w) - b(w,r) + b(u,q) + \varepsilon c(r,q)$$

is elliptic too.

Proof. We have

$$\begin{aligned} a_c((u,r),(u,r)) =& a(u,u) - b(u,r) + b(u,r) + \varepsilon c(r,r) = a(u,u) + \varepsilon c(r,r) \\ \geq& \alpha \|u\|^2 + \varepsilon\gamma \|r\|^2 \geq \min(\alpha;\ \varepsilon\gamma) \cdot \|(u,r)\|^2 , \end{aligned}$$

where the first estimate is a conclusion of the ellipticity of a and c and with $\alpha_c := \min(\alpha;\ \varepsilon\gamma) > 0$ for $\varepsilon > 0$ and hence the ellipticity of a_c. □

III

Error Estimates

Part III is not assigned to one of the previous parts – namely I Physics or II Mathematics – because we consider the intersection between both. We split the total error between the physical model of the real world and the numerical solution of an (even coarser) mathematical model into modelling and discretisation error (III.3). In III.1 we estimate the modelling error between the considered physical models, the Signorini- and vertical contact models (section III.1.1) as well as the different fluid models (section III.1.2). At next in section III.2 we present error estimates for the discretisation error, i. e. the difference between the mathematical model and the numerical solution. Finally in section III.3 we briefly discuss, how to refine both, the model and the numerical approximation in a balanced way.

The abstract setting is, that we have got a rather accurate model for any physical process

$$u_a \in V \text{ such that } \Phi_a(u_a) = 0 \tag{III.1}$$

and a coarser one:

$$u_c \in V \text{ such that } \Phi_c(u_c) = 0. \tag{III.2}$$

The functionals $\Phi_x(v)$ depend only on the restriction of v to a corresponding part of our domain $\Omega_x \subset \Omega$:

$$\Phi_x(v) = \Phi_x(v|_{\Omega_x}), \quad x \in \{a, c\}$$

with $\overline{\Omega_a \cup \Omega_c} = \overline{\Omega}$.
An example is given by the sub-dimensional Stokes equation (I.53) and its approximation by the Reynolds model (I.77).
The coarser model (III.2) will also be used on Ω_a to get an initial guess for the solution of the accurate problem (III.1).
Both models are approximated numerically, in our case by a finite element scheme (II.43):

$$\begin{aligned} u_{a,h} \in V_h(\Omega_a) \subset V(\Omega_a) \text{ such that } \Phi_a^h(u_{a,h}) = 0, \\ u_{c,h} \in V_h(\Omega_c) \subset V(\Omega_c) \text{ such that } \Phi_c^h(u_{c,h}) = 0. \end{aligned}$$

The total error e in any appropriate norm $\|\cdot\|$ can be split into **modelling error** and **discretisation error**:

$$\begin{aligned} \|e\| := \underbrace{\|u_a - u_c\|_{\Omega_c}}_{=: \|e_m\|} + \underbrace{\|u_a - u_{a,h}\|_{\Omega_a}}_{=: \|e_{d,a}\|} + \underbrace{\|u_c - u_{c,h}\|_{\Omega_c}}_{=: \|e_{d,c}\|} . \end{aligned} \tag{III.3}$$

In the remaining sections III.1 and III.2 we discuss these different contributions separate.

III.1 Error Estimates – Modelling Error

In this section we shortly describe the general handling of different models for a physical phenomenon. Therefor we introduce algorithm III.1 for model adaptivity and its variants for different refinement strategies – algorithm III.2 and algorithm III.3. In sections III.1.1 and III.1.2 the model error estimators for the different contact– and fluid–models respective are derived similar to Oden et al. [2001] and applied to algorithms III.2 and III.3.

Braack and Ern [2003] derive estimators for modelling errors by introducing a dual problem. Furthermore they introduce a strategy of balancing modelling and discretisation error.
The following algorithm III.1 solves a problem with a coarse and an accurate model on a fixed triangulation. It reduces the error by successive refinement of the model on single grid-cells until the modelling error is lower than a given bound $\varepsilon^m \leq \varepsilon_0$. The discretization error is not yet taken into account.

Algorithm III.1 (Model Adaptivity)
`create triangulation` $\mathbb{T}$ `of the domain` Ω
$\varepsilon_0 \in \mathbb{R}_{>0}$
$\mathbb{T}_c \leftarrow \mathbb{T}$
$\mathbb{T}_a \leftarrow \emptyset$
`calculate` $u \leftarrow u_c$ `on` Ω
$\varepsilon^m \leftarrow 0$
`for` $Q \in \mathbb{T}_c$
    `calculate` $\varepsilon^m(Q) \leftarrow \|e_m\|_Q$
    $(\varepsilon^m)^2 \leftarrow (\varepsilon^m)^2 + \varepsilon^m(Q)^2$
`while` $\varepsilon^m > \varepsilon_0$
    `find` $Q_{max} \in \mathbb{T}_c$ `with` $\forall Q \in \mathbb{T}_c : \ \varepsilon^m(Q_{max}) > \varepsilon^m(Q)$
    $\mathbb{T}_c \leftarrow \mathbb{T}_c \setminus \{Q_{max}\}$
    $\mathbb{T}_a \leftarrow \mathbb{T}_a \cup \{Q_{max}\}$
    $(\varepsilon^m)^2 \leftarrow (\varepsilon^m)^2 - (\varepsilon^m(Q_{max}))^2$
`calculate` $u \leftarrow u_a$ `on` Ω_a

$\mathbb{T}_c$ and $\mathbb{T}_a$ contain the cells of our triangulation $\mathbb{T}$, on which the coarse or the accurate model respective are active.
Usually $\varepsilon^m(Q)$ cannot be calculated exactly, but is estimated by the estimates in sections III.1.1 and III.1.2, that might be more accurate with the knowledge of u^a on a cell Q. Consequently ε^m in the following denotes the error estimate and not the error $\|e_m\|$ itself. Thus it might be appropriate to apply algorithm III.1 several times and successively refine or coarsen the model on each cell.

Therefor we modify algorithm III.1 in two different ways:

Firstly we follow a **fixed fraction strategy** (as we know it from grid-refinement). We always refine a percentage of p_r of the cells in $\mathbb{T}_c$ with the biggest error-estimate and coarsen the p_c percent of the cells in $\mathbb{T}_a$ with the least error-estimate ($0 \leq p_r;\ p_c \leq 1$), what results in algorithm III.2:

Algorithm III.2 (Model Adaptivity with fixed fraction strategy)

```
create triangulation 𝕋 of the domain Ω
ε_0 ∈ ℝ_{>0}
p_c, p_r ∈ [0;1]
N_max ∈ ℕ
N ← 0
𝕋_c ← 𝕋
𝕋_a ← ∅
calculate u ← u_c on Ω
ε^m ← 0
for Q ∈ 𝕋
    calculate the estimate ε^m(Q)
    if Q ∈ 𝕋_c
        (ε^m)^2 ← (ε^m)^2 + ε^m(Q)^2
while (N < N_max and ε^m > ε_0)
      n_c ← (1 − p_r) · |𝕋_c|
      while (|𝕋_c| > n_c)
            find Q_max ∈ 𝕋_c with ∀Q ∈ 𝕋_c : ε^m(Q_max) ≥ ε^m(Q)
            𝕋_c ← 𝕋_c \ {Q_max}
            𝕋_a ← 𝕋_a ∪ {Q_max}
      n_a ← (1 − p_c) · |𝕋_a|
      while (|𝕋_a| > n_a)
            find Q_min ∈ 𝕋_c with ∀Q ∈ 𝕋_c : ε^m(Q_min) ≤ ε^m(Q)
            𝕋_a ← 𝕋_a \ {Q_min}
            𝕋_c ← 𝕋_c ∪ {Q_min}
      calculate u ← u_c on 𝕋
      calculate u ← u_a on 𝕋_a
      ε^m ← 0
      for Q ∈ 𝕋
          calculate the estimate ε^m(Q)
          if Q ∈ 𝕋_c
              (ε^m)^2 ← (ε^m)^2 + ε^m(Q)^2
      N ← N + 1
```

Of course p_c and p_r have to be chosen in a way, that makes the error-estimate ε^m really decrease and not such that in one and the same run of the outer while-loop all cells that where refined are instantly coarsened.

The second way to introduce an error-estimate into algorithm III.1 is an **intuitive sorting of the error-contributions**, such that on any cell in $\mathbb{T}_c$ the estimate $\varepsilon^m(Q)$ is smaller than on those of $\mathbb{T}_a$:

$$\forall Q_c \in \mathbb{T}_c,\ Q_a \in \mathbb{T}_a : \quad \varepsilon^m(Q_c) \leq \varepsilon^m(Q_a).$$

This strategy is implemented in algorithm III.3:

Algorithm III.3 (Model Adaptivity with sorted error)

create triangulation $\mathbb{T}$ of the domain Ω
$\varepsilon_0 \in \mathbb{R}_{>0}$; $N_{max} \in \mathbb{N}$; $N \leftarrow 0$; $\varepsilon^m \leftarrow 0$; $p_c, p_r \in (0,1)$
$\mathbb{T}_c \leftarrow \mathbb{T}$; $\mathbb{T}_a \leftarrow \emptyset$
calculate $u \leftarrow u_c$ on Ω
for $Q \in \mathbb{T}$
    calculate the estimate $\varepsilon^m(Q)$
    if $Q \in \mathbb{T}_c$
        $(\varepsilon^m)^2 \leftarrow (\varepsilon^m)^2 + \varepsilon^m(Q)^2$
while ($N < N_{max}$ and $\varepsilon^m > \varepsilon_0$)
    sort the cells $Q_a \in \mathbb{T}_a$ with respect to $\varepsilon^m(Q_a)$:
        $\varepsilon^m(Q_a^{j-1}) \leq \varepsilon^m(Q_a^j),\ j = 2, 3, \ldots, |\mathbb{T}_a|$
    sort the cells $Q_c \in \mathbb{T}_c$ with respect to $\varepsilon^m(Q_c)$:
        $\varepsilon^m(Q_c^{j-1}) \leq \varepsilon^m(Q_c^j),\ j = 2, 3, \ldots, |\mathbb{T}_c|$
    while $\varepsilon^m(Q_c^{|\mathbb{T}_c|}) > \varepsilon(Q_a^1)$ //i.e. $\max\limits_{Q_c \in \mathbb{T}_c} \varepsilon^m(Q_c) > \min\limits_{Q_a \in \mathbb{T}_a} \varepsilon^m(Q_a)$
        if $((\varepsilon^m)^2 + \varepsilon^m(Q_a^1)^2 > \varepsilon_0^2)$
            $(\varepsilon^m)^2 \leftarrow (\varepsilon^m)^2 - \varepsilon(Q_c^{|\mathbb{T}_c|})^2$
            $\mathbb{T}_a \leftarrow \mathbb{T}_a \cup \{Q_c^{|\mathbb{T}_c|}\}$; $\mathbb{T}_c \leftarrow \mathbb{T}_c \setminus \{Q_c^{|\mathbb{T}_c|}\}$
            sort $\mathbb{T}_a$
        else
            $(\varepsilon^m)^2 \leftarrow (\varepsilon^m)^2 + \varepsilon(Q_a^1)^2$
            $\mathbb{T}_c \leftarrow \mathbb{T}_c \cup \{Q_a^1\}$; $\mathbb{T}_a \leftarrow \mathbb{T}_a \setminus \{Q_a^1\}$
            sort $\mathbb{T}_c$
    $n_c \leftarrow (1 - p_r) \cdot |\mathbb{T}_c|$
    while ($\varepsilon^m > \varepsilon_0$ and $|\mathbb{T}_c| > n_c$)
        $\mathbb{T}_a \leftarrow \mathbb{T}_a \cup \{Q_c^{|\mathbb{T}_c|}\}$; $\mathbb{T}_c \leftarrow \mathbb{T}_c \setminus \{Q_c^{|\mathbb{T}_c|}\}$
    $n_a \leftarrow (1 - p_c) \cdot |\mathbb{T}_a|$
    while ($(\varepsilon^m)^2 + \varepsilon^m(Q_a^1)^2 \leq \varepsilon_0^2$ and $|\mathbb{T}_a| > n_a$)
        $\mathbb{T}_c \leftarrow \mathbb{T}_c \cup \{Q_a^1\}$; $\mathbb{T}_a \leftarrow \mathbb{T}_a \setminus \{Q_a^1\}$
    calculate $u \leftarrow u_c$ on $\mathbb{T}$
    calculate $u \leftarrow u_a$ on $\mathbb{T}_a$
    $\varepsilon^m \leftarrow 0$
    for $Q \in \mathbb{T}$
        calculate the estimate $\varepsilon^m(Q)$
        if $Q \in \mathbb{T}_c$
            $(\varepsilon^m)^2 \leftarrow (\varepsilon^m)^2 + \varepsilon^m(Q)^2$
    $N \leftarrow N + 1$

In every cycle of the external while-loop after sorting and reorganising the cells, the error condition $\varepsilon^m > \varepsilon_0$ is checked and some of the coarse-model-cells $Q_c \in \mathbb{T}_c$ are refined if necessary. This refinement will only lead to a maximal reduction of the number of coarse

cells by the factor p_r.
After all, the algorithm will lead to $\mathbb{T}_a = \mathbb{T}$, in the extreme case, that the modelling error in each cell is bigger then the global bound ε_0: $\forall Q \in \mathbb{T} : \ \varepsilon^m(Q) > \varepsilon_0$. Therefore the algorithm will stop after a finite number of iterations.

III.1.1 Contact Models

In this section we estimate the difference between the Signorini model (I.21) and the coarser z-contact-model (I.20). Finally we reduce this estimate to that of the different projections on the contact surface (III.16).

The two considered models of contact descend the contact model (II.15)

$$s \in \Pi(V_0): \quad \forall r \in \Pi(V_0) = \begin{array}{l} \{r \in V_0 | r \cdot n \leq b \text{ on } x \in \Gamma_C\}: \\ a(s, r-s) - L(r-s) \geq 0, \end{array} \tag{III.4}$$

by introducing the two different types of projection (I.20) (one-direction-projection) and (I.21) (Signorini-Projection). As described in section I.1.4 the different projections just differ in the choice of n and b. In the case of the simple projection $n \in \mathbb{R}^d$ is a constant unit vector (e. g. $n = e_z$). In contrast to this in the case of the Signorini-projection

$$n : \Gamma_C \times V_0 \to \mathbb{R}^d$$

depends on the position in Γ_C *and* the deformation $s \in V_0$ itself. (In practical calculations this dependency will be circumvented by the approximaton of s with the help of the solution of a previous calculation.)
We call the solutions of the different problems s_z (simple contact) and s_s (Signorini contact).
The convex subsets of V_0, that contain the solutions s_z and s_s respectively, are

$$\begin{aligned} K_z :=& \{r \in V_0 | r \cdot n_z \leq b_z(x) \text{ on } x \in \Gamma_C\} \\ K_s :=& \{r \in V_0 | r \cdot n_s \leq b_s \text{ on } x \in \Gamma_C\} \\ =& \{r \in V_0 | (x+r) \cdot n_s \leq b_z(\Gamma_C((x+r)_{\perp,z}))\end{aligned}$$

and the projections into them are called P_z and P_s respective.
Because in this application the two considered models do not differ explicitly in the bilinearform but in the sets of possible solutions K_z and K_s we will go another way than Braack and Ern [2003], to obtain our modelling error estimator. But in the end ((III.7) and (III.8)) we also find that the modelling error e_{sz} can be estimated with the help of the norm of the considered (bi-)linear forms and that of the solution s_z.
For the examination of the modelling error $e_{sz} := s_s - s_z$, we recall the definition of the mappings a and L ((II.13) and (II.14)):

$$a(s, r) = 2\mu \left\langle \varepsilon_{ij}(s), \varepsilon_{ij}(r) \right\rangle_{L^2(\Omega)} + 2\lambda \left\langle \varepsilon_{ll}(s), \varepsilon_{jj}(r) \right\rangle_{L^2(\Omega)} \tag{III.5}$$

$$L(s) = \left\langle \rho f_i, s_i \right\rangle_{L^2(\Omega)} + \left\langle t_i, r_i \right\rangle_{L^2(\Gamma_\tau)} \tag{III.6}$$

with the abbreviation $t_i = \tau_{ij} n_j$.
We consider the ellipticity of $a(\cdot,\cdot)$ (theorem II.35):

$$\begin{aligned}
\alpha \|e_{sz}\|^2 \leq & a(e_{sz}, e_{sz}) = -a(s_s, s_z - s_s) - a(s_z, s_s - s_z) \\
= & - a(s_s, P_s(s_z) - s_s) + a(s_s, P_s(s_z) - s_z) + \\
& - a(s_z, P_z(s_s) - s_z) + a(s_z, P_z(s_s) - s_s) \\
\overset{(III.4)}{\leq} & - L(P_s(s_z) - s_s) - L(P_z(s_s) - s_z) + \\
& + a(s_s, P_s(s_z) - s_z) + a(s_z, P_z(s_s) - s_s) \\
\leq & \|L\| \|P_s(s_z) - P_z(s_z)\| + \|L\| \|P_s(s_s) - P_z(s_s)\| + \\
& + \|a\| \|s_s\| \|P_s(s_z) - P_z(s_z)\| + \|a\| \|s_z\| \|P_z(s_s) - P_s(s_s)\| . \\
& \qquad\qquad\qquad\qquad\qquad\qquad \text{(note } P_s(s_s) = s_s,\ P_z(s_z) = s_z)
\end{aligned}$$

With the help of

$$\begin{aligned}
\|a\| \|P_s(s_i) - P_z(s_i)\| \|e_{sz}\| \leq & \frac{1}{2\alpha} \left(\|a\| \|P_s(s_i) - P_z(s_i)\|\right)^2 + \frac{\alpha}{2} \|e_{sz}\|^2 \\
\text{and } \|s_i\| \leq & \|s_j\| + \|e_{sz}\| \qquad\qquad [\{s_i, s_j\} = \{s_s, s_z\}]
\end{aligned}$$

we achieve

$$\begin{aligned}
\frac{\alpha}{2} \|e_{sz}\|^2 \leq & (\|L\| + 2\|a\| \|s_z\|) \left(\|P_s(s_z) - P_z(s_z)\| + \|P_s(s_s) - P_z(s_s)\|\right) + \\
& + \frac{\left(\|a\| \|P_s(s_z) - P_z(s_z)\|\right)^2}{2\alpha} \qquad \text{(III.7)} \\
\text{and } \frac{\alpha}{2} \|e_{sz}\|^2 \leq & (\|L\| + 2\|a\| \|s_s\|) \left(\|P_s(s_z) - P_z(s_z)\| + \|P_s(s_s) - P_z(s_s)\|\right) + \\
& + \frac{\left(\|a\| \|P_s(s_s) - P_z(s_s)\|\right)^2}{2\alpha}. \qquad \text{(III.8)}
\end{aligned}$$

So at last the modelling error depends on the difference of the two projections

$$P_s(r) - P_z(r) \quad (r = s_z,\ s_s).$$

In the following we estimate this difference on the boundary part Γ_C. There we have

$$P_z(r)(x) = \begin{cases} r(x), & (Z) \\ r(x) + (y_z - (x + r)) \cdot n_z n_z & \neg(Z) \end{cases} \qquad \text{(III.9)}$$

$$P_s(r)(x) = \begin{cases} r(x), & (S) \\ r(x) + (y_s - (x + r)) \cdot n_s n_s, & \neg(S) \end{cases} \qquad \text{(III.10)}$$

where (Z) and (S) are the two contact-conditions

$$\begin{aligned}
(Z) :\Leftrightarrow & \quad (y_z - (x + r)) \cdot n_z \geq 0 \quad \Leftrightarrow \quad \eta_z - r \cdot n_z \geq 0 \\
(S) :\Leftrightarrow & \quad (y_s - (x + r)) \cdot n_s \geq 0 \quad \Leftrightarrow \quad \eta_s \geq 0
\end{aligned} \qquad \text{(III.11)}$$

with the intersections y_s and y_z of the obstacle $b(\Gamma_C)$ and the line spanned by n_s and n_z respective (figure III.1):

$$y_z = (x + \langle n_z \rangle) \cap b(\Gamma_C) = x + \eta_z n_z \qquad \text{(III.12)}$$

$$y_s = (x + r + \langle n_s \rangle) \cap b(\Gamma_C) = x + r + \eta_s n_s \qquad \text{(III.13)}$$

Furthermore we introduce the deviation of n_s from n_z and of y_s from y_z:

$$\varepsilon := y_s - y_z, \quad \nu := n_s - n_z. \tag{III.14}$$

For the estimate of the difference of (III.9) and (III.10) we have to divide the four possible cases:

- $(Z) \wedge (S)$:
$$(P_s r - P_z r)(x)^2 = 0 \tag{III.15}$$

- $(Z) \wedge \neg(S)$: This is the first of the three cases, that are scatched in figure III.1.

$$\begin{aligned} & 0 \overset{\neg(S)}{>} (y_s - (x+r)) \cdot n_s = -|(P_s r - P_z r)(x)| \\ \Rightarrow \quad & |(P_s r - P_z r)(x)| = -(y_z + \varepsilon - x - r) \cdot (n_z + \nu) \\ & = \underbrace{-(y_z - x - r) \cdot n_z}_{\leq 0,\ (Z)} - \varepsilon \cdot (n_z + \nu) - (y_z - x - r) \cdot \nu \\ & \overset{(Z)}{\leq} -\varepsilon \cdot n_z - (y_s - x - r) \cdot \nu \\ & = -\varepsilon_z - \eta_s n_s \cdot \nu \end{aligned}$$

  Here we used the abbreviations $f_z := n_z \cdot f$ and $f_\perp := f - f_z n_z$.

- $\neg(Z) \wedge (S)$: This is the second case in figure III.1, here we have

$$\begin{aligned} & 0 \overset{\neg(Z)}{>} (y_z - (x+r)) \cdot n_z = -|(P_s r - P_z r)(x)| \\ \Rightarrow \quad & |(P_s r - P_z r)(x)| = -(y_z - x - r) \cdot n_z \\ & = (y_s - y_z) \cdot n_z + (x+r)_z - y_s \cdot n_z \\ & = \varepsilon_z - \underbrace{(y_s - x - r) \cdot n_s}_{\geq 0,\ (S)} + (y_s - x - r) \cdot \nu \\ & \leq \varepsilon_z + \eta_s n_s \cdot \nu \end{aligned}$$

- $\neg(Z) \wedge \neg(S)$: In the third case of figure III.1 one can see

$$|(P_s(r) - P_z(r))(x)|^2 = \varepsilon_z^2 + (\eta_s n_s)_\perp^2 = \varepsilon_z^2 + \eta_s^2 (\nu_\perp)^2$$

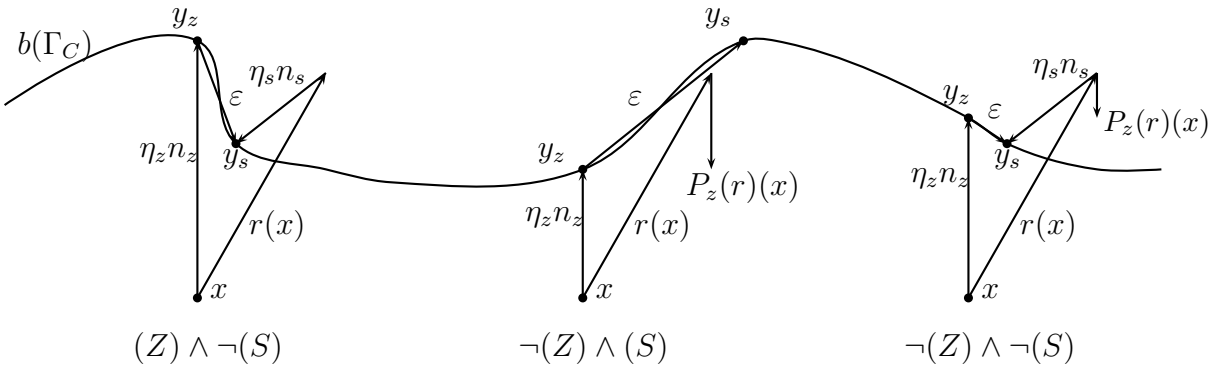

Figure III.1: Scatch of the three cases of obstacle penetration: In the left part the deformation $r(x)$ is valid with respect to the z-condition but not with respect to the Signorini-condition. In the second figure $r(x)$ is valid in Signorini's sence but not considering just the z-coordinate. In the right-hand-side the case is shown, where both projections have an effect on $r(x)$.

If we now take into account, that only the cases $r \in \{s_s, s_z\}$ have to be considered, we know, that for $r = s_s$ only the cases (S) are possible and for $r = s_z$ only the cases (Z) are possible and thus there holds

$$\begin{aligned} |P_s(r) - P_z(r)| \leq & |\varepsilon_z + \eta_s n_s \cdot \nu| \\ = & |(\eta_s n_s + r - \eta_z n_z) \cdot n_z + \eta_s n_s \cdot (n_s - n_z)| \\ = & |\eta_s - \eta_z + r \cdot n_z| \end{aligned}$$

and with (III.15)

$$|P_s(r) - P_z(r)| \leq \varepsilon_P(r) := \begin{cases} 0, & (S) \wedge (Z) \\ |\eta_s - \eta_z + r \cdot n_z|, & else \end{cases} \quad (r \in \{s_z, s_s\}). \tag{III.16}$$

We collect the above, to gain an estimate for the modelling error:

Theorem III.4
The modelling error of the contact problem (III.4) can be estimated with the help of the local differences of projections ε_P (III.16):

$$\|e_{sz}\|^2_{H^1(\Omega)} \leq C_P \left(\|\varepsilon_P(s_z)\|_{L^2(\Gamma_C)} + \|\varepsilon_P(s_z)\|^2_{L^2(\Gamma_C)} + \|\varepsilon_P(s_s)\|_{L^2(\Gamma_C)} + \|\varepsilon_P(s_s)\|^2_{L^2(\Gamma_C)} \right).$$

Proof. From (III.7) and (III.8) we conclude

$$\begin{aligned}\|e_{sz}\|^2_{H^1(\Omega)} \leq & C \cdot \Big(\|P_s(s_z) - P_z(s_z)\|_{H^1(\Omega)} + \|P_s(s_z) - P_z(s_z)\|^2_{H^1(\Omega)} + \\ & + \|P_s(s_s) - P_z(s_s)\|_{H^1(\Omega)} + \|P_s(s_s) - P_z(s_s)\|^2_{H^1(\Omega)} \Big).\end{aligned}$$

Analogue to (III.53) we can assume $\|P_s(s_x) - P_z(s_x)\|_{H^1(\Omega)} \leq C_s \|P_s(s_x) - P_z(s_x)\|_{L^2(\Gamma_C)}$ and thus we just have to consider the difference of the two projections on the contact boundary:

$$\begin{aligned}\|e_{sz}\|^2_{H^1(\Omega)} \leq & CC_s \cdot \Big(\|P_s(s_z) - P_z(s_z)\|_{L^2(\Gamma_C)} + \|P_s(s_z) - P_z(s_z)\|^2_{L^2(\Gamma_C)} + \\ & + \|P_s(s_s) - P_z(s_s)\|_{L^2(\Gamma_C)} + \|P_s(s_s) - P_z(s_s)\|^2_{L^2(\Gamma_C)} \Big).\end{aligned}$$

Insertion of (III.16) finally yields

$$\|e_{sz}\|^2_{H^1(\Omega)} \leq CC_s \left(\|\varepsilon_P(s_z)\|_{L^2(\Gamma_C)} + \|\varepsilon_P(s_z)\|^2_{L^2(\Gamma_C)} + \|\varepsilon_P(s_s)\|_{L^2(\Gamma_C)} + \|\varepsilon_P(s_s)\|^2_{L^2(\Gamma_C)} \right)$$

□

For the practical application of our estimate, we modify the general algorithms of model adaptivity III.2 and III.3, such that not the complete cells $Q \in \mathbb{T}$ of our triangulation are marked as Signorini- or Non-Signorini-cells, but only the faces $f \subset \Gamma_C$, hence the estimate (III.16) depends only on these domains.
Furthermore we approximate both s_s and s_z in the estimate of theorem III.4 by the momentary solution s_h and use the monotony of the estimate with regard to $\varepsilon(s_h)$.

III.1.2 Fluid Models

We consider three different fluid models:

- The three-dimensional Stokes model (I.29) with solution (v, p).
- The two-dimensional Stokes model (I.57) with solution (χ^S, ψ^S).
- The Reynolds model (I.77) with solution ψ^R.

In section I.2.5 we introduced the transformations between the solutions of these models.

III.1.2.1 Two-dimensional Stokes model to three-dimensional Stokes model

We consider the solution (v, p) of the original three-dimensional Stokes equation (I.29) and its two-dimensional approximation (I.89) (and (I.90) respective) and (I.85)

$$\begin{aligned} v_i^\chi =& v_i(z_0) + \frac{x_3 - z_0}{g}\delta v_i + \frac{6}{g^3}(x_3 - z_0)(z_1 - x_3)(\chi_i - g\overline{v}_i) \\ =& \overline{v}_i - \frac{\delta v_i}{2} + \frac{x_3 - \overline{z} + g/2}{g}\delta v_i + \frac{6}{g^3}\left(\frac{g^2}{4} - (x_3 - \overline{z})^2\right)(\chi_i - g\overline{v}_i), \qquad i = 1, 2, 3 \\ p^\psi =& \frac{\psi}{g} + \frac{g}{2}\left(\frac{(x_3 - z_0)^2}{g^2}\partial_3 p(s) - \frac{(z_1 - x_3)^2}{g^2}\partial_3 p(r)\right) \end{aligned}$$

with the solution (χ, ψ) of the two-dimensional Stokes problem (I.58):

$$\begin{aligned} \forall \xi \in \tilde{X}: \quad & \langle \partial_\mu \chi_\nu, \partial_\mu \xi_\nu \rangle_{L^2(\Omega_2)} + \langle \chi/g, \xi/g \rangle_{\Omega_2} - \left\langle \tfrac{\psi}{g}, \partial_\nu(\xi_\nu g) \right\rangle_{L^2(\Omega_2)} \\ & \qquad = \langle \kappa_\mu + \gamma_\mu, \xi_\mu \rangle_{L^2(\Omega_2)} - \langle \psi_0 n_\mu - (X_0)_\mu, \xi_\mu \rangle_{L^2(\partial\Omega_2)} \\ \forall \phi \in \tilde{\Psi}: \quad & \left\langle \tfrac{\phi}{g}, \partial_\nu(g\chi_\nu) \right\rangle_{L^2(\Omega_2)} = \langle \sigma_3, \phi \rangle_{L^2(\Omega_2)} \end{aligned}$$

and the auxillary problem (I.54):

$$\Delta\chi_3 - \frac{12}{g^2}\chi_3 - \delta p = -\kappa_3 - \gamma_3.$$

The Stokes-field

$$(\chi^v, \psi^p) = \int_{z_0}^{z_1} (v, p) dx_3$$

solves the exact two-dimensional problem

$$\begin{aligned} \forall \xi \in \tilde{X}: \quad & \langle \partial_\mu \chi_\nu^v, \partial_\mu \xi_\nu \rangle_{L^2(\Omega_2)} + \langle \chi_\nu^v/g, \xi_\nu/g \rangle_{\Omega_2} - \left\langle \frac{\psi^p}{g}, \partial_\nu(\xi_\nu g) \right\rangle_{L^2(\Omega_2)} \\ & = \langle \kappa_\mu + (\gamma_3 + \gamma_v + \gamma_p)_\mu, \xi_\mu \rangle_{L^2(\Omega_2)} - \langle \psi_0 n_\mu - (X_0)_\mu, \xi_\mu \rangle_{L^2(\partial\Omega_2)} \\ \forall \phi \in \tilde{\Psi}: \quad & \left\langle \frac{\phi}{g}, \partial_\nu(g\chi_\nu^v) \right\rangle_{L^2(\Omega_2)} = \langle \sigma_3 + \varepsilon_v, \phi \rangle_{L^2(\Omega_2)}. \end{aligned}$$

The difference of the corresponding equations of both problems yields a variational characterisation of the error $(\varepsilon^{S\chi}, \varepsilon^{S\psi}) = (\chi^v - \chi, \psi^p - \psi)$:

$$\forall \xi \in \tilde{X}: \quad \langle \partial_\mu(\chi^v_\nu - \chi_\nu), \partial_\mu \xi_\nu \rangle_{L^2(\Omega_2)} + \langle (\chi^v_\nu - \chi_\nu)/g, \xi_\nu/g \rangle_{\Omega_2} - \left\langle \frac{\psi^p - \psi}{g}, \partial_\nu(\xi_\nu g) \right\rangle_{L^2(\Omega_2)} = \langle (\gamma_v + \gamma_p)_\mu, \xi_\mu \rangle_{L^2(\Omega_2)} \tag{III.17}$$

$$\forall \phi \in \tilde{\Psi}: \quad \left\langle \frac{\phi}{g}, \partial_\nu(g(\chi^v_\nu - \chi_\nu)) \right\rangle_{L^2(\Omega_2)} = \langle \varepsilon_v, \phi \rangle_{L^2(\Omega_2)}. \tag{III.18}$$

In a more abstract notation (III.17) and (III.18) can be written as

$$\begin{aligned} \forall \xi \in \tilde{X}: \quad & a(\varepsilon^{S\chi}, \xi) - b(\xi, \varepsilon^{S\psi}) = \langle \gamma_{vp}, \xi \rangle_{L^2(\Omega_2)} \\ \forall \phi \in \tilde{\Psi}: \quad & b(\varepsilon^{S\chi}, \phi) = \langle \varepsilon_v, \phi \rangle_{L^2(\Omega_2)}, \end{aligned}$$

with the bilinearforms

$$\begin{aligned} a: & X \times X \to \mathbb{R}, \qquad (\xi, \eta) \to \langle \partial_\mu \xi_\nu, \partial_\mu \eta_\nu \rangle_{L^2(\Omega_2)} + \langle \xi^v_\nu/g, \eta_\nu/g \rangle_{\Omega_2} \\ b: & \Psi \times X \to \mathbb{R}, \qquad (\phi, \eta) \to \left\langle \frac{\phi}{g}, \partial_\nu(g\eta_\nu) \right\rangle_{L^2(\Omega_2)} \end{aligned}$$

and $\gamma_{vp} = \gamma_v + \gamma_p$.
Following corollary II.6 there exist linear mappings

$$A: X \to X, \quad B: \Psi \to X$$

such that the two equations above can be further transformed

$$\forall \xi \in \tilde{X}: \quad \left\langle A\varepsilon^{S\chi}, \xi \right\rangle_{L^2(\Omega_2)} - \left\langle B\varepsilon^{S\psi}, \xi \right\rangle_{L^2(\Omega_2)} = \langle \gamma_{vp}, \xi \rangle_{L^2(\Omega_2)} \tag{III.19}$$

$$\forall \phi \in \tilde{\Psi}: \quad \left\langle B\phi, \varepsilon^{S\chi} \right\rangle_{L^2(\Omega_2)} = \langle \varepsilon_v, \phi \rangle_{L^2(\Omega_2)}. \tag{III.20}$$

To get an estimate for the velocity-error $\varepsilon^{S\chi}$, we choose $\xi = \varepsilon^{S\chi}$ in (III.19) and apply the inequations of Cauchy-Schwarz and Poincaré (theorem II.28) as well as the definition of the Reynolds norm (II.10):

$$\begin{aligned} \left\| \partial_\nu \varepsilon^{S\chi}_\mu \right\|^2_{L^2(\Omega_2)} &= \left\langle A\varepsilon^{S\chi}_\mu, \varepsilon^{S\chi}_\mu \right\rangle_{L^2(\Omega_2)} = \left\langle \gamma_{vp}, \varepsilon^{S\chi} \right\rangle_{L^2(\Omega_2)} + \left\langle B\varepsilon^{S\psi}, \varepsilon^{S\chi} \right\rangle_{L^2(\Omega_2)} \\ &\le \|\gamma_{vp}\|_{L^2(\Omega_2)} \left\| \varepsilon^{S\chi} \right\|_{L^2(\Omega_2)} + \left\| B\varepsilon^{S\psi} \right\|_{L^2(\Omega_2)} \left\| \varepsilon^{S\chi} \right\|_{L^2(\Omega_2)} \\ &\le \left(\|\gamma_{vp}\|_{L^2(\Omega_2)} + \left\| \varepsilon^{S\psi} \right\|_R \right) C_P \left\| \partial_\nu \varepsilon^{S\chi}_\mu \right\|_{L^2(\Omega_2)} \\ \Rightarrow \quad \left\| \partial_\nu \varepsilon^{S\chi}_\mu \right\|_{L^2(\Omega_2)} &\le C_P \left(\|\gamma_{vp}\|_{L^2(\Omega_2)} + \left\| \varepsilon^{S\psi} \right\|_R \right) \end{aligned} \tag{III.21}$$

To gain an estimate for the pressure-error $\varepsilon^{S\psi}$, we choose $\xi = A^{-1}B\varepsilon^{S\psi}$ in (III.19):

$$\left\langle \gamma_{vp} + B\varepsilon^{S\psi}, A^{-1}B\varepsilon^{S\psi} \right\rangle_{L^2(\Omega_2)} = \left\langle A\varepsilon^{S\chi}, A^{-1}B\varepsilon^{S\psi} \right\rangle_{L^2(\Omega_2)} = \left\langle \varepsilon^{S\chi}, B\varepsilon^{S\psi} \right\rangle_{L^2(\Omega_2)}$$

and subtract (III.20) with $\phi = \varepsilon^{S\psi}$:

$$\begin{aligned}
0 =& \left\langle B\varepsilon^{S\psi}, A^{-1}(\gamma_{vp} + B\varepsilon^{S\psi})\right\rangle_{L^2(\Omega_2)} - \left\langle \varepsilon_v, \varepsilon^{S\psi}\right\rangle_{L^2(\Omega_2)} \\
\Rightarrow \quad \left\langle B\varepsilon^{S\psi}, A^{-1}B\varepsilon^{S\psi}\right\rangle_{L^2(\Omega_2)} =& \left\langle \varepsilon_v, \varepsilon^{S\psi}\right\rangle_{L^2(\Omega_2)} - \left\langle B\varepsilon^{S\psi}, A^{-1}\gamma_{vp}\right\rangle_{L^2(\Omega_2)} \\
\Rightarrow \quad \tilde{\alpha}\left\|B\varepsilon^{S\psi}\right\|^2_{L^2(\Omega_2)} \leq& \left\langle \varepsilon_v, \varepsilon^{S\psi}\right\rangle - \left\langle B\varepsilon^{S\psi}, A^{-1}\gamma_{vp}\right\rangle \qquad \text{(ellipticity of } A^{-1}\text{)} \\
\leq& \left\|\varepsilon^{S\psi}\right\|_{L^2(\Omega_2)} \left\|\varepsilon_v - B^*A^{-1}\gamma_{vp}\right\|_{L^2(\Omega_2)} \\
\leq& C_R \left\|\varepsilon^{S\psi}\right\|_R \left\|\varepsilon_v - B^*A^{-1}\gamma_{vp}\right\|_{L^2(\Omega_2)} \quad \text{(equivalence of } \|\cdot\|_R \\
& \qquad\qquad\qquad\qquad\qquad\qquad\qquad\qquad\qquad\qquad \text{and } \|\cdot\|_{H^1_0}\text{, lemma II.32)} \\
\Rightarrow \quad \left\|\varepsilon^{S\psi}\right\|_R \leq& \tfrac{C_R}{\tilde{\alpha}} \cdot \left\|\varepsilon_v - B^*A^{-1}\gamma_{vp}\right\|_{L^2(\Omega_2)}
\end{aligned}$$

For a further estimation of this upper bound, we use results of section I.2:

$$\begin{aligned}
\left\|\varepsilon^{S\psi}\right\|_R \leq& \frac{C_R}{\tilde{\alpha}} \left\|\varepsilon_v - B^*A^{-1}\gamma_{vp}\right\|_{L^2(\Omega_2)} \\
\leq& \frac{C_R}{\tilde{\alpha}} \left\|\varepsilon_v\right\|_{L^2(\Omega_2)} + \frac{C_R}{\tilde{\alpha}} \left\|B^*A^{-1}\right\|_{L^2(\Omega_2)} \left(\left\|\gamma_v\right\|_{L^2(\Omega_2)} + \left\|\gamma_p\right\|_{L^2(\Omega_2)}\right) \\
=& \frac{C_R}{12\tilde{\alpha}} \Big[\left\|g^2\partial_\mu g \partial_3^2 v_\mu(\zeta_v)\right\|_{L^2(\Omega_2)} + \\
& + \left\|B^*A^{-1}\right\|_{L^2(\Omega_2)} \Big(\left\|12g\partial_3^2 v_\mu(\overline{\zeta}) - 3g^2(\partial_3^3 v_\mu(s) - \partial_3^3 v_\mu(r))\right\|_{L^2(\Omega_2)} + \\
& + \left\|12g\partial_\mu\overline{z}\partial_3 p(\overline{z}) + \frac{3}{2}g^2\partial_\mu\overline{z}\left(\partial_3^2 p(r) - \partial_3^2 p(s)\right) + g^2\partial_\mu g\partial_3^2 p(\zeta_p)\right\|_{L^2(\Omega_2)} \Big) \Big] \\
& \qquad\qquad \Big(\text{(I.47)-(I.51) and (A.5) with } z = \overline{z}\Big) \\
\leq& \frac{C_R}{12\tilde{\alpha}} \Big[C_v \left\|g^2\partial_\mu g\right\|_{L^2(\Omega_2)} + \left\|B^*A^{-1}\right\|_{L^2(\Omega_2)} \Big(C_v\Big(12\left\|g\right\|_{L^2(\Omega_2)} + 6\left\|g^2\right\|_{L^2(\Omega_2)}\Big) + \\
& + C_p\Big(12\left\|g\partial_\mu\overline{z}\right\|_{L^2(\Omega_2)} + 3\left\|g^2\partial_\mu\overline{z}\right\|_{L^2(\Omega_2)} + \left\|g^2\partial_\mu g\right\|_{L^2(\Omega_2)}\Big)\Big)\Big] \\
=:& \frac{C_R}{\tilde{\alpha}} \Big[C_v M_\varepsilon + \left\|B^*A^{-1}\right\|_{L^2(\Omega_2)} (C_v M_v + C_p M_p)\Big] \qquad \text{(III.22)}
\end{aligned}$$

where C_v and C_p are constants with

$$\begin{aligned}
C_v \geq& \max\Big\{ \sup_{\mu=1,2;\, x\in\Omega_3} \left|\partial_3^2 v_\mu(x)\right| ; \sup_{\mu=1,2;\, x\in\Omega_3} \left|\partial_3^3 v_\mu(x)\right| \Big\} \\
C_p \geq& \max\left\{ \sup_{x\in\Omega_3} \left|\partial_3 p(x)\right| ; \sup_{x\in\Omega_3} \left|\partial_3^2 p(x)\right| \right\},
\end{aligned}$$

for the existence of C_v and C_p we assume that the velocity- and pressure-functions are sufficiantly smooth:

$$v_\mu \in \mathcal{C}^3(\Omega_3), \quad p \in \mathcal{C}^2(\Omega_3).$$

Furthermore we introduced the abbreviations

$$M_\varepsilon = \frac{1}{12} \left\| g^2 \partial_\mu g \right\|_{L^2(\Omega_2)} \tag{III.23}$$

$$M_v = \|g\|_{L^2(\Omega_2)} + \frac{1}{2} \left\| g^2 \right\|_{L^2(\Omega_2)} \tag{III.24}$$

$$M_p = \|g \partial_\mu \overline{z}\|_{L^2(\Omega_2)} + \frac{1}{4} \left\| g^2 \partial_\mu \overline{z} \right\|_{L^2(\Omega_2)} + \frac{1}{12} \left\| g^2 \partial_\mu g \right\|_{L^2(\Omega_2)} \tag{III.25}$$

Now we can subsume (III.21) and (III.22) to

Theorem III.5
Let (χ, ψ) be the solution of the two-dimensional Stokes problem (I.58) and (χ^v, ψ^p) the (via (I.87) and (I.84)) transformed solution of the three-dimensional Stokes problem (I.27)

$$v_i \in \mathcal{C}^3(\Omega_3), \quad p \in \mathcal{C}^2(\Omega_3).$$

Then there hold the estimates

$$\begin{aligned} \|\partial_\nu(\chi^v - \chi)\|_{L^2(\Omega_2)} \leq & C_P \left[\frac{1}{12}(C_v M_v + C_p M_p) + \|\psi^p - \psi\|_R \right] \\ \|\psi^p - \psi\|_R \leq & \frac{C_R}{\tilde{\alpha}} \left[C_v M_\varepsilon + \left\| B^* A^{-1} \right\|_{L^2(\Omega_2)} (C_v M_v + C_p M_p) \right] \end{aligned}$$

where the numbers M_ε, M_v and M_p are defined in (III.23), (III.24) and (III.25), $\tilde{\alpha}$ is the ellipticity-constant of A^{-1} and C_P the constant of the Poincaré inequation and C_R the equivalence constant of $\|\cdot\|_R$ and $\|\cdot\|_{H^1}$ (lemma II.32).

The conclusion of theorem III.5 is, that the errors of velocity and pressure $\varepsilon^{S\chi}$ and $\varepsilon^{S\psi}$ can be estimated by numbers, that only depend on the geometry of Ω_3 (in particular g, $d_\nu g$, $\overline{z}$ and $d_\nu \overline{z}$):

$$C_R,\ M_\varepsilon,\ M_v \text{ and } M_p$$

and those numbers, that depend on the derivatives of the three-dimensional velocity- and pressure-fields v and p:

$$C_v \text{ and } C_p.$$

$\|B^* A^{-1}\|_{L^2(\Omega_2)}$, $\tilde{\alpha}$ and C_P only implicitly depend on the geometry of Ω_2.
Crucial is, that the existance of C_R is only sure, if $C_P |\partial_\nu g / g| \leq \alpha$ can be estimated by $\alpha < 1$ (compare lemma II.32).

III.1.2.2 Reynolds-model to two-dimensional SubStokes model

At first we estimate the modelling error between the two-dimensional Stokes velocity χ_μ – the solution of (I.57) – and its approximation (I.86)

$$\chi_\mu^R := g\overline{v}_\mu + \frac{g^2}{12}\left[\Delta(g\overline{v}_\mu) - g\partial_\mu\frac{\psi^R}{g} + \kappa_\mu + (\gamma_3)_\mu\right].$$

To gain a repsesentation of the velocity error $\varepsilon^{R\chi} = \chi - \chi^R$, we solve the first equation of (I.57) for χ_μ:

$$\chi = \frac{g^2}{12}\left[\kappa + \gamma_3 + \frac{12}{g}\overline{v} - g\nabla\frac{\psi}{g} + \Delta\chi\right]$$

and subtract (I.86):

$$\begin{aligned}\varepsilon_\mu^{R\chi} =& \frac{g^2}{12}\left(-g\partial_\mu\frac{\psi-\psi^R}{g} + \Delta(\chi - g\overline{v})\right)\\ \overset{(I.69)}{=}& \frac{g^2}{12}\left(-g\partial_\mu\frac{\psi-\psi^R}{g} - \Delta(g^3\rho_\mu)\right)\\ \Rightarrow \qquad \left\|\varepsilon^{R\chi}\right\|_{L^2(\Omega_2)} \leq& \frac{1}{12}\left\|g^3\partial_\mu\frac{\varepsilon^{R\psi}}{g}\right\|_{L^2(\Omega_2)} + \frac{1}{12}\left\|g^2\Delta(g^3\rho_\mu)\right\|_{L^2(\Omega_2)},\end{aligned} \tag{III.26}$$

to estimate $\varepsilon^{R\chi}$ with the help of the estimate for the pressure-difference

$$\varepsilon^{R\psi} := \psi - \psi^R$$

below.

The natural norm for the pressure-error is given by (II.10): $\left\|\varepsilon^{R\psi}\right\|_R$.
ψ^R is the solution of (I.79), whereas ψ is the solution of (I.79) *including* the (undetermined) error term $R_\rho = \frac{g}{12}\partial_\mu(g\Delta(g^3\rho_\mu)) + 2\partial_\mu g g^2\rho_\mu$ (I.76).

$$-\left\langle \delta v_3 + \frac{g}{12}\cdot\partial_\nu\left(g\kappa_\nu\right) + R_1 + R_3 + R_\rho, \phi/g^2\right\rangle_{\Omega_2} = \frac{1}{12}\left\langle g\partial_\mu(\psi/g), g\partial_\mu(\phi/g)\right\rangle_{\Omega_2} \tag{III.27}$$

The difference of both equations (I.79) and (III.27) with $\phi = \varepsilon^\psi$ yields

$$\begin{aligned}\left\|\varepsilon^{R\psi}\right\|_R^2 =& \left\|g\partial_\mu\frac{\psi-\psi^R}{g}\right\|_{L^2(\Omega_2)}^2 = 12\left\langle -R_\rho, \frac{\varepsilon^{R\psi}}{g^2}\right\rangle_{L^2(\Omega_2)}\\ =& \left\langle \hat{R}_\mu, \partial_\mu\frac{\varepsilon^{R\psi}}{g}\right\rangle_{L^2(\Omega_2)} - \underbrace{\left\langle \hat{R}_\mu n_\mu, \frac{\varepsilon^{R\psi}}{g}\right\rangle_{L^2(\partial\Omega_2)}}_{=0}, \qquad \text{with } \frac{12R_\rho}{g} = \partial_\mu\hat{R}_\mu\\ \leq& \left\|\frac{\hat{R}_\mu}{g}\right\|_{L^2(\Omega_2)}\left\|g\partial_\mu\frac{\varepsilon^{R\psi}}{g}\right\|_{L^2(\Omega_2)}\\ \Rightarrow \quad \left\|\varepsilon^{R\psi}\right\|_R \leq& \left\|\frac{\hat{R}_\mu}{g}\right\|_{L^2(\Omega_2)}.\end{aligned} \tag{III.28}$$

To see the existence of $\hat{R}_\mu$, we assume, that $12R_\rho/g$ is sufficiantly smooth. Then there exists a function $\Phi \in H_0^2(\Omega_2)$ such that

$$\Delta\Phi = \frac{12R_\rho}{g}$$

and $\hat{R}_\mu = \partial_\mu\Phi$ is one possible choice. Furthermore there holds the stability inequality:

$$\|\partial_\nu\Phi\|_{L^2(\Omega_2)} \leq C \left\| \frac{12R_\rho}{g} \right\|_{L^2(\Omega_2)},$$

thus we can further estimate (III.28):

$$\begin{aligned}
\left\|\varepsilon^{R\psi}\right\|_R &\leq \left\| \frac{\hat{R}_\mu}{g} \right\|_{L^2(\Omega_2)} \leq \frac{C}{g_{\min}} \left\| \frac{12R_\rho}{g} \right\|_{L^2(\Omega_2)} \\
&\overset{\text{(I.76)}}{=} \frac{C}{g_{\min}} \left\| \partial_\mu \left(g\Delta(g^3\rho_\mu) \right) + 24g\partial_\mu g\rho_\mu \right\|_{L^2(\Omega_2)} \qquad \text{(III.29)} \\
&= \frac{C}{g_{\min}} \left\| \partial_\mu \left(g\Delta(g^3)\rho_\mu + 2g\partial_\nu(g^3)\partial_\nu\rho_\mu + g^4\Delta\rho_\mu \right) + 24g\partial_\mu g\rho_\mu \right\|_{L^2(\Omega_2)} \\
&= \frac{C}{g_{\min}} \Big\| \Big(\partial_\mu(g\Delta(g^3)) + 24g\partial_\mu g \Big) \rho_\mu + g\Delta(g^3)\partial_\mu\rho_\mu + 2\partial_\mu(g\partial_\nu(g^3))\partial_\nu\rho_\mu + \\
&\qquad + 2g\partial_\nu(g^3)\partial_\mu\partial_\nu\rho_\mu + \partial_\mu(g^4)\Delta\rho_\mu + g^4\partial_\mu\Delta\rho_\mu \Big\|_{L^2(\Omega_2)}.
\end{aligned}$$

For further estimates we define

$$C_{vR} := \max\Big\{ \sup_{\mu,\Omega_2} |\rho_\mu|;\ \sup_{\Omega_2} |\partial_\mu\rho_\mu|;\ \sup_{\mu,\nu;\Omega_2} |\partial_\nu\rho_\mu|;\ \sup_{\Omega_2,\nu} |\partial_\mu\partial_\nu\rho_\mu|;\ \sup_{\Omega_2,\mu} |\Delta\rho_\mu|;\ \sup_{\Omega_2} |\partial_\mu\Delta\rho_\mu| \Big\}.$$

which again is only defined, if v_μ is sufficiantly smooth: $v_\mu \in C^5(\Omega_3)$. (Compare the definition of ρ_μ (I.74).)

We conclude this section with

Theorem III.6
If the solution v of the three-dimensional Stokes equation (I.29) is continuously differentiable for five times:

$$v \in C^5(\Omega_3),$$

the modelling error between the two-dimensional Stokes model and the Reynolds-model can be estimated by

$$\begin{aligned}&\left\|\chi - \chi^R\right\|_{L^2(\Omega_2)}\\ \leq&\frac{\|g^2\|_\infty}{12}\left\|\psi - \psi^R\right\|_R + C \cdot C_{vR}\left(\left\|g^2\Delta(g^3)\right\|_{L^2(\Omega_2)} + \left\|g^5\right\|_{L^2(\Omega_2)} + 6\left\|g^4\nabla g\right\|_{L^2(\Omega)}\right)\end{aligned}$$

and the pressure error

$$\begin{aligned}\left\|\psi - \psi^R\right\|_R \leq&\frac{CC_{vR}}{g_{\min}}\Big(\left\|\partial_\mu(g\Delta(g^3)) + 24g\partial_\mu g\right\|_{L^2(\Omega_2)} + \left\|g\Delta(g^3)\right\|_{L^2(\Omega_2)} +\\ &+ 2\left\|\partial_\mu(g\partial_\nu(g^3))\right\|_{L^2(\Omega_2)} + 2\left\|g\partial_\nu(g^3)\right\|_{L^2(\Omega_2)} + \left\|\partial_\mu(g^4)\right\|_{L^2(\Omega_2)} + \left\|g^4\right\|_{L^2(\Omega_2)}\Big)\end{aligned}$$

Proof. The estimate for the velocity error $\varepsilon^{R\chi}$ is concluded of (III.26) by the estimate of ρ and its derivatives with the help of C_{vR} and the estimate for the pressure error is a consequence of (III.29):

$$\begin{aligned}\left\|\psi - \psi^R\right\|_R \leq&\ \tfrac{C}{g_{\min}}\Big\|\Big(\partial_\mu(g\Delta(g^3)) + 24g\partial_\mu g\Big)\rho_\mu + g\Delta(g^3)\partial_\mu\rho_\mu + 2\partial_\mu(g\partial_\nu(g^3))\partial_\nu\rho_\mu +\\ &+2g\partial_\nu(g^3)\partial_\mu\partial_\nu\rho_\mu + \partial_\mu(g^4)\Delta\rho_\mu + g^4\partial_\mu\Delta\rho_\mu\Big\|_{L^2(\Omega_2)}\\ \leq&\ \tfrac{CC_{vR}}{g_{\min}}\Big(\|\partial_\mu(g\Delta(g^3)) + 24g\partial_\mu g\|_{L^2(\Omega_2)} + \|g\Delta(g^3)\|_{L^2(\Omega_2)} +\\ &+2\|\partial_\mu(g\partial_\nu(g^3))\|_{L^2(\Omega_2)} + 2\|g\partial_\nu(g^3)\|_{L^2(\Omega_2)} + \|\partial_\mu(g^4)\|_{L^2(\Omega_2)} + \|g^4\|_{L^2(\Omega_2)}\Big)\end{aligned}$$

□

III.2 Error Estimates – Discretisation Error

In this section we discuss the discretisation error e_d in (III.3) for the case of a finite element discretisation.

Here we have not to distinguish the coarse and the accurate model ((III.2) and (III.1)). Furthermore in the following we specialize (III.2) $\Phi(u) = 0$ to the cases of elliptic and saddle-point (in-)equations. The solution will then be denoted by $v \in V$ or $(v, p) \in V \times \Pi$ respectively.

III.2.1 Elliptic Problems

III.2.1.1 A-priori Error for Elliptic Problems

Basically we follow Braess [1997], Glowinski [1984] and Ciarlet [1975] to develop a-priori-estimates for the discretization error of elliptic variational equations (III.31) and inequations (III.33). These estimates (corollary III.8 and theorem III.10) imply the convergence of the used FE-methods and furthermore they are of optimal order (with respect to the maximal cell-diameter h of the triangulation), i. e. of the same order as the interpolation error in the corresponding finite-dimensional spaces.

Variational Equations
Let V be a Hilbert space of $H^1(\Omega)$-functions, $a : V \times V \to \mathbb{R}$ a V-elliptic and continuous bilinear form:

$$\begin{aligned} \forall w \in V: \quad a(w,w) &\geq \alpha \|w\|^2_{H^1(\Omega)} \\ \forall u, w \in V: \quad a(u,v) &\leq C \|u\|_{H^1(\Omega)} \|v\|_{H^1(\Omega)} \end{aligned} \tag{III.30}$$

and $l \in V$. We examine the abstract elliptic problem

$$\text{Find } v \in V, \text{ such that } \forall w \in V: \quad a(v,w) = \langle l, w \rangle . \tag{III.31}$$

and its approximation for $V_h \subset V$:

$$\text{Find } v_h \in V_h, \text{ such that } \forall w \in V_h: \quad a(v_h,w) = \langle l, w \rangle . \tag{III.32}$$

For these we have

Lemma III.7 (Céa)
If $a : V \times V \to \mathbb{R}$ is a V-elliptic bilinear form, then for the solutions v and v_h of the elliptic problem (III.31) and its approximation (III.32), we have the estimate

$$\|v - v_h\| \leq \frac{C}{\alpha} \inf_{w \in V_h} \|v - w\| .$$

with the constants α and C, given in (III.30).

Proof. Braess [1997] □

From the Céa Lemma III.7 and theorem A.3 we conclude the convergence of the FE-method:

Corollary III.8
For $V \subset H^1(\Omega)$, a triangulation $\mathbb{T}$ of Ω with

$$h = \sup_{Q \in \mathbb{T}} \operatorname{diam}(Q),$$

a solution $v \in H^2(\Omega)$ of the elliptic problem (III.31) and its approximation, the solution v_h of (III.32) with $V_h = V \cap Q^m(\Omega)$, there holds

$$\|v - v_h\|_{H^1(\Omega)} = O(h^m).$$

Variational Inequations
For applications like the contact problem (section I.1.4) or cavitation in a fluid (sections I.2.2 and I.2.4.1), (III.31) is extended to a variational inequality (e. g. (II.15)):

$$\text{Find } v \in K, \text{ such that } \forall w \in K: \quad a(v, w - v) \geq \langle l, w - v \rangle \tag{III.33}$$

with a and l as above and a convex closed subset $K \subset V$.
The discrete approximation of (III.33) is

$$\text{Find } v_h \in K_h, \text{ such that } \forall w \in K_h: \quad a(v_h, w - v_h) \geq \langle l, w - v_h \rangle . \tag{III.34}$$

We remark, that in general $K_h \subset V_h$ is *not* a subset of K. E. g. for the approximation of an obstacle problem

$$K = \{v \in V | v(x) \geq \psi(x), x \in \Omega\}$$

with linear elements we set

$$K_h = \{v \in V_h | v(x_s) \geq \psi(x_s) \text{ for all support points } x_s\}$$

and might get a situation as scatched in figure III.2.

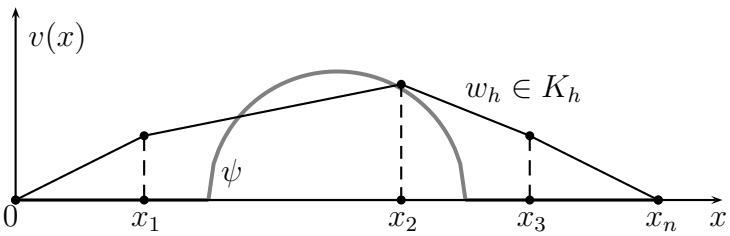

Figure III.2: Approximation of an obstacle problem. Example for a function $w_h \in K_h$, that does not hold the continuous obstacle condition $v \geq \psi$.

Ciarlet [1975] gives the following error estimates for the approximation (III.34). Therefor we recall, that we can write $a(\cdot,\cdot)$ as

$$a(u,v) = \langle Au, v\rangle$$

with a linear mapping $A : V \to V$, following corollary II.6.

Theorem III.9 (Falk I)
For $f,\ Av \in L^2(\Omega)$, there exists a constant $C > 0$, independend of V_h and K_h, such that for the solutions v of (III.33) and v_h of (III.34) there holds the estimate

$$\|v - v_h\|^2_{H^1(\Omega)} \leq C\left(\inf_{w_h\in K_h}\left(\|v - w_h\|^2_{H^1(\Omega)} + \|v - w_h\|_{L^2(\Omega)}\right) + \inf_{w\in K}\|v_h - w\|_{L^2(\Omega)}\right).$$

Proof. (Compare Ciarlet [1975].) In contrast to the case of elliptic equations, here we have no Galerkin orthogonality. Furthermore the approximation of K need not to be conform: $K_h \not\subset K$.
In the following calculation we circumvent this difficulties:

$$\begin{aligned}
\|v - v_h\|^2_{H^1(\Omega)} \leq& \frac{1}{\alpha}a(v - v_h, v - v_h) = \frac{1}{\alpha}\left(a(v - v_h, v - w_h) + a(v - v_h, w_h - v_h)\right)\\
\leq& \frac{1}{\alpha}\Big(\|a\|_{H^1(\Omega)}\|v - v_h\|_{H^1(\Omega)}\|v - w_h\|_{H^1(\Omega)} +\\
&\quad + a(v, w_h - v) + a(v, v - v_h) - a(v_h, w_h - v_h)\Big)\\
\leq& \frac{1}{2}\|v - v_h\|^2_{H^1(\Omega)} + \frac{\|a\|^2_{H^1(\Omega)}}{2\alpha^2}\|v - w_h\|^2_{H^1(\Omega)} +\\
&+ \frac{1}{\alpha}\Big(\langle Av, w_h - v\rangle_{L^2(\Omega)} + a(v, v - w) +\\
&\quad + \langle Av, w - v_h\rangle_{L^2(\Omega)} - \langle l, w_h - v_h\rangle_{L^2(\Omega)}\Big)\\
\Rightarrow\quad \|v - v_h\|^2_{H^1(\Omega)} \leq& \frac{\|a\|^2_{H^1(\Omega)}}{\alpha^2}\|v - w_h\|^2_{H^1(\Omega)} + \frac{2}{\alpha}\langle Av - l, w_h - v + w - v_h\rangle_{L^2(\Omega)}\\
\leq& \frac{\|a\|^2_{H^1(\Omega)}}{\alpha^2}\|v - w_h\|^2_{H^1(\Omega)} + \frac{2\|Av - l\|_{L^2(\Omega)}}{\alpha}\|v - w_h\|_{L^2(\Omega)} +\\
&+ \frac{2\|Av - l\|_{L^2(\Omega)}}{\alpha}\|v_h - w\|_{L^2(\Omega)}
\end{aligned}$$

□

Theorem III.10 (Falk II)
For the approximation (III.34) with linear elements, there holds the estimate

$$\|v - v_h\|_{H^1(\Omega)} = O(h).$$

Proof. The proof, given by Ciarlet [1975] is done for triangles, but can be adapted to elements on quadrilaterals, the geometry only enters through the interpolation-estimates, these are given in theorem A.3 for quadrilaterals too. □

This estimate is sufficiant for most applications, because a higher order of regularity than $v \in H^2(\Omega)$ cannot be assumed, what can be illustrated for the obstacle example above. In the regions, where the displacement v changes from contact to non-contact, the first derivative is continuous, but the second one is not any longer: See figure III.3.

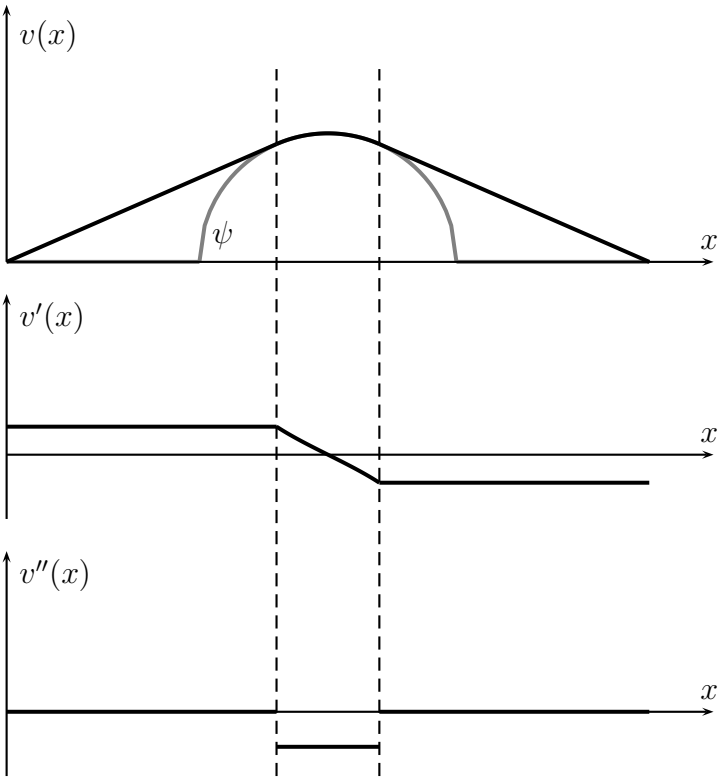

Figure III.3: Noncontinuous second derivative of the solution of the obstacle problem.

To complete this section, we recall, that all elliptic applications in this work fulfill the conditions, assumed by corollary III.8 and theorem III.9, that are basically continuity and ellipticity of the considered bilinear form (III.30):

- For the *deformation of a solid body* ellipticity is shown in lemma II.34, continuity is obvious:

$$|a(r,s)| = \frac{1}{2}\left\langle \partial_i r_j, \partial_i s_j + \partial_j s_i \right\rangle_{L^2} \leq \frac{1}{2}\left\|\partial_i r_j\right\|_{L^2} 2 \left\|\partial_i s_j\right\|_{L^2} \leq \|r\|_{H^1} \|s\|_{H^1}$$

- The bilinearform of the *Reynolds problem* can be written as scalar product $\langle \cdot, \cdot \rangle_R$. Because the induced norm $\|\cdot\|_R$ is equivalent to $\|\cdot\|_{H^1}$ (lemma II.32), $\langle \cdot, \cdot \rangle_R$ is H^1–elliptic and H^1–continuous.

III.2.1.2 A-posteriori Estimate for the Deformation of a Solid Body

We follow Braess [1997] section III.8.
We examine problem (II.11) and introduce the norm

$$\|r\|_a := \sqrt{a(r,r)} \tag{III.35}$$

with the bilinear form (II.13)

$$a(s,r) = 2\mu \langle \varepsilon_{ij}(s), \varepsilon_{ij}(r) \rangle_\Omega + 2\lambda \langle \varepsilon_{ll}(s), \varepsilon_{jj}(r) \rangle_\Omega .$$

$\|\cdot\|_a$ is equivalent to $\|\cdot\|_{H^1(\Omega)}$ on $V_0 = H^1_{0,\Gamma_0}(\Omega)$:

- $\|s\|_a \leq \|s\|_{H^1(\Omega)}$:

$$\begin{aligned}
\|s\|_a^2 =& \frac{\mu}{2} \langle \partial_i s_j + \partial_j s_i, \partial_i s_j + \partial_j s_i \rangle_{L^2(\Omega)} + 2\lambda \|\text{div } s\|^2_{L^2(\Omega)} \\
=& \mu \Big(\underbrace{\langle \partial_i s_j, \partial_i s_j \rangle_{L^2(\Omega)}}_{=\|\partial_i s_j\|^2_{L^2(\Omega)}} + \underbrace{\langle \partial_i s_j, \partial_j s_i \rangle_{L^2(\Omega)}}_{\leq \|\partial_i s_j\|_{L^2(\Omega)} \|\partial_j s_i\|_{L^2(\Omega)}} \Big) + 2\lambda \|\text{div } s\|^2_{L^2(\Omega)} \\
\leq& 2\mu \|\partial_i s_j\|^2_{L^2(\Omega)} + 2\lambda \|\text{div } s\|^2_{L^2(\Omega)} \leq (2\mu + 2\lambda) |s|^2_{H^1(\Omega)}
\end{aligned}$$

- $\|s\|_a^2 \geq c \cdot \|s\|^2_{H^1(\Omega)}$ is the content of Korn's inequality (lemma II.34).

The continuous problem (II.11) is

$$s \in V_0 : \quad \forall r \in V_0 : \; a(s,r) = \langle l, r \rangle \tag{III.36}$$

with

$$\langle l, r \rangle = \langle \rho f_i, r_i \rangle_{L^2(\Omega)} + \langle \tau_{ij} n_j, r_i \rangle_{L^2(\Gamma_\tau)} .$$

The discrete problem is

$$s_h \in (V_0)_h : \quad \forall r \in (V_0)_h : \; a(s_h, r) = \langle l, r \rangle \tag{III.37}$$

with $V_0 = (H^1_{0,\Gamma_0}(\Omega))^d$ and $(V_0)_h = V_0 \cap (Q_1(\Omega))^d$.
From a duality argument we have

$$\|s - s_h\|_a = \sup_{r \in V_0, \|r\|_a = 1} a(s - s_h, r). \tag{III.38}$$

Thus we estimate:

$$\begin{aligned}
a(s-s_h,r) &= 2\mu\left\langle\varepsilon_{ij}(s-s_h),\varepsilon_{ij}(r)\right\rangle_{L^2(\Omega)} + 2\lambda\left\langle\varepsilon_{ll}(s-s_h),\varepsilon_{jj}(r)\right\rangle_{L^2(\Omega)} \\
&\overset{\text{(III.36)}}{=} \left\langle\rho f_i, r_i\right\rangle_{L^2(\Omega)} + \left\langle\tau_{ij}n_j, r_i\right\rangle_{L^2(\Gamma_\tau)} - 2\mu\left\langle\varepsilon_{ij}(s_h),\varepsilon_{ij}(r)\right\rangle_{L^2(\Omega)} + \\
&\quad -2\lambda\left\langle\varepsilon_{ll}(s_h),\varepsilon_{jj}(r)\right\rangle_{L^2(\Omega)} \\
&= \left\langle\rho f_i, r_i\right\rangle_{L^2(\Omega)} + \left\langle\tau_{ij}n_j, r_i\right\rangle_{L^2(\Gamma_\tau)} + \\
&\quad - \sum_{Q\in\mathbb{T}_h}\Big(\mu\left\langle\partial_i(s_h)_j + \partial_j(s_h)_i, \partial_j r_i\right\rangle_{L^2(Q)} + 2\lambda\left\langle\partial_l(s_h)_l, \partial_j r_j\right\rangle_{L^2(Q)}\Big) \\
&= \sum_{Q\in\mathbb{T}_h}\Big(\left\langle\rho f_i + \mu(\partial_j\partial_i(s_h)_j + \partial_j\partial_j(s_h)_i) + 2\lambda\partial_i\partial_l(s_h)_l, r_i\right\rangle_{L^2(Q)} + \\
&\qquad + \left\langle\tau_{ij}n_j - \mu n_j(\partial_i(s_h)_j + \partial_j(s_h)_i) - 2\lambda n_i\partial_l(s_h)_l, r_i\right\rangle_{L^2(\partial Q)}\Big) \\
&\qquad \Big[\tau_{ij}|_{\Omega\setminus\Gamma_\tau} := 0\Big] \\
&= \sum_{Q\in\mathbb{T}_h}\Big(\left\langle\rho f_i + 2\mu\partial_j\varepsilon_{ij}(s_h) + 2\lambda\partial_i\partial_l(s_h)_l, r_i\right\rangle_{L^2(Q)} + \\
&\qquad + \tfrac{1}{2}\left\langle\left[\tau_{ij}n_j - 2\mu n_j\varepsilon_{ij}(s_h) - 2\lambda n_i\partial_l(s_h)_l\right], r_i\right\rangle_{L^2(\partial Q)}\Big) \\
&= \sum_{Q\in\mathbb{T}_h}\Big(\left\langle\rho f_i + 2\mu\partial_j\varepsilon_{ij}(s_h) + 2\lambda\partial_i\varepsilon_{ll}(s_h), (r-I_h(r))_i\right\rangle_{L^2(Q)} + \\
&\qquad + \tfrac{1}{2}\left\langle\left[\tau_{ij}n_j - 2\mu n_j\varepsilon_{ij}(s_h) - 2\lambda n_i\varepsilon_{ll}(s_h)\right], (r-I_hr)_i\right\rangle_{L^2(\partial Q)}\Big) \\
&\qquad \text{[Galerkin-orthogonality]} \\
&\leq \sum_{Q\in\mathbb{T}_h}\Big(\underbrace{\left\|\rho f_i + 2\mu\partial_j\varepsilon_{ij}(s_h) + 2\lambda\partial_i\varepsilon_{ll}(s_h)\right\|_{L^2(Q)}}_{\eta_Q}\left\|r-I_hr\right\|_{L^2(Q)} + \\
&\quad + \underbrace{\frac{1}{2}\left\|\left[\tau_{ij}n_j - 2\mu n_j\varepsilon_{ij}(s_h) - 2\lambda n_i\varepsilon_{ll}(s_h)\right]\right\|_{L^2(\partial Q)}}_{\eta_{\partial Q}}\left\|r-I_hr\right\|_{L^2(\partial Q)}\Big)
\end{aligned}$$

Here we used

Definition III.11 (Jump Operator)
In any boundary point $x \in \partial Q$ of a cell $Q \in \mathbb{T}_h$ of our triangulation with outer normal n, we define

$$[v](x) := \lim_{\delta\to 0}(-v(x+\delta n) + v(x-\delta n)).$$

For consistency at the boundary of the domain Ω we set

$$v(x+\delta n) := -v(x-\delta n) \text{ for } x \in \partial\Omega.$$

In Braess [1997], through the application of the Bramble-Hilbert-Lemma, the interpolation estimates

$$\left\|r-I_hr\right\|_{L^2(Q)} \leq ch_Q^{d/2}\left|r\right|_{H^1(Q)} \text{ and } \left\|r-I_hr\right\|_{L^2(\partial Q)} \leq ch_Q^{(d-1)/2}\left|r\right|_{H^1(Q)} \tag{III.39}$$

are shown. With the help of these we conclude

Theorem III.12
The approximation error $s - s_h$ of the deformation problem (III.36) and its approximation (III.37) can be estimated with regard to the energy norm

$$\|s - s_h\|_a^2 \leq c \sum_{Q \in \mathbb{T}_h} \left(\eta_Q^2 h_Q^d + \eta_{\partial Q}^2 h_Q^{d-1} \right)$$

with the cell-wise residuals

$$\begin{aligned} \eta_Q =& \|\rho f_i + 2\mu \partial_j \varepsilon_{ij}(s_h) + 2\lambda \partial_i \varepsilon_{ll}(s_h)\|_{L^2(Q)} \\ \eta_{\partial Q} =& \frac{1}{2} \left\| \left[\tau_{ij} n_j - 2\mu n_j \varepsilon_{ij}(s_h) - 2\lambda n_i \varepsilon_{ll}(s_h) \right] \right\|_{L^2(\partial Q)} . \end{aligned}$$

Proof. We collect the above:

$$\begin{aligned} \|s - s_h\|_a =& \sup_{r \in V_0} \frac{a(s - s_h, r)}{\|r\|_a} \\ \leq& \sup_{r \in V_0} \frac{\sum_{Q \in \mathbb{T}_h} \left(\eta_Q h_Q^{d/2} + \eta_{\partial Q} h_Q^{(d-1)/2} \right) c \|r\|_{H^1(Q)}}{\|r\|_{H^1(\Omega)}} \\ \leq& c \sqrt{\sum_{Q \in \mathbb{T}_h} \left(\eta_Q^2 h_Q^d + \eta_{\partial Q}^2 h_Q^{d-1} \right)}. \end{aligned}$$

□

III.2.1.3 A-posteriori Estimate for the Contact Problem

In this section we derive an a-posteriori estimate for the contact problem (III.40). Therefor we adapt the estimator for the Laplace problem, given in Chen and Nochetto [2000].

Further works dealing with energy norm estimates are Zou et al. [2011] and for pointwise estimates Nochetto et al. [2005] and Nochetto et al. [2003].
We recall our problem of deformation (II.15):

$$\text{Find } s \in \Pi(V_0): \quad \forall r \in \Pi(V_0): \quad a(s, r - s) - \langle l, r - s \rangle \geq 0. \tag{III.40}$$

with

$$\begin{aligned} a(q, r) =& \mu \langle \partial_i q_j, \partial_i r_j + \partial_j r_i \rangle_{L^2(\Omega)} + 2\lambda \langle \partial_l q_l, \partial_j r_j \rangle_{L^2(\Omega)} \\ \langle l, r \rangle =& \langle \rho f_i, r_i \rangle_{L^2(\Omega)} + \langle \tau_{ij} n_j, r_i \rangle_{L^2(\Gamma_\tau)} \\ \Pi(V_0) =& \left\{ r \in V_0 \middle| P(x + r(x)) = x + r(x),\ x \in \Gamma_C \right\} \\ P(\xi) =& \begin{cases} \xi, & \xi \cdot n \leq b(\xi) \\ \xi - (\xi \cdot n - b(\xi)) n, & \xi \cdot n > b(\xi) \end{cases} \end{aligned}$$

In the case of projection in z-direction, it is

$$n \equiv e_z \text{ and } b : \Gamma_C \to \mathbb{R}.$$

In the case of the Signorini-projection, we have

$$(n, b) : \Gamma_C \to \mathbb{R}^d \times \mathbb{R}. \tag{III.41}$$

The discrete problem is

$$\text{Find } s_h \in \Pi(V_h) : \quad \forall r \in \Pi(V_h) : \quad a(s_h, r - s_h) - \langle l, r - s_h \rangle \geq 0. \tag{III.42}$$

with

$$\Pi_h(V_h) = \{r \in (V_0)_h | P(\sigma + r(\sigma)) = \sigma + r(\sigma),\ \sigma \in \Sigma_C\}$$

and the set of contact support points

$$\Sigma_C := \Sigma_h \cap \Gamma_C. \tag{III.43}$$

Here

$$\Sigma_h := \{\sigma \in \overline{\Omega} | \sigma \text{ is support point}\}$$

denotes the set of support points and for any $\sigma \in \Sigma_h$ the corresponding basis function is ϕ_σ. As already mentioned in the context of the discretisation of the general variational inequation (III.34), the usual case is $\Pi(V_h) \not\subset \Pi(V_0)$.
To derive an a-posteriori estimate for an obstacle problem (with an active restriction on the whole domain Ω) Chen and Nochetto [2000] introduced the mapping

$$\Pi_h : L^1(\Omega) \to V_h; \quad (\Pi_h \varphi)(x) := \sum_{\sigma \in \Sigma_h} \left(\frac{1}{|\Delta_\sigma|} \int\limits_{\Delta_\sigma} \varphi(y) dy \right) \phi_\sigma(x) \tag{III.44}$$

with the ball Δ_σ of maximal size with $\Delta_\sigma \subset \text{supp}(\phi_\sigma)$ scatched in figure III.4.

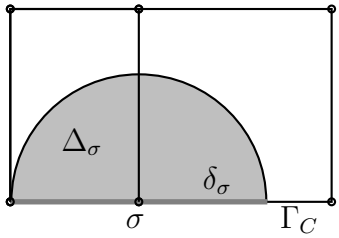

Figure III.4: The ball- and disk-like domains $\Delta\sigma$ and δ_σ for the projections Π_h and π_h.

Since our projection $P(x)$ only acts on Γ_C (Σ_C respective in the discrete case), we modify this mapping:

$$\begin{aligned}
&\pi_h : L^1(\partial\Omega) \to V_h \\
&(\pi_h\varphi)(x) := \begin{cases} \varphi(\sigma), & x = \sigma \in \Sigma_h \setminus \Gamma_C \\ \varphi(\sigma) + \Big(\frac{1}{|\delta_\sigma|}\int\limits_{\delta_\sigma} n\cdot\varphi - n(\sigma)\cdot\varphi(\sigma)\Big)n(\sigma), & x = \sigma \in \Sigma_C \\ \sum\limits_{\sigma\in\Sigma_h} \pi_h\varphi(\sigma)\phi_\sigma(x), & x \notin \Sigma_h. \end{cases}
\end{aligned} \tag{III.45}$$

In points $x \notin \Sigma_h$ (third case) the mapping just interpolates between the function values at the support points (first two cases).
In difference to (III.44) the mapping π_h (III.45) is the standard interpolation operator on the non-contact points of our domain $\Sigma_h \setminus \Sigma_C$, furthermore on Γ_C it averages over disc-like domains $\delta_\sigma = \Delta_\sigma \cap \Gamma_C$ instead of the balls Δ_σ, used in (III.44) (see figure III.4).
For linear elements, as we use here, π_h preserves positivity at least in the support points:

$$\forall x \in \Gamma_C : \ (n\cdot\varphi)(x) \geq 0 \quad \Rightarrow \quad \forall \sigma \in \Sigma_C : \ (n\cdot\pi_h\varphi)(\sigma) \geq 0. \tag{III.46}$$

This is seen via an elementary calculation:

$$\begin{aligned}
(n\cdot\pi_h\varphi)(\sigma) =& n(\sigma)\cdot\left(\varphi(\sigma) + \Big(\frac{1}{|\delta_\sigma|}\int\limits_{\delta_\sigma} n\cdot\varphi - n(\sigma)\cdot\varphi(\sigma)\Big)n(\sigma)\right) \\
=& \frac{1}{|\delta_\sigma|}\int\limits_{\delta_\sigma} n\cdot\varphi \geq 0.
\end{aligned} \tag{III.47}$$

For other points $x \in \Gamma_C$ we not yet state the same preservation.
Additional we state the following two lemmas:

Lemma III.13
For any cell of our triangulation $Q \in \mathbb{T}_h$, a face $e \subset Q$ and any function $\varphi \in (H^1(\Omega))^d$ there holds

$$\begin{aligned}
\|\varphi - \pi_h\varphi\|_{L^2(Q)} \leq& C\Big(h_Q \|\nabla\varphi\|_{L^2(Q)} + h_Q^{3/2} \|\nabla(n\cdot\varphi)\|_{L^2(\tilde{Q}\cap\Gamma_C)}\Big) \\
\|\varphi - \pi_h\varphi\|_{L^2(e)} \leq& C\Big(h_Q^{1/2} \|\nabla\varphi\|_{L^2(e)} + h_Q \|\nabla(n\cdot\varphi)\|_{L^2(\tilde{Q}\cap\Gamma_C)}\Big).
\end{aligned}$$

$\tilde{Q}$ and $\tilde{e}$ denote the union of the neighbour cells of Q or e respective.

Proof. We consider both cases at once by taking $A \in \{e, Q\}$.
Firstly we insert the standard interpolation of φ and apply the triangle inequation:

$$\|\varphi - \pi_h\varphi\|_{L^2(A)} \leq \|\varphi - I_h\varphi\|_{L^2(A)} + \|I_h\varphi - \pi_h\varphi\|_{L^2(A)}.$$

The first term is the standard interpolation error and can be estimated by

$$\|\varphi - I_h\varphi\|_{L^2(A)} \leq Ch_Q \|\nabla\varphi\|_{L^2(A)}.$$

From the definition of π_h (III.45) (and with the cases $A \in \{e, Q\}$) we can write the remaining term as

$$\begin{aligned}
&\|I_h\varphi - \pi_h\varphi\|^2_{L^2(A)} \\
&\quad= \int_A \Big(I_h\varphi(x) - \sum_{\sigma\in\Sigma_h} \varphi(\sigma)\phi_\sigma(x) + \\
&\qquad\qquad - \sum_{\sigma\in\Sigma_C} \Big(\frac{1}{|\delta_\sigma|} \int_{\delta_\sigma} n\cdot\varphi - n(\sigma)\cdot\varphi(\sigma) \Big) n(\sigma)\phi_\sigma(x) \Big)^2 dA \\
&\quad= \int_A \Big(\sum_{\sigma\in\Sigma_C} \int_{\delta_\sigma} (n\cdot\varphi(y) - n\cdot\varphi(\sigma))\, dy \frac{n(\sigma)}{|\delta_\sigma|}\phi_\sigma(x) \Big)^2 dA \\
&\quad= \int_A \Big(\sum_{\sigma\in\Sigma_C} \int_{\delta_\sigma} \int_0^1 \nabla(n\cdot\varphi)(\sigma + t(y-\sigma))\cdot(y-\sigma) dt dy \frac{n(\sigma)}{|\delta_\sigma|}\phi_\sigma(x) \Big)^2 dA \\
&\quad\leq C \sum_{\sigma\in\Sigma_C} \underbrace{\int_A (\phi_\sigma(x))^2 dA}_{\leq Ch_Q^{\dim A}} \underbrace{\frac{1}{|\delta_\sigma|^2}}_{\leq Ch_Q^{-2(d-1)}} \Big(\int_{\delta_\sigma} \int_0^1 \nabla(n\cdot\varphi)(\sigma + t(y-\sigma))\cdot(y-\sigma) dt dy \Big)^2 \\
&\quad\leq Ch_Q^{2+\dim A-2d} \sum_{\sigma\in\Sigma_C} \Big(\int_0^1 \int_{t\cdot\delta_\sigma} \nabla(n\cdot\varphi)(\xi)\cdot\frac{\xi-\sigma}{t^2} d\xi dt \Big)^2 \\
&\qquad\qquad\qquad\qquad (\text{with } t\delta_\sigma = \{\sigma + t(y-\sigma) | y\in\delta_\sigma\}) \\
&\quad\leq Ch_Q^{2+\dim A-2d} \sum_{\sigma\in\Sigma_C} \Big(\int_0^1 t^{-2} \underbrace{\|\nabla(n\cdot\varphi)\|_{t\delta_\sigma}}_{\leq\|\nabla(n\cdot\varphi)\|_{\delta_\sigma}} \underbrace{\|\xi-\sigma\|_{t\delta_\sigma}}_{\leq C(th_Q)^{(2+d-1)/2}} dt \Big)^2 \\
&\quad\leq Ch_Q^{3+\dim A-d} \sum_{\sigma\in\Sigma_C} \|\nabla(n\cdot\varphi)\|^2_{\delta_\sigma} \Big(\underbrace{\int_0^1 t^{(d-3)/2} dt}_{2/(d-1)} \Big)^2 \\
&\quad\leq Ch_Q^{3+\dim A-d} \|\nabla(n\cdot\varphi)\|^2_{\tilde{Q}\cap\Gamma_C}
\end{aligned}$$

□

If we assume a bilinear function φ_h and take a closer look on the proof of Lemma III.13 we note, that the interpolation-error $\varphi_h - I_h\varphi_h$ vanishes and there remains

Lemma III.14
For any cell of our triangulation $Q \in \mathbb{T}_h$, a face $e \subset Q$ and any function $\varphi_h \in (Q^1(\Omega))^d$ there holds

$$\begin{aligned}\|\varphi_h - \pi_h\varphi_h\|_{L^2(Q)} \leq & Ch_Q^{3/2} \|\nabla(n \cdot \varphi_h)\|_{L^2(\tilde{Q}\cap\Gamma_C)} \\ \|\varphi_h - \pi_h\varphi_h\|_{L^2(e)} \leq & Ch_Q \|\nabla(n \cdot \varphi_h)\|_{L^2(\tilde{Q}\cap\Gamma_C)} .\end{aligned}$$

If there would hold $s_h \in K := \Pi(V_0)$ and $\pi_h(s) \in K_h := \Pi_h(V_h)$, we could choose these as test functions in (III.40) and (III.42) respective, to obtain an estimate for the error $e = s - s_h$ in the a-norm (III.35):

$$\begin{aligned} 0 \leq & a(s, s_h - s) - \langle l, s_h - s\rangle + a(s_h, \pi_h(s) - s_h) - \langle l, \pi_h(s) - s_h\rangle \\ \Rightarrow \|e\|_a^2 = & a(s - s_h, s - s_h) \\ \leq & a(-s_h, s - s_h) + a(s_h, \pi_h(s) - s_h) + \langle l, s - \pi_h(s)\rangle \\ = & a(s_h, \pi_h(s) - s) - \langle l, \pi_h(s) - s\rangle \\ = & \underbrace{a(s_h, \pi_h(e) - e) - \langle l, \pi_h(e) - e\rangle}_{C} + \underbrace{a(s_h, \pi_h(s_h) - s_h) - \langle l, \pi_h(s_h) - s_h\rangle}_{D} . \end{aligned}$$

If $s_h \in K$ and $\pi_h(s) \in K_h$ do not hold, we have to project them in the following way:

$$r = s_h^* \text{ with } s_h^*(x) = \begin{cases} P(x + s_h(x)) - x & , \quad \text{for } x \in \Gamma_C \\ s_h(x) & , \quad x \in Q \in \mathbb{T}_h \text{ with } Q \cap \Gamma_C = \emptyset \\ \text{continuous extension} & , \quad \text{else} \end{cases}$$

in (III.42) (see figure III.5).
Analogue we take

$$s^*(x) = \begin{cases} P(\sigma + \pi_h s(\sigma)), & x = \sigma \in \Sigma_C \\ \pi_h s(x), & x \in \Sigma_h \setminus \Sigma_C \\ \sum\limits_{\sigma\in\Sigma_h} s^*(\sigma)\phi_\sigma(x), & x \notin \Sigma_h \end{cases}$$

in (III.40).

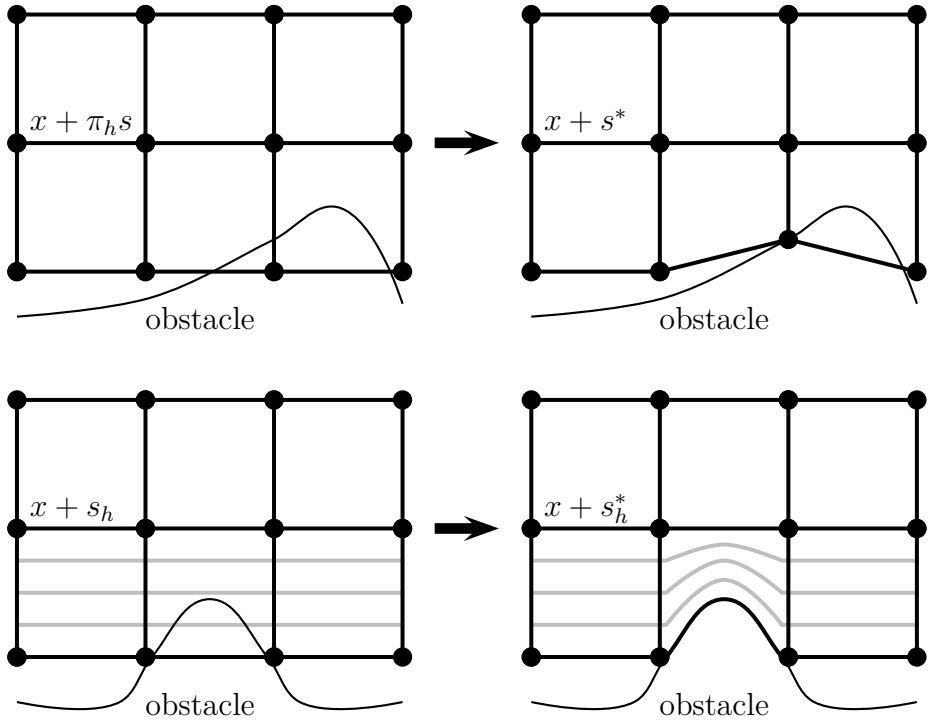

Figure III.5: Modification of the solution s of the continuous problem and of the discrete problem s_h. The bright lines denote the continuous extension in the definition of s_h^*.

Now there arise additional terms in the error estimate:

$$\begin{aligned}
\|e\|_a^2 &= a(s - s_h, s - s_h) \\
&= a(s, s - s_h^*) + a(s, s_h^* - s_h) + a(s_h, s_h - s^*) + a(s_h, s^* - s) \\
&\overset{\text{(III.40),(III.42)}}{\leq} \langle l, s - s_h^* \rangle + a(s, s_h^* - s_h) + \langle l, s_h - s^* \rangle + a(s_h, s^* - s) \\
&= a(s, s_h^* - s_h) - \langle l, s_h^* - s_h \rangle + a(s_h, s^* - \pi_h s) - \langle l, s^* - \pi_h s \rangle + \\
&\quad + a(s_h, \pi_h s - s) - \langle l, \pi_h s - s \rangle \\
&= \underbrace{a(s, s_h^* - s_h) - \langle l, s_h^* - s_h \rangle}_{A} + \underbrace{a(s_h, s^* - \pi_h s) - \langle l, s^* - \pi_h s \rangle}_{B} + \\
&\quad + \underbrace{a(s_h, \pi_h e - e) - \langle l, \pi_h e - e \rangle}_{C} + \underbrace{a(s_h, \pi_h s_h - s_h) - \langle l, \pi_h s_h - s_h \rangle}_{D}
\end{aligned} \tag{III.48}$$

We will discuss the four terms A, B, C and D separate. In this discussion we will employ the following Lagrange-formulation of the contact problem:

$$\Phi(s) := \frac{1}{2} a(s, s) - \langle l, s \rangle_{L^2(\Omega)} \to \min!$$

under the constraint

$$\gamma(s) = (x + s) \cdot n - b \leq 0 \quad \text{ on } \Gamma_C.$$

Then there exists a Lagrange multiplier $\lambda \in L^2(\Gamma_C)_{\geq 0}$, such that

$$\Phi'(s) + \int_{\Gamma_C} \lambda\gamma'(s) = 0 \text{ and } \int_{\Gamma_C} \lambda\gamma = 0$$

The first equation can be written as

$$\forall r \in V_0 : \quad a(s,r) - \langle l, r\rangle_{L^2(\Omega)} + \int_{\Gamma_C} \lambda n \cdot r = 0 \tag{III.49}$$

and its discrete variant:

$$\forall r \in (V_0)_h : \quad a(s_h,r) - \langle l, r\rangle_{L^2(\Omega)} = \sum_{\sigma\in\Sigma_C} -\lambda_h(\sigma)n(\sigma)\cdot r(\sigma) \tag{III.50}$$

with the support points on the contact surface (III.43).
Firstly we test with a function that vanishes on Γ_C:

$$r|_{\Gamma_C} = 0 \quad \Rightarrow \quad a(s_h,r) - \langle l, r\rangle_{L^2(\Omega)} = 0. \tag{III.51}$$

Now we choose an arbitrary $r \in (V_0)_h$, to establish an estimate for λ_h:

$$\begin{aligned}
&\sum_{\sigma\in\Sigma_C} \lambda_h(\sigma)n(\sigma)\cdot r(\sigma)\\
=& -a(s_h,r) + \langle l, r\rangle_{L^2(\Omega)}\\
=& \sum_{\sigma\in\Sigma_h} \left(-a(s_h, r(\sigma)\phi_\sigma) + \langle l, r(\sigma)\phi_\sigma\rangle_{L^2(\Omega)}\right)\\
\overset{\text{(III.51)}}{=}& \sum_{\sigma\in\Sigma_C} \left(-a(s_h, r(\sigma)\phi_\sigma) + \langle l, r(\sigma)\phi_\sigma\rangle_{L^2(\Omega)}\right)\\
=& \sum_{\sigma\in\Sigma_C} \Big(-\mu\left\langle \partial_i(s_h)_j + \partial_j(s_h)_i, \partial_i(r_j(\sigma)\phi_\sigma)\right\rangle_{L^2(\Omega)} +\\
&\qquad - 2\lambda\left\langle \partial_l(s_h)_l, \partial_j(r_j(\sigma)\phi_\sigma)\right\rangle_{L^2(\Omega)} + \langle l, r(\sigma)\phi_\sigma\rangle_{L^2(\Omega)}\Big)\\
=& \sum_{\sigma\in\Sigma_C}\sum_{Q\in\mathbb{T}_h} \Big(\langle \rho f_j + 2\mu\partial_i\varepsilon_{ij}(s_h) + 2\lambda\partial_j\partial_l(s_h)_l, r_j(\sigma)\phi_\sigma\rangle_{L^2(Q)} +\\
&\qquad - \left\langle 2\mu\varepsilon_{ij}(s_h)n_i^Q + 2\lambda\partial_l(s_h)_l n_j^Q - \tau_{ij}n_i^Q, r_j(\sigma)\phi_\sigma\right\rangle_{L^2(\partial Q)}\Big)\\
\leq& \sum_{Q\in\mathbb{T}_h}\sum_{\sigma\in\Sigma_C\cap Q} \Big(\underbrace{\|\rho f_j + 2\mu\partial_i\varepsilon_{ij}(s_h) + 2\lambda\partial_j\partial_l(s_h)_l\|_{L^2(Q)}}_{\eta_Q} |r(\sigma)|\,\|\phi_\sigma\|_{L^2(Q)} +\\
&\qquad + \underbrace{\left\|2\mu\varepsilon_{ij}(s_h)n_i^Q + 2\lambda\partial_l(s_h)_l n_j^Q - \tau_{ij}n_i^Q\right\|_{L^2(\partial Q)}}_{\eta_{\partial Q}} |r(\sigma)|\,\|\phi_\sigma\|_{L^2(\partial Q)}\Big)\\
\leq& C\sum_{Q\in\mathbb{T}_h}\sum_{\sigma\in\Sigma_C\cap Q} \left(\eta_Q\,|r(\sigma)|\,h_Q^{d/2} + \eta_{\partial Q}|r(\sigma)|h_Q^{(d-1)/2}\right)
\end{aligned} \tag{III.52}$$

with the same η_Q and $\eta_{\partial Q}$ as in theorem III.12. (Remark, that the λ occuring in η_Q and $\eta_{\partial Q}$ is *not* the Lagrange parameter, introduced in (III.49). Furthermore n^Q denotes the outer normal on the surface of Q in contrast to the vector field n (III.41), that defines the projection.)

A) If we have got a conform approximation, i. e. $\Pi_h(V_h) \subset \Pi(V_0)$ – for example in the case of a plane obstacle and a projection in z-direction, we have $s_h^* = s_h$ and A in (III.48) will vanish. Otherwise, we have

$$\begin{aligned} A =& a(s, s_h^* - s_h) - \langle l, s_h^* - s_h \rangle \overset{\text{(III.49)}}{=} - \int\limits_{\Gamma_C} \lambda n \cdot (s_h^* - s_h) \\ =& - \int\limits_{\Gamma_C} \lambda \Big(n \cdot (s_h^* + x) - n \cdot (s_h + x) \Big) \\ =& - \int\limits_{\Gamma_C} \lambda \Big(n \cdot (s_h^* + x) - I_h n \cdot (s_h + x) + (I_h n - n) \cdot (s_h + x) \Big) \end{aligned}$$

Pointwise, we have

$$n \cdot (s_h^* + x) - I_h n \cdot (s_h + x) = \begin{cases} b - I_h n \cdot (s_h + x), & x \in \Gamma_p \\ n \cdot (s_h + x) - I_h n \cdot (s_h + x), & x \notin \Gamma_p \end{cases}$$

with

$$\Gamma_p := \{ x \in \Gamma_C | n \cdot (s_h + x) > b \}$$

and hence

$$\begin{aligned} A \leq & - \int\limits_{\Gamma_C \setminus \Gamma_p} \lambda \Big((n - I_h n) \cdot (s_h + x) - (n - I_h n) \cdot (s_h + x) \Big) + \\ & - \int\limits_{\Gamma_p} \lambda \Big(b - I_h n \cdot (s_h + x) - (n - I_h n) \cdot (s_h + x) \Big) \\ = & - \int\limits_{\Gamma_p} \lambda \Big(b - n \cdot (s_h + x) \Big) \\ = & - \int\limits_{\Gamma_C} \lambda n \cdot \phi_n \quad \Big(\text{with } \phi_n(x) := 1_{\Gamma_p}(x) (b(x) - n(x) \cdot (s_h(x) + x)) n(x) \Big) . \end{aligned}$$

If we assume, that ϕ_n is the restriction of a function $\phi_n \in V_0$, defined on the whole domain Ω (and write ϕ_n for both of them) and

$$\| \phi_n \|_{H^1(\Omega)} \leq C_n \| \phi_n \|_{L^2(\Gamma_C)} , \tag{III.53}$$

we can re-replace λ:

$$\begin{aligned} A \leq & a(s, \phi_n) - \langle l, \phi_n \rangle \\ = & a(s - s_h, \phi_n) + a(s_h, \phi_n) - \langle l, \phi_n \rangle . \end{aligned} \tag{III.54}$$

Because a is continuous and elliptic, we can estimate

$$\begin{aligned} a(s - s_h, \phi_n) \leq & \|a\| \, \|s - s_h\|_{H^1(\Omega)} \cdot \|\phi_n\|_{H^1(\Omega)} \\ \leq & \frac{\|a\|}{2\varepsilon^2} \|s - s_h\|_{H^1(\Omega)}^2 + \frac{\|a\| \, \varepsilon^2}{2} \|\phi_n\|_{H^1(\Omega)}^2 \\ \leq & \frac{\|a\|}{2\varepsilon^2 \alpha} \|s - s_h\|_a^2 + \frac{\|a\| \, \varepsilon^2}{2} \|\phi_n\|_{H^1(\Omega)}^2 . \end{aligned}$$

With $\varepsilon^2 = 2\|a\|/\alpha$ and the stability-estimate (III.53) we have

$$a(s-s_h,\phi_n) \leq \frac{1}{4}\|s-s_h\|_a^2 + C\|\phi_n\|_{\Gamma_C}^2 .$$

The remaining part of (III.54) can be treated by partial integration:

$$\begin{aligned} a(s_h,\phi_n) - \langle l,\phi_n\rangle = &\sum_{Q\in\mathbb{T}_h}\Big(\langle -\rho f_j - 2\mu\partial_i\varepsilon_{ij}(s_h) - 2\lambda\partial_j\partial_l(s_h)_l, (\phi_n)_j\rangle_{L^2(Q)} + \\ &\qquad \left\langle -\tau_{ij}n_j^Q + 2\mu\varepsilon_{ij}(s_h)n_i^Q + 2\lambda\partial_l(s_h)_l n_j^Q, (\phi_n)_j\right\rangle_{L^2(\partial Q)}\Big) \\ \leq &\sum_{Q\in\mathbb{T}_h}\left(h_Q\eta_Q h_Q^{-1}\|\phi_n\|_{L^2(Q)} + \|(\phi_n)_j\|_{L^2(\partial Q)} h_Q^{-1/2}\cdot h_Q^{1/2}\eta_{\partial Q}\right) \\ \leq &c\sum_{Q\in\mathbb{T}_h}\left(h_Q^2\eta_Q^2 + h_Q^{-2}\|\phi_n\|_{L^2(Q)}^2 + h_Q\eta_{\partial Q}^2 + h_Q^{-1}\|(\phi_n)_j\|_{\partial Q}^2\right) \end{aligned}$$

With the trace inequality (given in Chen and Nochetto [2000])

$$\forall v\in H^1(\Omega): \quad \|v\|_{L^2(e)} \leq C\left(h^{-1/2}\|v\|_{L^2(\tilde{e})} + h^{1/2}|v|_{H^1(\tilde{e})}\right) \tag{III.55}$$

(with e one edge of the triangulation $\mathbb{T}_h$ and $\tilde{e}$ the union of its neighbor-cells), we can further estimate (III.54)

$$\begin{aligned} A \leq &\frac{1}{4}\|s-s_h\|_a^2 + C\|\phi_n\|_{\Gamma_C}^2 + \\ &+ C\sum_{Q\in\mathbb{T}_h}\left(h_Q\eta_{\partial Q}^2 + h_Q^{-2}\|\phi_n\|_{L^2(Q)}^2 + |\phi_n|_{H^1(Q)}^2 + h_Q^2\eta_Q^2\right) \\ \overset{\text{(III.53)}}{\leq} &\frac{1}{4}\|s-s_h\|_a^2 + C\left(1+(\min_Q h_Q)^{-2}\right)\|\phi_n\|_{\Gamma_C}^2 + \\ &+ C\sum_{Q\in\mathbb{T}_h}\left(h_Q\eta_{\partial Q}^2 + h_Q^2\eta_Q^2\right) \end{aligned}$$

We remark, that $\|\phi_n\|_{\Gamma_C}$ basically is an approximation-error:

$$0 \geq \phi_n(x)\cdot n = b - n\cdot s_h + x = \underbrace{b - n\cdot(s+x)}_{\geq 0} - n\cdot(s_h - s) \geq -n\cdot(s_h-s)$$

$$\Rightarrow \quad |\phi_n| \leq |s_h - s| = O(h^2).$$

Thus for linear elements there holds

$$\|\phi_n\|_{\Gamma_C}^2 = O(h_C^4) \text{ with } h_C = \max_{e\subset\Gamma_C,\ \text{edge}}|e|$$

which will outrun the term involving $h_{\min}^{-2}$, especially if the major part of refinement will take place at Γ_C.

B) With the help of (III.50) the second error contribution of (III.40) can be written as

$$B = a(s_h, s^* - \pi_h s) - \langle l, s^* - \pi_h s\rangle_{L^2(\Omega)} = -\sum_{\sigma\in\Sigma_C} \lambda_h(\sigma) I_h n(\sigma)\cdot(s^* - \pi_h s)(\sigma)$$

We examine the summands at the single support points $\sigma \in \Sigma_C \subset \Gamma_C$:

$$\begin{aligned}
\Big(I_h n\cdot(s^* - \pi_h s)\Big)(\sigma) &= \begin{cases} \Big(I_h n\cdot(\pi_h s - \pi_h s)\Big)(\sigma), & \sigma\notin\Sigma_{ph} \\ \Big(I_h b - I_h n\cdot(\sigma + \pi_h s)\Big)(\sigma), & \sigma\in\Sigma_{ph} \end{cases} \\
&\qquad [\text{with } \Sigma_{ph} := \{x\in\Sigma_C | (x + \pi_h(s)(x))\cdot I_h n(x) > I_h b(x)\}] \\
&= \begin{cases} 0, & \sigma\notin\Sigma_{ph} \\ (b - n\cdot\sigma - n\cdot\pi_h s)(\sigma), & \sigma\in\Sigma_{ph} \end{cases} \\
&\geq \begin{cases} 0, & \sigma\notin\Sigma_{ph} \\ b(\sigma) - n(\sigma)\cdot\sigma - n(\sigma)\cdot\pi_h(bn - x)(\sigma), & \sigma\in\Sigma_{ph} \end{cases} \\
&\qquad [\pi_h \text{ positivity preserving (III.46)}]
\end{aligned}$$

and use this for the further estimate of B:

$$\begin{aligned}
B &\leq -\sum_{\sigma\in\Sigma_{ph}} \lambda_h(\sigma)\Big(b - n\cdot(x + \pi_h(bn - x))\Big)(\sigma) \\
&= -\sum_{\sigma\in\Sigma_{ph}} \lambda_h(\sigma) n(\sigma)\cdot\Big(bn - x - \pi_h(bn - x)\Big)(\sigma) \\
&\overset{(III.52)}{\leq} c\sum_{Q\in\mathbb{T}_h}\sum_{\sigma\in\Sigma_{ph}\cap Q}\Big(\eta_Q h_Q^{d/2} + \eta_{\partial Q} h_Q^{(d-1)/2}\Big)\,|n\cdot(bn - x - \pi_h(bn - x))(\sigma)| \\
&\overset{(*)}{\leq} c\sum_{Q\in\mathbb{T}_h}\sum_{\sigma\in\Sigma_{ph}\cap Q}\Big(\eta_Q h_Q^{d/2} + \eta_{\partial Q} h_Q^{(d-1)/2}\Big)\cdot\Big(h_Q^{(3-d)/2}\,\|\nabla(n\cdot I_h(bn - x))\|_{L^2(\delta_\sigma)} + \\
&\qquad + h_Q^{-(d-1)/2}\,\|n\cdot(I_h(bn - x) - (bn - x))\|_{L^2(\delta_\sigma)}\Big) \\
&\leq c\sum_{Q\in\mathbb{T}_h}\sum_{\sigma\in\Sigma_{ph}\cap Q}\Big[h_Q^2\eta_Q^2 + h_Q\eta_{\partial Q}^2 + h_Q\,\|\nabla(n\cdot I_h(bn - x))\|_{L^2(\delta_\sigma)}^2 + \\
&\qquad + h_Q^{-1}\,\|n\cdot(I_h(bn - x) - (bn - x))\|_{L^2(\delta_\sigma)}^2\Big] \\
&\leq c\sum_{Q\in\mathbb{T}_h}\Big(h_Q^2\eta_Q^2 + h_Q\eta_{\partial Q}^2\Big) + \sum_{\substack{Q\in\mathbb{T}_h \\ Q\cap\Sigma_{ph}\neq\emptyset}}\Big(h_Q\,\|\nabla(n\cdot I_h(bn - x))\|_{L^2(\partial Q\cap\Gamma_C)}^2 + \\
&\qquad + h_Q^{-1}\,\|n\cdot(I_h(bn - x) - (bn - x))\|_{L^2(\partial Q\cap\Gamma_C)}^2\Big)
\end{aligned}$$

In step $(*)$ we used the following estimate for $f = bn - x$:

$$
\begin{aligned}
&|(f(\sigma) - \pi_h f(\sigma)) \cdot n(\sigma)| \\
\leq &|n(\sigma) \cdot (I_h f(\sigma) - \pi_h(I_h f(\sigma)))| + |n(\sigma) \cdot (\pi_h(I_h f - f)(\sigma))| \\
= &\frac{1}{|\delta_\sigma|} \left| \int_{\delta_\sigma} (I_h f(x) \cdot n(x) - I_h f(\sigma) \cdot n(\sigma)) dx \right| + \left| \frac{1}{|\delta_\sigma|} \int_{\delta_\sigma} (I_h f - f)(x) \cdot n(x) dx \right| \\
\leq &ch^{-(d-1)} \left| \int_{\delta_\sigma} \int_0^1 \nabla (I_h f \cdot n)(\sigma + t(x-\sigma)) \cdot (x - \sigma) dt dx \right| + \\
&+ \frac{1}{|\delta_\sigma|} \|1\|_{L^2(\delta_\sigma)} \|(I_h f - f) \cdot n\|_{L^2(\delta_\sigma)} \\
\leq &ch^{-d+1} \int_0^1 \left| \int_{\delta_\sigma} \nabla (n \cdot I_h f)(\sigma + t(x-\sigma)) \cdot (x - \sigma) dx \right| dt + \\
&+ ch^{-(d-1)/2} \|n \cdot (I_h f - f)\|_{L^2(\delta_\sigma)} \\
= &ch^{-(d-1)/2} \left(h^{-(d-1)/2} \int_0^1 \left| \int_{t\delta_\sigma} \nabla (n \cdot I_h f)(y) \cdot \frac{y - \sigma}{t} \cdot \frac{1}{t} dy \right| dt + \|n \cdot (I_h f - f)\|_{L^2(\delta_\sigma)} \right) \\
\leq &ch^{-(d-1)/2} \cdot \left(h^{-(d-1)/2} \int_0^1 \frac{1}{t^2} \underbrace{\|y - \sigma\|_{t\delta_\sigma}}_{\leq c(th)^{(d-1+2)/2}} \|\nabla (n \cdot I_h f)\|_{t\delta_\sigma} dt + \|n \cdot (I_h f - f)\|_{L^2(\delta_\sigma)} \right) \\
\leq &ch^{-(d-1)/2} \left(h \int_0^1 t^{(d-3)/2} \|\nabla (n \cdot I_h f)\|_{t\delta_\sigma} dt + \|n \cdot (I_h f - f)\|_{L^2(\delta_\sigma)} \right) \\
\leq &ch^{-(d-1)/2} \left(h \|\nabla (n \cdot I_h f)\|_{\delta_\sigma} \underbrace{\int_0^1 t^{\frac{d-3}{2}} dt}_{\leq 2} + \|n \cdot (I_h f - f)\|_{L^2(\delta_\sigma)} \right)
\end{aligned}
$$

C) For the third error contribution, we use lemma III.13:

$$
\begin{aligned}
C =& a(s_h, \pi_h e - e) - \langle l, \pi_h e - e\rangle \\
=& \sum_{Q\in\mathbb{T}_h} \Big(2\mu \left\langle \varepsilon_{ij}(s_h), \partial_i(\pi_h e - e)_j \right\rangle_{L^2(Q)} + 2\lambda \left\langle \partial_l(s_h)_l, \partial_j(\pi_h e - e)_j \right\rangle_{L^2(Q)} \Big) + \\
& - \langle l, \pi_h e - e\rangle \\
=& \sum_{Q\in\mathbb{T}_h} \Big(\left\langle -\rho f_i - 2\mu\partial_j \varepsilon_{ij}(s_h) - 2\lambda \partial_i\partial_l(s_h)_l, (\pi_h e - e)_i \right\rangle_{L^2(Q)} + \\
& + \left\langle 2\mu\varepsilon_{ij}(s_h) n_j^Q + 2\lambda\partial_l(s_h)_l n_i^Q - \tau_{ij} n_j^Q, (\pi_h e - e)_i \right\rangle_{L^2(\partial Q)} \Big) \\
\leq& \sum_{Q\in\mathbb{T}_h} \Big(\frac{h_Q^2}{2\delta^2}\eta_Q^2 + \frac{\delta^2}{2h_Q^2} \left\|\pi_h e - e\right\|_{L^2(Q)}^2 + \frac{h_Q}{2\delta^2}\eta_{\partial Q}^2 + \frac{\delta^2}{2h_Q} \left\|\pi_h e - e\right\|_{\partial Q}^2 \Big) \\
\leq& c \cdot \sum_{Q\in\mathbb{T}_h} \Big(\frac{h_Q^2}{2\delta^2}\eta_Q^2 + \frac{\delta^2}{2h_Q^2} \left\|\pi_h e - e\right\|_{L^2(Q)}^2 + \frac{h_Q}{2\delta^2}\eta_{\partial Q}^2 + \\
& + \frac{\delta^2}{2h_Q} \Big(h_Q^{-1} \left\|\pi_h e - e\right\|_{L^2(\tilde{Q})}^2 + h_Q \underbrace{\left\|\nabla(\pi_h e - e)\right\|_{L^2(\tilde{Q})}^2}_{\leq c\|\nabla e\|_{\tilde{Q}}^2,\ \pi_h \text{ continuous}} \Big) \Big) \qquad \text{(III.56)} \\
& \qquad \text{(trace inequality (III.55))} \\
\leq& c \cdot \sum_{Q\in\mathbb{T}_h} \Big(\frac{h_Q^2}{\delta^2}\eta_Q^2 + \frac{h_Q}{\delta^2}\eta_{\partial Q}^2 + \delta^2 \left\|\nabla e\right\|_Q^2 + \delta^2 h_Q \left\|\nabla(n\cdot e)\right\|_{L^2(\tilde{Q}\cap\Gamma_C)}^2 \Big) \\
& \qquad \text{(with lemma III.13)} \\
\leq& \frac{1}{4} \left\|e\right\|_a^2 + c \cdot \sum_{Q\in\mathbb{T}_h} \Big(h_Q^2\eta_Q^2 + h_Q\eta_{\partial Q}^2 \Big) \qquad \text{(with } \delta^2 = \alpha/(4c)\text{)}
\end{aligned}
$$

D) The last term D of (III.48) can be estimated with the help of lemma III.14:

$$
\begin{aligned}
D =& a(s_h, \pi_h s_h - s_h) - \langle l, \pi_h s_h - s_h \rangle \\
=& -\sum_{\sigma \in \Sigma_C} \lambda_h(\sigma) n(\sigma) \cdot (\pi_h s_h - s_h) && \text{(with (III.50))} \\
=& \sum_{\sigma \in \Sigma_{p1}} \lambda_h(\sigma) n(\sigma) \cdot (\pi_h s_h - s_h) \\
& && \text{(with } \Sigma_{p1} = \{\sigma \in \Sigma_C | n(\sigma) \cdot (s_h(\sigma) + \sigma) = b(\sigma)\} \\
& && \quad \text{and Lagrange condition } \lambda_h|_{\Sigma_C \setminus \Sigma_{p1}} = 0) \\
=& a(s_h, r_1) - \langle l, r_1 \rangle && \text{(with } r_1 = I_h((\pi_h s_h - s_h)(\sigma) 1_{\Sigma_{p1}}(\sigma))) \\
=& \sum_{Q \in \mathbb{T}_h} \Big(\mu \left\langle \partial_i (s_h)_j + \partial_j (s_h)_i, \partial_i (r_1) \right\rangle_{L^2(Q)} + \\
& \qquad + 2\lambda \left\langle \partial_l (s_h)_l, \partial_j (r_1)_j \right\rangle_{L^2(Q)} - \left\langle l_i, (r_1)_i \right\rangle_{L^2(Q)} \Big) \\
=& \sum_{Q \in \mathbb{T}_h} \Big(\left\langle 2\mu \varepsilon_{ij}(s_h) n_i^Q + 2\lambda \partial_l (s_h)_l n_j^Q - \tau_{ij} n_i^Q, (r_1)_j \right\rangle_{L^2(\partial Q)} + \\
& \qquad - \left\langle \rho f_j + 2\mu \partial_i \varepsilon_{ij}(s_h) + 2\lambda \partial_j \partial_l (s_h)_l, (r_1)_j \right\rangle_{L^2(Q)} \Big) \\
\leq& \sum_{Q \in \mathbb{T}_h} \left(\frac{h_Q}{2} \eta_{\partial Q}^2 + \frac{1}{2h_Q} \|r_1\|_{L^2(\partial Q)}^2 + \frac{h_Q^2}{2} \eta_Q^2 + \frac{1}{2h_Q^2} \|r_1\|_{L^2(Q)}^2 \right) \\
\leq& c \cdot \sum_{Q \in \mathbb{T}_h} \left(h_Q \eta_{\partial Q}^2 + h_Q^2 \eta_Q^2 \right) + \\
& + c \sum_{\substack{Q \in \mathbb{T}_h \\ Q \cap \Sigma_{p1} \neq \emptyset}} \left(\frac{1}{h_Q} \|\pi_h s_h - s_h\|_{L^2(\partial Q \cap \Gamma_C)}^2 + \frac{1}{h_Q^2} \|\pi_h s_h - s_h\|_{L^2(Q)}^2 \right) \\
\leq& c \cdot \sum_{Q \in \mathbb{T}_h} \left(h_Q \eta_{\partial Q}^2 + h_Q^2 \eta_Q^2 \right) + c \cdot \sum_{\substack{Q \in \mathbb{T}_h \\ Q \cap \Sigma_{p1} \neq \emptyset}} h_Q \|\nabla (n \cdot s_h)\|_{L^2(\tilde{Q} \cap \Gamma_C)}^2 && \text{(lemma III.14)}
\end{aligned}
$$

Collecting the estimates for A, B, C and D and (III.48) yields

Theorem III.15
For the error $s - s_h$ of the approximation (III.40) of the contact problem (III.42) there holds the a-posteriori-estimate

$$\|s - s_h\|_a^2 \leq c \cdot \left(1 + (\min_Q h_Q)^{-2}\right) \eta_{C2}^2 + c \cdot \sum_{Q \in \mathbb{T}_h} \left(h_Q \eta_{\partial Q}^2 + h_Q^2 \eta_Q^2 + h_Q \eta_{C,Q}^2 + h_Q^{-1} \eta_{-C,Q}^2\right)$$

the terms η_x are declared as

$$\begin{aligned}
\eta_Q =& \|\rho f_i + 2\mu \partial_j \varepsilon_{ij}(s_h) + 2\lambda \partial_i \varepsilon_{ll}(s_h)\|_{L^2(Q)} \\
\eta_{\partial Q} =& \frac{1}{2} \left\| \left[\tau_{ij} n_j - 2\mu n_j \varepsilon_{ij}(s_h) - 2\lambda n_i \varepsilon_{ll}(s_h)\right] \right\|_{L^2(\partial Q)} \\
\eta_{C,Q}^2 =& \left\{ \begin{array}{ll} \|\nabla(n \cdot s_h)\|_{\partial Q \cap \Gamma_C}^2, & Q \cap \Sigma_{p1} \neq \emptyset \\ 0, & \text{else} \end{array} \right\} + \\
& + \left\{ \begin{array}{ll} \|\nabla(n \cdot I_h(bn - x))\|_{L^2(\partial Q \cap \Gamma_C)}^2, & Q \cap \Sigma_{ph} \neq \emptyset \\ 0, & \text{else} \end{array} \right\} \\
\eta_{-C,Q}^2 =& \left\{ \begin{array}{ll} \|n \cdot (I_h(bn - x) - (bn - x))\|_{\partial Q \cap \Gamma_C}^2, & Q \cap \Sigma_{ph} \neq \emptyset \\ 0, & \text{else} \end{array} \right. \\
\eta_{C2} =& \|b - I_h b - (n - I_h n) \cdot (s_h + x)\|_{\Gamma_p}^2 .
\end{aligned}$$

with

$$\begin{aligned}
\Gamma_p =& \{x \in \Gamma_C | n \cdot (s_h + x) > b\} \\
\Sigma_{p1} =& \{\sigma \in \Sigma_C | n(\sigma) \cdot (s_h(\sigma) + \sigma) = b(\sigma)\} \\
\text{and } \Sigma_{ph} =& \{x \in \Sigma_C | (x + \pi_h(s)(x)) \cdot I_h n(x) > I_h b(x)\}.
\end{aligned}$$

In practical applications we will approximate the set Σ_{ph} by

$$\Sigma_{ph} \approx \Sigma_{p1},$$

if we do so, we have

$$\eta_{C,Q}^2 \approx \left\{ \begin{array}{ll} \|\nabla(n \cdot s_h)\|_{\partial Q \cap \Gamma_C}^2 + \|\nabla(n \cdot s_h)\|_{\partial Q \cap \Gamma_C}^2, & Q \cap \Sigma_{p1} \neq \emptyset \\ 0, & \text{else} \end{array} \right. .$$

III.2.1.4 A-posteriori Estimate for the Reynolds Equation

We proceed analogue to section III.2.1.2.
The Reynolds Equation is given by (II.37):

$$\text{Find } \psi \in \Psi_{R,D} : \ \forall \phi \in \tilde{\Psi}_R : \quad \langle \psi, \phi \rangle_R = \langle l_R, \phi \rangle_{L^2} . \tag{III.57}$$

and its approximation

$$\text{Find } \psi_h \in (\Psi_{R,D})_h : \ \forall \phi \in (\tilde{\Psi}_R)_h : \quad \langle \psi_h, \phi \rangle_R = \langle l_R, \phi \rangle_{L^2} . \tag{III.58}$$

Again, we calculate (with $\phi \in \tilde{\Psi}_R$)

$$\begin{aligned}
&\langle \psi - \psi_h, \phi \rangle_R \\
&= \sum_{Q \in \mathbb{T}_h} \langle \psi - \psi_h, \phi \rangle_{R,Q} \\
&= \sum_{Q \in \mathbb{T}_h} \left(\langle l_R, \phi \rangle_{L^2(Q)} - \langle \psi_h, \phi \rangle_{R,Q} \right) \\
&= \sum_{Q \in \mathbb{T}_h} \left(\langle l_R, \phi \rangle_{L^2(Q)} - \left\langle g^2 \partial_\mu \frac{\psi_h}{g}, \partial_\mu \frac{\phi}{g} \right\rangle_{L^2(Q)} \right) \\
&= \sum_{Q \in \mathbb{T}_h} \left(\left\langle l_R + \frac{1}{g} \partial_\mu \left(g^2 \partial_\mu \frac{\psi_h}{g} \right), \phi \right\rangle_{L^2(Q)} - \left\langle g \partial_n \frac{\psi_h}{g}, \phi \right\rangle_{L^2(\partial Q)} \right) \\
&= \sum_{Q \in \mathbb{T}_h} \left(\left\langle l_R + \frac{1}{g} \partial_\mu \left(g^2 \partial_\mu \frac{\psi_h}{g} \right), \phi - I_h \phi \right\rangle_{L^2(Q)} - \frac{1}{2} \left\langle \left[g \partial_n \frac{\psi_h}{g} \right], \phi - I_h \phi \right\rangle_{L^2(\partial Q)} \right)
\end{aligned}$$

and conclude the same way, we did in the proof of theorem III.12

Theorem III.16
For the Reynolds-model (III.57) and its approximation (III.58) with linear elements, there holds the a-posteriori estimate

$$\|\psi - \psi_h\|_R^2 \leq c \sum_{Q \in \mathbb{T}_h} \left(\rho_Q^2 h_Q^2 + \rho_{\partial Q}^2 h_Q \right) \tag{III.59}$$

with the residual terms

$$\begin{aligned}
\rho_Q &= \left\| l_R + \frac{1}{g} \partial_\mu \left(g^2 \partial_\mu \frac{\psi_h}{g} \right) \right\|_{L^2(Q)} \\
\rho_{\partial Q} &= \frac{1}{2} \left\| \left[g \partial_n \frac{\psi_h}{g} \right] \right\|_{L^2(\partial Q)} .
\end{aligned}$$

Proof. We used the same arguments as in theorem III.12, the interpolation estimate III.39 is here used for $d = 2$, because this is the appropriate dimension for the Reynolds-model. We can use it to estimate $\|\phi - I_h \phi\|_R$, after application of the duality argument, because of the equivalence of $\|\cdot\|_R$ and $\|\cdot\|_{H^1}$. □

III.2.1.5 A-posteriori Estimate for the Reynolds Problem with Cavitation

We examine the Reynolds Problem with cavitation II.39

$$\text{Find } \psi \in \Psi_{R,D,\geq 0} \colon \forall \phi \in \tilde{\Psi}_{R,\geq 0} : \ \langle \phi - \psi, \psi \rangle_R \geq \langle l_{R,c}, \phi - \psi \rangle_{L^2(\Omega_2)} . \tag{III.60}$$

$\langle \cdot, \cdot \rangle_R$ denotes the Reynolds product (II.9)

$$\langle \phi, \psi \rangle_R := \left\langle g \nabla \frac{\phi}{g}, g \nabla \frac{\psi}{g} \right\rangle_{L^2(\Omega_2)} .$$

The discretisation of (III.60) is

$$\text{Find } \psi_h \in (\Psi_{R,D,\geq 0})_h \colon \forall \phi \in (\tilde{\Psi}_{R,\geq 0})_h : \ \langle \phi - \psi_h, \psi_h \rangle_R \geq \langle l_{R,c}, \phi - \psi_h \rangle_{L^2(\Omega_2)} . \tag{III.61}$$

Because the solution is only restricted by a constant $\psi \geq 0$ and we use linear finite elements, the discretisation is conform:

$$(\Psi_{\geq 0})_h \subset \Psi_{\geq 0}$$

and we can choose $\phi = \psi_h$ in (III.60) and $\phi = I_h \psi$ in (III.61). The sum of both inequations is

$$\begin{aligned}
0 \leq & \langle \psi_h - \psi, \psi \rangle_R + \langle I_h \psi - \psi_h, \psi_h \rangle_R - \langle l_{R,c}, I_h \psi - \psi \rangle_{L^2(\Omega_2)} \\
\Rightarrow \quad \| \psi - \psi_h \|_R^2 \leq & \langle \psi_h, \psi_h - \psi \rangle_R + \langle I_h \psi - \psi_h, \psi_h \rangle_R - \langle l_{R,c}, I_h \psi - \psi \rangle_{L^2(\Omega_2)} \\
= & \sum_{Q \in \mathbb{T}_h} \left(\langle \psi_h, I_h \psi - \psi \rangle_{R,Q} - \langle l_{R,c}, I_h \psi - \psi \rangle_{L^2(\Omega_2)} \right) \\
= & \sum_{Q \in \mathbb{T}_h} \Bigg(- \left\langle \frac{1}{g} \partial_\mu \left(g^2 \partial_\mu \frac{\psi_h}{g} \right), I_h \psi - \psi \right\rangle_{L^2(Q)} + \left\langle g \partial_n \frac{\psi_h}{g}, I_h \psi - \psi \right\rangle_{L^2(\partial Q)} + \\
& \qquad - \langle l_{R,c}, I_h \psi - \psi \rangle_{L^2(\Omega_2)} \Bigg) \\
\leq & \sum_{Q \in \mathbb{T}_h} \Bigg(\left\| \frac{1}{g} \partial_\mu \left(g^2 \partial_\mu \frac{\psi_h}{g} \right) + l_{R,c} \right\|_{L^2(Q)} \| I_h \psi - \psi \|_{L^2(Q)} + \\
& \qquad + \frac{1}{2} \left\| \left[g \partial_n \frac{\psi_h}{g} \right] \right\|_{L^2(\partial Q)} \| I_h \psi - \psi \|_{L^2(\partial Q)} \Bigg) .
\end{aligned} \tag{III.62}$$

If the solution ψ is smooth enough, the interpolation error can be estimated by (III.39) again:

$$\begin{aligned}
\| I_h \psi - \psi \|_{L^2(Q)} = \| I_h(\psi - \psi_h) - (\psi - \psi_h) \|_{L^2(Q)} \leq & C \sqrt{|Q|} \, |\psi - \psi_h|_{H^1(Q)} \\
\| I_h \psi - \psi \|_{L^2(\partial Q)} = \| I_h(\psi - \psi_h) - (\psi - \psi_h) \|_{L^2(\partial Q)} \leq & C h^{\frac{d-1}{2}} \, |\psi - \psi_h|_{H^1(Q)}
\end{aligned}$$

with $d = 2$ for the Reynolds-equation.
We proceed with the estimate above:

Theorem III.17
The approximation error of the Reynolds cavitation problem (III.60) and its discretisation (III.61) can be estimated by

$$\|\psi - \psi_h\|_R^2 \leq C \sum_{Q \in \mathbb{T}_h} \left(\rho_{Q,c}^2 h_Q^2 + \rho_{\partial Q,c}^2 h_Q \right)$$

with

$$\begin{aligned} \rho_{Q,c} &= \left\| \frac{1}{g} \partial_\mu \left(g^2 \partial_\mu \frac{\psi_h}{g} \right) + l_{R,c} \right\|_{L^2(Q)} \\ \rho_{\partial Q,c} &= \frac{1}{2} \left\| \left[g \partial_n \frac{\psi_h}{g} \right] \right\|_{L^2(\partial Q)} . \end{aligned}$$

Proof. Insertion of the interpolation estimate (with $d = 2$) into (III.62) yields

$$\begin{aligned} \|\psi - \psi_h\|_R^2 &\leq C \sum_{Q \in \mathbb{T}_h} \left(\rho_{Q,c} h_Q + \rho_{\partial Q,c} h_Q^{1/2} \right) |\psi - \psi_h|_{H^1(Q)} \\ &\leq C \sqrt{\sum_{Q \in \mathbb{T}_h} \left(\rho_{Q,c} h_Q + \rho_{\partial Q,c} h_Q^{1/2} \right)^2} \, |\psi - \psi_h|_{H^1(\Omega_2)} \end{aligned}$$

□

III.2.2 Saddle Point Problems

In this section we give estimates for the approximation error of saddle-point-problems, following Braess [1997].

III.2.2.1 A-priori Estimate for Saddle Point Problems

This section gives a brief overview over error estimates for non stabilised saddle point problems. Especially we introduce the Taylor-Hood-Element (Corollary III.19), a stable element for the Stokes problem. Because in all our applications we only consider stabilised saddle point problems, this section is rather short and there are not given further estimates.

We examine the saddle-point-problem (II.1):

$$\text{Find } v \in V \text{ and } \lambda \in H \text{ such, that } \begin{array}{lrcl} \forall w \in V: & a(v,w) - b(w,\lambda) = & \langle f, w\rangle \\ \forall \mu \in H: & b(v,\mu) = & \langle g, \mu\rangle\,, \end{array} \tag{III.63}$$

and its approximation

$$\text{Find } v_h \in V_h \text{ and } \lambda_h \in H_h \text{ such, that } \begin{array}{lrcl} \forall w \in V_h: & a(v_h,w) - b(w,\lambda_h) = & \langle f, w\rangle \\ \forall \mu \in H_h: & b(v_h,\mu) = & \langle g, \mu\rangle\,. \end{array} \tag{III.64}$$

Then we have a first a-priori-error-estimate:

Theorem III.18
If the bilinear forms a and b fulfill the assumptions of theorem II.13 (ellipticity of a and inf-sup-condition for b) for both, the continuous spaces $V \times H$ and the discrete spaces $V_h \times H_h$, there holds the estimate

$$\|v - v_h\| + \|\lambda - \lambda_h\| \leq c \cdot \left(\inf_{w \in V_h} \|v - w\| + \inf_{\mu \in H_h} \|\lambda - \mu\| \right).$$

Proof. Braess [1997] □

Theorems III.18 and A.3 give us the opportunity to estimate the error $\|u - u_h\| + \|\lambda - \lambda_h\|$ with the help of the interpolant of (u, λ) in the discrete space $V_h \times H_h$:

Corollary III.19
If we approximate the space $V^{Stokes} \times \Pi$ with the subspaces $Q_2(\Omega_2)^d \times Q_1(\Omega_2)$ (the Taylor-Hood-Element) and assume $v, p \in H^{2,\infty}(\Omega_2)$, we have

$$\begin{aligned}\|v - v_h\|_{H^1(\Omega_2)} + \|p - p_h\|_{L^2(\Omega_2)} \leq & C \left(\sum_{Q \in \mathbb{T}} |Q| h_Q^4 \left(|v|^2_{H^{2,\infty}(Q)} + |p|^2_{H^{2,\infty}(Q)} \right) \right)^{1/2} \\ \leq & \tilde{C} h^2 \left(|v|_{H^{2,\infty}(\Omega_2)} + |p|_{H^{2,\infty}(\Omega_2)} \right) = O(h^2).\end{aligned}$$

$h = \sup_{Q \in \mathbb{T}} \operatorname{diam}(Q)$ denotes the maximal diameter of the quadrilaterals in our triangulation.

Proof. With the interpolants of v $I_h(v) \subset V_h$ and of p $I_h(p) \subset \Pi_h$, we conclude from theorem III.18:

$$\begin{aligned}& \|v - v_h\|_{H^1(\Omega_2)} + \|p - p_h\|_{L^2(\Omega_2)} \\ \leq & c \cdot \left(\|v - I_h(v)\|_{H^1(\Omega_2)} + \|p - I_h(p)\|_{L^2(\Omega_2)} \right) \\ \leq & c \cdot \sqrt{C} \left(\left[\sum_{Q \in \mathbb{T}} |Q| h_Q^4 \cdot |v|^2_{H^{2,\infty}(Q)} \right]^{1/2} + \left[\sum_{Q \in \mathbb{T}} |Q| h_Q^4 \cdot |p|^2_{H^{2,\infty}(Q)} \right]^{1/2} \right) && \text{(theorem A.3)} \\ \leq & c\sqrt{2C} \left[\sum_{Q \in \mathbb{T}} |Q| h_Q^4 \left(|v|^2_{H^{2,\infty}(Q)} + |p|^2_{H^{2,\infty}(Q)} \right) \right]^{1/2} && \text{(first estimate)} \\ \leq & \underbrace{c\sqrt{2C}\sqrt{|\Omega_2|}}_{\tilde{C}} h^2 \left[|v|^2_{H^{2,\infty}(\Omega_2)} + |p|^2_{H^{2,\infty}(\Omega_2)} \right]^{1/2} \\ \leq & \tilde{C} h^2 \left(|v|_{H^{2,\infty}(\Omega_2)} + |p|_{H^{2,\infty}(\Omega_2)} \right) && \text{(second estimate)}\end{aligned}$$

□

Finally, we recall, that the assumptions of theorem III.18 and II.39 respective hold in the two considered cases (the Stokes- and the Subdimensional Stokes-problem), and thus both the noncavitational and the caviational Stokes problem are well posed:

- Ellipticity and the inf-sup-conditon for the Stokes-problem (II.17) with the spaces given in theorem II.37 are shown in the proof of this theorem.
- The analogue statement for the subdimensional Stokes problem (II.32) and the spaces (II.34) and (II.35) is given in theorem II.40.

III.2.3 Stabilized Saddle Point Problems

Because in our applications we are mainly interested in the pressure and not in the velocity, we should avoid the use of higher order elements for the approximation of v than for that of p, but this is exactly, what we have to do, to let our approximaton $V_h \times H_h$ fulfill the inf-sup-condition II.3.
In section II.1.1.1 one possibility of stabilization is given, by insertion of the bilinear form $\varepsilon c(\cdot,\cdot)$ into the second of the two Stokes equations (II.5).

III.2.3.1 A-priori Estimates for the Stabilized Saddle Point Problem

In section III.2.3.1 we describe the stabilization of a saddle point problem, replace the inf-sup-condition by the generalised inf-sup-condition (III.70) and give error estimates for the stabilisation error (theorem III.20) on the one hand and for the total error of the stabilized problem (corollary III.21) on the other hand.

The general saddle point problem is given by (II.1):

$$\text{Find } (v,p) \in V \times H, \text{ such that: } \begin{array}{llll} \forall w \in V: & a(v,w) & -b(w,p) = & \langle f, w\rangle \\ \forall q \in H: & b(v,q) & = & \langle g, q\rangle \end{array}. \tag{III.65}$$

We assume, that the bilinear form $b : V \times H \to \mathbb{R}$ fulfills the inf-sup-condition (II.3)

$$\inf_{q\in H} \sup_{w\in V} \frac{b(w,q)}{\|w\|\,\|q\|} = \beta > 0 \tag{III.66}$$

and $a : V \times V \to \mathbb{R}$ is elliptic

$$\forall w \in V:\ a(w,w) \geq \alpha \|w\|^2 .$$

As described in section II.1.1.1 this problem can be stabilized:

$$\text{Find } (v^\varepsilon, p^\varepsilon) \in V \times H, \text{ such that: } \begin{array}{llll} \forall w \in V: & a(v^\varepsilon,w) & -b(w,p^\varepsilon) = & \langle f, w\rangle \\ \forall q \in H: & b(v^\varepsilon,q) & +\varepsilon c(q,p^\varepsilon) = & \langle g, q\rangle \end{array} \tag{III.67}$$

with the elliptic bilinear form $c : H \times H \to \mathbb{R}$:

$$\forall q \in H:\ c(q,q) \geq \gamma \|q\|^2 .$$

The error by stabilization can be estimated by theorem II.15:

$$\|v - v^\varepsilon\| + \|p - p^\varepsilon\| \leq K \cdot \varepsilon(\|f\| + \|g\|) \tag{III.68}$$

for sufficiantly small $\varepsilon > 0$.
This problem is elliptic (lemma II.44). For the discretisation, we introduce the finite dimensional subspaces $V_h \subset V$, $H_h \subset H$:

$$\text{Find } (v_h^\varepsilon, p_h^\varepsilon) \in V_h \times H_h, \text{ such that: } \begin{array}{llll} \forall w \in V_h: & a(v_h^\varepsilon,w) & -b(w,p_h^\varepsilon) = & \langle f, w\rangle \\ \forall q \in H_h: & b(v_h^\varepsilon,q) & +\varepsilon c(q,p_h^\varepsilon) = & \langle g, q\rangle \end{array} \tag{III.69}$$

and assume a generalised inf-sup-condition for the discrete spaces (compare Becker [1995]):

$$\inf_{q\in H_h}\left(\sup_{w\in V_h}\frac{b(w,q)^2}{\|q\|^2\,\|w\|^2}+\frac{\varepsilon c(q,q)}{\|q\|^2}\right)\geq\delta^2. \tag{III.70}$$

with $\delta>0$ independend of h and ε.
The discretisation error of the stabilized problem (III.67) can be estimated separate:

Theorem III.20
If the bilinearforms a, b and c of the stabilised saddle point problem (III.67) are continuous, a and c are elliptic and b and c fulfill the generalized inf-sup-condition (III.70), the discretisation error of (III.69) can be estimated by

$$\|v^\varepsilon-v_h^\varepsilon\|+\|p^\varepsilon-p_h^\varepsilon\|\leq K\left(\inf_{w\in V_h}\|v^\varepsilon-w\|+\inf_{q\in H_h}\|p^\varepsilon-q\|\right).$$

Proof. We will use the Schur complement of (III.67):

$$S_C=\varepsilon C+B^*A^{-1}B$$

where the operators $A,\ B$ and C are given as usual:

$$\begin{aligned}A:V\to V,&\qquad\langle Av,w\rangle=&a(v,w)\\ B:H\to V,&\qquad\langle w,Bq\rangle=&b(w,q)\\ C:H\to H,&\qquad\langle Cq,p\rangle=&c(q,p).\end{aligned}$$

Firstly we estimate $\|p_h^\varepsilon-q\|$ with the solution p_h^ε of (III.69) for an arbitrary $q\in H_h$:

$$\begin{aligned}\delta^2\|p_h^\varepsilon-q\|^2\leq&\ \|B^*(p_h^\varepsilon-q)\|_{V_h'}^2+\varepsilon c(p_h^\varepsilon-q,p_h^\varepsilon-q)\qquad\text{(with (III.70))}\\ \leq&\ \|A\|_{V'}^2\langle A^{-1}B^*(p_h^\varepsilon-q),A^{-1}B^*(p_h^\varepsilon-q)\rangle+\varepsilon c(p_h^\varepsilon-q,p_h^\varepsilon-q)\\ \leq&\ \tfrac{\|A\|_{V'}^2}{\alpha}\langle AA^{-1}B^*(p_h^\varepsilon-q),A^{-1}B^*(p_h^\varepsilon-q)\rangle+\varepsilon\langle C(p_h^\varepsilon-q),p_h^\varepsilon-q\rangle\\ \leq&\ \underbrace{\max\left\{1,\|A\|_{V'}^2/\alpha\right\}}_{=:M_\alpha}\langle p_h^\varepsilon-q,(BA^{-1}B^*+\varepsilon C)(p_h^\varepsilon-q)\rangle\\ =&\ M_\alpha\langle p_h^\varepsilon-q,(BA^{-1}B^*+\varepsilon C)(p^\varepsilon-q)\rangle\\ &\qquad\text{(with Galerkin-orthogonality of the Schur-complement)}\\ \leq&\ M_\alpha\cdot\left(\tfrac{\|B\|^2}{\|A\|}+\varepsilon\|C\|\right)\cdot\|p_h^\varepsilon-q\|\,\|p^\varepsilon-q\|\end{aligned}$$

Division by $\delta^2\|p_h^\varepsilon-q\|$ yields

$$\|p_h^\varepsilon-q\|\leq\frac{M_\alpha}{\delta^2}\left(\frac{\|B\|^2}{\|A\|}+\varepsilon\|C\|\right)\cdot\|p^\varepsilon-q\| \tag{III.71}$$

At next we derive an estimate for $\|v_h^\varepsilon - w\|$ with an arbitrary $w \in V_h$:

$$\begin{aligned}
\alpha \|v_h^\varepsilon - w\|^2 \leq & a(v_h^\varepsilon - w, v_h^\varepsilon - w) = a(v_h^\varepsilon - v^\varepsilon, v_h^\varepsilon - w) + a(v^\varepsilon - w, v_h^\varepsilon - w) \\
= & b(v_h^\varepsilon - w, p_h^\varepsilon - p^\varepsilon) + a(v^\varepsilon - w, v_h^\varepsilon - w) \\
& \qquad \text{(with the difference of (III.67) and (III.69))} \\
\leq & \left(\|b\| \, \|p_h^\varepsilon - p^\varepsilon\| + \|a\| \, \|v^\varepsilon - w\|\right) \|v_h^\varepsilon - w\| \\
\Rightarrow \qquad \|v_h^\varepsilon - w\| \leq & \frac{1}{\alpha} \left(\|b\| \, \|p_h^\varepsilon - p^\varepsilon\| + \|a\| \, \|v^\varepsilon - w\|\right) \qquad \text{(III.72)}
\end{aligned}$$

With the help of these estimates we can control the total discretisation error:

$$\begin{aligned}
& \|v^\varepsilon - v_h^\varepsilon\| + \|p^\varepsilon - p_h^\varepsilon\| \\
\leq & \|v^\varepsilon - w\| + \|w - v_h^\varepsilon\| + \|p^\varepsilon - q\| + \|q - p_h^\varepsilon\| \\
\leq & \|v^\varepsilon - w\| + \frac{1}{\alpha} \left(\|b\| \, \|p_h^\varepsilon - p^\varepsilon\| + \|a\| \, \|v^\varepsilon - w\|\right) + \qquad \text{(with (III.72))} \\
& + \|p^\varepsilon - q\| + \|p_h^\varepsilon - q\| \\
\leq & \left(1 + \frac{\|a\|}{\alpha}\right) \|v^\varepsilon - w\| + \\
& + \left[1 + \left(\frac{\|b\|}{\alpha} + 1\right) \frac{M_\alpha}{\delta^2} \left(\frac{\|B\|^2}{\|A\|} + \varepsilon \|C\|\right)\right] \|p^\varepsilon - q\| \qquad \text{(with (III.71))}
\end{aligned}$$

□

Alltogether the approximation error can be estimated by

Corollary III.21
If the bilinear forms of the saddle point problem (III.65) and its stabilization (III.67) and the discrete spaces $V_h \times H_h \subset V \times H$ fulfill the conditions of theorem II.15 and theorem III.20, the total error of the approximation $(v_h^\varepsilon, p_h^\varepsilon) \in V_h \times H_h$ of the solution $(v, p) \in V \times H$ of the saddle point problem (III.65) can be estimated by $\varepsilon > 0$ of the stabilized problem (III.67) and the interpolation-error of the discrete spaces:

$$\|v - v_h^\varepsilon\| + \|p - p_h^\varepsilon\| \leq K \cdot \varepsilon(\|f\| + \|g\|) + C \left(\inf_{w \in V_h} \|v^\varepsilon - w\| + \inf_{q \in H_h} \|p^\varepsilon - q\|\right).$$

Proof. Combination of theorem II.15 and theorem III.20 yields

$$\begin{aligned}
\|v - v_h^\varepsilon\| + \|p - p_h^\varepsilon\| \leq & \|v - v^\varepsilon\| + \|v^\varepsilon - v_h^\varepsilon\| + \|p - p^\varepsilon\| + \|p^\varepsilon - p_h^\varepsilon\| \\
\leq & K \cdot \varepsilon(\|f\| + \|g\|) + C \left(\inf_{w \in V_h} \|v^\varepsilon - w\| + \inf_{q \in H_h} \|p^\varepsilon - q\|\right).
\end{aligned}$$

□

Corollary III.21 implies, that the discretisation error and the stabilisation error are in balance, if ε is of the same order as the interpolation error in the discrete spaces V_h and H_h. For the bilinear elements, that we use in our applications, the discretisation error is of the order $O(h^2)$, thus we choose

$$\varepsilon = \delta_\varepsilon h^2$$

with a constant δ_ε to achieve a total error of

$$\|v - v_h^\varepsilon\| + \|v - v_h^\varepsilon\| = O(h^2).$$

For this case of *linear elements* $V_h \times H_h = (Q^1)^d \times Q^1$, we scatch the stabilisation process in detail:

- Initial point is the continuous saddle point problem (III.65) on the product space $V \times H$, that fulfills the inf-sup-condition (III.66). Thus theorem II.13 guarantees a well defined solution $(v, p) \in V \times H$ of (III.65). In section III.2.2.1 we learned, that the discretisation of this problem is rather expensive, because the discretised spaces have to fulfill the inf-sup-condition too.

- To weaken the inf-sup-condition – at least for the discrete spaces – we stabilize the saddle point problem with the help of an elliptic bilinearform $\varepsilon c : H \times H \to \mathbb{R}$, to gain the (still continuous) elliptic problem (III.67). Following (III.68), the choice of a sufficiantly small $\varepsilon > 0$ will reduce the stabilization error below a demanded border.
  In our application we use

  $$c(q, r) = \langle \nabla q, \nabla r \rangle_{L^2(\Omega_2)}$$

  (assuming $H \subset H^1(\Omega_2)$) and $\varepsilon = \delta_\varepsilon h^2$.

- For the application of theorem III.20, we have to ensure, that the bilinearforms

  $$\begin{aligned} b(w, q) &= \langle \operatorname{div} w, q \rangle_L^2 (\Omega) \\ \text{and } \varepsilon c(q, r) &= \delta_\varepsilon h^2 \langle \nabla q, \nabla r \rangle_{L^2(\Omega)} \end{aligned}$$

  fulfill the generalised inf-sup-condition (III.70)

  $$\exists \delta > 0 : \quad \|b(\cdot, q)\|_{V_h'}^2 + \varepsilon c(q, q) \geq \delta^2 \|q\|^2$$

  for linear elements $V_h \times H_h = (Q^1(\mathbb{T}_h))^d \times Q^1(\mathbb{T}_h)$. Therefor we refer to Hughes et al. [1986], Becker [1995] and Braack [1998].

  Following theorem III.20 we can estimate the discretisation error with the help of the interpolation error:

  $$\|v^\varepsilon - v_h^\varepsilon\| + \|p^\varepsilon - p_h^\varepsilon\| \leq C(\|v^\varepsilon - I_h v^\varepsilon\| + \|p^\varepsilon - I_h p^\varepsilon\|). \tag{III.73}$$

The interpolation error for H^2-functions v is of the order of h^2. The combination of the two estimates (III.68) and (III.73) and $\varepsilon = h^2$ leads to

---

Theorem III.22
The total error of the stabilized saddle point problem with linear elements is

$$\|v - v_h^\varepsilon\|_{H^1(\Omega_2)} + \|p - p_h^\varepsilon\|_{L^2(\Omega_2)} = O(h^2).$$

A closer look on this is taken in Becker [1995].

Finally we check, if the assumptions, stated in this section, hold for the Stokes- and the SubStokes-problem:

- The inf-sup-condition (III.66) and ellipticity of the involved bilinear forms a and b is proven for both problems in the proofs of theorems II.37 and II.40.
- For the generalised inf-sup-condition for linear elements we refer to Hughes et al. [1986], Becker [1995] and Braack [1998].

So, if the solutions of the Stokes- and the SubStokes-problem are sufficiantly regular, we can apply theorem III.20 and corollary III.21.

III.2.3.2 A-posteriori Estimate for the Stabilized SubStokes Problem

In this section we transform the estimate for the Stokes problem, that is given in Becker [1995] to the subdimensional problem (II.32). For a detailed discussion we refer to Becker [1995], Bochew and Gunzburger [2006] and to the following section III.2.3.3, where the detailed derivation for the cavitational problem is given.

Theorem III.23
If the SubStokes problem (II.32) is H^2-regular, then there holds

$$\|\chi - \chi_h\|_{H^1} + \|\psi - \psi_h\|_{L^2} \leq \eta_{sub}(\chi_h, \psi_h)$$

with the a-posteriori-expressions

$$\begin{aligned}\eta_{sub}(\chi_h, \psi_h) :=& C\Big[\left(\sum_Q h_Q^2 \left\|\kappa + \gamma + \Delta_h\chi_h - \frac{12}{g^2}\chi_h - g\nabla_h\frac{\psi_h}{g}\right\|_Q^2\right)^{1/2} + \\ &+ \left(\sum_Q h_Q \sum_{\Gamma\subset Q} \|[\psi_h n - \partial_n\chi_h]\|_\Gamma^2\right)^{1/2} + \\ &+ \left(\sum_Q \left\|\frac{1}{g}\mathrm{div}\,(g\chi_h) - \sigma_3\right\|_Q^2\right)^{1/2} + \left(\sum_Q \delta_Q^2 \|\nabla\psi_h - \kappa - \gamma\|_Q^2\right)^{1/2}\Big]\end{aligned}$$

and the abbreviations of theorem Becker [1995]:

$$(\Delta_h\chi_h - g\nabla_h\frac{\psi_h}{g})_Q := (\Delta\chi_h - g\nabla\frac{\psi_h}{g})_Q + \frac{|\Gamma|}{2|Q|}\sum_{\Gamma\subset Q}[\psi_h n - \partial_n\chi_h]_\Gamma$$

Proof. Becker [1995] □

III.2.3.3 A-posteriori Estimate for the Stabilized SubStokes Problem with Cavitation

We derive an a-posteriori error estimate for the SubStokes problem with cavitation (I.66). Therefor we proceed analogue to Gimbel et al. [2010], introducing an additional Lagrangian parameter. Furthermore we extend the estimate which is given there, by a sharper estimate for the pressure.

We recall the variational form of the SubStokes problem with cavitation (I.66):
Find $\chi \in X_D$ and $\psi \in (\Psi_D)_{\geq 0}$ such that

$$\begin{aligned}\forall \xi \in \tilde{X}: \quad & a_{2c}(\chi, \xi) - b_{2c}(\xi, \psi) - \underbrace{\langle \partial_\nu\chi_\nu, n_\mu\xi_\mu\rangle_{L^2(\partial\Omega_2)}}_{=0,\text{ see below}} = \langle \kappa_c, \xi\rangle_{L^2(\Omega_2)} \\ \forall \phi \in \tilde{\Psi}_{\geq 0}: \quad & b(\phi - \psi, \chi) \geq \langle \sigma_3, \phi - \psi\rangle_{L^2(\Omega_2)}.\end{aligned} \tag{III.74}$$

where we introduced the following abbreviations:

$$\begin{aligned} a_{2c}(\chi,\xi) &:= \langle \partial_\nu \chi_\mu, \partial_\nu \xi_\mu \rangle_{L^2(\Omega_2)} + 12 \left\langle \frac{\chi_\mu}{g}, \frac{\xi_\mu}{g} \right\rangle_{L^2(\Omega_2)} + \langle \partial_\nu \chi_\nu, \partial_\mu \xi_\mu \rangle_{L^2(\Omega_2)} \\ b_{2c}(\xi,\psi) &:= \langle \psi/g, \partial_\mu (g \xi_\mu) \rangle_{L^2(\Omega_2)} \\ \langle \kappa_c, \xi \rangle_{L^2(\Omega_2)} &:= \langle (\kappa + \gamma_c)_\mu, \xi_\mu \rangle_{L^2(\Omega_2)} + \langle (X_0 - \psi_0 n)_\mu, \xi_\mu \rangle_{L^2(\partial\Omega_2)} \end{aligned}$$

If we prescribe inhomogenous Dirichlet boundary conditions for the pressure

$$\psi|_{\partial\Omega_2} = \psi_0 > 0$$

and follow the variational argumentation of section I.2.3.3, there must hold

$$\text{div } \chi = 0 \quad \text{ on } \partial\Omega_2. \tag{III.75}$$

Thus in problem (III.74) there just remains the symmetric part of the bilinearform (coupling χ and ξ). We reformulate (III.74) with the help of the Lagrange multiplier $\lambda \in \Lambda = \{\rho \in L^2(\Omega_2) | \rho \geq 0 \text{ a. e.}\}$.

$$\begin{aligned} \forall \xi \in \tilde{X}: \quad a_{2c}(\chi,\xi) - b_{2c}(\xi,\psi) &= \langle \kappa_c, \xi \rangle_{L^2(\Omega_2)} \\ \forall \phi \in \tilde{\Psi}: \quad b(\phi,\chi) &= \langle \sigma_3, \phi \rangle_{L^2(\Omega_2)} + \langle \lambda, \phi \rangle_{L^2(\Omega_2)} \\ \forall \rho \in \Lambda: \quad \langle \psi, \rho - \lambda \rangle_{L^2(\Omega_2)} &\geq 0. \end{aligned} \tag{III.76}$$

After addition of a stabilisation term as introduced in section III.2.3 there remains the stabilized variational problem: Find $\chi^\varepsilon \in X_D$ and $\psi^\varepsilon \in (\Psi_D)_{\geq 0}$ with

$$\begin{aligned} \forall \xi \in \tilde{X}: \quad a_{2c}(\chi^\varepsilon,\xi) - b_{2c}(\xi,\psi^\varepsilon) &= \langle \kappa_c, \xi \rangle_{L^2(\Omega_2)} \\ \forall \phi \in \tilde{\Psi}_{\geq 0}: \quad b_{2c}(\phi - \psi^\varepsilon, \chi^\varepsilon) + \varepsilon c(\psi^\varepsilon, \phi - \psi^\varepsilon) &\geq \langle \sigma_3, \phi - \psi^\varepsilon \rangle_{L^2(\Omega_2)}. \end{aligned} \tag{III.77}$$

To gain an a-posteriori-estimate for problem (III.77) we proceed analoge to Gimbel et al. [2010] and introduce an additional Lagrangian multiplier to fulfill the inequality condition $\psi^\varepsilon \geq 0$:

$$\begin{aligned} \forall \xi \in \tilde{X}: \quad & a_{2c}(\chi^\varepsilon,\xi) - b_{2c}(\xi,\psi^\varepsilon) = \langle \kappa_c, \xi \rangle_{L^2(\Omega_2)} \\ \forall \phi \in \tilde{\Psi}: \quad & b_{2c}(\chi^\varepsilon,\phi) + \varepsilon c(\psi^\varepsilon,\phi) = \langle \sigma_3, \phi \rangle_{L^2(\Omega_2)} + \langle \lambda^\varepsilon, \phi \rangle_{L^2(\Omega_2)} \\ \forall \rho \in \Lambda: \quad & \langle \psi^\varepsilon, \rho - \lambda^\varepsilon \rangle_{L^2(\Omega_2)} \geq 0. \end{aligned} \tag{III.78}$$

The discretisation of (III.78) is

$$\begin{aligned} \forall \xi \in \tilde{X}_h: \quad & a_{2c}(\chi_h^\varepsilon,\xi) - b_{2c}(\xi,\psi_h^\varepsilon) = \langle \kappa_c, \xi \rangle_{L^2(\Omega_2)} \\ \forall \phi \in \tilde{\Psi}_h: \quad & b_{2c}(\chi_h^\varepsilon,\phi) + \varepsilon c(\psi_h^\varepsilon,\phi) = \langle \sigma_3, \phi \rangle_{L^2(\Omega_2)} + \langle \lambda_h^\varepsilon, \phi \rangle_{L^2(\Omega_2)} \\ \forall \rho \in \Lambda_h: \quad & \langle \psi_h^\varepsilon, \rho - \lambda_h^\varepsilon \rangle_{L^2(\Omega_2)} \geq 0. \end{aligned} \tag{III.79}$$

In the following we split the estimate of the total error $\chi - \chi_h^\varepsilon$ into three steps. In preparation therefor we recall the interpolation estimate (III.39) to remark, that there holds

$$\begin{aligned} \|r - I_h r\| &= \|(r - r_h) - I_h(r - r_h)\| \\ &\Rightarrow \; h_Q^{-1} \|r - I_h r\|_Q, \; h_Q^{-1/2} \|r - I_h r\|_{\partial Q} \leq C_S \cdot |r - r_h|_{H^1(Q)}. \end{aligned} \tag{III.80}$$

- Firstly we derive an upper bound for the discretisation error of the pressure, to extend Gimbel et al. [2010], where only an estimate of $\varepsilon c(\psi^\varepsilon - \psi_h^\varepsilon, \psi^\varepsilon - \psi_h^\varepsilon)$ is given.

$$
\begin{aligned}
\|\psi^\varepsilon - \psi_h^\varepsilon\|^2_{L^2(\Omega_2)} &= \sum_{Q\in\mathbb{T}_h} \|\psi^\varepsilon - \psi_h^\varepsilon\|^2_{L^2(Q)} \leq 2 \sum_{Q\in\mathbb{T}_h} \left[\|\psi^\varepsilon - I_h\psi^\varepsilon\|^2_{L^2(Q)} + \|I_h\psi^\varepsilon - \psi_h^\varepsilon\|^2_{L^2(Q)}\right] \\
&\overset{\text{(III.80)}}{\leq} 2 \sum_{Q\in\mathbb{T}} C_S^2 h_Q^2 \, |\psi^\varepsilon - \psi_h^\varepsilon|^2_{H^1(Q)} + 2 \, \|I_h\psi^\varepsilon - \psi_h^\varepsilon\|^2_{L^2(\Omega_2)} \\
&\overset{\text{(III.70)}}{\leq} 2C_S^2 \underbrace{\sum_{Q\in\mathbb{T}} h_Q^2 \, |\psi^\varepsilon - \psi_h^\varepsilon|^2_{H^1(Q)}}_{=\varepsilon c(\psi^\varepsilon-\psi_h^\varepsilon,\psi^\varepsilon-\psi_h^\varepsilon)/\delta_\varepsilon} + \\
&\quad + \frac{2}{\delta^2}\Big(\|b(\cdot, I_h\psi^\varepsilon - \psi_h^\varepsilon)\|^2_{V_h'} + \underbrace{\varepsilon c(I_h\psi^\varepsilon - \psi_h^\varepsilon, I_h\psi^\varepsilon - \psi_h^\varepsilon)}_{\substack{= \sum \delta_\varepsilon h^2 \left|I_h(\psi^\varepsilon - \psi_h^\varepsilon)\right|^2_{H^1(Q)} \\ \leq \sum \delta_\varepsilon h^2 \left|\psi^\varepsilon - \psi_h^\varepsilon\right|^2_{H^1(Q)}}} \Big) \\
&\leq \frac{2C_S^2}{\delta_\varepsilon} \varepsilon c(\psi^\varepsilon - \psi_h^\varepsilon, \psi^\varepsilon - \psi_h^\varepsilon) + \frac{2}{\delta^2} \varepsilon c(\psi^\varepsilon - \psi_h^\varepsilon, \psi^\varepsilon - \psi_h^\varepsilon) \\
&\quad + \frac{2}{\delta^2} \|b(\cdot, I_h\psi^\varepsilon - \psi_h^\varepsilon) + a(\cdot, \chi^\varepsilon - \chi_h^\varepsilon)\|^2_{V_h'} \\
&\leq \left(\frac{2C_S^2}{\delta_\varepsilon} + \frac{2}{\delta^2}\right) \varepsilon c(\psi^\varepsilon - \psi_h^\varepsilon, \psi^\varepsilon - \psi_h^\varepsilon) + \\
&\quad + \frac{4}{\delta^2} \|b\|^2 \underbrace{\|I_h\psi^\varepsilon - \psi_h^\varepsilon\|^2_{L^2(\Omega_2)}}_{\leq \sum_Q C_S^2 h_Q^2 \left|\psi^\varepsilon - \psi_h^\varepsilon\right|^2_{H^1(Q)}} + \frac{4}{\delta^2} \|a\|^2 \|\chi^\varepsilon - \chi_h^\varepsilon\|^2_{H^1(\Omega)} \\
&\leq \left(\frac{2C_S^2}{\delta_\varepsilon} + \frac{2}{\delta^2} + \frac{4\|b\|^2 C_S^2}{\delta^2\delta_\varepsilon}\right) \varepsilon c(\psi^\varepsilon - \psi_h^\varepsilon, \psi^\varepsilon - \psi_h^\varepsilon) + \\
&\quad + \frac{4}{\delta^2} \|a\|^2 \|\chi^\varepsilon - \chi_h^\varepsilon\|^2_{H^1(\Omega)} \\
&\leq C_1 \cdot \left(2\varepsilon c(\psi^\varepsilon - \psi_h^\varepsilon, \psi^\varepsilon - \psi_h^\varepsilon) + \alpha \|\chi^\varepsilon - \chi_h^\varepsilon\|^2_{H^1(\Omega)}\right)
\end{aligned}
$$

  with $C_1 := \frac{1}{\delta^2} \max\left\{ \left(C_S^2\delta^2 + \delta_\varepsilon + 2\|b\|^2 C_S^2\right)/\delta_\varepsilon;\ 2\|a\|^2/\alpha \right\}$.

- We extend this bound to an estimate for the discretisation error of both, the pressure

and the velocity, using techniques, presented in Gimbel et al. [2010]:

$$\begin{aligned}
&\frac{1}{2C_1}\left\|\psi^\varepsilon-\psi_h^\varepsilon\right\|^2_{L^2(\Omega)}+\frac{\alpha}{2}\left\|\chi^\varepsilon-\chi_h^\varepsilon\right\|^2_{H^1(\Omega)}\\
\leq&\alpha\left\|\chi^\varepsilon-\chi_h^\varepsilon\right\|^2_{H^1(\Omega)}+\varepsilon c(\psi^\varepsilon-\psi_h^\varepsilon,\psi^\varepsilon-\psi_h^\varepsilon)\\
\leq&a_{2c}(\chi^\varepsilon-\chi_h^\varepsilon,\chi^\varepsilon-\chi_h^\varepsilon)+\varepsilon c(\psi^\varepsilon-\psi_h^\varepsilon,\psi^\varepsilon-\psi_h^\varepsilon)\\
=&a_{2c}(\chi^\varepsilon-\chi_h^\varepsilon,\chi^\varepsilon-I_h\chi^\varepsilon)+a_{2c}(\chi^\varepsilon-\chi_h^\varepsilon,I_h\chi^\varepsilon-\chi_h^\varepsilon)+\varepsilon c(\psi^\varepsilon-\psi_h^\varepsilon,\psi^\varepsilon-\psi_h^\varepsilon)\\
=&\left\langle\kappa_c,\chi^\varepsilon-I_h\chi^\varepsilon\right\rangle_{L^2(\Omega_2}+b_{2c}(\chi^\varepsilon-I_h\chi^\varepsilon,\psi^\varepsilon)-a_{2c}(\chi_h^\varepsilon,\chi^\varepsilon-I_h\chi^\varepsilon)+\\
&+b_{2c}(I_h\chi^\varepsilon-\chi_h^\varepsilon,\psi^\varepsilon-\psi_h^\varepsilon)+\varepsilon c(\psi^\varepsilon-\psi_h^\varepsilon,\psi^\varepsilon-\psi_h^\varepsilon)\\
=&\left\langle\kappa_c,\chi^\varepsilon-I_h\chi^\varepsilon\right\rangle_{L^2(\Omega_2)}-a_{2c}(\chi_h^\varepsilon,\chi^\varepsilon-I_h\chi^\varepsilon)-b_{2c}(I_h\chi^\varepsilon-\chi_h^\varepsilon,\psi_h^\varepsilon)+\\
&+b_{2c}(\chi^\varepsilon-\chi_h^\varepsilon,\psi^\varepsilon)+\varepsilon c(\psi^\varepsilon-\psi_h^\varepsilon,\psi^\varepsilon-\psi_h^\varepsilon)\\
=&\left\langle\kappa_c,\chi^\varepsilon-I_h\chi^\varepsilon\right\rangle_{L^2(\Omega_2)}-a_{2c}(\chi_h^\varepsilon,\chi^\varepsilon-I_h\chi^\varepsilon)-b_{2c}(I_h\chi^\varepsilon-\chi^\varepsilon,\psi_h^\varepsilon)+\\
&+b_{2c}(\chi^\varepsilon-\chi_h^\varepsilon,\psi^\varepsilon-\psi_h^\varepsilon)+\varepsilon c(\psi^\varepsilon-\psi_h^\varepsilon,\psi^\varepsilon-\psi_h^\varepsilon)
\end{aligned}\tag{III.81}$$

The second last term can be estimated with the help of the Lagrange parameters λ^ε and λ_h^ε using the variational inequalities (III.78) and (III.79) respective:

$$\begin{aligned}
b_{2c}(\chi^\varepsilon-\chi_h^\varepsilon,\psi^\varepsilon-\psi_h^\varepsilon)\leq&b_{2c}(\chi^\varepsilon,\psi^\varepsilon-\psi_h^\varepsilon)-b_{2c}(\chi_h^\varepsilon,\psi^\varepsilon-\psi_h^\varepsilon)+\\
&+\underbrace{\left\langle(\lambda_h^\varepsilon+\lambda^\varepsilon)-\lambda^\varepsilon,\psi^\varepsilon\right\rangle_{L^2(\Omega_2)}}_{\geq0}+\underbrace{\left\langle0-\lambda_h^\varepsilon,\psi_h^\varepsilon\right\rangle_{L^2(\Omega_2)}}_{\geq0}\\
=&\left\langle\lambda_h^\varepsilon,\psi^\varepsilon-\psi_h^\varepsilon\right\rangle_{L^2(\Omega_2)}-b_{2c}(\chi_h^\varepsilon,\psi^\varepsilon-\psi_h^\varepsilon)+b_{2c}(\chi^\varepsilon,\psi^\varepsilon-\psi_h^\varepsilon)\\
=&\left\langle\lambda_h^\varepsilon,\psi^\varepsilon-\psi_h^\varepsilon\right\rangle_{L^2(\Omega_2)}-b_{2c}(\chi_h^\varepsilon,\psi^\varepsilon-\psi_h^\varepsilon)+\\
&+\left\langle\sigma_3+\lambda^\varepsilon,\psi^\varepsilon-\psi_h^\varepsilon\right\rangle_{L^2(\Omega_2)}-\varepsilon c(\psi^\varepsilon,\psi^\varepsilon-\psi_h^\varepsilon)\\
=&\left\langle\lambda_h^\varepsilon,\psi^\varepsilon-\psi_h^\varepsilon\right\rangle_{L^2(\Omega_2)}-b_{2c}(\chi_h^\varepsilon,\psi^\varepsilon-\psi_h^\varepsilon)+\left\langle\sigma_3,\psi^\varepsilon-\psi_h^\varepsilon\right\rangle_{L^2(\Omega_2)}+\\
&-\varepsilon c(\psi^\varepsilon,\psi^\varepsilon-\psi_h^\varepsilon)+\underbrace{\left\langle\lambda^\varepsilon,\psi^\varepsilon\right\rangle_{L^2(\Omega_2)}}_{=-\left\langle0-\lambda^\varepsilon,\psi^\varepsilon\right\rangle_{L^2(\Omega_2)}\leq0}-\underbrace{\left\langle\lambda^\varepsilon,\psi_h^\varepsilon\right\rangle_{L^2(\Omega_2)}}_{\geq0,\ \lambda^\varepsilon,\psi_h^\varepsilon\geq0\text{ a. e.}}\\
\leq&\left\langle\lambda_h^\varepsilon,\psi^\varepsilon-\psi_h^\varepsilon\right\rangle_{L^2(\Omega_2)}-b_{2c}(\chi_h^\varepsilon,\psi^\varepsilon-\psi_h^\varepsilon)+\left\langle\sigma_3,\psi^\varepsilon-\psi_h^\varepsilon\right\rangle_{L^2(\Omega_2)}+\\
&-\varepsilon c(\psi^\varepsilon,\psi^\varepsilon-\psi_h^\varepsilon)
\end{aligned}$$

We insert this into (III.81)

$$
\begin{aligned}
&\alpha \left\|\chi^\varepsilon - \chi_h^\varepsilon\right\|^2_{H^1(\Omega)} + \varepsilon c(\psi^\varepsilon - \psi_h^\varepsilon, \psi^\varepsilon - \psi_h^\varepsilon) \\
\leq\ & \left\langle \kappa_c, \chi^\varepsilon - I_h\chi^\varepsilon \right\rangle_{L^2(\Omega_2)} - a_{2c}(\chi_h^\varepsilon, \chi^\varepsilon - I_h\chi^\varepsilon) + b_{2c}(\chi^\varepsilon - I_h\chi^\varepsilon, \psi_h^\varepsilon) + \\
&+ \left\langle \lambda_h^\varepsilon + \sigma_3, \psi^\varepsilon - \psi_h^\varepsilon \right\rangle_{L^2(\Omega_2)} - b_{2c}(\chi_h^\varepsilon, \psi^\varepsilon - \psi_h^\varepsilon) - \varepsilon c(\psi^\varepsilon, \psi^\varepsilon - \psi_h^\varepsilon) + \varepsilon c(\psi^\varepsilon - \psi_h^\varepsilon, \psi^\varepsilon - \psi_h^\varepsilon) \\
\leq\ & \left\langle \kappa_c, \chi^\varepsilon - I_h\chi^\varepsilon \right\rangle_{L^2(\Omega_2)} - a_{2c}(\chi_h^\varepsilon, \chi^\varepsilon - I_h\chi^\varepsilon) + b_{2c}(\chi^\varepsilon - I_h\chi^\varepsilon, \psi_h^\varepsilon) + \\
&+ \left\langle \lambda_h^\varepsilon + \sigma_3, \psi^\varepsilon - \psi_h^\varepsilon \right\rangle_{L^2(\Omega_2)} - b_{2c}(\chi_h^\varepsilon, \psi^\varepsilon - \psi_h^\varepsilon) - \varepsilon c(\psi_h^\varepsilon, \psi^\varepsilon - \psi_h^\varepsilon) \\
\leq\ & \left\langle \kappa_c, \chi^\varepsilon - I_h\chi^\varepsilon \right\rangle_{L^2(\Omega_2)} - a_{2c}(\chi_h^\varepsilon, \chi^\varepsilon - I_h\chi^\varepsilon) + b_{2c}(\chi^\varepsilon - I_h\chi^\varepsilon, \psi_h^\varepsilon) + \\
&+ \left\langle \lambda_h^\varepsilon + \sigma_3, \psi^\varepsilon - I_h\psi^\varepsilon \right\rangle_{L^2(\Omega_2)} - b_{2c}(\chi_h^\varepsilon, \psi^\varepsilon - I_h\psi^\varepsilon) - \varepsilon c(\psi_h^\varepsilon, \psi^\varepsilon - I_h\psi^\varepsilon) \\
&\qquad\qquad\qquad\qquad\qquad\qquad\qquad\qquad\qquad\qquad\qquad\qquad\qquad\qquad \text{(with (III.79))} \\
=\ & \sum_{Q\in\mathbb{T}_h} \Bigg[\left\langle \kappa_c + \Delta\chi_h^\varepsilon - \frac{12\chi_h^\varepsilon}{g^2} + \nabla(\operatorname{div}\ \chi_h^\varepsilon) - g\nabla\frac{\psi_h^\varepsilon}{g}, \chi^\varepsilon - I_h\chi^\varepsilon \right\rangle_{L^2(Q)} + \\
&\quad + \frac{1}{2}\left\langle [-\partial_n\chi_h^\varepsilon + (\psi_h^\varepsilon - \operatorname{div}\ \chi_h^\varepsilon)n], \chi^\varepsilon - I_h\chi^\varepsilon \right\rangle_{L^2(\partial Q)} + \\
&\quad + \left\langle \lambda_h^\varepsilon + \sigma_3 - \frac{\operatorname{div}\ (g\chi_h^\varepsilon)}{g}, \psi^\varepsilon - I_h\psi^\varepsilon \right\rangle_{L^2(Q)} + \\
&\quad + \delta_\varepsilon h_Q^2 \left\langle -\nabla\psi_h^\varepsilon, \nabla(\psi^\varepsilon - I_h\psi^\varepsilon) \right\rangle_{L^2(Q)} \Bigg] \\
\leq\ & \sum_{Q\in\mathbb{T}_h} \Bigg[\left\| \kappa_c + \Delta\chi_h^\varepsilon - 12\chi_h^\varepsilon/g^2 + \nabla(\operatorname{div}\ \chi_h^\varepsilon) - g\nabla(\psi_h^\varepsilon/g) \right\|_{L^2(Q)} \cdot \left\|\chi^\varepsilon - I_h\chi^\varepsilon\right\|_{L^2(Q)} + \\
&\quad + \frac{1}{2}\left\|[(\psi_h^\varepsilon - \operatorname{div}\ \chi_h^\varepsilon)n - \partial_n\chi_h^\varepsilon]\right\|_{L^2(\partial Q)} \cdot \left\|\chi^\varepsilon - I_h\chi^\varepsilon\right\|_{L^2(\partial Q)} + \\
&\quad + \left\|\lambda_h^\varepsilon + \sigma_3 - (\operatorname{div}\ (g\chi_h^\varepsilon))/g\right\|_{L^2(Q)} \cdot \left\|\psi^\varepsilon - I_h\psi^\varepsilon\right\|_{L^2(Q)} + \\
&\quad + \delta_\varepsilon h_Q^2 \left\|\nabla\psi_h^\varepsilon\right\|_{L^2(Q)} \cdot \left\|\nabla(\psi^\varepsilon - I_h\psi^\varepsilon)\right\|_{L^2(Q)} \Bigg].
\end{aligned}
$$

With the interpolation estimate (III.80) we conclude

$$
\begin{aligned}
&\alpha \left\|\chi^\varepsilon - \chi_h^\varepsilon\right\|_{H^1(\Omega)}^2 + \varepsilon c(\psi^\varepsilon - \psi_h^\varepsilon, \psi^\varepsilon - \psi_h^\varepsilon) \\
&\leq \sum_{Q\in\mathbb{T}_h} \Big[\frac{C_S^2}{\alpha} h_Q^2 \left\| \kappa_c + \Delta\chi_h^\varepsilon - 12\chi_h^\varepsilon/g^2 + \nabla(\operatorname{div}\,\chi_h^\varepsilon) - g\nabla(\psi_h^\varepsilon/g) \right\|_{L^2(Q)}^2 + \\
&\qquad + \frac{\alpha}{4} \left\|\chi^\varepsilon - \chi_h^\varepsilon\right\|_{H^1(Q)}^2 + \frac{\alpha}{4} \left\|\chi^\varepsilon - \chi_h^\varepsilon\right\|_{H^1(Q)}^2 + \\
&\qquad + \frac{C_S^2}{4\alpha} h_Q \left\| [(\psi_h^\varepsilon - \operatorname{div}\,\chi_h^\varepsilon)n - \partial_n \chi_h^\varepsilon] \right\|_{L^2(\partial Q)}^2 + \\
&\qquad + \frac{C_S^2}{\delta_\varepsilon} \left\| \lambda_h + \sigma_3 - (\operatorname{div}\,(g\chi_h^\varepsilon))/g \right\|_{L^2(Q)}^2 + \\
&\qquad + \frac{1}{4}\delta_\varepsilon h_Q^2 \left|\psi^\varepsilon - \psi_h^\varepsilon\right|_{H^1(Q)}^2 + \frac{1}{4}\delta_\varepsilon h_Q^2 \underbrace{\left|\psi^\varepsilon - I_h\psi^\varepsilon\right|_{H^1(Q)}^2}_{\substack{= \left|(\psi^\varepsilon - \psi_h^\varepsilon) - I_h(\psi^\varepsilon - \psi_h^\varepsilon)\right|_{H^1(Q)}^2 \\ \leq \left|\psi^\varepsilon - \psi_h^\varepsilon\right|_{H^1(Q)}^2}} + \qquad \text{(III.82)} \\
&\qquad + \delta_\varepsilon h_Q^2 \left\|\nabla\psi_h^\varepsilon\right\|_{L^2(Q)}^2 \Big]
\end{aligned}
$$

The sum over the term in line (III.82) is equal to $\frac{1}{2}\varepsilon c(\psi^\varepsilon - \psi_h^\varepsilon, \psi^\varepsilon - \psi_h^\varepsilon)$ such that we can subtract $\frac{\alpha}{2}\left\|\chi^\varepsilon - \chi_h^\varepsilon\right\|_{H^1(\Omega_2)}^2 + \frac{1}{2}\varepsilon c(\psi^\varepsilon - \psi_h^\varepsilon, \psi^\varepsilon - \psi_h^\varepsilon)$ and yield

$$
\begin{aligned}
&\frac{1}{2}\alpha \left\|\chi^\varepsilon - \chi_h^\varepsilon\right\|_{H^1(\Omega)}^2 + \frac{1}{2}\varepsilon c(\psi^\varepsilon - \psi_h^\varepsilon, \psi^\varepsilon - \psi_h^\varepsilon) \\
&\leq \sum_{Q\in\mathbb{T}_h} \Big[\frac{C_S^2}{\alpha} h_Q^2 \left\| \kappa_c + \Delta\chi_h^\varepsilon - 12\chi_h^\varepsilon/g^2 + \nabla(\operatorname{div}\,\chi_h^\varepsilon) - g\nabla(\psi_h^\varepsilon/g) \right\|_{L^2(Q)}^2 + \\
&\qquad + \frac{C_S^2}{4\alpha} h_Q \left\| [(\psi_h^\varepsilon - \operatorname{div}\,\chi_h^\varepsilon)n - \partial_n \chi_h^\varepsilon] \right\|_{L^2(\partial Q)}^2 + \\
&\qquad + \frac{C_S^2}{\delta_\varepsilon} \left\| \lambda_h + \sigma_3 - (\operatorname{div}\,(g\chi_h^\varepsilon))/g \right\|_{L^2(Q)}^2 + \delta_\varepsilon h_Q^2 \left\|\nabla\psi_h^\varepsilon\right\|_{L^2(Q)}^2 \Big] \qquad \text{(III.83)}
\end{aligned}
$$

- For the stabilisation error we assume a stability estimate for the solutions of (III.76) and (III.78) on each cell $Q \in \mathbb{T}_h$:

$$
\left|\psi - \psi^\varepsilon\right|_{H^1(Q)} \leq C_T \left|\psi^\varepsilon\right|_{H^1(Q)} \qquad \text{(III.84)}
$$

and estimate the stabilisation error:

$$
\begin{aligned}
&\|\psi-\psi^\varepsilon\|^2_{L^2(\Omega)}+\|\chi-\chi^\varepsilon\|^2_{H^1(\Omega)}\\
\leq&\sup_{\xi\in X}\frac{(b_{2c}(\xi,\psi-\psi^\varepsilon))^2}{\|\xi\|^2_{H^1(\Omega)}}+\|\chi-\chi^\varepsilon\|^2_{H^1(\Omega)} && \text{(inf-sup-condition for } b_{2c})\\
=&\sup_{\xi\in X}\frac{(a_{2c}(\xi,\chi-\chi^\varepsilon))^2}{\|\xi\|^2_{H^1(\Omega)}}+\|\chi-\chi^\varepsilon\|^2_{H^1(\Omega)} && \text{(with (III.76), (III.78))}\\
\leq&\|a_{2c}\|^2\cdot\|\chi-\chi^\varepsilon\|^2_{H^1(\Omega)}+\|\chi-\chi^\varepsilon\|^2_{H^1(\Omega)}\\
\leq&\frac{\|a_{2c}\|^2+1}{\alpha}a_{2c}(\chi-\chi^\varepsilon,\chi-\chi^\varepsilon) && \text{(ellipticity of } a_{2c})\\
\leq&\frac{\|a_{2c}\|^2+1}{\alpha}\cdot\Big(a_{2c}(\chi-\chi^\varepsilon,\chi-\chi^\varepsilon)+\varepsilon c(\psi-\psi^\varepsilon,\psi-\psi^\varepsilon)\Big)\\
=&\frac{\|a_{2c}\|^2+1}{\alpha}\cdot\Big(b_{2c}(\chi-\chi^\varepsilon,\psi-\psi^\varepsilon)+\varepsilon c(\psi-\psi^\varepsilon,\psi-\psi^\varepsilon)\Big)\\
=&\frac{\|a_{2c}\|^2+1}{\alpha}\cdot\Big(\langle\lambda-\lambda^\varepsilon,\psi-\psi^\varepsilon\rangle+\varepsilon c(\psi,\psi-\psi^\varepsilon)\Big) && \text{(with (III.76), (III.78))}\\
=&\frac{\|a_{2c}\|^2+1}{\alpha}\cdot\Big(-\underbrace{\langle 0-\lambda,\psi\rangle}_{\geq 0}-\underbrace{\langle(\lambda^\varepsilon+\lambda)-\lambda,\psi\rangle}_{\geq 0}-\underbrace{\langle\lambda-\lambda^\varepsilon,\psi^\varepsilon\rangle}_{\geq 0}+\varepsilon c(\psi,\psi-\psi^\varepsilon)\Big)\\
\leq&\frac{\|a_{2c}\|^2+1}{\alpha}\cdot\sum_{Q\in\mathbb{T}_h}\delta_\varepsilon h_Q^2\,\langle\nabla\psi,\nabla(\psi-\psi^\varepsilon)\rangle_{L^2(Q)}\\
\leq&\frac{\|a_{2c}\|^2+1}{\alpha}\cdot\sum_{Q\in\mathbb{T}_h}\delta_\varepsilon h_Q^2\left(\|\nabla(\psi-\psi^\varepsilon)\|^2_{L^2(Q)}+\|\nabla\psi^\varepsilon\|_{L^2(Q)}\,\|\nabla(\psi-\psi^\varepsilon)\|_{L^2(Q)}\right)\\
\leq&\frac{\|a_{2c}\|^2+1}{\alpha}\cdot\sum_{Q\in\mathbb{T}_h}\delta_\varepsilon h_Q^2\left(C_T^2\,|\psi^\varepsilon|^2_{H^1(Q)}+C_T\,|\psi^\varepsilon|^2_{H^1(Q)}\right) && \text{(with (III.84))}\\
\leq&\frac{\|a_{2c}\|^2+1}{\alpha}\cdot\sum_{Q\in\mathbb{T}_h}\delta_\varepsilon h_Q^2\cdot 2\cdot(C_T^2+C_T)\left(|\psi^\varepsilon-\psi_h^\varepsilon|^2_{H^1(Q)}+|\psi_h^\varepsilon|^2_{H^1(Q)}\right)\\
=&\frac{\|a_{2c}\|^2+1}{\alpha}\cdot 2\cdot C_T(C_T+1)\cdot(\varepsilon c(\psi^\varepsilon-\psi_h^\varepsilon,\psi^\varepsilon-\psi_h^\varepsilon)+\varepsilon c(\psi_h^\varepsilon,\psi_h^\varepsilon)) && \text{(III.85)}
\end{aligned}
$$

Now we can state:

Theorem III.24
The total error (discretisation and stabilisation error) of the stabilized SubStokes Cavitation problem (III.74) can be estimated by

$$\begin{aligned}
&\|\psi-\psi_h^\varepsilon\|^2_{L^2(\Omega_2)}+\|\chi-\chi_h^\varepsilon\|^2_{H^1(\Omega_2)}\\
\leq& K\cdot\sum_{Q\in\mathbb{T}_h}\Big[h_Q^2\left\|\kappa_c+\Delta\chi_h^\varepsilon-12\chi_h^\varepsilon/g^2+\nabla(\operatorname{div}\,\chi_h^\varepsilon)-g\nabla(\psi_h^\varepsilon/g)\right\|^2_{L^2(Q)}+\\
&\qquad+h_Q\left\|[(\psi_h^\varepsilon-\operatorname{div}\,\chi_h^\varepsilon)n-\partial_n\chi_h^\varepsilon]\right\|^2_{L^2(\partial Q)}+\\
&\qquad+\|\lambda_h+\sigma_3-(\operatorname{div}\,(g\chi_h^\varepsilon))/g\|^2_{L^2(Q)}+\delta_\varepsilon h_Q^2\|\nabla\psi_h^\varepsilon\|^2_{L^2(Q)}\Big].
\end{aligned}$$

Proof. We collect the estimates (III.81), (III.83) and (III.85):

$$\begin{aligned}
&\|\psi-\psi_h^\varepsilon\|^2_{L^2(\Omega_2)}+\|\chi-\chi_h^\varepsilon\|^2_{H^1(\Omega_2)}\\
\leq\;& 2\|\psi-\psi^\varepsilon\|^2_{L^2(\Omega_2)}+2\|\chi-\chi^\varepsilon\|^2_{H^1(\Omega_2)}+2\|\psi^\varepsilon-\psi_h^\varepsilon\|^2_{L^2(\Omega_2)}+2\|\chi^\varepsilon-\chi_h^\varepsilon\|^2_{H^1(\Omega_2)}\\
\overset{(III.85)}{\leq}&\frac{4(\|a_{2c}\|^2+1)\cdot C_T(C_T+1)}{\alpha}\cdot(\varepsilon c(\psi^\varepsilon-\psi_h^\varepsilon,\psi^\varepsilon-\psi_h^\varepsilon)+\varepsilon c(\psi_h^\varepsilon,\psi_h^\varepsilon))+\\
&+2\|\psi^\varepsilon-\psi_h^\varepsilon\|^2_{L^2(\Omega)}+2\|\chi^\varepsilon-\chi_h^\varepsilon\|^2_{H^1(\Omega_2)}\\
\overset{(III.81)}{\leq}&\frac{4(\|a_{2c}\|^2+1)\cdot C_T(C_T+1)}{\alpha}\cdot(\varepsilon c(\psi^\varepsilon-\psi_h^\varepsilon,\psi^\varepsilon-\psi_h^\varepsilon)+\varepsilon c(\psi_h^\varepsilon,\psi_h^\varepsilon))+\\
&+4\cdot\max\{C_1;\;1/\alpha\}\cdot\left(\alpha\|\chi^\varepsilon-\chi_h^\varepsilon\|^2_{H^1(\Omega_2)}+\varepsilon c(\psi^\varepsilon-\psi_h^\varepsilon,\psi^\varepsilon-\psi_h^\varepsilon)\right)\\
=\;&\frac{4(\|a_{2c}\|^2+1)\cdot C_T(C_T+1)}{\alpha}\cdot\varepsilon c(\psi_h^\varepsilon,\psi_h^\varepsilon)+\\
&+\frac{4}{\alpha}\cdot\max\left\{(\|a_{2c}\|^2+1)\cdot C_T(C_T+1);\;\alpha C_1;\;1\right\}\cdot\\
&\quad\cdot\left(\alpha\|\chi^\varepsilon-\chi_h^\varepsilon\|^2_{H^1(\Omega_2)}+\varepsilon c(\psi^\varepsilon-\psi_h^\varepsilon,\psi^\varepsilon-\psi_h^\varepsilon)\right)\\
\overset{(III.83)}{\leq}&\frac{4(\|a_{2c}\|^2+1)\cdot C_T(C_T+1)}{\alpha}\cdot\varepsilon c(\psi_h^\varepsilon,\psi_h^\varepsilon)+\\
&+\frac{4}{\alpha}\cdot\max\left\{(\|a_{2c}\|^2+1)\cdot C_T(C_T+1);\;\alpha C_1;\;1\right\}\cdot\\
&\quad\cdot 2\cdot\sum_{Q\in\mathbb{T}_h}\Big[\frac{C_S^2}{\alpha}h_Q^2\left\|\kappa_c+\Delta\chi_h^\varepsilon-12\chi_h^\varepsilon/g^2+\nabla(\operatorname{div}\,\chi_h^\varepsilon)-g\nabla(\psi_h^\varepsilon/g)\right\|^2_{L^2(Q)}+\\
&\qquad+\frac{C_S^2}{4\alpha}h_Q\left\|[(\psi_h^\varepsilon-\operatorname{div}\,\chi_h^\varepsilon)n-\partial_n\chi_h^\varepsilon]\right\|^2_{L^2(\partial Q)}+\\
&\qquad+\frac{C_S^2}{\delta_\varepsilon}\|\lambda_h+\sigma_3-(\operatorname{div}\,(g\chi_h^\varepsilon))/g\|^2_{L^2(Q)}+\delta_\varepsilon h_Q^2\|\nabla\psi_h^\varepsilon\|^2_{L^2(Q)}\Big]
\end{aligned}$$

□

The estimate given in theorem III.24 is sharper than that, given in Gimbel et al. [2010]. There $p - p_h^\varepsilon$ only is estimated in the h-dependant norm

$$\sum_{Q\in\mathbb{T}} \delta \cdot h_Q^2 \left|\psi - \psi_h^\varepsilon\right|^2_{H^1(Q)} .$$

III.2.3.4 Uzawa Algorithm

In the last sections we learned, how to stabilize a saddle point problem. In this section we briefly discuss, how to handle the resulting system of equations algorithmically. We follow Braess [1997], Girault and Raviart [1979], Girault and Raviart [1986], Kim [2009].

As general problem in this section we examine the discrete system

$$\text{Find } v \in \mathbb{R}^n, \quad p \in \mathbb{R}^m : \quad \left\{ \begin{array}{rrcl} Av & -Bp & = & f \\ B^T v & +Cp & = & g \end{array} \right\} \tag{III.86}$$

where $f \in \mathbb{R}^n$, $g \in \mathbb{R}^m$, $A \in \mathbb{R}^{n\times n}$, $B \in \mathbb{R}^{n\times m}$ and $C \in \mathbb{R}^{m\times m}$.
The Schur-complement of this system is

$$\Big(B^T A^{-1} B + C\Big) p = g - B^T A^{-1} f.$$

Treatment of this equation with the Jacobi-Solver and additional v-update by the first equation of (III.86) yields the following algorithm:

$$\begin{aligned} &p^0 \in \mathbb{R}^m \\ &\texttt{for } k = 0, 1, 2, 3, \ldots \\ &\qquad v^k := A^{-1}(f + Bp^k) \\ &\qquad p^{k+1} := p^k + A_p^{-1}(g - B^T A^{-1} f - B^T A^{-1} B p^k - C p^k) = p^k + A_p^{-1}(g - B^T v^k - C p^k) \end{aligned} \tag{III.87}$$

with a suitable preconditioner $A_p \in \mathbb{R}^{m\times m}$.
One example of a system of the form (III.86) is given by the stabilized Stokes-problem

$$\begin{aligned} \forall w \in V_h : \qquad & \langle \partial_i v_j, \partial_i w_j \rangle_\Omega - \langle \partial_j w_j, p \rangle_\Omega = \langle f, v \rangle_\Omega \\ \forall \psi \in P_h : \qquad & \langle \partial_i v_j, p \rangle_\Omega + \sum_{Q\in\mathbb{Q}} h_Q^2 \langle \partial_j \psi, \partial_j p \rangle_Q = \langle g, p \rangle_\Omega \end{aligned} \tag{III.88}$$

with the choice $f = 0$, $g = 0$ and bilinear elements for the spaces V_h and P_h.
On the domain $\Omega = [0;4]^2$ there are given Dirichlet (boundary-)conditions for velocity and pressure:

$$\begin{aligned} v &= \begin{pmatrix} y \cdot (4-y) \\ 0 \end{pmatrix}, && x = 0 \\ v &= 0, && y = 4 \vee x = 4 \vee x > 1,5 \wedge y = 0 \\ v &= 0, && 1,5 \le x \le 2 \wedge y \le 1,5 \vee 2 \le x \le 3 \wedge 1 \le y \le 1,5 \\ p &= 0 && y = 0 \wedge 0 \le x \le 1,5 \end{aligned}$$

The numbers of degrees of freedom are $\dim V_h = 2178$ and $\dim P_h = 1089$ respectively.

Testing the different variants of the Uzawa algorithm
The considered algorithms vary in the choice of the preconditioner A_p^{-1}:

- The most simple variant is $A_p = I$.
- Another obvious choice is the diagonal of the Schur-Complement $A_p = D = \text{diag } S = \text{diag } (B^T A^{-1} B + C)$. Therefore prior the execution of the Uzawa-loop, we have to invert A for n_p times (n_p=number of degrees of freedom in pressure space). If we choose the ssor-method in the following, it is sufficiant, to calculate $A_p = \text{diag } (B^T \text{diag}(A)^{-1} B + C)$.

$$\begin{array}{l} p^0 \in \mathbb{R}^m \\ D := \texttt{diag } \left(B^T A^{-1} B + C\right) \\ \texttt{for } k = 0, 1, 2, 3, \ldots \\ \qquad v^k := A^{-1}(f + Bp^k) \\ \qquad p^{k+1} := p^k + D^{-1}\left(g - B^T v^k - Cp^k\right) \end{array} \tag{III.89}$$

- The next improvement is the successive treatment of the system, which means, that we for every calculation of

$$\left(p^{k+1} - p^k\right)_k = \left(A_p^{-1}(g - B^T v^k - Cp^k)\right)_k$$

we use the already calculated p_i^{k+1} $(i < k)$.

$$\begin{array}{l} p^0 \in \mathbb{R}^m \\ D := \texttt{diag } \left(B^T A^{-1} B + C\right) \\ \texttt{for } k = 0, 1, 2, 3, \ldots \\ \qquad v^k := A^{-1}(f + Bp^k) \\ \qquad \texttt{for } j = 1, \ldots, m \\ \qquad\qquad p_j^{k+1} := p_j^k + \frac{1}{D_{jj}}\left(g_j - (B^T v^k)_j - \sum_{i=1}^{j-1} C_{ji} p_i^{k+1} - \sum_{i=j}^{m} C_{ji} p_i^k\right) \end{array} \tag{III.90}$$

- This SOR-method can be symmetrized to a SSOR-variant.

$$\begin{array}{l} p^0 \in \mathbb{R}^m \\ D := \texttt{diag } \left(B^T A^{-1} B + C\right) \\ \texttt{for } k = 0, 1, 2, 3, \ldots \\ \qquad v^k := A^{-1}(f + Bp^k) \\ \qquad \texttt{for } j = 1, \ldots, m \\ \qquad\qquad p_j^{k+\frac{1}{2}} := p_j^k + \frac{1}{D_{jj}}\left(g_j - (B^T v^k)_j - \sum_{i=1}^{j-1} C_{ji} p_i^{k+\frac{1}{2}} - \sum_{i=j}^{m} C_{ji} p_i^k\right) \\ \qquad v^{k+\frac{1}{2}} := A^{-1}(f + Bp^{k+\frac{1}{2}}) \\ \qquad \texttt{for } j = m, \ldots, 1 \\ \qquad\qquad p_j^{k+1} := p_j^{k+\frac{1}{2}} + \frac{1}{D_{jj}}\left(g_j - (B^T v^{k+\frac{1}{2}})_j - \sum_{i=1}^{j} C_{ji} p^{k+\frac{1}{2}} - \sum_{i=j+1}^{m} C_{ji} p_i^{k+1}\right) \end{array} \tag{III.91}$$

- The last acceleration, we consider at this point, is the implementation of one cg-step in every loop:

$$
\begin{aligned}
&p^0 \in \mathbb{R}^m \\
&D := \texttt{diag}\ \left(B^T A^{-1} B + C\right) \\
&\texttt{for}\ k = 0, 1, 2, 3, \ldots \\
&\qquad v^k := A^{-1}(f + Bp^k) \\
&\qquad \texttt{for}\ j = 1, \ldots, m \\
&\qquad\qquad p_j^{k+\frac{1}{4}} := p_j^k + \tfrac{1}{D_{jj}} \left(g_j - (B^T v^k)_j - \sum_{i=1}^{j-1} C_{ji} p_i^{k+\frac{1}{4}} - \sum_{i=j}^{m} C_{ji} p_i^k \right) \\
&\qquad v^{k+\frac{1}{2}} := A^{-1}(f + Bp^{k+\frac{1}{4}}) \\
&\qquad \texttt{for}\ j = m, \ldots, 1 \\
&\qquad\qquad p_j^{k+\frac{1}{2}} := p_j^{k+\frac{1}{4}} + \tfrac{1}{D_{jj}} \left(g_j - (B^T v^{k+\frac{1}{2}})_j - \sum_{i=1}^{j} C_{ji} p^{k+\frac{1}{4}} - \sum_{i=j+1}^{m} C_{ji} p_i^{k+\frac{1}{2}} \right) \\
&\qquad g = p^{k+\frac{1}{2}} - p^k \\
&\qquad \texttt{if}\ k > 0 \\
&\qquad\qquad \beta := \tfrac{(Sp^k - b)^T \left(d^T S g g - g^T S g d \right)}{g^T S g d^T S d - (g^T S d)^2} \\
&\qquad\qquad \alpha := \tfrac{g^T \left(b - S(\beta d + p^k) \right)}{g^T S g} \\
&\qquad\qquad p^{k+1} := p^k + \alpha g + \beta d \\
&\qquad \texttt{else} \\
&\qquad\qquad p^{k+1} := p^{k+\frac{1}{2}} \\
&\qquad d = p^{k+1} - p^k
\end{aligned}
\tag{III.92}
$$

The inversions A^{-1} are calculated by a simple cg-solver. Crucial for the convergence of the Uzawa algorithm is the accuracy of these internal solvers. The residuals of these should be less than square of the gained Uzawa residual. The convergence of the algorithm with the different preconditioners for the model problem (III.88) is illustrated in figure III.6. The comparison implies the supremacy of the cg-accelerated solver.

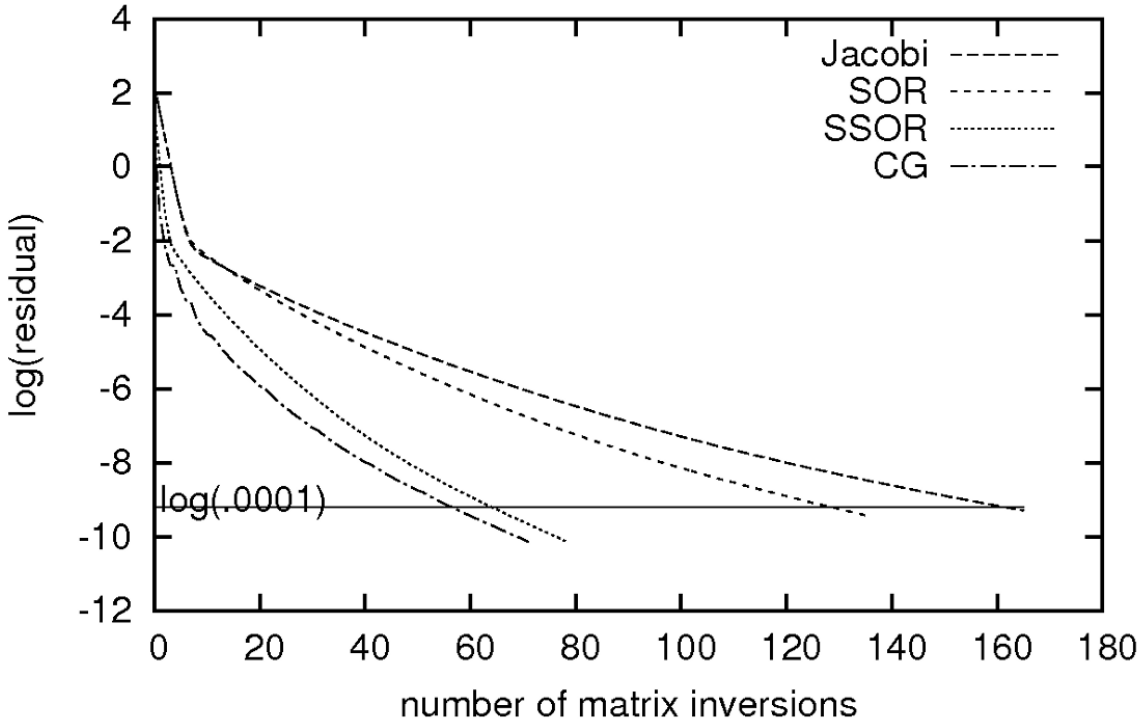

Figure III.6: Residual $\sqrt{\|Av - Bp - f\|_2^2 + \|B^T v + Cp - g\|_2^2}$ of the Uzawa-Algorithm with the different pre-conditioners.

III.3 Balance of Model- and Discretisation-Error

In this section we discuss, how to refine both, the model, that is used in different parts of the domain and the mesh, that underlies the FE-discretisation, in a balanced way.

The challange in this section is to combine the estimates for the modelling error of section III.1 and the estimates for the discretisation error of section III.2 to use the correct model on the one hand and a sufficiently fine mesh on the other hand.
To avoid an unappropriate numerically accurate calculation of a very rough model or the use of an accurate (expensive) model on a rough grid, the refinment has to be performed in a balanced way. This is discussed in Braack and Ern [2003].
There, the local error indicators are modified in the following way: (we use the notation of (III.3))

$$\tilde{\varepsilon}_{m,Q} := \begin{cases} \|e_m\|_Q\,, & \|e_m\|_Q \geq \alpha \|e_d\|_Q \\ 0, & else \end{cases}$$
$$\tilde{\varepsilon}_{d,Q} := \begin{cases} \|e_d\|_Q\,, & \|e_d\|_Q \geq \alpha \|e_m\|_Q \\ 0, & else \end{cases}, \quad \text{with } \alpha \in (0;1). \tag{III.93}$$

The refinement of the model takes place with the help of these modified indicators analogue one of the algorithms for model-refinenement III.2 or III.3 and the grid-refinement takes place in the usual way of fixed fraction strategy, i. e. in every cycle about thirty percent of the cells with highest error indicator $\tilde{\varepsilon}_{d,Q}$ are refined, while the three percent of the cells with the lowest error are coarsened. This results in algorithm III.25

Algorithm III.25 (Balance of Model- and Grid-Refinement)
create triangulation $\mathbb{T}$ of the domain Ω
$\varepsilon_0 \in \mathbb{R}_{>0}$; $N_{max} \in \mathbb{N}$; $N \leftarrow 0$; $\varepsilon^m \leftarrow 0$; $\varepsilon^d \leftarrow 0$; $p_c \in (0,1)$; $p_a \in (0,1)$
$\mathbb{T}_c \leftarrow \mathbb{T}$; $\mathbb{T}_a \leftarrow \emptyset$
calculate $u \leftarrow u_c$ on Ω
for $Q \in \mathbb{T}$
    calculate the estimate $\varepsilon^m(Q)$
    if $Q \in \mathbb{T}_c$
        $(\varepsilon^m)^2 \leftarrow (\varepsilon^m)^2 + \varepsilon^m(Q)^2$
        calculate the estimate $\varepsilon^d(Q)$
        $(\varepsilon^d)^2 \leftarrow (\varepsilon^d)^2 + \varepsilon^d(Q)$
while ($N < N_{max}$ and $(\varepsilon^m)^2 + (\varepsilon^d)^2 > \varepsilon_0$)
      refine model using $\tilde{\varepsilon}^m(Q)$
      refine grid using $\tilde{\varepsilon}^d(Q)$
      calculate $u \leftarrow u_c$ on $\mathbb{T}$
      calculate $u \leftarrow u_a$ on $\mathbb{T}_a$
      $\varepsilon^m \leftarrow 0$
      $\varepsilon^d \leftarrow 0$
      for $Q \in \mathbb{T}$
          calculate the estimate $\varepsilon^m(Q)$

`if` $Q \in \mathbb{T}_c$
$(\varepsilon^m)^2 \leftarrow (\varepsilon^m)^2 + \varepsilon^m(Q)^2$
`calculate the estimate` $\varepsilon^d(Q)$
$(\varepsilon^d)^2 \leftarrow (\varepsilon^d)^2 + \varepsilon^d(Q)$
$N \leftarrow N + 1$

IV

Applications

In this section we give some applications of the models, error estimates and algorithms, introduced in sections I, II and III.

IV.1 Deformation

We apply our model for linear elasticity (I.17) to a rather simple geometry (IV.1) for different cases of external force fields to test the error estimators for these examples.

In sections IV.1.1-IV.1.5 we always consider the two-dimensional problem of deformation (I.17):

$$\forall r \in V_0 : \ 2\mu \left\langle \varepsilon_{ij}(s), \varepsilon_{ij}(r) \right\rangle_{L^2(\Omega)} + 2\lambda \left\langle \varepsilon_{ll}(s), \varepsilon_{jj}(r) \right\rangle_{L^2(\Omega)} = \left\langle \rho f_i, r_i \right\rangle_{L^2(\Omega)} + \left\langle \tau_{ij} n_j, r_i \right\rangle_{\Gamma_\tau}$$

on the domain

$$\Omega = [-16; 16] \times [0; 1], \text{ with } \Gamma_0 = \{\pm 16\} \times [0; 1], \ \Gamma_\tau = \partial\Omega \setminus \Gamma_0. \tag{IV.1}$$

and the function space

$$V_0 = H^1_{0,\Gamma_0}(\Omega).$$

All computations start on an initial grid of 64 cells and refine it adaptively using the estimator of theorem III.12 and a fixed-fraction strategy (see e. g. Suttmeier [2008]): We refine the 30% of the cells with the highest error per cell, which results in about doubling of the cells. Furthermore we coarsen 3% of the cells with the smallest error.

IV.1.1 Deformation of a box domain under a constant load

We consider the two dimensional problem of deformation (I.17) with

$$\begin{aligned} \rho f_i &= 0.0004 \cdot \delta_{i2} \\ \tau &= 0 \end{aligned}$$

on the domain (IV.1). The sequence of refined grids is shown in figure IV.1 and the final solution in figure IV.2.

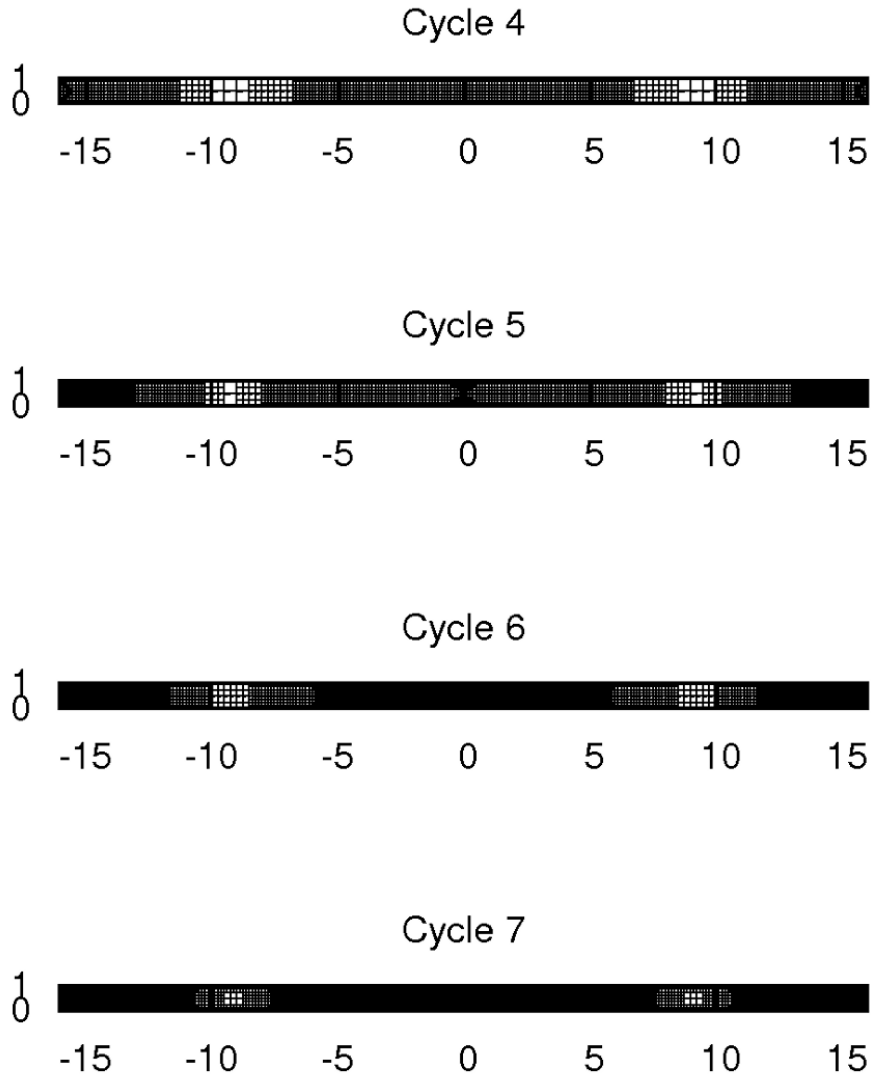

Figure IV.1: Adaptively refined grids, after 4 to 7 refinement cycles. There is drawn the domain $[-16; 16] \times [0; 1]$.

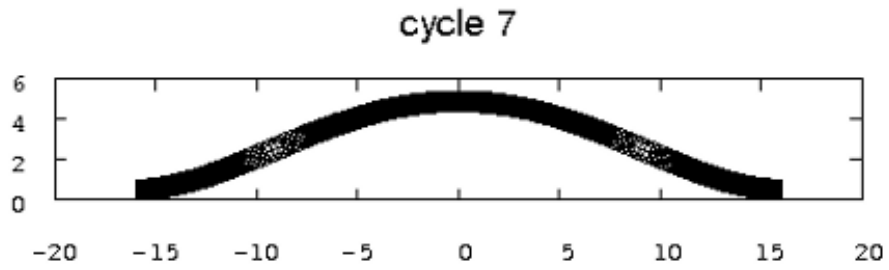

Figure IV.2: The solution of the considered problem. There is shown the deformed domain (IV.1).

The following table IV.1 shows the results of one run of our algorithm:

cycle	# active cells	# dofs	a-posteriori-estimate	ratio
0	128	390	0.6881	inf
1	245	676	0.5118	0.7439
2	464	1200	0.3743	0.7312
3	884	2138	0.2860	0.7642
4	1682	3906	0.2025	0.7081
5	3197	7152	0.1536	0.7583

Table IV.1: The convergence of one run of our algorithm for the deformation problem.

We see the decrease of the estimator by the factor $1/\sqrt{2}$, which indicates the expected order

$$\|s - s_h\|_a = O(n_{dofs}^{-1/2}).$$

IV.1.2 Deformation of a box domain under a constant surface-stress

We consider the two dimensional problem of deformation (I.17) with

$$\begin{aligned} \rho f_i &= 0 \\ \tau_{ij} n_j &= \begin{cases} 0, & x_2 = 0 \\ 0.001 \cdot \delta_{i2}, & x_2 = 1 \end{cases} . \end{aligned}$$

on the domain (IV.1).
This example is of certain practical importance, because all forces on a work-piece of our

technichal application are applied through surface-stresses. Especially the pressure of the considered lubricant is applied this way:

$$\tau_{ij} n_j = p_{\text{fluid}} n_i.$$

The final solution is shown in figure IV.3.

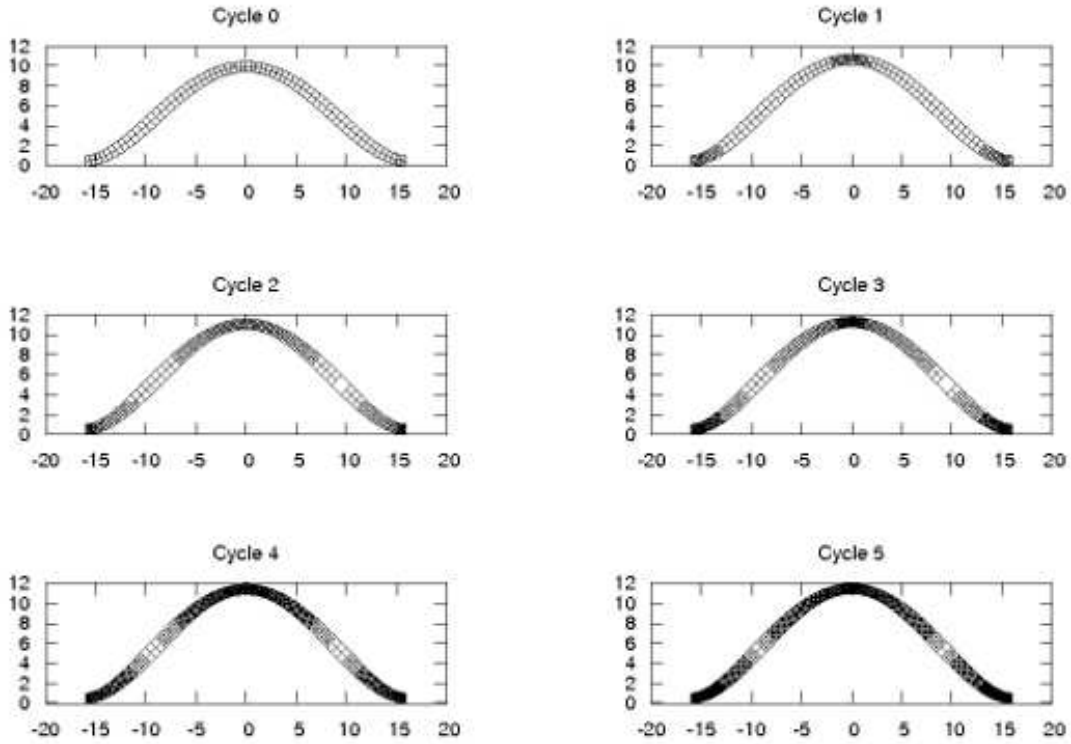

Figure IV.3: The solution of the considered problem.

The following table shows the results of one run of our algorithm: The following table IV.2 shows the results of one run of our algorithm:

cycle	# active cells	# dofs	a-posteriori-estimate	ratio
0	128	390	1.7202	inf
1	245	676	1.2788	0.7434
2	464	1200	0.9356	0.7316
3	884	2138	0.7146	0.7638
4	1682	3906	0.5063	0.7085
5	3197	7152	0.3837	0.7578

Table IV.2: The convergence of one run of our algorithm for the deformation problem.

We see the decrease of the estimator by the factor $1/\sqrt{2}$, which indicates the expected order

$$\|s - s_h\|_a = O(n_{dofs}^{-1/2}).$$

IV.1.3 Deformation of a box domain under an elliptic load

We consider the two dimensional problem of deformation (I.17) with

$$\begin{aligned} \rho f_i &= \frac{0.0004}{16^2} \cdot x_1^2 \cdot \delta_{i2} \\ \tau &= 0 \end{aligned}$$

on the domain (IV.1). The sequence of refined grids is shown in figure IV.4 and the final solution in figure IV.5.

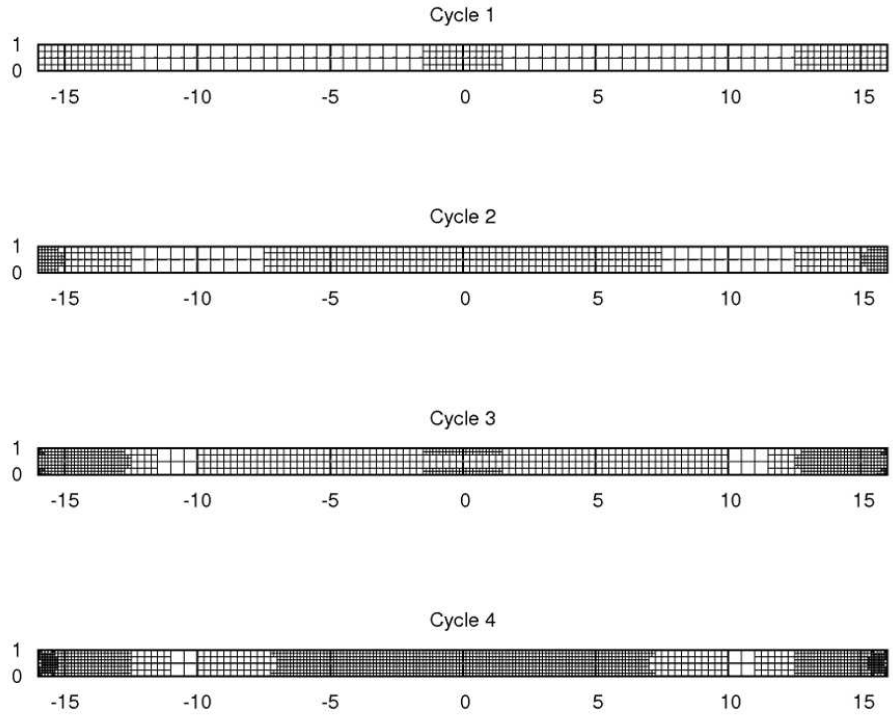

Figure IV.4: Adaptively refined grids. There is drawn the domain $[-16; 16] \times [0; 1]$.

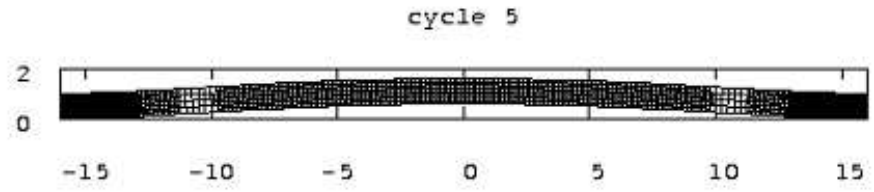

Figure IV.5: The solution of the considered problem.

The following table IV.3 shows the results of one run of our algorithm:

cycle	# active cells	# dofs	a-posteriori-estimate	ratio
0	128	390	0.1021	inf
1	248	682	0.0723	0.7077
2	476	1218	0.0527	0.7296
3	908	2234	0.0390	0.7398
4	1736	4022	0.0291	0.7463
5	3314	7418	0.0204	0.6999

Table IV.3: The convergence of one run of our algorithm for the deformation problem.

We see the decrease of the estimator by the factor $1/\sqrt{2}$, which indicates the expected order

$$\|s - s_h\|_a = O(n_{dofs}^{-1/2}).$$

IV.1.4 Deformation of a box domain under a jump load

We consider the two dimensional problem of deformation (I.17) with

$$\rho f_i(x) = \begin{cases} 0.0004 \cdot \delta_{i2} & x_1 > 0 \\ 0 & \text{else} \end{cases}$$
$$\tau = 0$$

on the domain (IV.1). The sequence of refined grids is shown in figure IV.6 and the final solution in figure IV.7.

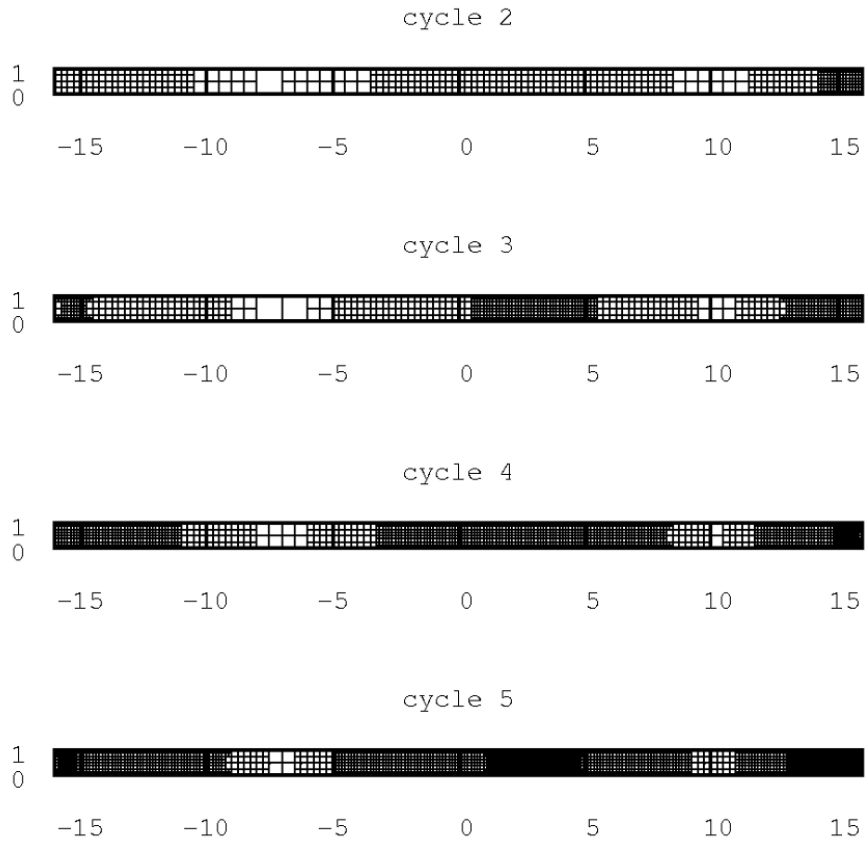

Figure IV.6: Adaptively refined grids, after 2 to 5 refinement cycles. There is drawn the domain $[-16; 16] \times [0; 1]$.

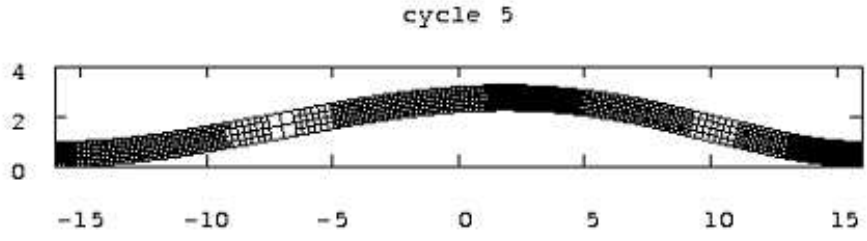

Figure IV.7: The solution of the considered problem.

The following table IV.4 shows the results of one run of our algorithm:

cycle	# active cells	# dofs	a-posteriori-estimate	ratio
0	128	390	0.3676	inf
1	248	682	0.2660	0.7236
2	473	1202	0.1910	0.7181
3	896	2158	0.1475	0.7726
4	1706	3922	0.1042	0.7063
5	3242	7202	0.0798	0.7661

Table IV.4: The convergence of one run of our algorithm for the deformation problem.

We see the decrease of the estimator by the factor $1/\sqrt{2}$, which indicates the expected order

$$\|s - s_h\|_a = O(n_{dofs}^{-1/2}).$$

IV.1.5 Deformation of a box domain under a periodic load

We consider the two dimensional problem of deformation (I.17) with

$$\begin{aligned} \rho f_i(x) =& 0.004 \cdot \sin \frac{x_1 \cdot \pi}{16} \cdot \delta_{i2} \\ \tau =& 0 \end{aligned}$$

on the domain (IV.1). The sequence of refined grids is shown in figure IV.8 and the final solution in figure IV.9.

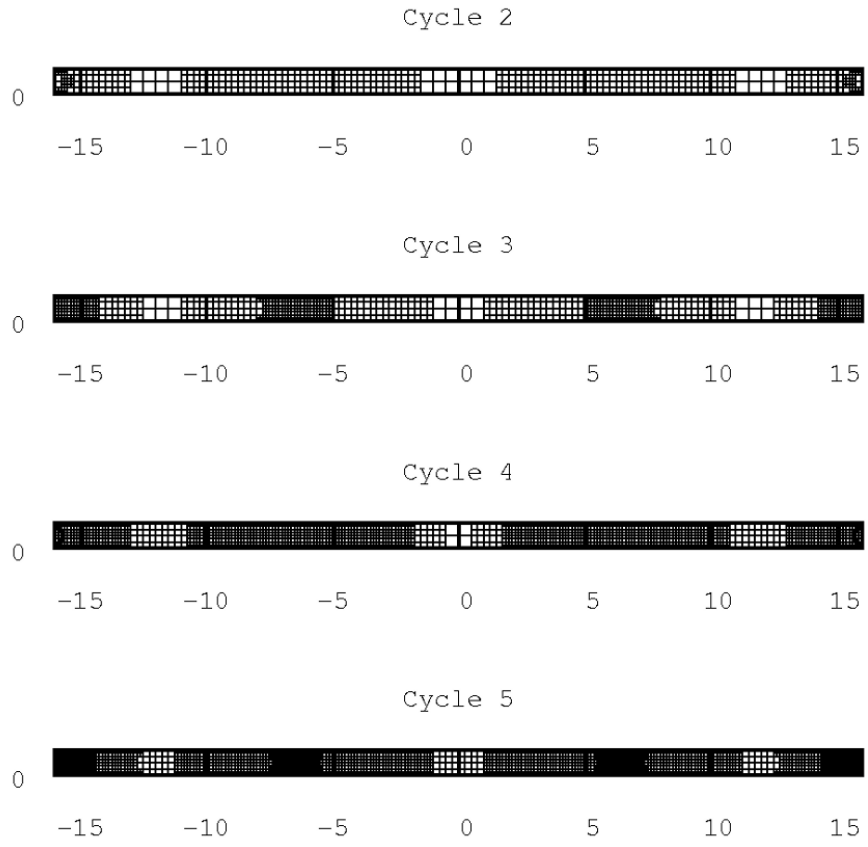

Figure IV.8: Adaptively refined grids, after 2 to 5 refinement cycles. There is drawn the domain $[-16; 16] \times [0; 1]$.

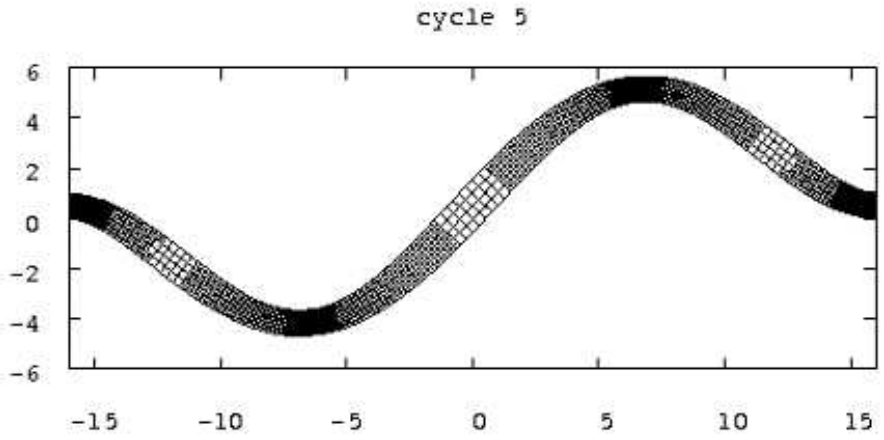

Figure IV.9: The solution of the considered problem.

The following table IV.5 shows the results of one run of our algorithm:

cycle	# active cells	# dofs	a-posteriori-estimate	ratio
0	128	390	2.0788	inf
1	248	686	1.5901	0.7649
2	476	1234	1.1394	0.7165
3	908	2202	0.8947	0.7853
4	1736	4030	0.6127	0.6848
5	3308	7394	0.4827	0.7879

Table IV.5: The convergence of one run of our algorithm for the deformation problem.

We see the decrease of the estimator by the factor $1/\sqrt{2}$, which indicates the expected order

$$\|s - s_h\|_a = O(n_{dofs}^{-1/2}).$$

For all five examples, we considered in sections IV.1.1– IV.1.5, we see that the error estimate of theorem III.12 decreases with the expected order of $O(n_{dofs}^{-1/2})$ that corresponds the reduction of the estimate by the factor $1/\sqrt{2}$. Also the output of the adaptively refined grids shows a refinement in zones of high stresses and rather coarse cells in regions of low stresses.

IV.2 Contact Mechanics

IV.2.1 Single Direction Contact

In this section we apply a grid-adaptive algorithm, using the a-posteriori-error of theorem III.15 to the contact problem (I.23) with the simple projection in only one direction.

The considered probelms are described by (I.23): For all $r \in \Pi_n(V_0)$:

$$2\mu \langle \varepsilon_{ij}(s), \varepsilon_{ij}(r-s)\rangle_\Omega + 2\lambda \langle \varepsilon_{ll}(s), \varepsilon_{jj}(r-s)\rangle_\Omega \geq \langle \rho f_i, r - s_i\rangle_\Omega + \langle \tau_{ij} n_j, r - s_i\rangle_{\Gamma_\tau} \quad \text{(IV.2)}$$

with $\mu = \lambda = 1$.
The set of allowed displacements

$$\Pi_n(V_0) = \{r \in V_0 | P_n(x + r(x)) = x + r(x),\ x \in \Gamma_C\}$$

is given by the projection in z-direction (I.20):

$$P_n(\xi) = \begin{cases} \xi, & \xi \cdot n \leq b(\xi_\perp) \\ \xi - (\xi \cdot n - b(\xi_\perp))n, & \xi \cdot n > b(\xi_\perp) \end{cases}$$

In all applications in sections IV.2.1.1-IV.2.1.5 we consider the same domain (IV.1) as in the previous section IV.1

$$\Omega = [-16; 16] \times [0; 1],\ \text{with } \Gamma_0 = \{\pm 16\} \times [0; 1]$$

and the function space

$$V_0 = H^1_{0,\Gamma_0}(\Omega).$$

The contact-boundary Γ_C will be declared for each example separately while the Neumann-boundary will always be

$$\Gamma_\tau = \partial\Omega \setminus (\Gamma_0 \cup \Gamma_C).$$

Again the computations start on an initial grid of 64 cells and refine it adaptively using the estimator of theorem III.15 to refine the 30% of the cells with the highest error per cell, which results in about doubling of the cells. Furthermore we coarsen 3% of the cells with the smallest error.

IV.2.1.1 Contact Problem: Box domain with constant load and constant obstacle

We consider the two dimensional contact problem (IV.2) with

$$\begin{aligned} \rho f_i(x) &= -\,0.004 \cdot \delta_{i2} \\ \tau &= 0. \end{aligned}$$

The displacement is restricted at the lower boundary

$$\Gamma_C = \{x \in \partial\Omega | x_2 = 0\}$$

by the obstacle

$$s_2(x) \geq -2.$$

The process of grid-refinement is shown in figure IV.10.

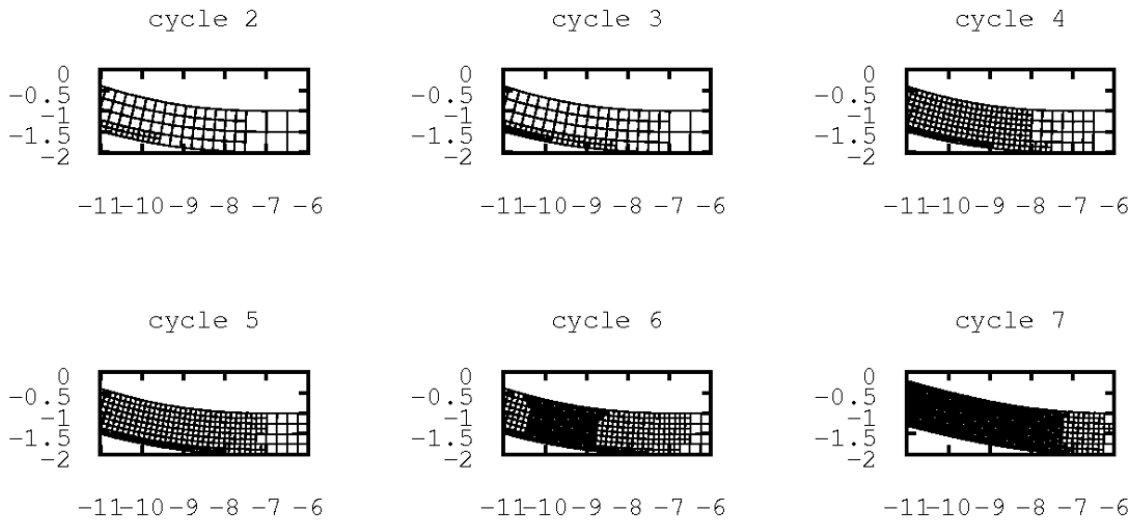

Figure IV.10: Adaptively refined grids, after 2 to 7 refinement cycles.

The result of one run of the algorithm is shown in figure IV.11.

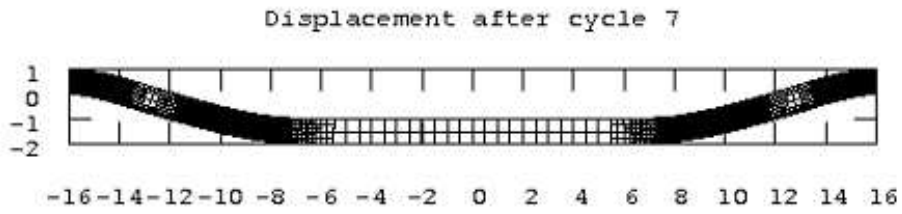

Figure IV.11: The solution of the considered problem.

The following table IV.6 shows the behaviour of the error estimate during one run of our algorithm:

cycle	# active cells	# dofs	a-posteriori-estimate	ratio
0	128	390	1.2261	inf
1	248	702	0.8474	0.6911
2	476	1290	0.6233	0.7355
3	905	2368	0.4603	0.7386
4	1721	4382	0.3478	0.7555
5	3272	8182	0.2558	0.7356
6	6224	15438	0.1935	0.7564
7	11834	28930	0.1443	0.7459

Table IV.6: The convergence of one run of our algorithm for the contact problem.

We see the decrease of the estimator by the factor $1/\sqrt{2}$, which indicates the expected order

$$\|s - s_h\|_a = O(n_{dofs}^{-1/2}).$$

Ãij

IV.2.1.2 Contact Problem: Box domain with constant load and periodic obstacle

We consider the two dimensional contact problem (IV.2) with

$$\begin{aligned} \rho f_i(x) &= -.002\delta_{i2} \\ \tau &= 0 \end{aligned}$$

The displacement is restricted at the lower boundary

$$\Gamma_C = \{x \in \partial\Omega | x_2 = 0\}$$

by the obstacle

$$s_2(x) \geq -2 + 1.2 \cdot \sin \frac{2 \cdot 2\pi \cdot (x_1 + 16)}{32}.$$

The process of grid-refinement is shown in figure IV.12.

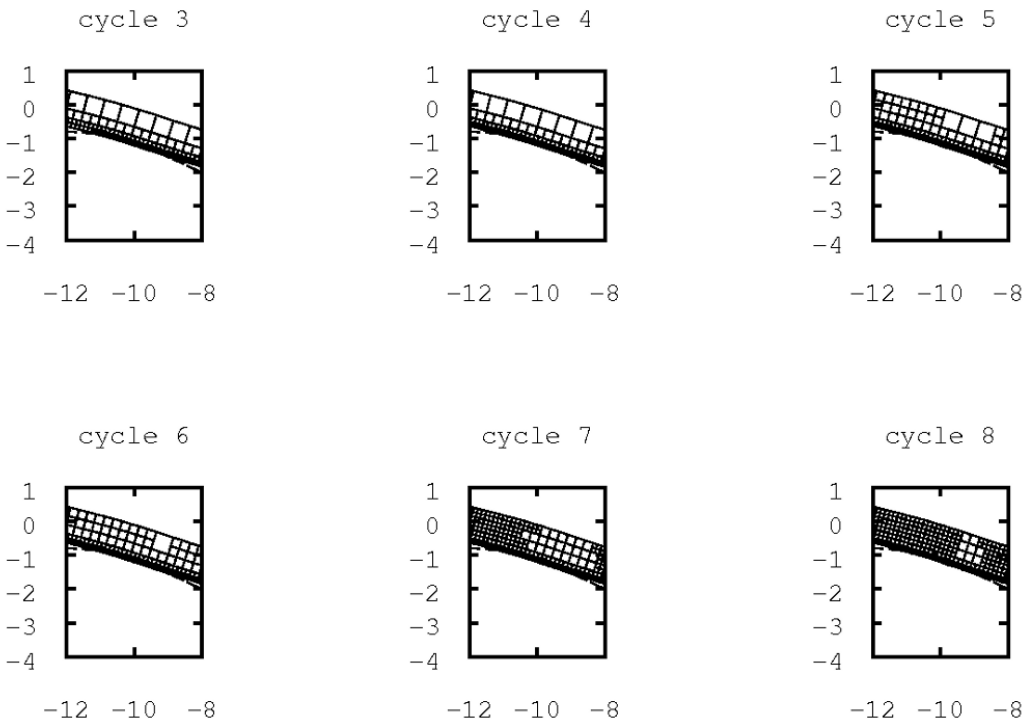

Figure IV.12: Adaptively refined grids, after 3 to 8 refinement cycles.

The result of one run of the algorithm is shown in figure IV.13.

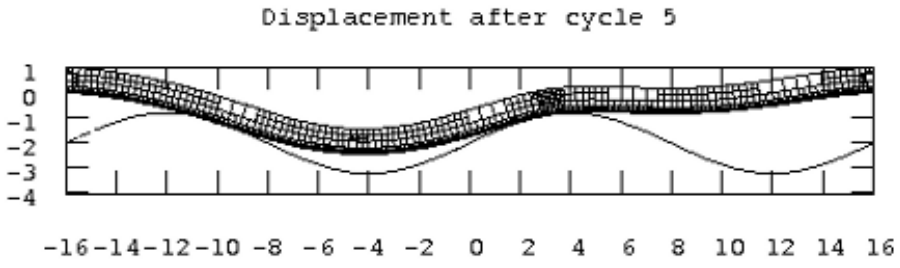

Figure IV.13: The solution of the considered problem.

Table IV.7 shows the results of one run of our algorithm:

cycle	# active cells	# dofs	a-posteriori-estimate	ratio
0	128	390	2.4851	inf
1	245	706	2.0555	0.8271
2	467	1300	1.5981	0.7775
3	890	2406	1.2118	0.7583
4	1694	4516	0.9050	0.7468
5	3221	8546	0.6813	0.7528
6	6122	16046	0.5120	0.7515
7	11633	30458	0.3845	0.7510
8	22103	57094	0.2812	0.7313

Table IV.7: The convergence of one run of our algorithm for the contact problem.

IV.2.1.3 Contact Problem: Box domain with no load and periodic obstacle

We consider the two dimensional contact problem (IV.2) with

$$\begin{aligned} \rho f_i(x) &= 0 \\ \tau &= 0 \end{aligned}$$

The displacement is restricted at the lower boundary

$$\Gamma_C = \{x \in \partial\Omega | x_2 = 0\}$$

on the domain

$$\Omega = [-16; 16] \times [0; 1], \text{ with } \Gamma_0 = \{\pm 16\} \times [0; 1], \ \Gamma_\tau = \partial\Omega \setminus \Gamma_0.$$

The displacement is restricted at the lower boundary

$$\Gamma_C = \{x \in \partial\Omega | x_2 = 0\}$$

by the obstacle

$$s_2(x) \geq 1.2 \cdot \sin \frac{2 \cdot 2\pi \cdot (x_1 + 16)}{32}.$$

The process of grid-refinement is shown in figure IV.14.

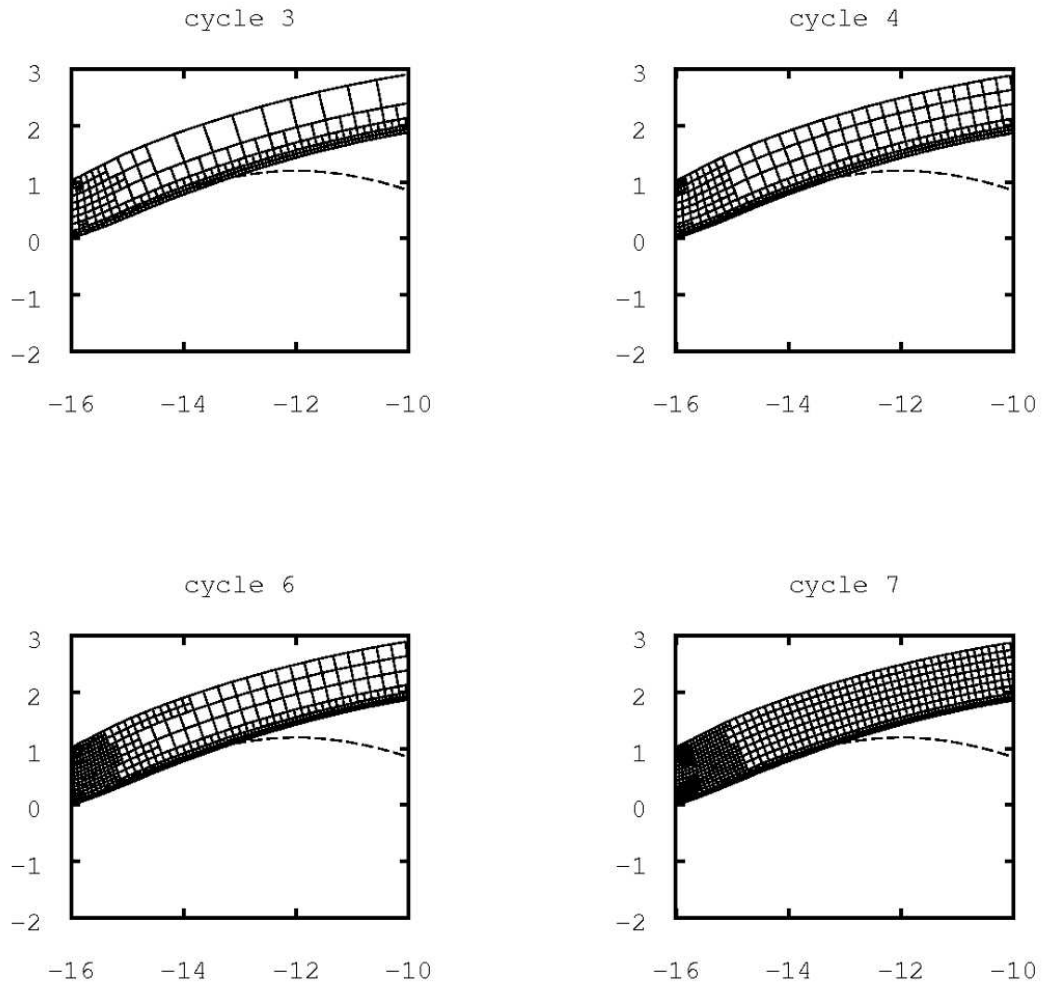

Figure IV.14: Adaptively refined grids, after 3 to 7 refinement cycles.

The result of one run of the algorithm is shown in figure IV.15.

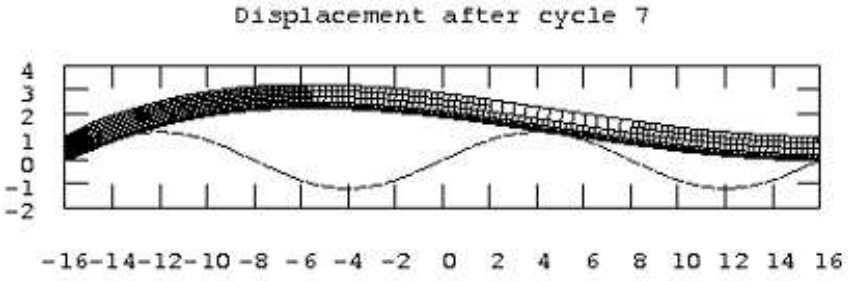

Figure IV.15: The solution of the considered problem.

The following table IV.8 shows the results of one run of our algorithm:

cycle	# active cells	# dofs	a-posteriori-estimate	ratio
0	128	390	2.5942	inf
1	245	704	2.0888	0.8052
2	467	1300	1.5994	0.7657
3	893	2424	1.1878	0.7427
4	1697	4538	0.8801	0.7410
5	3227	8562	0.6520	0.7408
6	6134	16242	0.4926	0.7555
7	11660	30614	0.3649	0.7408
8	22160	58024	0.2674	0.7328
9	42107	109668	0.2005	0.7498

Table IV.8: The convergence of one run of our algorithm for the contact problem.

IV.2.1.4 Contact Problem: Box domain with constant load, one jump-obstacle and a single Dirichlet boundary

We consider the two dimensional contact problem (IV.2) with

$$\begin{aligned} \rho f_i(x) =& 0.0001 \cdot \delta_{i2} \\ \tau =& 0. \end{aligned}$$

For the description of the obstacle we first introduce the Heavyside-like function

$$\theta_s(x) = \frac{x + \sqrt{s^2 + x^2}}{2\sqrt{s^2 + x^2}}, \tag{IV.3}$$

which is continuously differentiable and models a jump in the origin

$$\theta_s(x) \underset{x\to-\infty}{\longrightarrow} 0 \text{ and } \theta_s(x) \underset{x\to\infty}{\longrightarrow} +1,$$

which is the sharper the smaller s^2 is (compare figure IV.16).

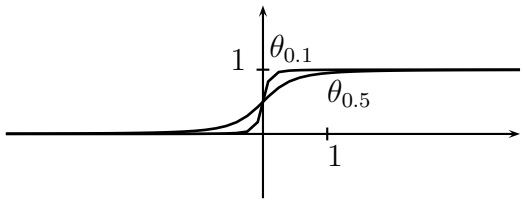

Figure IV.16: Scatch of the Heavyside like function θ_s for different s.

In our application the displacement is restricted at the upper boundary

$$\Gamma_C = \{x \in \partial\Omega | x_2 = 1\}$$

by the obstacle

$$s_2(x) \leq 2 + (10 - 2) \cdot \theta_{0.01}(x_1).$$

The process of grid-refinement is shown in figure IV.17.

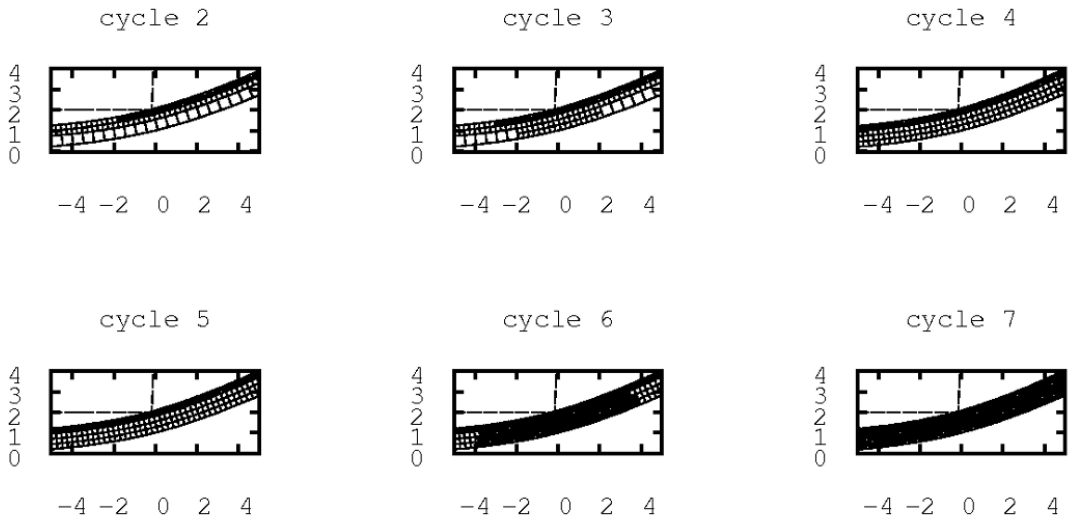

Figure IV.17: Adaptively refined grids, after 2 to 7 refinement cycles.

The result of one run of the algorithm is shown in figure IV.18.

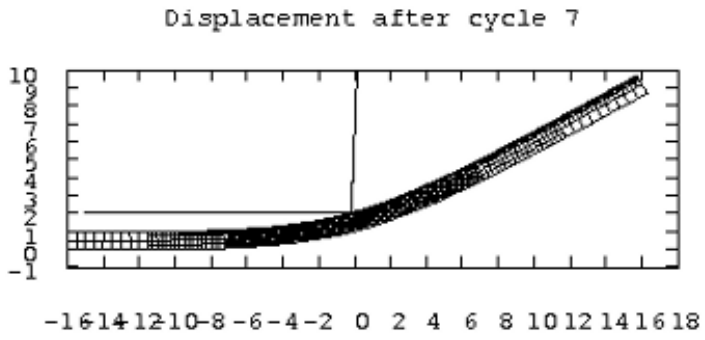

Figure IV.18: The solution of the considered problem.

The following table IV.9 shows the results of one run of our algorithm:

cycle	# active cells	# dofs	a-posteriori-estimate	ratio
0	128	390	2.7874	inf
1	245	704	2.2537	0.8085
2	467	1298	1.4261	0.6328
3	890	2416	1.6342	1.1459
4	1694	4538	1.2802	0.7833
5	3221	8592	0.8778	0.6857
6	6122	16140	0.6255	0.7126
7	11633	30664	0.4463	0.7135
8	22103	57768	0.3182	0.7129
9	41999	109916	0.2265	0.7119

Table IV.9: The convergence of one run of our algorithm for the contact problem.

We see, that in the beginning the error-estimate does not reduce with the factor $1/\sqrt{2}$, as we expect from the theory and the other test calculations. The reason for this is, that the grid has to be fine enough, to approximate the jump-like θ_s–function well enough. After we achieved a sufficiantly accurate grid the error estimate decreases in the way, we expect.

IV.2.1.5 Box domain with zero load, two obstacles and a single Dirichlet boundary

We consider the two dimensional contact problem (IV.2) with

$$\begin{aligned} \rho f_i(x) &= 0 \\ \tau &= 0 \end{aligned}$$

The displacement is restricted at the lower boundary

$$\Gamma_{C1} = \{x \in \partial\Omega | x_2 = 0\}$$

by the obstacle

$$s_2(x) \geq 0 - 10 \cdot \theta_{0.01}(x_1 - (-1))$$

and at the upper boundary

$$\Gamma_{C2} = \{x \in \partial\Omega | x_2 = 1\}$$

by the obstacle

$$s_2(x) \leq 2 + ((-2) - 2) \cdot \theta_{0.01}(x_1 - 2).$$

(See (IV.3) for the definition of $\theta_{0.01}$.)
The use of the θ_s–function smoothes the modeled jump-obstacle (compare figure IV.20), such that it can be handeled by the a-posteriori-estimate of theorem III.15.

The process of grid-refinement is shown in figure IV.19.

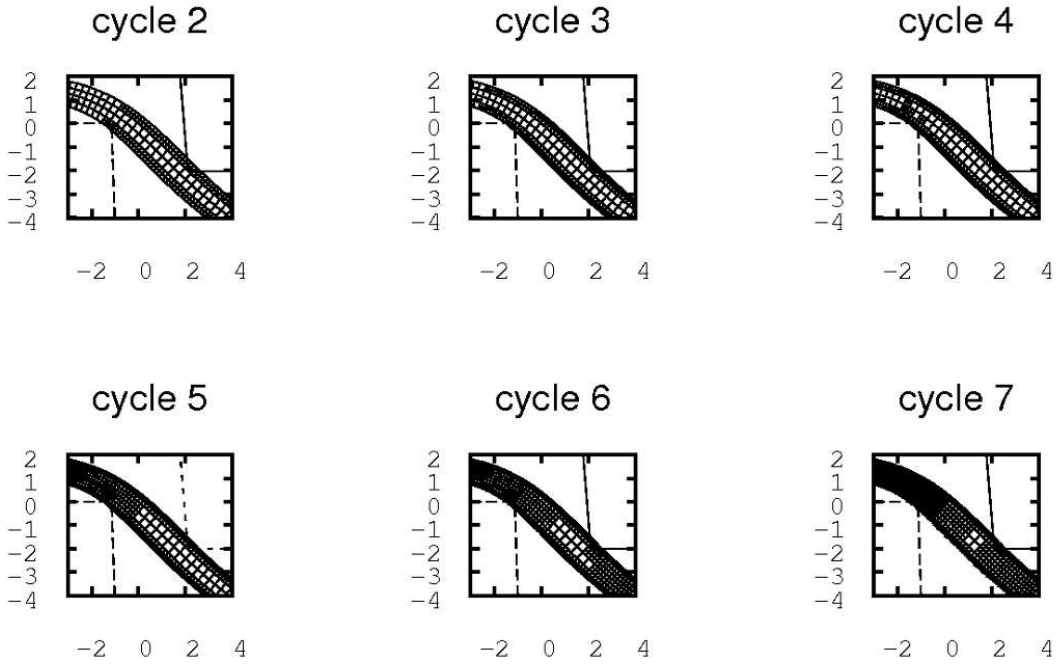

Figure IV.19: Adaptively refined grids, after 2 to 7 refinement cycles.

The result of one run of the algorithm is shown in figure IV.20.

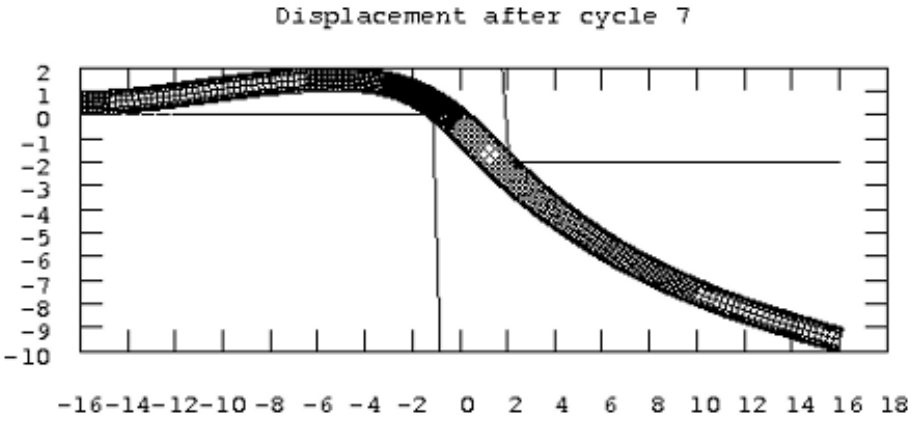

Figure IV.20: The solution of the considered problem.

The following table IV.10 shows the results of one run of our algorithm:

cycle	# active cells	# dofs	a-posteriori-estimate	ratio
0	128	390	4.3910	inf
1	245	668	3.8791	0.8834
2	467	1234	4.3927	1.1324
3	890	2354	2.7027	0.6153
4	1694	4476	2.1071	0.7796
5	3221	8452	1.4823	0.7035
6	6122	16066	1.0761	0.7260
7	11636	30228	0.7761	0.7213
8	22112	57656	0.5618	0.7238
9	42014	108684	0.4053	0.7215

Table IV.10: The convergence of one run of our algorithm for the contact problem.

As in the previous example, we see, that in the beginning the error-estimate does not reduce with the factor $1/\sqrt{2}$, as we expect from the theory and the other test calculations. The reason for this is, that the grid has to be fine enough, to approximate the jump-like tanh-function well enough. After we achieved a sufficiantly accurate grid the error estimate decreases in the way we expect.

IV.2.1.6 Contact Problem: Box domain with constant load and saw obstacle

We consider the two dimensional contact problem (IV.2) with

$$\rho f_i(x) = -.05\delta_{i2}$$
$$\tau = 0$$

The displacement is restricted at the lower boundary

$$\Gamma_C = \{x \in \partial\Omega | x_2 = 0\}.$$

With the help of the Heavyside-like function θ_s (IV.3) we can model a piecewise linear lower obstacle on Γ_C (compare figure IV.22):

$$\begin{aligned} s_2(x) \geq & \theta_s(x_2+4)\theta_s(-2-x_2)\frac{-1-0}{-2-(-4)}(x_2+4) + \theta_s(x_2+2)\theta_s(1-x_2)\frac{0-(-1)}{1-(-2)}(x_2+2) + \\ & + \theta_s(x_2-1)\theta_s(5-x_2)\frac{2-0}{5-1}(x_2-1) + \theta_s(x_2-5)\theta_s(6-x_2)\frac{0-2}{6-5}(x_2-5) \end{aligned}$$

The process of grid-refinement is shown in figure IV.21.

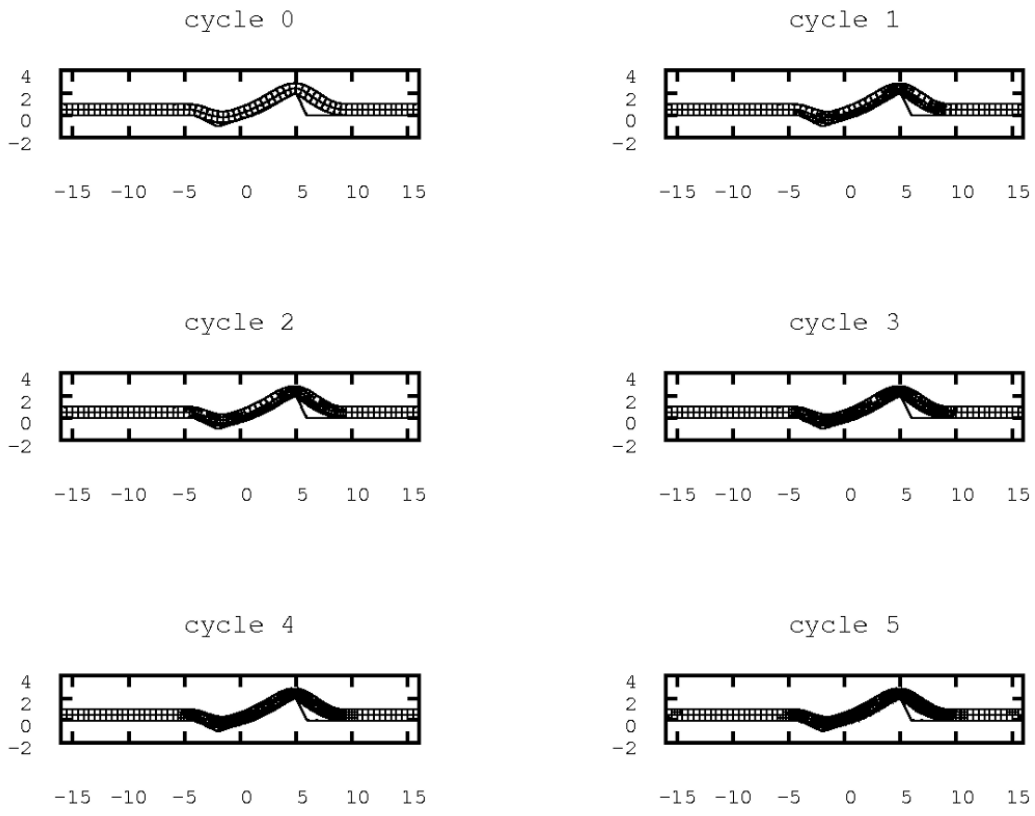

Figure IV.21: Adaptively refined grids, after the first five refinement cycles.

The result of one run of the algorithm is shown in figure IV.22.

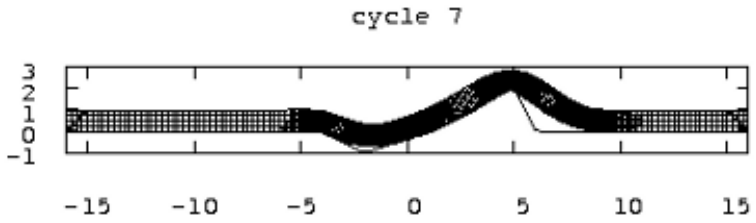

Figure IV.22: The solution of the considered problem.

Table IV.11 shows the results of one run of our algorithm:

cycle	# active cells	# dofs	a-posteriori-estimate	ratio
0	128	390	4.8653	inf
1	245	686	3.3950	0.6978
2	467	1246	2.3945	0.7053
3	890	2290	1.7322	0.7234
4	1691	4274	1.2467	0.7197
5	3215	8048	0.9076	0.7280
6	6113	14970	0.6528	0.7193
7	11615	28294	0.4722	0.7234
8	22070	52770	0.3394	0.7187

Table IV.11: The convergence of one run of our algorithm for the contact problem.

Of all computations, presented in sections IV.2.1.1 – IV.2.1.6, we can conclude, that the error estimate in theorem III.15 is of optimal order, because all convergence tables basically show the decrease of the estimate with the order of $O(n_{dofs}^{1/2})$ as we expect for the energy-norm under adaptive refinement. In the cases of the jump-like obstacles (sections IV.2.1.4 and IV.2.1.5 the grid has to be refined around the jump regions before the error estimate decreases with the expired speed. This can be seen in the corresponding tables IV.9 and IV.10. These critical regions are localised correct by our estimate too. Furthermore the plotted grid series (e. g. figure IV.19 and IV.21) illustrate the geometrical correct refinement near the contact zones especially at the rather rough parts of the obstacles. On the other hand the grids stay coarse in regions of a plain obstacle.

IV.2.2 Signorini Contact

In this section we apply a grid-adaptive algorithm to the contact problem with the more accurate Signorini projection. We consider the same examples as in section IV.2.1.

We consider the same examples as in section IV.2.1, the definition of the problem (IV.2) is given there, but now we have to use the Signorini projection (I.21):
For all $r \in \Pi_S(V_0)$:

$$2\mu \langle \varepsilon_{ij}(s), \varepsilon_{ij}(r-s) \rangle_\Omega + 2\lambda \langle \varepsilon_{ll}(s), \varepsilon_{jj}(r-s) \rangle_\Omega \geq \langle \rho f_i, r - s_i \rangle_\Omega + \langle \tau_{ij} n_j, r - s_i \rangle_{\Gamma_\tau} \quad \text{(IV.4)}$$

with $\mu = \lambda = 1$ and

$$P_s(\xi) = \begin{cases} \xi, & \xi \cdot n(\xi) \leq b(\xi_\perp) \\ \xi - (\xi \cdot n(\xi) - b(\xi_\perp)) n(\xi), & \xi \cdot n(\xi) > b(\xi_\perp) \\ \xi, & \xi \notin \partial\Omega \end{cases}$$

for the definition of

$$\Pi_S(V_0) = \{ r \in V_0 | P_s(x + r(x)) = x + r(x),\ x \in \Gamma_C \}\,.$$

The initial guess s_0 for the displacement (which is need to run the Signorini algorithm) is usually the result of either a prior run of the Signorini- or the simple z-projection-algorithm. With the help of s_0, we calculate the normal-vector n and the gap-width g in each vertex, with these there must hold

$$(s - s_0) \cdot n \leq g \quad \Rightarrow \quad n \cdot (s + x) \leq g + n \cdot (x + s_0)$$

such, that the functions n and b of theorem III.15 are chosen in the following way:

$$\begin{aligned} n :=& n \\ b :=& g + n \cdot (x + s_0). \end{aligned}$$

We start on an initial grid of 64 cells and refine it adaptively using the estimator of theorem III.15 to refine the 30% of the cells with the highest error per cell, which results in about doubling of the cells. Furthermore we coarsen 3% of the cells with the smallest error.
All tables in this section show not only the total a-posteriori error estimate (theorem III.15) but also the different contributions, owed by the contact-problem:

$$\sqrt{\sum_Q h_Q \eta_{C,Q}^2} \quad \text{and} \quad \sqrt{\sum_Q h_Q^{-1} \eta_{-C,Q}^2}.$$

For each of these numbers we give the ratio of the actual value and that of the previous cycle.

IV.2.2.1 Signorini Problem: Box domain with constant load and constant obstacle

We consider the two dimensional contact problem (IV.4) with

$$\begin{aligned} \rho f_i(x) &= -\,0.004 \cdot \delta_{i2} \\ \tau &= 0. \end{aligned}$$

The displacement is restricted at the lower boundary

$$\Gamma_C = \{x \in \partial\Omega | x_2 = 0\}$$

by the obstacle

$$s_2(x) \geq -2.$$

The process of grid-refinement is shown in figure IV.23.

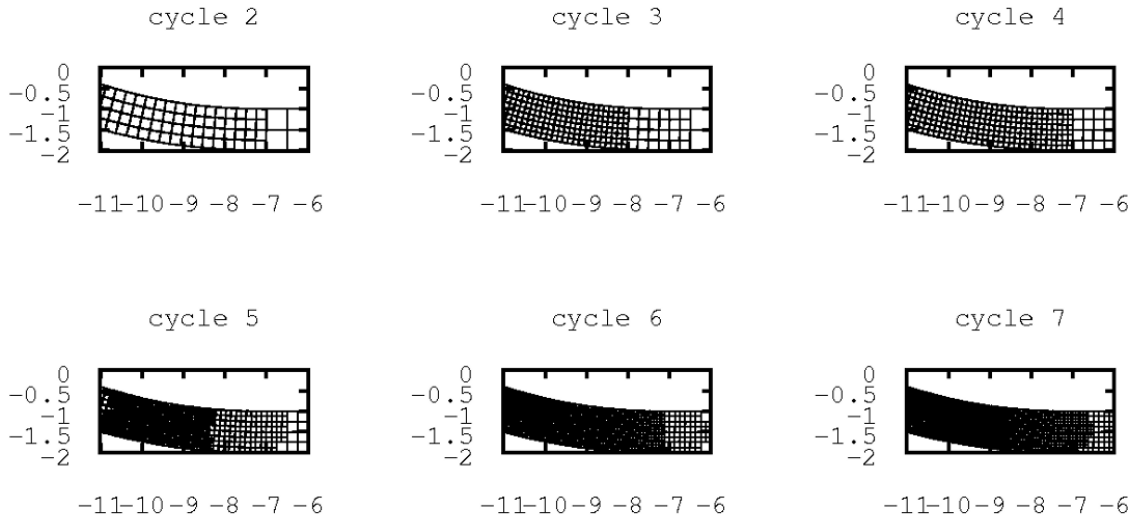

Figure IV.23: Adaptively refined grids, after 2 to 7 refinement cycles.

The result of one run of the algorithm is shown in figure IV.24.

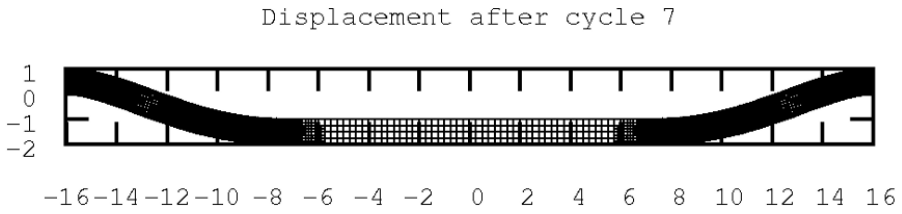

Figure IV.24: The solution of the considered problem.

Table IV.12 shows the results of one run of our algorithm:

	# dofs	a-posteriori estimate	ratio	$\sqrt{\sum_Q h_Q \eta_{C,Q}^2}$	ratio	$\sqrt{\sum_Q h_Q^{-1} \eta_{-C,Q}^2}$	ratio
0	390	0.8374	inf	2.1000e-03	inf	5.0001e-04	inf
1	680	0.5160	0.6161	4.7949e-03	2.2833	1.1744e-03	2.3487
2	1190	0.3468	0.6721	2.0436e-03	0.4262	4.8724e-04	0.4149
3	2142	0.2564	0.7395	1.1185e-03	0.5473	2.7295e-04	0.5602
4	3824	0.1798	0.7011	5.1125e-04	0.4571	1.2185e-04	0.4464
5	7082	0.1362	0.7578	2.8441e-04	0.5563	6.9013e-05	0.5664
6	13076	0.0954	0.7003	1.2434e-04	0.4372	2.9386e-05	0.4258
7	24474	0.0723	0.7573	6.6399e-05	0.5340	1.5486e-05	0.5270
8	45662	0.0508	0.7036	1.6885e-05	0.2543	3.8065e-06	0.2458
9	85968	0.0383	0.7528	1.1212e-06	0.0664	2.1964e-07	0.0577

Table IV.12: The convergence of one run of our algorithm for the contact problem.

We see the decrease of the estimator by the factor $1/\sqrt{2}$, which indicates the expected order

$$\|s - s_h\|_a = O(n_{dofs}^{-1/2}).$$

IV.2.2.2 Signorini Problem: Box domain with constant load and periodic obstacle

We consider the two dimensional contact problem (IV.4) with

$$\begin{aligned} \rho f_i(x) &= -\,0.002 \cdot \delta_{i2} \\ \tau &= 0 \end{aligned}$$

The displacement is restricted at the lower boundary

$$\Gamma_C = \{x \in \partial\Omega | x_2 = 0\}$$

by the obstacle

$$s_2(x) \geq -2 + 1.2 \cdot \sin \frac{2 \cdot 2\pi \cdot (x_1 + 16)}{32}.$$

The process of grid-refinement is shown in figure IV.25.

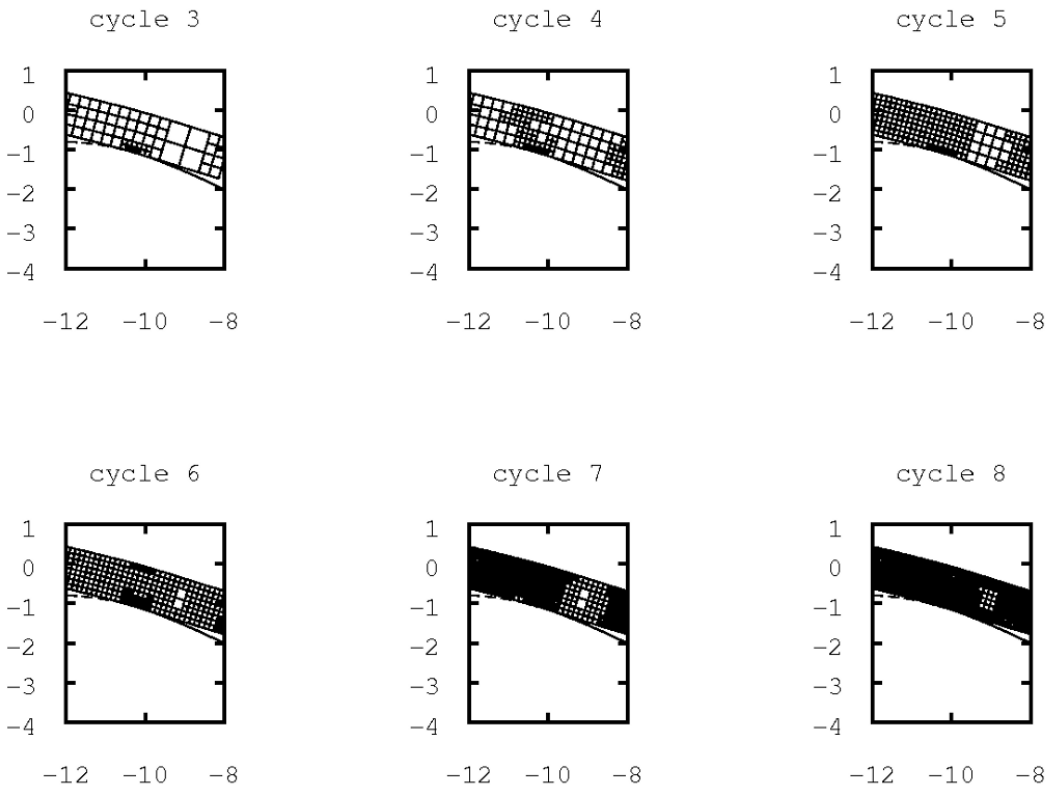

Figure IV.25: Adaptively refined grids, after 3 to 8 refinement cycles.

The result of one run of the algorithm is shown in figure IV.26.

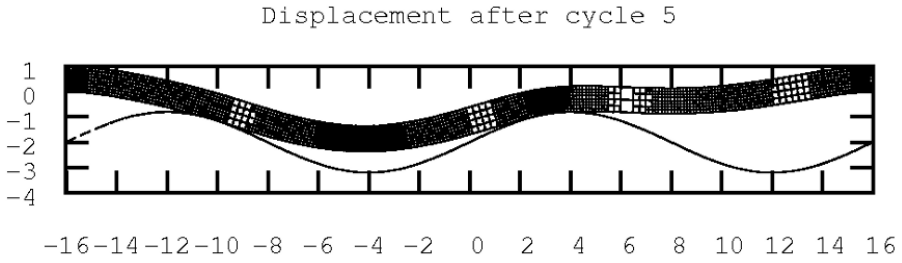

Figure IV.26: The solution of the considered problem.

Table IV.13 shows the results of one run of our algorithm:

	# dofs	a-posteriori estimate	ratio	$\sqrt{\sum_Q h_Q \eta_{C,Q}^2}$	ratio	$\sqrt{\sum_Q h_Q^{-1} \eta_{-C,Q}^2}$	ratio
0	390	0.6869	inf	0.1901	inf	4.0000e-03	inf
1	682	0.4867	0.7086	0.1279	0.6727	2.1536e-03	0.5384
2	1258	0.3691	0.7583	0.0868	0.6789	6.3596e-04	0.2953
3	2196	0.2759	0.7476	0.0762	0.8775	3.4062e-04	0.5356
4	4058	0.2014	0.7299	0.0522	0.6850	1.4796e-04	0.4344
5	7416	0.1521	0.7551	0.0391	0.7489	6.1968e-05	0.4188
6	13844	0.1072	0.7049	0.0279	0.7130	3.4355e-05	0.5544
7	25766	0.0818	0.7627	0.0204	0.7333	1.8998e-05	0.5530
8	48294	0.0567	0.6941	0.0145	0.7081	1.9023e-05	1.0013
9	90782	0.0432	0.7606	0.0099	0.6833	2.1443e-05	1.1272

Table IV.13: The convergence of one run of our algorithm for the contact problem.

We see the decrease of the estimator by the factor $1/\sqrt{2}$, which indicates the expected order

$$\|s - s_h\|_a = O(n_{dofs}^{-1/2}).$$

IV.2.2.3 Signorini Problem: Box domain with no load and periodic obstacle

We consider the two dimensional contact problem (IV.4) with

$$\begin{aligned} \rho f_i(x) &= 0 \\ \tau &= 0 \end{aligned}$$

The displacement is restricted at the lower boundary

$$\Gamma_C = \{x \in \partial\Omega | x_2 = 0\}$$

by the obstacle

$$s_2(x) \geq 1.2 \cdot \sin \frac{2 \cdot 2\pi \cdot (x_1 + 16)}{32}.$$

The process of grid-refinement is shown in figure IV.27.

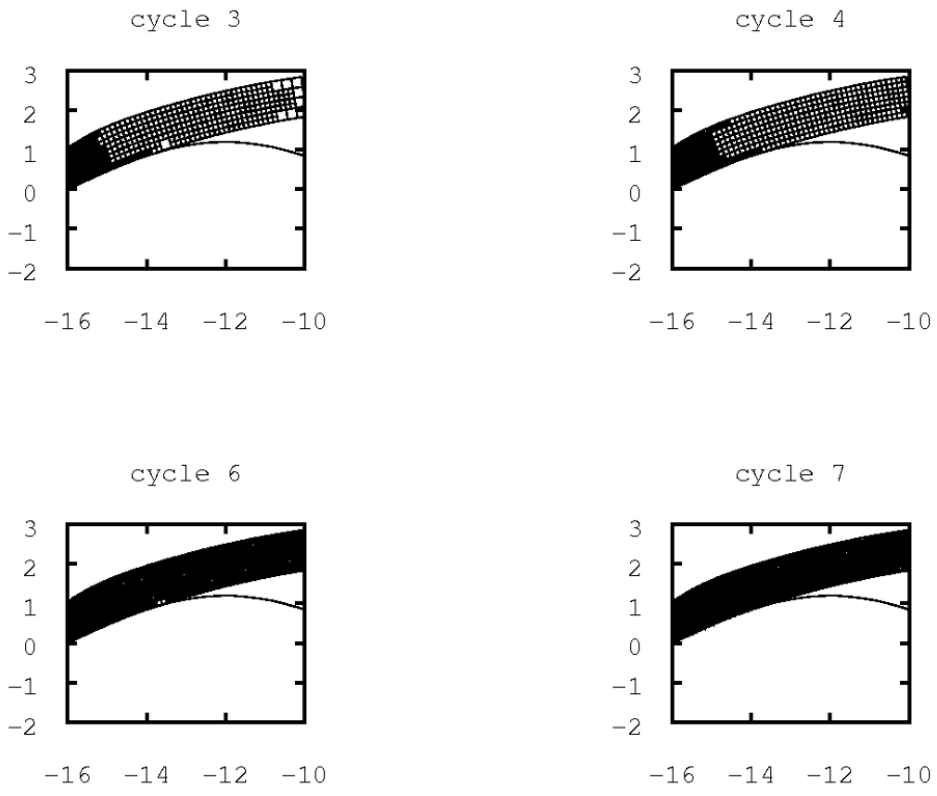

Figure IV.27: Adaptively refined grids, after 3,4,6 and 7 refinement cycles. There is drawn the left part of the domain.

The result of one run of the algorithm is shown in figure IV.28.

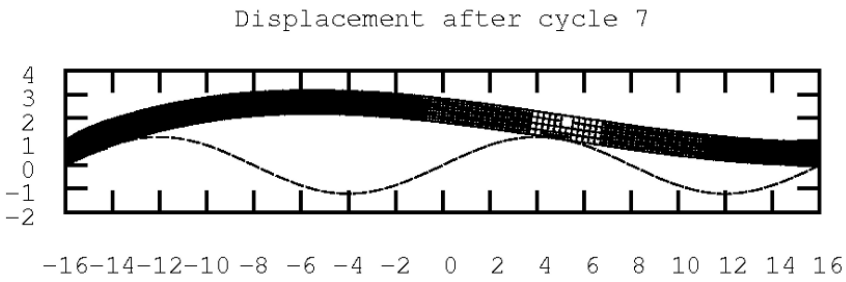

Figure IV.28: The solution of the considered problem.

Table IV.14 shows the results of one run of our algorithm:

	# dofs	a-posteriori estimate	ratio	$\sqrt{\sum_Q h_Q \eta_{C,Q}^2}$	ratio	$\sqrt{\sum_Q h_Q^{-1} \eta_{-C,Q}^2}$	ratio
0	390	1.0825	inf	0.4143	inf	3.3000e-03	inf
1	668	0.7145	0.6600	0.3250	0.7843	3.4825e-03	1.0553
2	1198	0.4695	0.6571	0.2490	0.7664	1.5730e-03	0.4517
3	2148	0.3144	0.6697	0.1786	0.7169	8.6328e-04	0.5488
4	3968	0.2172	0.6908	0.1255	0.7027	2.5337e-04	0.2935
5	7394	0.1538	0.7082	0.0904	0.7203	1.0016e-04	0.3953
6	13788	0.1098	0.7137	0.0634	0.7021	3.4775e-05	0.3472
7	25852	0.0769	0.7005	0.0439	0.6924	2.2506e-05	0.6472
8	48632	0.0537	0.6978	0.0268	0.6106	2.1633e-05	0.9612
9	91158	0.0369	0.6874	0.0172	0.6413	1.9649e-05	0.9083

Table IV.14: The convergence of one run of our algorithm for the contact problem.

We see the decrease of the estimator by the factor $1/\sqrt{2}$, which indicates the expected order

$$\|s - s_h\|_a = O(n_{dofs}^{-1/2}).$$

IV.2.2.4 Box domain with constant load, one jump-obstacle and a single Dirichlet boundary

We consider the two dimensional contact problem (IV.4) with

$$\begin{aligned} \rho f_i(x) =& 0.0001 \cdot \delta_{i2} \\ \tau =& 0 \end{aligned}$$

The displacement is restricted at the upper boundary

$$\Gamma_C = \{x \in \partial\Omega | x_2 = 1\}$$

by the obstacle

$$s_2(x) \leq 2 + (10 - 2) \cdot \theta_{0.01}(x_1)$$

with the jump-function (IV.3). The process of grid-refinement is shown in figure IV.29.

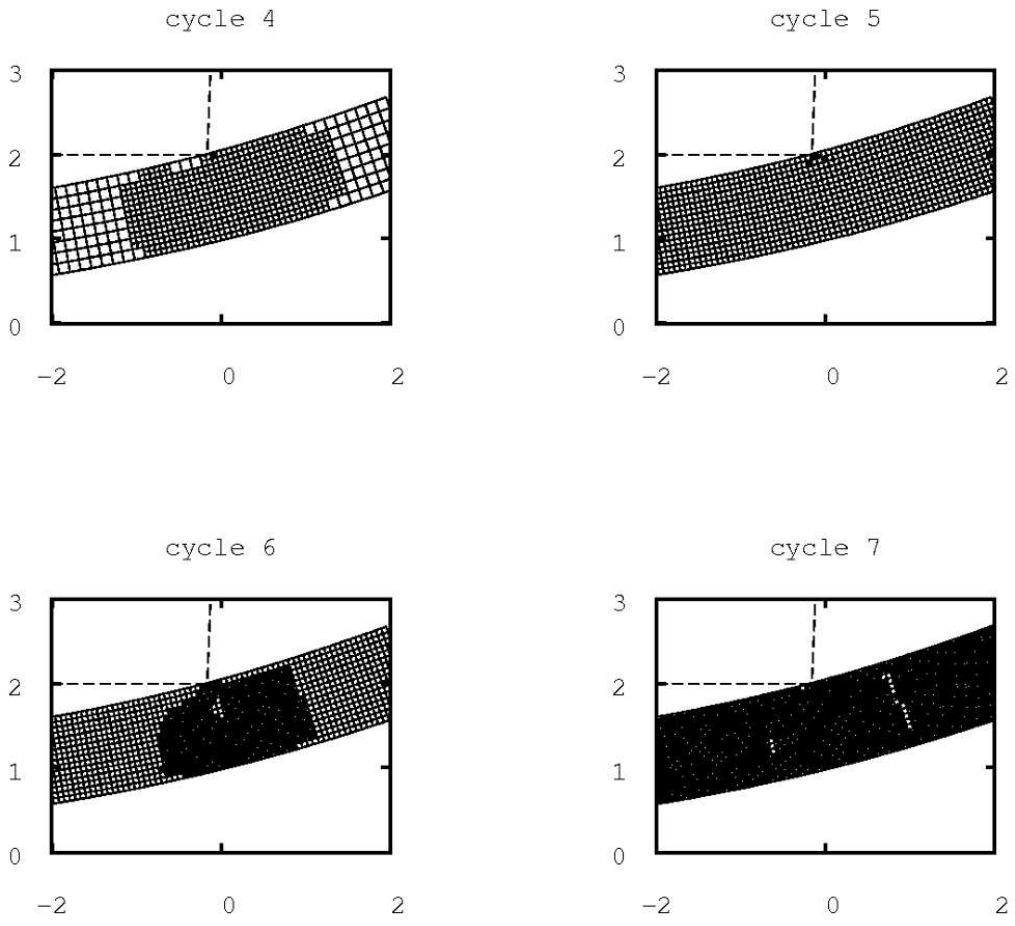

Figure IV.29: Adaptively refined grids, after 4 to 7 refinement cycles.

The result of one run of the algorithm is shown in figure IV.30.

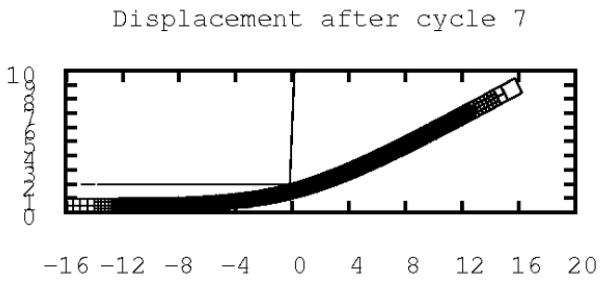

Figure IV.30: The solution of the considered problem.

Table IV.15 shows the results of one run of our algorithm:

	# dofs	a-posteriori estimate	ratio	$\sqrt{\sum h_Q \eta_{C,Q}^2}$	ratio	$\sqrt{\sum h_Q^{-1} \eta_{-C,Q}^2}$	ratio
0	390	0.2455	inf	0.0000	nan	0.0000	nan
1	668	0.1620	0.6599	0.0000	nan	0.0000	nan
2	1164	0.1228	0.7581	0.0000	nan	0.0000	nan
3	2070	0.1672	1.3614	0.0921	inf	0.1097	inf
4	3750	0.1474	0.8819	0.1050	1.1407	0.0792	0.7218
5	6904	0.1148	0.7788	0.0707	0.6731	0.0775	0.9780
6	12846	0.0476	0.4148	0.0258	0.3656	0.0190	0.2447
7	23862	0.0380	0.7985	0.0230	0.8901	0.0167	0.8807
8	44854	0.0250	0.6569	0.0137	0.5959	0.0095	0.5709
9	83428	0.0193	0.7712	0.0110	0.8046	0.0079	0.8263

Table IV.15: The convergence of one run of our algorithm for the contact problem.

As in the previous calculations with jump-like obstacles it takes some cycles, to approximate the obstacle accurate enough, such that the estimator decreases by the factor $2^{-1/2}$, which indicates the expected order

$$\|s - s_h\|_a = O(n_{dofs}^{-1/2}).$$

IV.2.2.5 Box domain with two jump-obstacles and a single Dirichlet boundary

We consider the two dimensional contact problem (IV.4) with

$$\begin{aligned} \rho f_i(x) &= 0 \\ \tau &= 0 \end{aligned}$$

The displacement is restricted at the lower boundary

$$\Gamma_{C1} = \{x \in \partial\Omega | x_2 = 0\}$$

by the obstacle

$$s_2(x) \geq -10 \cdot \theta_{0.01}(x_1 + 1)$$

and at the upper boundary

$$\Gamma_{C2} = \{x \in \partial\Omega | x_2 = 1\}$$

by the obstacle

$$s_2(x) \leq 2 - 4 \cdot \theta_{0.01}(x_1 - 2).$$

The use of the θ_s-function smoothes the modeled jump-obstacle (compare figure IV.32), such that it can be handeled by the a-posteriori estimate of theorem III.15.
A series of grid refinement is shown in figure IV.31.

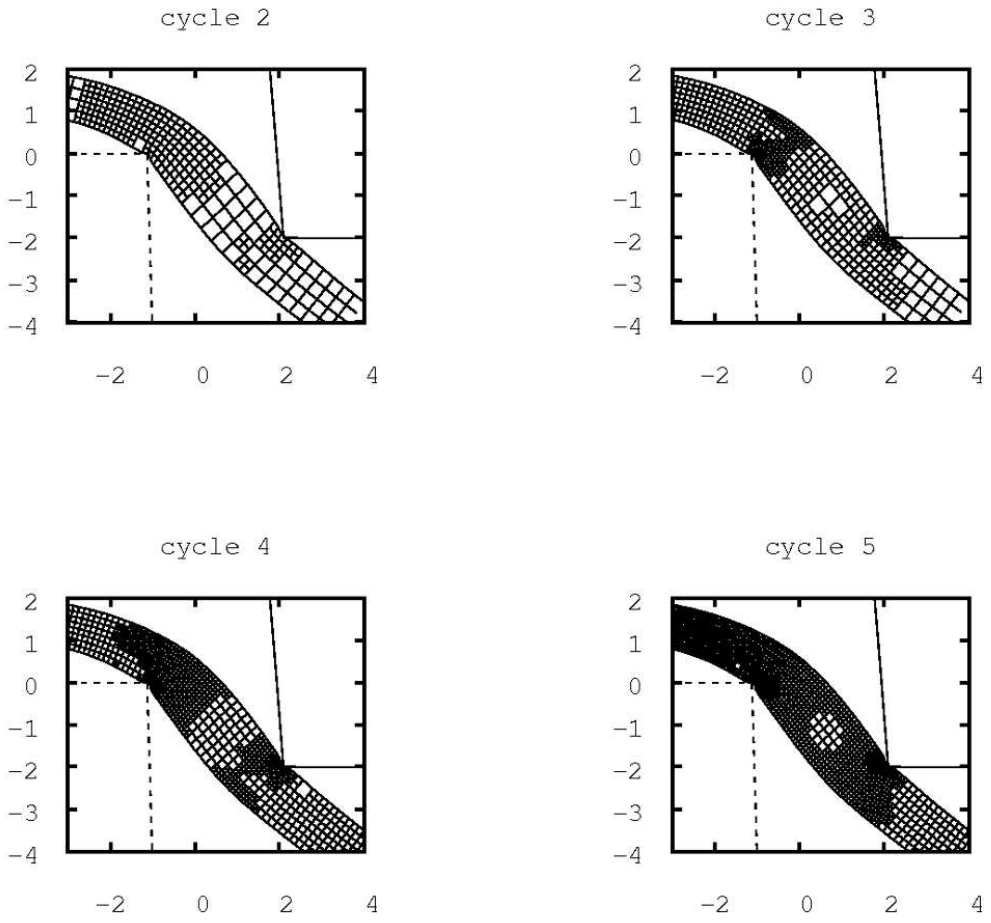

Figure IV.31: Adaptively refined grids, after 2 to 5 refinement cycles.

Figure IV.32 shows the solution of the calculation.

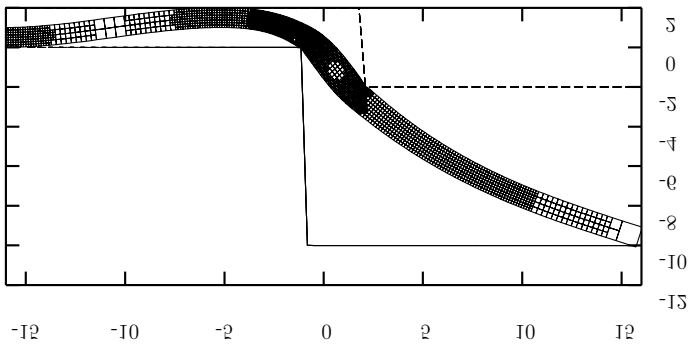

Figure IV.32: The solution of the considered problem.

Table IV.16 shows the results of one run of our algorithm:

	# dofs	a-posteriori estimate	ratio	$\sqrt{\sum h_Q \eta^2_{C,Q}}$	ratio	$\sqrt{\sum h_Q^{-1} \eta^2_{-C,Q}}$	ratio
0	390	1.5696	inf	0.4026	inf	1.5488e-02	inf
1	672	0.9679	0.6166	0.4515	1.1216	2.2390e-02	1.4456
2	1180	0.9225	0.9530	0.4077	0.9029	1.1909e-02	0.5319
3	2130	0.6700	0.7262	0.3220	0.7898	5.5518e-03	0.4661
4	3888	0.4459	0.6655	0.2165	0.6724	2.3127e-03	0.4165
5	7140	0.2934	0.6580	0.1418	0.6547	7.6336e-04	0.3300
6	15010	0.2024	0.6899	0.0976	0.6889	2.5630e-04	0.3357
7	27826	3.6292	17.926	3.6257	37.114	1.0362e-01	404.29
8	51840	0.1014	0.0279	0.0481	0.0132	3.2908e-05	0.0003
9	97214	0.0729	0.7194	0.0342	0.7113	1.4350e-05	0.4360

Table IV.16: The convergence of one run of our algorithm for the contact problem.

A rather interesting question is, why the a-posteriori error increases in cycle 6 (compare table IV.16) just to proceed decreasing with the expected rate in the following cycles.

IV.2.2.6 Signorini Problem: Box domain with constant load and saw obstacle

We consider the two dimensional contact problem (IV.4) with

$$\rho f_i(x) = -\,0.05 \cdot \delta_{i2}$$
$$\tau = 0$$

The displacement is restricted at the lower boundary

$$\Gamma_C = \{x \in \partial\Omega | x_2 = 0\}$$

by the obstacle

$$s_2(x) \geq \theta_s(x_2+4)\theta_s(-2-x_2)\frac{-1-0}{-2-(-4)}(x_2+4) + \theta_s(x_2+2)\theta_s(1-x_2)\frac{0-(-1)}{1-(-2)}(x_2+2) +$$
$$+\,\theta_s(x_2-1)\theta_s(5-x_2)\frac{2-0}{5-1}(x_2-1) + \theta_s(x_2-5)\theta_s(6-x_2)\frac{0-2}{6-5}(x_2-5)$$

which is defined with the help of the Heavyside like function (IV.3). The process of grid-refinement is shown in figure IV.33.

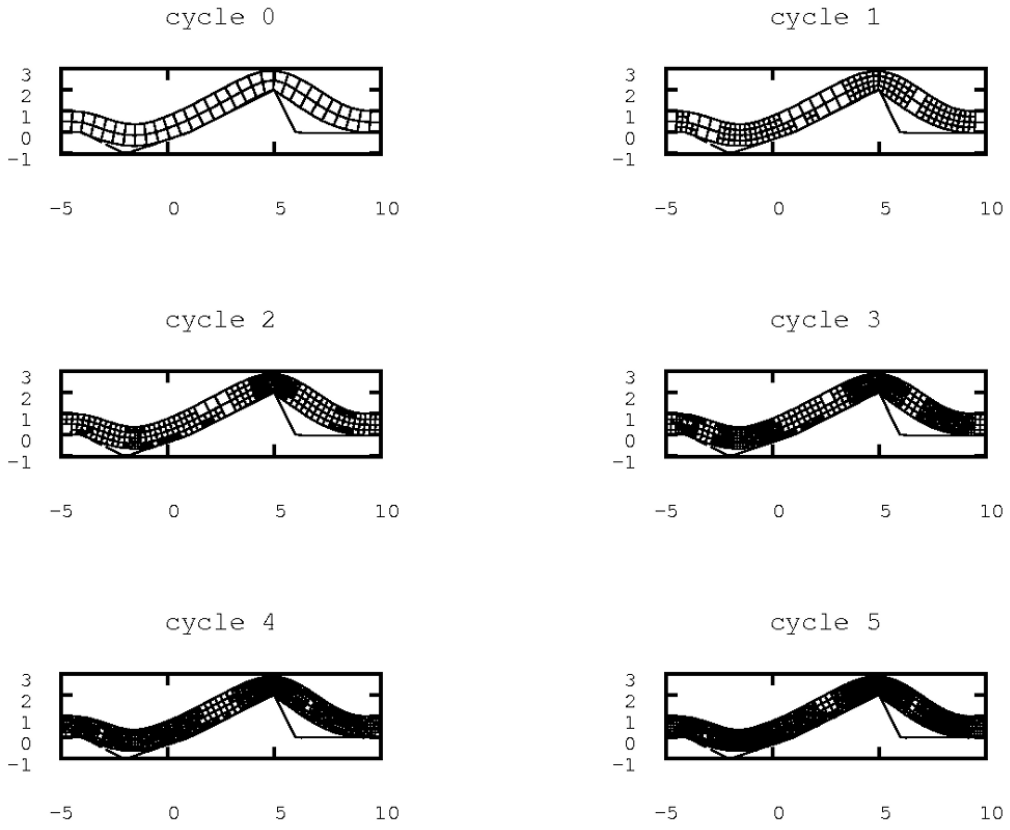

Figure IV.33: Adaptively refined grids, after 0 to 5 refinement cycles.

The result of one run of the algorithm is shown in figure IV.34.

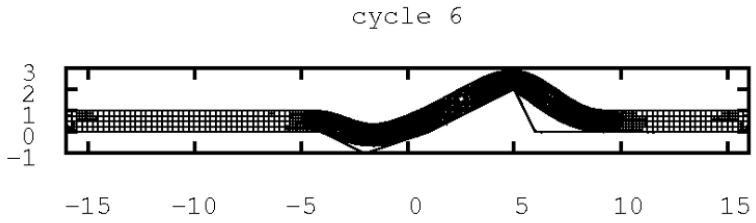

Figure IV.34: The solution of the considered problem.

Table IV.17 shows the results of one run of our algorithm:

	# dofs	a-posteriori estimate	ratio	$\sqrt{\sum_Q h_Q \eta_{C,Q}^2}$	ratio	$\sqrt{\sum_Q h_Q^{-1} \eta_{-C,Q}^2}$	ratio
0	390	0.6869	inf	0.1901	inf	4.0000e-03	inf
1	682	0.4867	0.7086	0.1279	0.6727	2.1536e-03	0.5384
2	1258	0.3691	0.7583	0.0868	0.6789	6.3596e-04	0.2953
3	2196	0.2759	0.7476	0.0762	0.8775	3.4062e-04	0.5356
4	4058	0.2014	0.7299	0.0522	0.6850	1.4796e-04	0.4344
5	7416	0.1521	0.7551	0.0391	0.7489	6.1968e-05	0.4188
6	13844	0.1072	0.7049	0.0279	0.7130	3.4355e-05	0.5544
7	25766	0.0818	0.7627	0.0204	0.7333	1.8998e-05	0.5530
8	48294	0.0567	0.6941	0.0145	0.7081	1.9023e-05	1.0013
9	90782	0.0432	0.7606	0.0099	0.6833	2.1443e-05	1.1272

Table IV.17: The convergence of one run of our algorithm for the contact problem.

We see the decrease of the estimator by the factor $1/\sqrt{2}$, which indicates the expected order

$$\|s - s_h\|_a = O(n_{dofs}^{-1/2}).$$

As before for the one direction contact also the calculations for Signorini contact presented in sections IV.2.2.1 – IV.2.2.6 supply sufficiant results. The zones of high stress and rough obstacles are detected correctly (compare e. g. figures IV.31 and IV.33).
Furthermore we see the advantage of the Signorini solver regarding rough obstacles and rather high deformations. Especially a comparison of the result of the z-solver (figure IV.19) and the one of the Signorini solver (figure IV.31) for the two-obstacle-problem illustrates, that the Signorini solver does not hurt the contact condition, while the z-projection results in an obstacle penetration. This advantage is balanced out against the higher speed of the z-solver in section IV.2.3.

IV.2.3 Model adaptive Contact

For each of the six examples considered in the previous sections IV.2.1 and IV.2.2 we now apply the model adaptive schemes based on algorithm III.1 to a constant grid.

For each example we apply both algorithms III.2 and III.3 to achieve a sufficiant distribution of the different contact models with the help of the model error estimate (III.16). We recall the numerical problem again:
Find $s \in \Pi_{zs}(V_0)$, such that for all $r \in \Pi_{zs}(V_0)$:

$$2\mu \left\langle \varepsilon_{ij}(s), \varepsilon_{ij}(r-s) \right\rangle_\Omega + 2\lambda \left\langle \varepsilon_{ll}(s), \varepsilon_{jj}(r-s) \right\rangle_\Omega \geq \left\langle \rho f_i, r - s_i \right\rangle_\Omega + \left\langle \tau_{ij} n_j, r - s_i \right\rangle_{\Gamma_\tau} . \quad \text{(IV.5)}$$

with $\mu = \lambda = 1$.
The projected space

$$\Pi_{zs}(V_0) = \{ r \in V_0 | P_\Xi(x + r(x)) = x + r(x),\ x \in \Gamma_\Xi, \ \text{ for } \Xi = n, S \} ,$$

now is declared more complex than in the previous one-model-calculations. We use the partition of the contact boundary

$$\Gamma_C = \overline{\Gamma_n \cup \Gamma_S},\ \Gamma_n \cap \Gamma_S = \emptyset$$

and both types of projection

$$P_n(\xi) = \begin{cases} \xi, & \xi \cdot n \leq b(\xi_\perp) \\ \xi - (\xi \cdot n - b(\xi_\perp))n, & \xi \cdot n > b(\xi_\perp), \end{cases}$$

$$P_s(\xi) = \begin{cases} \xi, & \xi \cdot n(\xi) \leq b(\xi_\perp) \\ \xi - (\xi \cdot n(\xi) - b(\xi_\perp))n(\xi), & \xi \cdot n(\xi) > b(\xi_\perp) \\ \xi, & \xi \notin \partial\Omega. \end{cases}$$

All other declarations stay the same as in sections IV.2.1 and IV.2.2:

$$\begin{aligned} \Omega =& [-16; 16] \times [0; 1] \\ \lambda = \mu =& 1. \end{aligned}$$

In this section the grid we use, will not be refined adaptively but we use a fixed grid of 2×64 coarse cells, that will be refined three times at the contact surfaces. For contact at one of the upper or the lower surface of Ω this results in 3980 degrees of freedom. For contact on both the upper and the lower surface we have 7442 degrees of freedom.
For both algorithms, the fixed-fraction algorithm III.2 and the one with the sorted error strategy III.3 we set

$$p_c = 1\% \quad \text{and} \quad p_r = 2\%.$$

IV.2.3.1 Box domain with constant load and constant obstacle

We consider the two dimensional contact problem (IV.5) with

$$\begin{aligned} \rho f_i(x) =& -0.004 \cdot \delta_{i2} \\ \tau =& 0. \end{aligned}$$

The displacement is restricted at the lower boundary

$$\Gamma_C = \{x \in \partial\Omega | x_2 = 0\}$$

by the obstacle

$$s_2(x) \geq -2.$$

The process of model-refinement is shown in figure IV.35.

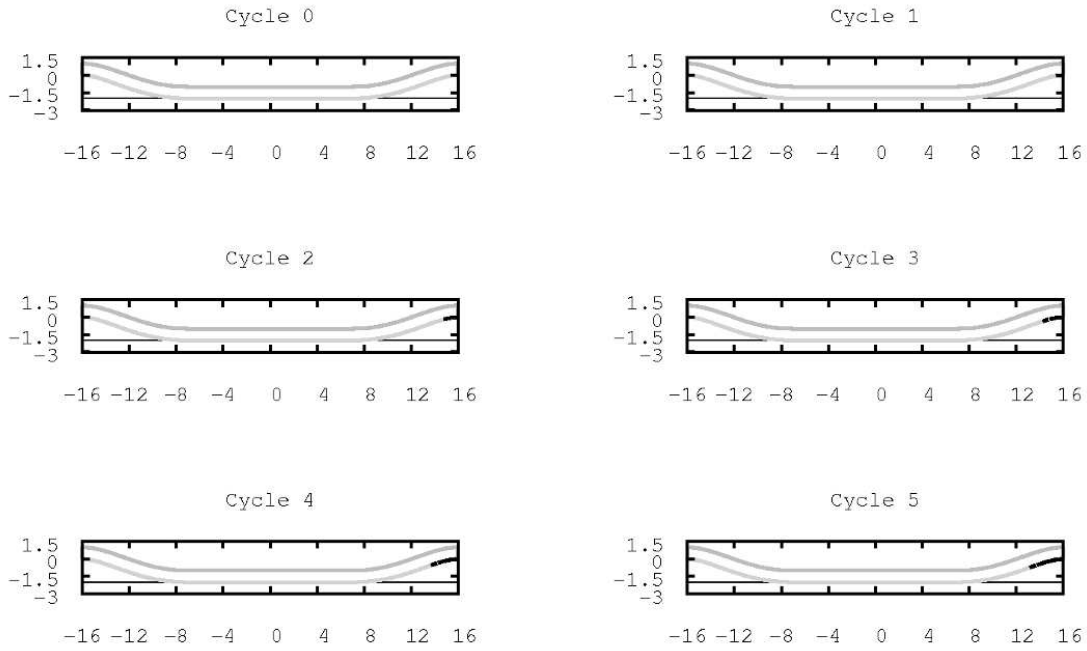

Figure IV.35: Adaptively refined model. The zone of Signorini contact is colored black. the zone of z-direction contact light gray.

Table IV.18 shows the results of one run of our algorithm:

cycle	# coarse faces	# accurate faces	# active cells	# dofs	model error estimate
0	512	0	1472	3980	0.0000e+00
1	502	10	1472	3980	0.0000e+00
2	492	20	1472	3980	0.0000e+00
3	483	29	1472	3980	0.0000e+00
4	474	38	1472	3980	0.0000e+00
5	465	47	1472	3980	0.0000e+00
6	456	56	1472	3980	0.0000e+00
7	447	65	1472	3980	0.0000e+00
8	439	73	1472	3980	0.0000e+00
9	431	81	1472	3980	0.0000e+00

Table IV.18: The convergence of one run of algorithm III.2 for the contact problem.

We see, that the modelling error vanishes right from the beginning. This is no surprise, because for a constant obstacle the conditions (S) and (Z) (III.11) are the same and thus the estimate (III.16) is zero.
Consequently the only criterion for the enforced model refinment of our strategy is the (ultimatly geometrical) order of the contact faces.
The results of the application of algorithm III.3 we see in table IV.19.

	# coarse faces	# accurate faces	# active cells	# dofs	model error estimate
0	512	0	1472	3980	0.0000e+00
1	512	0	1472	3980	0.0000e+00
2	512	0	1472	3980	0.0000e+00
3	512	0	1472	3980	0.0000e+00
4	512	0	1472	3980	0.0000e+00
5	512	0	1472	3980	0.0000e+00
6	512	0	1472	3980	0.0000e+00
7	512	0	1472	3980	0.0000e+00
8	512	0	1472	3980	0.0000e+00
9	512	0	1472	3980	0.0000e+00

Table IV.19: The convergence of one run of algorithm III.3 for the contact problem.

Because the modelling error is zero from the beginning, the model is not refined anywhere.

IV.2.3.2 Box domain with constant load and periodic obstacle

We consider the two dimensional contact problem (IV.5) with

$$\begin{aligned} \rho f_i(x) &= -\,0.002 \cdot \delta_{i2} \\ \tau &= 0 \end{aligned}$$

The displacement is restricted at the lower boundary

$$\Gamma_C = \{x \in \partial\Omega | x_2 = 0\}$$

by the obstacle

$$s_2(x) \geq -2 + 1.2 \cdot \sin \frac{2 \cdot \cdot 2\pi \cdot (x_1 + 16)}{32}.$$

The process of model-refinement is shown in figure IV.36.

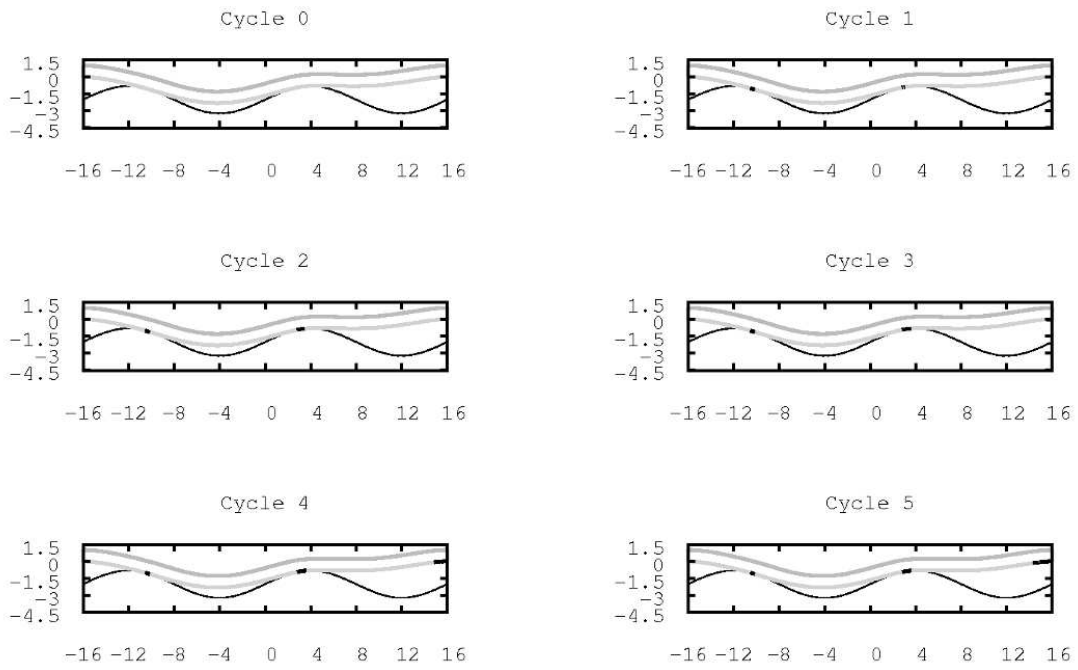

Figure IV.36: Adaptively refined model. The zone of Signorini contact is colored black, the zone of z-direction contact light gray.

Table IV.20 shows the results of one run of our algorithm:

cycle	# coarse faces	# accurate faces	# active cells	# dofs	model error estimate
0	512	0	1472	3980	2.8320e-02
1	502	10	1472	3980	6.5693e-03
2	492	20	1472	3980	8.7384e-04
3	483	29	1472	3980	0.0000e+00
4	474	38	1472	3980	0.0000e+00
5	465	47	1472	3980	0.0000e+00
6	456	56	1472	3980	0.0000e+00
7	447	65	1472	3980	0.0000e+00
8	439	73	1472	3980	0.0000e+00
9	431	81	1472	3980	0.0000e+00

Table IV.20: The convergence of one run of algorithm III.2 for the contact problem.

The results of the application of algorithm III.3 we see in table IV.21.

cycle	# coarse faces	# accurate faces	# active cells	# dofs	model error estimate
0	512	0	1472	3980	2.8320e-02
1	500	12	1472	3980	4.8450e-03
2	492	20	1472	3980	1.0290e-11
3	492	20	1472	3980	0.0000e+00
4	492	20	1472	3980	0.0000e+00
5	492	20	1472	3980	0.0000e+00
6	492	20	1472	3980	0.0000e+00
7	492	20	1472	3980	0.0000e+00
8	492	20	1472	3980	0.0000e+00
9	492	20	1472	3980	0.0000e+00

Table IV.21: The convergence of one run of algorithm III.3 for the contact problem.

The different stages of model refinement is shown in figure IV.37.

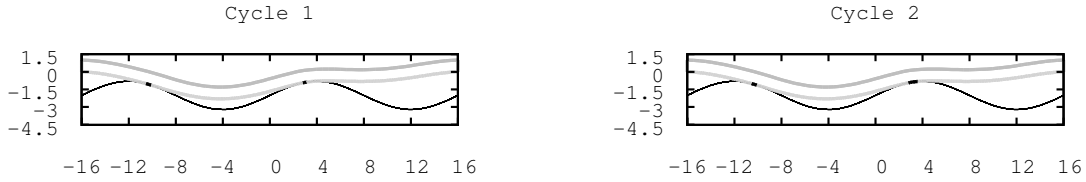

Figure IV.37: By algorithm III.3 adaptively refined model. The zone of Signorini contact is colored black, the zone of z-direction contact light gray.

IV.2.3.3 Box domain with no load and periodic obstacle

We consider the two dimensional contact problem (IV.5) with

$$\begin{aligned} \rho f_i(x) &= 0 \\ \tau &= 0 \end{aligned}$$

The displacement is restricted at the lower boundary

$$\Gamma_C = \{x \in \partial\Omega | x_2 = 0\}$$

by the obstacle

$$s_2(x) \geq 1.2 \cdot \sin \frac{2 \cdot 2\pi \cdot (x_1 + 16)}{32}.$$

The process of model-refinement is shown in figure IV.38.

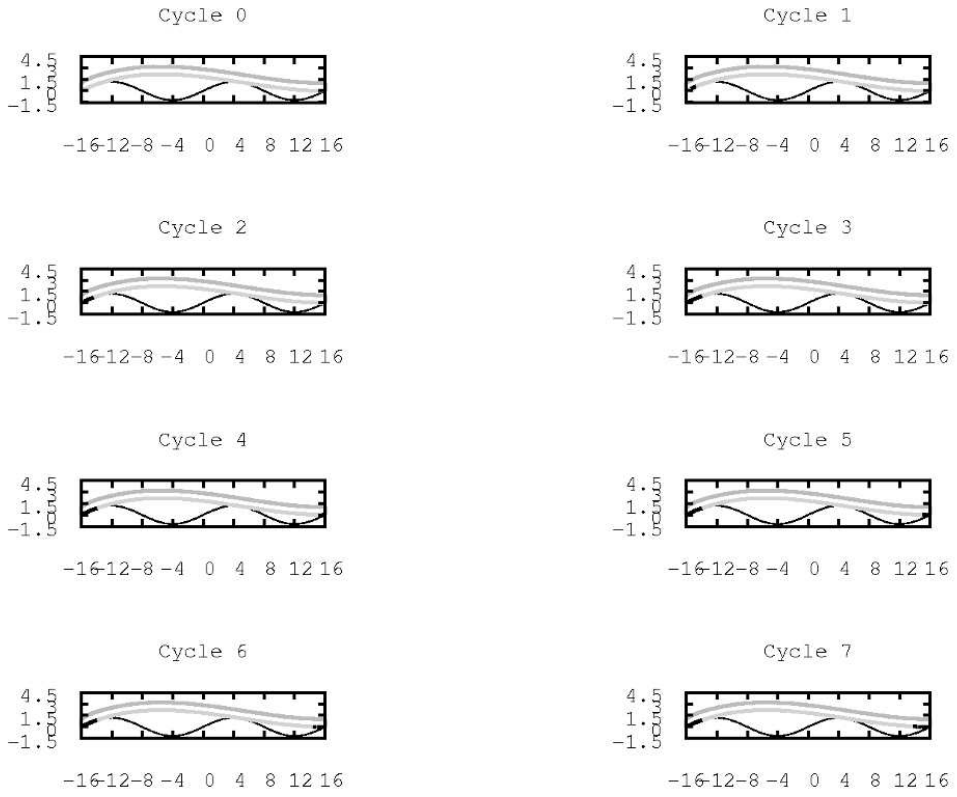

Figure IV.38: Adaptively refined model. The zone of Signorini contact is colored black, the zone of z-direction contact light gray.

Table IV.22 shows the results of one run of our algorithm:

cycle	# coarse faces	# accurate faces	# active cells	# dofs	model error estimate
0	512	0	1472	3980	6.8251e-02
1	502	10	1472	3980	4.6785e-02
2	492	20	1472	3980	2.9573e-02
3	483	29	1472	3980	9.0867e-03
4	474	38	1472	3980	0.0000e+00
5	465	47	1472	3980	0.0000e+00
6	456	56	1472	3980	0.0000e+00
7	447	65	1472	3980	0.0000e+00
8	439	73	1472	3980	0.0000e+00
9	431	81	1472	3980	0.0000e+00

Table IV.22: The convergence of one run of algorithm III.2 for the contact problem.

The results of the application of algorithm III.3 we see in table IV.23.

cycle	# coarse faces	# accurate faces	# active cells	# dofs	model error estimate
0	512	0	1472	3980	6.8251e-02
1	500	12	1472	3980	4.2782e-02
2	490	22	1472	3980	2.5894e-02
3	480	32	1472	3980	3.0801e-10
4	481	31	1472	3980	0.0000e+00
5	481	31	1472	3980	0.0000e+00
6	481	31	1472	3980	0.0000e+00
7	481	31	1472	3980	0.0000e+00
8	481	31	1472	3980	0.0000e+00
9	481	31	1472	3980	0.0000e+00

Table IV.23: The convergence of one run of algorithm III.3 for the contact problem.

The process of model-refinement is shown in figure IV.39.

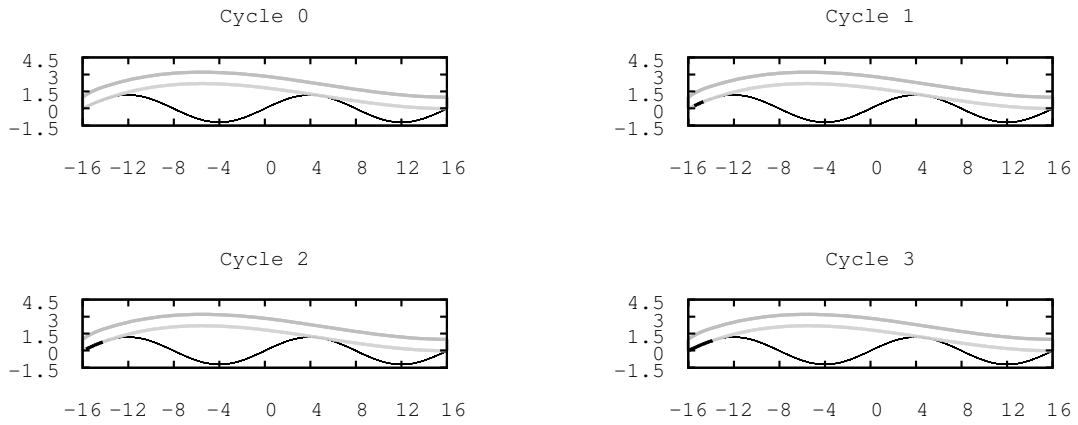

Figure IV.39: By algorithm III.3 adaptively refined model. The zone of Signorini contact is colored black, the zone of z-direction contact light gray.

IV.2.3.4 Box domain with constant load, one jump-obstacle and a single Dirichlet boundary

We consider problem (IV.5) with

$$\begin{aligned}\rho f_i(x) =& 0.0001 \cdot \delta_{i2}\\ \tau =& 0\end{aligned}$$

on the domain

$$\Omega = [-16;16] \times [0;1], \text{ with } \Gamma_0 = \{-16\} \times [0;1],\ \Gamma_\tau = \{+16\} \times [0;1].$$

The displacement is restricted at the upper boundary

$$\Gamma_C = \{x \in \partial\Omega | x_2 = 1\}$$

with the help of the Heavyside-like function θ_s (IV.3):

$$s_2(x) \leq 2 + 8 \cdot \theta_{0.01}(x_1).$$

The process of model-refinement is shown in figure IV.40.

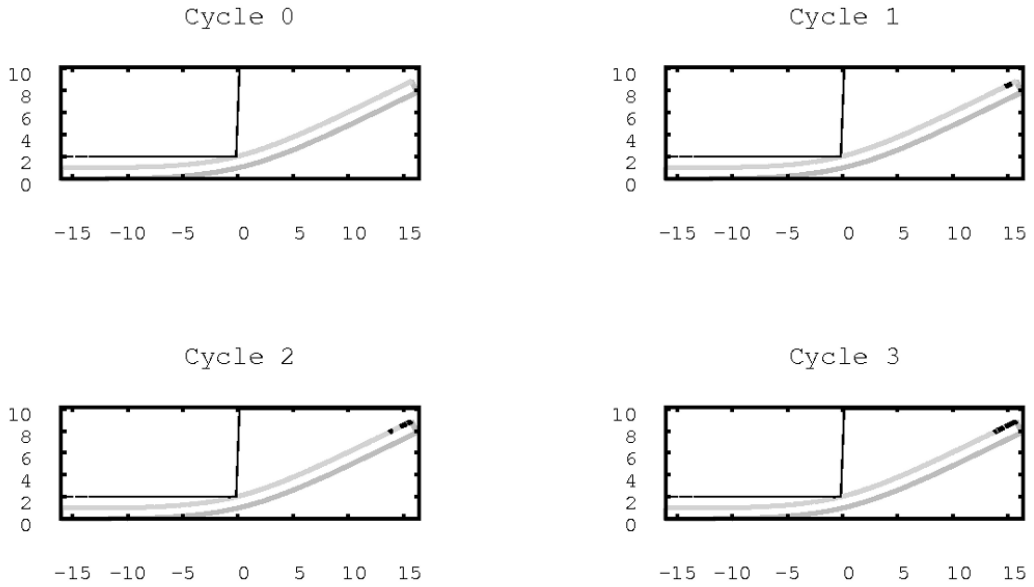

Figure IV.40: Adaptively refined model.

Table IV.24 shows the results of one run of our algorithm:

cycle	# coarse faces	# accurate faces	# active cells	# dofs	model error estimate
0	512	0	1472	3980	2.2176e-01
1	502	10	1472	3980	0.0000e+00
2	492	20	1472	3980	0.0000e+00
3	483	29	1472	3980	0.0000e+00
4	474	38	1472	3980	0.0000e+00
5	465	47	1472	3980	0.0000e+00
6	456	56	1472	3980	0.0000e+00
7	447	65	1472	3980	0.0000e+00
8	439	73	1472	3980	0.0000e+00
9	431	81	1472	3980	0.0000e+00

Table IV.24: The convergence of one run of algorithm III.2 for the contact problem.

From figure IV.40 and table IV.24 we see, that the model error estimate is greater than zero only at the jump region of the obstacle. There the model is refined. After the first step of refinement the error vanishes and the refinement takes only place in the geometrical

order as described above. Table IV.25 shows the results of the application of algorithm III.3 we see in table

cycle	# coarse faces	# accurate faces	# active cells	# dofs	model error estimate
0	512	0	1472	3980	2.2176e-01
1	511	1	1472	3980	0.0000e+00
2	511	1	1472	3980	0.0000e+00
3	511	1	1472	3980	0.0000e+00
4	511	1	1472	3980	0.0000e+00
5	511	1	1472	3980	0.0000e+00
6	511	1	1472	3980	0.0000e+00
7	511	1	1472	3980	0.0000e+00
8	511	1	1472	3980	0.0000e+00
9	511	1	1472	3980	0.0000e+00

Table IV.25: The convergence of one run of algorithm III.3 for the contact problem.

In contrast to the refinement strategy of algorithm III.2 table IV.25 shows, that the model refinement stops after the first cycle of algorithm III.3, because then the modelling error already vanishes.
The process of model-refinement is shown in figure IV.41.

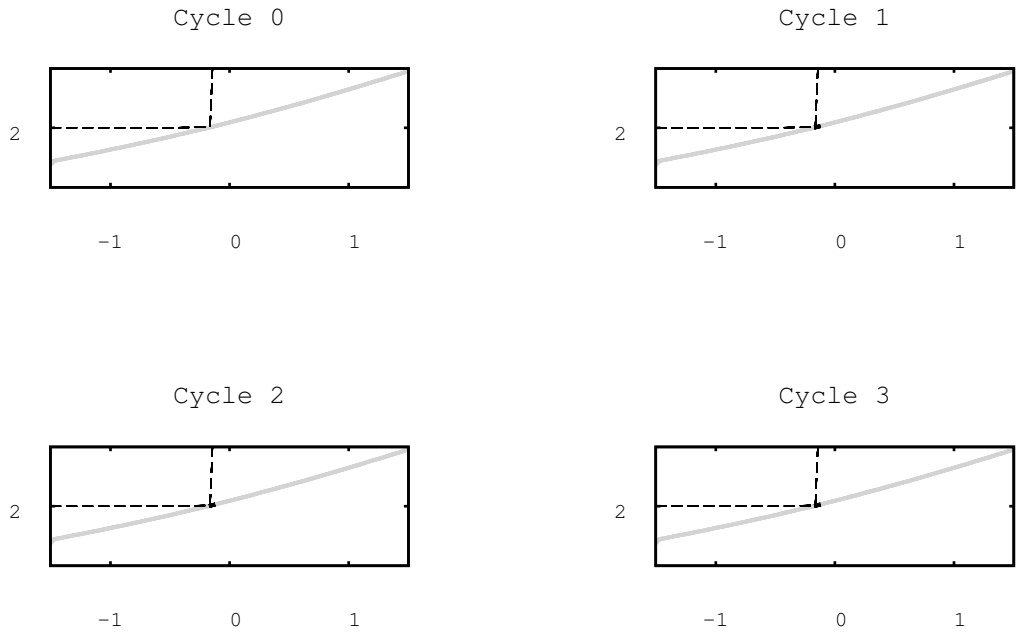

Figure IV.41: By algorithm III.3 adaptively refined model. The zone of Signorini contact is colored black, the zone of z-direction contact light gray.

IV.2.3.5 Box domain with two jump-obstacles and a single Dirichlet boundary

We consider the two dimensional contact problem (IV.4) with

$$\begin{aligned} \rho f_i(x) &= 0 \\ \tau &= 0 \end{aligned}$$

The displacement is restricted at the lower boundary

$$\Gamma_{C1} = \{x \in \partial\Omega | x_2 = 0\}$$

by the obstacle

$$s_2(x) \geq -10 \cdot \theta_{0.01}(x_1 + 1)$$

and at the upper boundary

$$\Gamma_{C2} = \{x \in \partial\Omega | x_2 = 1\}$$

by the obstacle

$$s_2(x) \leq 2 - 4 \cdot \theta_{0.01}(x_1 - 2).$$

The process of model-refinement is shown in figure IV.42.

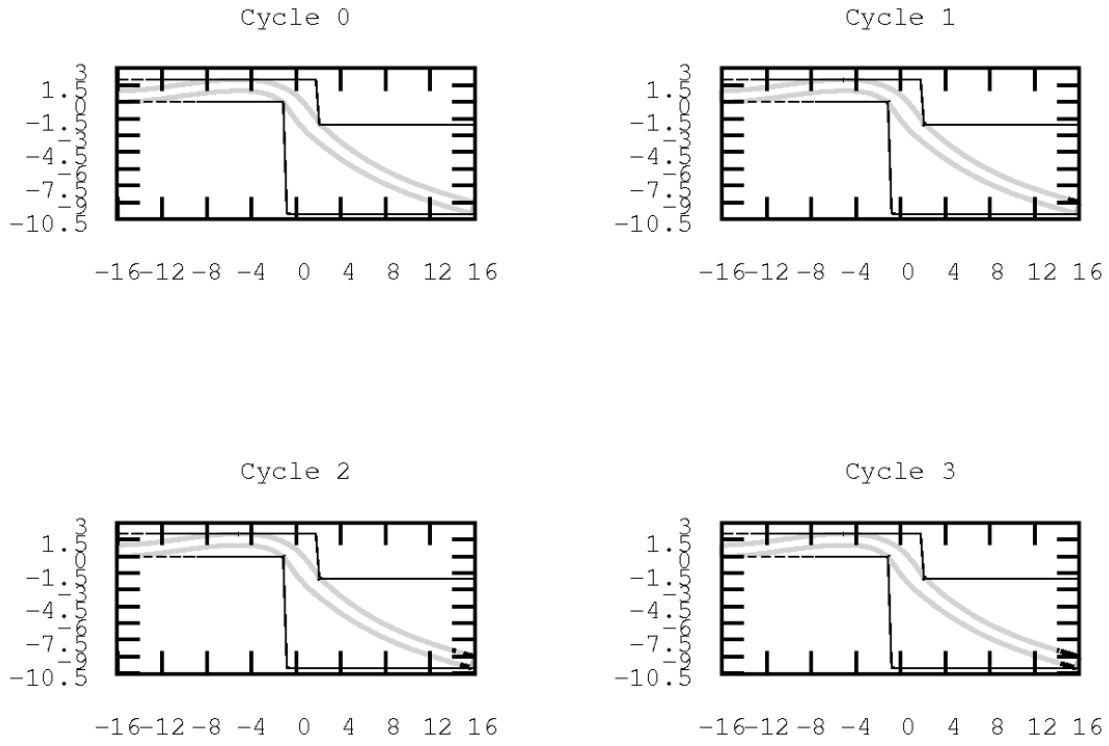

Figure IV.42: Adaptively refined model.

Table IV.26 shows the results of one run of our algorithm:

cycle	# coarse faces	# accurate faces	# active cells	# dofs	model error estimate
0	512	0	1280	3342	3.2220e+00
1	502	10	1280	3342	0.0000e+00
2	492	20	1280	3342	0.0000e+00
3	483	29	1280	3342	0.0000e+00
4	474	38	1280	3342	0.0000e+00
5	465	47	1280	3342	0.0000e+00
6	456	56	1280	3342	0.0000e+00
7	447	65	1280	3342	0.0000e+00
8	439	73	1280	3342	0.0000e+00
9	431	81	1280	3342	0.0000e+00

Table IV.26: The convergence of one run of algorithm III.2 for the contact problem.

As for the previous example, from figure IV.42 and table IV.26 we see, that the model error estimate is greater than zero only near the jump region. There the model is refined. After the first step of refinement the error vanishes and the refinement takes only place in the geometrical order as before. Table IV.27 shows the results of the application of algorithm III.3.

cycle	# coarse faces	# accurate faces	# active cells	# dofs	model error estimate
0	512	0	1280	3342	3.2220e+00
1	500	12	1280	3342	2.9744e-08
2	501	11	1280	3342	0.0000e+00
3	502	10	1280	3342	0.0000e+00
4	503	9	1280	3342	0.0000e+00
5	504	8	1280	3342	0.0000e+00
6	505	7	1280	3342	0.0000e+00
7	506	6	1280	3342	0.0000e+00
8	507	5	1280	3342	0.0000e+00
9	508	4	1280	3342	0.0000e+00

Table IV.27: The convergence of one run of algorithm III.3 for the contact problem.

In table IV.27 we recognize, that the model is even coarsened from cycle 2 on, while the model error stays zero.
The process of model-refinement is shown in figure IV.43.

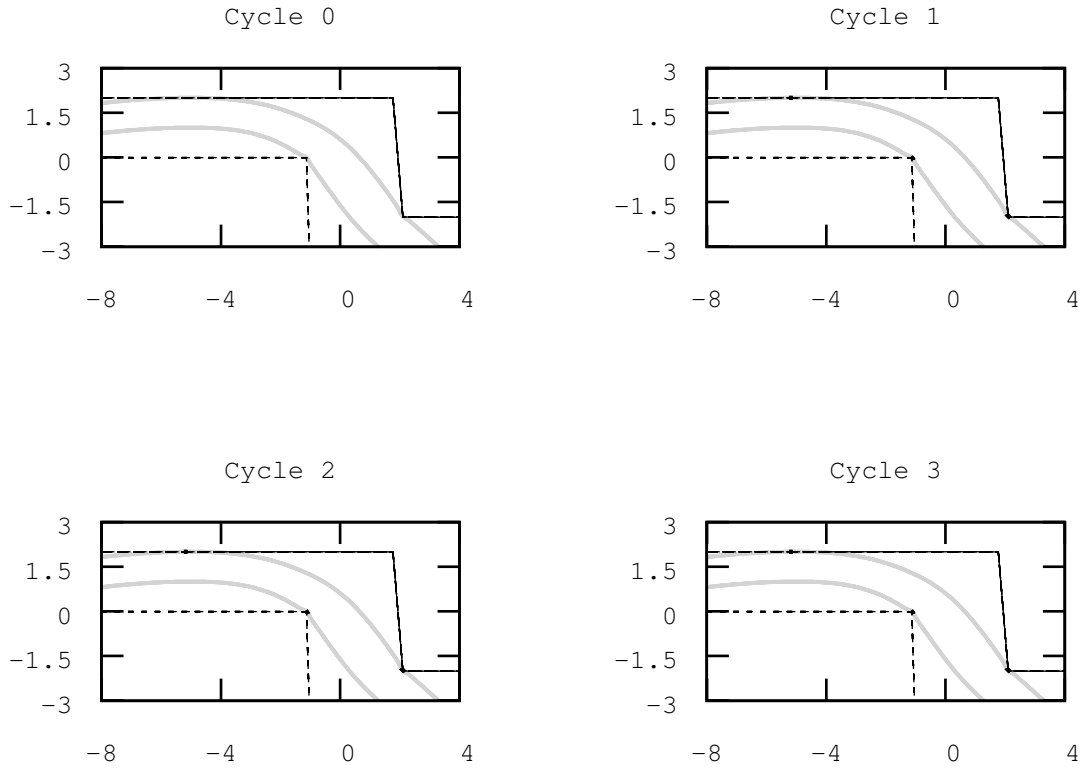

Figure IV.43: By algorithm III.3 adaptively refined model. The zone of Signorini contact is colored black, the zone of z-direction contact light gray.

IV.2.3.6 Box domain with constant load and saw obstacle

We consider the two dimensional contact problem (IV.5) with

$$\begin{aligned}\rho f_i(x) =& -0.05 \cdot \delta_{i2}\\ \tau =& 0\end{aligned}$$

The displacement is restricted at the lower boundary

$$\Gamma_C = \{x \in \partial\Omega | x_2 = 0\}$$

by the obstacle

$$\begin{aligned}s_2(x) \geq& \theta_s(x_2+4)\theta_s(-2-x_2)\frac{-1-0}{-2-(-4)}(x_2+4) + \theta_s(x_2+2)\theta_s(1-x_2)\frac{0-(-1)}{1-(-2)}(x_2+2)+\\ &+\theta_s(x_2-1)\theta_s(5-x_2)\frac{2-0}{5-1}(x_2-1) + \theta_s(x_2-5)\theta_s(6-x_2)\frac{0-2}{6-5}(x_2-5)\end{aligned}$$

which is defined with the help of the Heavyside like function (IV.3). The process of model-refinement is shown in figure IV.44.

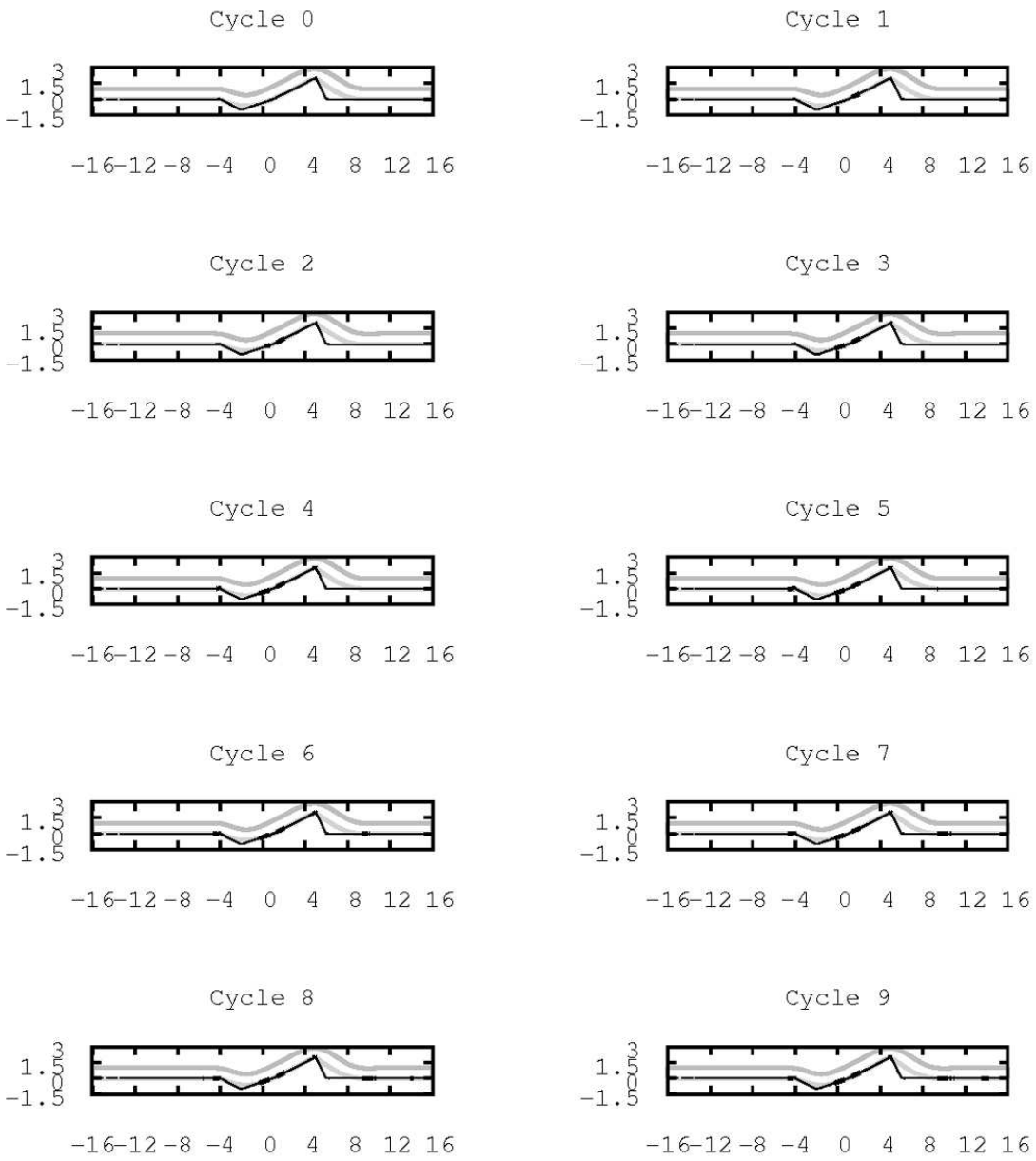

Figure IV.44: Adaptively refined model. The Signorini-faces are colored black, the z-contact-faces light grey.

Table IV.28 shows the results of one run of our algorithm:

cycle	# coarse faces	# accurate faces	# active cells	# dofs	model error estimate
0	512	0	1472	3980	8.9521e-02
1	502	10	1472	3980	4.7881e-02
2	492	20	1472	3980	2.0086e-02
3	483	29	1472	3980	7.8890e-03
4	474	38	1472	3980	1.5994e-04
5	465	47	1472	3980	4.9509e-06
6	456	56	1472	3980	1.9047e-06
7	447	65	1472	3980	1.2415e-06
8	439	73	1472	3980	1.0035e-06
9	431	81	1472	3980	7.2138e-07

Table IV.28: The convergence of one run of algorithm III.2 for the contact problem.

In this more interesting case, we see, that the model refinement expecially takes place, where the surface is rather rough, i. e. in the ankles of the obstacle. The results of the application of algorithm III.3 we see in table IV.29.

cycle	# coarse faces	# accurate faces	# active cells	# dofs	model error estimate
0	512	0	1472	3980	8.9521e-02
1	500	12	1472	3980	3.5290e-02
2	490	22	1472	3980	1.7733e-02
3	480	32	1472	3980	2.5448e-03
4	470	42	1472	3980	3.7550e-05
5	460	52	1472	3980	2.5973e-06
6	450	62	1472	3980	1.3668e-06
7	441	71	1472	3980	1.0632e-06
8	432	80	1472	3980	7.6012e-07
9	423	89	1472	3980	4.5011e-07

Table IV.29: The convergence of one run of algorithm III.3 for the contact problem.

The process of model-refinement is shown in figure IV.45.

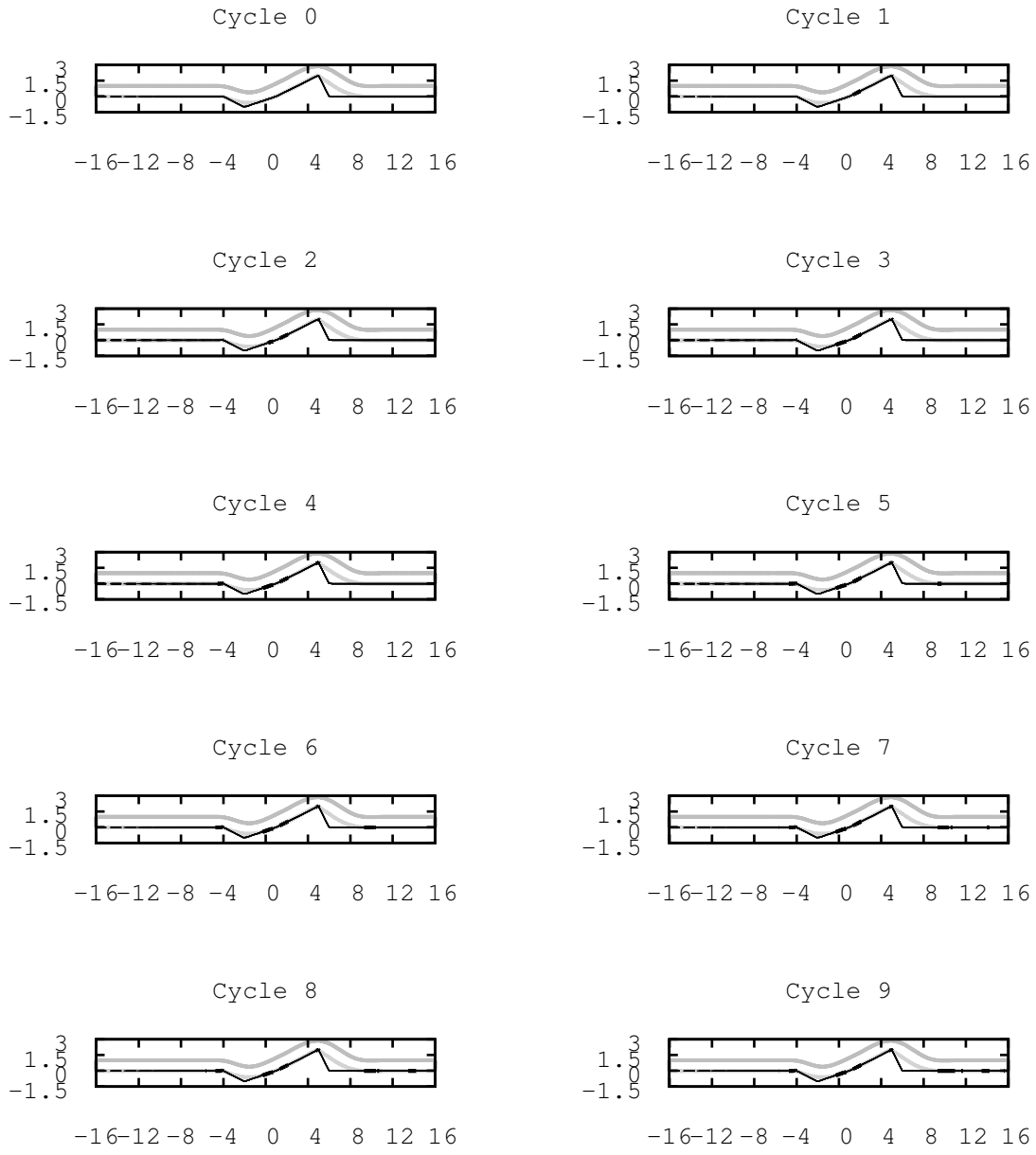

Figure IV.45: By algorithm III.3 adaptively refined model. The zone of Signorini contact is colored black, the zone of z-direction contact light gray.

A comparison of the two tables IV.28 and IV.29 illustrates, that the second strategy, namely algorithm III.3 reduces the error faster than algrorithm III.2 by the fast identification of the faces with a high model error contribution. This correct localisation is also seen in the plots of the model-series IV.44 and IV.45

In the application of the different model refinement schemes – namely algorithm III.2 for the fixed fraction strategy and algorithm III.3 for the sorted error strategy – to our model examples (sections IV.2.3.1 – IV.2.3.6) we see that the modelling error estimate (III.16) decreases for both strategies. Furthermore we see the supremacy of the sorted error strategy over the fixed fraction strategy. Especially in section IV.2.3.5 (table IV.27) we see, that the number of accurate faces can be reduced without an increase of the modelling error estimate. In general we can say that after the same number of refinement cycles the error estimate for the sorted error algorithm is lower than that of the fixed-fraction algorithm and demands for the more expensive model on a lower number of faces.

IV.2.4 Model- and Grid-adaptive Contact

For each of the six examples considered in the previous sections IV.2.1 and IV.2.2 we now apply algorithm III.25, that refines the contact model and the grid in a balanced way.

Because of the results of the previous section IV.2.3, that indicate, that the sorted-error strategy for model refinement deliveres the better results, we only implement this strategy in algorithm III.25 to refine the model.
The estimator for the **modelling error** is given in (III.16). The estimators for the **discretisation error** on both contact boundary parts (the z-contact-boundary as well as the Signorini-boundary) are based upon theorem III.15 and are implemented as in sections IV.2.1 and IV.2.2.

We recall the numerical problem again:
Find $s \in \Pi_{zs}(V_0)$, such that for all $r \in \Pi_{zs}(V_0)$:

$$2\mu \left\langle \varepsilon_{ij}(s), \varepsilon_{ij}(r-s) \right\rangle_\Omega + 2\lambda \left\langle \varepsilon_{ll}(s), \varepsilon_{jj}(r-s) \right\rangle_\Omega \geq \left\langle \rho f_i, r - s_i \right\rangle_\Omega + \left\langle \tau_{ij} n_j, r - s_i \right\rangle_{\Gamma_\tau} . \quad \text{(IV.6)}$$

with $\mu = \lambda = 1$.
The projected space

$$\Pi_{zs}(V_0) = \{ r \in V_0 | P_\Xi(x + r(x)) = x + r(x),\ x \in \Gamma_\Xi, \ \text{ for } \Xi = n, S \} ,$$

now is declared more complex than in the previous one-model-calculations. We use the partition of the contact boundary

$$\Gamma_C = \overline{\Gamma_n \cup \Gamma_S},\ \Gamma_n \cap \Gamma_S = \emptyset$$

and both types of projection

$$P_n(\xi) = \begin{cases} \xi, & \xi \cdot n \leq b(\xi_\perp) \\ \xi - (\xi \cdot n - b(\xi_\perp))n, & \xi \cdot n > b(\xi_\perp), \end{cases}$$

$$P_s(\xi) = \begin{cases} \xi, & \xi \cdot n(\xi) \leq b(\xi_\perp) \\ \xi - (\xi \cdot n(\xi) - b(\xi_\perp))n(\xi), & \xi \cdot n(\xi) > b(\xi_\perp) \\ \xi, & \xi \notin \partial\Omega. \end{cases}$$

All other declarations stay the same as in the previous sections:

$$\begin{aligned} \Omega =& [-16; 16] \times [0; 1] \\ \lambda = \mu =& 1. \end{aligned}$$

We start all calculations on an initial grid with 2×64 cells, that will be refined by the usual fixed-fraction strategy, i. e. we refine the 30% of the cells with the highest discretisation error estimate and coarsen the 3% of the cells with the lowest discretisation error estimate. For the sorted error strategy III.3 of model refinement we set

$$p_c = 1\% \quad \text{and} \quad p_r = 2\%$$

again.
We remind, that for both modelling- and grid-refinement we use the modified estimators $\tilde{\varepsilon}_m$ and $\tilde{\varepsilon}_d$ (III.93).
In tables IV.30–IV.35 we print out the numbers of z-contact- and Signorini-faces (called z- and S-faces), the number of degrees of freedom, the model error estimate (which of coarse only appears on the z-faces). The last three columns of each table contain the discretisation error estimate on the two different contact-boundary-parts and on the interiour of the domain. Because on the internal of Ω both the Signorini- as well as the z-contact-estimator do not deviate sharply, we ommit the output of the latter.

IV.2.4.1 Box domain with constant load and constant obstacle

We consider the two dimensional contact problem (IV.6) with

$$\begin{aligned} \rho f_i(x) &= -\,0.004 \cdot \delta_{i2} \\ \tau &= 0. \end{aligned}$$

The displacement is restricted at the lower boundary

$$\Gamma_C = \{x \in \partial\Omega | x_2 = 0\}$$

by the obstacle

$$s_2(x) \geq -2.$$

The process of grid- and model-refinement is shown in figure IV.46.

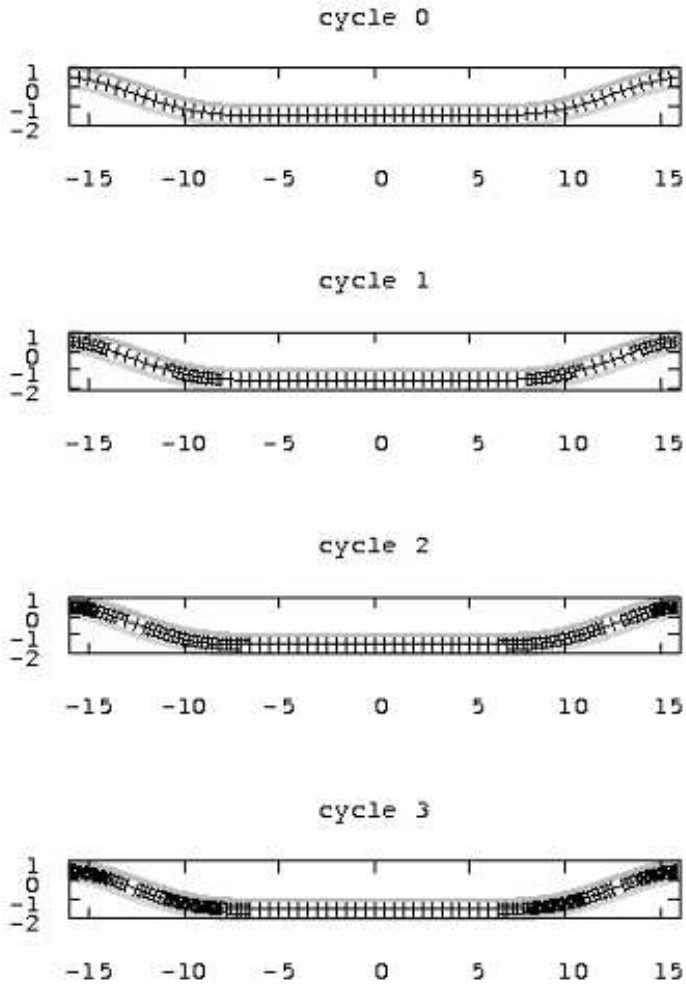

Figure IV.46: Adaptively refined model. The zone of Signorini contact is colored black, the zone of z-direction contact light gray.

Table IV.30 shows the results of one run of our algorithm:

	z-faces	S-faces	dofs	model error estimate	discretisation error estimate on z-boundary	S-boundary	interior S
0	64	0	390	0.0000e+00	0.5941	0.0000	0.6213
1	82	0	682	0.0000e+00	0.3087	0.0000	0.4270
2	107	0	1192	0.0000e+00	0.1710	0.0000	0.3079
3	143	0	2156	0.0000e+00	0.1067	0.0000	0.2364
4	188	0	3866	0.0000e+00	0.0646	0.0000	0.1689
5	258	0	7138	0.0000e+00	0.0426	0.0000	0.1298
6	348	0	13182	0.0000e+00	0.0259	0.0000	0.0920
7	498	0	24654	0.0000e+00	0.0162	0.0000	0.0704
8	668	0	46020	0.0000e+00	0.0100	0.0000	0.0498
9	960	0	86660	0.0000e+00	0.0062	0.0000	0.0376

Table IV.30: The convergence of one run of our algorithm for the contact problem.

As in section IV.2.3.1 we see, that the modelling error vanishes right from the beginning. As mentioned there, the reason for this is, that for a constant obstacle the conditions (S) and (Z) (III.11) are the same and thus the estimate (III.16) is zero.
Because the modelling error is zero from the beginning, again the model is not refined anywhere.

IV.2.4.2 Box domain with constant load and periodic obstacle

We consider the two dimensional contact problem (IV.6) with

$$\begin{aligned} \rho f_i(x) &= -\,0.002 \cdot \delta_{i2} \\ \tau &= 0 \end{aligned}$$

The displacement is restricted at the lower boundary

$$\Gamma_C = \{x \in \partial\Omega | x_2 = 0\}$$

by the obstacle

$$s_2(x) \geq -2 + 1.2 \cdot \sin \frac{2 \cdot \cdot 2\pi \cdot (x_1 + 16)}{32}.$$

The process of grid- and model-refinement is shown in figure IV.47.

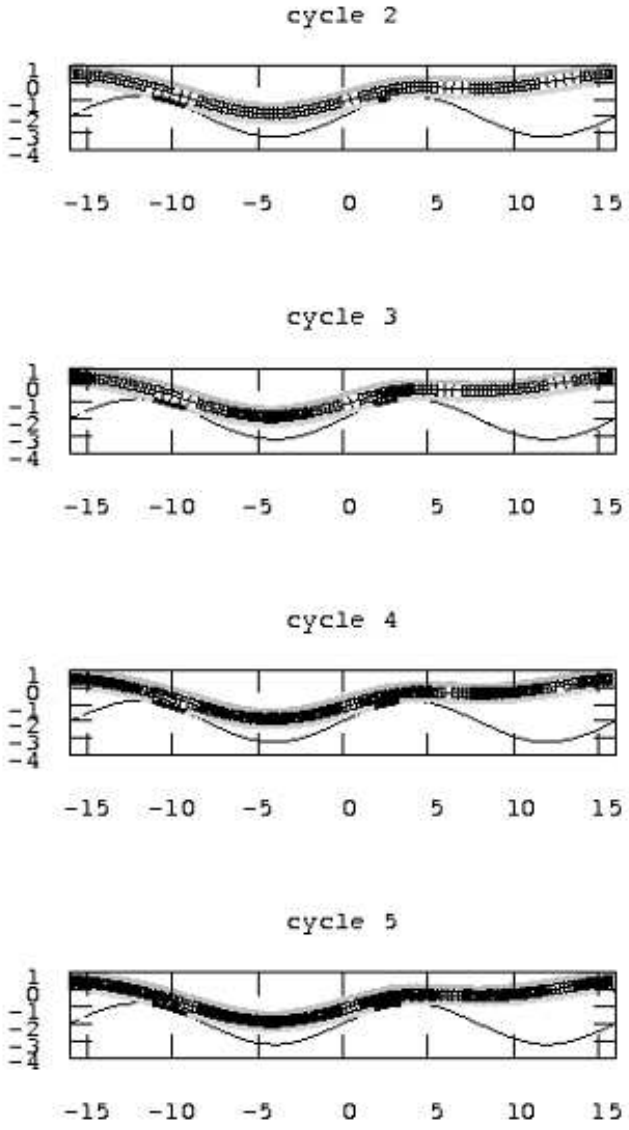

Figure IV.47: Adaptively refined model. The zone of Signorini contact is colored black, the zone of z-direction contact light gray.

Table IV.31 shows the results of one run of our algorithm:

	z-faces	S-faces	dofs	model error estimate	discretisation error estimate on z-boundary	S-boundary	interior S
0	64	0	390	6.7274e-02	0.6129	0.0000	0.4857
1	79	3	682	6.3054e-02	0.3516	0.0795	0.3651
2	108	7	1244	1.9130e-02	0.2007	0.0648	0.3093
3	138	11	2180	2.9914e-03	0.1245	0.0758	0.2287
4	197	17	4044	1.9883e-03	0.0710	0.0484	0.1784
5	253	29	7330	1.1630e-03	0.0462	0.0402	0.1336
6	371	51	13732	4.5371e-02	0.0239	0.0215	0.0977
7	463	66	25440	0.0000e+00	0.0179	0.0181	0.0739
8	703	88	47728	1.5992e-02	0.0093	0.0108	0.0522
9	881	126	89660	0.0000e+00	0.0069	0.0075	0.0400

Table IV.31: The convergence of one run of our algorithm for the contact problem.

IV.2.4.3 Box domain with no load and periodic obstacle

We consider the two dimensional contact problem (IV.6) with

$$\begin{aligned} \rho f_i(x) &= 0 \\ \tau &= 0 \end{aligned}$$

The displacement is restricted at the lower boundary

$$\Gamma_C = \{x \in \partial\Omega | x_2 = 0\}$$

by the obstacle

$$s_2(x) \geq 1.2 \cdot \sin \frac{2 \cdot 2\pi \cdot (x_1 + 16)}{32}.$$

The process of grid- and model-refinement is shown in figure IV.48.

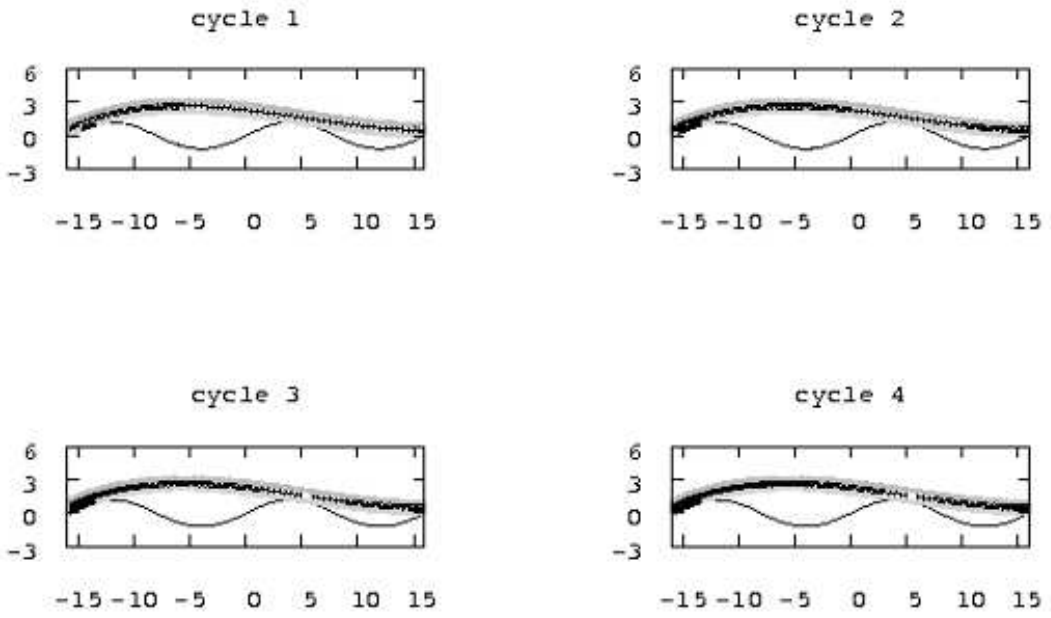

Figure IV.48: Adaptively refined model. The zone of Signorini contact is colored black, the zone of z-direction contact light gray.

Table IV.32 shows the results of one run of our algorithm:

	z-faces	S-faces	dofs	model error estimate	discretisation error estimate on z-boundary	S-boundary	interior S
0	64	0	390	8.1963e-02	0.7849	0.0000	0.8367
1	79	3	676	4.9143e-02	0.4130	0.1190	0.5691
2	101	8	1218	2.5517e-02	0.2416	0.0930	0.3676
3	123	13	2178	2.2491e-02	0.1361	0.0749	0.2396
4	159	19	4008	6.1885e-03	0.0831	0.0490	0.1612
5	210	30	7434	2.6031e-03	0.0505	0.0280	0.1140
6	284	41	13824	9.2567e-04	0.0305	0.0209	0.0807
7	395	62	25928	1.1677e-02	0.0184	0.0118	0.0578
8	543	81	48556	3.1042e-04	0.0114	0.0082	0.0418
9	764	119	91430	8.7972e-04	0.0069	0.0047	0.0298

Table IV.32: The convergence of one run of our algorithm for the contact problem.

IV.2.4.4 Box domain with constant load, one jump-obstacle and a single Dirichlet boundary

We consider the two dimensional contact problem (IV.6) with

$$\begin{aligned} \rho f_i(x) =& 0.0001 \cdot \delta_{i2} \\ \tau =& 0 \end{aligned}$$

The displacement is restricted at the upper boundary

$$\Gamma_C = \{x \in \partial\Omega | x_2 = 1\}$$

by the obstacle

$$s_2(x) \leq 2 + (10 - 2) \cdot \theta_{0.01}(x_1)$$

with the jump-function (IV.3).
The process of grid- and model-refinement is shown in figure IV.49.

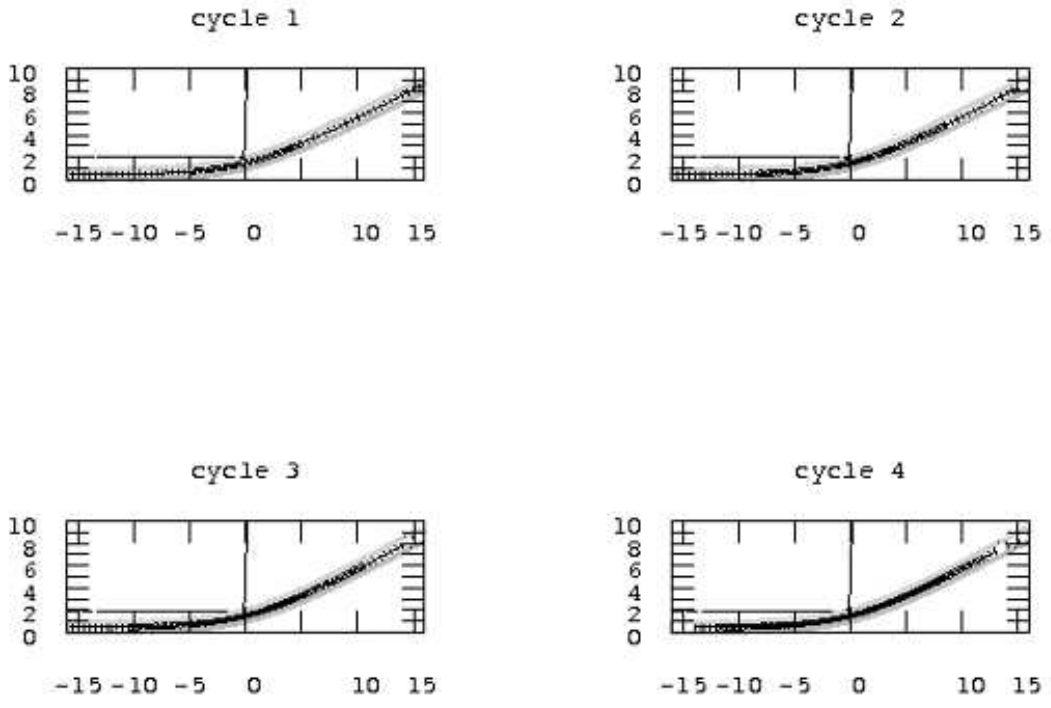

Figure IV.49: Adaptively refined model. The zone of Signorini contact is colored black, the zone of z-direction contact light gray.

Table IV.33 shows the results of one run of our algorithm:

	z-faces	S-faces	dofs	model error estimate	discretisation error estimate on z-boundary	S-boundary	interior S
0	64	0	390	4.7396e-02	0.1737	0.0000	0.1800
1	82	1	670	2.0446e+00	0.0919	0.0430	0.1324
2	102	3	1178	0.0000e+00	0.0610	0.0240	0.1059
3	143	2	2090	0.0000e+00	0.0349	0.0205	0.0774
4	183	4	3802	0.0000e+00	0.0243	0.0104	0.0610
5	261	4	6986	0.0000e+00	0.0144	0.0095	0.0436
6	345	5	12998	0.0000e+00	0.0095	0.0075	0.0341
7	489	5	24124	0.0000e+00	0.0058	0.0074	0.0243
8	680	7	45300	5.5859e-03	0.0034	0.0056	0.0184
9	915	9	84330	0.0000e+00	0.0023	0.0056	0.0134

Table IV.33: The convergence of one run of our algorithm for the contact problem.

IV.2.4.5 Box domain with two jump obstacles, no load and a single Dirichlet boundary

We consider the two dimensional contact problem (IV.6) with

$$\begin{aligned} \rho f_i(x) &= 0 \\ \tau &= 0 \end{aligned}$$

The displacement is restricted at the lower boundary

$$\Gamma_{C1} = \{x \in \partial\Omega | x_2 = 0\}$$

by the obstacle

$$s_2(x) \geq -10 \cdot \theta_{0.01}(x_1 + 1)$$

and at the upper boundary

$$\Gamma_{C2} = \{x \in \partial\Omega | x_2 = 1\}$$

by the obstacle

$$s_2(x) \leq 2 - 4 \cdot \theta_{0.01}(x_1 - 2).$$

The use of the θ_s-function smoothes the modeled jump-obstacle (compare figure IV.50), such that it can be handeled by the a-posteriori estimate of theorem III.15.

The process of grid- and model-refinement is shown in figure IV.50.

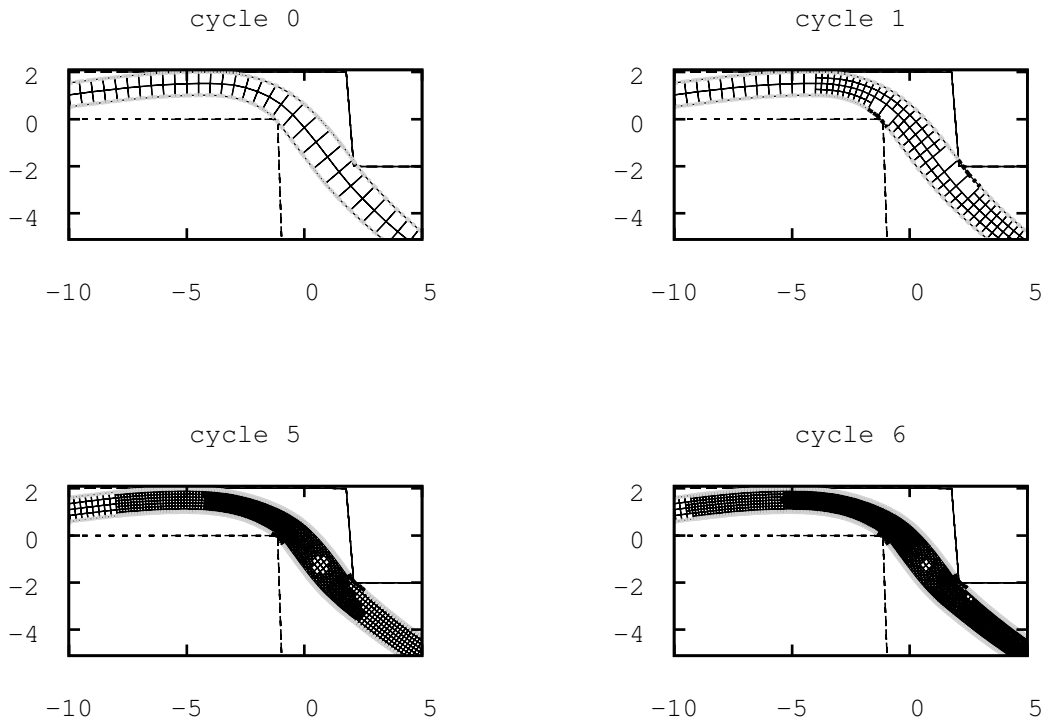

Figure IV.50: Adaptively refined model. The zone of Signorini contact is colored black, the zone of z-direction contact light gray.

Table IV.34 shows the results of one run of our algorithm:

	z-faces	S-faces	dofs	model error estimate	discretisation error estimate on z-boundary	S-boundary	interior S
0	128	0	390	4.0969	1.5170	0	0
1	90	4	676	0	0.6221	0.6659	0.4866
2	212	7	1212	0	0.3621	0.3478	0.3942
3	302	8	2188	0	0.2093	0.3796	0.3289
4	384	12	3966	0	0.1365	0.3668	0.2758
5	545	18	7280	0	0.0824	0.4304	0.2138
6	725	24	13536	2.0661e-02	0.0559	0.3336	0.1794
7	1020	35	28210	1.3227e-01	0.0357	0.3559	0.1433
8	1567	61	80326	1.3578e-01	0.0247	0.1043	0.1043
9	2335	122	149376	1.6617e-02	0.0101	0.0833	0.0833

Table IV.34: The convergence of one run of our algorithm for the contact problem. (Because in cycle 0 all cells have got a contact-face, the discretisation error on the interiour is zero.)

IV.2.4.6 Box domain with constant load and saw obstacle

We consider the two dimensional contact problem (IV.6) with

$$\begin{aligned}\rho f_i(x) =& -0.05 \cdot \delta_{i2}\\ \tau =& 0\end{aligned}$$

The displacement is restricted at the lower boundary

$$\Gamma_C = \{x \in \partial\Omega | x_2 = 0\}$$

by the obstacle

$$\begin{aligned}s_2(x) \geq& \theta_s(x_2+4)\theta_s(-2-x_2)\frac{-1-0}{-2-(-4)}(x_2+4) + \theta_s(x_2+2)\theta_s(1-x_2)\frac{0-(-1)}{1-(-2)}(x_2+2)+\\ &+\theta_s(x_2-1)\theta_s(5-x_2)\frac{2-0}{5-1}(x_2-1) + \theta_s(x_2-5)\theta_s(6-x_2)\frac{0-2}{6-5}(x_2-5)\end{aligned}$$

which is defined with the help of the Heavyside like function (IV.3).
The process of grid- and model-refinement is shown in figure IV.51.

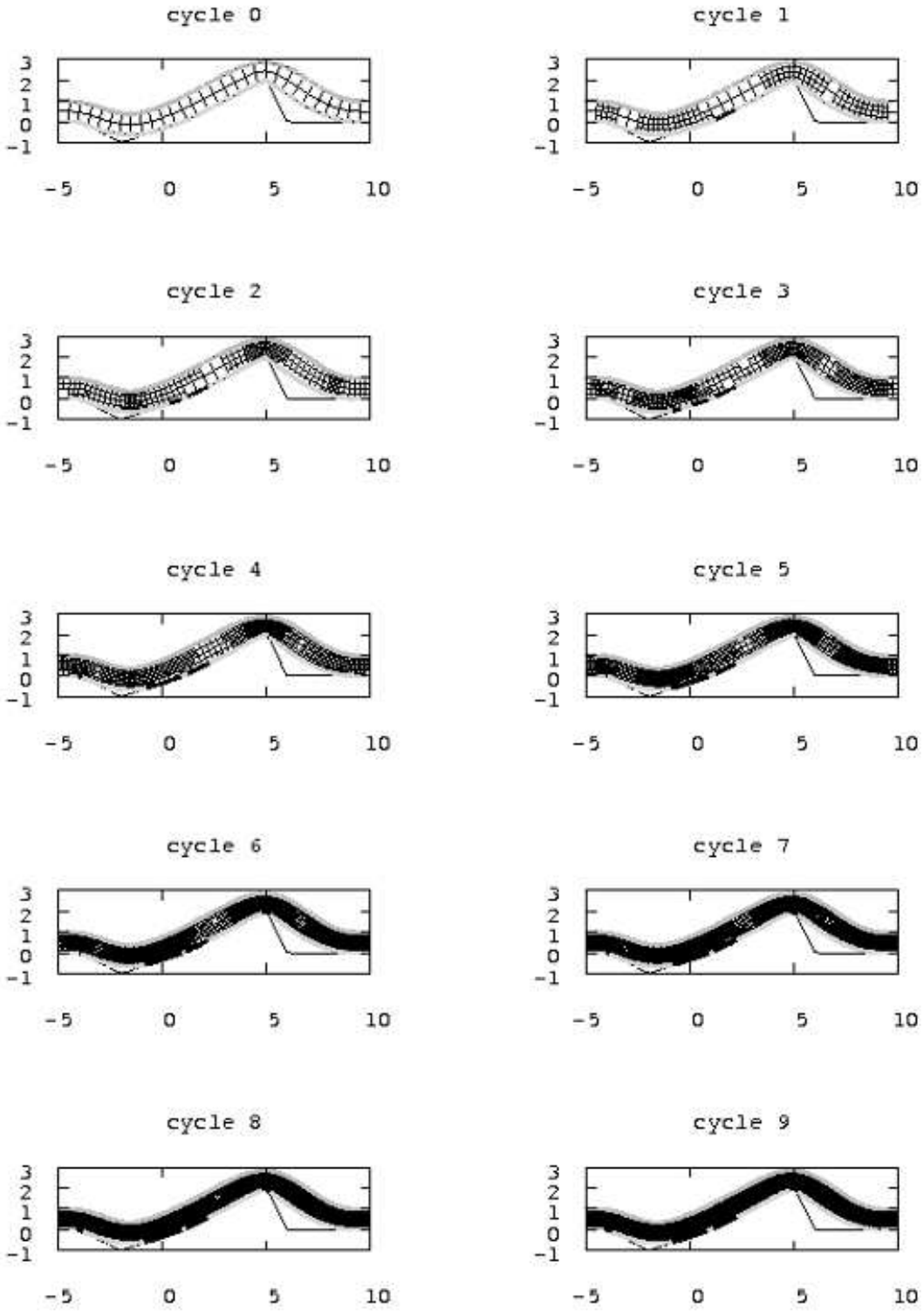

Figure IV.51: Adaptively refined model. The zone of Signorini contact is colored black, the zone of z-direction contact light gray.

Table IV.35 shows the results of one run of our algorithm:

	z-faces	S-faces	dofs	model error estimate	discretisation error estimate on z-boundary	S-boundary	interior S
0	64	0	390	1.0894e-01	1.5514	0.0000	1.4578
1	82	2	680	7.7317e-02	0.7985	0.1035	0.9830
2	103	4	1216	5.3323e-02	0.4829	0.1227	0.7099
3	128	8	2200	3.4506e-01	0.3306	0.1129	0.5213
4	174	18	4064	2.3523e-01	0.1965	0.1765	0.4051
5	245	30	7442	2.6093e-02	0.1160	0.1338	0.3008
6	317	55	13878	1.2878e-03	0.0585	0.1098	0.2275
7	445	94	25728	6.0828e-04	0.0306	0.0998	0.1673
8	538	143	48260	1.3063e-02	0.0229	0.0762	0.1248
9	844	199	90556	1.7468e-02	0.0117	0.0439	0.0925

Table IV.35: The convergence of one run of our algorithm for the contact problem.

In figure IV.51 we see, that the model is refined in the same critical points, that where already detected in section IV.2.3.6, while the grid-refinement takes place in the expected araeas.

A comparison of the results of the model- and grid-adaptive solvers (MGA-solver) with the model-refinement-solver (MA-solver), e. g. figure IV.51 and IV.44, affirms, that the critical points for the contact are detected correctly. If we compare the number of contact-faces, that are marked as Signorini-faces, we see, that the MGA-solver marks up to twice as much S-faces in comparison to the MA-solver. This is a consequence of the simultanuous grid-refinement, which also increases the number of faces.
If we compare the results of the MGA-solver with the ones of the Signorini-solver (given in section IV.2.2) we see, that the grid is refined in the same regions of high stress or rough obstacle respective as before.
Furthermore in tables IV.31– IV.35 we see, that the balanced refinement strategy of algorithm III.25 lets the error contributions of modelling-error and discretisation error converge to the same order from initially different orders, as already seen in Braack and Ern [2003]. For example in table IV.35 the estimates start at $\|e_m\| = O(0.1)$ and $\|e_d\| = O(1.0)$ and reach $\|e_m\|, \|e_d\| = O(0.01)$.

IV.2.4.7 U-O-Forming

In this section we briefly present the results of the simulation of an U-O-forming process in steel-forming.

Within the U-O-forming process a sheet of metall is formed into a pipe. The process can be split into three steps (figure IV.52):

1) The bending of the plane sheet into a U-shape.

2) The bending of the U-shaped sheet into an O-shape.

3) The welding of the work piece to a pipe.

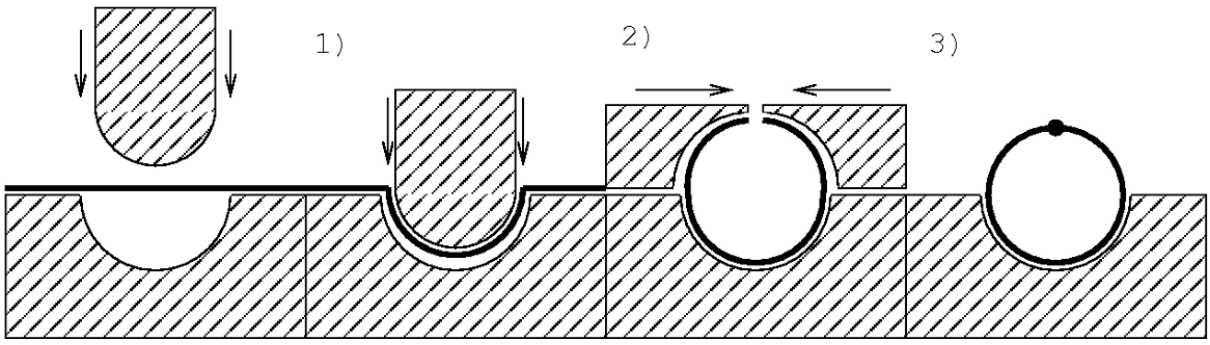

Figure IV.52: The three steps of the U-O-process.

Here the calculations for the U-forming process (step 1)) are presented. Because of the problems symmetry, we reduce our calculations to the right half of the U-shape – effectively we consider a J-forming process.

In the end the steel sheet shall not behave elastic. Thus we model a kind of plasticity, that is not described in section I.1.3. In difference to Hook's law (I.11) we do not assume a linear relation between tension σ and deformation ε, but one, that is scatched in figure IV.53. The tension-deformation-graph is not a line, but a hysteresis loop. That means, the deformed material stays in its deformed state, even after relaxation.

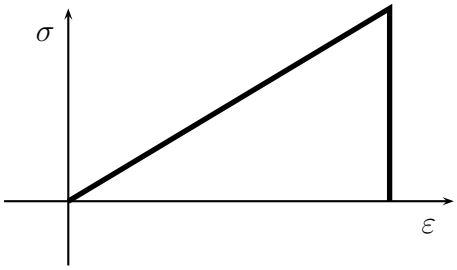

Figure IV.53: Material law for plasticity. After the vanishing load of the solid body the deformation remains.

In our calculation we model this kind of plasticity in the following way. We split the whole process in 25 single parts. In each of these parts we assume an elastic problem (IV.6) with

$$\begin{aligned} \rho f_i(x) =& 0 \\ \tau =& 0. \end{aligned}$$

For each step we perform 4 (model- and grid-) refinement cycles. After this we add to each vertex of the grid the local deformation and use this deformed grid for the next step, with the lowered upper obstacle.
The geometry of the lower obstacles is given by the radii of the upper and lower half circle

$$r^U = 8.8, \quad r^L = 10$$

and their initial centers

$$c_0^U = (-16; 10), \quad c_0^L = (-16, 0)$$

as well as the height of the plain obstacle parts:

$$H_0^U = 1.2, \quad H_0^L = 0.0$$

The complete lower obstacle and the plain part of the higher obstacle rises in each step by 10/24:

$$c_j^L = \left(-16, j \cdot \frac{10}{24}\right), \; H_j^U = 1.2 + j \cdot \frac{10}{24}, \; H_j^L = j \cdot \frac{10}{24} \quad (j = 0, 1, \ldots, 24).$$

As before the departure from the half-circle- to the plain parts of the obstacles is smoothed with the help of the θ_s-function (IV.3).
Homogenous Dirichlet conditions are only applied to the left boundary of the domain, on the right side we apply homogenuous Neumann conditions to allow following with the sheet.
Some of the results are shown in figure IV.54.

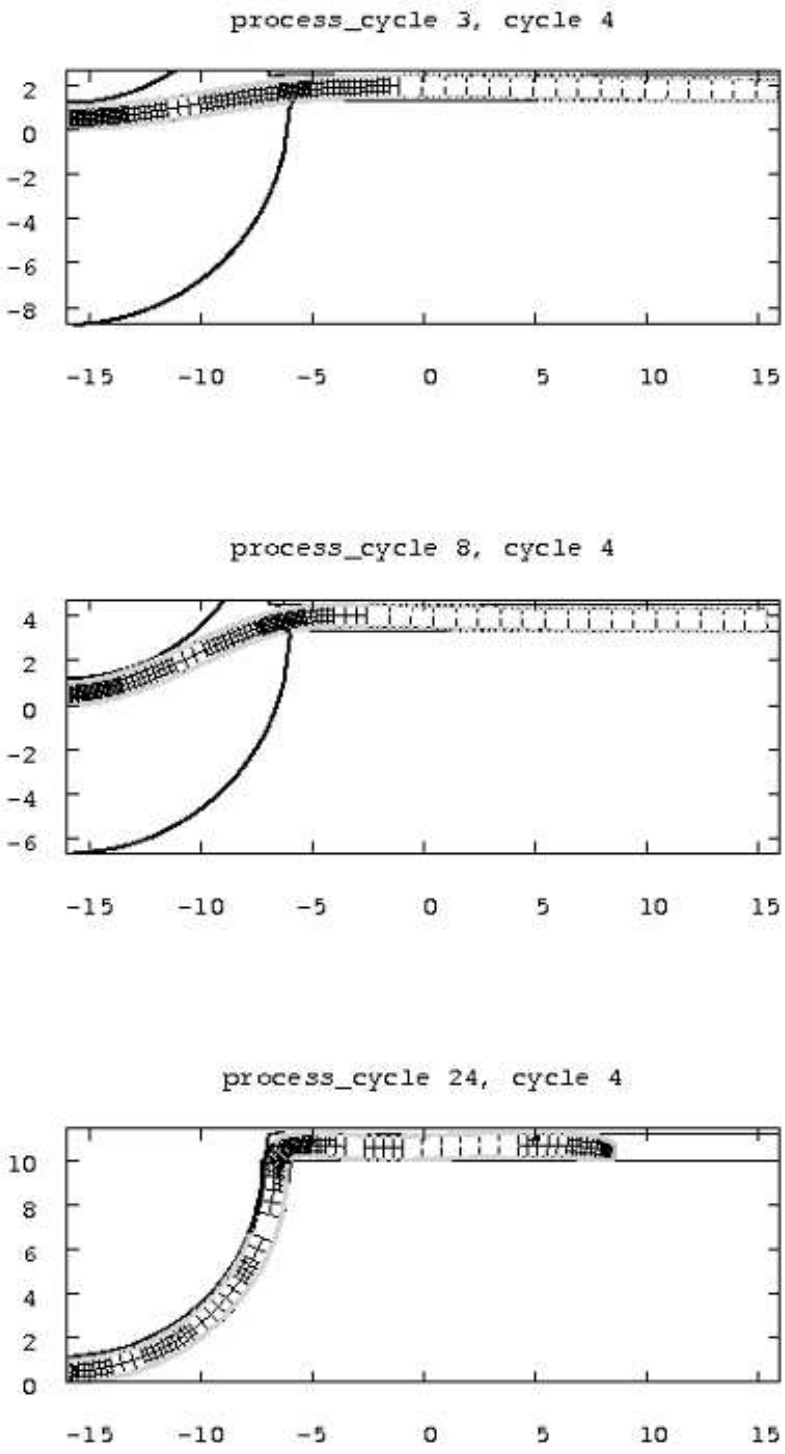

Figure IV.54: Results of the U process calculations. The y-range of the plot moves up in each step, thus the lower obstacle seems to rest.

IV.3 Hydrodynamics

In sections IV.3.1 – IV.3.6 we present numerical results for the Reynolds– and SubStokes–model with and without cavitation considering the following prototype examples on the unit square

$$\Omega_2 = [0;1] \times [0;1]$$

For every example we set the inhomogenuous boundary condition for the pressure

$$\psi|_{\partial\Omega_2} = 200$$

and the geometrical properties of the lower surface

$$z_0 = 0, \quad v(z_0) = 0.$$

The prototype examples differ in the geometry and the velocity of the upper surface.

- Plain surface and downward velocity

$$\begin{gathered} g = 2\overline{z} = 0.1, \\ \delta v_3 = 2\overline{v}_3 = -10.0, \quad \delta v_\mu = 2\overline{v}_\mu = 0 \ (\mu = 1;2) \end{gathered} \tag{IV.7}$$

- Plain surface and upward velocity

$$\begin{gathered} g = 2\overline{z} = 0.1, \\ \delta v_3 = 2\overline{v}_3 = 10.0, \quad \delta v_\mu = 2\overline{v}_\mu = 0 \ (\mu = 1;2) \end{gathered} \tag{IV.8}$$

- Plain surface and horizontal velocity

$$\begin{gathered} g = 2\overline{z} = 0.1, \\ \delta v_1 = 2\overline{v}_1 = 10.0, \quad \delta v_2 = 2\overline{v}_2 = 0; \ \delta v_3 = 2\overline{v}_3 = 0 \end{gathered} \tag{IV.9}$$

- Steep surface and downward velocity

$$\begin{gathered} g = 2\overline{z} = 0.1 + 0.05 \cdot x_1, \\ \delta v_3 = 2\overline{v}_3 = -10.0, \quad \delta v_\mu = 2\overline{v}_\mu = 0 \ (\mu = 1;2) \end{gathered} \tag{IV.10}$$

- Steep surface and upward velocity

$$\begin{gathered} g = 2\overline{z} = 0.1 + 0.05 \cdot x_1, \\ \delta v_3 = 2\overline{v}_3 = 10.0, \quad \delta v_\mu = 2\overline{v}_\mu = 0 \ (\mu = 1;2) \end{gathered} \tag{IV.11}$$

- Steep surface and horizontal velocity in direction of the ascent

$$\begin{gathered} g = 2\overline{z} = 0.1 + 0.05 \cdot x_1, \\ \delta v_1 = 2\overline{v}_1 = 10.0, \quad \delta v_2 = 2\overline{v}_2 = 0; \ \delta v_3 = 2\overline{v}_3 = 0 \end{gathered} \tag{IV.12}$$

- Steep surface and horizontal velocity against direction of the ascent

$$\begin{gathered} g = 2\overline{z} = 0.1 + 0.05 \cdot x_1, \\ \delta v_1 = 2\overline{v}_1 = -10.0,\ \delta v_2 = 2\overline{v}_2 = 0;\ \delta v_3 = 2\overline{v}_3 = 0 \end{gathered} \tag{IV.13}$$

- Steep surface and horizontal velocity perpendicular to the ascent

$$\begin{gathered} g = 2\overline{z} = 0.1 + 0.05 \cdot x_1, \\ \delta v_2 = 2\overline{v}_2 = 10.0, \quad \delta v_1 = 2\overline{v}_1 = 0;\ \delta v_3 = 2\overline{v}_3 = 0 \end{gathered} \tag{IV.14}$$

- Wave surface and downward velocity

$$\begin{gathered} g = 2\overline{z} = 0.1 + 0.07 \cdot \sin(2\pi \cdot 2x_1), \\ \delta v_3 = 2\overline{v}_3 = -10.0, \quad \delta v_\mu = 2\overline{v}_\mu = 0\ (\mu = 1; 2) \end{gathered} \tag{IV.15}$$

- Wave surface and upward velocity

$$\begin{gathered} g = 2\overline{z} = 0.1 + 0.07 \cdot \sin(2\pi \cdot 2x_1), \\ \delta v_3 = 2\overline{v}_3 = 10.0, \quad \delta v_\mu = 2\overline{v}_\mu = 0\ (\mu = 1; 2) \end{gathered} \tag{IV.16}$$

- Wave surface and horizontal velocity

$$\begin{gathered} g = 2\overline{z} = 0.1 + 0.07 \cdot \sin(2\pi \cdot 2x_1), \\ \delta v_1 = 2\overline{v}_1 = 40.0, \quad \delta v_2 = 2\overline{v}_2 = 0;\ \delta v_3 = \overline{v}_3 = 0 \end{gathered} \tag{IV.17}$$

- Hilly surface and downward velocity

$$\begin{gathered} g = 2\overline{z} = 0.1 + 0.07 \cdot \sin^2(2\pi \cdot 2x_1) \cdot \sin^2(2\pi \cdot 2x_2), \\ \delta v_3 = 2\overline{v}_3 = -10.0, \quad \delta v_\mu = 2\overline{v}_\mu = 0\ (\mu = 1; 2) \end{gathered} \tag{IV.18}$$

- Hilly surface and upward velocity

$$\begin{gathered} g = 2\overline{z} = 0.1 + 0.07 \cdot \sin^2(2\pi \cdot 2x_1) \cdot \sin^2(2\pi \cdot 2x_2), \\ \delta v_3 = 2\overline{v}_3 = 10.0, \quad \delta v_\mu = 2\overline{v}_\mu = 0\ (\mu = 1; 2) \end{gathered} \tag{IV.19}$$

- Hilly surface and horizontal velocity

$$\begin{gathered} g = 2\overline{z} = 0.1 + 0.07 \cdot \sin^2(2\pi \cdot 2x_1) \cdot \sin^2(2\pi \cdot 2x_2), \\ \delta v_1 = 2\overline{v}_1 = 1000, \quad \delta v_2 = 2\overline{v}_2 = 0;\ \delta v_3 = 2\overline{v}_3 = 0 \end{gathered} \tag{IV.20}$$

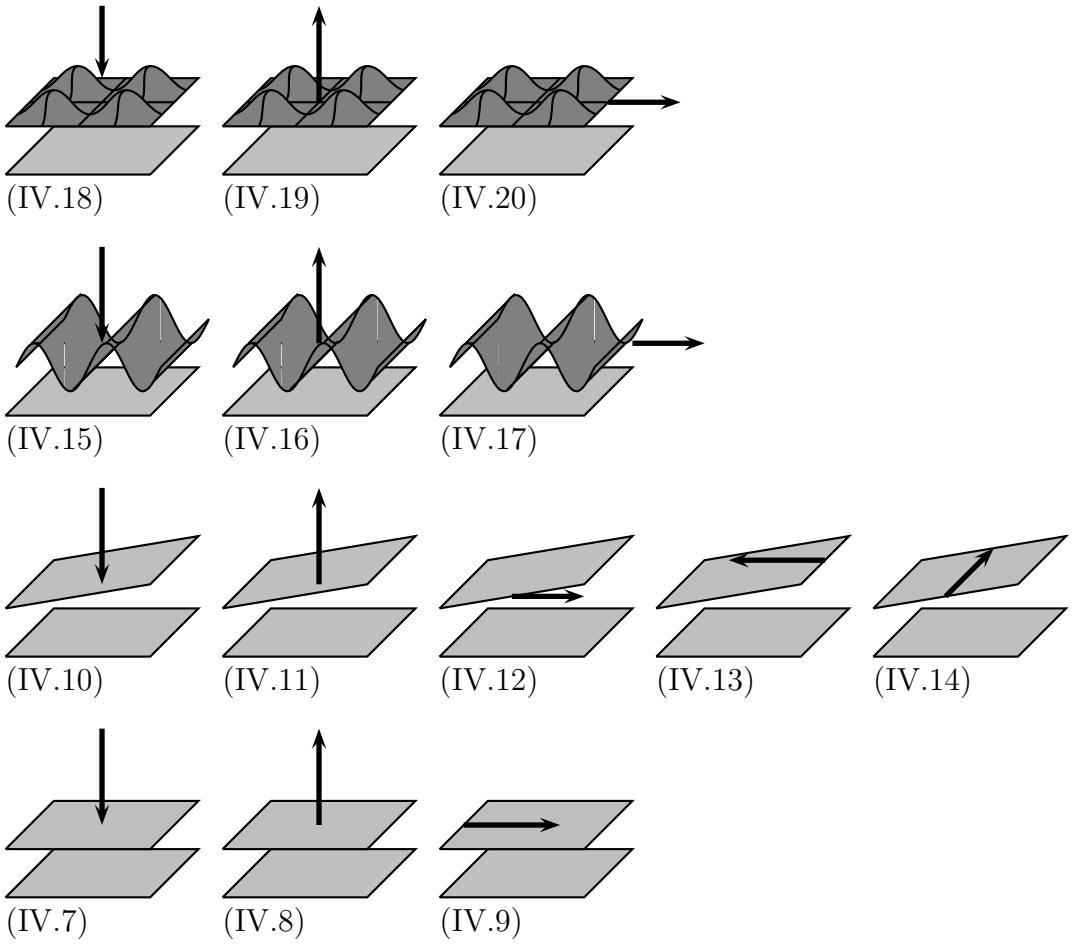

Figure IV.55: Scatch of the example applications for the fluid calculations. We see the lower and upper surface ($z_0(\Omega_2)$ and $z_1(\Omega_2)$) (gray) and the velocity $v(z_1)$ (black arrow).

IV.3.1 Reynolds Model without cavitation

We solve the Reynolds equation (I.77) for different examples (IV.7)–(IV.20).
All computations start on an initial grid of $64 \times 64 = 4096$ cells and refine it adaptively using the estimator of theorem III.16 and a fixed-fraction strategy, as already done in section IV.1: We refine the 30% of the cells with the highest error per cell, which results in about doubling of the cells. Furthermore we coarsen 3% of the cells with the smallest error.

IV.3.1.1 Plain surface and vertical downward velocity

We consider the Reynolds problem (I.77) with the upper surface given by (IV.7). The sequence of refined grids is shown in figure IV.56 and the solution in figure IV.57.

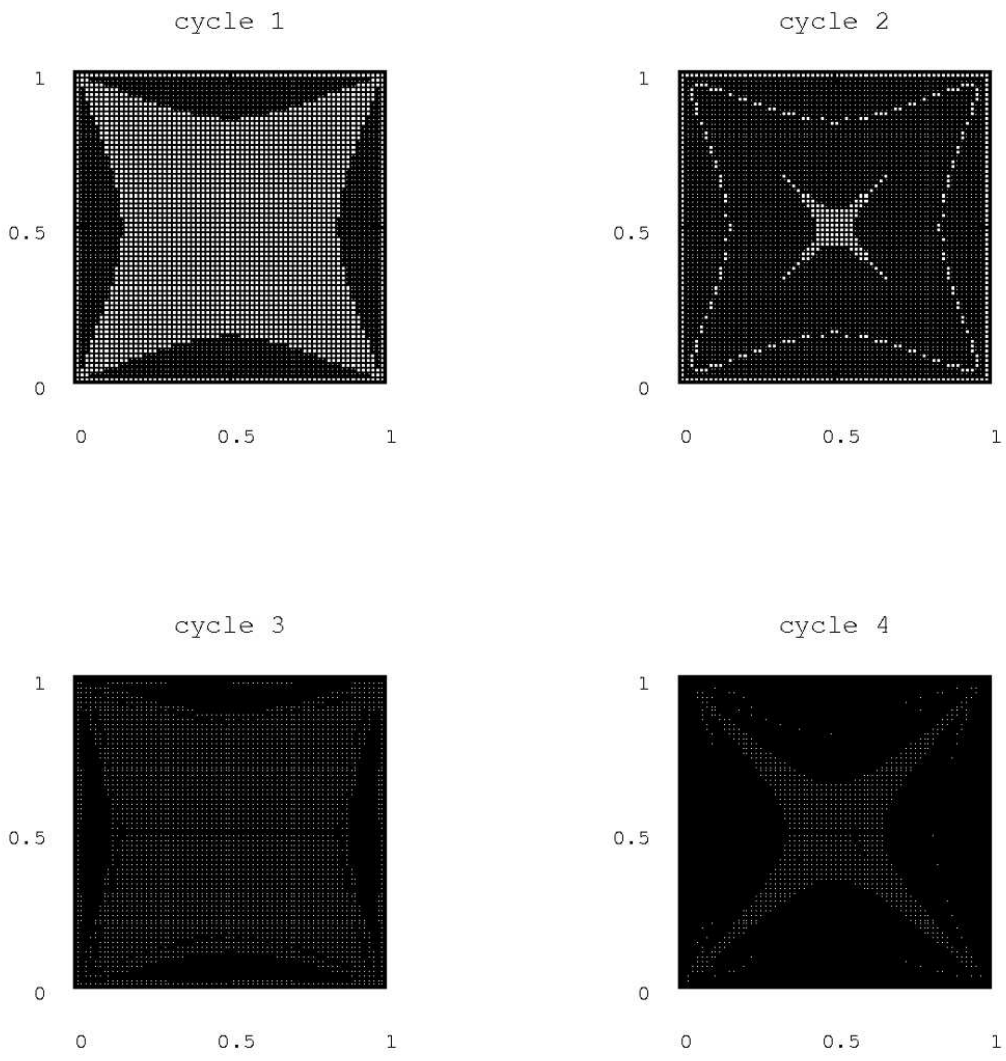

Figure IV.56: Adaptively refined grids.

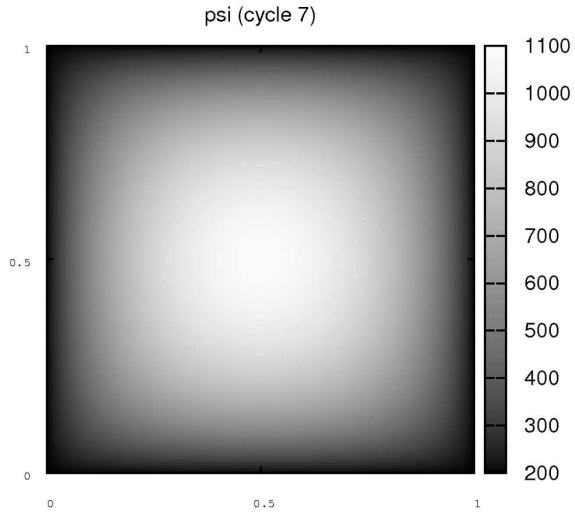

Figure IV.57: The solution of the considered problem.

The following table IV.36 shows the results of one run of our algorithm:

cycle	# active cells	# dofs	a-posteriori-estimate	ratio
0	7783	8180	1.2206e+02	inf
1	14788	15349	1.0096e+02	0.8271
2	28099	30166	6.6559e+01	0.6593
3	53389	54849	5.3681e+01	0.8065
4	101440	105418	3.8222e+01	0.7120
5	192739	196208	2.7900e+01	0.7300
6	365893	373228	2.0964e+01	0.7514
7	695170	703363	1.4430e+01	0.6883

Table IV.36: The convergence of one run of our algorithm for the considered problem.

We see the decrease of the estimator by the factor $1/\sqrt{2}$, which indicates the expected order $O(n_{dofs}^{-1/2})$.

IV.3.1.2 Plain surface and vertical upward velocity

We consider the Reynolds problem (I.77) with the upper surface given by (IV.8). The sequence of refined grids is shown in figure IV.58 and the final solution in figure IV.59.

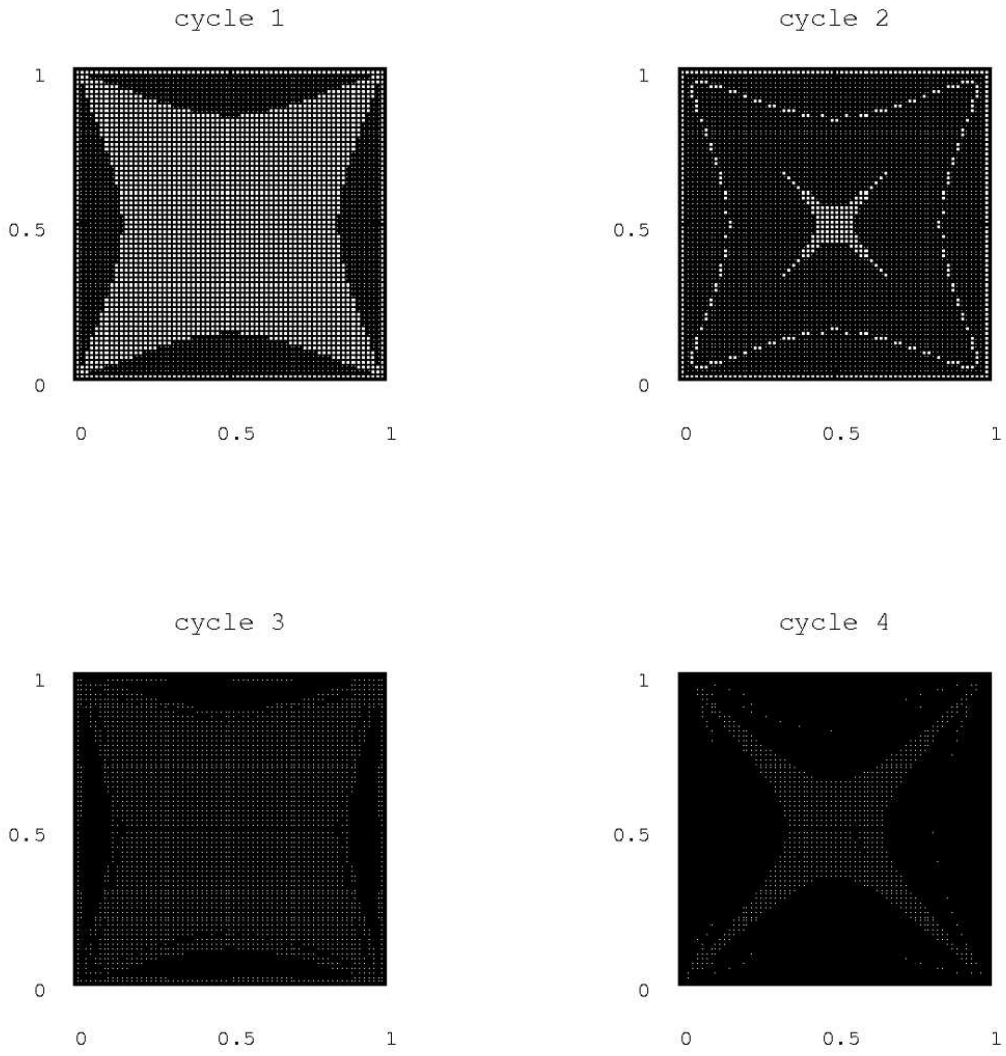

Figure IV.58: Adaptively refined grids.

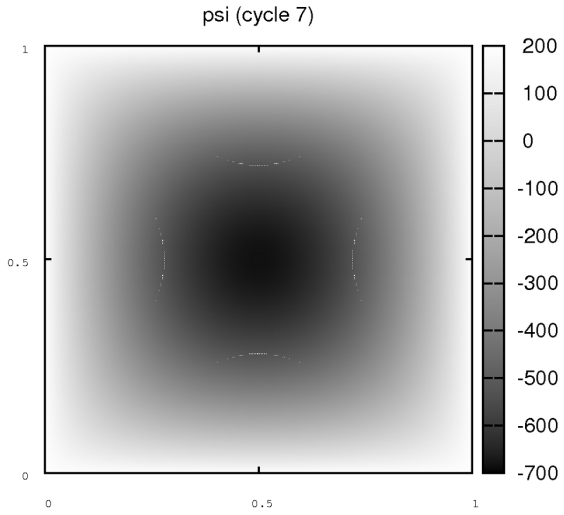

Figure IV.59: The solution of the considered problem.

The following table IV.37 shows the results of one run of our algorithm:

cycle	# active cells	# dofs	a-posteriori-estimate	ratio
0	7783	8180	1.2206e+02	inf
1	14788	15349	1.0096e+02	0.8271
2	28099	30166	6.6559e+01	0.6593
3	53389	54847	5.3681e+01	0.8065
4	101440	105413	3.8221e+01	0.7120
5	192739	196212	2.7901e+01	0.7300
6	365899	373223	2.0964e+01	0.7514
7	695179	703408	1.4430e+01	0.6883

Table IV.37: The convergence of one run of our algorithm for the considered problem.

We see almost exactly the results of the last section, because we consider a symmetric problem, as far as we do not allow cavitation. The decrease of the estimator by the factor $1/\sqrt{2}$, which indicates the expected order $O(n_{dofs}^{-1/2})$.

IV.3.1.3 Plain surface and horizontal velocity

We consider the Reynolds problem (I.77) with the upper surface given by (IV.9). The sequence of refined grids is shown in figure IV.60 and the final solution in figure IV.61.

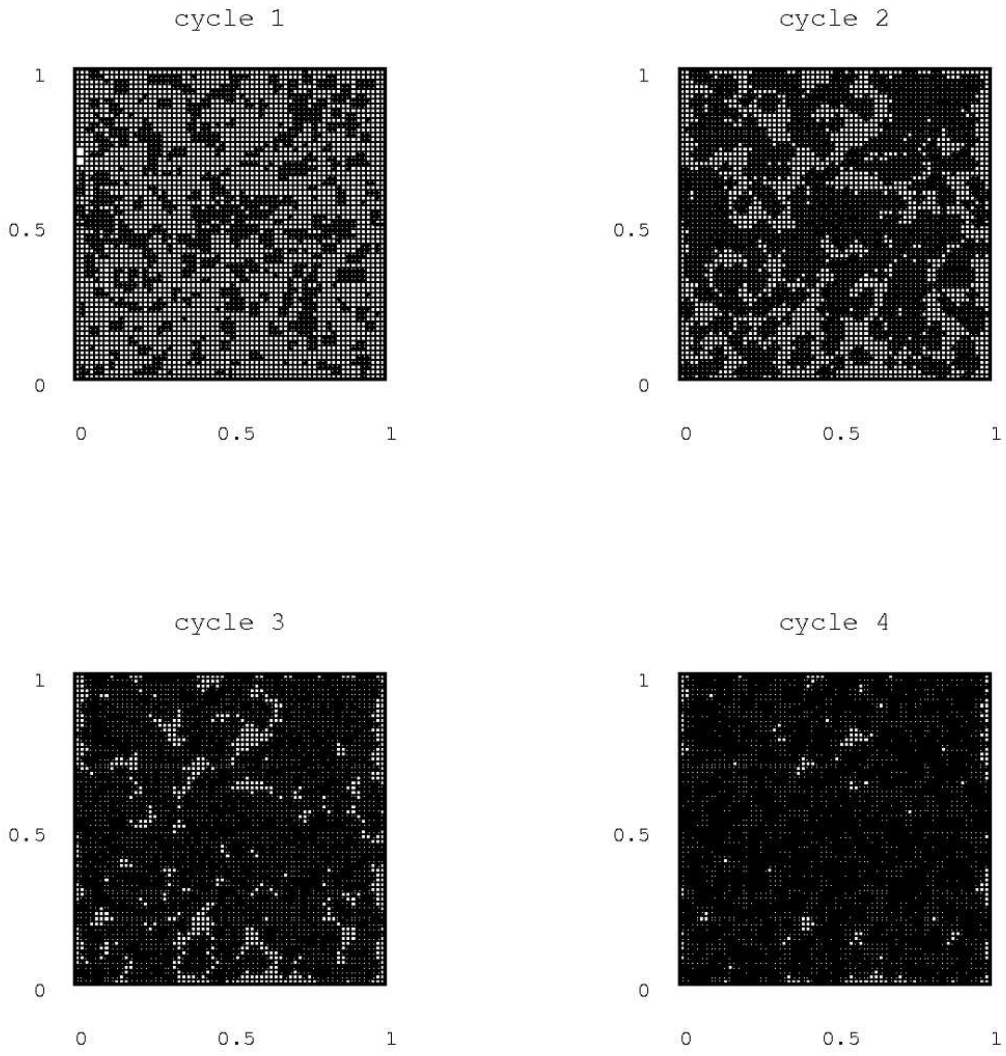

Figure IV.60: Adaptively refined grids.

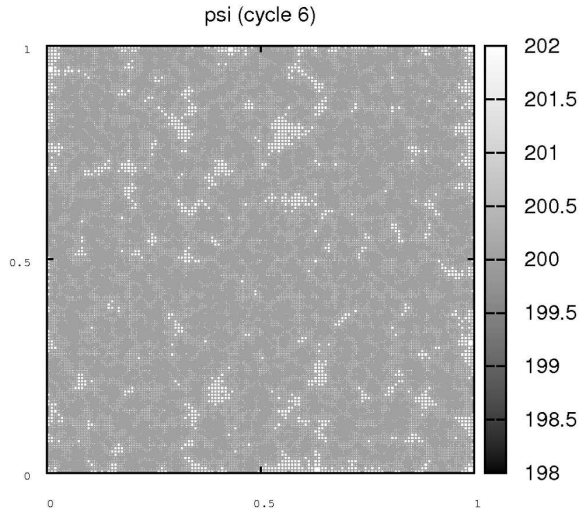

Figure IV.61: The solution of the considered problem.

The following table IV.38 shows the results of one run of our algorithm:

cycle	# active cells	# dofs	a-posteriori-estimate	ratio
0	7777	8915	9.0397e-12	inf
1	15109	18091	4.8579e-05	5373940.4810
2	30685	37268	8.2058e-05	1.6892
3	61021	73390	1.2200e-04	1.4868
4	123142	148322	1.6785e-04	1.3758
5	253699	305692	2.4323e-04	1.4491
6	504409	606014	3.5228e-04	1.4483
7	1038358	1250391	4.9273e-04	1.3987

Table IV.38: The convergence of one run of our algorithm for the considered problem.

The behaviour of the error estimate and especially the ratio seems a bit awkward. But it is obvious, that the estimate cannot decrease, because the correct solution is constant and cannot be further optimized and basicly remains at a constant order. The only fluctuations (and expecially the steep increase in the first step) can be explained by computational uncertainties.

IV.3.1.4 Steep surface and vertical downward velocity

We consider the Reynolds problem (I.77) with the upper surface given by (IV.10). The sequence of refined grids is shown in figure IV.62 and the final solution in figure IV.63.

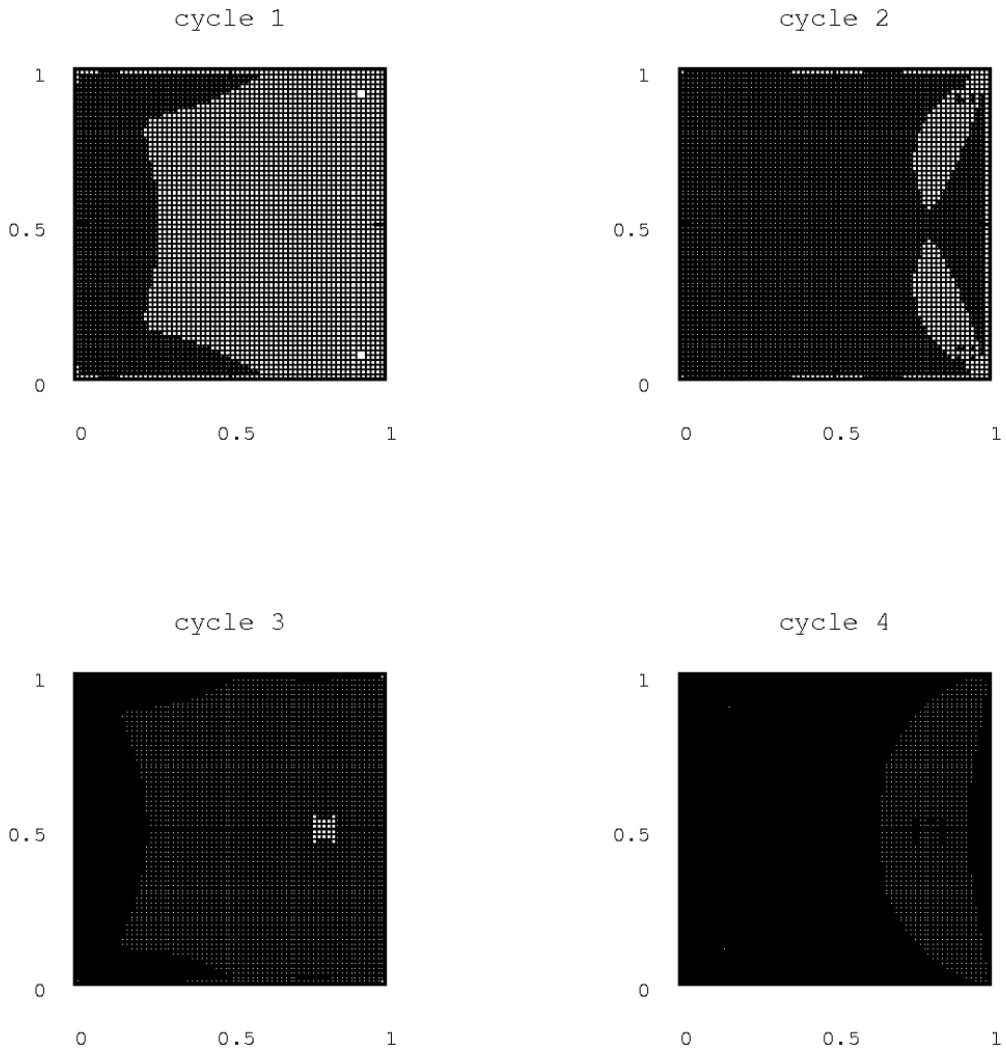

Figure IV.62: Adaptively refined grids.

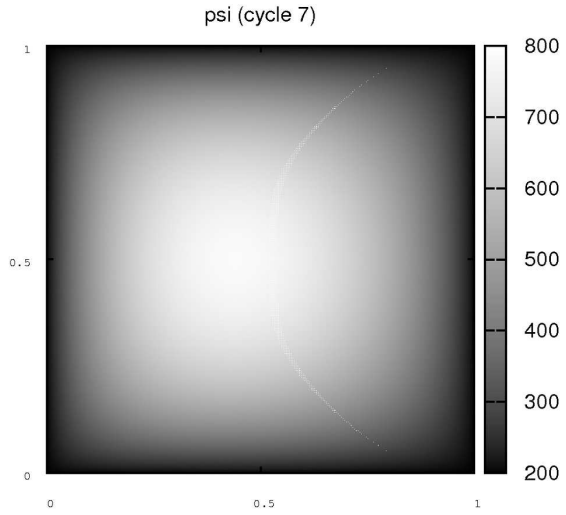

Figure IV.63: The solution of the considered problem.

The following table IV.39 shows the results of one run of our algorithm:

cycle	# active cells	# dofs	a-posteriori-estimate	ratio
0	7777	8039	8.4418e+01	inf
1	14779	15124	6.5770e+01	0.7791
2	28009	28599	4.5545e+01	0.6925
3	53206	53938	3.4981e+01	0.7680
4	100765	102019	2.4846e+01	0.7103
5	190837	192761	1.8357e+01	0.7388
6	360223	364025	1.3405e+01	0.7302
7	680902	685158	9.6615e+00	0.7208

Table IV.39: The convergence of one run of our algorithm for the considered problem.

We see the decrease of the estimator by the factor $1/\sqrt{2}$, which indicates the expected order $O(n_{dofs}^{-1/2})$.

IV.3.1.5 Steep surface and vertical upward velocity

We consider the Reynolds problem (I.77) with the upper surface given by (IV.11). The sequence of refined grids is shown in figure IV.64 and the final solution in figure IV.65.

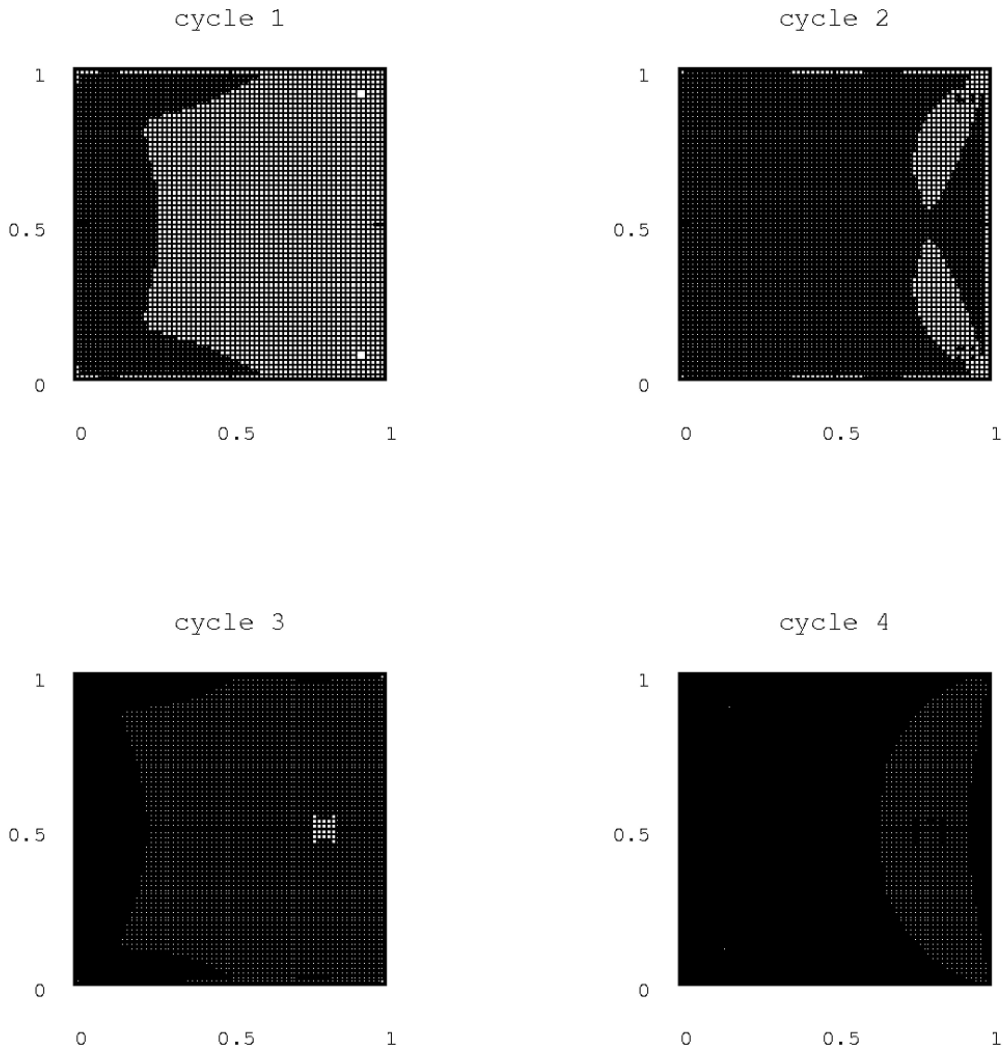

Figure IV.64: Adaptively refined grids.

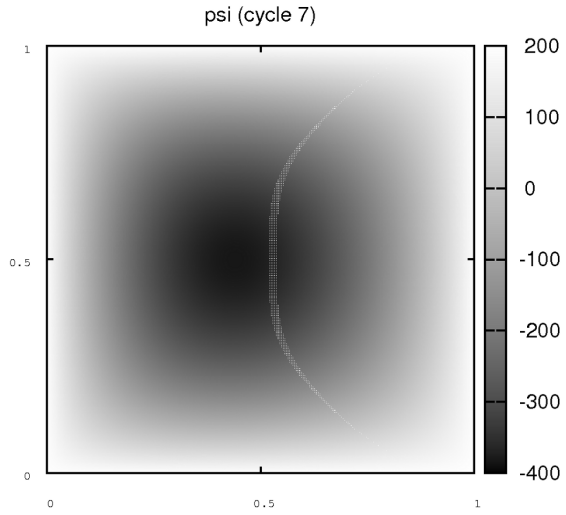

Figure IV.65: The solution of the considered problem.

The following table IV.40 shows the results of one run of our algorithm:

cycle	# active cells	# dofs	a-posteriori-estimate	ratio
0	7777	8039	8.4418e+01	inf
1	14779	15124	6.5768e+01	0.7791
2	28009	28599	4.5542e+01	0.6925
3	53200	53934	3.4984e+01	0.7682
4	100753	102010	2.4848e+01	0.7103
5	190816	192743	1.8359e+01	0.7389
6	360196	363999	1.3404e+01	0.7301
7	680548	684823	9.6701e+00	0.7214

Table IV.40: The convergence of one run of our algorithm for the considered problem.

We see the decrease of the estimator by the factor $1/\sqrt{2}$, which indicates the expected order $O(n_{dofs}^{-1/2})$.

IV.3.1.6 Steep surface and horizontal velocity against the direction of the surfaces gradient

We consider the Reynolds problem (I.77) with the surface given by (IV.13). The sequence of refined grids is shown in figure IV.66 and the final solution in figure IV.67.

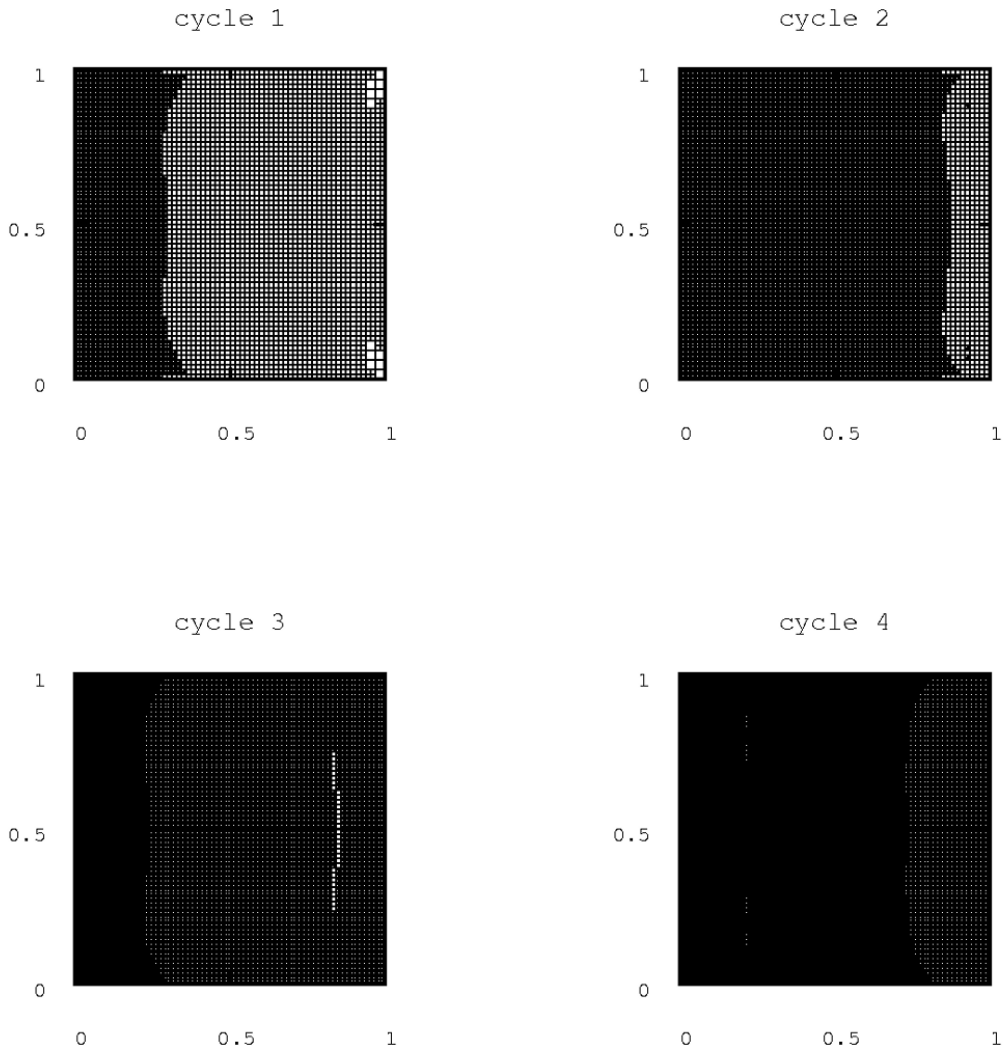

Figure IV.66: Adaptively refined grids.

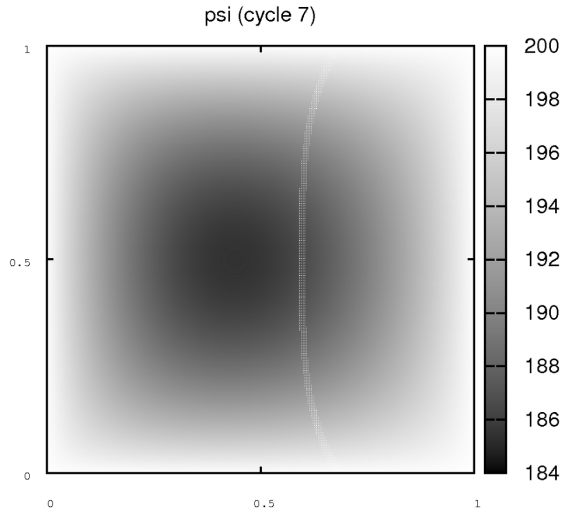

Figure IV.67: The solution of the considered problem.

The following table IV.41 shows the results of one run of our algorithm:

cycle	# active cells	# dofs	a-posteriori-estimate	ratio
0	7747	7973	5.0186e+00	inf
1	14722	14985	4.0404e+00	0.8051
2	27874	28345	2.7538e+00	0.6816
3	52798	53370	2.1335e+00	0.7748
4	99568	100666	1.5232e+00	0.7140
5	188017	189296	1.1627e+00	0.7633
6	353950	356432	8.7326e-01	0.7511
7	666985	669493	6.7544e-01	0.7735

Table IV.41: The convergence of one run of our algorithm for the considered problem.

We see the decrease of the estimator by the factor $1/\sqrt{2}$, which indicates the expected order $O(n_{dofs}^{-1/2})$.

IV.3.1.7 Steep surface and horizontal velocity in the direction of the surface's gradient

We consider the Reynolds problem (I.77) with the surface given by (IV.12). The sequence of refined grids is shown in figure IV.68 and the final solution in figure IV.69.

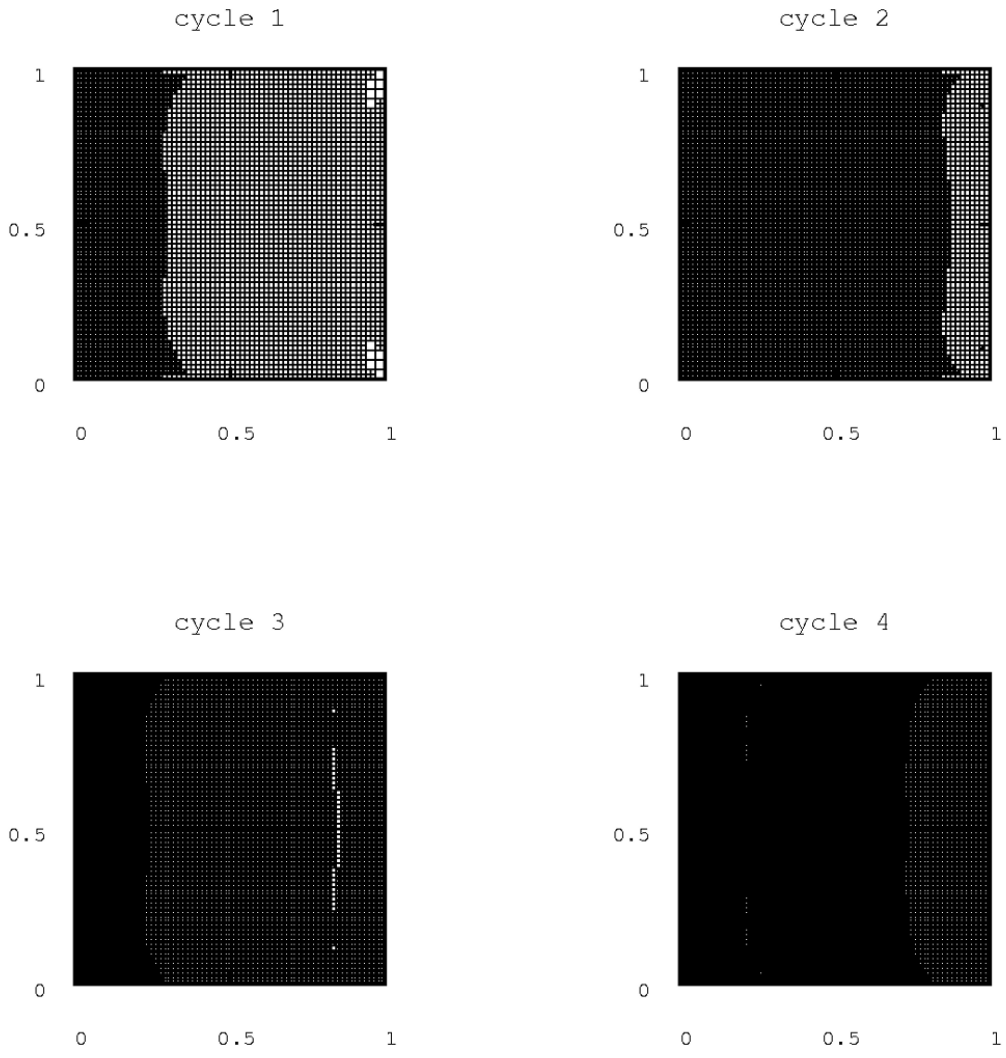

Figure IV.68: Adaptively refined grids.

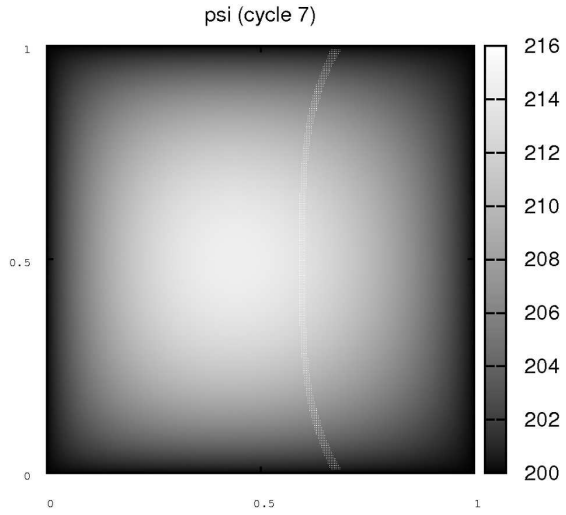

Figure IV.69: The solution of the considered problem.

The following table IV.42 shows the results of one run of our algorithm:

cycle	# active cells	# dofs	a-posteriori-estimate	ratio
0	7747	7973	5.0186e+00	inf
1	14722	14983	4.0417e+00	0.8053
2	27865	28339	2.7547e+00	0.6816
3	52762	53342	2.1356e+00	0.7753
4	99523	100638	1.5246e+00	0.7139
5	188374	189612	1.1627e+00	0.7626
6	354610	357066	8.7132e-01	0.7494
7	668851	671329	6.7516e-01	0.7749

Table IV.42: The convergence of one run of our algorithm for the considered problem.

Again see the decrease of the estimator by the factor $1/\sqrt{2}$, which indicates the expected order $O(n_{dofs}^{-1/2})$..

IV.3.1.8 Steep surface and horizontal velocity perpendicular to the surface's gradient

We consider the Reynolds problem (I.77) with the surface given by (IV.14). The sequence of refined grids is shown in figure IV.70 and the final solution in figure IV.71.

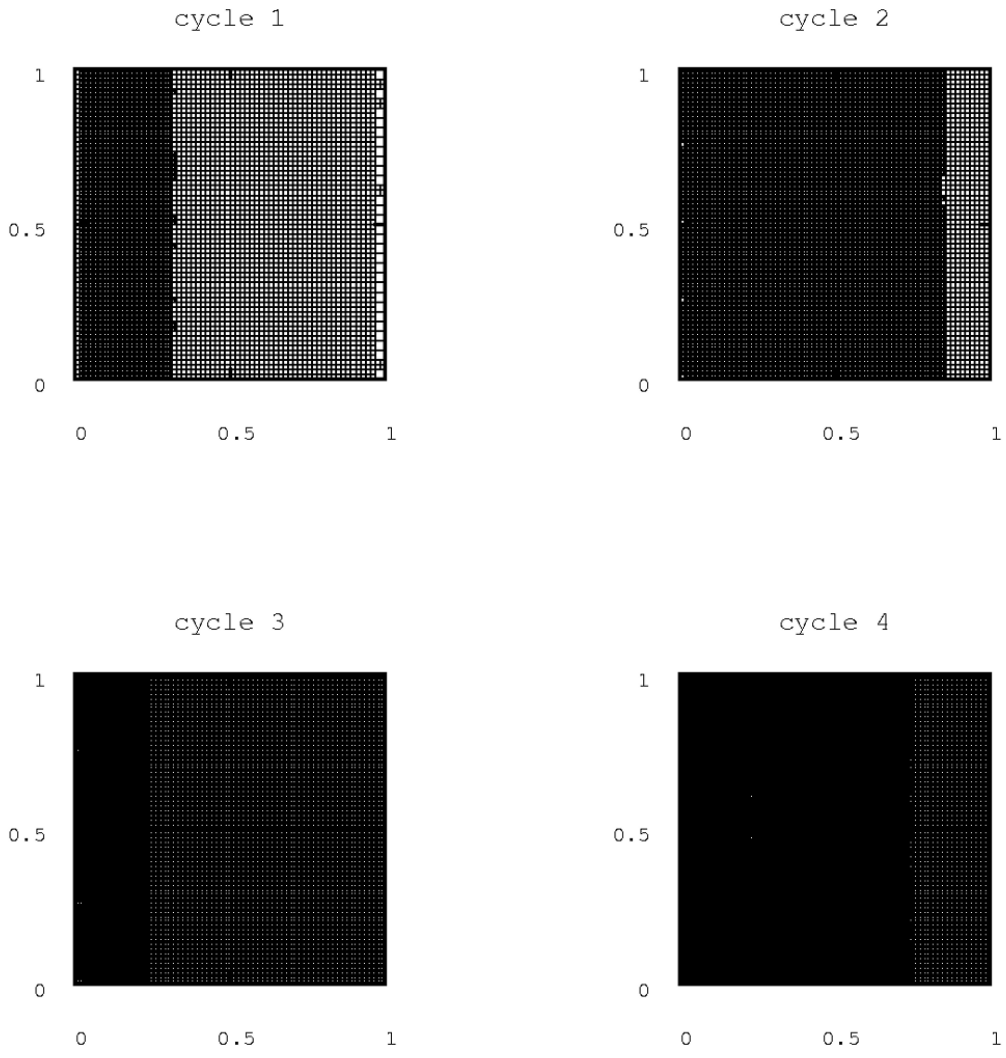

Figure IV.70: Adaptively refined grids.

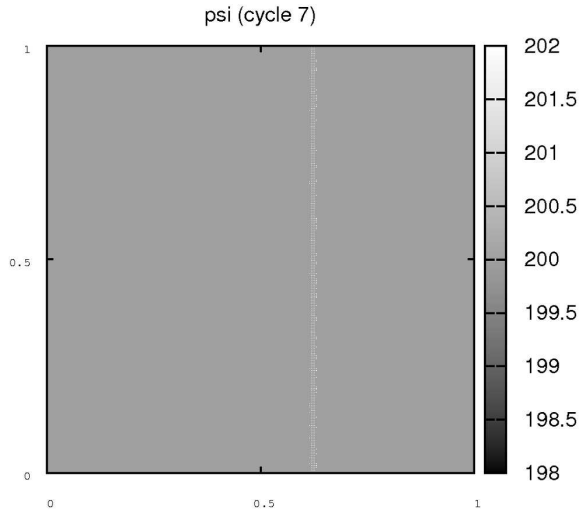

Figure IV.71: The solution of the considered problem.

The following table IV.43 shows the results of one run of our algorithm:

cycle	# active cells	# dofs	a-posteriori-estimate	ratio
0	7699	7920	3.4038e-01	inf
1	14629	14882	3.3826e-01	0.9938
2	27796	28233	3.4107e-01	1.0083
3	52798	53299	3.4139e-01	1.0010
4	99664	100791	3.4143e-01	1.0001
5	188269	189551	3.4204e-01	1.0018
6	355183	357404	3.4217e-01	1.0004
7	669220	671701	3.4266e-01	1.0014

Table IV.43: The convergence of one run of our algorithm for the considered problem.

As already in section IV.3.1.3 the solution is constant and cannot be optimized, what results in a constant but low error estimate .

IV.3.1.9 Wave surface and vertical downward velocity

We consider the Reynolds problem (I.77) with the upper surface given by (IV.15). The sequence of refined grids is shown in figure IV.72 and the final solution in figure IV.73.

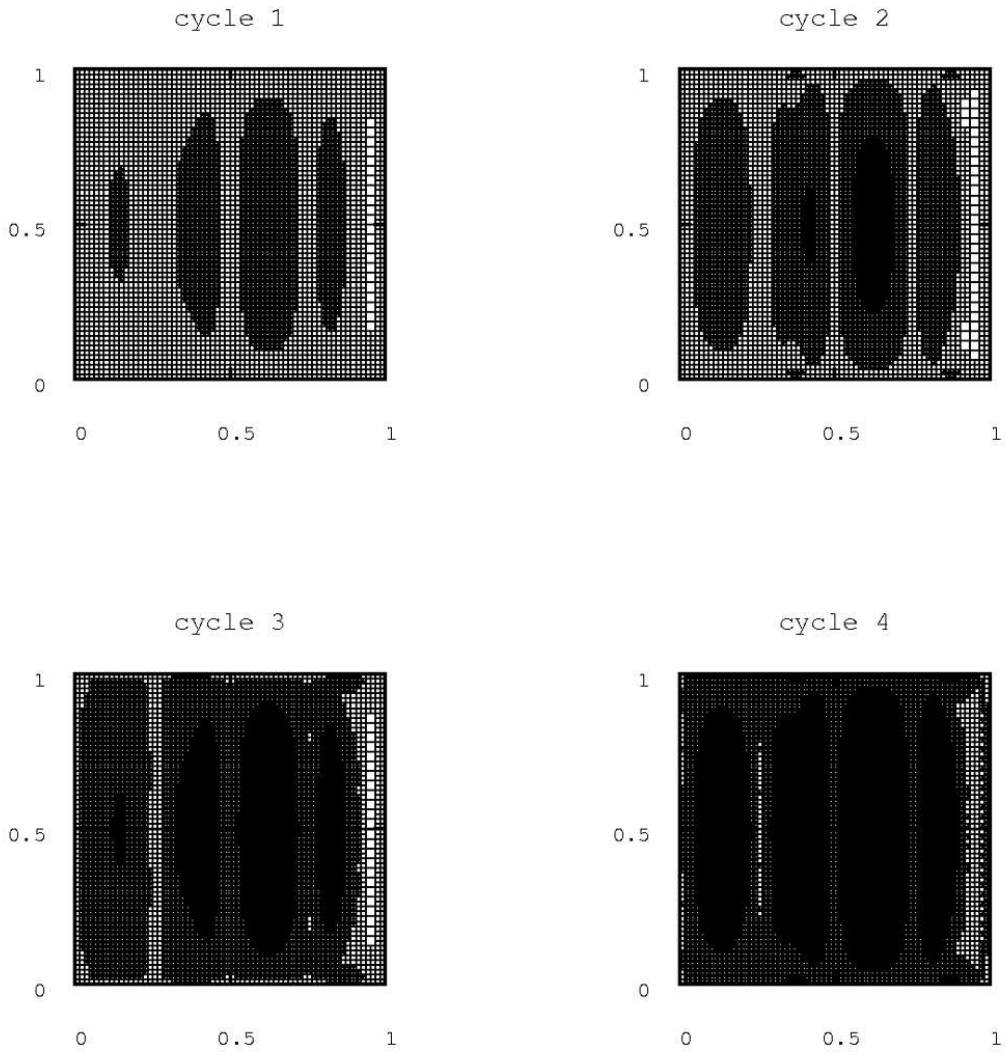

Figure IV.72: Adaptively refined grids.

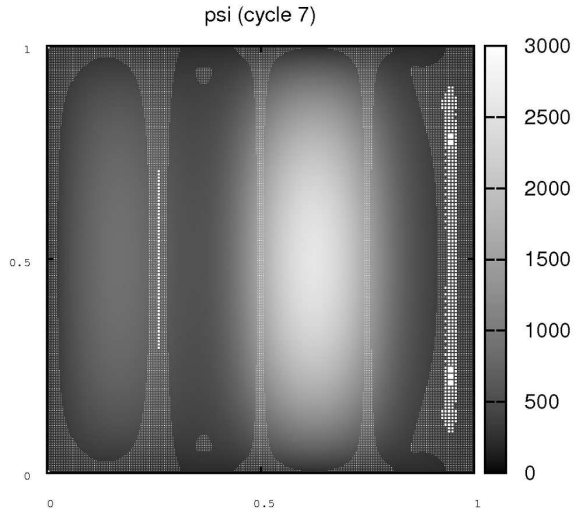

Figure IV.73: The solution of the considered problem.

The following table IV.44 shows the results of one run of our algorithm:

cycle	# active cells	# dofs	a-posteriori-estimate	ratio
0	7717	8066	7.0753e+02	inf
1	14629	15221	4.3339e+02	0.6125
2	27796	28534	3.1732e+02	0.7322
3	52813	53976	2.2682e+02	0.7148
4	100345	101992	1.6856e+02	0.7432
5	190675	192904	1.2068e+02	0.7159
6	361789	365161	8.9117e+01	0.7385
7	686368	691780	6.4382e+01	0.7224

Table IV.44: The convergence of one run of our algorithm for the considered problem.

We see the decrease of the estimator by the factor $1/\sqrt{2}$, which indicates the expected order $O(n_{dofs}^{-1/2})$.

IV.3.1.10 Wave surface and vertical upward velocity

We consider the Reynolds problem (I.77) with the upper surface given by (IV.16). The sequence of refined grids is shown in figure IV.74 and the final solution in figure IV.75.

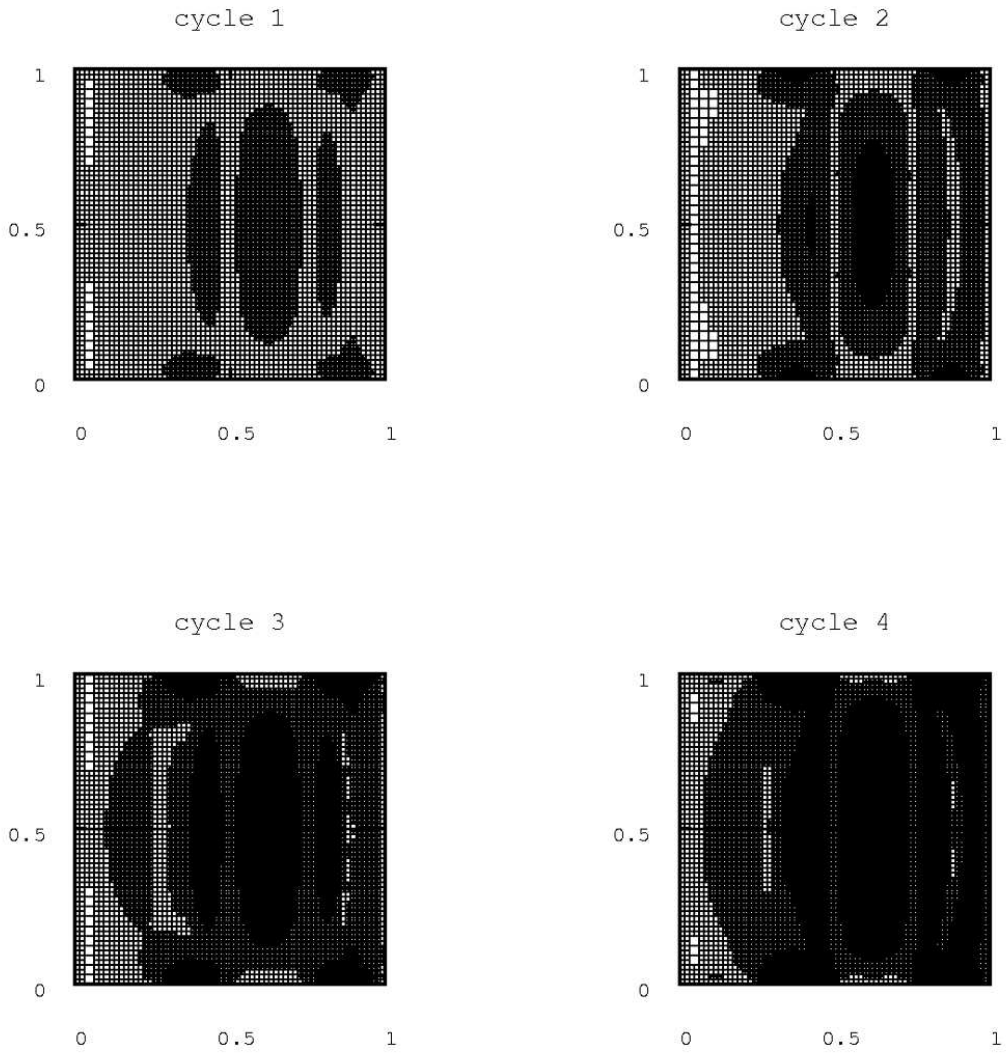

Figure IV.74: Adaptively refined grids.

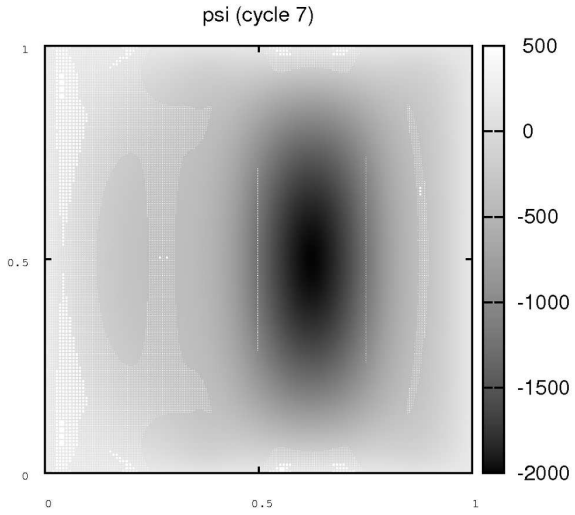

Figure IV.75: The solution of the considered problem.

The following table IV.45 shows the results of one run of our algorithm:

cycle	# active cells	# dofs	a-posteriori-estimate	ratio
0	7729	8112	5.1594e+02	inf
1	14590	15269	3.0637e+02	0.5938
2	27724	28644	2.2246e+02	0.7261
3	52666	53984	1.5826e+02	0.7114
4	100066	101794	1.1836e+02	0.7479
5	190114	192821	8.4082e+01	0.7104
6	360697	364395	6.2929e+01	0.7484
7	684409	690819	4.5122e+01	0.7170

Table IV.45: The convergence of one run of our algorithm for the considered problem.

We see the decrease of the estimator by the factor $1/\sqrt{2}$, which indicates the expected order $O(n_{dofs}^{-1/2})$.

IV.3.1.11 Wave surface and horizontal velocity

We consider the Reynolds problem (I.77) with the upper surface given by (IV.17). The sequence of refined grids is shown in figure IV.76 and the final solution in figure IV.77.

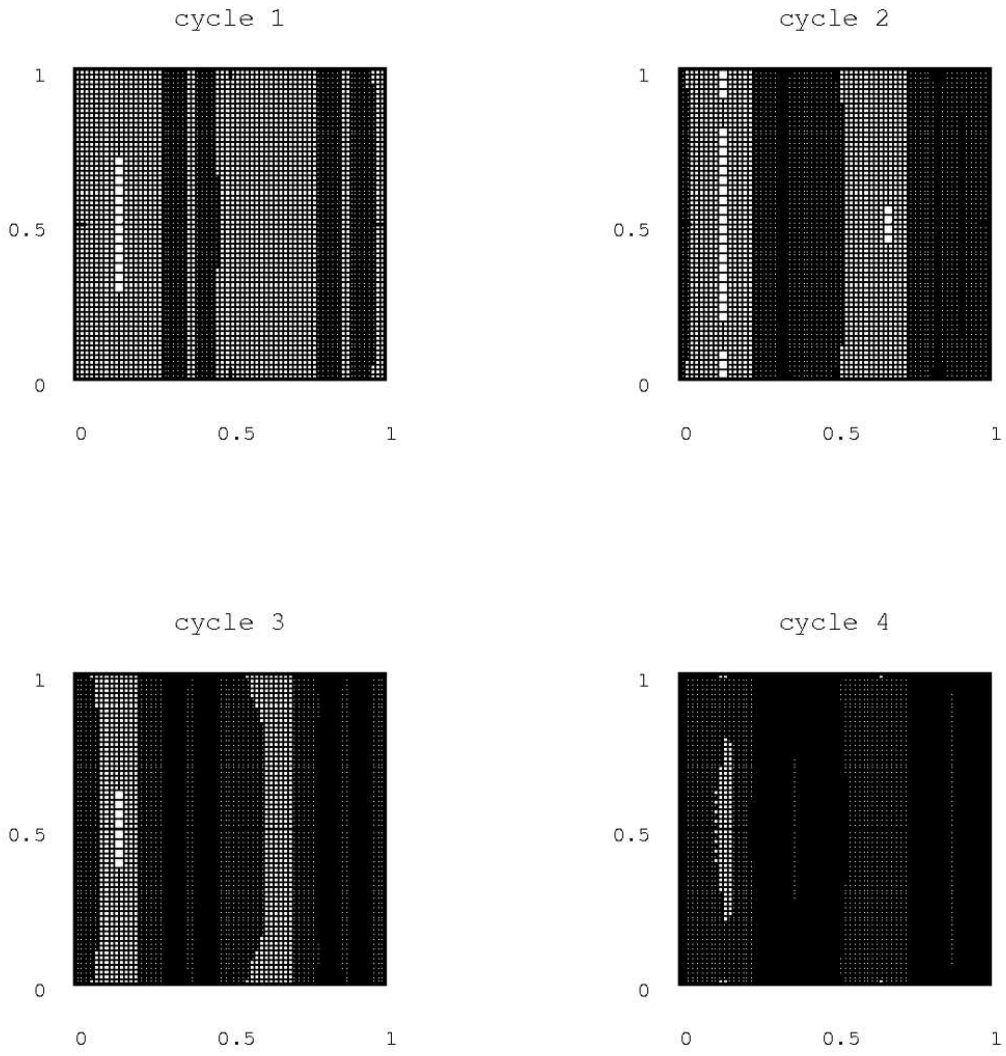

Figure IV.76: Adaptively refined grids.

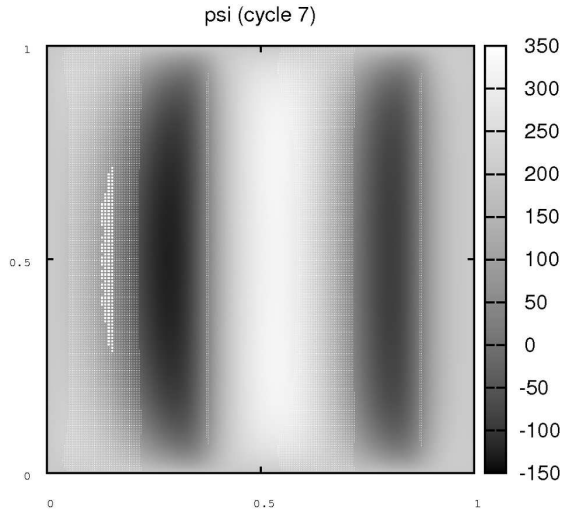

Figure IV.77: The solution of the considered problem.

The following table IV.46 shows the results of one run of our algorithm:

cycle	# active cells	# dofs	a-posteriori-estimate	ratio
0	7741	8161	8.3075e+02	inf
1	14662	15564	5.2266e+02	0.6291
2	27859	28798	3.9513e+02	0.7560
3	52933	54709	2.7206e+02	0.6885
4	100573	102448	2.0591e+02	0.7568
5	191089	194164	1.4606e+02	0.7094
6	362872	367127	1.0695e+02	0.7322
7	689458	694188	7.8311e+01	0.7322

Table IV.46: The convergence of one run of our algorithm for the considered problem.

We see the decrease of the estimator by the factor $1/\sqrt{2}$, which indicates the expected order $O(n_{dofs}^{-1/2})$.

IV.3.1.12 Hilly surface and vertical downward velocity

We consider the Reynolds problem (I.77) with the upper surface given by (IV.18). The sequence of refined grids is shown in figure IV.78 and the final solution in figure IV.79.

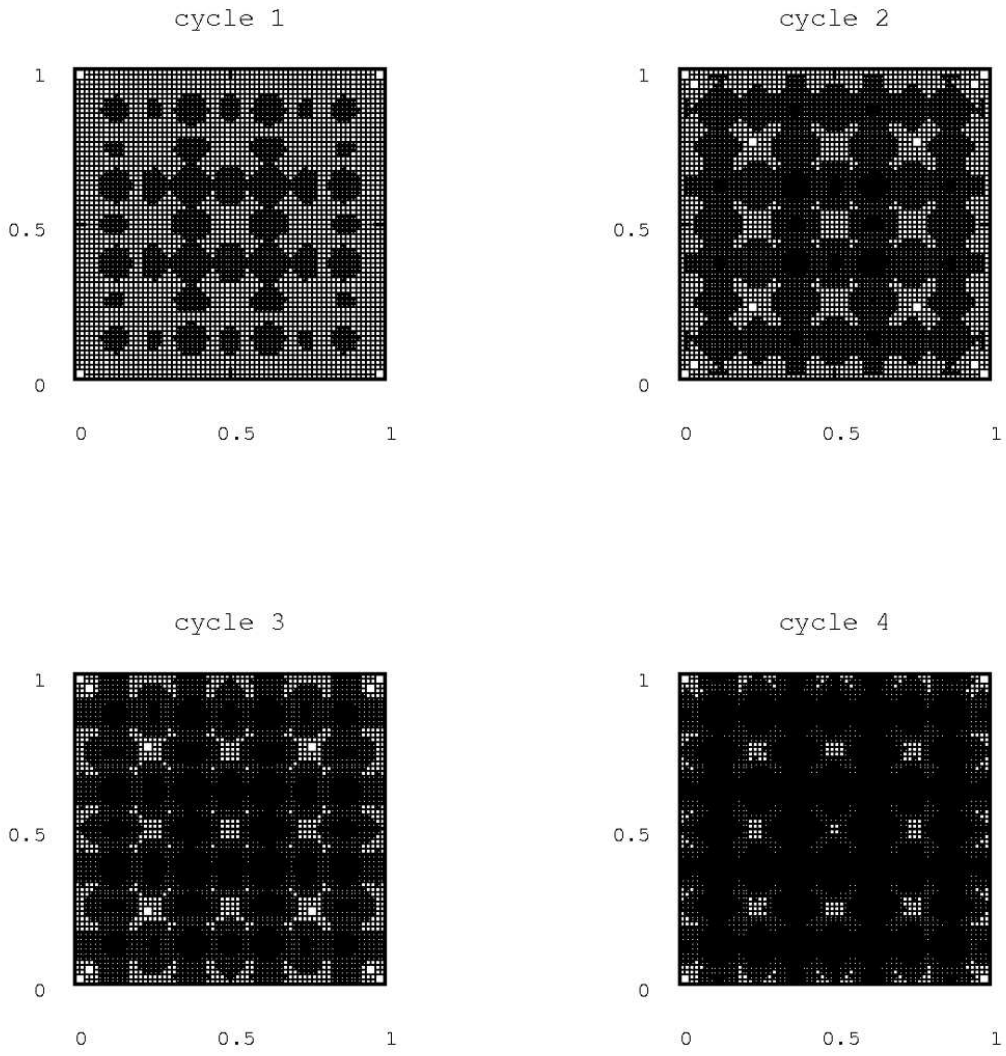

Figure IV.78: Adaptively refined grids.

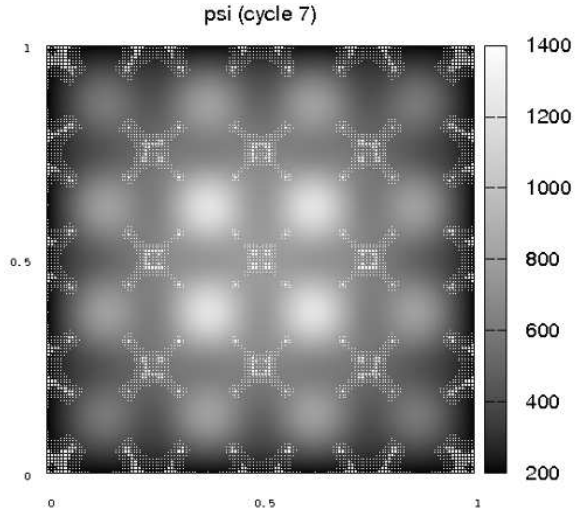

Figure IV.79: The solution of the considered problem.

The following table IV.47 shows the results of one run of our algorithm:

cycle	# active cells	# dofs	a-posteriori-estimate	ratio
0	7717	8066	7.0753e+02	inf
1	14629	15221	4.3339e+02	0.6125
2	27796	28534	3.1732e+02	0.7322
3	52813	53976	2.2682e+02	0.7148
4	100345	101992	1.6856e+02	0.7432
5	190675	192904	1.2068e+02	0.7159
6	361789	365161	8.9117e+01	0.7385
7	686368	691780	6.4382e+01	0.7224

Table IV.47: The convergence of one run of our algorithm for the considered problem.

We see the decrease of the estimator by the factor $1/\sqrt{2}$, which indicates the expected order $O(n_{dofs}^{-1/2})$.

IV.3.1.13 Hilly surface and vertical upward velocity

We consider the Reynolds problem (I.77) with the upper surface given by (IV.19). The sequence of refined grids is shown in figure IV.80 and the final solution in figure IV.81.

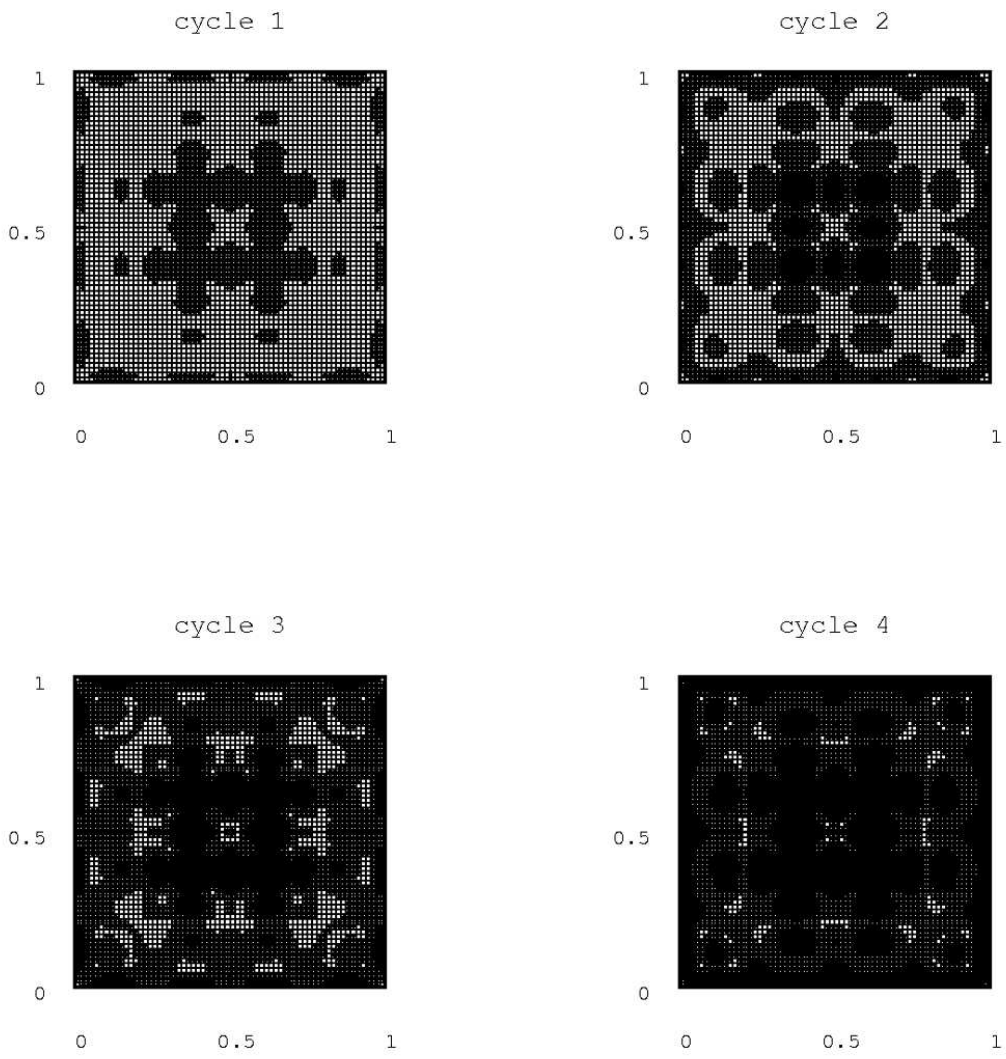

Figure IV.80: Adaptively refined grids.

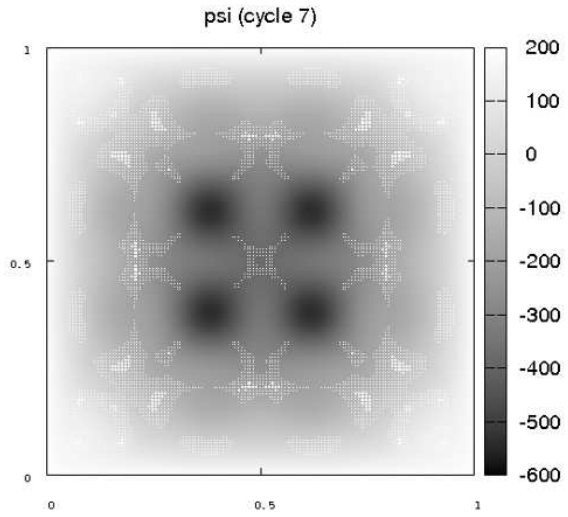

Figure IV.81: The solution of the considered problem.

The following table IV.48 shows the results of one run of our algorithm:

cycle	# active cells	# dofs	a-posteriori-estimate	ratio
0	7729	8112	5.1594e+02	inf
1	14590	15269	3.0637e+02	0.5938
2	27724	28644	2.2246e+02	0.7261
3	52666	53984	1.5826e+02	0.7114
4	100066	101794	1.1836e+02	0.7479
5	190114	192821	8.4082e+01	0.7104
6	360697	364395	6.2929e+01	0.7484
7	684409	690819	4.5122e+01	0.7170

Table IV.48: The convergence of one run of our algorithm for the considered problem.

We see the decrease of the estimator by the factor $1/\sqrt{2}$, which indicates the expected order $O(n_{dofs}^{-1/2})$.

IV.3.1.14 Hilly surface and horizontal velocity

We consider the Reynolds problem (I.77) with the upper surface given by (IV.20). The sequence of refined grids is shown in figure IV.82 and the final solution in figure IV.83.

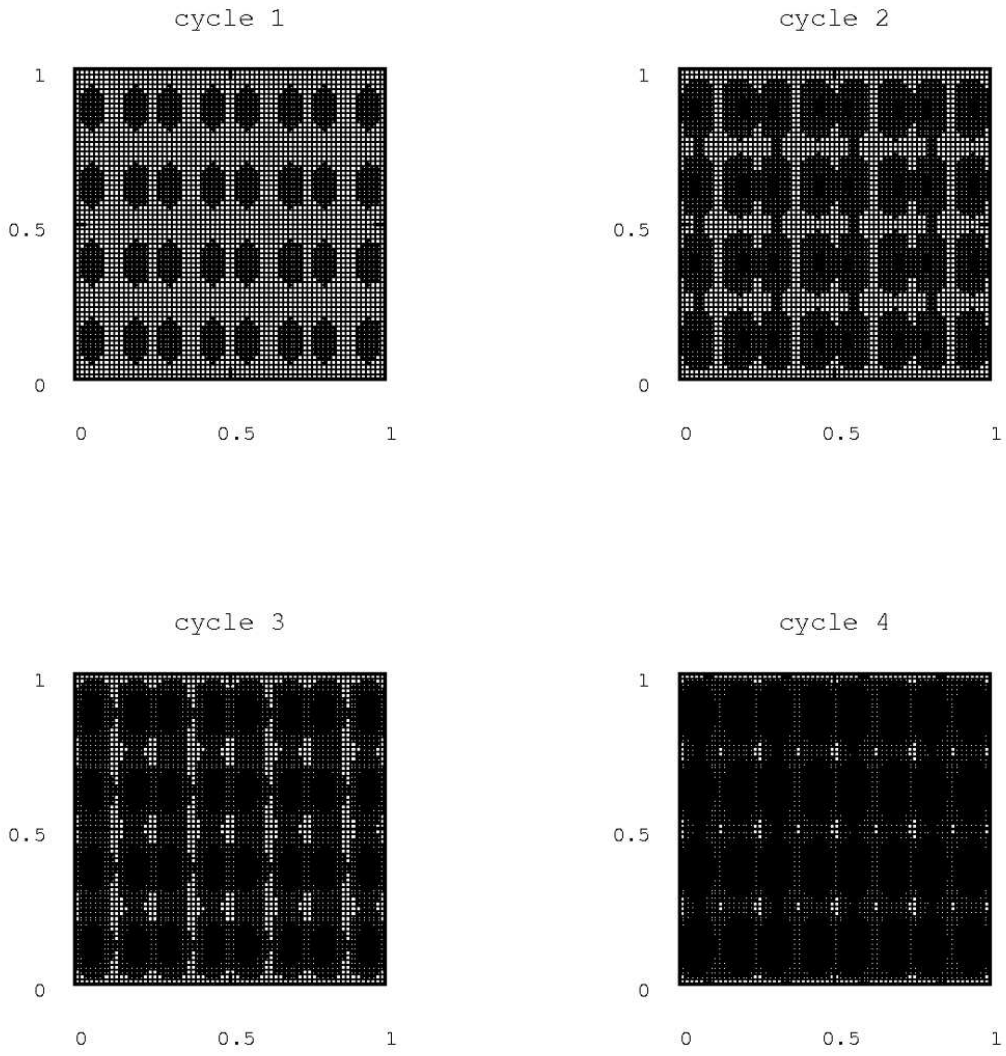

Figure IV.82: Adaptively refined grids.

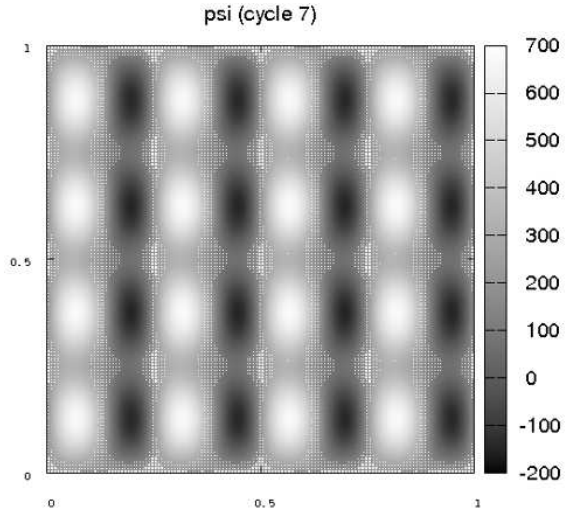

Figure IV.83: The solution of the considered problem.

The following table IV.49 shows the results of one run of our algorithm:

cycle	# active cells	# dofs	a-posteriori-estimate	ratio
0	7741	8161	8.3075e+02	inf
1	14662	15564	5.2266e+02	0.6291
2	27859	28798	3.9513e+02	0.7560
3	52933	54709	2.7206e+02	0.6885
4	100573	102448	2.0591e+02	0.7568
5	191089	194164	1.4606e+02	0.7094
6	362872	367127	1.0695e+02	0.7322
7	689458	694188	7.8311e+01	0.7322

Table IV.49: The convergence of one run of our algorithm for the considered problem.

We see the decrease of the estimator by the factor $1/\sqrt{2}$, which indicates the expected order $O(n_{dofs}^{-1/2})$.

Most calculations in sections IV.3.1.1–IV.3.1.14 show a decrease of the error estimate, given in theorem III.16, of the expected order $O(n_{dofs}^{1/2})$. The only exceptions are the plain or steep gap-width with a velocity perpendicular to the gap-width's gradient (sections IV.3.1.3 and IV.3.1.8), which have constant solutions and thus do not result in an decreasing error estimate. For the more sophisticated gap-shapes, the wave– and hill–gaps (sections IV.3.1.9–IV.3.1.14), one sees that the grid refinement, controlled by the estimate of theorem III.16, takes place around the most wide and most narrow parts of the gap, if the surface's velocity is just in vertical direction (figures IV.72, IV.74, IV.78 and IV.80). For the horizontal velocity (section IV.3.1.11 and IV.3.1.14) we see, that the grid refinment is concentrated on the narrow regions for the wave-shaped gap (see figure IV.76). In the case of a hilly gap we observe different behaviours in the directions parallel and perpendicular to the surface's movement. In the latter one (the y-direction in figure IV.82) the main refinement takes place in the regions, where the surface's normal is parallel to direction of the surface's movement. The least refinement takes place, where the fluid's movement is parallel to the surface.

IV.3.2 SubStokes Model without Cavitation

In the following sections we always consider the SubStokes Problem (I.58) on the domain

$$\Omega = [0;1] \times [0;1]$$

with the Dirichlet boundary conditions

$$\psi|_{\partial\Omega} = 200.0$$

and the boundary condition (I.56) for χ. The surface- and velocity-data on the underside of the fluid film are zero:

$$z_0 = 0, \quad v(z_0) = 0$$

while the data on the upper side differ in each example.
All computations start on an initial grid of 64 cells and refine it adaptively using the estimator of theorem III.23 and a fixed-fraction strategy, as already done in section IV.3.1: We refine the 30% of the cells with the highest error per cell, which results in about doubling of the cells. Furthermore we coarsen 3% of the cells with the smallest error.
Additional to the pressure results, we print out the velocity field, although this is not in the focus of interest in this work.

IV.3.2.1 Plain surface and vertical downward velocity

We consider the SubStokes problem (I.58) with the upper surface given by (IV.7). The sequence of refined grids is shown in figure IV.84 and the solution for pressure and velocity in figure IV.85.

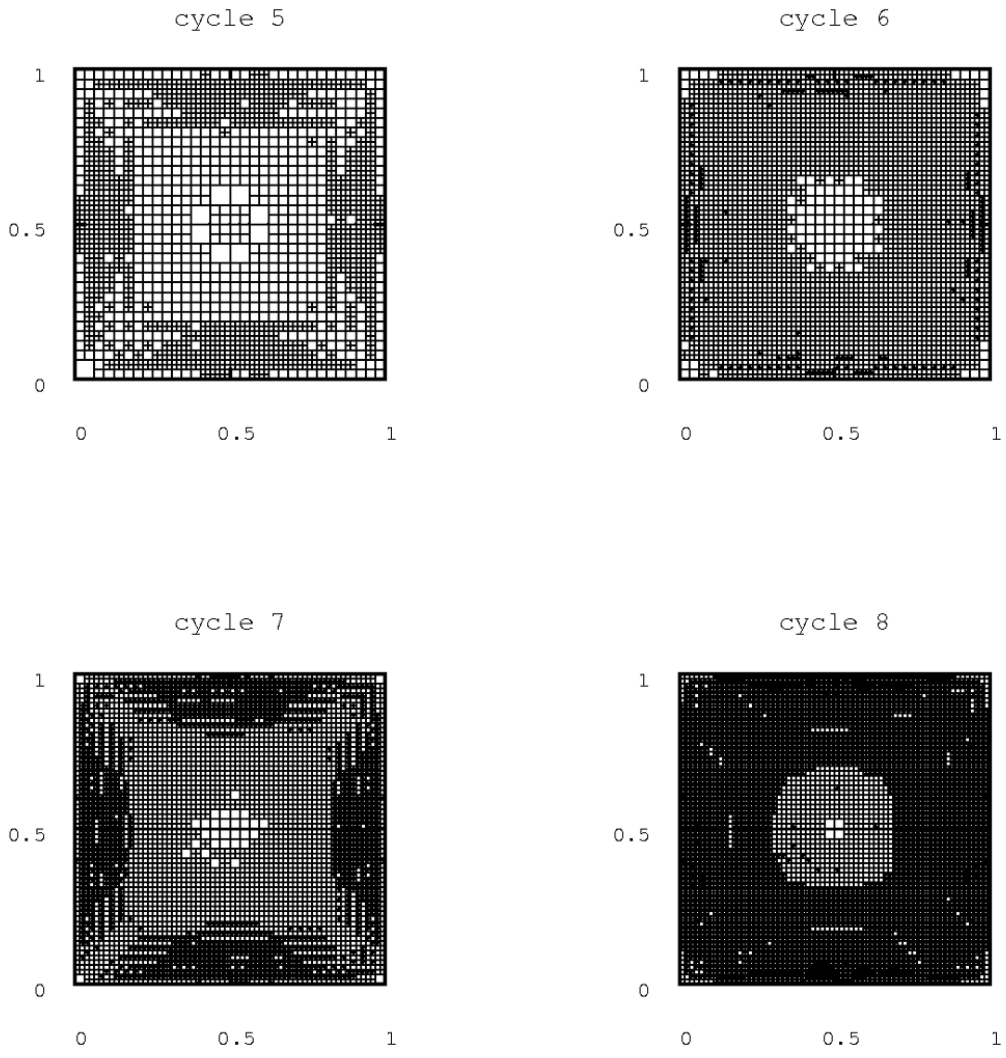

Figure IV.84: Adaptively refined grids.

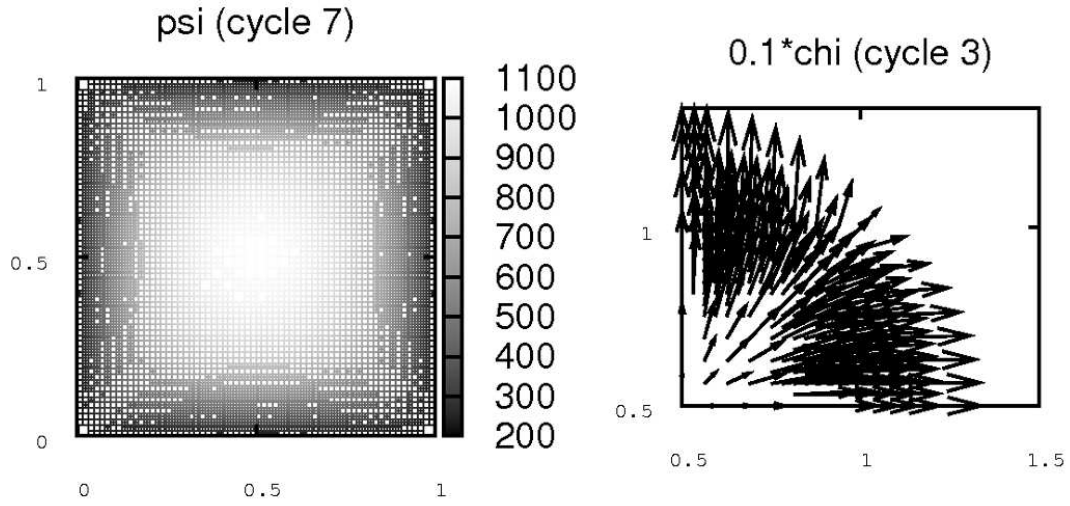

Figure IV.85: The solution of the considered problem. Due to symmetry we only show the velocity-field in one quarter of the domain.

The following table IV.50 shows the results of one run of our algorithm:

cycle	# active cells	# dofs	a-posteriori-estimate	ratio
0	124	483	4.0477e+02	inf
1	286	1059	2.6686e+02	0.6593
2	550	1965	2.0894e+02	0.7830
3	1138	3927	1.4059e+02	0.6729
4	2173	7452	1.0769e+02	0.7660
5	4363	14466	7.6128e+01	0.7069
6	8302	27651	5.6377e+01	0.7406
7	16339	53154	4.1621e+01	0.7383

Table IV.50: The convergence of one run of our algorithm for the considered problem.

We see the decrease of the estimator by the factor $1/\sqrt{2}$, which indicates the expected order $O(n_{dofs}^{-1/2})$.

IV.3.2.2 Plain surface and vertical upward velocity

We consider the SubStokes problem (I.58) with the upper surface given by (IV.8). The sequence of refined grids is shown in figure IV.86 and the solution for pressure and velocity in figure IV.87.

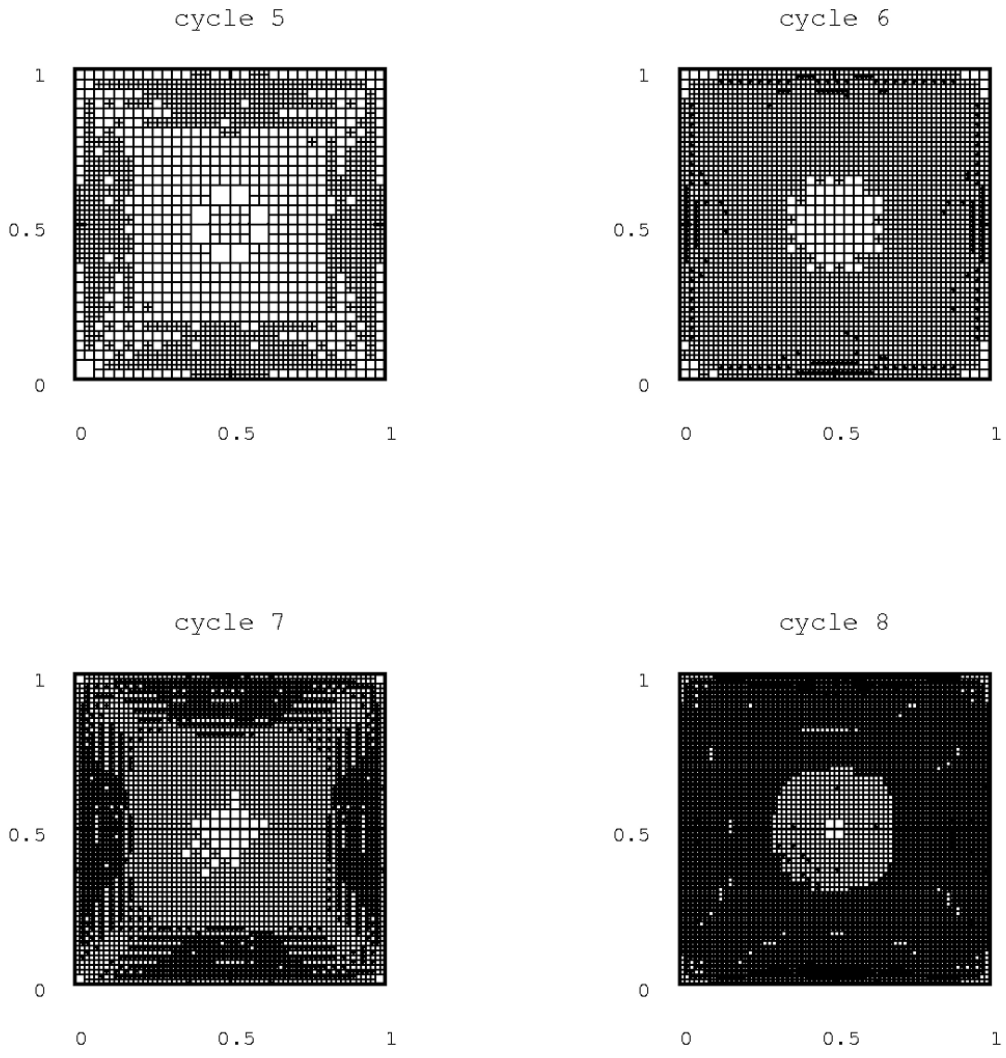

Figure IV.86: Adaptively refined grids.

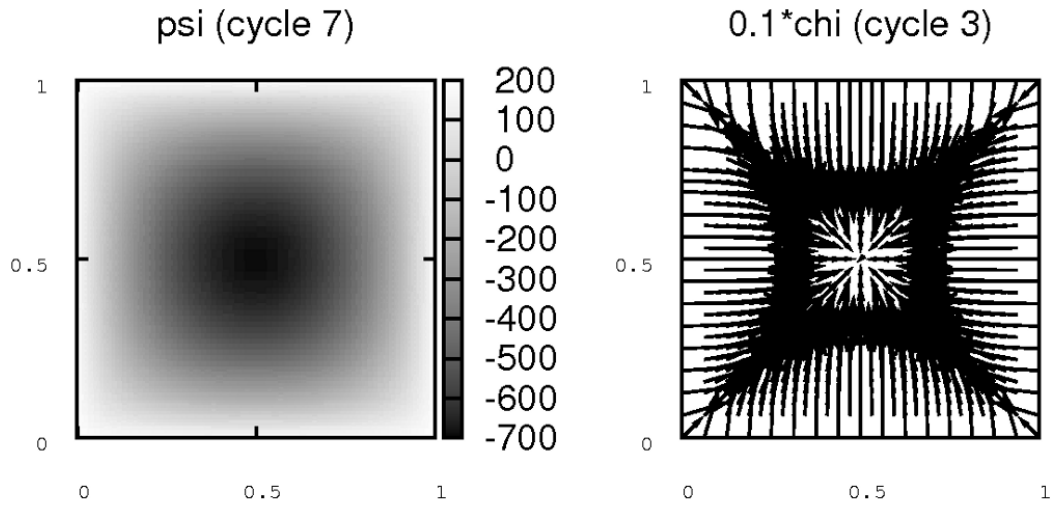

Figure IV.87: The solution of the considered problem.

The following table IV.51 shows the results of one run of our algorithm:

cycle	# active cells	# dofs	a-posteriori-estimate	ratio
0	124	483	4.0477e+02	inf
1	286	1059	2.6686e+02	0.6593
2	553	1977	2.0922e+02	0.7840
3	1153	4005	1.4033e+02	0.6707
4	2200	7521	1.0703e+02	0.7627
5	4399	14589	7.6258e+01	0.7125
6	8365	28032	5.6169e+01	0.7366
7	16495	53664	4.1378e+01	0.7367

Table IV.51: The convergence of one run of our algorithm for the considered problem.

As in the Reynolds case the results for the upward velocity are basically the same as in the case of downward velocity. We see the decrease of the estimator by the factor $1/\sqrt{2}$, which indicates the expected order $O(n_{dofs}^{-1/2})$.

IV.3.2.3 Plain surface and horizontal velocity

We consider the SubStokes problem (I.58) with the upper surface given by (IV.9). The sequence of refined grids is shown in figure IV.88 and the solution for pressure and velocity in figure IV.89.

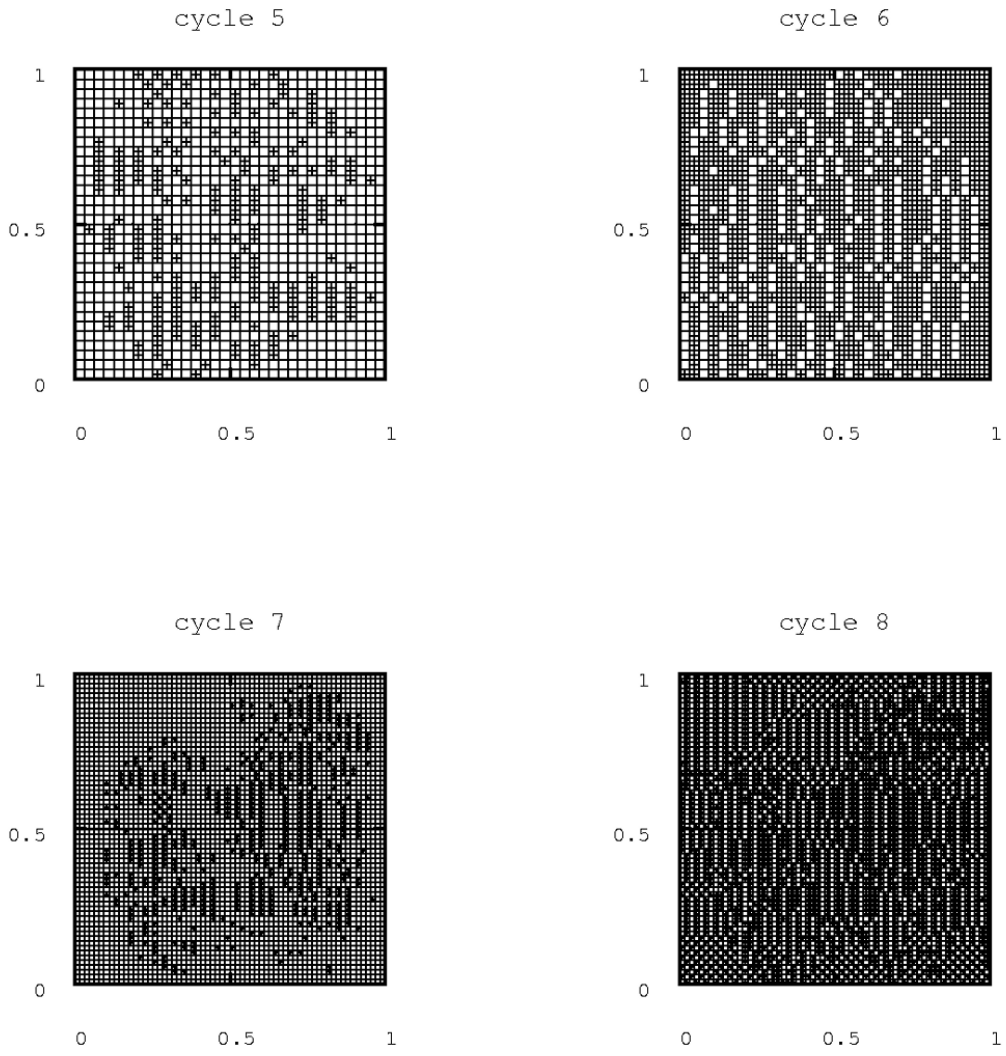

Figure IV.88: Adaptively refined grids.

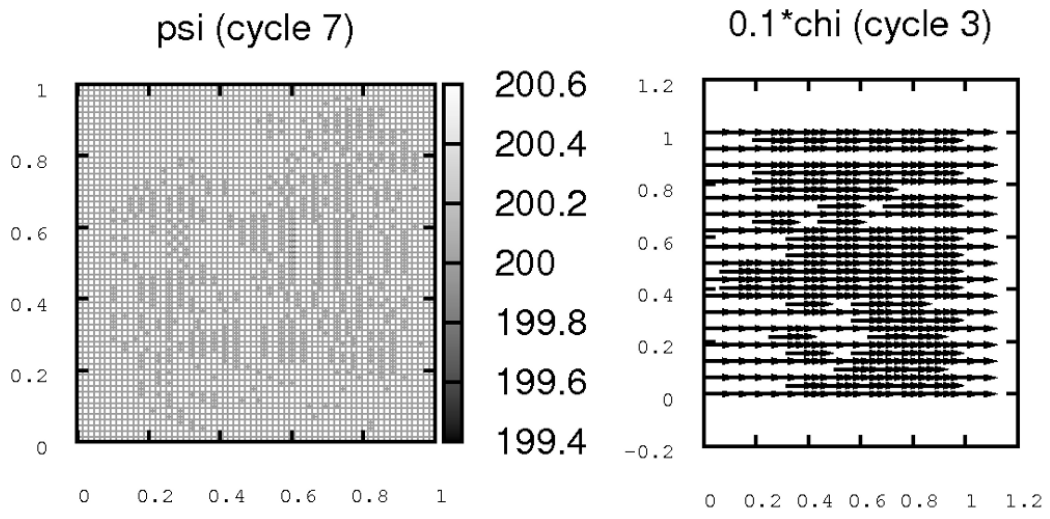

Figure IV.89: The solution of the considered problem.

The following table IV.52 shows the results of one run of our algorithm:

cycle	# active cells	# dofs	a-posteriori-estimate	ratio
0	124	486	1.0607e+02	inf
1	238	846	9.2808e+01	0.8750
2	454	1770	6.0029e+01	0.6468
3	865	3018	4.7631e+01	0.7935
4	1645	6066	3.3761e+01	0.7088
5	3127	11025	2.4424e+01	0.7234
6	5944	20757	1.8497e+01	0.7573
7	11296	41133	1.2488e+01	0.6752

Table IV.52: The convergence of one run of our algorithm for the considered problem.

We see the decrease of the estimator by the factor $1/\sqrt{2}$, which indicates the expected order $O(n_{dofs}^{-1/2})$.
In contrast to the Reynolds calculation for this application, the error estimate decreases. The reason therefor is the additional calculation of the velocity field, whose error is estimated as well. Furthermore initial grid is coarser then that of the Reynolds calculations.

IV.3.2.4 Steep surface and vertical downward velocity

We consider the SubStokes problem (I.58) with the upper surface given by (IV.10). The sequence of refined grids is shown in figure IV.90 and the final solution in figure IV.91.

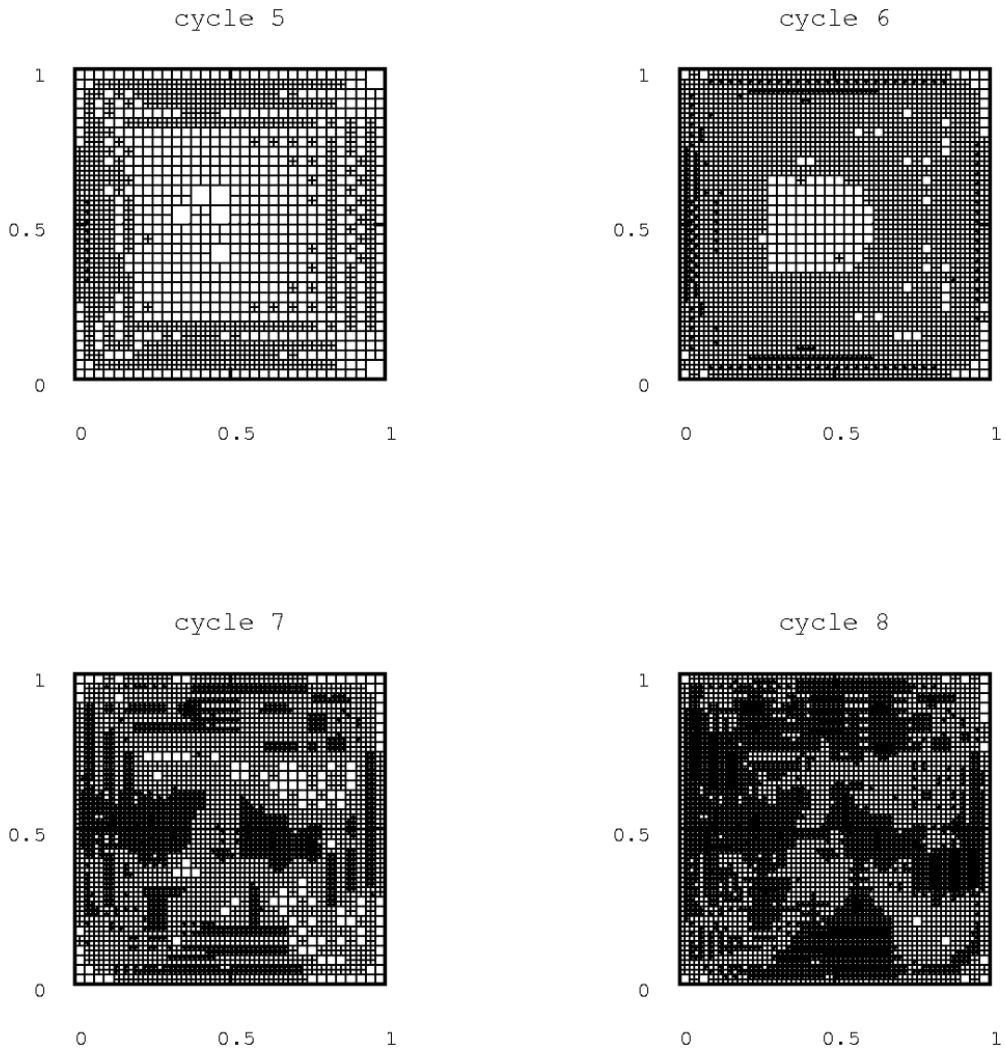

Figure IV.90: Adaptively refined grids.

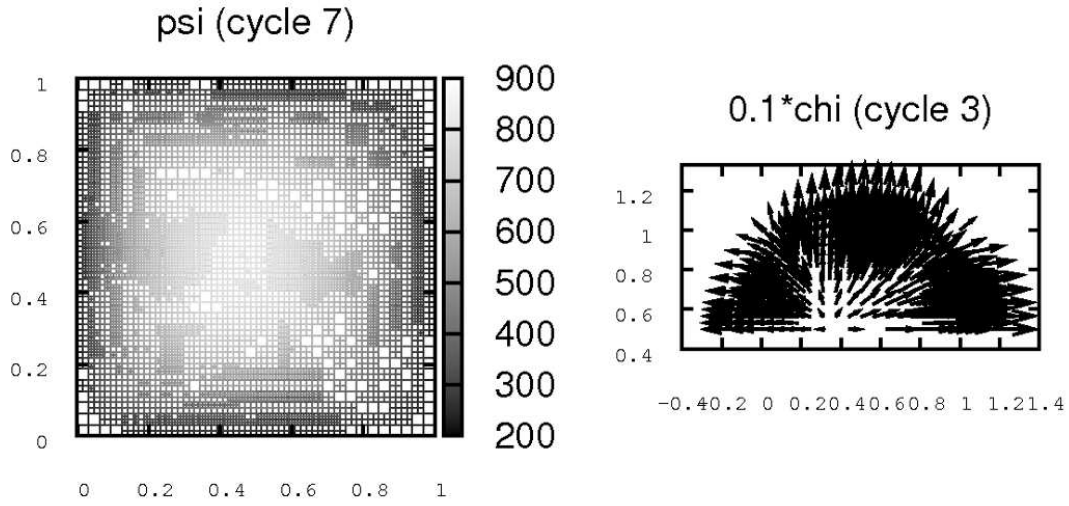

Figure IV.91: The solution of the considered problem. Due to symmetry we only show the upper half of the velocity field.

The following table IV.53 shows the results of one run of our algorithm:

cycle	# active cells	# dofs	a-posteriori-estimate	ratio
0	124	483	2.6850e+02	inf
1	283	1053	1.8419e+02	0.6860
2	538	1926	1.3731e+02	0.7455
3	1111	3822	9.5768e+01	0.6975
4	2140	7539	7.2528e+01	0.7573
5	4300	14484	5.0866e+01	0.7013
6	8284	28344	3.7853e+01	0.7442
7	16114	53661	2.8453e+01	0.7517

Table IV.53: The convergence of one run of our algorithm for the considered problem.

We see the decrease of the estimator by the factor $1/\sqrt{2}$, which indicates the expected order $O(n_{dofs}^{-1/2})$.

IV.3.2.5 Steep surface and vertical upward velocity

We consider the SubStokes problem (I.58) with the upper surface given by (IV.11). The sequence of refined grids is shown in figure IV.92 and the solution of ψ and χ in figure IV.93.

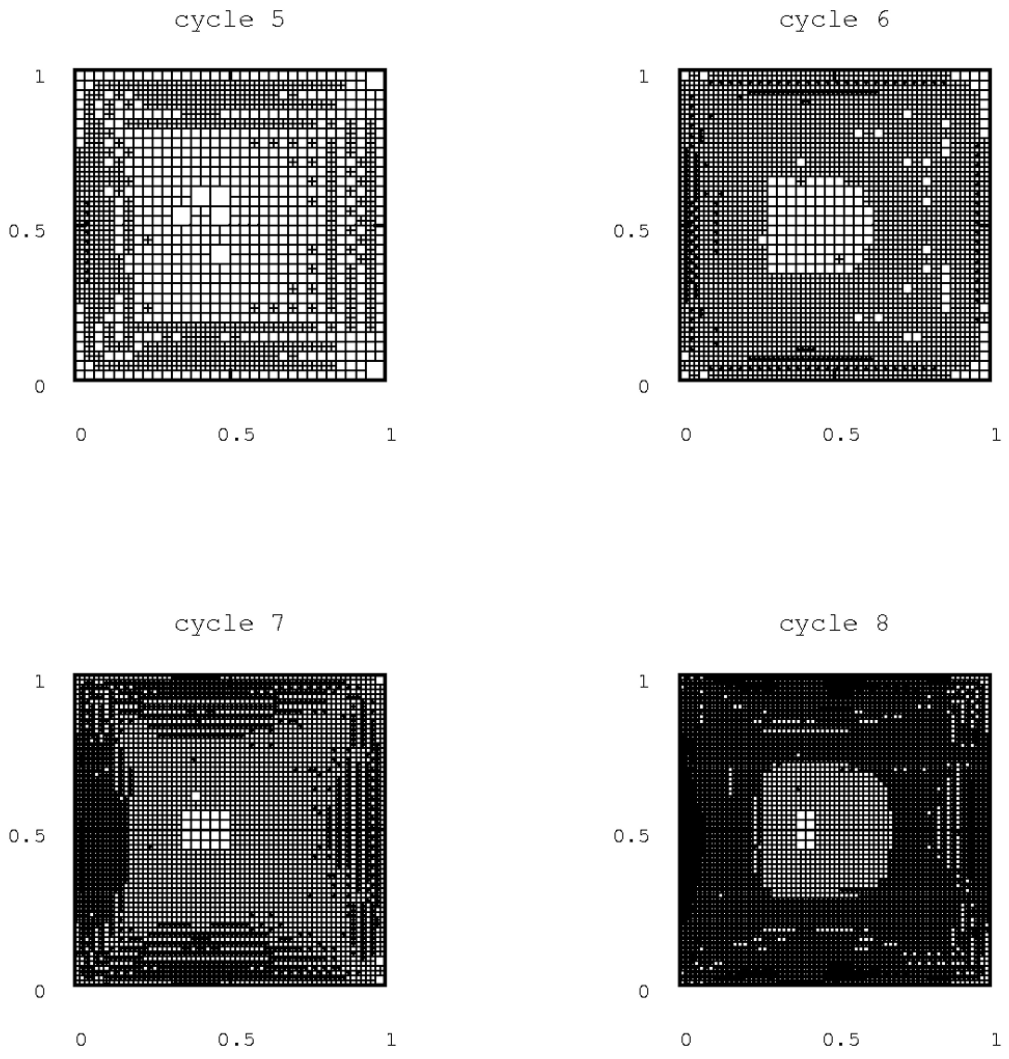

Figure IV.92: Adaptively refined grids.

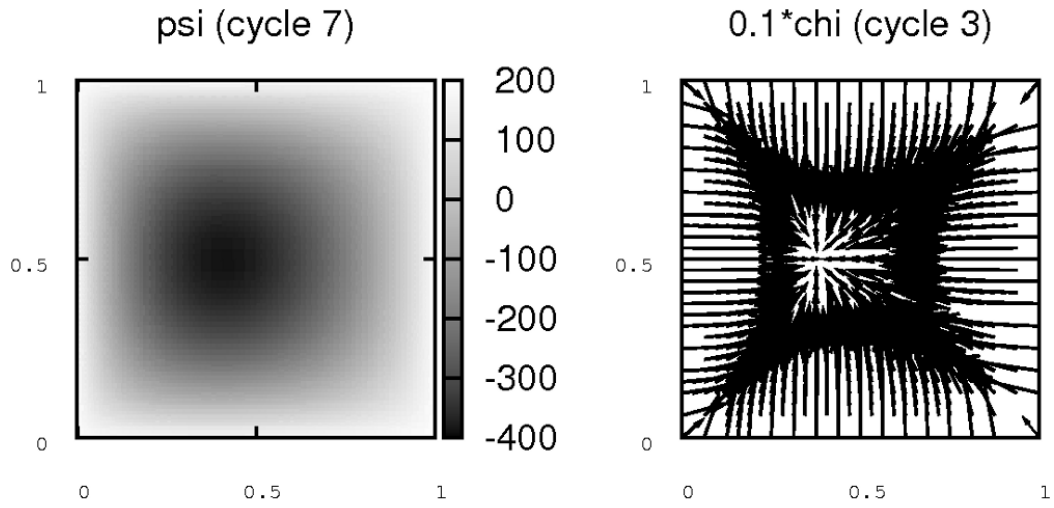

Figure IV.93: The solution of the considered problem.

The following table IV.54 shows the results of one run of our algorithm:

cycle	# active cells	# dofs	a-posteriori-estimate	ratio
0	124	483	2.7293e+02	inf
1	283	1053	1.8716e+02	0.6857
2	538	1926	1.3958e+02	0.7458
3	1111	3822	9.7334e+01	0.6974
4	2140	7539	7.3700e+01	0.7572
5	4297	14460	5.1682e+01	0.7013
6	8272	28257	3.8431e+01	0.7436
7	16108	53715	2.8990e+01	0.7543

Table IV.54: The convergence of one run of our algorithm for the considered problem.

We see the decrease of the estimator by the factor $1/\sqrt{2}$, which indicates the expected order $O(n_{dofs}^{-1/2})$.

IV.3.2.6 Steep surface and horizontal velocity against gradient direction of the surface

We consider the SubStokes problem (I.58) with the upper surface given by (IV.13). The sequence of refined grids is shown in figure IV.94 and the final solution in figure IV.95.

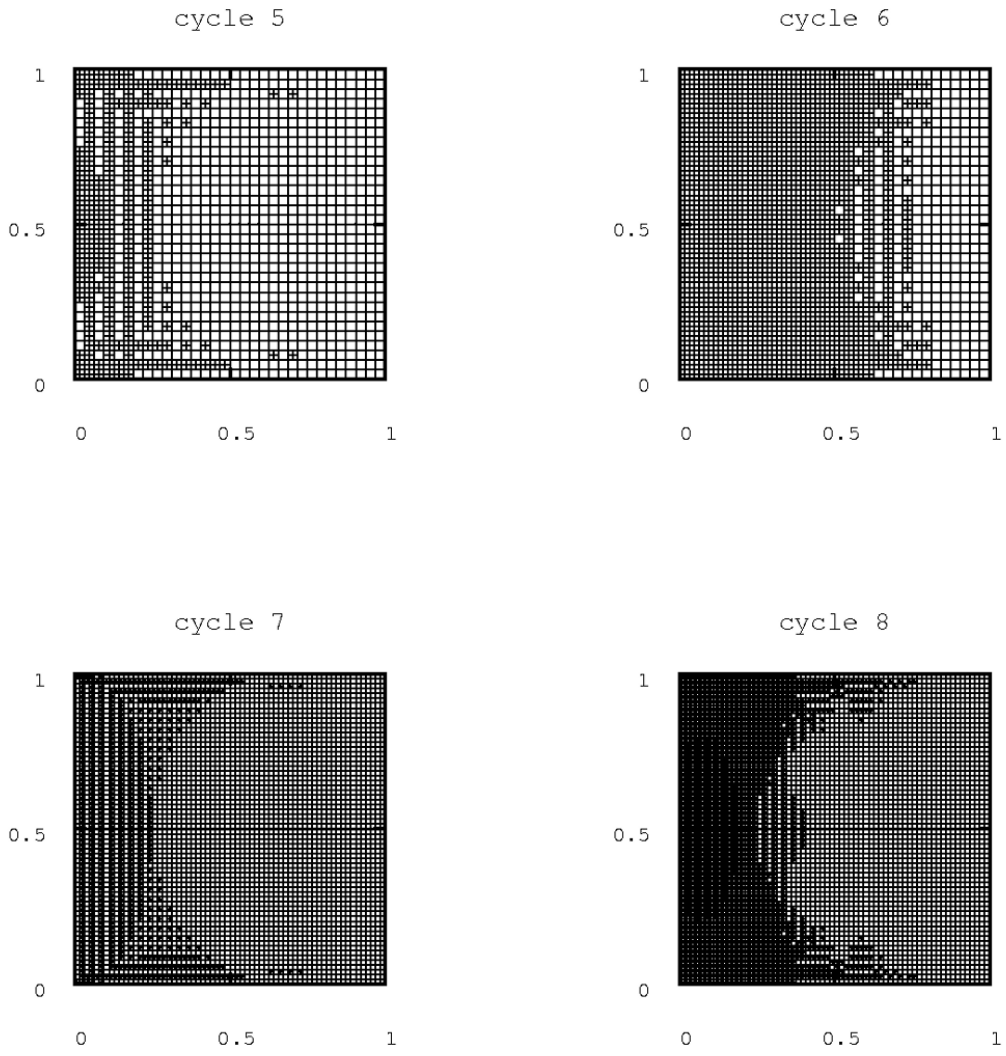

Figure IV.94: Adaptively refined grids.

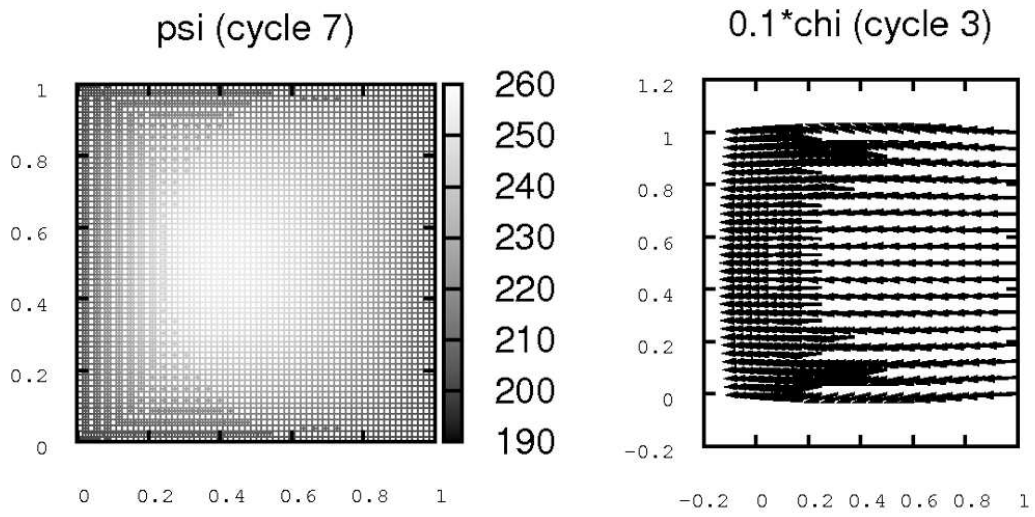

Figure IV.95: The solution of the considered problem.

The following table IV.55 shows the results of one run of our algorithm:

cycle	# active cells	# dofs	a-posteriori-estimate	ratio
0	124	465	8.9965e+01	inf
1	238	813	7.5522e+01	0.8395
2	454	1596	4.9308e+01	0.6529
3	865	2817	3.9058e+01	0.7921
4	1645	5646	2.7342e+01	0.7000
5	3127	10005	2.0323e+01	0.7433
6	5944	20301	1.5044e+01	0.7403
7	11293	36606	1.3106e+01	0.8712

Table IV.55: The convergence of one run of our algorithm for the considered problem.

Basically we see the decrease of the estimator by the factor $1/\sqrt{2}$, which indicates the expected order $O(n_{dofs}^{-1/2})$. The weakening of this decrease in the last step might be caused by numerical inaccuracies of the linear system solver.

IV.3.2.7 Steep surface and horizontal velocity in direction of the gradient of the surface

We consider the SubStokes problem (I.58) with the upper surface given by (IV.12). The sequence of refined grids is shown in figure IV.96 and the final solution in figure IV.97.

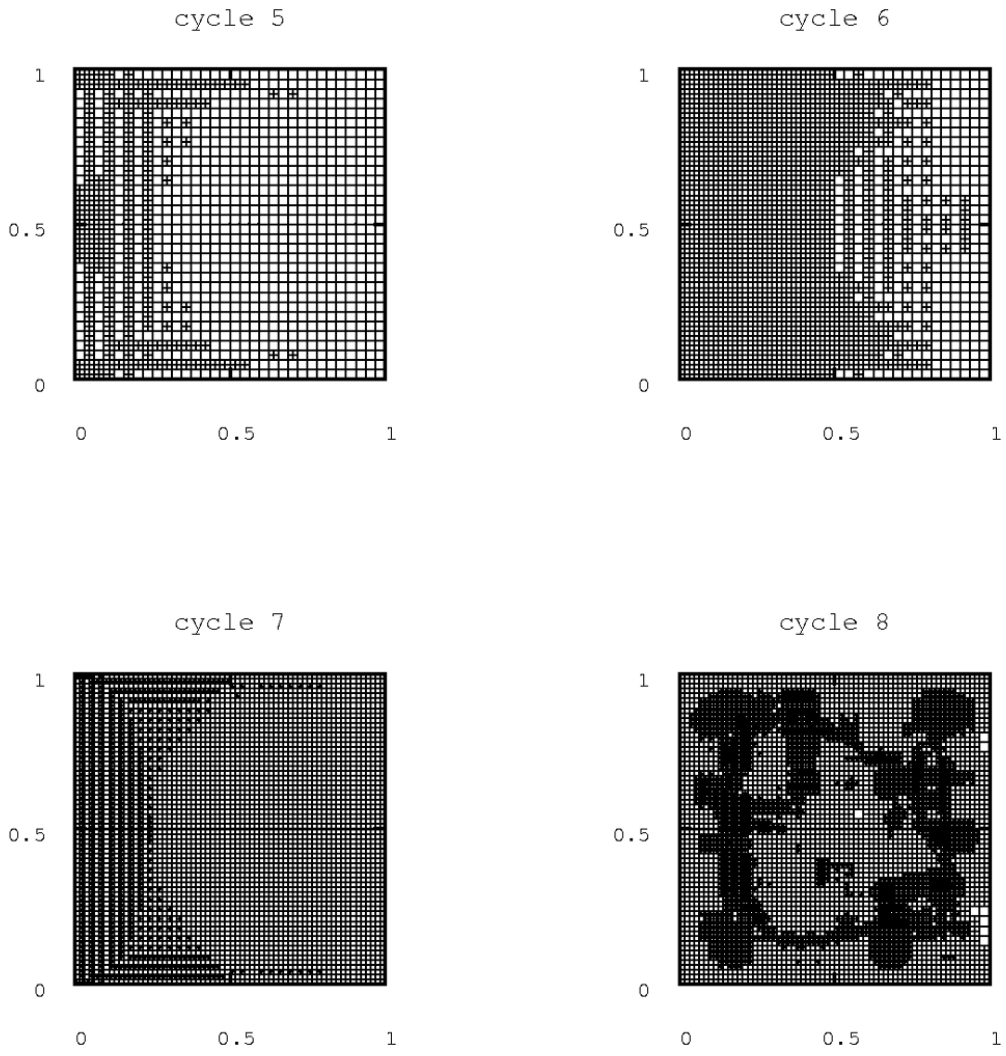

Figure IV.96: Adaptively refined grids.

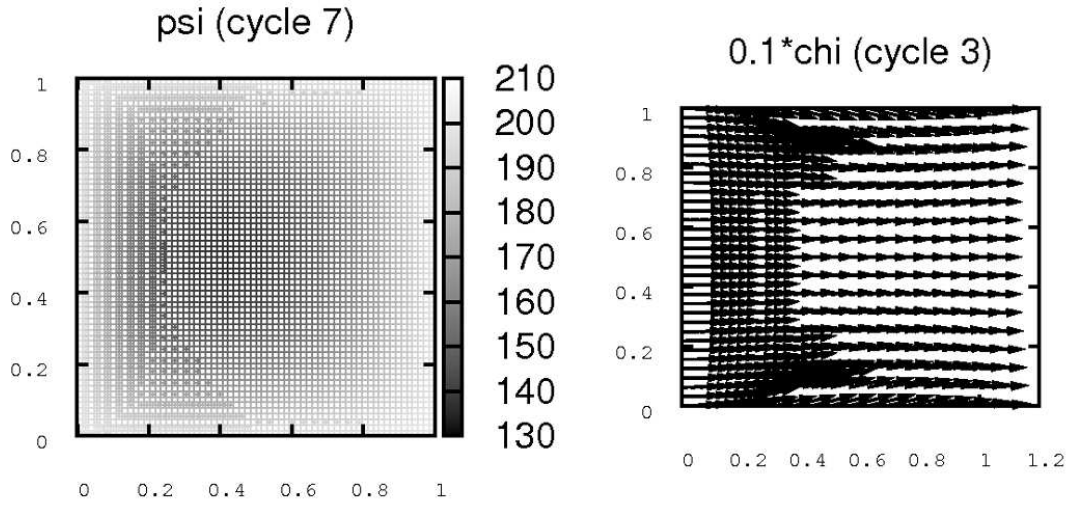

Figure IV.97: The solution of the considered problem. Due to the problems symmetry we only show the upper half of the velocity field.

The following table IV.56 shows the results of one run of our algorithm:

cycle	# active cells	# dofs	a-posteriori-estimate	ratio
0	124	465	9.1266e+01	inf
1	238	813	7.6561e+01	0.8389
2	454	1596	5.0021e+01	0.6533
3	865	2811	3.9643e+01	0.7925
4	1645	5688	2.7797e+01	0.7012
5	3127	10134	2.0585e+01	0.7405
6	5944	20364	1.5278e+01	0.7422
7	11293	36480	1.2086e+01	0.7910

Table IV.56: The convergence of one run of our algorithm for the considered problem.

We see the decrease of the estimator by the factor $1/\sqrt{2}$, which indicates the expected order $O(n_{dofs}^{-1/2})$.

IV.3.2.8 Steep surface and horizontal velocity orthogonal to the gradient of the surface

We consider the SubStokes problem (I.58) with the upper surface given by (IV.14). The sequence of refined grids is shown in figure IV.98 and the final solution in figure IV.99.

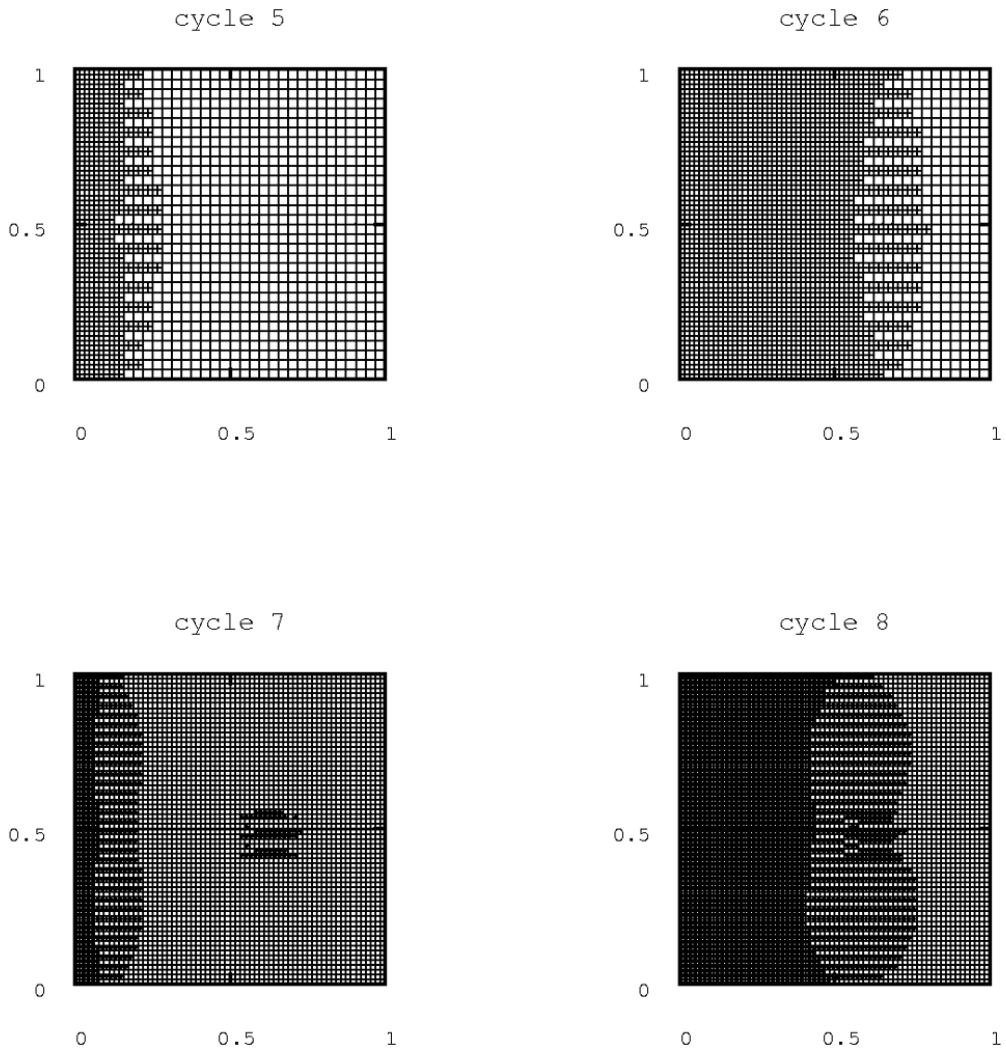

Figure IV.98: Adaptively refined grids.

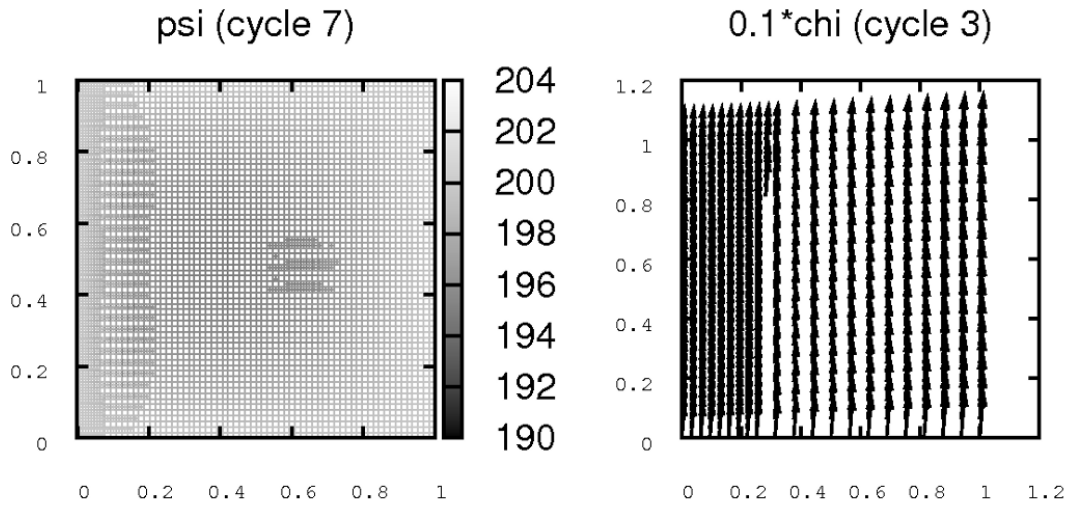

Figure IV.99: The solution of the considered problem.

The following table IV.57 shows the results of one run of our algorithm:

cycle	# active cells	# dofs	a-posteriori-estimate	ratio
0	124	456	6.9961e+02	inf
1	259	912	4.2463e+02	0.6069
2	496	1725	2.1069e+02	0.4962
3	937	3126	3.1243e+02	1.4829
4	1798	5937	1.1018e+02	0.3527
5	3403	11430	5.1031e+01	0.4632
6	6442	21450	2.5968e+01	0.5089
7	12217	41049	1.4589e+01	0.5618

Table IV.57: The convergence of one run of our algorithm for the considered problem.

We see the decrease of the estimator is much faster than before, which is caused by the simple solution (a constant pressure) of this problem.

IV.3.2.9 Wave surface and vertical downwards velocity

We consider the SubStokes problem (I.58) with the upper surface given by (IV.15). The sequence of refined grids is shown in figure IV.100 and the solution for pressure and velocity in figure IV.101.

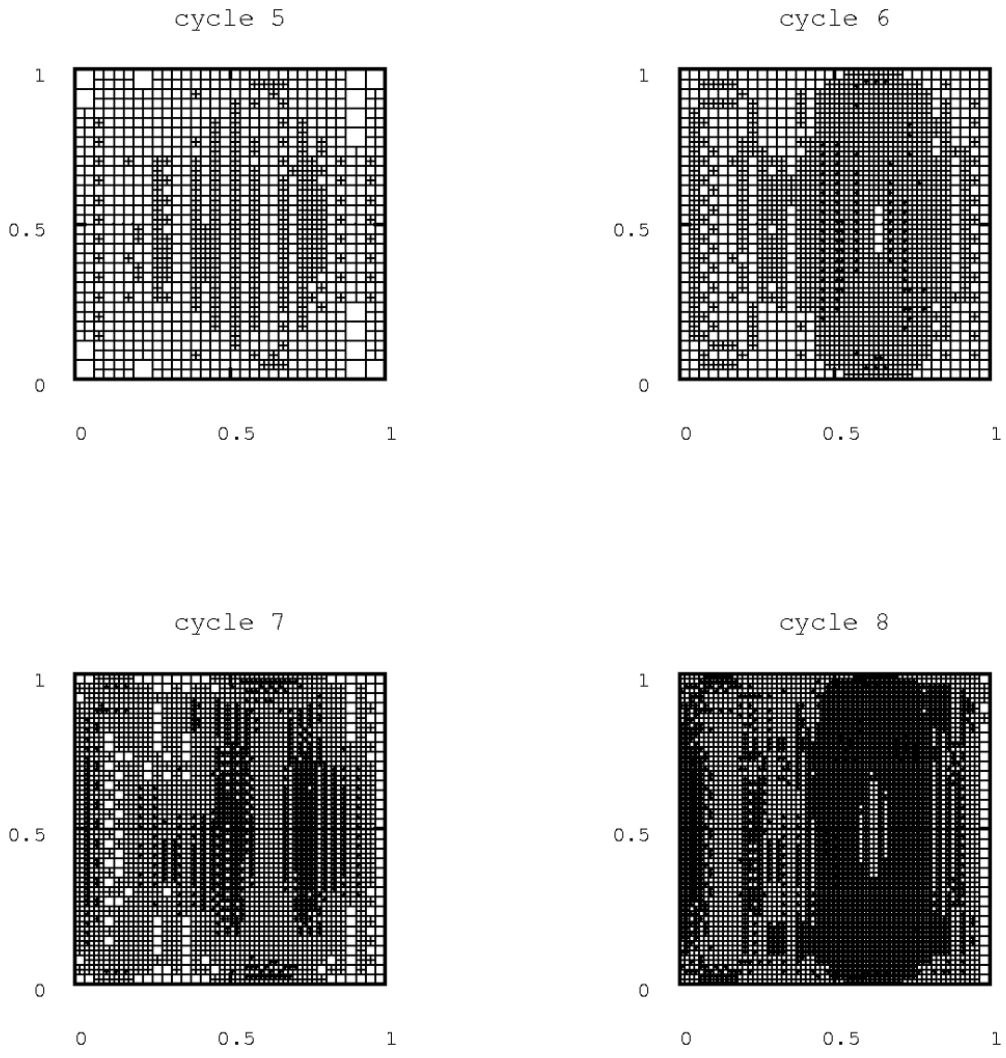

Figure IV.100: Adaptively refined grids.

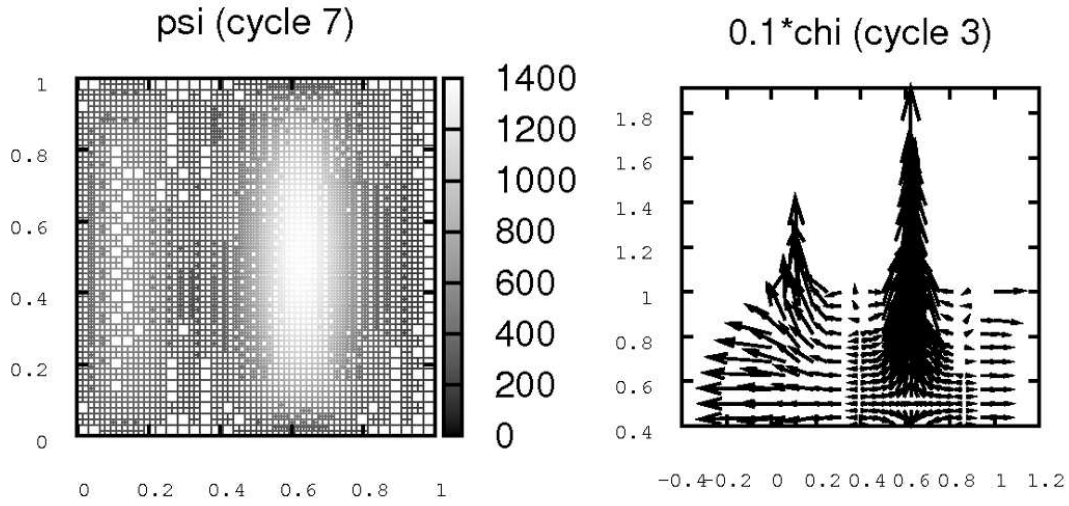

Figure IV.101: The solution of the considered problem. Due to symmetry we show the velocity field only in the upper half of the domain.

The following table IV.58 shows the results of one run of our algorithm:

cycle	# active cells	# dofs	a-posteriori-estimate	ratio
0	124	453	7.5111e+02	inf
1	238	843	4.9990e+02	0.6656
2	454	1557	3.4858e+02	0.6973
3	865	2961	2.4226e+02	0.6950
4	1678	6021	2.1445e+02	0.8852
5	3190	11079	1.2994e+02	0.6059
6	6109	21318	9.7503e+01	0.7504
7	11701	39018	6.9762e+01	0.7155

Table IV.58: The convergence of one run of our algorithm for the considered problem.

We see the decrease of the estimator by the factor $1/\sqrt{2}$, which indicates the expected order $O(n_{dofs}^{-1/2})$.

IV.3.2.10 Wave surface and vertical upwards velocity

We consider the SubStokes problem (I.58) with the upper surface given by (IV.16). The sequence of refined grids is shown in figure IV.102 and the solution for pressure and velocity in figure IV.103.

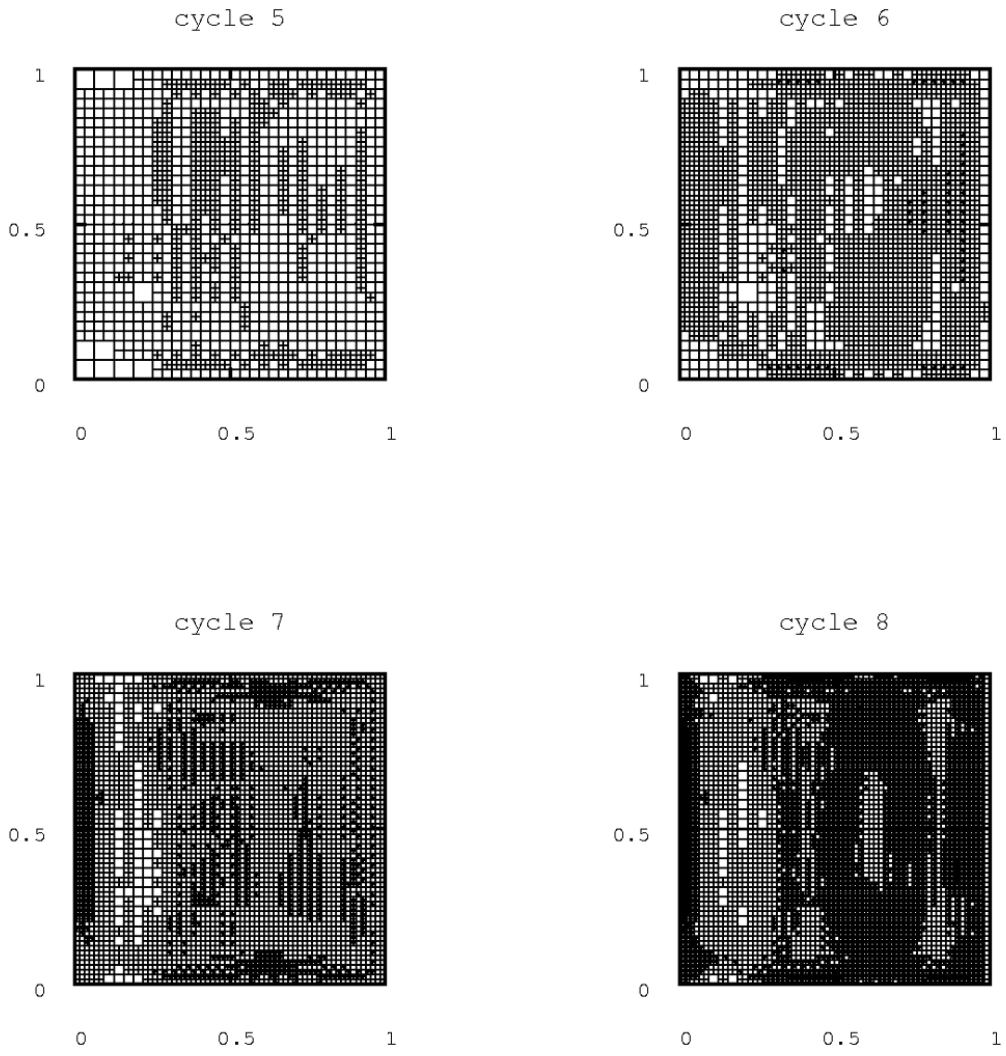

Figure IV.102: Adaptively refined grids.

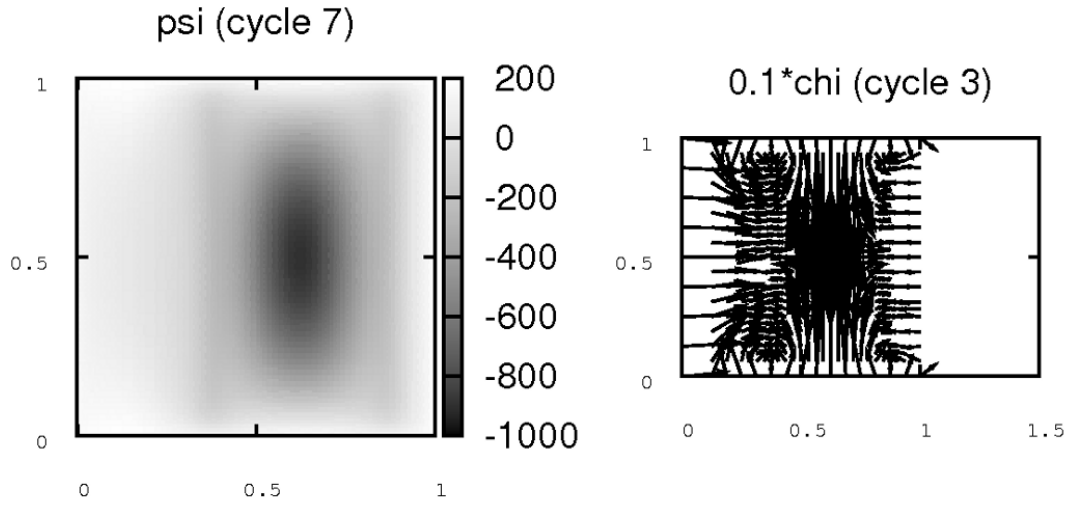

Figure IV.103: The solution of the considered problem.

The following table IV.59 shows the results of one run of our algorithm:

cycle	# active cells	# dofs	a-posteriori-estimate	ratio
0	124	465	5.9748e+02	inf
1	241	861	4.1687e+02	0.6977
2	460	1722	2.9501e+02	0.7077
3	925	3213	2.1165e+02	0.7174
4	1759	6225	1.8388e+02	0.8688
5	3466	11679	1.1807e+02	0.6421
6	6658	23274	8.9109e+01	0.7547
7	12799	41808	5.8437e+01	0.6558

Table IV.59: The convergence of one run of our algorithm for the considered problem.

We see the decrease of the estimator by the factor $1/\sqrt{2}$, which indicates the expected order $O(n_{dofs}^{-1/2})$.

IV.3.2.11 Wave surface and horizontal velocity

We consider the SubStokes problem (I.58) with the upper surface given by (IV.17). The sequence of refined grids is shown in figure IV.104 and the solution for pressure and velocity in figure IV.105.

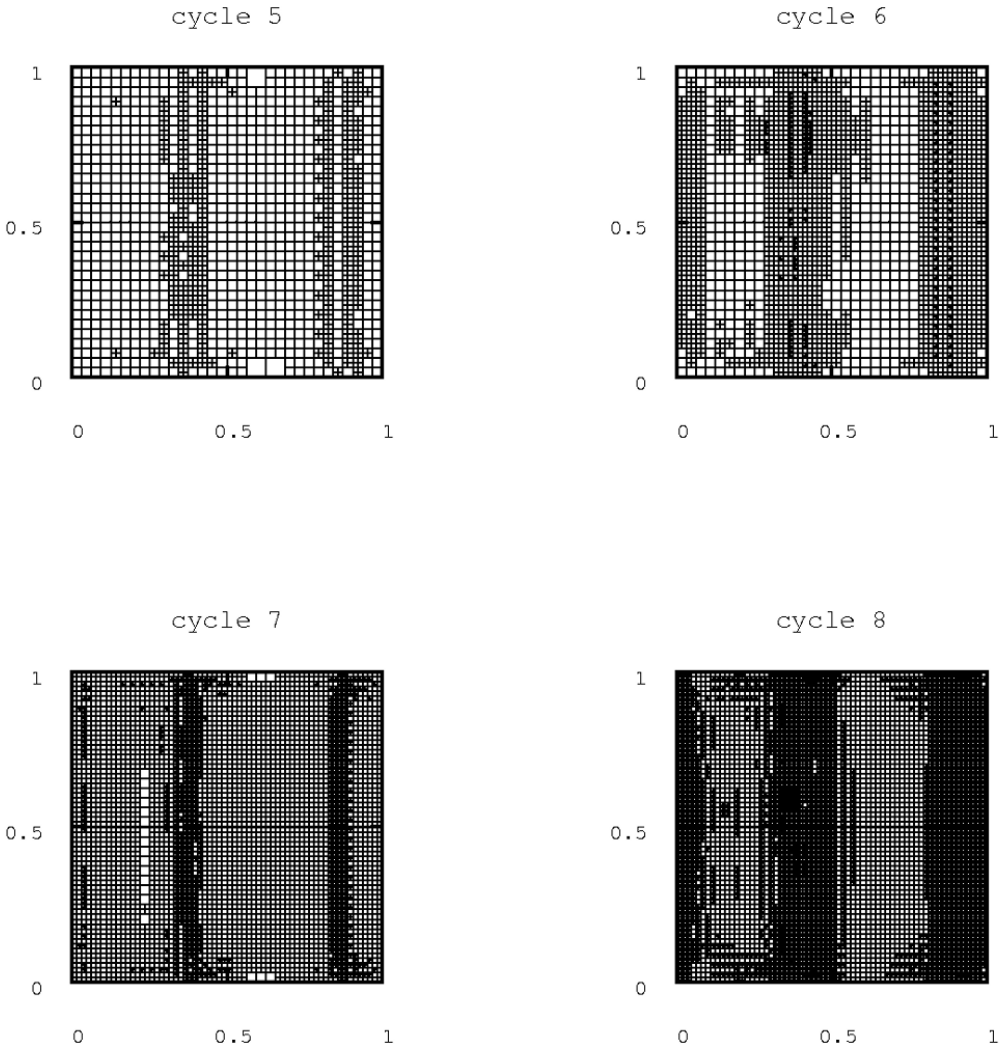

Figure IV.104: Adaptively refined grids.

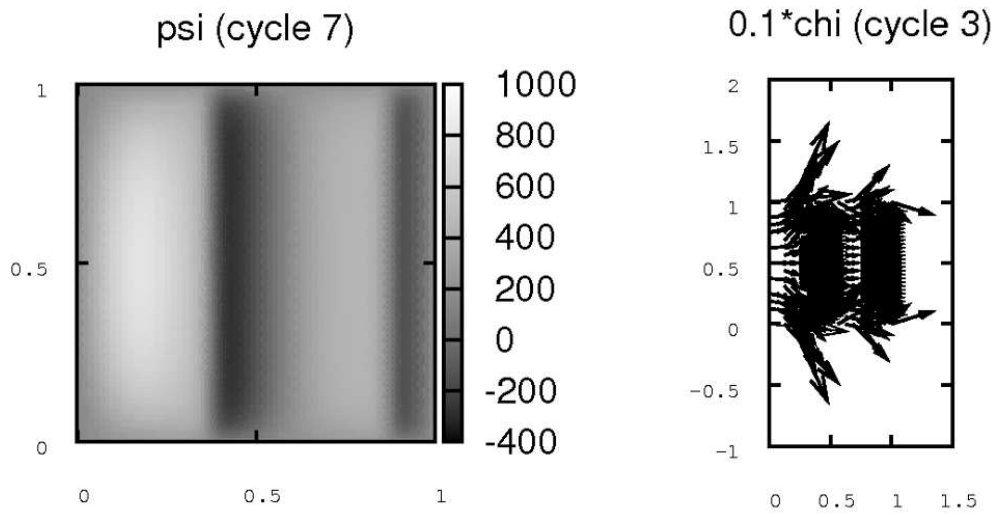

Figure IV.105: The solution of the considered problem. Due to symmetry we only show the upper half of the velocity solution.

The following table IV.60 shows the results of one run of our algorithm:

cycle	# active cells	# dofs	a-posteriori-estimate	ratio
0	124	492	1.2260e+03	inf
1	241	852	1.1404e+03	0.9302
2	460	1668	6.7518e+02	0.5921
3	877	3111	4.8271e+02	0.7149
4	1669	5745	3.4009e+02	0.7045
5	3280	11214	2.6865e+02	0.7899
6	6211	20217	1.6441e+02	0.6120
7	11860	38838	1.2598e+02	0.7663

Table IV.60: The convergence of one run of our algorithm for the considered problem.

We see the decrease of the estimator by the factor $1/\sqrt{2}$, which indicates the expected order $O(n_{dofs}^{-1/2})$.

IV.3.2.12 Hilly surface and vertical downwards velocity

We consider the SubStokes problem (I.58) with the upper surface given by (IV.18). The sequence of refined grids is shown in figure IV.106 and the final solution in figure IV.107.

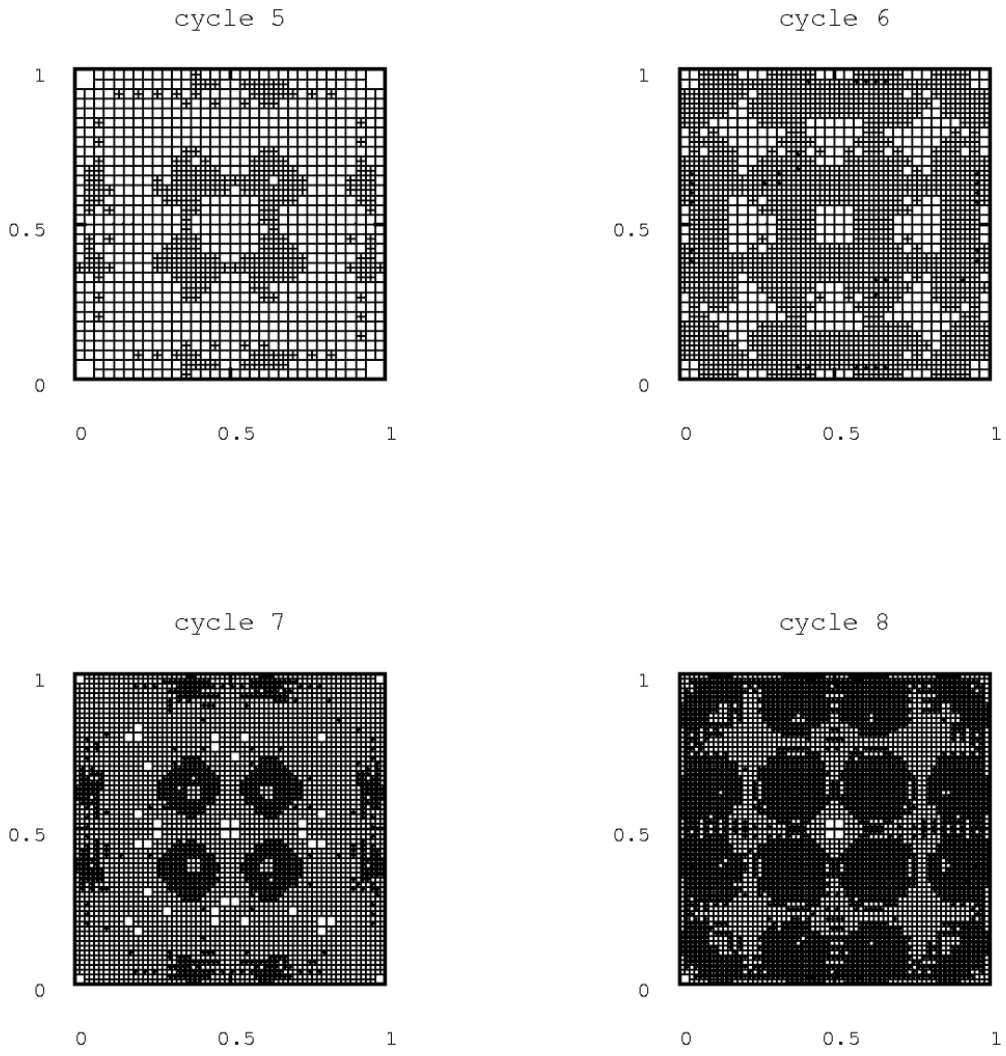

Figure IV.106: Adaptively refined grids.

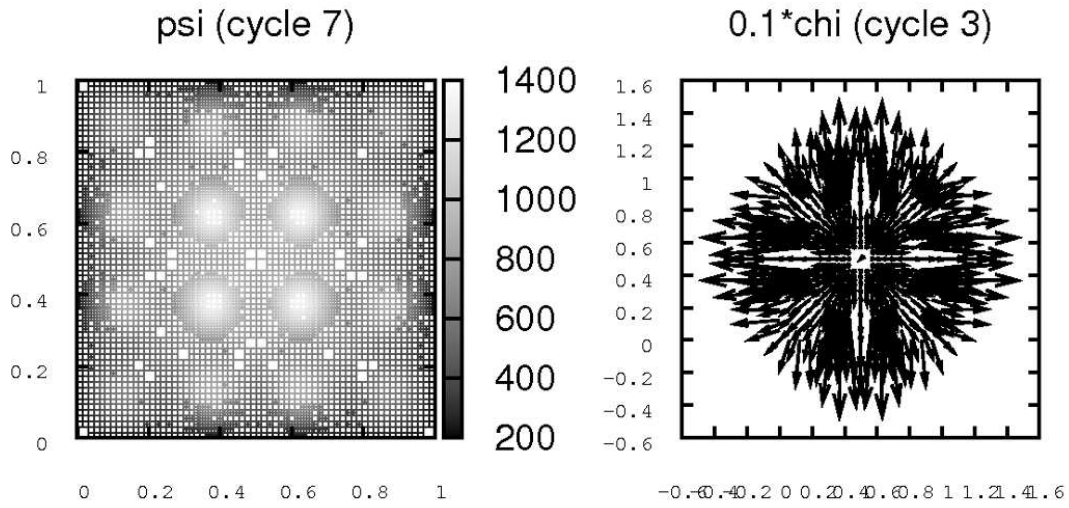

Figure IV.107: The solution of the considered problem.

The following table IV.61 shows the results of one run of our algorithm:

cycle	# active cells	# dofs	a-posteriori-estimate	ratio
0	124	459	9.5969e+02	inf
1	238	819	7.3641e+02	0.7673
2	454	1671	4.3459e+02	0.5901
3	904	3177	3.0502e+02	0.7019
4	1720	5922	2.1014e+02	0.6889
5	3337	11133	1.5015e+02	0.7145
6	6457	21456	1.0684e+02	0.7115
7	12361	40212	7.8983e+01	0.7393

Table IV.61: The convergence of one run of our algorithm for the considered problem.

We see the decrease of the estimator by the factor $1/\sqrt{2}$, which indicates the expected order $O(n_{dofs}^{-1/2})$.

IV.3.2.13 Hilly surface and vertical upwards velocity

We consider the SubStokes problem (I.58) with the upper surface given by (IV.19). The sequence of refined grids is shown in figure IV.108 and the final solution in figure IV.109.

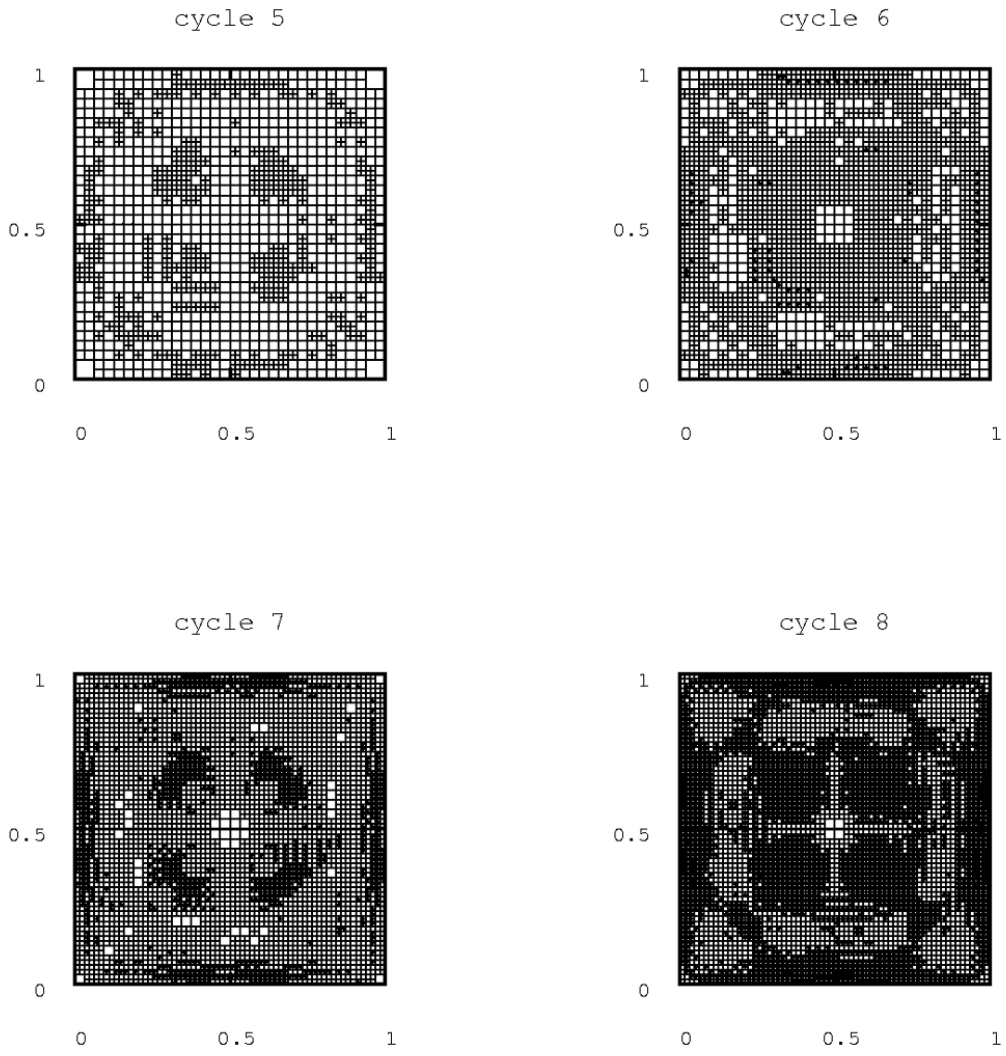

Figure IV.108: Adaptively refined grids.

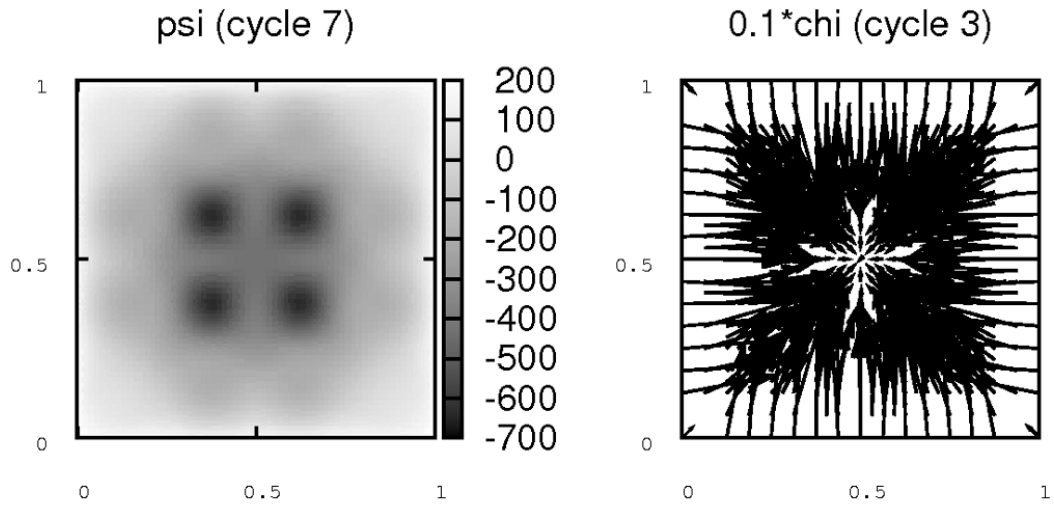

Figure IV.109: The solution of the considered problem.

The following table IV.62 shows the results of one run of our algorithm:

cycle	# active cells	# dofs	a-posteriori-estimate	ratio
0	124	459	6.1867e+02	inf
1	256	975	5.3628e+02	0.8668
2	487	1800	3.0248e+02	0.5640
3	952	3288	2.0598e+02	0.6810
4	1810	6423	1.3691e+02	0.6647
5	3475	11907	9.1506e+01	0.6683
6	6613	22518	6.7980e+01	0.7429
7	12724	42714	4.7173e+01	0.6939

Table IV.62: The convergence of one run of our algorithm for the considered problem.

We see the decrease of the estimator by the factor $1/\sqrt{2}$, which indicates the expected order $O(n_{dofs}^{-1/2})$.

IV.3.2.14 Hilly surface and horizontal velocity

We consider the SubStokes problem (I.58) with the upper surface given by (IV.20). The sequence of refined grids is shown in figure IV.110 and the final solution in figure IV.111.

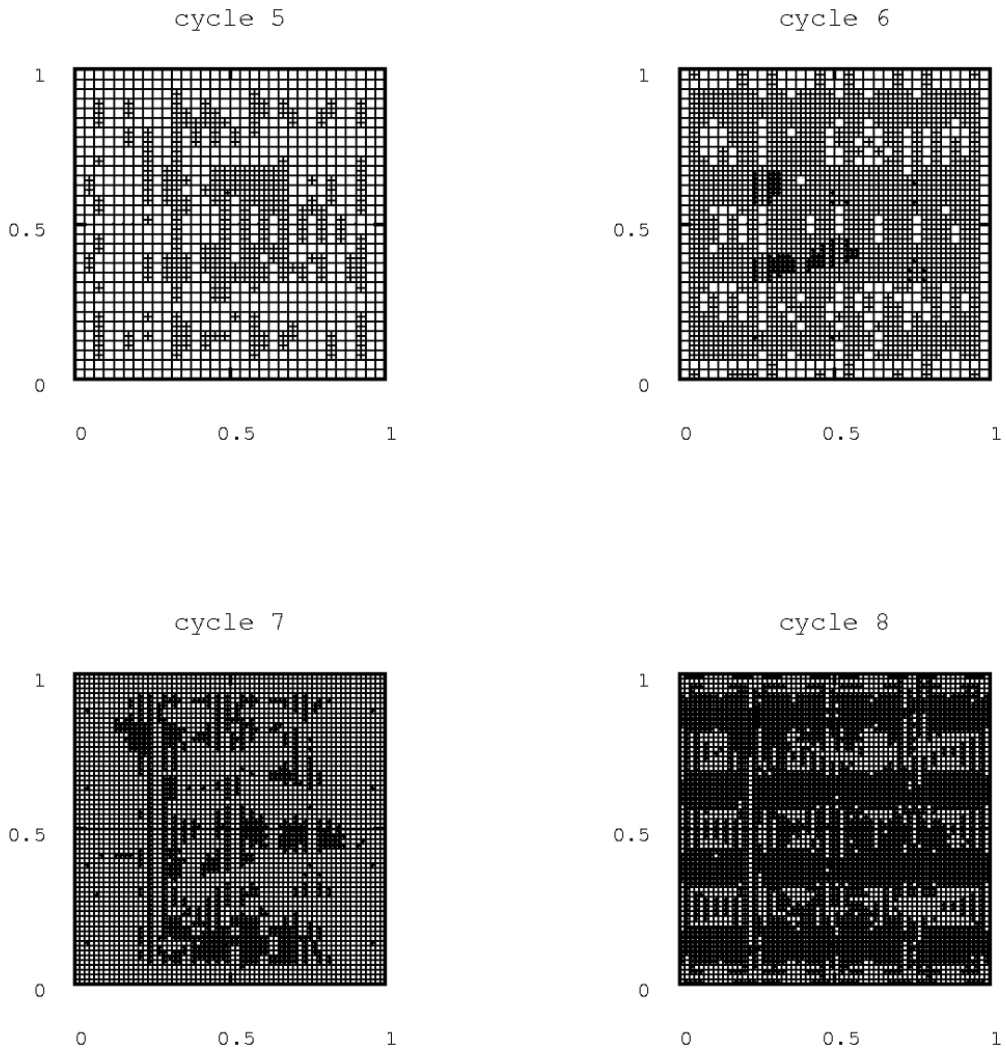

Figure IV.110: Adaptively refined grids.

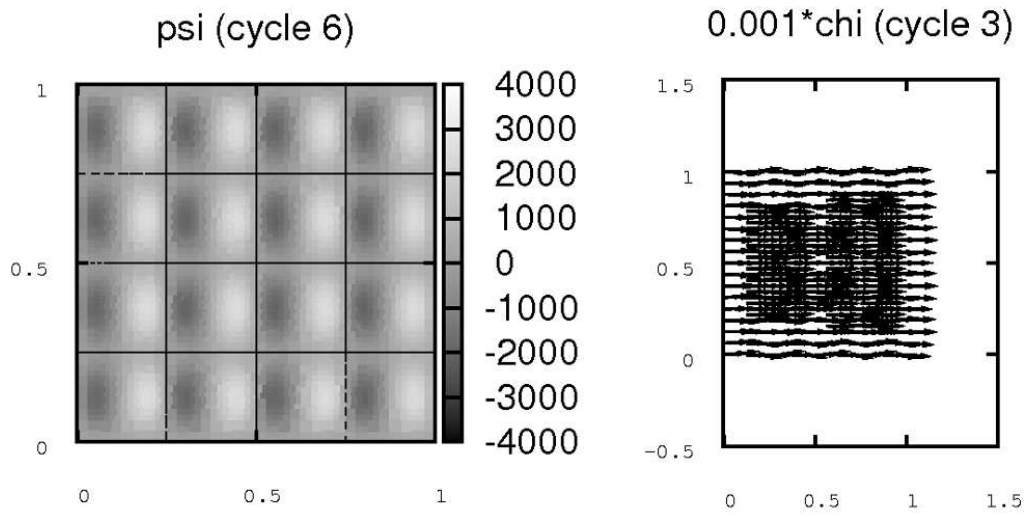

Figure IV.111: The solution of the considered problem.

The following table IV.63 shows the results of one run of our algorithm:

cycle	# active cells	# dofs	a-posteriori-estimate	ratio
0	124	486	9.4571e+03	inf
1	262	930	1.7331e+04	1.8326
2	499	1779	1.2569e+04	0.7252
3	952	3249	8.9031e+03	0.7083
4	1813	6375	4.6075e+03	0.5175
5	3463	11676	3.4023e+03	0.7384
6	6568	22119	2.8801e+03	0.8465
7	12541	41412	1.5758e+03	0.5471

Table IV.63: The convergence of one run of our algorithm for the considered problem.

We see the decrease of the estimator by the factor $1/\sqrt{2}$, which indicates the expected order $O(n_{dofs}^{-1/2})$.

All calculations in sections IV.3.2.1–IV.3.2.14 show a decrease of the error estimate, given in theorem III.23, of the expected order $O(n_{dofs}^{1/2})$. The grid-refinement for the wave-gap and vertical velocities (sections IV.3.2.9–IV.3.2.10) is not as concentrated around the maxima as it was in the Reynolds case. For the hilly gap and downward velocity (section IV.3.2.12) the refinement is clearly concentrated around the maxima of the gap width. For a upward velocity (section IV.3.2.13) this is the case in the interiour of the domain, while the refinement around the maxima near the boundary is not as strong as before. For the horizontal velocity (section IV.3.2.14) refinement takes place at the widest regions of the gap too. In the direction parallel to the fluid's velocity the refinement is not as strongly localized, as in the perpendicular direction. (compare figure IV.110)

IV.3.3 Comparison of the Reynolds- and the SubStokes-Model

There remains a comparison between both – the Reynolds model without cavitation and the SubStokes model without cavitation. Therefor in figure IV.112 we see a cut of the pressure profile for examples out of (IV.7)–(IV.14) and in figure IV.113 for examples (IV.15)–(IV.20).
The line of the cut is positioned at the maximum altitude of the hills for examples (IV.18)–(IV.20) (at $y = 0.375$) and in the middle of the domain ($y = 0.5$) for all other examples to circumvent boundary effects.
For sake of a clear presentation, we choose the results of low refinement for the plot. We do not plot the results for examples (IV.9) and (IV.8) because the latter one is just the reflection of (IV.7) while the first one is constant.
We see, that in the cases of vertical velocity of the surface the Reynolds pressure (i. e. (IV.7), (IV.10), (IV.11), (IV.15), (IV.16), (IV.18) and (IV.19)) is equal or at least very closed to the SubStokes pressure.
If the gradient of the gap width is perpendicular to the velocity field (example (IV.14), ψ^R is constant, which is a rather good approximation of ψ^s.
In the remaining cases of horizontal velocities the Reynolds model seemingly fails. If we compare the pressures for examples (IV.12), (IV.13), (IV.17) and (IV.20), we find, that the curvature of ψ^R is mostly the opposite of the curvature of the result ψ^s of the SubStokes calculation. Furthermore the absolute value of the pressure is under-estimated by the Reynolds model.
Even the comparison of the three dimensional pressure

$$p \approx \frac{\psi}{g}$$

in figure IV.114 does not improve this observation – although the results for the steep velocity (figure IV.114 (IV.12) and (IV.13) and for the wave surface (figure IV.114 (IV.17)) show, that one might use the Reynolds model as rough guess for the SubStokes model for these cases.
But for the case of the hilly surface and horizontal velocity (figure (IV.114) (IV.20)) the pressure approximations p^R and p^s do not coincide at all.
However, the velocity fields χ^R and χ^s of these examples are rather similair (figure IV.115) and come along with the surface velocities in sight.

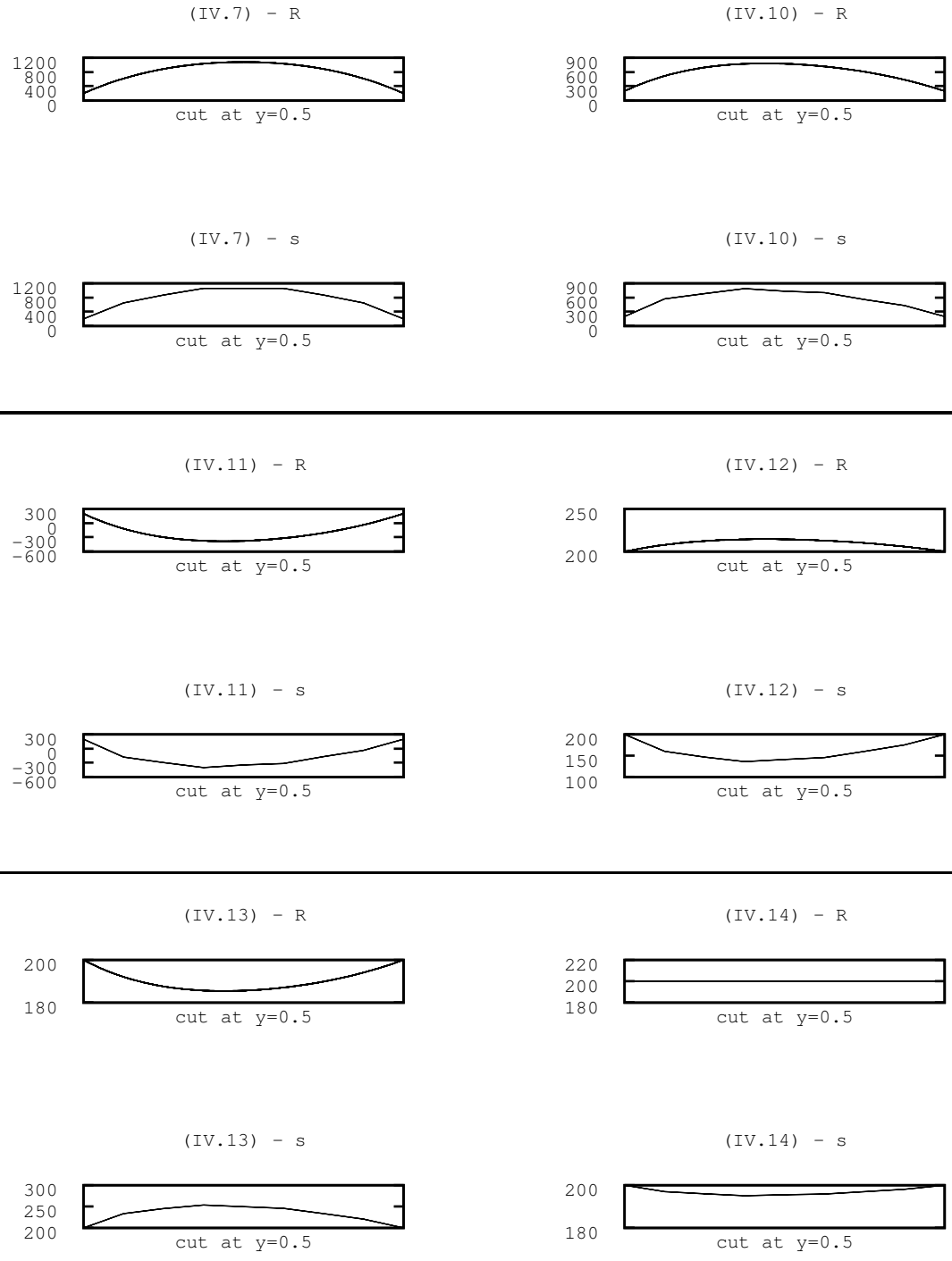

Figure IV.112: Comparison of the Reynolds– and the SubStokes–model: We see the cut of the pressures ψ^R (upper plot – R) and ψ^s (lower plot – s) for the different example applications (IV.7)–(IV.14).

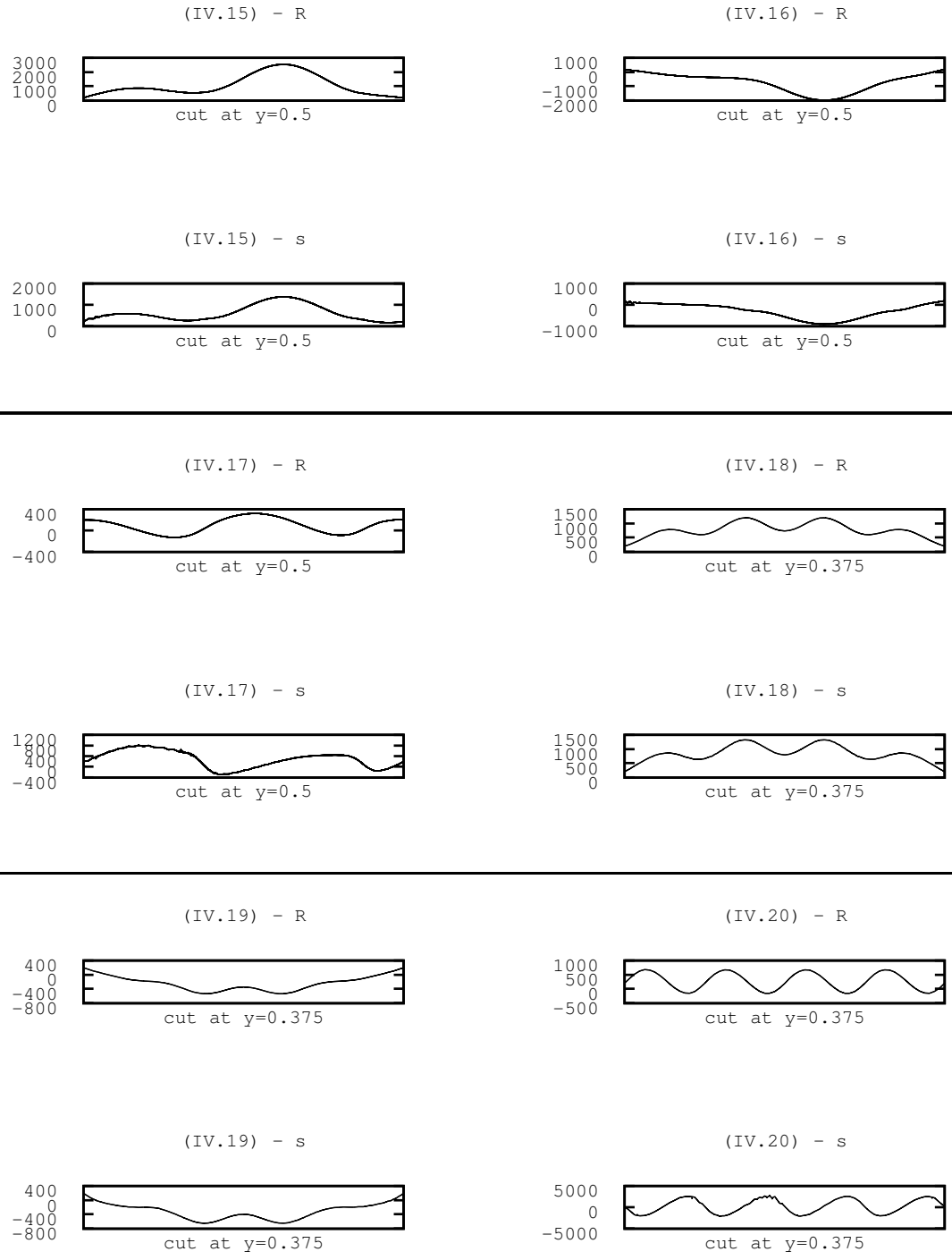

Figure IV.113: Comparison of the Reynolds– and the SubStokes–model: We see the cut of the pressures ψ^R (upper plot – R) and ψ^s (lower plot – s) for the different example applications (IV.15)–(IV.20).

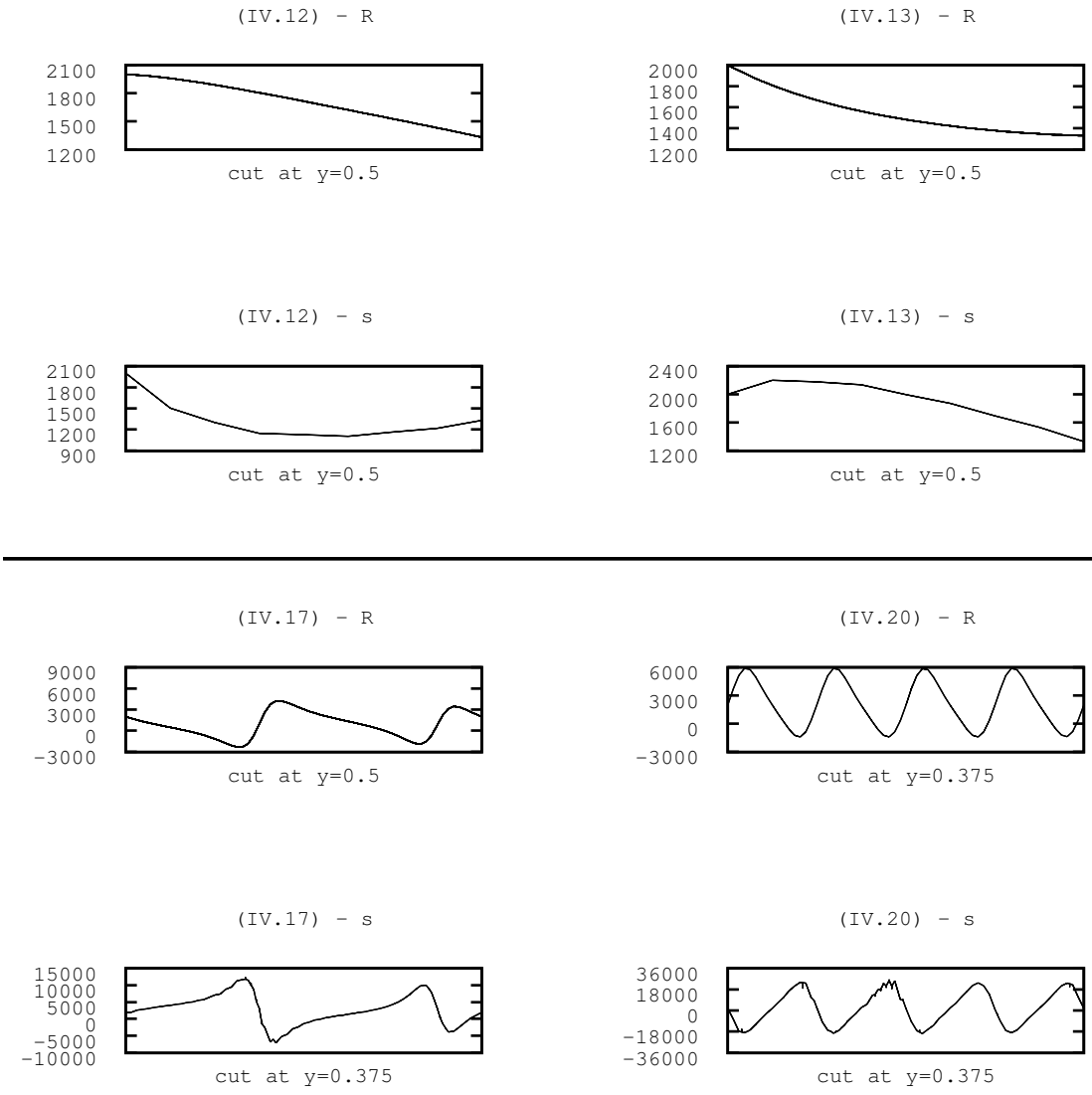

Figure IV.114: Comparison of the Reynolds– and the SubStokes–model: We see the cut of the three dimensional pressures $p^R \approx \psi^R/g$ (upper plot – R) and $p^s \approx \psi^s/g$ (lower plot – s) for the different example applications with horizontal velocities.

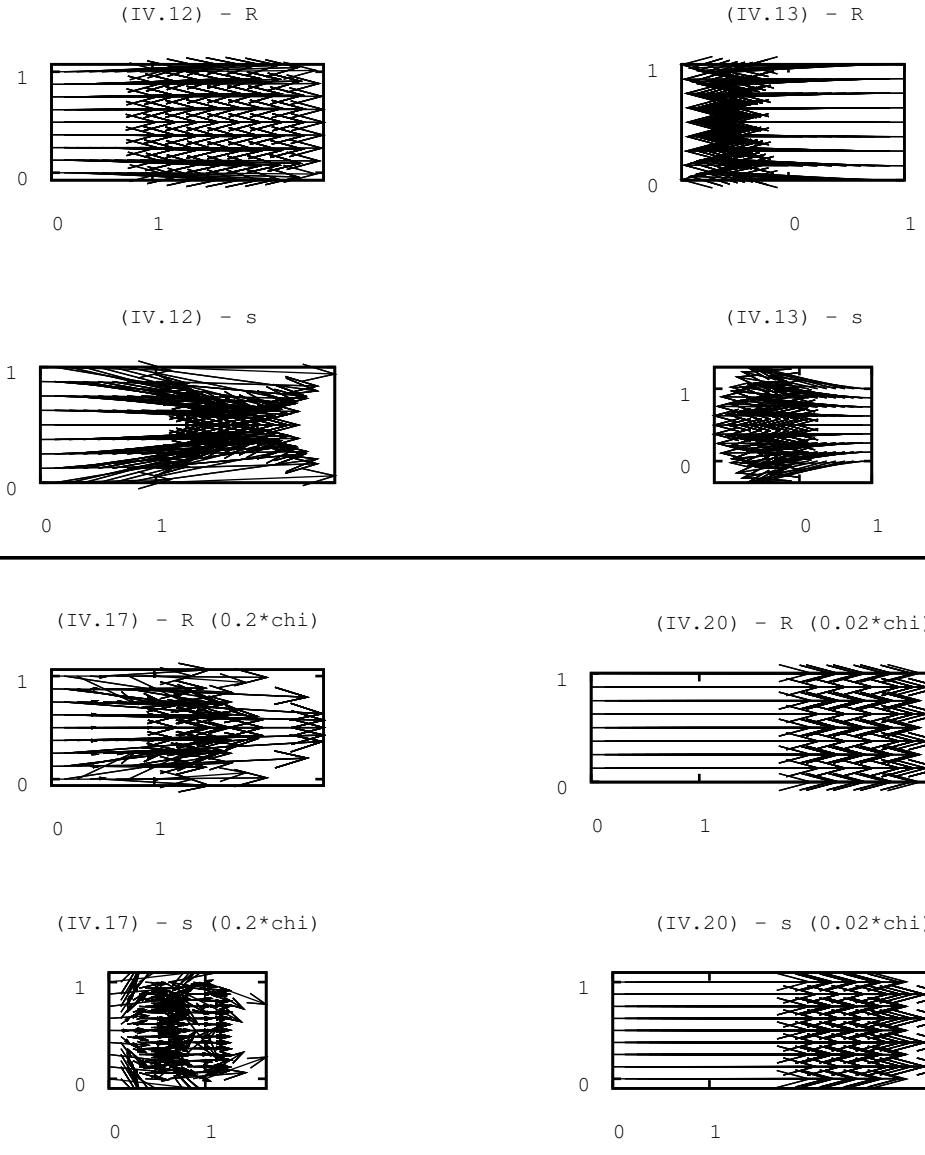

Figure IV.115: Comparison of the Reynolds– and the SubStokes–model: We see the velocity-fields χ^R and χ^s for the different example applications with horizontal velocities.

IV.3.4 Model Adaptive Fluid Simulation

In this section we give one brief example for model adaptivity for fluids, combining the Reynolds model (I.77) and SubStokes-model (I.58) using the model error estimate of theorem III.6 and the strategies of section III.3.

We consider only the example application (IV.17).
As described in section III.3 we divide the domain

$$\Omega_2 = [0;1] \times [0;1]$$

into the subdomains Ω^R and Ω^s

$$\overline{\Omega^R \cup \Omega^s} = \overline{\Omega_2}, \quad \Omega^R \cap \Omega^s = \emptyset.$$

On Ω^R we solve the Reynolds equation (I.77), on Ω^s we solve the SubStokes problem (I.58).
For both we take inhomogenous Dirichlet boundary conditions for the pressure

$$\psi|_{\partial\Omega_2} = 200$$

and in the case of the SubStokes model the boundary condition (I.56) for χ.
The surface- and velocity-data on the underside of the fluid film are zero:

$$z_0 = 0, \quad v(z_0) = 0$$

while the data on the upper side differ in each example.
The computations start on an initial grid of 64 Reynolds-cells.
The grid refinement is organised as before: We refine the 30% of the cells with the highest error per cell and coarsen 3% of the cells with the smallest error. Therefor we use the estimates of theorems III.16 and III.23.
In each step on 5% of the Reynolds cells the model is refined with the help of the estimate in theorem III.6, using the sorted error model refinement algorithm III.3.

The sequence of refined grids and models is shown in figure IV.116.

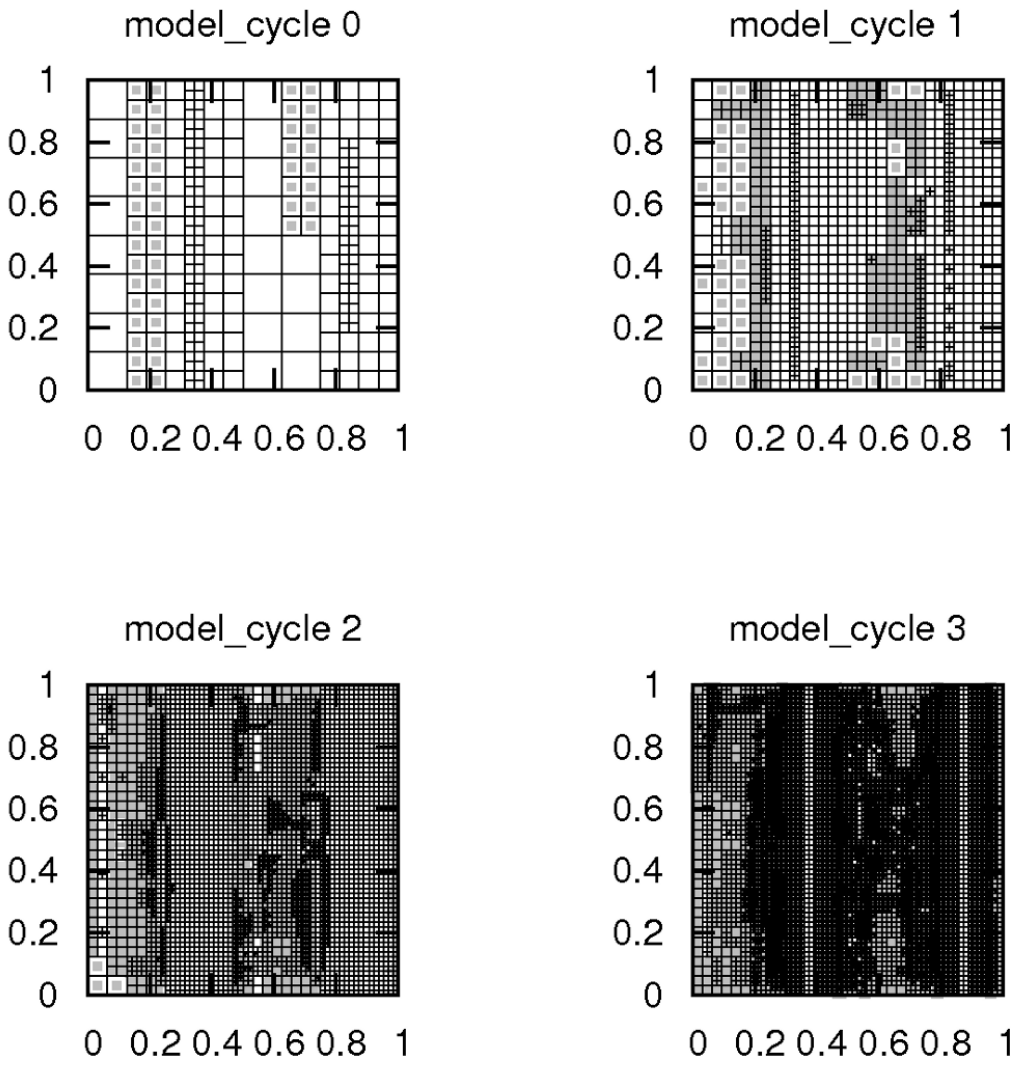

Figure IV.116: Adaptively refined model and grids. The cells of the SubStokes model are marked grey.

The decrease of the total error, i. e. the discretisation error estimate (of theorem III.23) and the model error, versus the number of SubStokes cells for the model adaptive calculation in comparison to the results of the pure SubStokes simulation (section IV.3.2.11) is shown in figure IV.117.

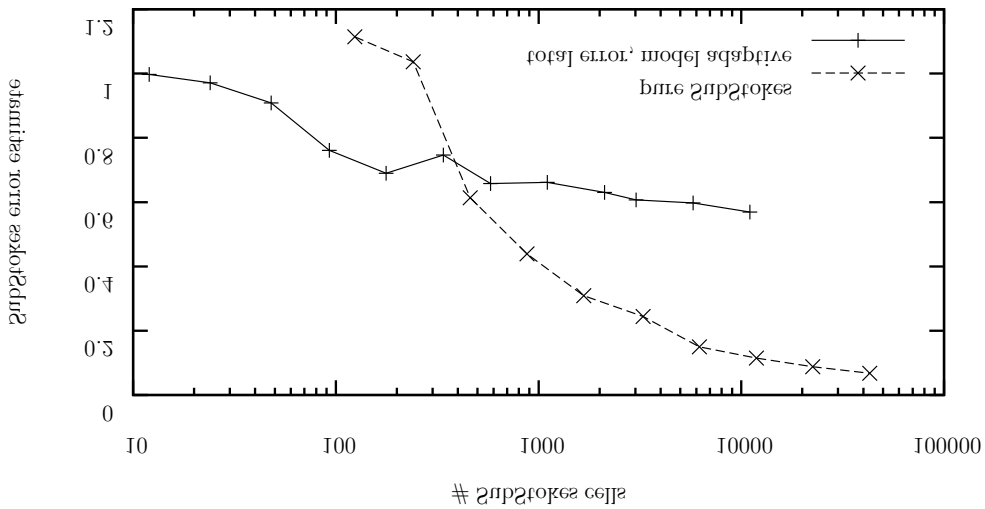

Figure IV.117: A-posteriori estimate of the SubStokes solution versus the number of SubStokes cells.

The comparison of a cut of one preliminary solution of the model adaptive algorithm to the solution of the pure Reynolds calculation (section IV.3.1.11) and the one of the pure SubStokes calculation (section IV.3.2.11) is shown in figure IV.118.

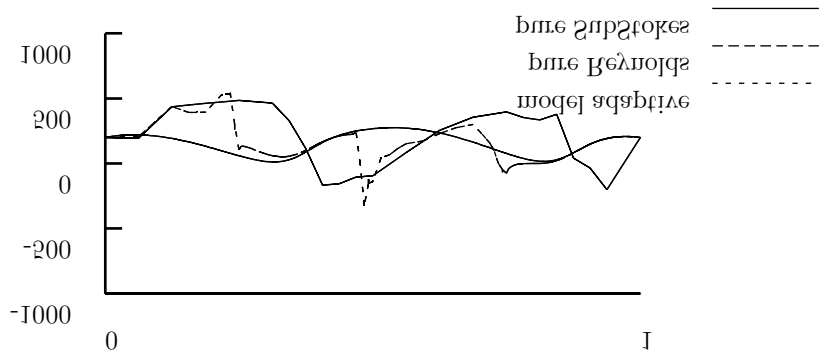

Figure IV.118: The solution of the model adaptive calculation and the ones of the pure Reynolds and pure SubStokes calculation.

The series of refined grids and models, shows that refinement takes place in regions of a wide gap, what is reasonable, because there the Reynolds approximation (I.56) is rather inaccurate.
In figure IV.118 we see, that the model adaptive solution fluctuates between the pure Reynolds and the pure SubStokes solution. At some of the interfaces between both models the fluctuation is rather sharp.
The decrease of the error estimate (figure IV.117) is not as strong as one could hope for. This gives hints to a possible improvement of the model error estimate (theorem III.6), which by now only depends on the geometrical properties of the fluid gap.
Furthermore the refinement parameters of this single application are not chosen optimal and the solver can be balanced, to avoid the sharp fluctuations of the solution and to accelerate the convergence.

IV.3.5 Reynolds Model with cavitation

The results of section IV.3.1 give hints for the occurance of cavitation for examples (IV.8), (IV.11), (IV.16), (IV.17), (IV.19) and (IV.20). Thus we only consider these in the following.
For each example we solve the Reynolds inequation (II.39).
All computations start on an initial grid of $64 \times 64 = 4096$ cells and refine it adaptively using the estimator of theorem III.17 and a fixed-fraction strategy, as already done before: We refine the 30% of the cells with the highest error per cell, which results in about doubling of the cells. Furthermore we coarsen 3% of the cells with the smallest error.

IV.3.5.1 Plain surface and vertical upward velocity

We consider the Reynolds cavitation problem (II.39) with the upper surface given by (IV.8). The sequence of refined grids is shown in figure IV.119 and the final solution in figure IV.120.

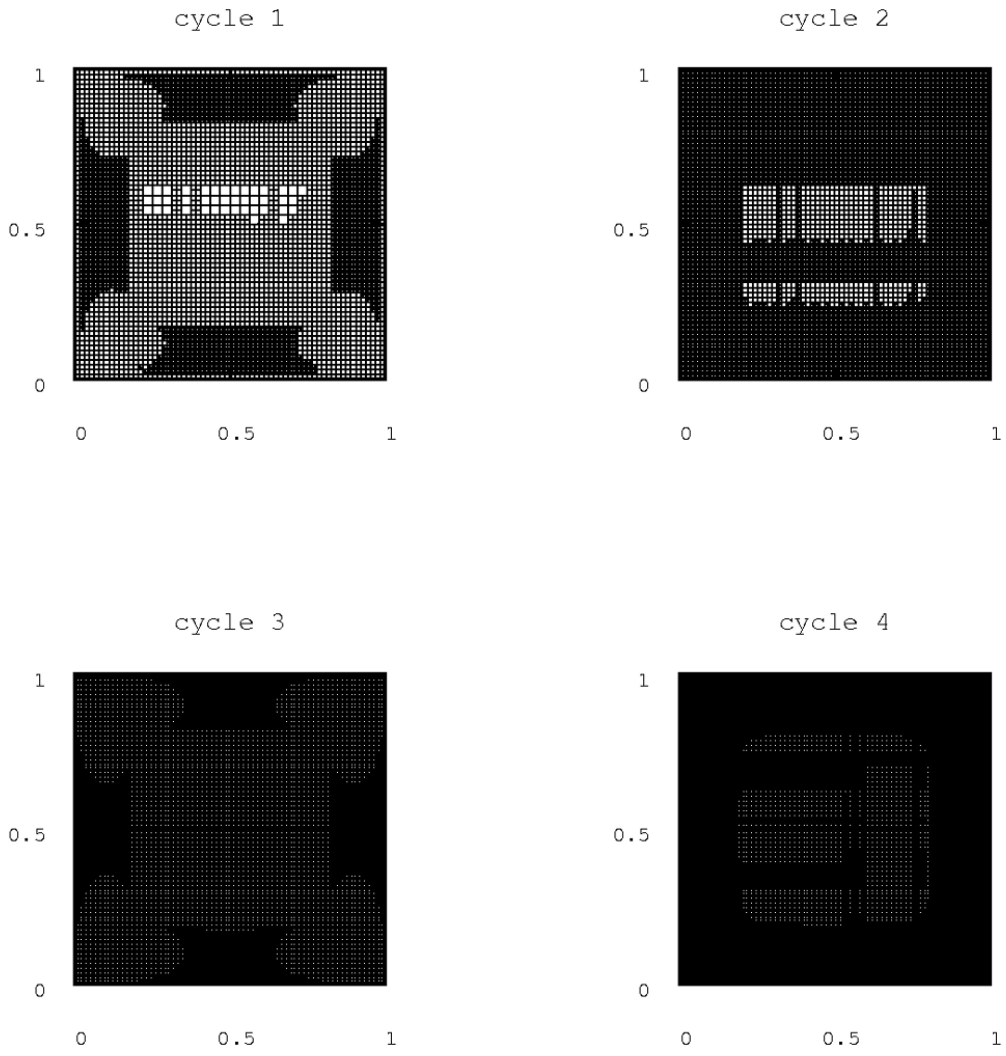

Figure IV.119: Adaptively refined grids.

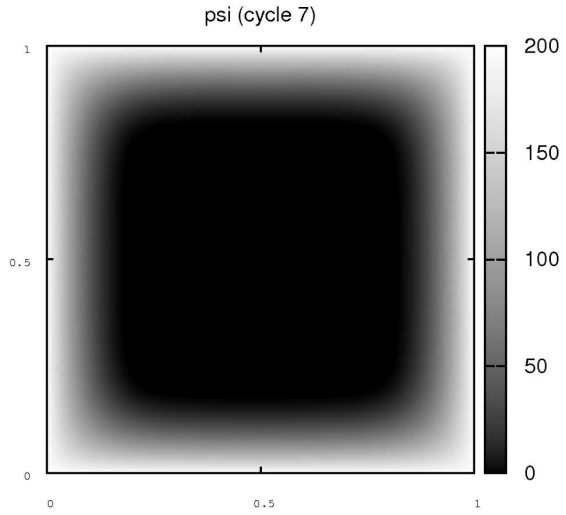

Figure IV.120: The solution of the considered problem.

The following table IV.64 shows the results of one run of our algorithm:

cycle	# active cells	# dofs	a-posteriori-estimate	ratio
0	7657	8028	2.8677e+02	inf
1	14782	15205	2.6335e+02	0.9183
2	28087	28793	1.6601e+02	0.6304
3	54115	56098	1.2809e+02	0.7716
4	102820	104297	9.0809e+01	0.7089
5	197185	202472	6.5822e+01	0.7248
6	374653	378102	4.8854e+01	0.7422
7	710065	714426	3.3724e+01	0.6903

Table IV.64: The convergence of one run of our algorithm for the considered problem.

We see the decrease of the estimator by the factor $1/\sqrt{2}$, which indicates the expected order $O(n_{dofs}^{-1/2})$.

IV.3.5.2 Steep surface and vertical upward velocity

We consider the Reynolds cavitation problem (II.39) with the upper surface given by (IV.11). The sequence of refined grids is shown in figure IV.121 and the final solution in figure IV.122.

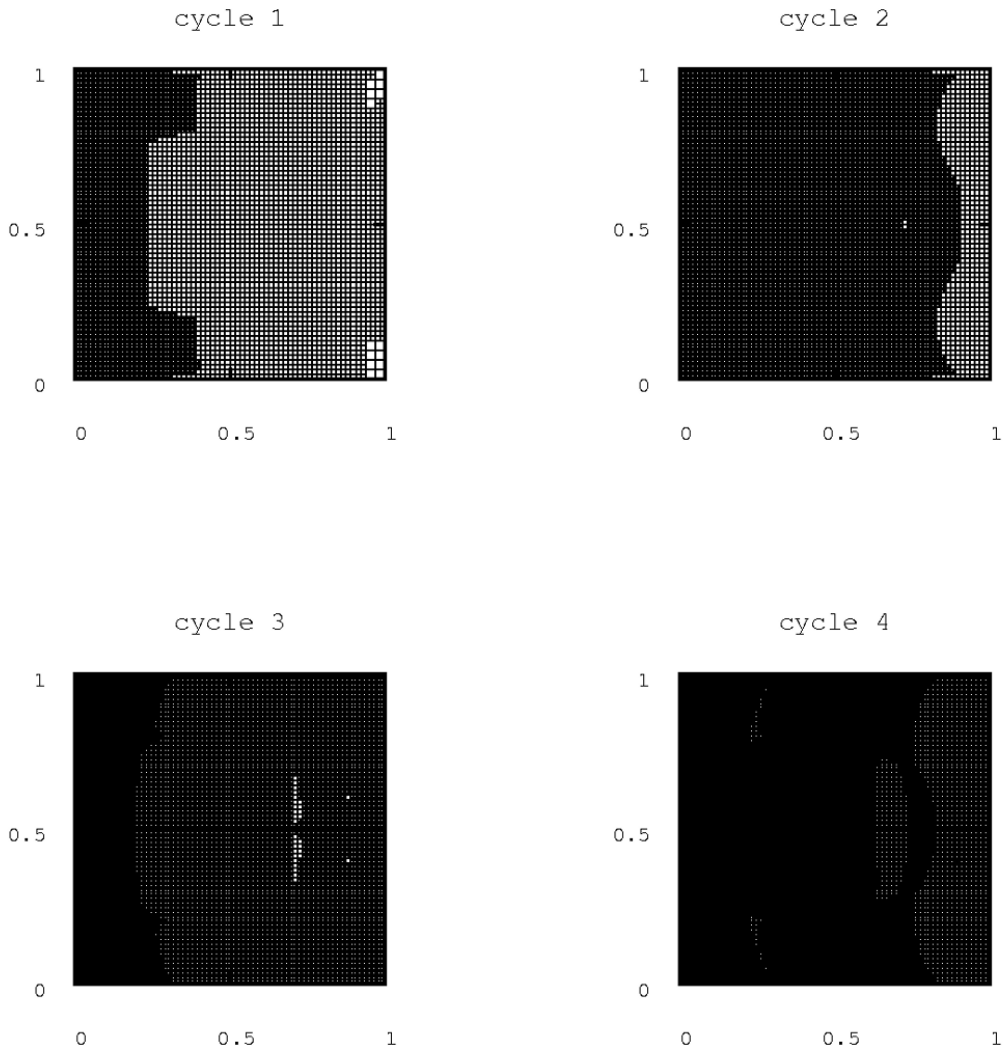

Figure IV.121: Adaptively refined grids.

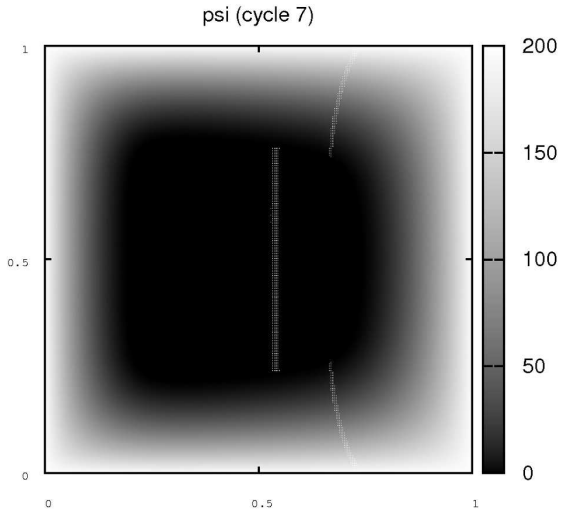

Figure IV.122: The solution of the considered problem.

The following table IV.65 shows the results of one run of our algorithm:

cycle	# active cells	# dofs	a-posteriori-estimate	ratio
0	7741	7973	1.9849e+02	inf
1	14710	14972	1.5882e+02	0.8001
2	27862	28338	1.0873e+02	0.6846
3	52612	53284	8.2898e+01	0.7624
4	99565	100607	5.9410e+01	0.7167
5	187753	189187	4.3484e+01	0.7319
6	353995	356321	3.1972e+01	0.7353
7	666943	669642	2.2920e+01	0.7169

Table IV.65: The convergence of one run of our algorithm for the considered problem.

We see the decrease of the estimator by the factor $1/\sqrt{2}$, which indicates the expected order $O(n_{dofs}^{-1/2})$.

IV.3.5.3 Wave surface and vertical upward velocity

We consider the Reynolds cavitation problem (II.39) with the upper surface given by (IV.16). The sequence of refined grids is shown in figure IV.123 and the final solution in figure IV.124.

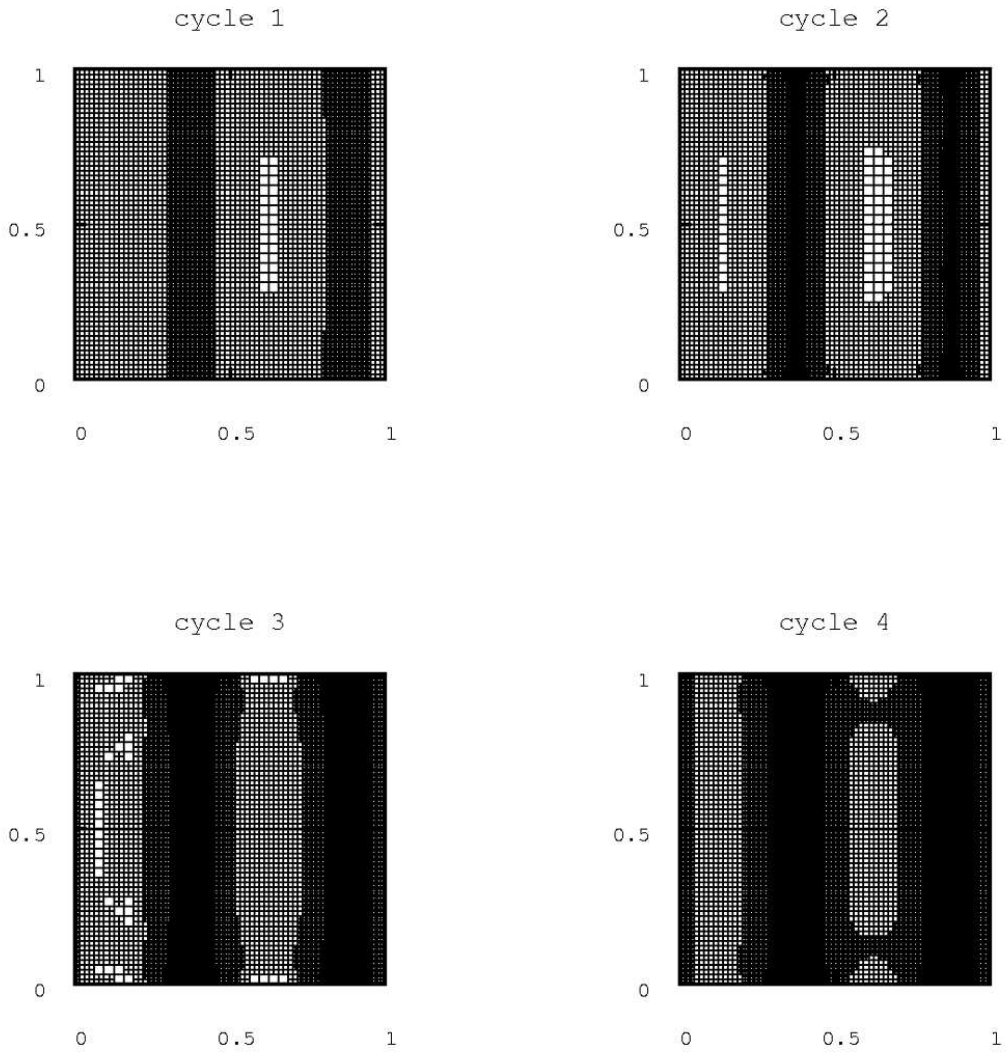

Figure IV.123: Adaptively refined grids.

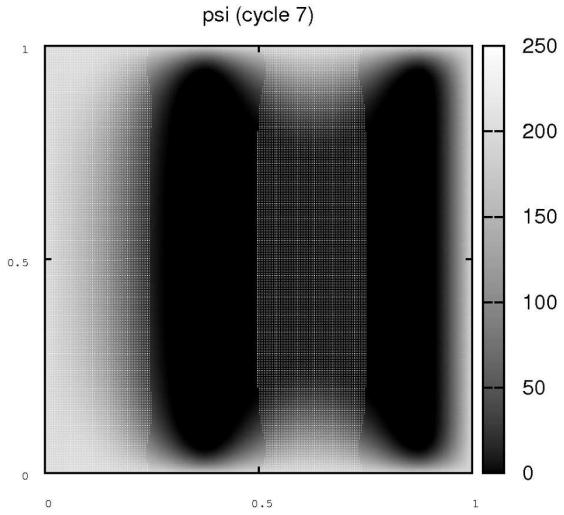

Figure IV.124: The solution of the considered problem.

The following table IV.66 shows the results of one run of our algorithm:

cycle	# active cells	# dofs	a-posteriori-estimate	ratio
0	7720	8014	1.1707e+03	inf
1	14575	15186	6.3064e+02	0.5387
2	27580	28405	4.4943e+02	0.7127
3	52369	53683	3.2029e+02	0.7126
4	99502	100911	2.3918e+02	0.7468
5	188911	191466	1.6526e+02	0.6910
6	358933	361319	1.2710e+02	0.7691
7	681964	687221	8.6529e+01	0.6808

Table IV.66: The convergence of one run of our algorithm for the considered problem.

We see the decrease of the estimator by the factor $1/\sqrt{2}$, which indicates the expected order $O(n_{dofs}^{-1/2})$.

IV.3.5.4 Wave surface and horizontal velocity

We consider the Reynolds cavitation problem (II.39) with the upper surface given by (IV.17). The sequence of refined grids is shown in figure IV.125 and the final solution in figure IV.126.

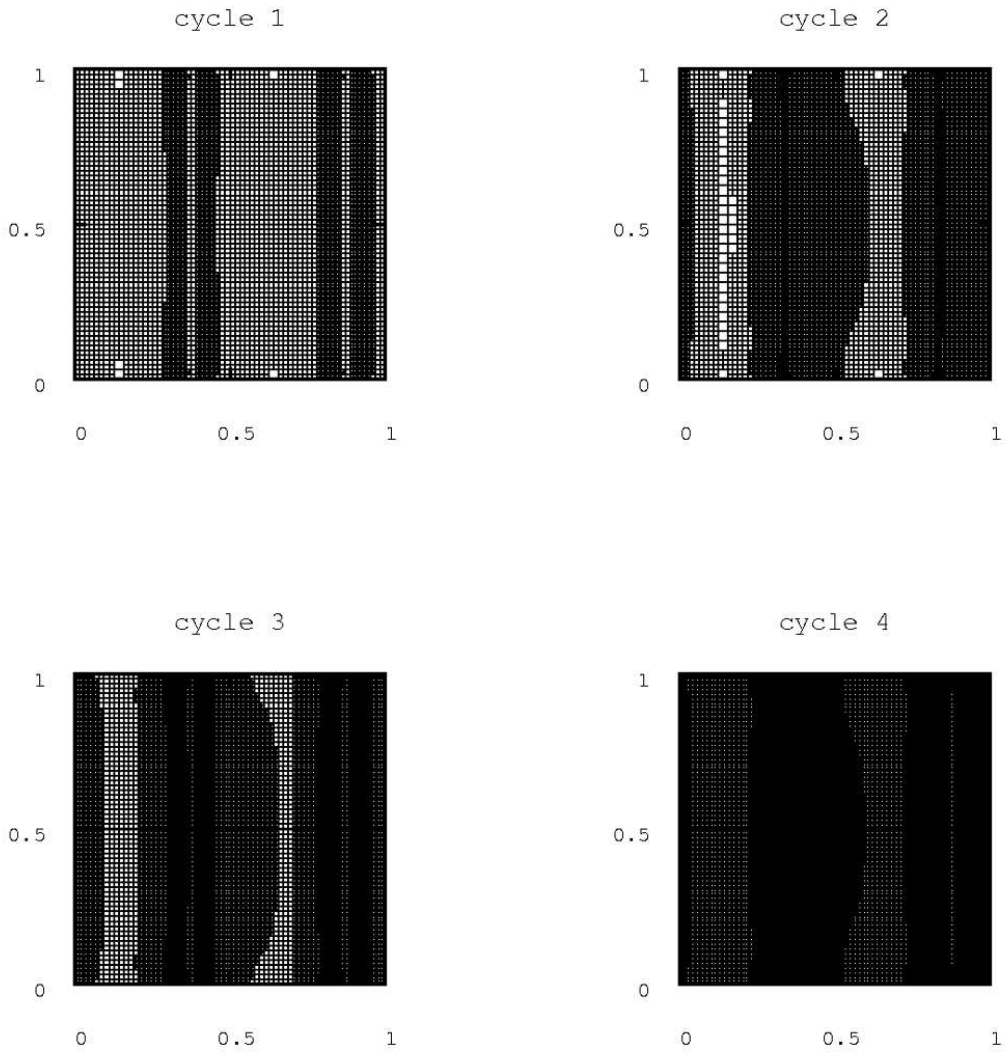

Figure IV.125: Adaptively refined grids.

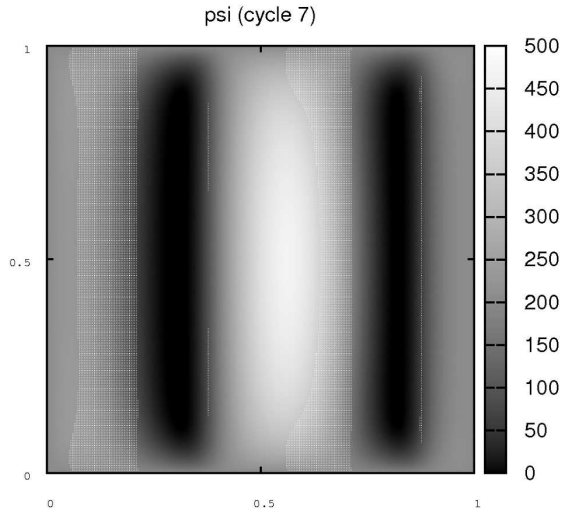

Figure IV.126: The solution of the considered problem.

The following table IV.67 shows the results of one run of our algorithm:

cycle	# active cells	# dofs	a-posteriori-estimate	ratio
0	7765	8182	7.7868e+02	inf
1	14659	15340	5.0724e+02	0.6514
2	27853	28788	3.8257e+02	0.7542
3	52921	54325	2.6947e+02	0.7044
4	100552	102418	1.9911e+02	0.7389
5	191050	193873	1.4433e+02	0.7249
6	362176	366698	1.0370e+02	0.7185
7	688111	692338	7.7484e+01	0.7472

Table IV.67: The convergence of one run of our algorithm for the considered problem.

We see the decrease of the estimator by the factor $1/\sqrt{2}$, which indicates the expected order $O(n_{dofs}^{-1/2})$.

IV.3.5.5 Hilly surface and vertical upward velocity

We consider the Reynolds problem (II.39) with the upper surface given by (IV.19). The sequence of refined grids is shown in figure IV.127 and the final solution in figure IV.128.

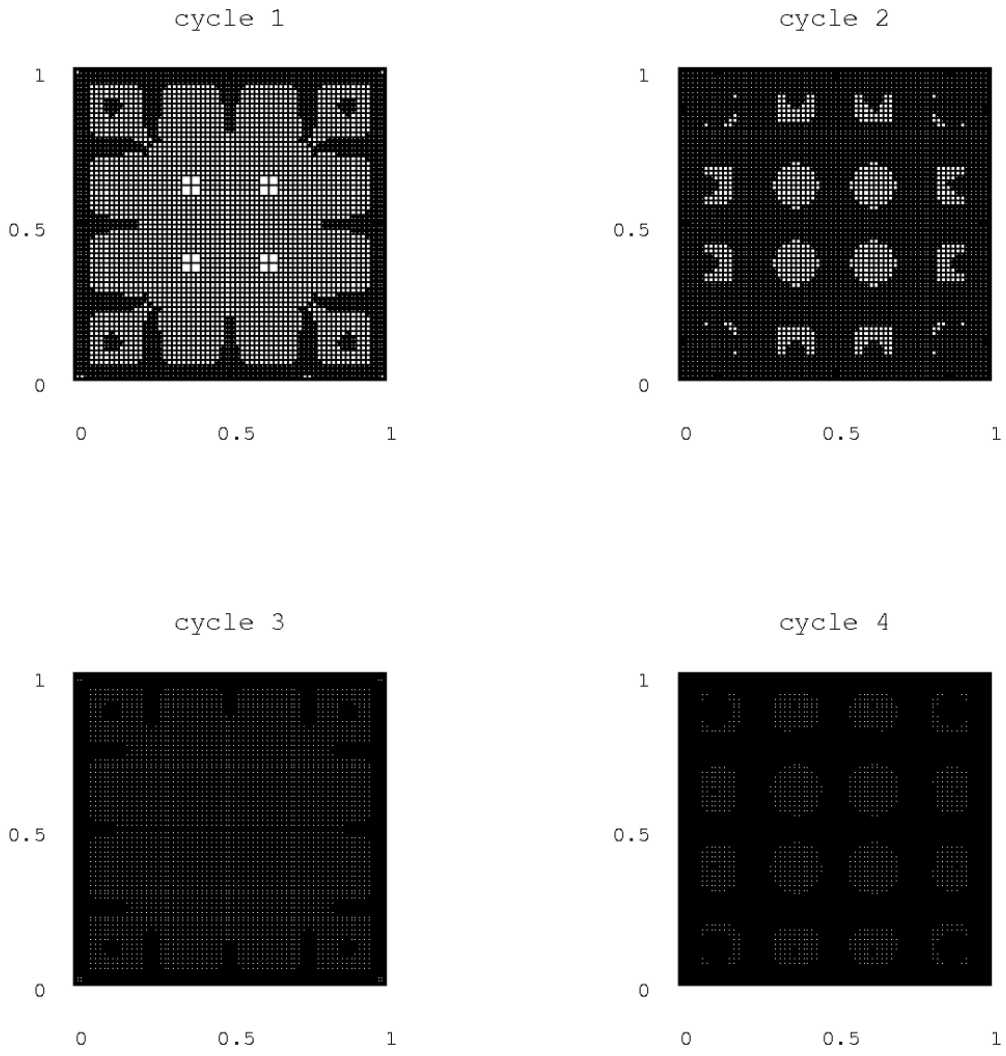

Figure IV.127: Adaptively refined grids.

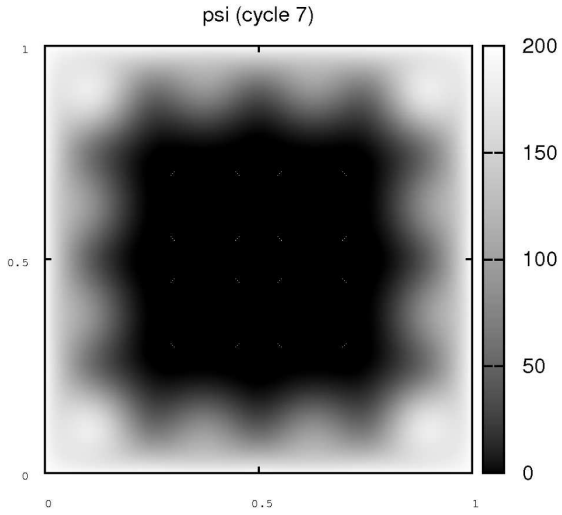

Figure IV.128: The solution of the considered problem.

The following table IV.68 shows the results of one run of our algorithm:

cycle	# active cells	# dofs	a-posteriori-estimate	ratio
0	7735	8309	2.7145e+02	inf
1	14698	15253	2.1151e+02	0.7792
2	27928	28949	1.4597e+02	0.6901
3	53065	54282	1.1104e+02	0.7607
4	100825	102910	7.8420e+01	0.7062
5	191377	194014	5.8171e+01	0.7418
6	363475	367364	4.2161e+01	0.7248
7	688861	694819	3.0467e+01	0.7226

Table IV.68: The convergence of one run of our algorithm for the considered problem.

We see the decrease of the estimator by the factor $1/\sqrt{2}$, which indicates the expected order $O(n_{dofs}^{-1/2})$.

IV.3.5.6 Hilly surface and horizontal velocity

We consider the Reynolds problem (II.39) with the upper surface given by (IV.20). The sequence of refined grids is shown in figure IV.129 and the final solution in figure IV.130.

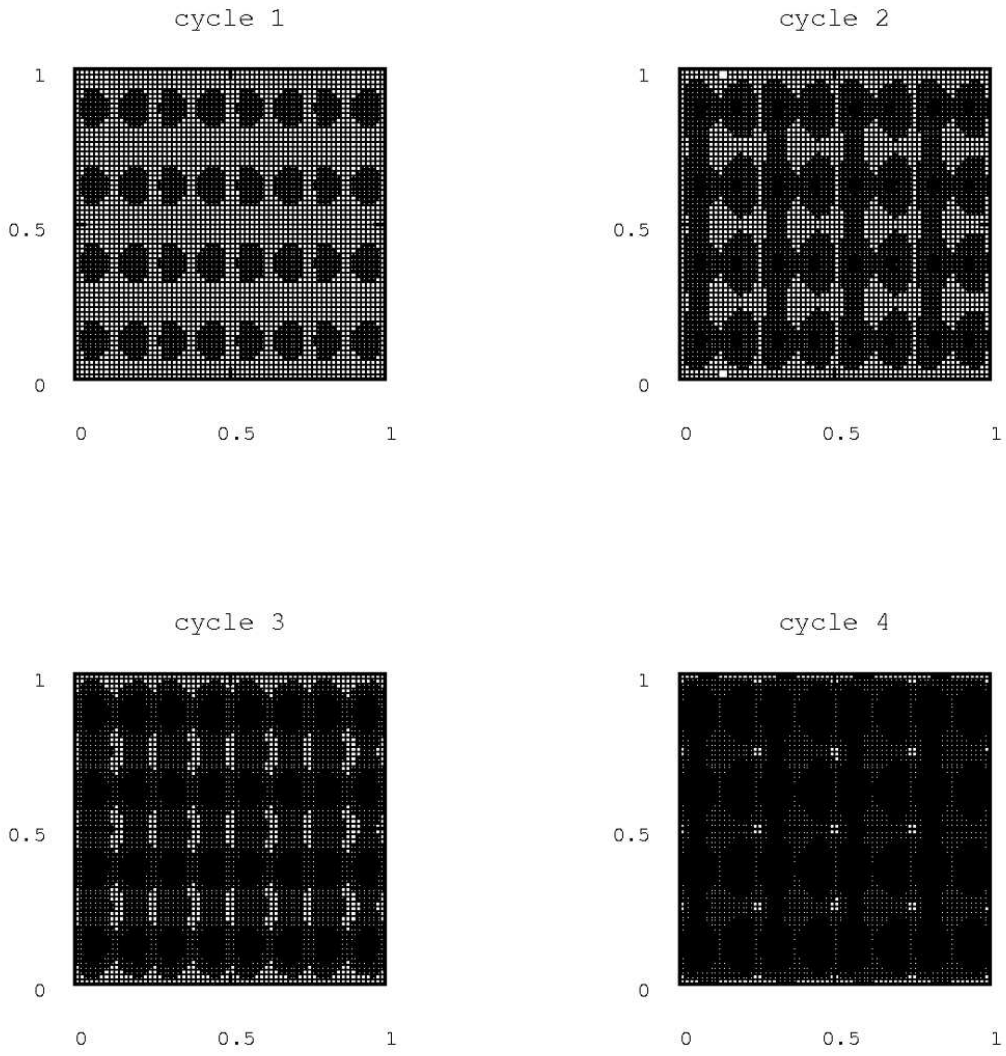

Figure IV.129: Adaptively refined grids.

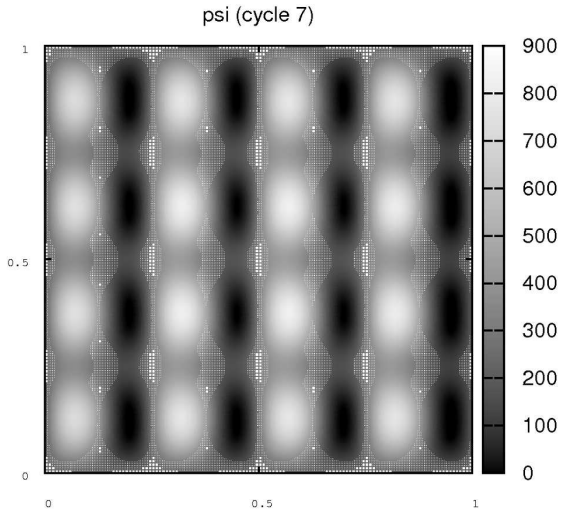

Figure IV.130: The solution of the considered problem.

The following table IV.69 shows the results of one run of our algorithm:

cycle	# active cells	# dofs	a-posteriori-estimate	ratio
0	7783	8360	3.2459e+03	inf
1	14782	15902	2.0670e+03	0.6368
2	28087	29538	1.5421e+03	0.7461
3	53368	55652	1.0731e+03	0.6958
4	101401	104445	8.0302e+02	0.7484
5	192664	197167	5.6948e+02	0.7092
6	366064	372271	4.1880e+02	0.7354
7	695482	703806	3.0349e+02	0.7247

Table IV.69: The convergence of one run of our algorithm for the considered problem.

We see the decrease of the estimator by the factor $1/\sqrt{2}$, which indicates the expected order $O(n_{dofs}^{-1/2})$.

All calculations in sections IV.3.5.1–IV.3.5.6 show a decrease of the error estimate, given in theorem III.17, of the expected order $O(n_{dofs}^{1/2})$. For most of the more sophisticated gap-shapes, the wave– and hill–gaps (sections IV.3.5.3–IV.3.5.5), one sees that the grid refinement, controlled by the estimate of theorem III.17, takes place around the most narrow parts of the gap (figures IV.123, IV.125, IV.127). The only exception is the case of a hilly surface and a horizontal velocity (section IV.3.5.6). There the regions of a surface gradient in direction of the horizontal velocity are refined as well as the narrow regions that have an extension orthogonal to the surface velocity (the vertical valleys in figure IV.129). A comparison with the results of section IV.3.1 shows, that the regions of cavitation are detected correctly. Unfortunately the grid is not coarsened in these regions of constant pressure.

IV.3.6 SubStokes Model with Cavitation

We solve the SubStokes problem for cavitation (I.66) for different cases.

As in the Reynolds case the results of section IV.3.2 give hints for cavitation for examples (IV.8), (IV.11), (IV.16), (IV.17), (IV.19) and (IV.20). Thus we only consider these in the following.
For each example we solve the SubStokes problem for cavitation (I.66) on the domain

$$\Omega_2 = [0;1] \times [0;1]$$

with inhomogenous boundary conditions

$$\psi|_{\partial\Omega_2} = 200.0$$

and the boundary condition (I.56) for χ. The surface- and velocity-data on the underside of the fluid film are zero:

$$z_0 = 0, \quad v(z_0) = 0$$

while the data on the upper side differ in each example.
All computations start on an initial grid of 64 cells and refine it adaptively using the estimator of theorem III.24 and a fixed-fraction strategy, as already done in section IV.3.2: We refine the 30% of the cells with the highest error per cell, which results in about doubling of the cells. Furthermore we coarsen 3% of the cells with the smallest error.

IV.3.6.1 Plain surface and vertical upward velocity

We consider the SubStokes problem for cavitation (I.66) with the upper surface given by (IV.8). The sequence of refined grids is shown in figure IV.131 and the final solution in figure IV.132.

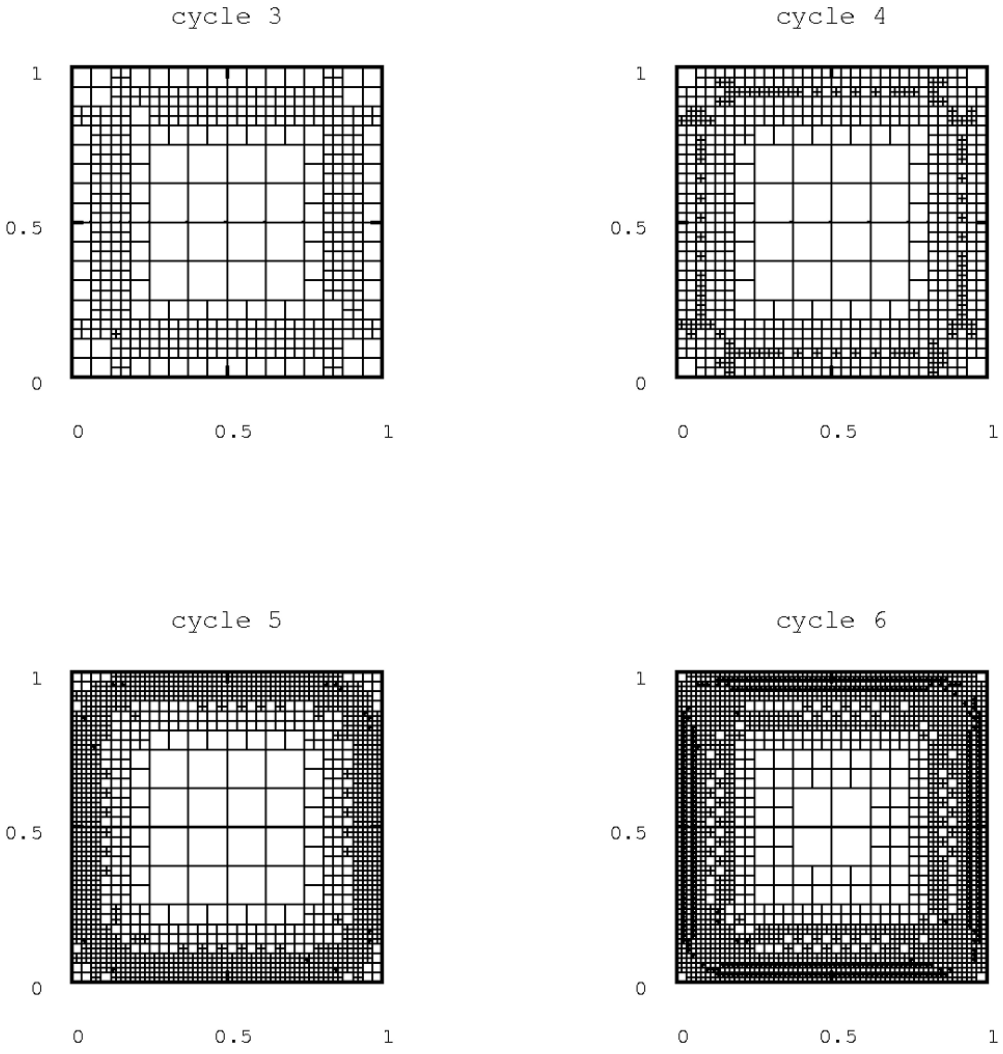

Figure IV.131: Adaptively refined grids.

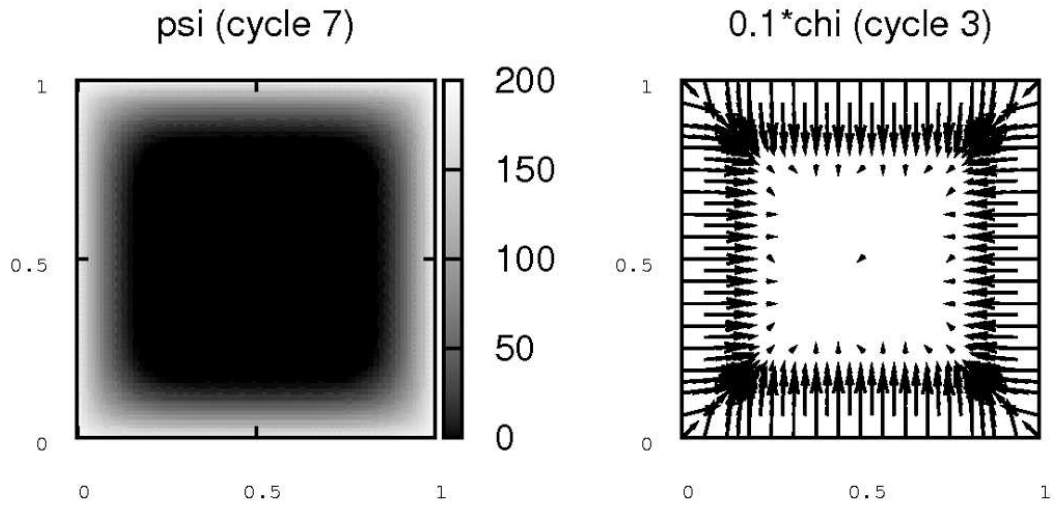

Figure IV.132: The solution of the considered problem.

The following table IV.70 shows the results of one run of our algorithm:

cycle	# active cells	# dofs	a-posteriori-estimate	ratio
0	124	483	1.6619e+02	inf
1	265	1050	1.0048e+02	0.6047
2	505	1818	8.5107e+01	0.8470
3	961	3540	5.8047e+01	0.6821
4	1861	6420	4.4709e+01	0.7702
5	3694	13323	3.0358e+01	0.6790
6	7033	25020	2.5496e+01	0.8399
7	13477	48240	1.9207e+01	0.7533

Table IV.70: The convergence of one run of our algorithm for the considered problem.

We see the decrease of the estimator by the factor $1/\sqrt{2}$, which indicates the expected order $O(n_{dofs}^{-1/2})$.

IV.3.6.2 Steep surface and vertical upward velocity

We consider the SubStokes problem for cavitation (I.66) with the upper surface given by (IV.7). The sequence of refined grids is shown in figure IV.133 and the final solution in figure IV.134.

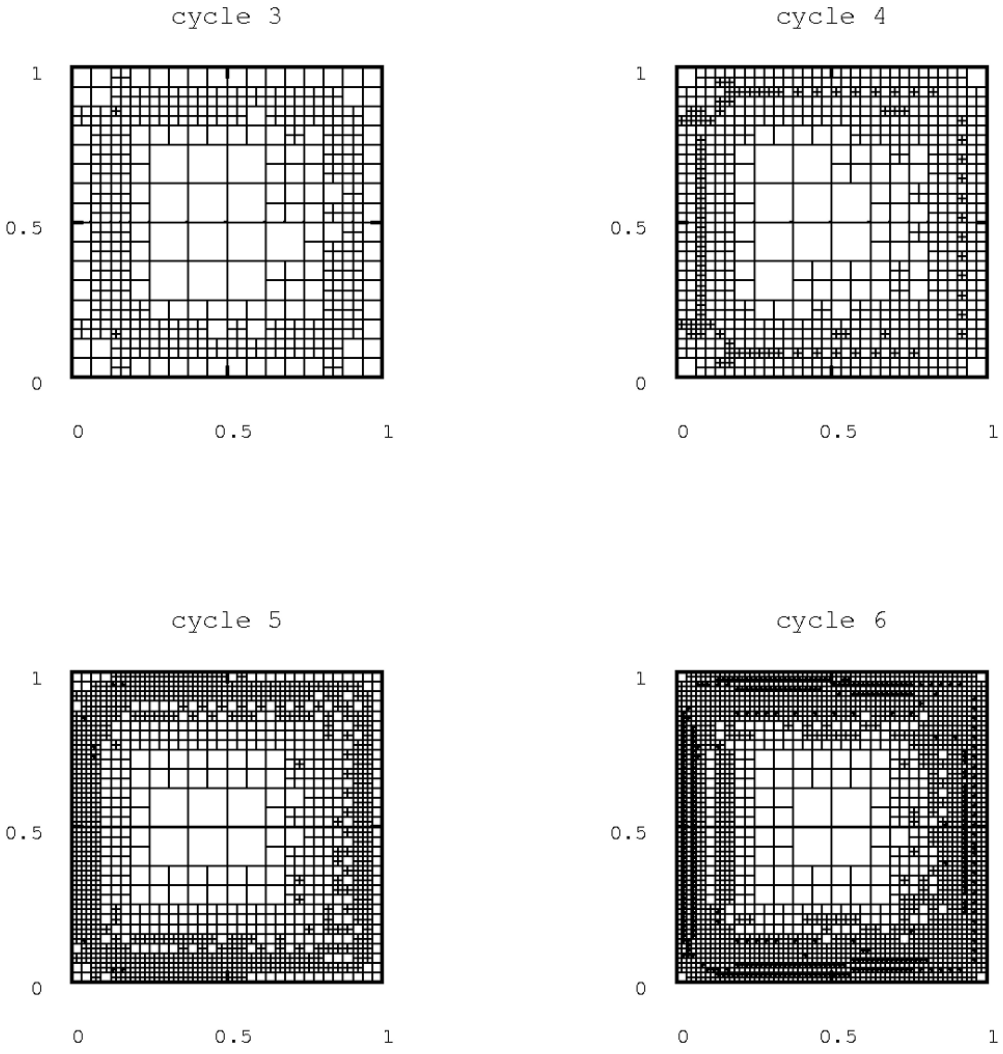

Figure IV.133: Adaptively refined grids.

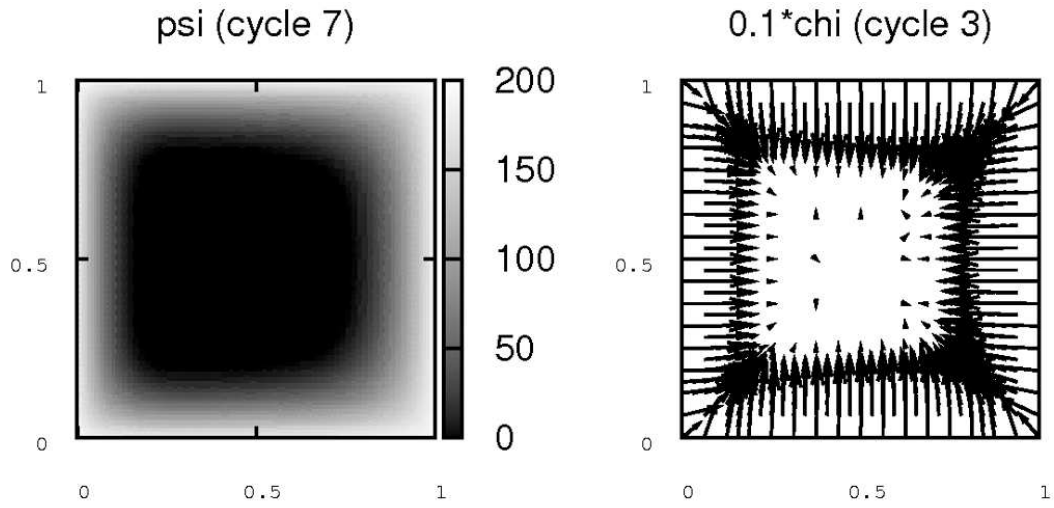

Figure IV.134: The solution of the considered problem.

The following table IV.71 shows the results of one run of our algorithm:

cycle	# active cells	# dofs	a-posteriori-estimate	ratio
0	124	483	1.4772e+02	inf
1	265	1050	9.6524e+01	0.6534
2	505	1827	7.7142e+01	0.7992
3	988	3612	5.4198e+01	0.7026
4	1906	6672	4.1638e+01	0.7683
5	3733	13383	3.0241e+01	0.7263
6	7153	25362	2.4633e+01	0.8145
7	13729	48588	2.0866e+01	0.8471

Table IV.71: The convergence of one run of our algorithm for the considered problem.

We see the decrease of the estimator by the factor $1/\sqrt{2}$, which indicates the expected order $O(n_{dofs}^{-1/2})$. The decrease becomes weaker, while the number of cells rises. This can be compensated by the use of a more accurate solver for the linear equations.

IV.3.6.3 Wave surface and vertical upward velocity

We consider the SubStokes problem for cavitation (I.66) with the upper surface given by (IV.16). The sequence of refined grids is shown in figure IV.135 and the final solution in figure IV.136.

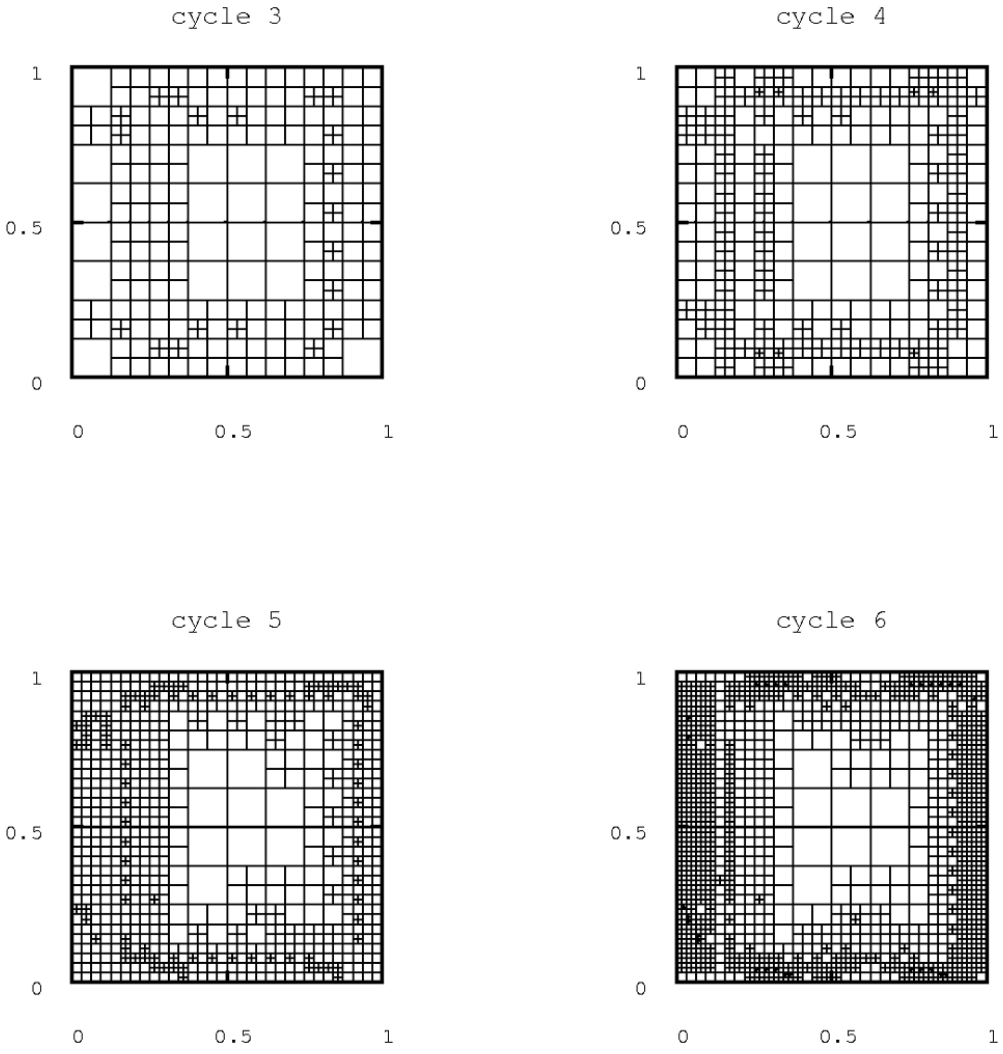

Figure IV.135: Adaptively refined grids.

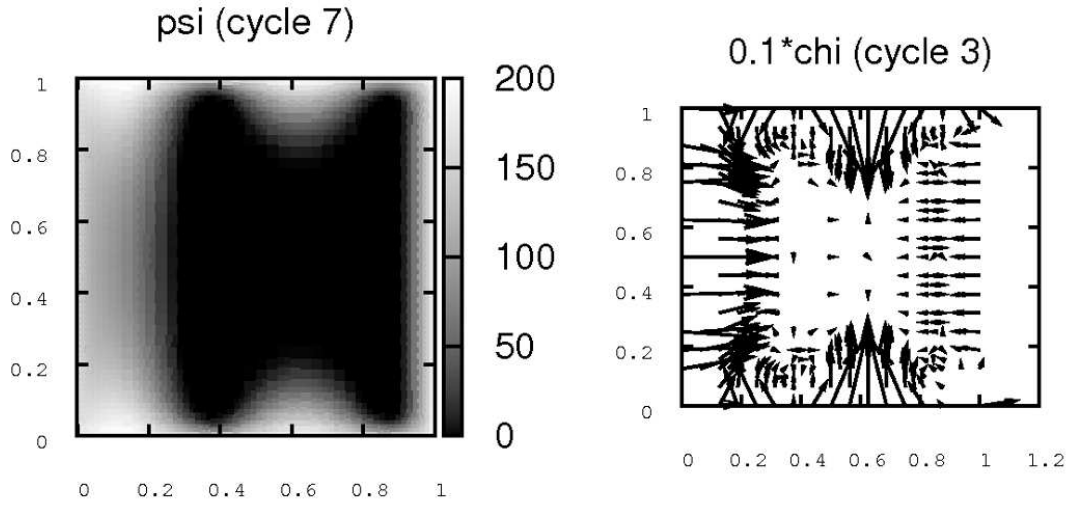

Figure IV.136: The solution of the considered problem.

The following table IV.72 shows the results of one run of our algorithm:

cycle	# active cells	# dofs	a-posteriori-estimate	ratio
0	64	243	nan	nan
1	124	486	1.6557e+02	nan
2	259	1008	1.1540e+02	0.6970
3	505	1920	1.0301e+02	0.8927
4	997	3702	8.8505e+01	0.8592
5	1933	6819	6.5495e+01	0.7400
6	3718	12942	4.8833e+01	0.7456
7	7153	24108	3.8346e+01	0.7853

Table IV.72: The convergence of one run of our algorithm for the considered problem.

We see the decrease of the estimator by the factor $1/\sqrt{2}$, which indicates the expected order $O(n_{dofs}^{-1/2})$.

IV.3.6.4 Wave surface and horizontal velocity

We consider the SubStokes problem for cavitation (I.66) with the upper surface given by (IV.17). The sequence of refined grids is shown in figure IV.137 and the final solution in figure IV.138.

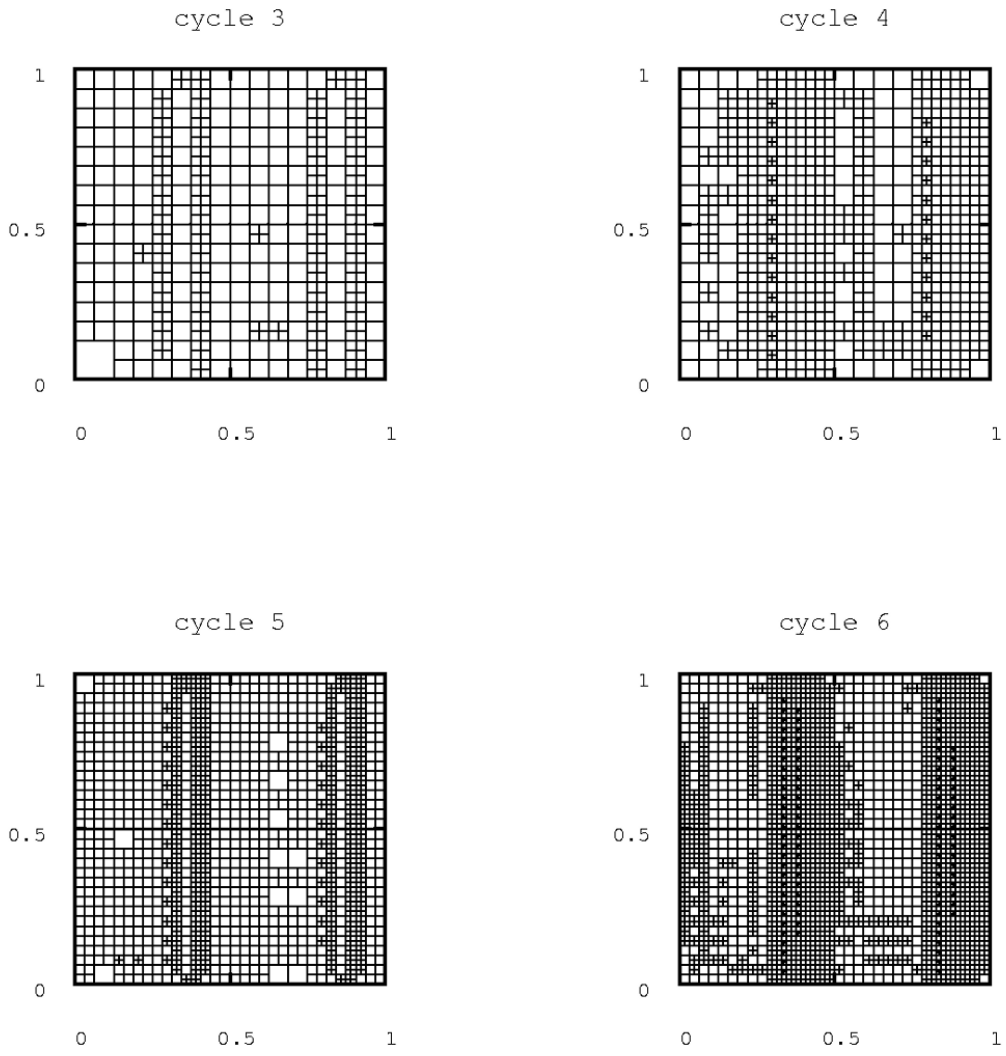

Figure IV.137: Adaptively refined grids.

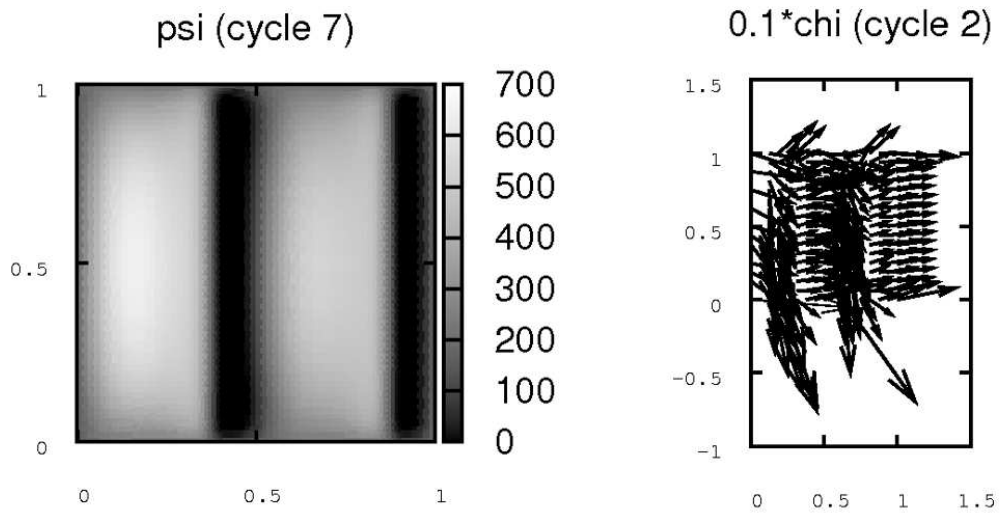

Figure IV.138: The solution of the considered problem.

The following table IV.73 shows the results of one run of our algorithm:

cycle	# active cells	# dofs	a-posteriori-estimate	ratio
0	124	498	1.0366e+03	inf
1	238	861	7.8220e+02	0.7546
2	454	1680	6.4840e+02	0.8289
3	865	3054	4.2011e+02	0.6479
4	1651	5682	2.9543e+02	0.7032
5	3139	10848	2.1495e+02	0.7276
6	5977	19401	1.5535e+02	0.7227
7	11359	36213	1.1587e+02	0.7458

Table IV.73: The convergence of one run of our algorithm for the considered problem.

Basically we see the decrease of the estimator by the factor $1/\sqrt{2}$, which indicates the expected order $O(n_{dofs}^{-1/2})$.

IV.3.6.5 Hilly surface and vertical upward velocity

We consider the SubStokes problem for cavitation (I.66) with the upper surface given by (IV.19). The sequence of refined grids is shown in figure IV.139 and the final solution in figure IV.140.

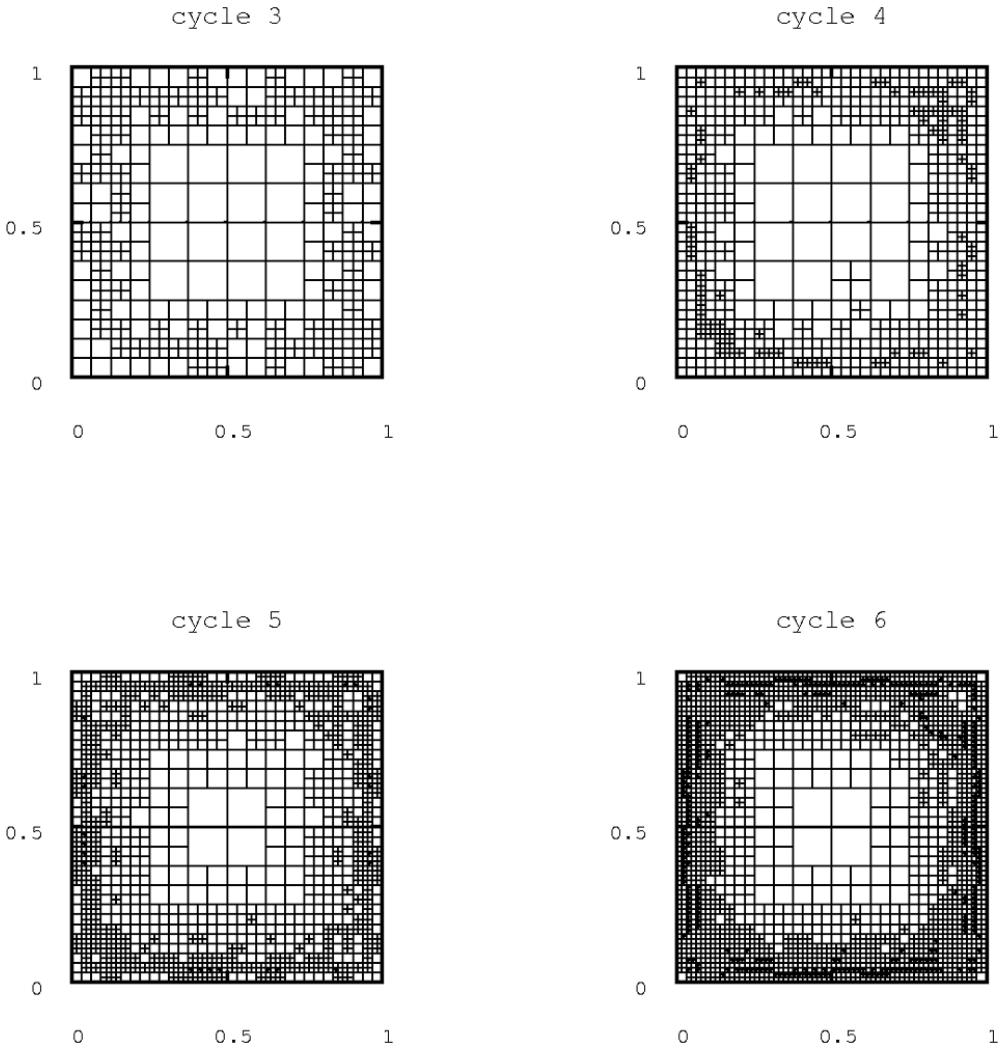

Figure IV.139: Adaptively refined grids.

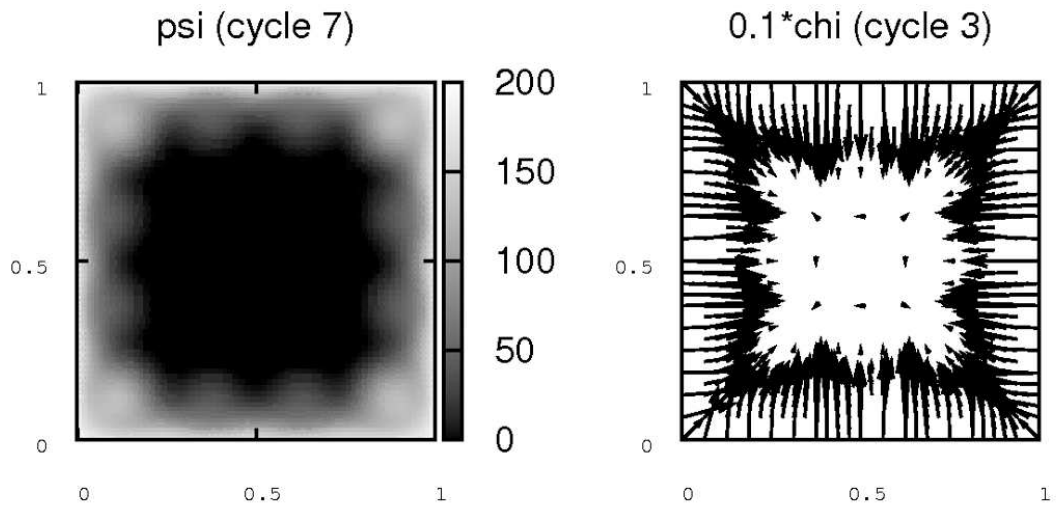

Figure IV.140: The solution of the considered problem.

The following table IV.74 shows the results of one run of our algorithm:

cycle	# active cells	# dofs	a-posteriori-estimate	ratio
0	124	483	1.6324e+02	inf
1	250	993	1.4159e+02	0.8674
2	478	1803	1.2178e+02	0.8601
3	916	3414	8.4274e+01	0.6920
4	1792	6474	5.3722e+01	0.6375
5	3421	12249	3.9649e+01	0.7380
6	6766	23871	2.9725e+01	0.7497
7	12925	45690	2.1654e+01	0.7285

Table IV.74: The convergence of one run of our algorithm for the considered problem.

We see the decrease of the estimator by the factor $1/\sqrt{2}$, which indicates the expected order $O(n_{dofs}^{-1/2})$.

IV.3.6.6 Hilly surface and horizontal velocity

We consider the SubStokes problem for cavitation (I.66) with the upper surface given by (IV.20). The sequence of refined grids is shown in figure IV.141 and the final solution in figure IV.142.

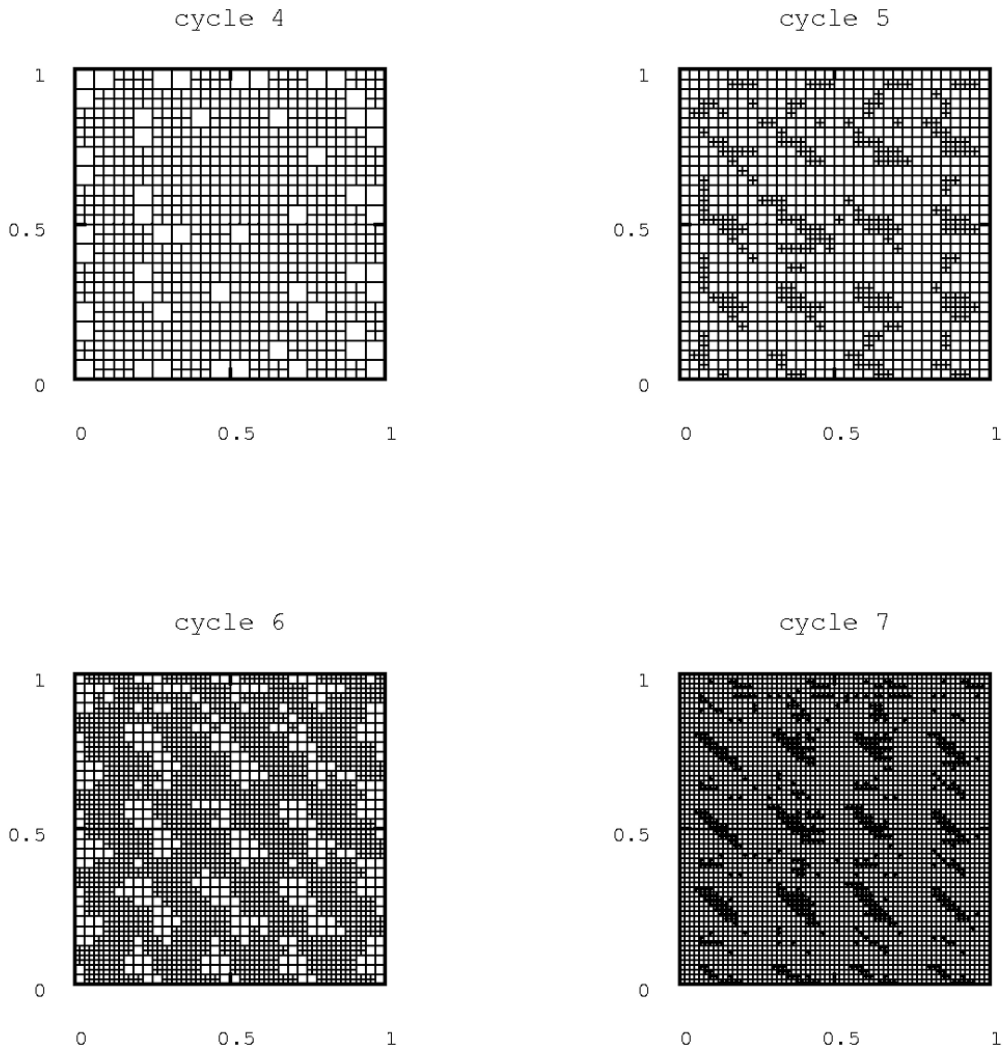

Figure IV.141: Adaptively refined grids.

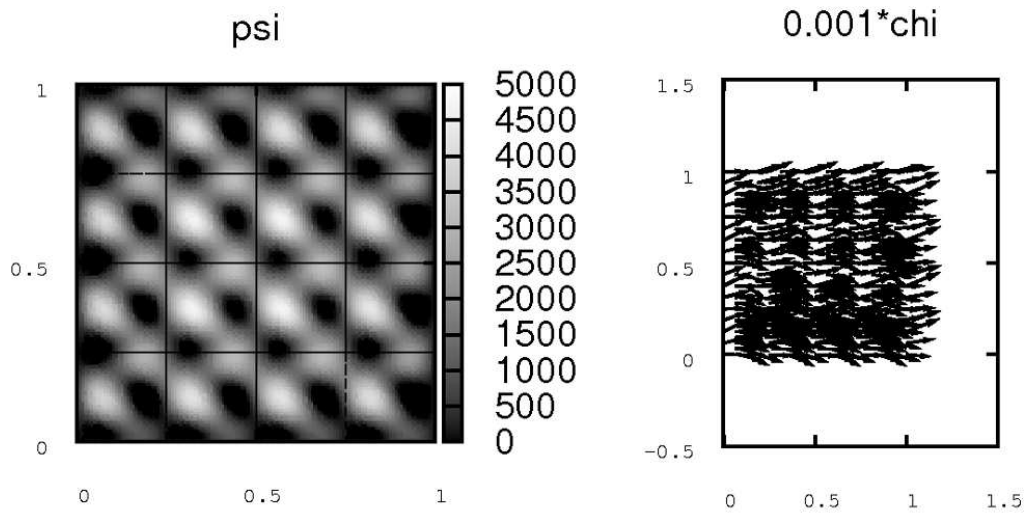

Figure IV.142: The solution of the considered problem.

The following table IV.75 shows the results of one run of our algorithm:

cycle	# active cells	# dofs	a-posteriori-estimate	ratio
0	124	543	1.4042e+04	inf
1	238	828	1.0804e+04	0.7694
2	454	1695	1.0642e+04	0.9850
3	865	2940	7.9724e+03	0.7492
4	1645	5850	4.8928e+03	0.6137
5	3127	10449	3.7023e+03	0.7567
6	5944	20133	2.5870e+03	0.6987
7	11296	36786	1.9644e+03	0.7593

Table IV.75: The convergence of one run of our algorithm for the considered problem.

We see the decrease of the estimator by the factor $1/\sqrt{2}$, which indicates the expected order $O(n_{dofs}^{-1/2})$.

All calculations in sections IV.3.6.1–IV.3.6.6 show a decrease of the error estimate, given in theorem III.24, of the expected order $O(n_{dofs}^{1/2})$. The most visible effect regarding the grid-refinement is, that in regions of cavitation (where ψ is constant) the grid is rather coarse (compare e. g. figure IV.136). The most refined regions are those where the variation of ψ is rather high. A comparison with the results of section IV.3.2 shows, that the regions of cavitation are detected correctly.

IV.3.7 Comparison of the Reynolds- and the SubStokes-Model for Cavitation

Analogue to section IV.3.3 we compare the cuts of the pressure profiles for the examples considered in sections IV.3.6.1–IV.3.6.6, that are drawn in figure IV.143.

The line of the cut is positioned at the maximum altitude of the hills for examples (IV.19) and (IV.20) (at $y = 0.375$) and in the middle of the domain ($y = 0.5$) for all other examples to circumvent boundary effects.
As in the noncavitational case we see, that in the examples with vertical velocity of the surface the Reynolds pressure (i. e. (IV.8), (IV.11), (IV.16) and (IV.19)) is equal or at least very closed to the SubStokes pressure.
In the remaining cases of horizontal velocities the Reynolds model again does not deliver optimal results in comparison to the SubStokes model. Never the less the projection seems to correct some of the deviation and the Reynolds pressure ψ^R is a better guess for ψ^s than in the non cavitational case.

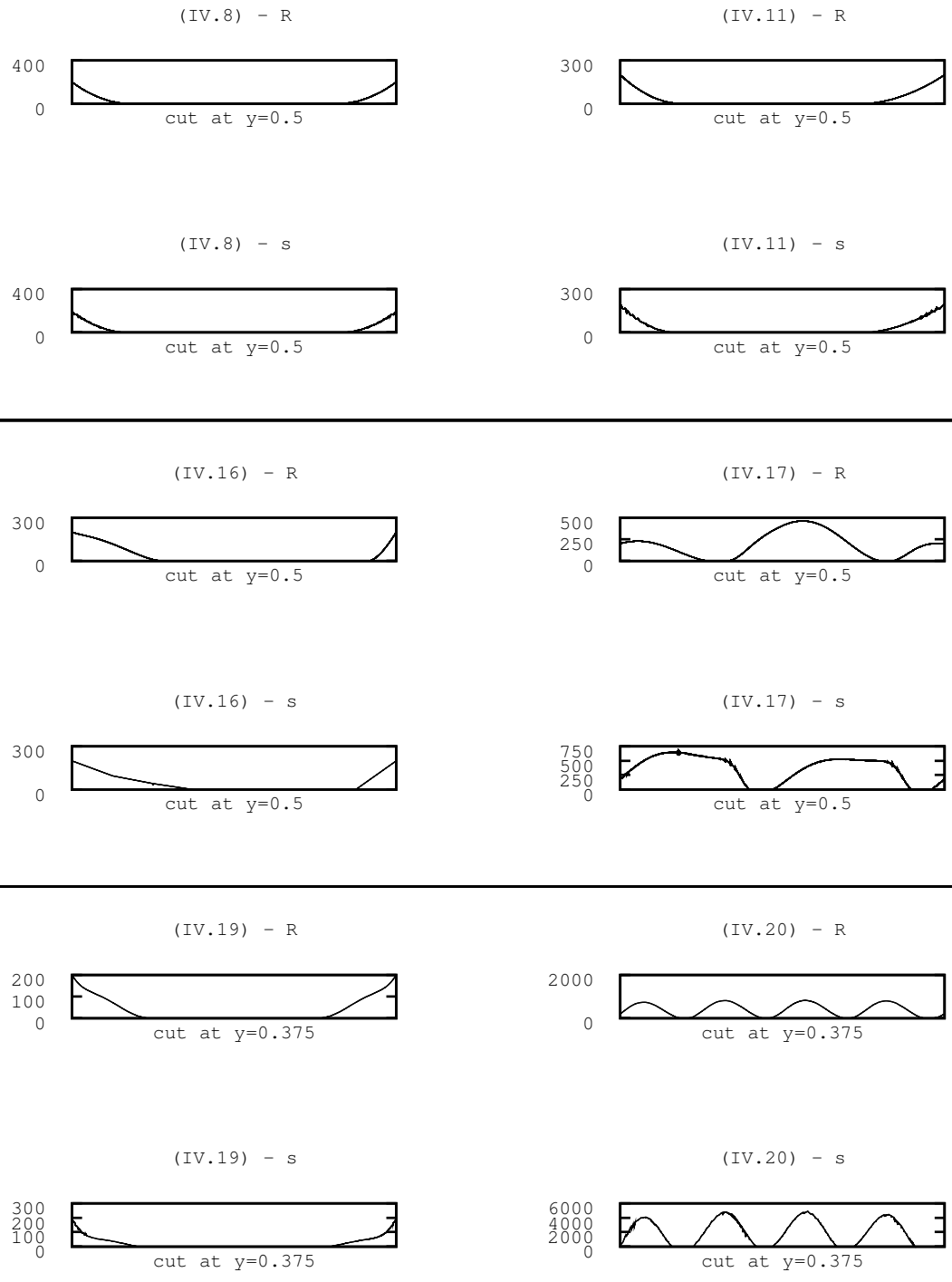

Figure IV.143: Comparison of the Reynolds– and the SubStokes–model: We see the cut of the pressures ψ^R (upper plot – R) and ψ^s (lower plot – s) for the different example applications (IV.7)–(IV.14).

Outlook

The thesis on hand considers the simulation of a steel forming process including the lubricant between tool and workpiece.
The steel sheet is simulated as elastic material. In Frohne [2011] this model is extended to consider plasticity and gives numerical results of an implementation for three-dimensional contact too.

Here the simulation of the contact problem and the fluid problem is discussed separately to allow the independend analysis of each part. Current work considers implementations of Fluid-Structure-Interaction, to cover the complete forming process by two interchanging processes. The first one simulates the plastic material. The second one simulates the fluid. Both exchange their results to each other in a quasi stationary loop and use the results of the other process as as boundary condition: The Fluid-Simulator gets the shape and velocity of the Structure-Simulator as boundary condition and to define the domain, while the Structure simulation uses the pressure, calculated by the Fluid-Simulator as external force.

An obvious improvement of the simulation of the lubricant is the computation of the full three-dimensional Stokes model, such that we use the three models – Stokes, SubStokes and Reynolds – simultanuously in an adaptive process. Therefor the model estimate between Stokes and SubStokes-model has to be improved. Furthermore computational resources have to be aquired.
In future the internal cg-solver in the Uzawa-algorithm for the Stokes-Solver can be replaced by a direct solver, to avoid instabilities. With the problem of cavitation in sight, it is crucial for this replacement, that the new solver should implement a projection, as the projected cg-method does.

Future work will be done to achieve a more accurate estimate of the modelling error between the SubStokes model and the Reynolds model. The estimate given in theorem III.6 only depends on the fluid film's geometry and might be improved by the use of the given boundary condition for the velocity-field and the calculated approximation of the velocity- and pressure-fields themselves.
To validate these estimates and to optimize model adaptive fluid simulations some computational effort is necessary.

Appendix A

Results of Taylor approximation

In this section we scatch some general results for the approximation of one-dimensional functions and their error-estimates.

We consider the function

$$f : I := [z_0; z_1] \to \mathbb{R} \tag{A.1}$$

to have a continuous third derivative.

The Taylor-formula up to the second order for f around the point $z \in I$ yields

$$\begin{aligned} f(z_1) =& f(z) + (z_1 - z)\partial_z f(z) + \frac{1}{2}(z_1 - z)^2 \partial_z \partial_z f(r) \\ f(z_0) =& f(z) - (z - z_0)\partial_z f(z) + \frac{1}{2}(z - z_0)^2 \partial_z \partial_z f(s) \end{aligned} \tag{A.2}$$

with sufficiant values r, s with $z_0 \leq s \leq z \leq r \leq z_1$. By an appropriate linear combination of these two equations we eliminate the terms containing $\partial_z f(z)$:

$$\begin{aligned} (z - z_0)f(z_1) + (z_1 - z)f(z_0) =& (z_1 - z_0)f(z) + \\ &+ \frac{1}{2}(z_1 - z)(z - z_0)\Big((z_1 - z)\partial_z^2 f(r) + (z - z_0)\partial_z^2 f(s)\Big) \end{aligned}$$

With the abbreviations

$$\begin{aligned} g =& z_1 - z_0; & \overline{z} =& \frac{1}{2}(z_0 + z_1) \\ \delta f =& f(z_1) - f(z_0); & \overline{f} =& \frac{1}{2}(f(z_1) + f(z_0)) \end{aligned}$$

this yields

$$\begin{aligned} f(z) =& \frac{z\delta f + z_1 f(z_0) - z_0 f(z_1)}{g} - \frac{1}{2g}(z_1 - z)(z - z_0)\Big((z_1 - z)\partial_z^2 f(r) + (z - z_0)\partial_z^2 f(s)\Big) \\ =& \frac{z\delta f - \overline{z}\delta f + g\overline{f}}{g} - \frac{(z_1 - z)(z - z_0)}{2g}\Big((z_1 - z)\partial_z^2 f(r) + (z - z_0)\partial_z^2 f(s)\Big). \end{aligned} \tag{A.3}$$

To achieve a quadrature-formula we integrate this equation:

$$\begin{aligned}\int_I f(z)dz =& \frac{(z_1^2 - z_0^2)\delta f}{2g} - \overline{z}\delta f + g\overline{f} + \\ & - \frac{1}{2g}\int_I \Big((z_1 - z)^2(z - z_0)\partial_z^2 f(r(z)) + (z_1 - z)(z - z_0)^2\partial_z^2 f(s(z)) \Big) dz.\end{aligned}$$

To evaluate the remaining integral we employ the mean value theorem for the first summand

$$\frac{1}{2g}\int_{z_0}^{z_1}(z_1 - z)^2(z - z_0)\partial_z^2 f(r(z))dz = \frac{1}{2g}\partial_z^2 f(\overline{r})\int_{z_0}^{z_1}(z_1 - z)^2(z - z_0)dz = \frac{g^3}{24}\partial_z^2 f(\overline{r})$$

with $z_0 \le \overline{r} \le z_1$ and analogue for the second summand and yield

$$\begin{aligned}\int_I f(z)dz =& \frac{g\overline{z}\delta f}{g} - \overline{z}\delta f + g\overline{f} - \frac{g^3}{24}\Big(\partial_z^2 f(\overline{r}) + \partial_z^2 f(\overline{s})\Big) \\ =& g\overline{f} - \frac{g^3}{12}\partial_z^2 f(\overline{\zeta}) \qquad (A.4)\end{aligned}$$

with $z_0 \le \overline{\zeta} \le z_1$ according to the mean value theorem for the continuous function $\partial_z^2 f(z)$. With (A.4) we finally reached the **trapezoidal quadrature rule**.

If we combine equations (A.2), to eliminate the terms involving $f(z)$ we gain

$$\partial_z f(z) = \frac{f(z_1) - f(z_0)}{z_1 - z_0} + \frac{1}{2(z_1 - z_0)}\left((z - z_0)^2\partial_z^2 f(s) - (z_1 - z)^2\partial_z^2 f(r)\right). \qquad (A.5)$$

To gain a higher order quadrature formula, we can extend (A.4) to (we use the abbreviations $\overline{z} = \frac{1}{2}(z_0 + z_1)$ and $g = z_1 - z_0$)

$$\begin{aligned}& f(z) = f(\overline{z}) + \partial_z f(\overline{z})(z - \overline{z}) + \frac{1}{2}\partial_z^2 f(\overline{z})(z - \overline{z})^2 + \frac{1}{6}\partial_z^3(\zeta_z)(z - \overline{z})^3 \\ \Rightarrow \quad & \int_{z_0}^{z_1} f(z)dz = gf(\overline{z}) + \frac{1}{2}\partial_z^2 f(\overline{z})\frac{2g^3}{3\cdot 8} + g^4 O(\left\|\partial_z^3 f\right\|_\infty) \\ & = gf(\overline{z}) + \frac{g^3}{24}\partial_z^2 f(\overline{z}) + g^4 O(\left\|\partial_z^3 f\right\|_\infty) \\ & = g\overline{f} - \frac{g^3}{8}\partial_z^2 f(\overline{z}) + g^4 O(\left\|\partial_z^3 f\right\|_\infty) + \frac{g^3}{24}\partial_z^2 f(\overline{z}) \\ & = g\overline{f} - \frac{g^3}{12}\partial_z^2 f(\overline{z}) + g^4 O(\left\|\partial_z^3 f\right\|_\infty) \qquad (A.6)\end{aligned}$$

A.1 Interpolation error

This section collects a view results of interpolation of function spaces $V(\Omega)$ by polynomial functions. These are essentially need, for error estimates of finite element approximation in section III.2.

Definition A.1 (Interpolant)
Let $V_h \subset V$ be a (finite-dimensional) subspace of the Hilbert-space V.
For any function $\varphi \in V$ we call $I_h\varphi \in V_h$ interpolant of φ, if

$$\|\varphi - I_h\varphi\| = \inf_{\chi \in V} \|\varphi - \chi\| .$$

Theorem A.2
If V_h is complete, for any $\varphi \in V$, $I_h\varphi$ exists and is unique.

Proof. Because $V_h \subset V$ is a subspace, it is convex, hence the projection of any element $\varphi \in V$ on V_h exists and is unique (theorem II.11). But definition A.1 is equivalent to that of the projection II.10. □

Theorem A.3
Let $Q^m(\Omega) \subset H^1(\Omega)$ $(m = 0, 1, 2, \ldots)$ be the space of polynomial functions on a triangulation $\mathbb{T}$ of Ω into quadrilaterals Q (hexaeders in $\mathbb{R}^3$ respective) with diameter h_Q. And $\varphi \in H^{m+1}(\Omega)$ with $\|\varphi\|_{H^2} < \infty$ there hold

$$\begin{aligned} \|\varphi - I_h\varphi\|^2_{L^2(\Omega)} \leq & C \sum_{Q \in \mathbb{T}} |Q| \left(h_Q^{m+1} \, |\varphi|_{H^{m+1,\infty}(Q)} \right)^2 \\ |\varphi - I_h\varphi|^2_{H^1(\Omega)} \leq & C \sum_{Q \in \mathbb{T}} |Q| \left(h_Q^{m} \, |\varphi|_{H^{m+1,\infty}(Q)} \right)^2 . \end{aligned}$$

Proof. At first we examine the situation on one quadrilateral $Q \in \mathbb{T}$. Let $\pi \in Q^m(Q)$ be the Taylor-polynom with respect to one vertex p_Q of Q up to the order of m.

Then for $x \in Q$ we have the Taylor-error

$$\begin{aligned}
|\varphi(x) - \pi(x)| &= \left| \frac{1}{(m+1)!} \sum_{k \in \mathbb{N}^d, |k|=m+1} \partial_k \varphi(\xi)(x-p_Q)_1^{k_1} \dots (x-p_Q)_d^{k_d} \right| \\
&\leq \frac{1}{(m+1)!} \sum_k |\partial_k \varphi(\xi)| (x-p_Q)_1|^{k_1} \dots |(x-p_Q)_d|^{k_d} \\
&\leq \frac{h_Q^{m+1}}{(m+1)!} \sum_k |\partial_k \varphi(\xi)| \\
\Rightarrow \qquad |\varphi(x) - \pi(x)|^2 &\leq \frac{h_Q^{2(m+1)}}{((m+1)!)^2} \left(\sum_k |\partial_k \varphi(\xi)| \right)^2 \\
&\leq \frac{2^{d^{m+1}-1}}{((m+1)!)^2} h_Q^{2(m+1)} \sum_k |\partial_k \varphi(\xi)|^2 \\
&\leq \frac{2^{d^{m+1}}}{2((m+1)!)^2} h_Q^{2(m+1)} \cdot d^{m+1} |\varphi|^2_{H^{m+1,\infty}(Q)} \\
\Rightarrow \qquad \|\varphi - \pi\|^2_{L^2(Q)} &\leq C \cdot |Q| \cdot h_Q^{2(m+1)} |\varphi|^2_{H^{m+1,\infty}(Q)}
\end{aligned}$$

Summation over all $Q \in \mathbb{T}$ yields the first estimate.
The analogue calculation for the derivative $\partial_i \varphi$ yields the second estimate. □

With the same techniques as in the proof for theroem A.3 one can proove:

Corollary A.4
Let there hold the same assumptions as in theorem A.3 for $m = 1$. Then we can conclude the following cell-wise estimates:

$$\begin{aligned}
\|v - I_h v\|_{L_2(Q)} &\leq c_i h_Q |v|_{H^1(Q)} \\
|v - I_h v|_{H^1(Q)} &\leq c_i |v|_{H^1(Q)} \\
\|v - I_h v\|_{L^2(\partial Q)} &\leq c_i h_Q^{1/2} |v|_{H^1(Q)} .
\end{aligned} \tag{A.7}$$

Bibliography

W. Bangerth and G. Kanschat. `deal.II` *Differential Equations Analysis Library, Technical Reference*, 2005. URL `http://www.dealii.org`. `http://www.dealii.org`.

W. Bangerth, R. Hartmann, and G. Kanschat. deal.II – a general purpose object oriented finite element library. *ACM Trans. Math. Softw.*, 33(4):24/1–24/27, 2007.

R. Becker. *An Adaptive Finite Element Method for the Incompressible Navier-Stokes Equations on Time-dependent Domains*. PhD thesis, Universität Heidelberg, 1995.

H. Blum, D. Braess, and F.-T. Suttmeier. A cascadic multigrid algorithm for variational inequalities. *Computing and Visualization in Science*, 7:153–157, 2004.

P. Bochew and M. Gunzburger. Least-squares finite element methods. 2006.

M. Braack. *An Adaptive Finite Element Method for Reactive-Flow Problems*. PhD thesis, Universität Heidelberg, 1998.

M. Braack and A. Ern. A posteriori control of modeling errors and discretization errors. *Multiscale Model. Simul.*, 1:221–238, 2003.

D. Braess. *Finite Elemente: Theorie, schnelle Löser und Anwendungen in der Elastizitätstheorie*. Springer, Berlin [u.a.], 1997.

J. H. Bramble and J. E. Pasciak. A preconditioning technique for indefinite systems resulting from mixed approximations of elliptic problems. *Math. Comp.*, 50:1–17, 1988.

S. Brandt and H. D. Dahmen. *Mechanik: eine Einführung in Experiment und Theorie*. Springer, Berlin [u.a.], 1996.

H. Brezis. *Functional Analysis, Sobolev Spaces and Partial Differential Equations*. Springer, Berlin, 2010.

Z. Chen and R. H. Nochetto. Residual type a posteriori error estimates for elliptic obstacle problems. *Numer. Math*, 84:527–548, 2000.

P. G. Ciarlet. *Lectures on the finite element method*. Tata Institute of Fundamental Research, 1975.

P. G. Ciarlet. *The Finite Element Method for elliptic problems*. Studies in mathematics and its applications. North-Holland, Amsterdam, 1978.

M. L. Denis Laxalde. Nonlinear modal analysis of mechanical systems with frictionless contact interfaces. *Comput. Mech*, 47:469–478, 2011.

M. Dobrowolski. *Angewandte Funktionalanalysis: Funktionalanalysis, Sobolev-Räume und elliptische Differentialgleichungen*. Springer, Berlin [u.a.], 2006.

E. Domke. *Vektoranalysis: Einführung für Ingenieure und Naturwissenschaftler*. BI-Wiss.-Verl., Mannheim [u.a.], 1990.

T. Dupont and R. Scott. Polynomial approximation of functions in sobolev spaces. *Mathematics of Computation*, 34(150):441–463, 1980.

T. Fließbach. *Mechanik*. Spektrum Lehrbuch. Spektrum Akad. Verl., Heidelberg [u.a.], 4. aufl. edition, 2003.

J. Frohne. *FEM-Simulation der Umformtechnik metallischer Oberflächen im Mikrokosmos*. PhD thesis, Universität Siegen, 2011.

F. Gimbel, P. Hansbo, and F.-T. Suttmeier. An adaptive low-order fe-scheme for stokes flow with cavitation. *Journal of Numerical Mathematics*, 18/3:177–185, 2010.

V. Girault and P.-A. Raviart. *Finite element approximation of the Navier-Stokes equations*, volume 749. Springer, 1979. ISBN 3-540-09557-8.

V. Girault and P.-A. Raviart. *Finite element methods for Navier-Stokes equations: theory and algorithms*. Springer, 1986.

R. Glowinski. *Numerical methods for nonlinear variational problems*. (Springer series in computational physics). Springer, New York, Berlin, Heidelberg [usw.], 1984.

R. Glowinski, J. L. Lions, and R. Trémolières. *Numerical analysis of variational inequalities*. (Studies in mathematics and its applications. North-Holland Publ. Co., Amsterdam [u.a.], 1981.

P. M. Gresho and R. L. Sani. On pressure boundary conditions for the incompressible navier-stokes equations. *International Journal for numerical Methods in Fluids*, 7: 1111–1145, 1987.

C. Großmann and H.-G. Roos. *Numerik partieller Differentialgleichungen*. Teubner-Studienbücher: Mathematik. Teubner, Stuttgart, 1992.

P. Hansbo and B. Nielsson. Weak coupling of a reynolds model and a stokes model for hydrodynamic lubrication. *Int. J. Numer. Meth. Fluids*, 66, 2010.

K. H. Huebner. *The Finite Element Method for Engineers*. John Wiley & Sons, New York, 1975.

T. J. Hughes, L. P. Franca, and M. Balestra. A new finite element formulation for computational fluid dynamics: V. circumventing the babuÅąka-brezzi condition: a stable petrov-galerkin formulation of the stokes problem accommodating equal-order interpolations. *Computer Methods in Applied Mechanics and Engineering*, 59(1):85 – 99, 1986.

C. Johnson. *Numerical solution of partial differential equations by the finite element method*. Cambridge Univ. Pr., Cambridge [u.a.], 1987.

S. D. Kim. Uzawa algorithms for coupled stokes equations from the optimal control problem. *Calcolo*, 46, 2009.

D. Kinderlehrer and G. Stampacchia. *An introduction to variational inequalities and their applications*. Acad. Press, New York [u.a.], 1980.

R. Krahl and E. Bänsch. Computational comparison between the taylor-hood and the conforming crouzeix-raviart element, 2005.

E. Kreyszig. *Introductory Functional Analysis with Applications*. John Wiley & Sons, New York, 1978.

W. Lin and D. B. Bogy. A generalized compressible reynolds lubrication equation with bounded contact pressure. *Physics of Fluids*, 13, 2001.

B. Nilsson and P. Hansbo. Adaptive finite element methods for hydrodynamic lubrication with cavitation. *International journal for numerical methods in engineering*, 72(13): 1584–1604, 2007. ISSN 00295981. URL `http://dx.doi.org/10.1002/nm3.2051`.

B. Nilsson and P. Hansbo. A stokes model with cavitation for the numerical simulation of hydrodynamic lubrication. *preprint*, 2008. ISSN 16529715.

R. H. Nochetto, K. G. Siebert, and A. Veeser. Pointwise a posteriori error control for elliptic obstacle problems. *Numerische Mathematik*, 95:163–195, 2003.

R. H. Nochetto, K. G. Siebert, and A. Veeser. Fully localized a posteriori error estimators and barrier sets for contact problems. *SIAM Journal on numerical analysis*, 42:2118–2135, 2005.

J. T. Oden, S. Prudhomme, D. C. Hammerand, and M. W. Kuczma. Modeling error and adaptivity in nonlinear continuum mechanics. *Comput. Methods Appl. Mech. Engrg.*, 190:6663–6684, 2001.

R. Plato. *Numerische Mathematik kompakt: Grundlagenwissen für Studium und Praxis*. Vieweg, Wiesbaden, 2., überarb. aufl. edition, 2004.

J. Qin and S. Zhang. Stability and approximability of the p1-p0 element for stokes equations. *International Journal for Numerical Methods in Fluids*, 54(5):497–515, 2007.

F. Sahlin. *Hydrodynamic Lubrication of Rough Surfaces*. PhD thesis, Luleå University of Technology, 2005.

L. San Andrés. Modern lubrication theory, lecture notes, 2009. URL {\url{http://rotorlab.tamu.edu/me626/}}.

H. R. Schwarz. *Methode der finiten Elemente: Eine Einführung unter besonderer Berücksichtigung der Rechenpraxis*. Teubner, Stuttgart, 1984.

B. K. Shivamoggi. *Theoretical fluid dynamics*. Nijhoff, Dordrecht, 1985. ISBN 90-247-2999-8.

J. H. Spurk. *Strömungslehre: Einführung in die Theorie der Strömungen*. Springer, Berlin [u.a.], 1989.

O. Steinbach. *Numerische Näherungsverfahren für elliptische Randwertprobleme*. Teubner, Stuttgart [u. a.], 2003.

H. Stephani and G. Kluge. *Theoretische Mechanik: Punkt- und Kontinuumsmechanik*. Spektrum-Lehrbuch. Spektrum, Heidelberg [u.a.], 1995.

F. Stummel and K. Hainer. *Praktische Mathematik*. Teubner, Stuttgart, 1971.

F.-T. Suttmeier. Adaptive computational methods for variational inequalities based on mixed formulations. *International Journal for Numerical Methods in Engineering*, 68 (11), 2006.

F.-T. Suttmeier. *Numerical solution of variational inequalities by adaptive finite elements*. Vieweg + Teubner, Wiesbaden, 2008.

R. Temam. *Navier-Stokes equations*. North-Holland, 1985.

H. Wobker and S. Turek. Numerical studies of Vanka–type smoothers in computational solid mechanics. *Advances in Applied Mathematics and Mechanics*, 1(1):29–55, 2009.

P. Wriggers. *Computational contact mechanics*. CISM courses and lectures. Springer, Wien [u.a.], 2008.

O. C. Zienkiewicz and J. Z. Zhu. A simple error estimator and adaptive procedure for practical engineering analysis. *International Journal for Numerical Methods in Engineering*, 24:337–357, 1987.

Q. Zou, A. Veeser, R. Kornhuber, and C. Gräser. Hierarchical error estimates for the energy functional in obstacle problems. *Numerische Mathematik*, 117, 2011.